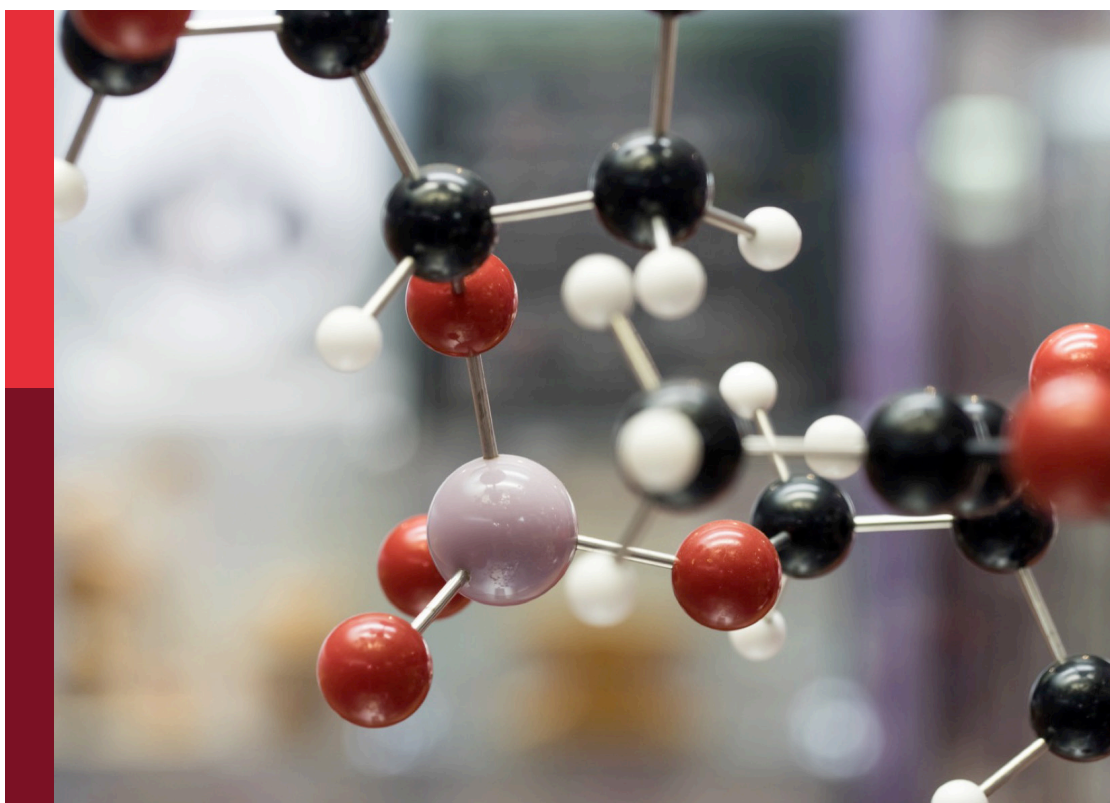


Frontiers in Chemistry: 10 years anniversary

Edited by
Steve Suib

Published in
Frontiers in Chemistry



FRONTIERS EBOOK COPYRIGHT STATEMENT

The copyright in the text of individual articles in this ebook is the property of their respective authors or their respective institutions or funders. The copyright in graphics and images within each article may be subject to copyright of other parties. In both cases this is subject to a license granted to Frontiers.

The compilation of articles constituting this ebook is the property of Frontiers.

Each article within this ebook, and the ebook itself, are published under the most recent version of the Creative Commons CC-BY licence. The version current at the date of publication of this ebook is CC-BY 4.0. If the CC-BY licence is updated, the licence granted by Frontiers is automatically updated to the new version.

When exercising any right under the CC-BY licence, Frontiers must be attributed as the original publisher of the article or ebook, as applicable.

Authors have the responsibility of ensuring that any graphics or other materials which are the property of others may be included in the CC-BY licence, but this should be checked before relying on the CC-BY licence to reproduce those materials. Any copyright notices relating to those materials must be complied with.

Copyright and source acknowledgement notices may not be removed and must be displayed in any copy, derivative work or partial copy which includes the elements in question.

All copyright, and all rights therein, are protected by national and international copyright laws. The above represents a summary only. For further information please read Frontiers' Conditions for Website Use and Copyright Statement, and the applicable CC-BY licence.

ISSN 1664-8714
ISBN 978-2-8325-6076-1
DOI 10.3389/978-2-8325-6076-1

About Frontiers

Frontiers is more than just an open access publisher of scholarly articles: it is a pioneering approach to the world of academia, radically improving the way scholarly research is managed. The grand vision of Frontiers is a world where all people have an equal opportunity to seek, share and generate knowledge. Frontiers provides immediate and permanent online open access to all its publications, but this alone is not enough to realize our grand goals.

Frontiers journal series

The Frontiers journal series is a multi-tier and interdisciplinary set of open-access, online journals, promising a paradigm shift from the current review, selection and dissemination processes in academic publishing. All Frontiers journals are driven by researchers for researchers; therefore, they constitute a service to the scholarly community. At the same time, the *Frontiers journal series* operates on a revolutionary invention, the tiered publishing system, initially addressing specific communities of scholars, and gradually climbing up to broader public understanding, thus serving the interests of the lay society, too.

Dedication to quality

Each Frontiers article is a landmark of the highest quality, thanks to genuinely collaborative interactions between authors and review editors, who include some of the world's best academicians. Research must be certified by peers before entering a stream of knowledge that may eventually reach the public - and shape society; therefore, Frontiers only applies the most rigorous and unbiased reviews. Frontiers revolutionizes research publishing by freely delivering the most outstanding research, evaluated with no bias from both the academic and social point of view. By applying the most advanced information technologies, Frontiers is catapulting scholarly publishing into a new generation.

What are Frontiers Research Topics?

Frontiers Research Topics are very popular trademarks of the *Frontiers journals series*: they are collections of at least ten articles, all centered on a particular subject. With their unique mix of varied contributions from Original Research to Review Articles, Frontiers Research Topics unify the most influential researchers, the latest key findings and historical advances in a hot research area.

Find out more on how to host your own Frontiers Research Topic or contribute to one as an author by contacting the Frontiers editorial office: frontiersin.org/about/contact

Frontiers in Chemistry: 10 years anniversary

Topic editor

Steve Suib — University of Connecticut, United States

Citation

Suib, S., ed. (2025). *Frontiers in Chemistry: 10 years anniversary*.
Lausanne: Frontiers Media SA. doi: 10.3389/978-2-8325-6076-1

Table of contents

- 05 **Editorial: Frontiers in Chemistry: 10 years anniversary**
Steven L. Suib
- 08 **Big peptide drugs in a small molecule world**
Laszlo Otvos Jr. and John D. Wade
- 18 **A novel optimal formula of nickel extraction: arsenic removal from niccolite by controlling arsenic-containing phases**
Xiaowei Tang and Yuehui He
- 30 **Catalytic divergencies in the mechanism of L-arginine hydroxylating nonheme iron enzymes**
Hafiz Saqib Ali and Sam P. de Visser
- 44 **A minireview on covalent organic frameworks as stationary phases in chromatography**
Raquel Gavara, Sergio Royuela and Félix Zamora
- 55 **Luminescent Ln^{3+} -based silsesquioxanes with a β -diketonate antenna ligand: toward the design of efficient temperature sensors**
Gautier Félix, Alena N. Kulakova, Saad Sene, Victor N. Khrustalev, Miguel A. Hernández-Rodríguez, Elena S. Shubina, Tristan Pelluau, Luís D. Carlos, Yannick Guari, Albano N. Carneiro Neto, Alexey N. Bilyachenko and Joulia Larionova
- 69 **Fragment-based drug discovery for disorders of the central nervous system: designing better drugs piece by piece**
Bill W. G. L. Chan, Nicholas B. Lynch, Wendy Tran, Jack M. Joyce, G. Paul Savage, Wim Meutermans, Andrew P. Montgomery and Michael Kassiou
- 90 **Recent advances in catalytic asymmetric synthesis**
Ashna Garg, Dominick Rendina, Hersh Bendale, Takahiko Akiyama and Iwao Ojima
- 118 **A review on transition metal oxides in catalysis**
Sanjubala Sahoo, Kaveendra Y. Wickramathilaka, Elsa Njeri, Dilshan Silva and Steven L. Suib
- 132 **Unveiling the chemical kinetics of aminomethanol ($\text{NH}_2\text{CH}_2\text{OH}$): insights into O.H and O_2 photo-oxidation reactions and formamide dominance**
Naga Venkateswara Rao Nulakani and Mohamad Akbar Ali
- 149 **New synthesis of oligosaccharides modelling the M epitope of the *Brucella* O-polysaccharide**
Yury E. Tsvetkov, Timur M. Volkov, Sergei A. Eremin, Oleg D. Sklyarov, Yuri K. Kulakov, Vadim B. Krylov and Nikolay E. Nifantiev

- 163 **Toward the identification of cyano-astroCOMs via vibrational features: benzonitrile as a test case**
Yanting Xu and Malgorzata Biczysko
- 176 ***In-situ* FTIR spectroscopy of epoxy resin degradation: kinetics and mechanisms**
Marianna Pannico, Giuseppe Mensitieri and Pellegrino Musto



OPEN ACCESS

EDITED AND REVIEWED BY

Serge Cosnier,
UMR5250 Département de Chimie Moléculaire
(DCM), France

*CORRESPONDENCE

Steven L. Suib,
✉ steven.suib@uconn.edu

RECEIVED 06 February 2025

ACCEPTED 13 February 2025

PUBLISHED 20 February 2025

CITATION

Suib SL (2025) Editorial: Frontiers in Chemistry:
10 years anniversary.
Front. Chem. 13:1572259.
doi: 10.3389/fchem.2025.1572259

COPYRIGHT

© 2025 Suib. This is an open-access article distributed under the terms of the [Creative Commons Attribution License \(CC BY\)](#). The use, distribution or reproduction in other forums is permitted, provided the original author(s) and the copyright owner(s) are credited and that the original publication in this journal is cited, in accordance with accepted academic practice. No use, distribution or reproduction is permitted which does not comply with these terms.

Editorial: Frontiers in Chemistry: 10 years anniversary

Steven L. Suib*

Department of Chemistry, University of Connecticut, Storrs, CT, United States

KEYWORDS

chemistry, research, anniversary, 10th year, review

Editorial on the Research Topic

Frontiers in Chemistry: 10 years anniversary

We are thrilled to celebrate a significant milestone for *Frontiers in Chemistry*—our 10-year anniversary! To commemorate this remarkable occasion, we have meticulously curated an extraordinary anniversary collection, featuring a series of groundbreaking papers, including insightful contributions from our esteemed Specialty Chief Editors. These works illuminate the cutting-edge frontiers and diverse domains of modern chemistry. With this Anniversary Research Topic, our aim is to present both new research and reviews of the most exciting areas of current chemical research.

[Pannico et al.](#) have studied the thermal oxidation of flexible epoxy resins using *in situ* FTIR. We report on an *in situ* FTIR study of the thermo-oxidative degradation of a flexible epoxy resin. A unique feature was the normal coordinate analysis used to help interpret the vibrational data. The structure of such resins is a network as determined by using two-dimensional correlation spectroscopy. This paper is an excellent combination of spectroscopy, modeling, kinetics, and synthesis.

A team led by [Félix et al.](#) has also focused on excellent characterization of luminescent cage-like tetranuclear silsesquioxanes. Synthesis, X-ray diffraction, magnetism, and luminescence studies of single crystals were done. Such systems are a series of seven-coordinate lanthanides that have a one-capped trigonal prismatic structure. Luminescence was sensitized by acetylacetonate ligands when excitation was in the UV and visible spectral regions. Computational modeling of intramolecular energy transfer and multiphonon rates was used to study thermal interactions in mixed lanthanide ions. Such research has led to the development of luminescent thermometers. These optical sensing materials may lead to numerous other applications.

[Xu and Biczysko](#) have used vibrational spectroscopy with the James Webb Space Telescope to investigate molecules in interstellar space. This truly unique work focused on cyano-based derivatives of aromatics. A key molecule that was identified was benzonitrile. This molecule was used as a model via computational modeling to try to observe similar but heretofore unknown molecules. Anharmonic simulations of infrared data were compared to experimental Fourier transform infrared data. Their calculations provided excellent match to experimental data, suggesting that this methodology could provide reliable predictions of vibrational data for a large variety of cyano-based interstellar species.

[Gavara et al.](#) have reviewed the use of Covalent organic frameworks (COFs) as chromatographic solid stationary phases. They suggest that COFs have various structural motifs with different chemical and physical properties that allow these separations. In their review, the types of ideas that have been used to lead to

chromatographic applications primarily as stationary phases. They have also suggested that this research is novel, still in development, and may lead to other types of chromatographic applications to solve different analytical problems.

The above characterization studies provide a wealth of information regarding the use of characterization methods to study a wide variety of materials for a diverse set of applications. Indeed, the development of new and modified methods both *ex situ* and *in situ* are the focus of many research groups around the world. New instrumentation, new sample holders, combined methods, and studies of unique systems have all revolutionized the field of chemistry.

Another area of recent and continuing interest is catalysis. Garg et al.'s group has emphasized and reviewed the significance of asymmetric catalysis for efficient synthesis of enantiopure chiral systems. Transition metals are key to transformations with chiral ligands that are important in this type of catalysis. Phosphines and carbenes are types of species used to form chiral C-x and C-C bonds. This leads to specific control of stereochemistry. Photocatalytic, electrocatalytic, and biocatalytic systems have been covered in this review. Sustainability, atom-efficiency, environmentally friendly, and versatility properties are all important in this area of research. Enantioselective organocatalytic reactions have also been covered. The novelty of flow methods in asymmetric catalysis was mentioned as transformative. Hybrid approaches with different strategies that are synergistic have been incorporated to attack challenging problems.

Ali and Visser have contributed a paper on catalytic divergencies in the mechanism of L-arginine hydroxylating nonheme iron enzymes. Such enzymes can be important in the biosynthesis of natural products. Their focus has been on mechanistic studies of L-Arg-activating nonheme iron dioxxygenases. As with many of the above papers in this anniversary Research Topic, computational modeling, molecular dynamics, and quantum mechanical methods have been used to predict a variety of properties such as electrostatics and electronics. These studies suggest that changes in electric fields and electric dipole moments can strengthen or weaken C-H bonds. This can lead to unique reactivity of such enzymes and their novel reaction pathways.

Tsvetkov et al. have studied Brucellosis which is a dangerous disease caused by bacteria. This work aimed at new methods for diagnosing brucellosis. Specific methodologies were summarized and the authors pointed out that false positives are observed. Synthetic oligosaccharides can improve the reliability of these tests. This epitope is characterized by an α -(1→3)-linkage between d-perosamine units and is unique to *Brucella*. They developed a set of four protected oligosaccharides of two trisaccharides and a tetrasaccharide to improve diagnostic reliability. They plan to extend such an approach to both animals and humans, and to developing potential vaccines.

The work of Chan et al. concerns fragment-based drug discovery for treating central nervous system disorders. This approach uses screening of libraries of thousands of small molecular fragments. This approach allows a more strategic starting point than typical high throughput screening methods. Advantages of using such fragments include compactness, good binding affinities, important in drug candidate development. This method can allow for precise modifications to improve activity and

pharmacokinetics. There has been commercial success of this methodology and has promise for fast drug discovery and development. This review suggests how this approach can be integrated into drug discovery.

Otvos and Wade have reviewed big peptide drugs. Designer peptide drugs developed by biotechnology companies are injectable and have been useful for orphan and small volume diseases like type 2 diabetes. Successful oral doses have been used for chronic constipation. Careful choices of targets, modification of intrachain and terminal amino acids, correct conjugation for stabilizing enhancers, unique delivery methods, and marketing strategies focused on patients have been successfully used to create useful treatments. Improvement in peptide drug modification and formulation has led to significant growth and acceptance of designer peptide drugs as desirable alternatives to small molecule compounds.

Nulakani and Ali have studied the chemical kinetics of aminomethanol ($\text{NH}_2\text{CH}_2\text{OH}$) systems for insight into O.H and O_2 photo-oxidation reactions. Aminomethanol has been released into the atmosphere via burning of biomass and from other pathways. The chemical kinetics of aminomethanol in relation to hydroxyl radicals have been investigated using a variety of computational modeling methods and studies. Computational modeling as a sole source of analysis as well as in conjunction with experimental methods has been another theme that links many of the papers in this Anniversary Research Topic. Activation energies for these reactions, rate constants, and branching paths of radical species were pursued. They also studied detrimental effects of formamide. Formamide can react with hydroxyl radicals to form toxic materials like HNCO.

Another original article by Tang and He concerns ways to remove arsenic from nickel-based systems. Thermodynamic calculations and studies of roasting and reduction methods were described. Roasting under oxidizing conditions was not productive. However, sulfur was used as a reducing agent and this reacted with arsenic to form arsenic sulfide, which is volatile and can be removed. Use of FeS under oxidizing conditions was not as promising due to reactions of nickel with arsenic at high temperatures. On the other hand, use of FeS under reducing conditions appears to be the best method that was studied here for removal of arsenic.

The above articles are excellent reviews and original research that highlight many of the current and new directions being used in the field of chemistry. Some unique underlying themes include advanced characterization, new synthetic strategies, and the use of computational modeling to understand all these types of systems described above.

Author contributions

SS: Conceptualization, Formal Analysis, Writing—original draft, Writing—review and editing.

Funding

The author(s) declare that no financial support was received for the research, authorship, and/or publication of this article.

Conflict of interest

The author declares that the research was conducted in the absence of any commercial or financial relationships that could be construed as a potential conflict of interest.

Generative AI statement

The author(s) declare that no Generative AI was used in the creation of this manuscript.

Publisher's note

All claims expressed in this article are solely those of the authors and do not necessarily represent those of their affiliated organizations, or those of the publisher, the editors and the reviewers. Any product that may be evaluated in this article, or claim that may be made by its manufacturer, is not guaranteed or endorsed by the publisher.



OPEN ACCESS

EDITED BY

Steve Suib,
University of Connecticut, United States

REVIEWED BY

Weijun Shen,
The Scripps Research Institute,
United States
Daniel Conole,
The University of Auckland, New Zealand
Nitin Aniruddha Patil,
Monash University, Australia

*CORRESPONDENCE

Laszlo Otvos Jr.,
✉ lotvos@comcast.net
John D. Wade,
✉ john.wade@florey.edu.au

RECEIVED 26 September 2023

ACCEPTED 24 November 2023

PUBLISHED 07 December 2023

CITATION

Otvos L Jr. and Wade JD (2023), Big
peptide drugs in a small molecule world.
Front. Chem. 11:1302169.
doi: 10.3389/fchem.2023.1302169

COPYRIGHT

© 2023 Otvos and Wade. This is an open-access article distributed under the terms of the [Creative Commons Attribution License \(CC BY\)](#). The use, distribution or reproduction in other forums is permitted, provided the original author(s) and the copyright owner(s) are credited and that the original publication in this journal is cited, in accordance with accepted academic practice. No use, distribution or reproduction is permitted which does not comply with these terms.

Big peptide drugs in a small molecule world

Laszlo Otvos Jr.^{1,2*} and John D. Wade^{3,4*}

¹Institute of Medical Microbiology, Semmelweis University, Budapest, Hungary, ²OLPE Pharmaceutical Consultants, Audubon, PA, United States, ³Florey Institute of Neuroscience and Mental Health, Parkville, VIC, Australia, ⁴School of Chemistry, University of Melbourne, Parkville, VIC, Australia

A quarter of a century ago, designer peptide drugs finally broke through the glass ceiling. Despite the resistance by big pharma, biotechnology companies managed to develop injectable peptide-based drugs, first against orphan or other small volume diseases, and later for conditions affecting large patient populations such as type 2 diabetes. Even their lack of gastrointestinal absorption could be utilized to enable successful oral dosing against chronic constipation. The preference of peptide therapeutics over small molecule competitors against identical medical conditions can be achieved by careful target selection, intrachain and terminal amino acid modifications, appropriate conjugation to stability enhancers and chemical space expansion, innovative delivery and administration techniques and patient-focused marketing strategies. Unfortunately, however, pharmacoeconomical considerations, including the strength of big pharma to develop competing small molecule drugs, have somewhat limited the success of otherwise smart peptide-based therapeutics. Yet, with increasing improvement in peptide drug modification and formulation, these are continuing to gain significant, and growing, acceptance as desirable alternatives to small molecule compounds.

KEYWORDS

peptide drugs, small molecules, peptide pharmaceuticals, pharma, peptide drug design and development

Introduction

Almost a decade ago, we summarized the advantages of peptide-based drugs over small molecule counterparts and the necessary target selection, lead optimization and formulation steps required to make synthetic peptide therapeutics both useful and appreciated alternatives from human therapy and pharmaceutical investment perspectives (Otvos and Wade, 2014). Our recommendations included identification of targets to which traditional organic chemistry leads are not available, insufficiently active or induce serious side reactions, taking advantage of the fast peak serum concentration of peptides and favorable medium-term pharmacodynamics parameters. We also described the utilization of innovative sequence modification and formulation strategies to improve their activity profile, *in vivo* half-life and thus mitigate patient compliance disadvantages. In the current report, we highlight the successes (and partial frustrations) of peptide-based drugs from a clinical point of view. A review article from last year lists 36 peptide drugs approved for clinical use since 2000, acting specifically on 26 targets or non-specific biological assemblies (Wang et al., 2022). We have selected 10 peptide drugs from this list that represent various aspects of peptide drug development strategies including both blockbusters and less widely used examples (the word “failure” is not allowed in this review article). The peptide-based drugs (Table 1) are compared with small molecule competitors

acting on identical targets or prescribed for the same indications. Note that none of these are considered biologics (in contrast to the insulin family of drugs). According to current Food and Drug Administration (FDA) guidelines, peptides up to 50 residues are regarded non-biological drugs (as opposed to therapeutic proteins, including antibodies and vaccines), mostly driven by the fully synthetic nature of their preparation (Carton and Strohl, 2013). In keeping with the theme of high specificity targets (Kaspar and Reichert, 2013), we do not discuss peptide drugs that act purely via their physical properties (e.g., Lucinactant, formerly known as KL (4) surfactant used for the prevention of neonatal respiratory distress syndrome, Moen et al., 2005), act on complexes of proteins (Carfilzomib (Kyprolis), a proteasome inhibitor against multiple myeloma, Vij et al., 2012), or oligoamides that are recognized as molecular patterns rather than well-defined amino acid sequences (Mifamurtide, a muramyl-dipeptide derivative used for the treatment of osteosarcoma, Myers et al., 2008). Rather, we outline peptide drug development and application concepts instead of an exhaustive review of all approved peptide drugs.

What the doctor will order—with limitations

Peptide drugs are still mostly developed by biotechnology companies at least until late-stage clinical trials (Anand et al., 2023) with big pharma acquiring the products at close-to-market opportunities. The goals of the research process reflect typical biotech thinking: let's have a receptor antagonist or, better yet, agonist for which no satisfactory small molecule drug is available, select indications where “on demand” injectable therapies with high initial plasma concentration are acceptable such as acutely life-saving or highly desired life-style medications carrying as little side effects as possible. Ease of preparation (low cost of goods) can also be a fringe benefit during the clinical development process.

One of the latest peptide drugs, Bremelanotide (Vyleesi), was approved in 2019 for increasing the sexual appetite of premenopausal women with hypoactive sexual desire disorder (HSDD) (Table 1). It is a non-selective agonist of the melanocortin receptors. Bremelanotide is prescribed for women who have not had problems with low sexual desire in the past. The recommended dosage is 1.75 mg injected subcutaneously in the abdomen or thigh at least 45 min before intercourse. The peptide induces improvements in desire, arousal, and orgasm scores (Edinoff et al., 2022). It represents only a very small segment of the drug market with gross product sales to pharmacy distributors for the second quarter of 2022 being \$2.3 million, and net product revenue of only \$771,000 to Palatin Technologies. Nevertheless, product sales increased by 79% over the prior quarter and by 91% over the comparable quarter in 2021. In 2012, the FDA identified female sexual dysfunction as one of 20 disease areas of high priority and, at the time of approval, considered Bremelanotide a first-in-class medication. The company's objective is re-licensing the US rights to a committed women's healthcare company. Bremelanotide is a short peptide without any activity enhancers but carries typical designer peptide drug modifications: a blocked amino terminus, and inclusion of D- and other unnatural amino

acid residues. The sequence is Ac-Nle-cyclo [Asp-His-DPhe-Arg-Trp-Lys]-OH.

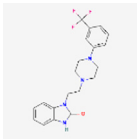
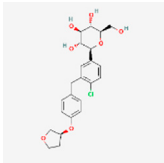
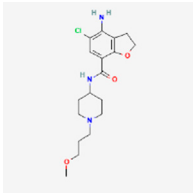
Bremelanotide's small molecule competitor is Flibanserin (Addyi), a serotonin agonist. New drugs for HSDD were clearly needed, as the FDA had rejected Flibanserin in 2010 and 2013 but succumbed to the pressure and approved it in 2015 although it required several black-box warnings (Sorscher, 2017). While Flibanserin is an oral medication, it mediates a series of drug interactions, particularly with alcohol, central nervous system (CNS) depressants, histamine 2 (H2) blockers and protein pump (PP) inhibitors as well as serotonin uptake inhibitors. It has low efficacy (Dooley et al., 2017) and the manufacturer had legal issues with investors about excessive expectations for activity and business income (Stempel, 2016). The significantly more efficacious peptide interacts only with a very small number of drugs (naltrexone, indomethacin), carries no legal concerns and, assuming that the market share keeps growing at the pace of the first 2 years, can be expected to assume a dominant role in the female HSDD market for quite some time.

A peptide drug for male erectile dysfunction (ED) has traveled a much choppier road. Aviptadil (Zyesami), a human vasoactive intestinal peptide (VIP), was approved in 2000 with phentolamine mesylate for ED (Keijers, 2001). The peptide was originally proposed to treat acute respiratory distress syndrome (ARDS). It is administered as an intracavernosal injection before sexual intercourse. The advent of oral phosphodiesterase-5 inhibitors (Huang and Lie, 2012) and the availability of intracavernosal Alprostadil injections (ICAI) compounded by regulatory issues for Invicorp have limited its use and availability. Currently it is a third line option for men who have failed most non-surgical treatment for ED. The competitor, Alprostadil (prostaglandin E1, Caverject, Edex, Prostin VR), makes blood vessels expand and is similarly administered as intracavernosal injection. When the two drugs are compared, Aviptadil/phentolamine induces a remarkably greater incidence of facial flushing relative to Alprostadil injections (16% versus 3%). Aviptadil is a typical example of unsuccessful peptide drug development. After its little impact as an erectile disorder treatment, during COVID-19 the peptide returned as a potential ARDS treatment as it was initially intended. Given via intravenous injection (a kiss of death), the peptide did not provide any positive primary output measure or anti-inflammatory activity (Youssef et al., 2022) and the FDA declined emergency use authorization in 2021 and 2022 (NRx Pharmaceuticals, 2022). Then a nebulized administration variant was tested in clinically ill patients with COVID-19 in 2022 although no clinical benefits were recorded either. The sequence of the peptide is H-His-Ser-Asp-Ala-Val-Phe-Thr-Asp-Asn-Tyr-Thr-Arg-Leu-Arg-Lys-Gln-Met-Ala-Val-Lys-Lys-Tyr-Leu-Asn-Ser-Ile-Leu-Asn-NH₂.

Whoa, ho ho, it's magic, yesss

The past decade has witnessed the rise of several blockbuster peptide drugs. When Pilot, a one-hit-wonder Scottish rock band, patented the song It's Magic in 1974 (Whoa ho ho ho, it's magic), nobody ever thought that this would be the most broadcast tune in 2023 on US television. This remarkable success came from the

TABLE 1 Peptide drugs and their small molecule competitors discussed in detail in this article.

Medical condition	Peptide drug				Small molecule competitor			
	Brand Name	Chemical Name and Primary Sequence	Approval Year	Target	Brand Name	Chemical Name and Structure	Approval Year	Target
HSDD	Vyleesi ✓	Bremelanotide Ac-Nle-cyclo[Asp-His-DPhe-Arg-Trp-Lys]-OH	2019	MCR	Addyi	Flibanserin 	2015	5-HT1A
ED	Aviptadil	Zyesami Invicorp H-His-Ser-Asp-Ala-Val-Phe-Thr-Asp-Asn-Tyr-Thr-Arg-Leu-Arg-Lys-Gln-Met-Ala-Val-Lys-Lys-Tyr-Leu-Asn-Ser-Ile-Leu-Asn-NH ₂	2000	VPAC	Caverjet Edex ✓	Alprostadil PGE1 	2002	PGR
Type 2 diabetes/obesity	Ozempic Wegovy ✓	Semaglutide H-His-Aib-Glu-Gly-Thr-Phe-Thr-Ser-Asp-Val-Ser-Ser-Tyr-Leu-Glu-Gly-Gln-Ala-Ala-N6-[N-(17-carboxy-1-oxoheptadecyl-L-α-glutamyl[2-(2-aminoethoxy)ethoxy]acetyl [2-(2-aminoethoxy)ethoxy]acetyl]-Lys-Glu-Phe-Ile-Ala-Trp-Leu-Val-Arg-Gly-Arg-Gly-OH	2017	GLP-1R	Jardiance	Empagliflozin 	2014	SGLT-2
IBS-C	Linzess ✓	Linacotide H-Cys-Cys-Glu-Tyr-Cys-Cys-Asn-Pro-Ala-Cys-Thr-Gly-Cys-Tyr-OH	2012	GC-C	Motegrity	Prucalopride 	2018	5-HT4
Anemia due to chronic kidney disease	Omontys	Peginesatide 	2012; Withdrawn 2013	Erythropoietin receptor				

(Continued on following page)

TABLE 1 (Continued) Peptide drugs and their small molecule competitors discussed in detail in this article.

Medical condition	Peptide drug				Small molecule competitor			
Acute decompensated heart failure	Natrecor	Nesiritide H-Ser-Pro-Lys-Met-Val-Gln-Gly-Ser-Gly-Cys-Phe-Gly-Arg-Lys-Met-Asp-Arg-Ile-Ser-Ser-Ser-Ser-Gly-Leu-Gly-Cys-Lys-Val-Leu-Arg-Arg-His-OH	2001	NPR-A	Tridil \checkmark	Nitroglycerin 	2000	Vascular smooth muscles
Secondary hyperparathyroidism in chronic kidney disease	Parsabiv	Etelcalcetide Ac-DCys (Cys)-DAla-DArg-DArg-DArg-DAla-DArg-NH ₂	2016	CaSR	Sensipar \checkmark	Cinacalcet 	2004	CaSR
AIDS	Fuzeon	Enfivirtide T-20 Ac-Tyr-Thr-Ser-Leu-Ile-His-Ser-Leu-Ile-Glu-Glu-Ser-Gln-Asn-Gln-Gln-Glu-Lys-Asn-Glu-Gln-Glu-Leu-Leu-Glu-Leu-Asp-Lys-Trp-Ala-Ser-Leu-Trp-Asn-Trp-Phe-NH ₂	2003	gp41	Selzentry Celzentry \checkmark	Maraviroc 	2007	CCR5
Chronic pain	Prialt	Ziconitide H-Cys-Lys-Gly-Lys-Gly-Ala-Lys-Cys-Ser-Arg-Leu-Met-Tyr-Asp-Cys-Cys-Thr-Gly-Ser-Cys-Arg-Ser-Gly-Lys-Cys-NH ₂	2004	N-type calcium channel	None			
HIV-induced lipodystrophy	Egrifta	Tesamorelin Hexenoil-Tyr-Ala-Asp-Ala-Ile-Phe-Thr-Asn-Ser-Tyr-Arg-Lys-Val-Leu-Gly-Gln-Leu-Ser-Ala-Arg-Lys-Leu-Leu-Gln-Asp-Ile-Met-Ser-Arg-Gln-Gln-Gly-Glu-Ser-Asn-Gln-Glu-Arg-Gly-Ala-Arg-Ala-Arg-Leu-NH ₂	2010	GHR	None			

¹Checkmarks indicate the clinical preference in current medical practice (as seen by these authors).

²Please note that with the exception of Etelcalcetide/Cinacalcet, the peptide/small molecule pairs act on different receptors and targets. Accordingly, their binding characteristics cannot be directly compared.

³The table shows only the primary peptide sequences. For cysteine bridges in disulfide-containing peptides, please refer to the text. Peginesatide is shown as a full sequence for understanding the spatial contribution of the PEG moiety.

Abbreviations: 5-HT_{1A}, serotonin type 1A receptor; 5-HT₄, serotonin type 4 receptor; CCR5, C-C chemokine receptor type 5; CaSR, calcium-sensing receptor; ED, erectile disorder; HSDD, hypoactive sexual desire disorder; IBS-C, irritable bowel syndrome with constipation; GC-C, guanylate cyclase-C; GHR, human growth hormone receptor; GLP-1R, glucagon like peptide 1 receptor; MCR, melanocortin receptors; NPR-A, atrial natriuretic peptide receptor; PGR, prostaglandin receptor; SGLT-2, sodium-glucose cotransporter-2; VPAC, vasoactive intestinal peptide receptor.

commercial remake of the song to advertise Ozempic (Semaglutide, Whoa ho, ho, Ozempic), a GLP-1 analog (Mahapatra et al., 2022). GLP-1 agonists stimulate glucose-dependent insulin release from pancreatic islets as their primary effect (Lee and Jun, 2014). Other main effects are to slow gastric emptying and to reduce appetite (Nauck et al., 1997). According to the Centers for Disease Control and Prevention (CDC), about 35 million Americans suffer from type 2 diabetes. This figure is 460 million patients worldwide, about 6.3% of the total population. Just to show how big a business the production of anti-diabetic drugs, it is enough to say that the worldwide incidence of all cancer types is 1.3% (Roser and Ritchie, 2015). Native incretin peptides were originally not suitable for drug development but the enormous need for an anti-diabetic drug forced research to make GLP-1 receptor agonists ultimately druggable (Todd and Bloom, 2007). For Semaglutide, the tide-turning substitutions are a glycine → 2-aminoisobutyric acid (Aib) replacement at position 2 and the attachment of an octadecanoic diacid to the side chain of Lys-26. The peptide chain modifications render the native peptide increasingly resistant to the proteolytic enzyme DPP-4, and the presence of the fatty acid moiety results in a high binding affinity to serum albumin increasing the half-life to approximately 7 days in humans (van Witteloostuijn, et al., 2016). Semaglutide, built on a human GLP-1 backbone, was initially approved in 2017, is administered at 0.25 mg subcutaneously weekly. Other GLP-1 receptor peptide agonists include Dulaglutide (Trulicity, injected weekly); Liraglutide (Victoza, Saxenda, daily) both also built on the human GLP-1 backbone, and Exenatide (Byetta, twice daily), Exenatide extended release (Bydureon bcise, weekly), Lixisenatide (Adlyxin, daily), the last ones being built on the exendin-4 backbone. Novo Nordisk, the manufacturer of Semaglutide, has rapidly grown so large that the company is reshaping the Danish economy. Ozempic and Wegovy (the latter contains higher doses up to 2.4 mg of Semaglutide and is designed for weight loss) have been proclaimed as revolutionary in the field of obesity. Ozempic and Wegovy sales are \$12 billion and \$4 billion a year respectively. Denmark's recent economic growth can be attributed solely to Novo Nordisk's booming success. In the past few weeks, Novo Nordisk's market value has exceeded the size of the entire Danish economy (Nelson, 2023). Part of Wegovy's success is the auto-injection device that is a piece of art. The patient does not even see the needle or needs to engage a frightening button. Just push the drug autoinjector tube against the abdomen and wait until the color gauge indicates complete loading of Semaglutide. The Semaglutide sequence is: H-His-Aib-Glu-Gly-Thr-Phe-Thr-Ser-Asp-Val-Ser-Ser-Tyr-Leu-Glu-Gly-Gln-Ala-Ala-N6-[N-(17-carboxy-1-oxoheptadecyl)-L-α-glutamyl [2-(2-aminoethoxy)ethoxy] acetyl [2-(2-aminoethoxy)ethoxy]acetyl]-Lys-Glu-Phe-Ile-Ala-Trp-Leu-Val-Arg-Gly-Arg-Gly-OH.

The non-peptide competitor of Ozempic is Jardiance (Empagliflozin), a sodium glucose co-transporter 2 (SGLT-2) inhibitor. SGLT-2 inhibitors are used to lower high blood glucose levels in people with type 2 diabetes. They may also be called gliflozins. Jardiance dose is a 10 mg tablet daily. Its sales are \$6 billion a year, nothing to sneeze at, yet significantly below the sales of Semaglutide. This is probably due to better patient

experience with the peptide than with its small molecule partner. According to [Drugs.com](#), the overall user rating of Ozempic is 6.0, with 46% positive and 32% negative experience. The values for Jardiance are 5.2 overall, 39% positive and 43% negative. Other approved small molecule SGLT-2 inhibitors include Brenzavvy (Bexagliflozin), Invokana (Canagliflozin) and Farxiga (Dapagliflozin).

Ozempic/Wegovy achieved blockbuster status through extended activity changes and a patient compliant administration mode, a quasi-oral injectable strategy. Yet, the final goal of all peptide drugs is truly oral administration and Semaglutide is not an exception. Clinical trials with 25–50 mg Semaglutide pills are in progress (Aroda et al., 2023; spoiler: good efficacy but 80% of patients reported adverse effects). In contrast, another huge peptide drug owes its success to the lack of adsorption after oral administration. Linaclotide (Linzess) is a guanylate cyclase 2C (GC-C) agonist (McCormack, 2014). It is a first-in-class agent approved in 2012 for the treatment of adult patients with moderate to severe irritable bowel syndrome with constipation (IBS-C). Linaclotide does not get absorbed in the gastrointestinal tract; rather it binds the receptor on the intestine surface. Upon binding, the peptide stimulates fluid secretion, increases colonic transit, and reduces abdominal pain (Camilleri, 2015). The daily oral dose is 0.15–0.3 mg. Linaclotide is an unmodified *Echerichia coli* enterotoxin ST sequence. H-Cys-Cys-Glu-Tyr-Cys-Cys-Asn-Pro-Ala-Cys-Thr-Gly-Cys-Tyr-OH, Cys bridges between residues 1–6, 2–10, 5–13. The low dose needed reflects Nature's evolutionary pressure to optimize the native peptide for its biological function i.e., travelers' diarrhea. Linzess' annual sales reached \$1 billion in 2021 which is an impressive figure especially if we consider that the treatment success is not a television-friendly result (as opposed to the addictive Ozempic tune) for commercials. Patients in Linzess television commercials do express verbally what most of us do after a productive morning event, yesss. Linaclotide's peptide sequence is somewhat similar to that of Plecanatide. Plecanatide is sold under the trade name Trulance. Plecanatide is uroguanilin, a hexadecapeptide, expressed by a gain-of-function mutation of GC-C and similarly prescribed for chronic idiopathic constipation (CIC) and IBS-C in adults (Kamuda and Mazzola, 2018).

The major non-peptide competitor of Linzess is Motegrity (Prucalopride), a selective serotonin type 4 (5-HT₄) receptor agonist against CIC. Motegrity at a daily dose of 2 mg sells at a dramatically lower volume of \$75 million annually. Currently no generic variant is available for either medication. Linzess' 30 day costs are \$400; with health insurance, \$10. Once again, the peptide drug enjoys its business success due to patient preference. The overall ratings at [Drugs.com](#) are 6.6 for Linzess and 5.4 for Motegrity, with 14% more patients reporting positive experience and 14% less reporting negative experience with the peptide compared to the non-peptide competitor.

Lessons learned from other peptide drugs

Peptide drug developers must be very cautious with the selection of covalent additives or formulation enhancers. Peginesatide (Omontys) is a pegylated peptide against anemia due to chronic

kidney disease. It is a dimer of the erythropoietin-mimetic peptide (EMP-1) that activates the erythropoietin receptor but bears no resemblance to erythropoietin (Wrighton et al., 1996). As EMP-1 had no potency, a dimeric peptide was made and conjugated to polyethylene glycol (PEG) to enhance the half-life to 50 h after intravenous administration (McDougall et al., 2009). The final composition is a heterodetic cyclic peptide composed of two identical 21-amino acid cyclic peptide units (including 3 non-natural residues) covalently bonded via a linker derived from iminodiacetic acid and β -alanine to a lysine-branched 40 kDa poly (ethylene glycol) chain. Omontys was approved in 2012. However, in Phase IV clinical trials, serious adverse drug reactions (sADRs) were reported including not only cardiovascular events but actual mortality (Hermanson et al., 2016). The approval was withdrawn in 2013. When the causal factors of the sADRs were investigated, experts pointed to the conjugated polyethylene glycol moiety. Soon after the withdrawal of Omontys, a large clinical trial was terminated early due to anaphylaxis following intravenous administration of REG1, a novel anticoagulation system containing a synthetic pegylated anticoagulant (Lincoff et al., 2015). In general, since the time of the Pegineside saga, it has been recognized that pegylation of polyamide therapeutics candidates is not without potentially game stopping disadvantages (Zhang et al., 2014).

Pharmacoeconomical considerations can sink otherwise promising peptide drugs. Nesiritide (Natrecor) is a human B-type natriuretic peptide approved in 2001 against acute decompensated heart failure. H-Ser-Pro-Lys-Met-Val-Gln-Gly-Ser-Gly-Cys-Phe-Gly-Arg-Lys-Met-Asp-Arg-Ile-Ser-Ser-Ser-Ser-Gly-Leu-Gly-Cys-Lys-Val-Leu-Arg-Arg-His-OH (disulfide bridge between the two cysteines). The target of the peptide is the natriuretic peptide receptor. It is a relatively long and complex peptide and competes with the non-peptide drug Nitroglycerin, arguably the simplest and probably least expensive small molecule medication of all. In acute (as opposed to chronic) heart failure, both drugs are administered intravenously. When added to standard care in hospitals, the peptide improves hemodynamic functions better than Nitroglycerin. Pulmonary capillary wedge pressure decrease (the standard readout of heart failure therapy efficacy) in 3–24 h is 25%–60% larger with Nesiritide compared to Nitroglycerin (Young, 2002). However, Nesiritide treatment (drug price plus continuous infusion, 2 days more treatment time) costs 40 times more than that of Nitroglycerin. Hospitals and insurance agencies agree that improvements in mortality and morbidity upon peptide administration do not warrant the considerably higher medical costs. The recommendations suggest that, in spite of the better clinical efficacy, the peptide should not be considered as first line therapy (Noviaski et al., 2003).

While it is a common trend to replace marketed peptide therapeutics with competing small molecule drugs, it does not seem to be a good idea to go the other way around. Cinacalcet (Sensipar) is an orally administered non-peptide allosteric modulator of the calcium sensing receptor (Balman Balfour, and Scott, 2005). CaSR is predominantly expressed in the parathyroids and kidneys (Thakker, 2012). Cinacalcet was approved in 2004 and is marketed by Amgen. Sensipar (cinacalcet) sales are now under \$100 million annually. The sales recently decreased 70% year-over-year, primarily driven by volume decline in response to generic

competition. Amgen purchased a company selling a peptidic direct CaSR agonist for \$315 million in 2017. One can speculate that this move was to maintain the market dominance in the secondary hyperparathyroidism in patients undergoing hemodialysis field. Etelcalcetide (Parsabiv) was approved in 2016. The peptide is administered intravenously 3 times a week. Ac-DCys (Cys)-DAla-DArg-DArg-DAla-DArg-NH₂.

The peptide reduces parathyroid hormone (PTH) better than Sensipar in hemodialysis patients, with 11.4% more patients being below the threshold clinical level than with the small molecule drug (Patel and Bridgeman, 2018). Etelcalcetide works so well that one of the major side effects is hypocalcaemia (Block et al., 2016). Unfortunately, the observed prolonged QT interval upon peptide treatment cannot be disentangled from the low serum calcium concentration. Another problem is that the peptide was studied only in hospitals, so no early data for at-home hemodialysis, for children and peritoneal dialysis (where oral non-peptide works well) are available. It is also unclear whether the PTH reduction eliminates actual clinical symptoms (bone fracture rate, cardiovascular morbidity, Pereira et al., 2018). Health insurance involvement did not help peptide sales either. Parsabiv sales reached \$186 million in the second quarter of 2020 but dropped to \$71 million in the same period of 2021. With Etelcalcetide's inclusion in the US end-stage renal disease bundled payment system, dialysis clinics rapidly implemented new treatment protocols, switching from Etelcalcetide to a generic version of oral Cinacalcet. To make everything worse, a new non-peptide competitor started to dominate the market.

Calcifediol (Ryaldee) is prescribed for hyperparathyroidism secondary to renal impairment (Sprague et al., 2017). The molecule is 25-hydroxyvitamin D₃, approved in 2016. It is a prohormone of the active ingredient, calcitriol that binds to the vitamin D receptor in target tissues and activates vitamin D responsive pathways resulting in increased intestinal absorption of calcium and phosphorus and reduced parathyroid hormone synthesis. Ryaldee dosing is 30 μ g tablets administered orally once daily at bedtime. At this point, Ryaldee is upcoming and is very popular. The overall Drugs.com rating is 7.9, with 57% of patients reporting positive feelings and 0% negative. Annual sales reached \$35 million in 2022 and are constantly increasing. Unlike for Cinacalcet, no lower cost generic is available. Apparently, the impact of Etelcalcetide to human health will never reach its originally anticipated potential.

How did textbook examples fare so far?

The end of the last century was not good for polyamide-based drugs. If drug developers had followed the infamous, and now widely criticized, “Pfizer rule of five” or “Lipinski’s rule of five,” peptide drugs would have never made the market (Muller-Kuhrt, 2003; Love, 2021). Luckily, pioneering and innovative biotechnology companies swam against the current and developed peptide therapeutics that served as encouragement for further oligoamide drug development. The following three examples were highly inspirational for peptide scientists, at least for the authors of this review article. Let’s take a look how they managed to keep peptide drugs viable alternatives to small molecules over time.

One of the first designer peptide drugs that received considerable public interest was Fuzeon (Enfuvirtide, T-20) which was approved in 2003. It binds to human immunodeficiency virus (HIV) gp41 and competitively inhibits the energy supplying six-helix viral bundle for cell fusion (Wild et al., 1993). While Fuzeon was an eye-opener and switched the negative public view against peptides as possible therapeutics, it still suffers from the activity and administration limitations of early peptide drugs. It is a peptide that mimicks the HR2 region of gp41 containing only natural amino acid residues and has to be subcutaneously injected twice daily. Its structure is Ac-Tyr-Thr-Ser-Leu-Ile-His-Ser-Leu-Ile-Glu-Glu-Ser-Gln-Asn-Gln-Gln-Glu-Lys-Asn-Glu-Gln-Glu-Leu-Leu-Glu-Leu-Asp-Lys-Trp-Ala-Ser-Leu-Trp-Asn-Trp-Phe-NH₂. Primary HIV-1 virus isolates exhibit variable susceptibilities to Enfuvirtide and thus resistance induction is a major concern (Poveda et al., 2005). Fuzeon is considered a second-line anti-retroviral agent (Qian et al., 2009). The authors of this article have always been concerned about optimization of peptide drug leads. For a 36-residue peptide, it is nearly impossible not to find a better analog in terms of covering extended chemical space, stability and pharmacodynamic properties. When we posed the personal question to a Trimeris lead scientist in 2004 whether they identified a more potent analog, the answer was yes, but investors and drug developers did not want to spend additional money for a potentially better version. The official answer is that a second-generation analog, Tifuvirtide, was found to be 10-times more active (Lalazari et al., 2005) but clinical development was discontinued due to formulation issues. A few additional peptidic fusion inhibitors were identified but never approved.

The significantly larger resources of big pharma usually allows the systematic improvements of small molecule peptide drug competitors and can develop a successful formula. Maraviroc (Selzentry, Celzentry in Europe) from Pfizer is a non-peptide inhibiting HIV gp120 attachment to binding to the CCR5 co-receptor. It is administered twice daily as an oral solution. On the way to approval in 2007, a number of problems associated with the original lead (Dorr et al., 2005) had to be solved by one-by-one medicinal chemistry optimization (Armour et al., 2006): a) high lipophilicity; b) side reaction as a potent CYP 2D6 inhibitor; c) a tropane-based analog turned to be a hERG ion channel inhibitor; and d) two additional structural changes were introduced leading to the final drug composition. Maraviroc works only for 50%–80% of patients, but around 2010 had generated 6–7 times more money than Enfuvirtide (these are the only two approved HIV fusion inhibitors). The monthly patient costs of the peptide are more than double that of the non-peptide.

Although we focus here on peptide drugs acting on well-defined targets, we cannot leave this review without briefly mentioning Prialat (Ziconotide). Approved in 2004, it was seminal to establishing positive public opinion to peptide drugs. Prialat is derived from the cone snail *Conus magus*, comprises 25 amino acids with three disulfide bonds and it acts as an N-type calcium channel blocker for the management of chronic pain (Miljanich, 2004). Its primary structure is H-Cys-Lys-Gly-Lys-Gly-Ala-Lys-Cys-Ser-Arg-Leu-Met-Tyr-Asp-Cys-Cys-Thr-Gly-Ser-Cys-Arg-Ser-Gly-Lys-Cys-NH₂ (disulfide bonds Cys1-Cys16, Cys8-Cys20, and Cys15-Cys25). Remarkably, Ziconotide has no approved competitor of any drug class. To

date, Ziconotide is the only calcium channel blocking peptide approved for use by the FDA. Prialat reached a textbook example status among pain medications because of the lack of signs of dependence and of no apparent tolerance. Ziconotide is administered intrathecally over 1 hour. Given the intrathecal administration and low membrane permeability due to its size, Ziconotide is expected to remain primarily in the cerebrospinal fluid (CSF); plasma levels, where detected, remain constant up to 9 months following administration (McGivern, 2007). For cancer pain, morphine is also recommended as first line therapy, but the consensus is to use Prialat without hesitation unless contraindicated (Deer et al., 2019). However, for its long standing as cancer pain killer, a remarkable 73 tons of morphine for cancer was produced in 2023 (14% of 523 tons total, van Zee, 2009) compared to Prialat which sold for a total of \$27 million in 2017. To be fair to morphine, monotherapy with the peptide costs 2.5 times of that of the opioid (Lambe et al., 2023).

Our last example has a personal connection to these authors. We have provided a few examples for replacing approved peptide drugs with small molecule therapeutics. Due to our interest in adipokine receptor modulators namely, leptin and adiponectin receptor agonists and antagonists (Otvos et al., 2009; Otvos, 2019), we submitted tens of public and private grant proposals for replacing Tesamorelin against lipodystrophy with a leptin receptor agonist peptide drug but to no avail. Apparently, the benefits of Tesamorelin would not justify the development of any peptide competitor. Tesamorelin (Egrifta) is a human growth hormone-releasing factor (GRF) analog for lipodystrophy induced by antiviral therapy in AIDS patients (Lake et al., 2021) and has the primary structure Hexenol-Tyr-Ala-Asp-Ala-Ile-Phe-Thr-Asn-Ser-Tyr-Arg-Lys-Val-Leu-Gly-Gln-Leu-Ser-Ala-Arg-Lys-Leu-Leu-Gln-Asp-Ile-Met-Ser-Arg-Gln-Gln-Gly-Glu-Ser-Asn-Gln-Glu-Arg-Gly-Ala-Arg-Ala-Arg-Leu-NH₂. Approved in 2010, it is still produced by the same biotechnology company which developed it (Theratechnologies). Tesamorelin is administered once daily by subcutaneous injection. The peptide has no competitor for HIV-related lipodystrophy. For generalized lipodystrophy metreleptin (Myalept), a recombinant leptin derivative can be used but even this competitor is a biologic medication.

Engrifta fills a hole in lipodystrophy drugs. The 16:0 FDA approval, a sign of desperate need for lipodystrophy treatments, came despite pronounced anabolic effects and even more evident adverse effects (liver and kidney findings, anaemia, clinical chemistry changes, organ weight effects) observed in dogs after repeat daily subcutaneous injections, which were all attributed to prolonged exposure to supraphysiological levels of the growth hormone and/or the insulin-like growth factor (IGF)-1 (Ferdinandi et al., 2007). Despite these side effects, this medication is truly needed, documented by the sales volume in 2021 of \$41 million and \$50 million in 2022 indicating constant, if not increased, usage even a dozen years after approval. While Tesamorelin is not a blockbuster, it is an especially useful addition to the human pharmaceutical arsenal helping 1,000–2,000 patients annually and producing a constant revenue stream for the developers. Most of us peptide therapeutics designers and developers would be very happy to produce a drug like that.

Some additional approved peptide drug targets—and the lack thereof

While discussing the merits of peptide therapeutics, experts pointed out a few additional successful peptide drugs on the market and several others in late clinical development stage. Since more than half of drug candidates passing phase II trials fail in phase III (van Norman, 2019), listing these peptides would be premature in the context of this review article. However, some additional approved peptide drugs are worth briefly mentioning. Pasireotide is a hexamer homodetic cyclic somatostatin analog approved in 2012 for the treatment of Cushing disease caused by a tumor or excess growth (hyperplasia) of the pituitary gland (Pivonello et al., 2019). Pasireotide was included in the reference review article (Wang et al., 2022) as was another anti-tumor peptide, Degarelix, approved in 2008, an antagonist of gonadotropin-releasing hormones (GnRH) for the treatment of advanced prostate cancer. It distinguishes itself among the sea of GnRH agonists used for androgen deprivation therapy (Sciarra et al., 2016). What was approved before 2000 (exactly in 1987 and accordingly not listed) is another prostate (and breast) cancer treatment, Goserelin, a synthetic analog of the luteinizing hormone-releasing hormone that acts by reducing secretion of gonadotropins from the pituitary (Bolla et al., 1997). Goserelin earned the fame of being a member of the World Health Organization's List of Essential Medicines. For targeting diseases mostly affecting women, two remarkable peptide drugs are Abaloparatide, utilized in osteoporosis management and Elagolix, employed in the relief of endometriosis-associated pain and the management of heavy menstrual bleeding. While Abaloparatide is an N-terminal analog of parathyroid hormone-related protein (PTHrP) 4 and an agonist at the parathyroid hormone type 1 (PTH1) receptor (Pioszak et al., 2009, first approval date: 2017), Elagolix, approved in 2018, is yet another gonadotropin releasing hormone receptor antagonist and is used to treat moderate to severe pain in endometriosis. It is a rare orally-administered peptide drug that inhibits endogenous GnRH signaling by binding competitively to GnRH receptors in the pituitary gland (Leyland et al., 2021).

Remarkably, what is missing from this list are antimicrobial peptides (AMP). Although as many as 3,000 AMPs have been reported and characterized, only 7 are approved by the FDA (gramicidin D, daptomycin, vancomycin, oritavancin, dalbavancin, colistin and telavancin), all acting on bacterial membranes, and none of them are classical peptide therapeutics regarding their structure and all lack of specific molecular targets (Chen and Lu, 2020). Although early preclinical studies show quite promising results against resistant bacterial infections (Ostorhazi et al., 2018), in late preclinical assays and clinical trials AMPs failed to show sufficient antimicrobial activity (Silver, 2011). Their poor performance may derive from differences between the clinical setting and the screening conditions (Luo et al., 2023). Declining current public investment in new antimicrobial drugs does not help the situation either (World Health Organization, 2020).

An interesting aspect of “de-orphanization” of rare G-protein-coupled receptors (GPCR) with peptide ligands is to expand peptide drug coverage (Hauser et al., 2020). In fact, we took exactly the

opposite approach. While our adiponectin receptor (hardly an orphan GPCR) targeting peptide agonist, ADP 355 (Otvos et al., 2011), did not show pronounced activity in an initial phase 3 clinical trial against the multibillion dollar dry eye disease, it shows remarkable efficacy in animal models of orphan diseases such as Duchenne muscular dystrophy syndrome (Dubuisson et al., 2023). Phase 1 clinical trials of a systemic formulation (as opposed to the eyedrop) will start in Q1 2024.

Concluding remarks

It is undeniable that peptides, natural biomolecules, have contributed enormously to the advance of chemical and biological science and have profoundly impacted the development of the modern pharmaceutical industry. Because of their high specificity and low toxicity profiles in humans, designer peptide drugs are now sought-after alternatives to small molecule therapeutics and a major focus for creating next-generation products (Otvos and Wade, 2014; Fosgerau and Hoffmann, 2015). Despite the challenges with their development as outlined above and previously (Otvos and Wade, 2014), today, the peptide market is growing nearly *twice* as fast as the overall pharmaceutical market due to an increased number of therapeutic targets and improved delivery methodologies. There are now 80 therapeutic peptides on the market, 200 in clinical phases, and 600 in advanced pre-clinical stages (Henninot et al., 2018). Worldwide sales of peptide drugs are projected to reach a staggering \$75 billion by 2028 (Arora, 2022). It is clear that their promise is being increasingly realized in the pharmacy and that with further inevitable advances in drug design, formulation and delivery systems, they will continue to be critically important alternatives to small molecules for therapy. The current trend of designing a road map to help identify the best course for selecting drug targets in light of recent clinical developments would be a useful set of guidelines for even more successful competition with traditional drug classes.

Author contributions

LO: Conceptualization, Writing—original draft. JW: Conceptualization, Writing—original draft.

Funding

The author(s) declare financial support was received for the research, authorship, and/or publication of this article. Studies at the Florey Institute of Neuroscience and Mental Health are supported in part by the Victorian Government's Operational Infrastructure Support Program.

Conflict of interest

Author LO was employed by OLPE Pharmaceutical Consultants.

The remaining author declares that the research was conducted in the absence of any commercial or financial relationships that could be construed as a potential conflict of interest.

The authors declared that they were editorial board members of Frontiers, at the time of submission. This had no impact on the peer review process and the final decision.

References

- Anand, U., Bandyopadhyay, A., Jha, N. K., Pérez de la Lastra, J. M., and Dej, A. (2023). Translational aspect in peptide drug discovery and development: an emerging therapeutic candidate. *Biofactors* 49 (2), 251–269. doi:10.1002/biof.1913
- Armour, D., de Groot, M. J., Edwards, M., Perros, M., Price, D. A., Stammen, B. L., et al. (2006). The discovery of CCR5 receptor antagonists for the treatment of HIV infection: hit-to-lead studies. *ChemMedChem* 1 (7), 706–709. doi:10.1002/cmdc.200600031
- Aroda, V. R., Aberle, J., Bardtrum, L., Christiansen, E., Knop, F. K., Gabery, S., et al. (2023). Efficacy and safety of once-daily oral semaglutide 25 mg and 50 mg compared with 14 mg in adults with type 2 diabetes (PIONEER PLUS): a multicentre, randomised, phase 3b trial. *Lancet* 402 (10403), 693–704. doi:10.1016/S0140-6736(23)01127-3
- Arora, R. (2022). *Global peptide therapeutics market USD 75 billion opportunity*. Des Moines, Iowa: Biospace.
- Barman Balfour, J. A., and Scott, L. J. (2005). Cinacalcet hydrochloride. *Drugs* 65 (2), 271–281. doi:10.2165/00003495-200565020-00007
- Block, G. A., Bushinsky, D. A., Cunningham, J., Drueke, T. B., Ketteler, M., Kewalramani, R., et al. (2016). Effect of etelcalcetide vs placebo on serum parathyroid hormone in patients receiving hemodialysis with secondary hyperparathyroidism: two randomized clinical trials. *JAMA* 317 (2), 146–155. doi:10.1001/jama.2016.19456
- Bolla, M., Gonzalez, D., Warde, P., Dubois, J. B., Mirimanoff, R. O., Storme, G., et al. (1997). Improved survival in patients with locally advanced prostate cancer treated with radiotherapy and goserelin. *N. Engl. J. Med.* 337 (5), 295–300. doi:10.1056/NEJM199707313370502
- Camilleri, M. (2015). Guanylate cyclase C agonists: emerging gastrointestinal therapies and actions. *Gastroenterology* 148, 483–487. doi:10.1053/j.gastro.2015.01.003
- Carton, J. M., and Strohl, W. R. (2013). “Protein therapeutics (Introduction to biopharmaceuticals),” in *Biological and small molecule drug research and development*. Editors R. Ganelin, R. Jefferts, and S. Roberts (Waltham, MA, USA: Academic Press), 127–159.
- Chen, C. H., and Lu, T. K. (2020). Development and challenges of antimicrobial peptides for therapeutic applications. *Antibiot. (Basel)* 9 (1), 24. doi:10.3390/antibiotics9010024
- Deer, T. R., Pope, J. E., Hanes, M. C., and McDowell, G. C. (2019). Intrathecal therapy for chronic pain: a review of Morphine and Ziconotide as firstline options. *Pain Med.* 20 (4), 784–798. doi:10.1093/pm/pny132
- Dooley, E. M., Miller, M. K., and Clayton, A. H. (2017). Flibanserin: from bench to bedside. *Sex. Med. Rev.* 5 (4), 461–469. doi:10.1016/j.sxmr.2017.06.003
- Dorr, P., Westby, M., Dobbs, S., Griffin, P., Irvine, B., Macartney, M., et al. (2005). Maraviroc (UK-427,857), a potent, orally bioavailable, and selective small-molecule inhibitor of chemokine receptor CCR5 with broad-spectrum anti-human immunodeficiency virus type 1 activity. *Antimicrob. Agents Chemother.* 49 (11), 4721–4732. doi:10.1128/AAC.49.11.4721-4732.2005
- Dubuisson, N., Verselle, R., Davis-López de Carrizosa, M. A., Selvais, C. M., Noel, L., Planchon, C., et al. (2023). The adiponectin receptor agonist, ALY688: a promising therapeutic for fibrosis in the dystrophic muscle. *Cells* 12 (16), 2101. doi:10.3390/cells12162101
- Edinoff, A. N., Sanders, N. M., Lewis, K. B., Apgar, T. L., Cornett, E. M., Kaye, A. M., et al. (2022). Bremelanotide for treatment of female hypoactive sexual desire. *Neurol. Int.* 14 (1), 75–88. doi:10.3390/neurolint14010006
- Ferdinand, E. S., Brazeau, P., High, K., Procter, B., Fennell, S., and Dubreuil, P. (2007). Non-clinical pharmacology and safety evaluation of TH9507, a human growth hormone-releasing factor analogue. *Basic Clin. Pharmacol. Toxicol.* 100 (1), 49–58. doi:10.1111/j.1742-7843.2007.00008.x
- Fosgerau, K., and Hoffmann, T. (2015). Peptide therapeutics: current status and future directions. *Drug Discov. Today* 20, 122–128. doi:10.1016/j.drudis.2014.10.003
- Hauser, A. S., Gloriam, D. E., Bräuner-Osborne, H., and Foster, S. R. (2020). Novel approaches leading towards peptide GPCR de-orphanisation. *Br. J. Pharmacol.* 177 (5), 961–968. doi:10.1111/bph.14950
- Henninot, A., Collins, J. C., and Nuss, J. M. (2018). The current state of peptide drug discovery. *J. Med. Chem.* 61, 1382–1414. doi:10.1021/acs.jmedchem.7b00318
- Hermanson, T., Bennett, C. L., and Macdougall, I. C. (2016). Peginesatide for the treatment of anemia due to chronic kidney disease - an unfulfilled promise. *Expert Opin. Drug Saf.* 15 (10), 1421–1426. doi:10.1080/14740338.2016.1218467
- Huang, S. A., and Lie, J. D. (2012). Phosphodiesterase-5 inhibitors in the management of erectile dysfunction. *P. Trans.* 38 (7), 414–419.
- Kamuda, J. A., and Mazzola, N. (2018). Plecanatide (Trulance) for chronic idiopathic constipation and irritable bowel syndrome with constipation. *Pharm. Ther.* 43 (4), 207–232.
- Kaspar, A. A., and Reichert, J. M. (2013). Future directions for peptide therapeutics development. *Drug Discov. Today* 18, 807–817. doi:10.1016/j.drudis.2013.05.011
- Keijzers, G. B. (2001). Aviptadil (senatek). *Curr. Opin. Investig. Drugs* 2 (4), 545–549.
- Lake, J. E., La, K., Erlandson, K. M., Adrian, S., Yenokyan, G., Scherzinger, A., et al. (2021). Tesamorelin improves fat quality independent of changes in fat quantity. *AIDS* 35 (9), 1395–1402. doi:10.1097/QAD.0000000000002897
- Lalezari, J. P., Bellos, N. C., Sathasivam, K., Richmond, G. J., Cohen, C. J., Myers, R. A., Jr, et al. (2005). T-1249 retains potent antiretroviral activity in patients who had experienced virological failure while on an enfuvirtide-containing treatment regimen. *J. Infect. Dis.* 191 (7), 1155–1163. doi:10.1086/427993
- Lambe, T., Duarte, R., Eldabe, R., Copley, S., Kansal, A., Black, S., et al. (2023). Ziconotide for the management of cancer pain: a budget impact analysis. *Neuromodulation* 26 (6), 1226–1232. doi:10.1016/j.neurom.2022.08.458
- Lee, Y. S., and Jun, H. S. (2014). Anti-diabetic actions of glucagon-like peptide-1 on pancreatic beta-cells. *Metabolism* 63 (1), 9–19. doi:10.1016/j.metabol.2013.09.010
- Leyland, N., Estes, S. J., Lessey, B. A., Advincula, A. P., and Taylor, H. S. (2021). A clinician's guide to the treatment of endometriosis with Elagolix. *J. Womens Health (Larchmt)*. 30 (4), 569–578. doi:10.1089/jwh.2019.8096
- Lincoff, A. M., Mehran, R., Povsic, T. J., Zelenkofske, S. L., Huang, Z., Armstrong, P. W., et al. (2016). Effect of the REG1 anticoagulation system versus bivalirudin on outcomes after percutaneous coronary intervention (REGULATE-PCI): a randomised clinical trial. *Lancet* 387 (10016), 349–356. doi:10.1016/S0140-6736(15)00515-2
- Love, D. (2021). *Ruling out the rule of five*. London, United Kingdom: Royal Society of Chemistry.
- Luo, X., Chen, H., Song, Y., Qin, Z., Xu, L., He, N., et al. (2023). Advancements, challenges and future perspectives on peptide-based drugs: focus on antimicrobial peptides. *Eur. J. Pharm. Sci.* 181, 106363. doi:10.1016/j.ejps.2022.106363
- Macdougall, I. C., Rossert, J., Casadevall, N., Stead, R. B., Duliege, A. M., Froissart, M., et al. (2009). A peptide-based erythropoietin-receptor agonist for pure red-cell aplasia. *N. Engl. J. Med.* 361 (19), 1848–1855. doi:10.1056/NEJMoa074037
- Mahapatra, M. K., Karuppusamy, M., and Sahoo, B. M. (2022). Semaglutide, a glucagon like peptide-1 receptor agonist with cardiovascular benefits for management of type-2 diabetes. *Rev. Endocr. Metab. Disord.* 23 (3), 521–539. doi:10.1007/s11154-021-09699-1
- McCormack, P. L. (2014). Linaclotide: a review of its use in the treatment of irritable bowel syndrome with constipation. *Drugs* 74 (1), 53–60. doi:10.1007/s40265-013-0157-5
- McGivern, J. G. (2007). Ziconotide: a review of its pharmacology and use in the treatment of pain. *Neuropsychiatr. Dis. Treat.* 3 (1), 69–85. doi:10.2147/ndt.2007.3.1.69
- Meyers, P. A., Schwartz, C. L., Krailo, M. D., Healey, J. H., Bernstein, M. L., Betcher, D., et al. (2008). Osteosarcoma: the addition of muramyl tripeptide to chemotherapy improves overall survival—a report from the children's oncology group. *J. Clin. Oncol.* 26 (4), 633–638. doi:10.1200/JCO.2008.14.0095
- Miljanich, G. P. (2004). Ziconotide: neuronal calcium channel blocker for treating severe chronic pain. *Curr. Med. Chem.* 11 (23), 3029–3040. doi:10.2174/0929867043363884
- Moen, M. D., Perry, C. M., and Wellington, K. (2005). Lucinactant: in neonatal respiratory distress syndrome. *Treat. Respir. Med.* 4 (2), 139–145. doi:10.2165/00151829-200504020-00008
- Muller-Kuhrt, L. (2003). Putting nature back into drug discovery. *Nat. Biotechnol.* 21, 602. doi:10.1038/nbt0603-602

Publisher's note

All claims expressed in this article are solely those of the authors and do not necessarily represent those of their affiliated organizations, or those of the publisher, the editors and the reviewers. Any product that may be evaluated in this article, or claim that may be made by its manufacturer, is not guaranteed or endorsed by the publisher.

- Nauck, M. A., Niedereichholz, U., Ettler, R., Holst, J. J., Orskov, C., Ritzel, R., et al. (1997). Glucagon-like peptide 1 inhibition of gastric emptying outweighs its insulinotropic effects in healthy humans. *Am. J. Physiol.* 273 (5), E981–E988. doi:10.1152/ajpendo.1997.273.5.E981
- Nelson, E. (2023). *How Ozempic and weight loss drugs are reshaping Denmark's economy*. New York City, New York, USA: The New York Times.
- Noviasky, J. A., Kelberman, M., Whalen, K. M., Guharoy, R., and Darko, W. (2003). Science or fiction: use of nesiritide as a first-line agent? *Pharmacotherapy* 23 (8), 1081–1083. doi:10.1592/phco.23.8.1081.32882
- NRx Pharmaceuticals (2022). *FDA declines emergency use authorization for ZYESAMI® (aviptadil) for subgroup of patients with critical COVID-19 at immediate risk of death from respiratory failure despite treatment with approved therapy, including remdesivir*. Chicago, IL, United States: Cision PR Newswire.
- Ostorhazi, E., Hoffmann, R., Herth, N., Wade, J. D., Kraus, C. N., and Otvos, L., Jr. (2018). Advantage of a narrow spectrum host defense (antimicrobial) peptide over a broad spectrum analog in preclinical drug development. *Front. Chem.* 6, 359. doi:10.3389/fchem.2018.00359
- Otvos, L., Jr. (2019). Potential adiponectin receptor response modifier therapeutics. *Front. Endocrinol. (Lausanne)* 10, 539. doi:10.3389/fendo.2019.00539
- Otvos, L., Jr., Haspinger, E., La Russa, F., Maspero, F., Graziano, P., Kovalszky, I., et al. (2011). Design and development of a peptide-based adiponectin receptor agonist for cancer treatment. *BMC Biotechnol.* 11, 90. doi:10.1186/1472-6750-11-90
- Otvos, L., Jr., Cassone, M., Terrasi, M., Cascio, S., Mateo, G. D., Knappe, D., et al. (2009). Agonists and partial antagonists acting on the leptin-leptin receptor interface. *Adv. Exp. Med. Biol.* 611, 497–498. doi:10.1007/978-0-387-73657-0_215
- Otvos, L., Jr. and Wade, J. D. (2014). Current challenges in peptide-based drug discovery. *Front. Chem.* 2, 62. doi:10.3389/fchem.2014.00062
- Patel, J., and Bridgeman, M. B. (2018). Etelcalcetide (Parsabiv) for secondary hyperparathyroidism in adults with chronic kidney disease on hemodialysis. *Pharm. Ther.* 43 (7), 396–399.
- Pereira, L., Meng, C., Marques, D., and Frazão, J. M. (2018). Old and new calcimimetics for treatment of secondary hyperparathyroidism: impact on biochemical and relevant clinical outcomes. *Clin. Kidney J.* 11 (1), 80–88. doi:10.1093/ckj/sfx125
- Pioszak, A. A., Parker, N. R., Gardella, T. J., and Xu, H. E. (2009). Structural basis for parathyroid hormone-related protein binding to the parathyroid hormone receptor and design of conformation-selective peptides. *J. Biol. Chem.* 284 (41), 28382–28391. doi:10.1074/jbc.M109.022905
- Pivonello, R., Arnaldi, G., Scaroni, C., Giordano, C., Cannavò, S., Iacuanello, D., et al. (2019). The medical treatment with pasireotide in Cushing's disease: an Italian multicentre experience based on “real-world evidence”. *Endocrine* 64 (3), 657–672. doi:10.1007/s12020-018-1818-7
- Poveda, E., Rodés, B., Lebel-Binay, S., Faudon, J. L., Jimenez, V., and Soriano, V. (2005). Dynamics of enfuvirtide resistance in HIV-infected patients during and after long-term enfuvirtide salvage therapy. *J. Clin. Virol.* 34 (4), 295–301. doi:10.1016/j.jcv.2005.02.004
- Qian, K., Morris-Natschke, S. L., and Lee, K. H. (2009). HIV entry inhibitors and their potential in HIV therapy. *Med. Res. Rev.* 29 (2), 369–393. doi:10.1002/med.20138
- Roser, M., and Ritchie, H. (2015). Cancer. Our world in data. <https://ourworldindata.org/cancer>.
- Sciarra, A., Fasulo, A., Ciardi, A., Petrangeli, E., Gentilucci, A., Maggi, M., et al. (2016). A meta-analysis and systematic review of randomized controlled trials with degarelix versus gonadotropin-releasing hormone agonists for advanced prostate cancer. *Med. Baltim.* 95 (27), e3845. doi:10.1097/MD.0000000000003845
- Silver, L. L. (2011). Challenges of antibacterial discovery. *Clin. Microbiol. Rev.* 24 (1), 71–109. doi:10.1128/CMR.00030-10
- Sorscher, S. (2017). *Maker of 'female viagra' sued as sales fizzle*. Washington, DC, USA: Public Citizen.
- Sprague, S. M., Strugnell, S. A., and Bishop, C. W. (2017). Extended-release calcifediol for secondary hyperparathyroidism in stage 3–4 chronic kidney disease. *Expert Rev. Endocrinol. Metab.* 12 (5), 289–301. doi:10.1080/17446651.2017.1347501
- Stempel, J. (2016). *Valeant sued for botching marketing of female libido pill*. London, United Kingdom: Reuters.
- Thakker, R. V. (2012). Calcium-sensing receptor: role in health and disease. *Indian J. Endocrinol. Metab.* 16 (Suppl. 2), S213–S216. doi:10.4103/2230-8210.104041
- Tood, J. F., and Bloome, S. R. (2007). Incretins and other peptides in the treatment of diabetes. *Diabet. Med.* 24 (3), 223–232. doi:10.1111/j.1464-5491.2006.02071.x
- Van Norman, G. A. (2019). Phase II Trials in drug development and adaptive trial design. *JACC Basic Transl. Sci.* 4 (3), 428–437. doi:10.1016/j.jacbs.2019.02.005
- van Witteloostuijn, S. B., Pedersen, S. L., and Jensen, K. J. (2016). Half-life extension of biopharmaceuticals using chemical methods: alternatives to PEGylation. *ChemMedChem* 11 (22), 2474–2495. doi:10.1002/cmdc.201600374
- van Zee, A. (2009). The promotion and marketing of oxycontin: commercial triumph, public health tragedy. *Am. J. Public Health* 99 (2), 221–227. doi:10.2105/AJPH.2007.131714
- Vij, R., Wang, M., Kaufman, J. L., Lonial, S., Jakubowski, A. J., Stewart, A. K., et al. (2012). An open-label, single-arm, phase 2 (PX-171-004) study of single-agent carfilzomib in bortezomib-naïve patients with relapsed and/or refractory multiple myeloma. *Blood* 119 (24), 5661–5670. doi:10.1182/blood-2012-03-414359
- Wang, L., Wang, N., Zhang, W., Cheng, X., Yan, Z., Shao, G., et al. (2022). Therapeutic peptides: current applications and future directions. *Signal Trans. Target. Ther.* 7, 48. doi:10.1038/s41392-022-00904-4
- Wild, C., Greenwell, T., and Matthews, T. (1993). A synthetic peptide from HIV-1 gp41 is a potent inhibitor of virus-mediated cell-cell fusion. *AIDS Res. Hum. Retroviruses* 9 (11), 1051–1053. doi:10.1089/aid.1993.9.1051
- World Health Organization, (2020). *Lack of new antibiotics threatens global efforts to contain drug-resistant infections*. Geneva, Switzerland: World Health Organization.
- Wrighton, N. C., Farrell, F. X., Chang, R., Kashyap, A. K., Barbone, F. P., Mulcahy, L. S., et al. (1996). Small peptides as potent mimetics of the protein hormone erythropoietin. *Science* 273 (5274), 458–463. doi:10.1126/science.273.5274.458
- Young, J. B. (2002). Intravenous nesiritide vs nitroglycerin for treatment of decompensated congestive heart failure: a randomized controlled trial. *JAMA* 287 (12), 1531–1540. doi:10.1001/jama.287.12.1531
- Youssef, J. G., Lavin, P., Schoenfeld, D. A., Lee, R. A., Lenhardt, R., Park, D. J., et al. (2022). The use of IV vasoactive intestinal peptide (Aviptadil) in patients with critical COVID-19 respiratory failure: results of a 60-day randomized controlled trial. *Crit. Care Med.* 50 (11), 1545–1554. doi:10.1097/CCM.0000000000005660
- Zhang, F., Liu, M. R., and Wan, H. T. (2014). Discussion about several potential drawbacks of PEGylated therapeutic proteins. *Biol. Pharm. Bull.* 37 (3), 335–339. doi:10.1248/bpb.b13-00661



OPEN ACCESS

EDITED BY

Steve Suib,
University of Connecticut, United States

REVIEWED BY

Qifan Zhong,
Central South University, China
Kang Yan,
Jiangxi University of Science and
Technology, China
Zhen Yao,
Guizhou Normal University, China

*CORRESPONDENCE

Yuehui He,
✉ yuehui@mail.csu.edu.cn

RECEIVED 08 September 2023

ACCEPTED 27 November 2023

PUBLISHED 07 December 2023

CITATION

Tang X and He Y (2023), A novel optimal
formula of nickel extraction: arsenic
removal from niccolite by controlling
arsenic-containing phases.
Front. Chem. 11:1290831.
doi: 10.3389/fchem.2023.1290831

COPYRIGHT

© 2023 Tang and He. This is an open-
access article distributed under the terms
of the [Creative Commons Attribution
License \(CC BY\)](#). The use, distribution or
reproduction in other forums is
permitted, provided the original author(s)
and the copyright owner(s) are credited
and that the original publication in this
journal is cited, in accordance with
accepted academic practice. No use,
distribution or reproduction is permitted
which does not comply with these terms.

A novel optimal formula of nickel extraction: arsenic removal from niccolite by controlling arsenic-containing phases

Xiaowei Tang¹ and Yuehui He^{1,2*}

¹Powder Metallurgy Research Institute, Central South University, Changsha, China, ²State Key Laboratory of Powder Metallurgy, Central South University, Changsha, China

Objective: Niccolite, a rare nickel arsenide mineral, has emerged as a promising source for nickel extraction. However, its processing is limited and often associated with toxicity concerns. This study aims to search for efficient separation of arsenic during the roasting process of niccolite.

Methods: The arsenic-containing phase was optimized through changing the contents of oxygen, additive S, and additive FeS in the system to achieve efficient separation of arsenic during the roasting process of niccolite. Thermodynamic analysis was performed using the equilibrium composition module with HSC Chemistry.

Results: The thermodynamic results showed that in direct roasting, the product contained ferric arsenate which immobilized arsenic in the solid phase, increasing the difficulty in separation. In the presence of sulfur, the arsenic may escape completely in the form of gas (As_2O_3 , As_4O_4 , As_4O_6). The use of FeS as the reductant significantly reduced the residual arsenic content.

Conclusion: The FeS reduction in roasting process is an optimal strategy for arsenic removal from niccolite. This provides a novel technique for nickel extraction in industry.

KEYWORDS

nickel, arsenic, niccolite, roasting, S, FeS

1 Introduction

Nickel is an important strategic metal with widespread applications in stainless steel and clean energy fields (Pariser et al., 2018; Poole et al., 2022). The consumption of nickel has reached 2.89 million tons in 2022 and the International Nickel Study Group (INSG) expects this to reach 3.22 million tons in 2023 (INSG, 2013). In recent years, the growth of nickel consumption has mainly come from the increasing demand for power batteries, which has reached 15% of the total consumption of nickel (Wang et al., 2022; Zhou et al., 2022). China alone accounts for close to 52% of world nickel demand. Annual production of electric vehicles (comprising 49%–60% Ni wt%) will reach 31 million in 2025, increasing high pure demand from 33 kt in 2017 to 570 kt in 2025 (Meshram et al., 2019). However, the world reserves of nickel are estimated at 74 million tons of Ni metal content (U.S.-Geological-Survey, 2018). Australia (25%), Brazil (16%), Russia (10%), Cuba (7%), Indonesia (6%), South Africa (5%), Canada (3.6%) and China (3.9%) together account for around 75% of the nickel reserves. The nickel mined comes from two types of ore deposits, magmatic sulfide

deposits and laterites. Sulfide nickel ore, due to a long-term excavation, has seen a constant decline in production in China (Murofushi et al., 2022), and more than 60% of nickel ore is laterite nickel ore (Pandey et al., 2023) presently. Nevertheless, due to Indonesia's embargoes on raw ore exports (Hobson, 2013; Shi and Ju, 2023), diminishing production from Philippines' mines (Lee, 2017), and the Russian-Ukrainian war causing significant restrictions on the export of nickel (Erickson, 2022), the price of nickel ore shows an overall upward trend, with the discord between supply and demand becoming increasingly conspicuous. Thus, certain minerals, which were formerly deemed to be of low value, such as nickel arsenide ore, have become prospective contenders for nickel extraction.

Nicolite (NiAs), an ore mineral of nickel, is commonly associated with other nickel arsenides and sulfides, and classified in a group of sulfide minerals (Liu et al., 2023). NiAs is rarely used as a source of nickel due to the presence of arsenic, which is deleterious to most smelting and milling techniques. When nickel sulfide ore deposits are altered to produce NiAs, the presence of arsenic often renders the ore uneconomic when concentrations of As reach several hundred parts per million. However, arsenic bearing nickel ore may be treated by blending with "clean" ore sources, to produce a blended feedstock that can be handled with acceptable recovery by the mill and smelter. Thus, as a general rule, smelters do not accept ores containing more than 4% arsenic (China, 2015). Presently, the treatment of NiAs is primarily involved in flotation process (Iwasaki et al., 1986; Nakazawa and Iwasaki, 1986b; a; Dai et al., 2005; Senior et al., 2009). This method causes a significant water pollution, and does not effectively utilize nickel and arsenic.

To address the above problem, a method of arsenic removal from red arsenic nickel ore was proposed using sulfur roasting in the present study. In this methods, pure oxidized arsenic can be extracted by filtering the dust with porous materials. Currently, the application and development of porous intermetallic materials in gas-solid separation has proven to be an effective solution to the toxicity problem of arsenic bearing mineral (Zhang et al., 2017). The thermal stability, corrosion resistance, and high toughness of this material enable it to directly filter the high-temperature flue gas generated by the roasting process (Gao et al., 2009; Sheng et al., 2010; Jiang et al., 2018). Through filtration of dust at high-temperature and condensed arsenic compounds at low-temperature, this material may separate and extract arsenic elements from the source of smelting.

The aim of this study is to explore an arsenic removal from NiAs by controlling arsenic-containing phases. The process of arsenic removal by sulfur roasting was proposed by comparing thermodynamic data, and additions of S and FeS were verified a suggestion methods.

2 Raw materials and methods

2.1 Raw materials

The raw materials used in the experiment came from the mines in Yunnan. The results of mineral elements detected by ICP showed that the main elements were As (18.6 wt%) and Ni (16.1 wt%). The

mineral composition was analyzed by XRD, and the main mineral components were NiAs (34.7 wt%) and SiO₂ (65.3 wt%).

2.2 Thermodynamic approaches

Thermodynamic analysis was performed using the equilibrium composition module in HSC Chemistry[®] 6.0. The thermodynamic data of specific substances were obtained from database module of HSC and CRC handbook of chemistry and physics (Internet Version 2016) (96th). Specifically, the Gibbs free energy (GFE) of all reactions can be calculated by Formula 1 and the occurrence of the reaction in the corresponding temperature range can be determined by Formula 1.

$$\Delta_r G_m(T) = \Delta_r H_m(T) - T \Delta_r S_m(T) \quad (1)$$

In the equation, $\Delta_r G_m$ is GFE, $\Delta_r H_m$ is enthalpy, $\Delta_r S_m$ is entropy, and T is temperature.

The relationship between GFE and reactants was established by Formula 2.

$$\Delta_r G_m(T) = \Delta_r G_m^\theta(T) + RT \ln Q \quad (2)$$

When the reaction is in equilibrium, $\Delta_r G_m(T) = 0$ and $Q = K^\theta$, thus Formula 3 can be derived.

$$\Delta_r G_m^\theta(T) = -RT \ln K^\theta \quad (3)$$

In the equation, $\Delta_r G_m^\theta$ is standard GFE, R is molar gas constant, Q is reaction quotient, and K^θ is equilibrium quotient.

K^θ , as derived from Formula 4, is the ratio of the concentration entropy of the products to that of the reactants at equilibrium, and the gas components are the ratio of partial pressures.

$$K^\theta = \prod (P_j \hat{n}_j)_{\text{product}} / \prod (P_i \hat{n}_i)_{\text{reactant}} \quad (4)$$

In the equation, P is partial pressures, j is product, i is reactant, and n is chemical coefficient.

Finally, Formula 5 was used to obtain the ratio of molar amounts of the gas components as the ratio of partial pressures:

$$PV = nRT \quad (5)$$

By combining the above formulas, the equilibrium molar amount of each component of the reactants at a specific temperature may be calculated step by step.

2.3 TG/DTA method

Concurrent TG/DTA (SDT 650, WATERS CORPORATION) was used to identify various reactions on the basis of weight changes as well as thermal effects. Tests were done under flowing nitrogen or air and at a heating rate of 20°C/min.

2.4 Experimental method

A schematic diagram of the roasting setup is presented in Figure 1. The air was pumped into the gas mixing system through

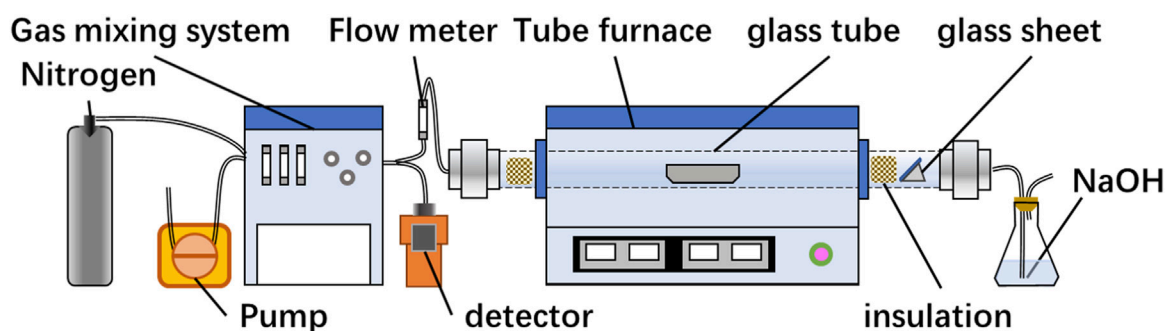


FIGURE 1
Roasting experimental setup.

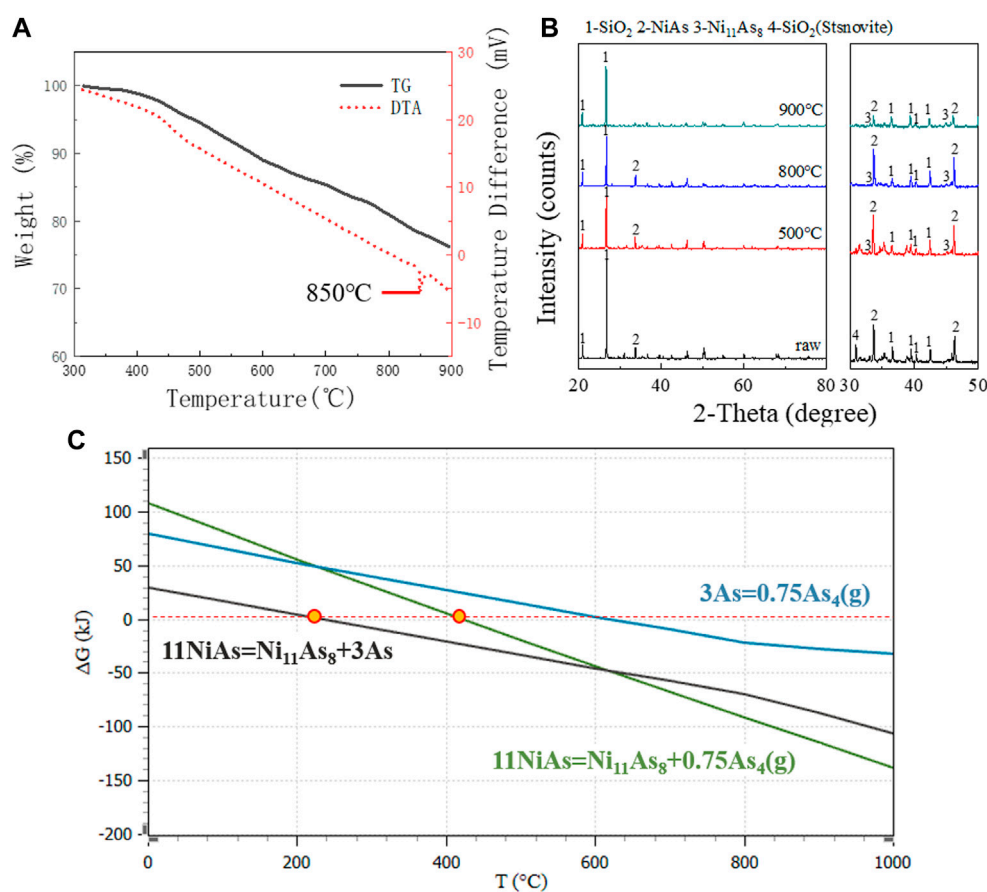


FIGURE 2
DTA, TG and XRD images in anaerobic conditions. (A) TG/DTA diagram for raw ore in nitrogen. (B) XRD patterns for raw ore roasting at 900°C, 800°C, and 500°C. (C) GFE for decomposition reaction of NiAs.

a peristaltic pump and combined with nitrogen. The resultant mixture was then divided into two parts, one part entering the gas detector for oxygen content detection and other part entering the tube furnace, regulated by the gas flow meter. For each experiment, the crucible containing a mineral of the requisite

mass was placed in a furnace and heated to the specified temperature. The glass pane was situated behind the insulation to collect the volatilized condensate from the concentrate. Subsequently, the gas was purified using a sodium hydroxide solution before being discharged.

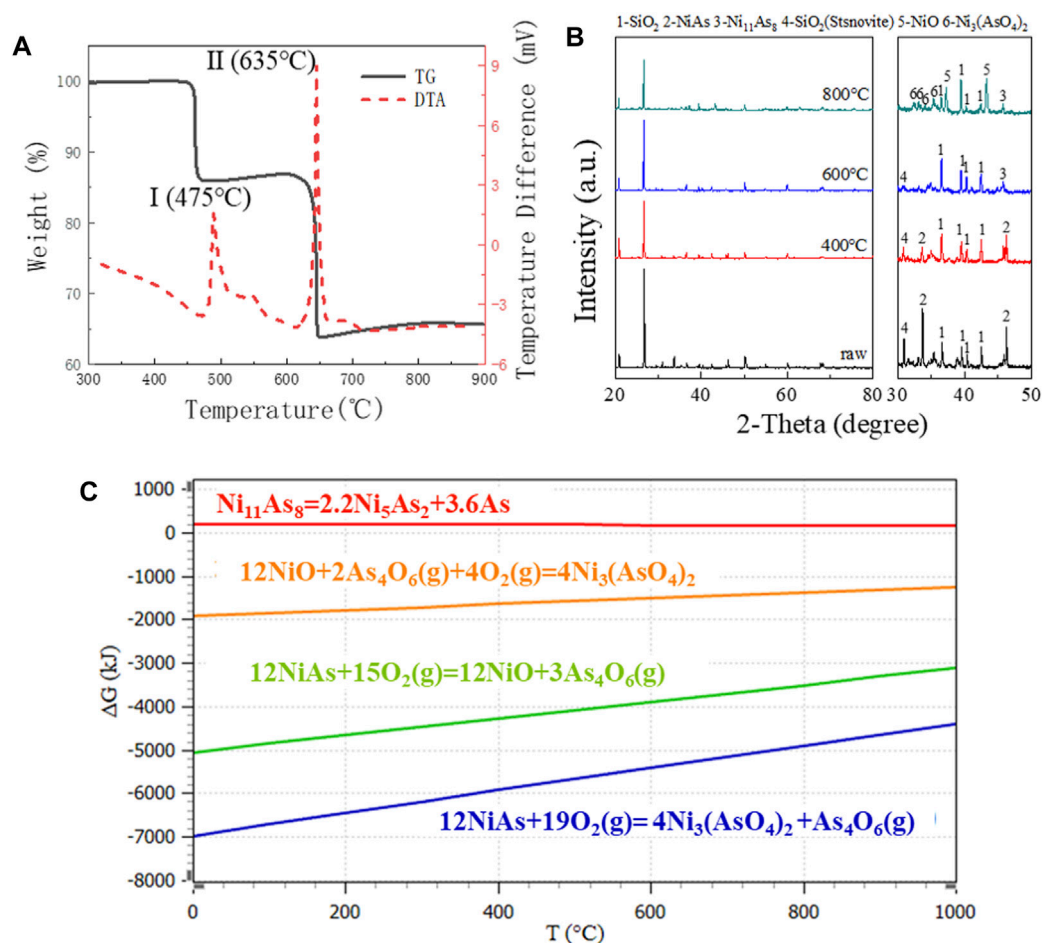


FIGURE 3

TG diagram, XRD pattern and GFE data in oxygen presence at various temperatures. (A) TG/DTA diagram for raw ore in air. (B) XRD pattern for raw ore roasting in 800°C, 600°C, and 400°C. (C) GFE for oxidation reaction of NiAs.

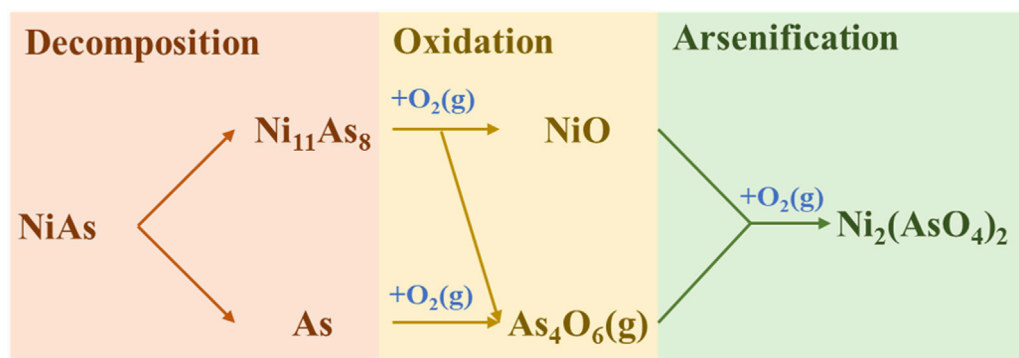


FIGURE 4

Reaction mechanism of direct roasting.

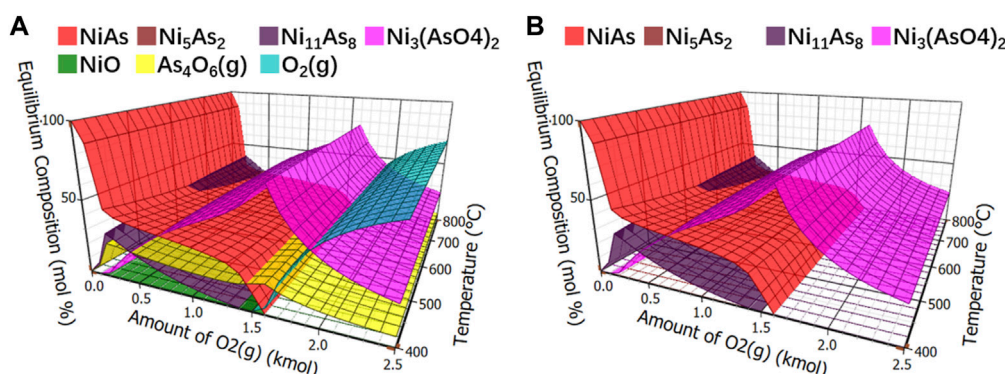


FIGURE 5

Calculation of equilibrium components in oxidation roasting. (A), Equilibrium component of oxidative roasting. (B), Equilibrium component of arsenide nickel and arsenate nickel in oxidative roasting.

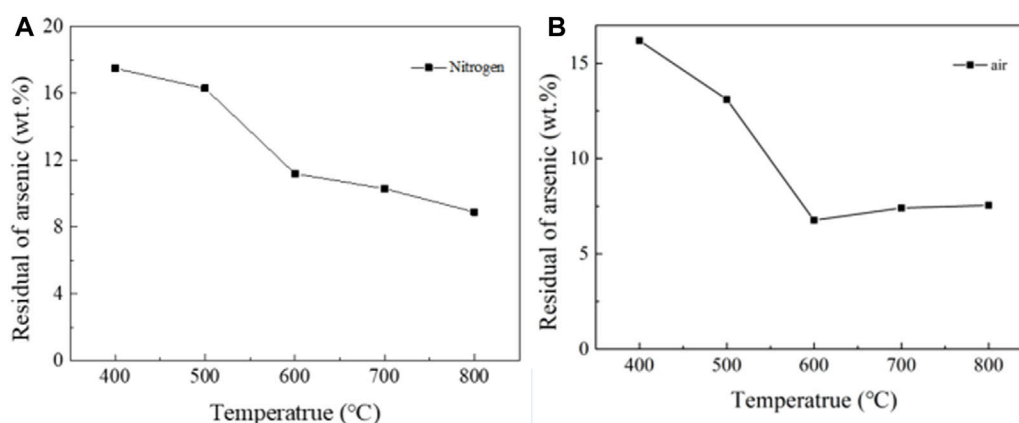


FIGURE 6

Roasting experiment of NiAs in nitrogen and air. (A), Roasting experiment of NiAs in nitrogen. (B), Roasting experiment of NiAs in air.

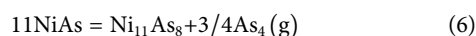
3 Results and discussion

3.1 The limitation of direct roasting

3.1.1 Reaction mechanism

Direct roasting refers to adjusting the reaction only by controlling the oxygen content without addition.

In anaerobic conditions, DTA and TG images showed a continuous decrease after 300°C (Figure 2A). The XRD images showed that $\text{Ni}_{11}\text{As}_8$ was generated at 500°C, 800°C and 900°C (Figure 2B). According to the report of L.J Wilson (Wilson and Mikhail, 1987), $\text{Ni}_{11}\text{As}_8$ decomposes according to reaction (6).



However, by comparing the XRD images, it was found that the peak of NiAs changed little at 500°C and 800°C, and the peak of NiAs decreased significantly when the temperature reached 900°C. This indicates that the main temperature of reaction (6) is above 800°C. The DTA image showed that there is an endothermic peak around 850°C, which corresponds to the

boiling temperature of Arsenic (816°C). Finally, by comparing the GFE (Figure 2C) of reaction, the reaction of NiAs decomposing to produce As started at about 248°C, while the reaction of NiAs decomposing to produce $\text{As}_4(\text{g})$ started at about 420°C. Comparing the two reactions, the reaction of NiAs decomposing to produce As was more consistent with the process of weight loss shown by the TG image. And the GFE of NiAs decomposition reaction was less than that of As volatilization reaction. The above evidence shows that NiAs decomposition may be divided into two reactions (7) and (8).



In the presence of oxygen, the thermal activities which appear on the DTA diagram and the corresponding weight changes on the TG diagram of Figure 3A may be explained as follows.

Peak I, The oxidation of NiAs in air started around 475°C, and resulted in a substantial exothermic peak. XRD results (Figure 3B) indicated that the reaction product associated with peak I is $\text{Ni}_{11}\text{As}_8$, and the reaction at this stage may be represented by the following equation.

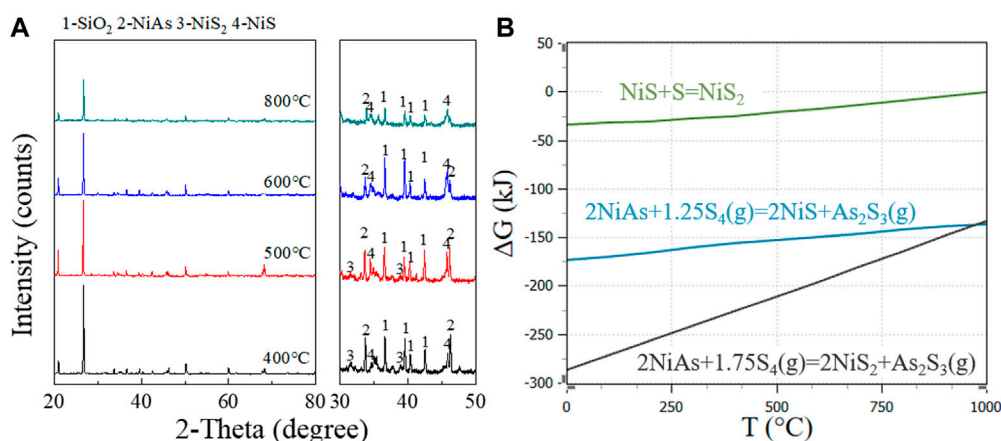


FIGURE 7

NiS₂ and NiS formation at different temperatures in sulfidation roasting. (A), XRD patterns for adding sulfide roasting at 800°C, 600°C, 500°C, and 400°C. (B), GFE for adding sulfide reaction of NiAs.

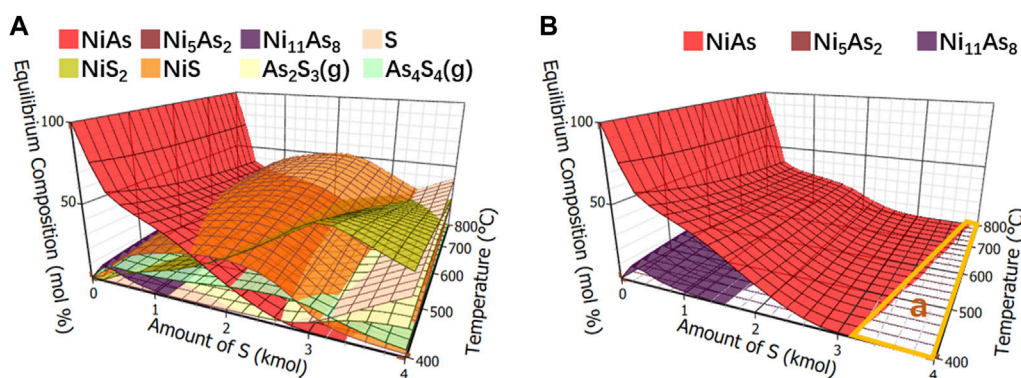


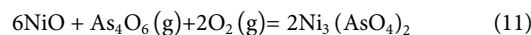
FIGURE 8

Calculation of equilibrium components in sulfide roasting. (A), Equilibrium component of adding sulfide roasting. (B), Equilibrium component of arsenide nickel and arsenate nickel in adding sulfide roasting.



It is possible that the reaction (9) occurs via a two-step mechanism which consists of an endothermic thermal dissociation of NiAs reaction (7) and a highly exothermic reaction between As₄ and O₂(g) to form As₄O₆(g) vapour. However, the reaction free energy profile suggests that the GFE of the reaction between As₄ and O₂(g) to form As₄O₆(g) is considerably lower than that of reaction (7), indicating that As₄ would be oxidized immediately upon formation, thus reaction (9) should be regarded as a whole.

Peak II, When the temperature exceeded 635°C, the second peak of DTA was generated, while the TG experienced a significant weight loss. XRD results indicated that the reaction product associated with peak I was NiO and Ni₃(AsO₄)₂ (Figure 3B), at this stage, it may be represented by the following Eqs 10, 11.



The reaction (10) occurs through a two-step mechanism which consists of an endothermic thermal dissociation of Ni₁₁As₈ and oxidation of Ni₅As₂. However, the reaction GFE data suggested that the GFE of dissociation of Ni₁₁As₈ to Ni₅As₂ was higher than zero, indicating that the reaction did not proceed spontaneously and the presence of Ni₅As₂ cannot be found in the XRD image, thus the reaction cannot be regarded as two steps. Meanwhile, due to the low GFE of formation of Ni₃(AsO₄)₂, Ni₃(AsO₄)₂ may definitely be generated during NiAs oxidation (Figure 3C).

In summary, the direct oxidation process of NiAs may be concluded into three stages (Figure 4). Firstly, the decomposition, where part of the As in NiAs volatilizes to form Ni₁₁As₈. Secondly, oxidation, where the oxidation of As yields As₄O₆ and the oxidation of Ni₁₁As₈ yields NiO and As₄O₆. Lastly, the excessive oxidation of NiO yields Ni₃(AsO₄)₂.

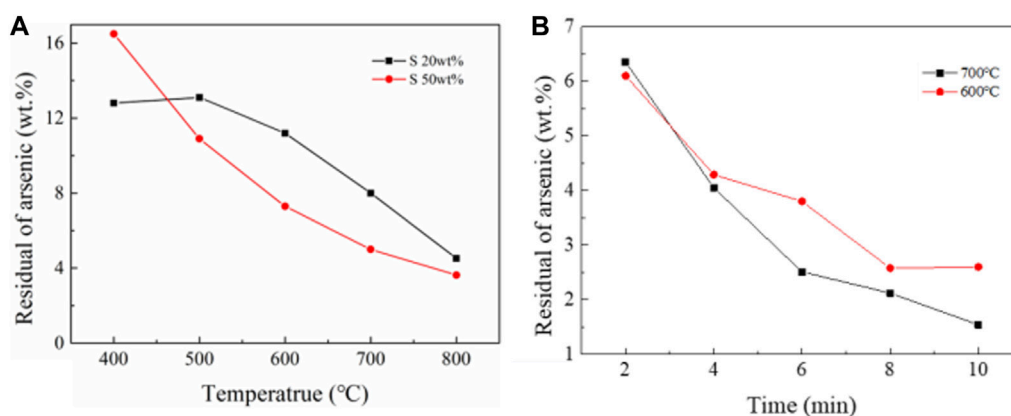


FIGURE 9

NiAs roasting experiments. (A), Oxidation roasting experiment of NiAs. (B), Reduction roasting experiment of NiAs.

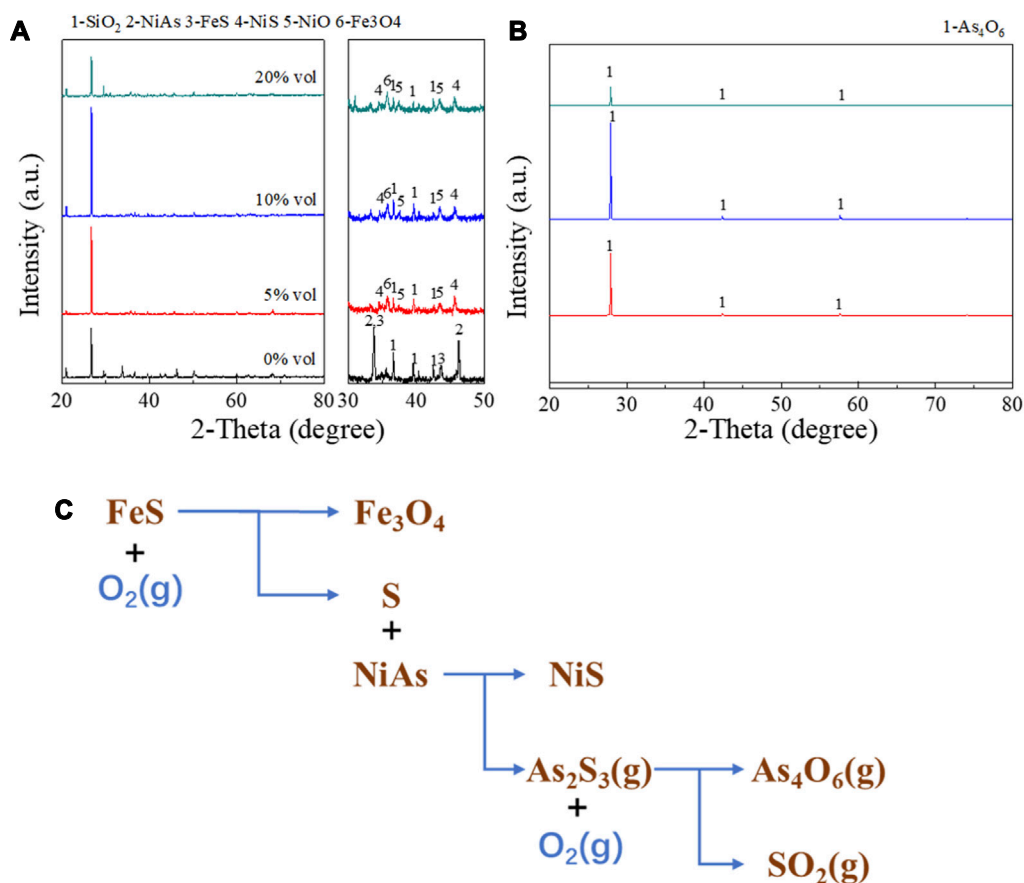


FIGURE 10

XRD detection on the roasted products and condensates with various oxygen content. (A), XRD pattern of roasted products. (B), XRD pattern of condensates. (C), Reaction mechanism of adding FeS roasting.

3.1.2 Thermodynamic equilibrium component

Controlling the amount of oxygen is the most direct method for controlling oxygen content. The initial quantity of thermodynamic

equilibrium components was 1 kmol NiAs, and different contents of oxygen were added to observe the content of products in mol percentage at different temperatures. The calculation results of

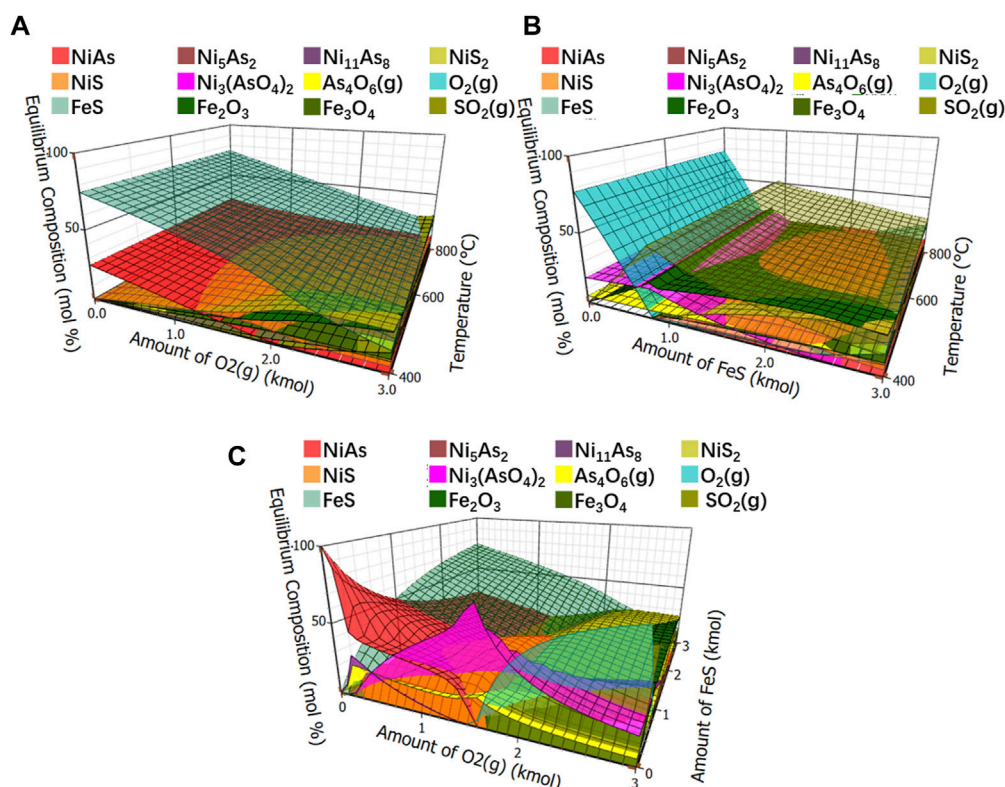


FIGURE 11

Equilibrium compositions of roasted arsenic nickel ore. (A), Equilibrium component of fixed ratio of NiAs to FeS. (B), Equilibrium component of fixed ratio of NiAs to O_2 . (C), Equilibrium component of fixed temperature to 400°C.

components in oxidation roasting balance were shown in Figure 5A, which are relatively complex. In order to facilitate observation, other compounds were removed, and arsenide nickel and arsenate nickel were simplified, as shown in Figure 5B.

In Figure 5B, arsenide nickel and arsenate nickel were overlapped. Under low oxygen condition, the reaction of NiAs was not complete, and the product $Ni_{11}As_8$ still contained a large amount of arsenic. When the oxygen level was slightly increased, it may generate the difficult-to-volatilize $Ni_3(AsO_4)_2$. Therefore, arsenate nickel or arsenide nickel is definitely produced in the oxidation roasting process.

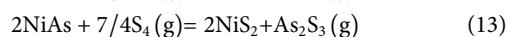
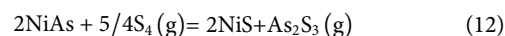
3.1.3 Roasting experiment

The results of NiAs roasting experiment were shown in Figure 6, the roasting conditions were 30 min of time and 1L/min of gas flow rate. When roasting in nitrogen, the arsenic content gradually decreased and reached 8.9 wt% at 800°C, which shows that the effect of roasting without oxygen is poor (Figure 6A). When roasting in air, the arsenic content suddenly decreased when the temperature reached 600°C and kept around 5.5 wt% at subsequent temperatures (Figure 6B). The roasting effect was still not satisfactory. Therefore, direct roasting needs to reduce the roasting of $Ni_3(AsO_4)_2$ and then oxidize the roasting to remove arsenic. Such a process was repeated to reduce the arsenic content, which makes the direct roasting process for removing arsenic complicated and tedious.

3.2 Research on adding sulfide roasting

3.2.1 Reaction mechanism

Adding sulfur as a carrier for arsenic volatilization may change the oxidation process to sulfidation process. After sulfidation, the main substances formed are $As_2S_3(g)$, NiS, NiS_2 , and S. The roasting process without oxygen prevents the occurrence of arsenic oxidation. Figure 7A shows the substances formed at different temperatures during the sulfidation roasting of the ore. NiS_2 and NiS are the main products. The reaction equation is inferred as follows (12) and (13).



Additionally, sulfur started to break the cycle from S_8 when heated to form a long chain, and the chain shortened with increasing temperature and finally boil at 444.6°C. At this time, there were molecules such as $S_8(g)$, $S_6(g)$, $S_4(g)$, $S_2(g)$ in sulfur vapor. Here, $S_4(g)$ with the lowest molar GFE was chosen for reaction equation discussion.

From the reaction GFE (Figure 7B), under lower temperature and sufficient sulfur condition, NiS_2 was preferentially formed. With the increase of temperature, NiS_2 gradually decreased while NiS increased gradually, which is consistent with the change of peak in the XRD pattern.

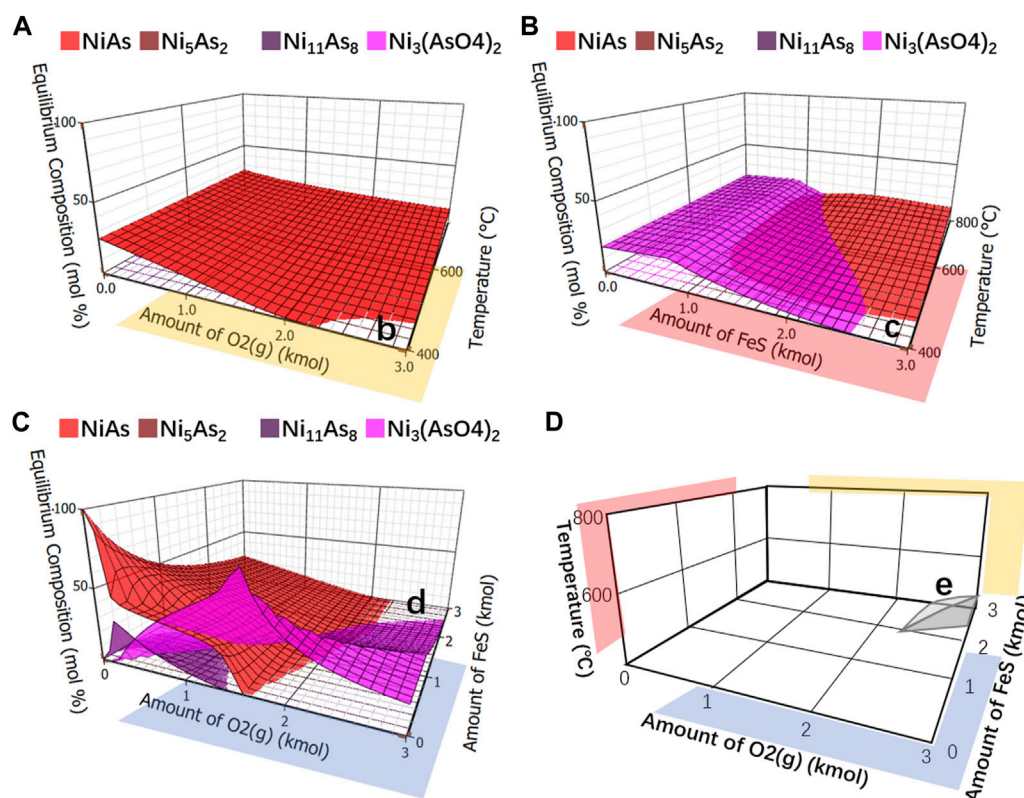


FIGURE 12

Equilibrium component of arsenide nickel and arsenate nickel. (A), Analysis of arsenide nickel and arsenate nickel O_2 as x-axis and temperature as y-axis. (B), Analysis of arsenide nickel and arsenate nickel FeS as x-axis and temperature as y-axis. (C), Integrate analysis of arsenide nickel and arsenate nickel O_2 as x-axis and FeS as y-axis. (D), Merging areas of b, c, (D) using temperature as z-axis, FeS as y-axis, and O_2 as x-axis.

3.2.2 Thermodynamic equilibrium component

The calculation results of components in adding sulfide roasting balance were shown in Figure 8A. Other compounds were removed and only arsenide nickel and arsenate nickel were simplified, as shown in Figure 8B. Since there was no oxygen, arsenate nickel was not produced. It was found that when the addition of S is greater than 3 kmol, an area “a” appears where no arsenate nickel or arsenide nickel is produced. Collectively, the arsenic removal of arsenide nickel needs to be carried out under adding sulfide roasting.

3.2.3 Roasting experiment

The results of NiAs adding sulfide roasting experiment were shown in Figure 9A. When the roasting conditions were time of 30 min, nitrogen atmosphere, and gas flow rate of 1L/min, the remaining arsenic content decreased gradually with the increase of temperature. And the higher the sulfur content, the better the arsenic removal effect. However, at 400°C, the arsenic removal efficiency of high sulfur content was lower, which was due to the low volatilization rate of sulfur at 400°C and hindered the volatilization of arsenic sulfide. However, when the gas flow rate increased to 2 L/min, the roasting effect with sulfur addition was significantly improved. In Figure 9B, the roasting conditions were nitrogen atmosphere, gas flow rate of 2 L/min, and sulfur content 20 wt%, the reaction was almost completed in 10 min, and the arsenic content dropped to 1.54 wt% at 700°C.

In summary, sulfur is used as reducing agent, and arsenic volatilizes in the form of arsenic sulfide. Due to the poor volatility of arsenic sulfide, high gas flow rate is needed to reduce the partial pressure of arsenic sulfide in the roasting environment. When the gas flow rate is high, roasting with sulfur addition has a good effect on arsenic removal.

3.3 Research on adding FeS roasting

3.3.1 Reaction mechanism

In Figure 10, the experiment conducted XRD detection on the roasted products and condensates with oxygen content of 0% vol, 5% vol, 10% vol and 20% vol, with other conditions of 1h roasting time and 1 L/min gas flow rate. The results were shown in Figures 10A, B. When the oxygen content rose to 5%–20%, the roasted products were NiS, NiO, and Fe_3O_4 , and the condensate was pure As_4O_6 . This indicated that in this range of oxygen content, arsenic may be removed in the form of As_4O_6 . And it may be represented by the reaction Eq. 14.



However, when there was no oxygen, NiAs and FeS did not react basically, and the condensate obtained was also basically zero. This suggested that FeS cannot react directly with NiAs. Experiments

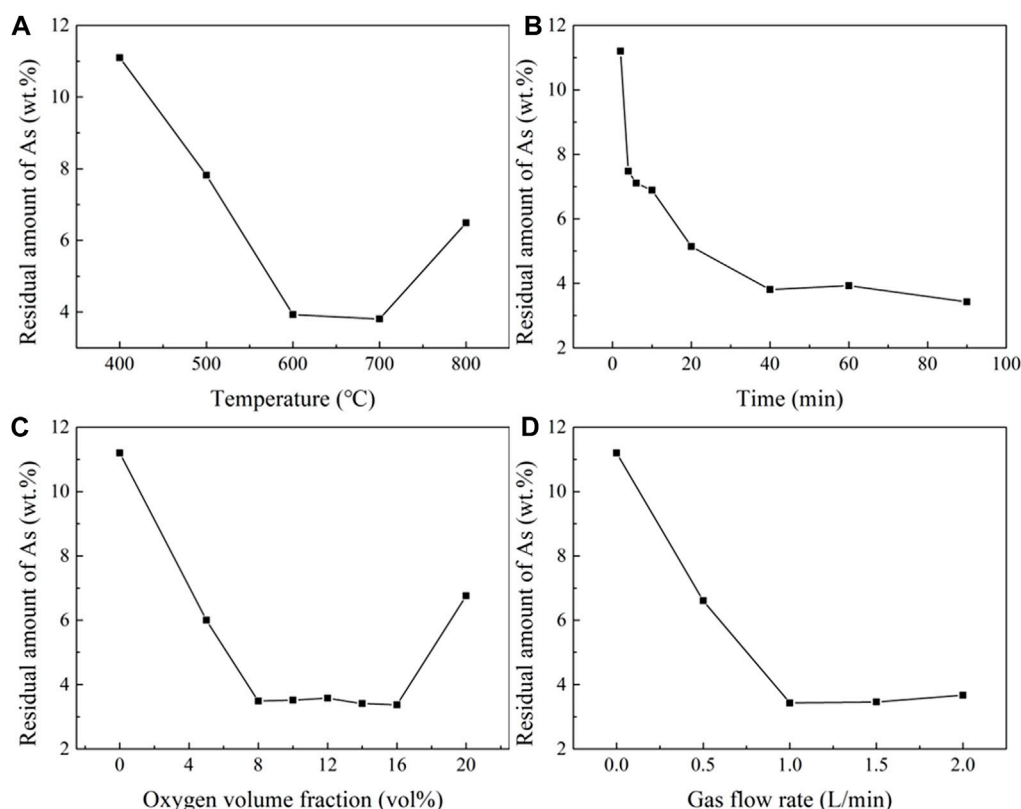
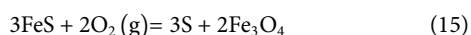


FIGURE 13

Influence of temperature, time, oxygen, and gas flow velocity on residual arsenic. (A), Effect of temperature (time 60 min, Flow rate 1 L/min, oxygen volume fraction 10 vol%). (B), Effect of time (temperature 600°C, flow rate 1 L/min, oxygen volume fraction 10 vol%). (C), Oxygen volume fraction (temperature 600°C, time 60 min, flow rate 1L/min). (D), Effect of flow rate (temperature 700°C, time 30 min, oxygen volume fraction 10% vol).

conducted by J.G.Dunn (Dunn, 1997) has explained this issue, where FeS generated S during oxidation and proposed a reaction (15) for this phenomenon.



Therefore, it may be concluded that the reaction (14) is decomposed into reactions (12), reaction (15), and oxidation of arsenic sulfide.

The final process of the roasting with FeS addition was summarized by Figure 10C, and the entire process is divided into three stages. Firstly, the decomposition of FeS occurs, then the sulfuration of NiAs, and finally the oxidation of arsenic sulfide.

3.3.2 Thermodynamic equilibrium component analysis

The equilibrium compositions of the roasted arsenic nickel ore after adding FeS were shown in Figure 11. Figure 11A shows the effect of oxygen and temperature on the equilibrium composition with a fixed ratio of NiAs to FeS of 1:3. Figure 11B shows the effect of FeS and temperature on the equilibrium composition with a fixed ratio of NiAs to O₂ of 1:3. Figure 11C shows the effect of O₂ and FeS on the equilibrium composition with a fixed temperature of 400°C and a ratio of 1:3.

After being removed other compounds and left only arsenic nickel and arsenate nickel, the simplified ones were respectively showed in Figures 12A–C. It was observed blank areas b, c and d in

Figures 12A–C, and no arsenate nickel or arsenic nickel was generated in these areas. By merging these areas, with temperature as the z-axis, the amount of FeS as the y-axis and the amount of O₂ as the x-axis, Figure 12D is formed, in which the three-dimensional area e is the area where no arsenate nickel or arsenic nickel is generated. Observing this area, it may be found that the higher the reaction temperature, the higher the FeS and O₂ required, which indicates that arsenic needs to be reduced as much as possible to reduce the reaction temperature.

3.3.3 Roasting experiment

The optimizing conditions during roasting experiment were explored with a 5g sample and a ratio of 2:1 between the mineral and FeS. In Figure 13A, the influence of temperature on the residual arsenic content was displayed a rapid decrease as the temperature increased from 500°C to 700°C. However, as the temperature continued to increase, the arsenic content began to rise due to the rapid decrease in the free energy of Ni₁₁As₈. Thus, it is necessary to control the roasting temperature below 600°C, when the residual arsenic content is 3.93 wt%.

In Figure 13B, the influence of time on the residual arsenic content was shown that at a minimum value at 40 min most of the arsenic was removed. When the time was extended to 60 min, the amount of residual arsenic increased due to the continuous volatilization of sulfur in the FeS, and the residual arsenic content dropped to 3.43 wt% when the time reached 90 min.

Figure 13C illustrates the impact of oxygen content on the residual arsenic content. The slight fluctuations were observed in the oxygen content range 8%–16% vol. The lowest residual arsenic content achieved was 3.37 wt% at 16 vol% oxygen content.

Figure 13D shows the effect of gas flow velocity on the residual arsenic content. The lowest residual arsenic content was seen at 3.34 wt% when the gas flow was 1 L/min. However, the residual arsenic content increased when the flow rate exceeded this value, due to the influence of gas flow velocity on the total amount of oxygen. When S was added as the reductant, the residual arsenic content was reduced to 1.54 wt% at 700°C and a gas flow rate of 2.0 L/min. When FeS was added as the reductant, the residual arsenic content was reduced to 3.34 wt% at 600°C, roasting time of 60 min, oxygen volume fraction of 10 vol%, and gas flow rate of 1.0 L/min.

4 Conclusion

Through thermodynamic calculation and comparison of oxidation roasting and reduction roasting, it was confirmed that oxidation roasting process cannot be used for arsenic removal from NiAs. Sulfur is employed as a reducing agent, and arsenic volatilizing as arsenic sulfide is produced. As arsenic sulfide has low volatility, a high rate of gas flow is required to reduce the partial pressure of arsenic sulfide in the roasting atmosphere. When the gas flow rate is increased, sulfur addition proves to be effective in removing arsenic.

In the thermodynamic analysis of FeS roasting, the following three points were found: 1) The high roasting temperature produces nickel arsenate or nickel arsenide, which is not conducive to arsenic removal; 2) The addition of oxygen is necessary for FeS reduction roasting process, and the control of oxygen has a great influence on the process; 3) There is an area where nickel arsenate or nickel arsenide should be avoided when FeS and oxygen are in a certain proportion.

Finally, the FeS reduction roasting process is an optimal strategy for for arsenic removal from NiAs. The use of FeS as the reductant significantly reduces the residual arsenic content.

Data availability statement

The original contributions presented in the study are included in the article/Supplementary Material, further inquiries can be directed to the corresponding author.

References

- China, M. (2015). *Non ferrous metal industry standards of the people's Republic of China*. Beijing, China: Standards Press of China.
- Dai, Z., Garritsen, J., Wells, P. F., and Xu, M. (2005). Arsenic rejection in the flotation of garson Ni-Cu Ore. <https://www.ausimm.com/publications/conference-proceedings/centenary-of-flotation-symposium/arsenic-rejection-in-the-flotation-of-garson-ni-cu-ore/>.
- Dunn, J. G. (1997). The oxidation of sulphide minerals. *Thermochim. Acta* 300 (1), 127–139. doi:10.1016/S0040-6031(96)03132-2
- Erickson, C. (2022). Nickel price spike during Russia-Ukraine conflict could drive up EV costs. Available: <https://www.spglobal.com/marketintelligence/en/news-insights/latest-news-headlines/nickel-price-spike-during-russia-ukraine-conflict-could-drive-up-ev-costs-69130867>.
- Gao, H., He, Y., Shen, P., Zou, J., Xu, N., Jiang, Y., et al. (2009). Porous FeAl intermetallics fabricated by elemental powder reactive synthesis. *Intermetallics* 17 (12), 1041–1046. doi:10.1016/j.intermet.2009.05.007
- Hobson, M. (2013). Indonesia ore export banrnsen boosting nickel prices. *Platt's Met. Dly.* 2 (247), 9–10.
- INSG (2013). Nickel usage. Available: <https://insg.org/index.php/about-nickel/production-usage/> (Accessed August, 2021).
- Iwasaki, I., Weiblen, P. W., Reid, K. J., Ryan, P. J., and Malicsi, A. S. (1986). Platinum group and arsenide minerals in copper-nickel sulfide bearing duluth gabbro and their flotation recoveries. *Trans. SME AIME* 280, 1983–1988.
- Jiang, Y., He, Y., and Liu, C. T. (2018). Review of porous intermetallic compounds by reactive synthesis of elemental powders. *Intermetallics* 93, 217–226. doi:10.1016/j.intermet.2017.06.003
- Lee, W. (2017). Philippines DMCI's H1 nickel ore shipments fall 71% on year. *Platts Met. Dly.* (6-161).
- Liu, J., Li, Z., Zhou, Y., Wang, L., Wang, G., Jiang, P., et al. (2023). Distribution, geology and development status of nickel deposits. *Geol. China* 40 (1), 118–132. doi:10.12029/gc20210225002

Author contributions

XT: Investigation, Writing–original draft. YH: Conceptualization, Project administration, Writing–review and editing.

Funding

The author(s) declare financial support was received for the research, authorship, and/or publication of this article. This work was supported in part by the National Key Research and Development Plan of Ministry of Science and Technology of China (2019YFF0216502), and Major Science and Technological Innovation Project of Hunan Province (2021SK1020-4).

Acknowledgments

We thank Professor Chaoqun Peng in Central South University for contribution and helpful discussion. We appreciate the contribution of the various members in the Powder Metallurgy Research Institute and the State Key Laboratory of Powder Metallurgy, Central South University.

Conflict of interest

The authors declare that the research was conducted in the absence of any commercial or financial relationships that could be construed as a potential conflict of interest.

The reviewer QZ declared a shared affiliation with the authors to the handling editor at the time of review.

Publisher's note

All claims expressed in this article are solely those of the authors and do not necessarily represent those of their affiliated organizations, or those of the publisher, the editors and the reviewers. Any product that may be evaluated in this article, or claim that may be made by its manufacturer, is not guaranteed or endorsed by the publisher.

- Meshram, P., Abhilash, and Pandey, B. D. (2019). Advanced review on extraction of nickel from primary and secondary sources. *Mineral Process. Extr. Metallurgy Rev.* 40 (3), 157–193. doi:10.1080/08827508.2018.1514300
- Murofushi, A., Otake, T., Sanematsu, K., Ya, K. Z., Ito, A., Kikuchi, R., et al. (2022). Mineralogical evolution of a weathering profile in the Tagaung Taung Ni laterite deposit: significance of smectite in the formation of high-grade Ni ore in Myanmar. *Miner. Deposita* 57 (7), 1107–1122. doi:10.1007/s00126-021-01089-6
- Nakazawa, H., and Iwasaki, I. (1986a). Flotation behavior of nickel arsenide. *Int. J. Mineral Process.* 18 (3–4), 191–202. doi:10.1016/0301-7516(86)90017-7
- Nakazawa, H., and Iwasaki, I. (1986b). Galvanic contact between nickel arsenide and pyrrhotite and its effect on flotation. *Int. J. Mineral Process.* 18 (3–4), 203–215. doi:10.1016/0301-7516(86)90018-9
- Pandey, N., Tripathy, S. K., Patra, S. K., and Jha, G. (2023). Recent progress in hydrometallurgical processing of nickel lateritic ore. *Trans. Indian Inst. Metals* 76 (1), 11–30. doi:10.1007/s12666-022-02706-2
- Pariser, H. H., Backeberg, N. R., Masson, O. C. M., and Bedder, J. C. M. (2018). Changing nickel and chromium stainless steel markets-a review. *J. South. Afr. Inst. Min. Metallurgy* 118 (6), 563–568. doi:10.17159/2411-9717/2018/v118n6a1
- Poole, J., Thornhill, J., Lee, A., Zhu, W., and Suga, M. (2022). How skyrocketing nickel prices may impact the clean energy drive. *Environ. Energy Rep.* (3).
- Senior, G. D., Smith, L. K., Silvester, E., and Bruckard, W. J. (2009). The flotation of gersdorffite in sulphide nickel systems - a single mineral study. *Int. J. Mineral Process.* 93 (2), 165–171. doi:10.1016/j.minpro.2009.07.009
- Sheng, P., Gao, L., Gao, H., and He, Y. (2010). High-temperature sulfidation behavior and application in SO₂-containing gas cleanup of porous FeAl intermetallics. *Mater. Sci. Eng. Powder Metallurgy* 15 (1), 38–43. doi:10.1097/00007890-197412000-00013
- Shi, C., and Ju, Y., (2023). China's Lygend produces first batch of nickel sulfate in Indonesia. *Platts Met. Dly.*
- U.S.-Geological-Survey, (2018). *Mineral commodity summaries 2017*. Virginia, VA, USA: U.S. Geological Survey.
- Wang, L., Wang, J., Wang, L., Zhang, M., Wang, R., and Zhan, C. (2022). A critical review on nickel-based cathodes in rechargeable batteries. *Int. J. Minerals Metallurgy Mater.* 29 (5), 925–941. doi:10.1007/s12613-022-2446-z
- Wilson, L. J., and Mikhail, S. A. (1987). Investigation of the oxidation of niccolite by thermal analysis. *Thermochim. Acta* 112 (2), 197–213. doi:10.1016/0040-6031(87)88277-1
- Zhang, H., Liu, X., Jiang, Y., Gao, L., Yu, L., Lin, N., et al. (2017). Direct separation of arsenic and antimony oxides by high-temperature filtration with porous FeAl intermetallic. *J. Hazard. Mater.* 338, 364–371. doi:10.1016/j.jhazmat.2017.05.049
- Zhou, D., Guo, X., Zhang, Q., Shi, Y., Zhang, H., Yu, C., et al. (2022). Nickel-Based materials for advanced rechargeable batteries. *Adv. Funct. Mater.* 32 (12). doi:10.1002/adfm.202107928



OPEN ACCESS

EDITED BY

Steve Suib,
University of Connecticut, United States

REVIEWED BY

Lixue Cheng,
Microsoft Research, Germany
Qiyuan Zhao,
University of Michigan, United States

*CORRESPONDENCE

Hafiz Saqib Ali,
✉ hafiz.ali@chem.ox.ac.uk
Sam P. de Visser,
✉ sam.devisser@manchester.ac.uk

RECEIVED 04 January 2024

ACCEPTED 22 January 2024

PUBLISHED 08 February 2024

CITATION

Ali HS and de Visser SP (2024), Catalytic divergencies in the mechanism of L-arginine hydroxylating nonheme iron enzymes.
Front. Chem. 12:1365494.
doi: 10.3389/fchem.2024.1365494

COPYRIGHT

© 2024 Ali and de Visser. This is an open-access article distributed under the terms of the [Creative Commons Attribution License \(CC BY\)](https://creativecommons.org/licenses/by/4.0/). The use, distribution or reproduction in other forums is permitted, provided the original author(s) and the copyright owner(s) are credited and that the original publication in this journal is cited, in accordance with accepted academic practice. No use, distribution or reproduction is permitted which does not comply with these terms.

Catalytic divergencies in the mechanism of L-arginine hydroxylating nonheme iron enzymes

Hafiz Saqib Ali^{1*} and Sam P. de Visser^{2*}

¹Chemistry Research Laboratory, Department of Chemistry and the INEOS Oxford Institute for Antimicrobial Research, University of Oxford, Oxford, United Kingdom, ²Manchester Institute of Biotechnology and Department of Chemical Engineering, The University of Manchester, Manchester, United Kingdom

Many enzymes in nature utilize a free arginine (L-Arg) amino acid to initiate the biosynthesis of natural products. Examples include nitric oxide synthases, which generate NO from L-Arg for blood pressure control, and various arginine hydroxylases involved in antibiotic biosynthesis. Among the groups of arginine hydroxylases, several enzymes utilize a nonheme iron(II) active site and let L-Arg react with dioxygen and α -ketoglutarate to perform either C₃-hydroxylation, C₄-hydroxylation, C₅-hydroxylation, or C₄–C₅-desaturation. How these seemingly similar enzymes can react with high specificity and selectivity to form different products remains unknown. Over the past few years, our groups have investigated the mechanisms of L-Arg-activating nonheme iron dioxygenases, including the viomycin biosynthesis enzyme VioC, the naphthyridinomycin biosynthesis enzyme NapI, and the streptothricin biosynthesis enzyme OrfP, using computational approaches and applied molecular dynamics, quantum mechanics on cluster models, and quantum mechanics/molecular mechanics (QM/MM) approaches. These studies not only highlight the differences in substrate and oxidant binding and positioning but also emphasize on electronic and electrostatic differences in the substrate-binding pockets of the enzymes. In particular, due to charge differences in the active site structures, there are changes in the local electric field and electric dipole moment orientations that either strengthen or weaken specific substrate C–H bonds. The local field effects, therefore, influence and guide reaction selectivity and specificity and give the enzymes their unique reactivity patterns. Computational work using either QM/MM or density functional theory (DFT) on cluster models can provide valuable insights into catalytic reaction mechanisms and produce accurate and reliable data that can be used to engineer proteins and synthetic catalysts to perform novel reaction pathways.

KEYWORDS

QM/MM, cluster models, enzyme catalysis, inorganic reaction mechanisms, iron enzymes, dioxygenases

1 Introduction

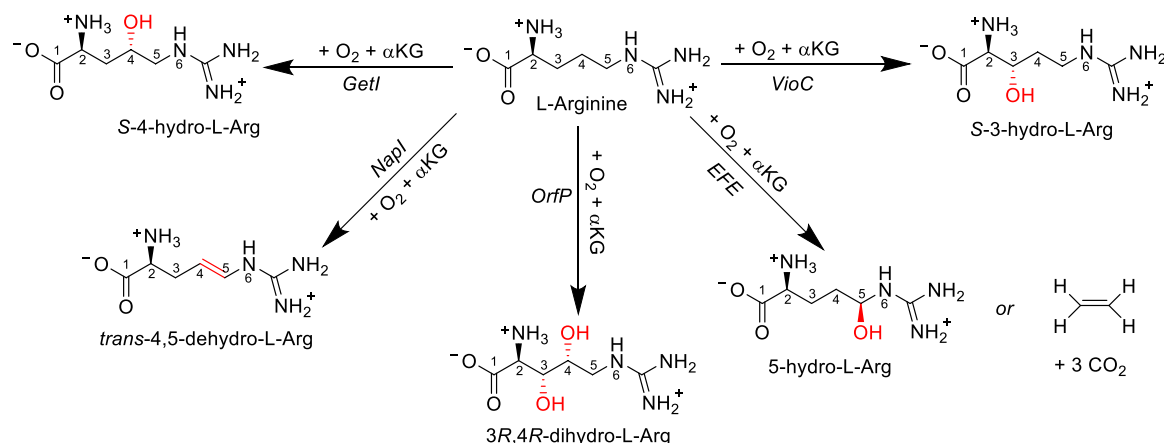
The 20 standard amino acids play crucial roles in biology and serve as fundamental building blocks in the design of many biological structures and natural products. They serve as both the constituents of macromolecular protein polymers and as platforms for the synthesis of small-molecule metabolites with functions related to biological defense, e.g., antibiotics and antifungal, or as signaling molecules in biosystems (Walsh, 2006; White and Flashman, 2016; Dunham and Arnold, 2020; Morita et al., 2021). In either role, specific modifications of these amino acids by enzymes contribute to the biochemical diversity essential for their various functions. For instance, a free L-tryptophan amino acid forms the starting point of the biosynthesis of the hormones serotonin and melatonin that function as neurotransmitters in the brain and trigger mood swings and happiness (Roberts and Fitzpatrick, 2013; Höglund et al., 2019). The conversion of a proline amino acid in a peptide chain to R-4-hydroxyproline by proline-4-hydroxylase enzymes enables crosslinking of collagen strands that gives them their strength (McDonough et al., 2006; Koski et al., 2009; Gorres and Raines, 2010). As a result, a major constituent of collagen is 4-hydroxyproline that plays a vital role in maintaining the integrity and resilience of various bodily tissues and organs in humans.

Many amino acids serve as essential building blocks in the biosynthesis of various antibiotics and natural products in microorganisms like bacteria and fungi (Bérdy, 2005; Liu et al., 2013; Herisse et al., 2020). A notable example of a natural amino acid used in a range of bioreactions in biology is L-arginine (L-Arg). This amino acid falls into the category of semi-essential or conditionally essential amino acids due to its synthesis by the body, which can vary depending on development stages, health conditions, or injuries (Barbul, 1986; Visek, 1986; Beaumier et al., 1996; Wu et al., 2009). The most common enzymatic use of L-Arg is within the group of nitric oxide synthase (NOS) enzymes, where L-Arg reacts on a heme center with dioxygen to form L-citrulline and NO (Stuehr, 1999; Groves and Wang, 2000). In the human body, NO has functions including blood pressure control through dilating blood vessels, as well as immunological functions. Other uses of L-Arg in biosystems include serving as a building block for the biosynthesis of a range of natural products with remarkable metabolic versatility, contributing to the synthesis of various compounds such as urea, ornithine, citrulline, creatine, agmatine, glutamate, proline, hydroxyls, and polyamines (Wu and Morris, 1998). Consequently, its metabolic processes are intricate and tightly regulated, which is unsurprising considering its diverse roles (Morris, 2002). The intricate nature of L-Arg metabolism stems not just from the array of enzymes engaged in its breakdown and its metabolites but also from their distinctive patterns of expression within cells (Morris, 2009).

One significant enzyme superfamily responsible for a substantial portion of known oxidative L-Arg modifications is the iron(II)- and α -ketoglutarate-dependent (Fe/ α KG) oxygenase superfamily. In eukaryotic organisms, Fe/ α KG enzymes primarily hydroxylate side chain functional groups of amino acids and mainly operate on protein or peptide substrates, serving structural or regulatory functions (Krebs et al., 2007; de Visser and Kumar, 2011; Martinez and Hausinger, 2015; Simaan et al., 2015; Herr and Hausinger, 2018). In contrast, in prokaryotes, Fe/ α KG oxidants can target

monomeric amino acids, leading to diverse reaction outcomes. A prominent example is clavamate synthase (CAS), an α KG-dependent oxygenase (α KG is also called 2-oxoglutarate), which catalyzes sequential hydroxylation, oxidative cyclization, and desaturation reactions on an L-Arg derivative during the biosynthesis of the β -lactamase inhibitor known as clavulanic acid (Marsh et al., 1992). In several other antibiotic biosynthesis reactions, Fe/ α KG oxidants play a crucial role in selectively hydroxylating or desaturating an L-Arg amino acid residue during the initial reaction step, highlighting the significance of enzyme activity in antibiotic production. For example, enzymes such as the viomycin biosynthesis enzyme VioC, nonribosomal peptide biosynthesis enzyme GetI, the streptothricin biosynthesis enzyme OrfP, and the naphthyridinomycin biosynthesis enzyme NapI all act on L-Arg. Despite the fact that all of these enzymes share >50% sequence similarity (Berman et al., 2000), they target different positions on the amino acid side chain and produce distinct products (Scheme 1). VioC selectively hydroxylates L-Arg at the C₃ position within the viomycin pathway (Thomas et al., 2003; Barkei et al., 2009; Dunham et al., 2018a; Ali et al., 2021a), while GetI functions as a C₄-hydroxylase of L-Arg (Zwick et al., 2019). OrfP is responsible for dihydroxylations at both the C₃ and C₄ positions of L-Arg in the streptothricin pathways (Chang et al., 2014; Ali et al., 2021b), and NapI performs the C₄–C₅ desaturation of L-Arg in the naphthyridinomycin pathway (Scott and Williams, 2002; Pu et al., 2013; Dunham et al., 2018b; Ali et al., 2023). Although the ethylene-forming enzymes (EFEs) allow the reaction of α KG on an iron(II) center with dioxygen to convert α KG into ethene and CO₂ molecules, a side reaction leads to the hydroxylation of a free L-Arg at the C₅ position (Martinez and Hausinger, 2016; Chaturvedi et al., 2021; Copeland et al., 2021; Yeh et al., 2022). It is unclear whether this L-Arg hydroxylation is part of the bioreaction or whether L-Arg binding is related to creating specific charge, electric dipole, and electric field perturbations to the active site (Chaturvedi et al., 2021). Nevertheless, the 5-hydroxyarginine product decomposes spontaneously into guanidine L- Δ^1 -pyrroline-5-carboxylate products.

Structurally, Fe/ α KG-dependent dioxygenases exhibit an iron(II) resting state, where the metal is bound to the protein via interactions involving the side chains of two histidine residues and either a carboxylate group from a Glu or Asp residue. The two residues located in the equatorial plane, one His residue and one carboxylate group of Glu or Asp, are typically separated by two residues within the protein loop, denoted as residues X and X + 2 along the protein chain (Berman et al., 2000; Ali et al., 2021a). An analysis of various protein structures of L-Arg-activating nonheme iron dioxygenases, retrieved from the Protein Data Bank (Berman et al., 2000), is shown in Figure 1 and contains both L-Arg and α KG. The structures reveal that the α KG group forms a bidentate ligand to iron(II), connecting through both the carboxylate and keto groups. Moreover, in these structures, it was observed that the terminal carboxylate group of α KG forms a salt bridge with the side chain of a preserved Arg residue. This Arg residue is on the same chain and positioned several residues away from the axial His residue in most α KG-dependent nonheme iron dioxygenases. The chain forms a loop around the α KG co-substrate that holds it in a specific orientation and position in the active site. Extracts of crystal structures of the selected L-Arg hydroxylases are shown in



SCHEME 1
Enzymatic conversion of L-Arg by various Fe/αKG-dependent enzymes and obtained products.

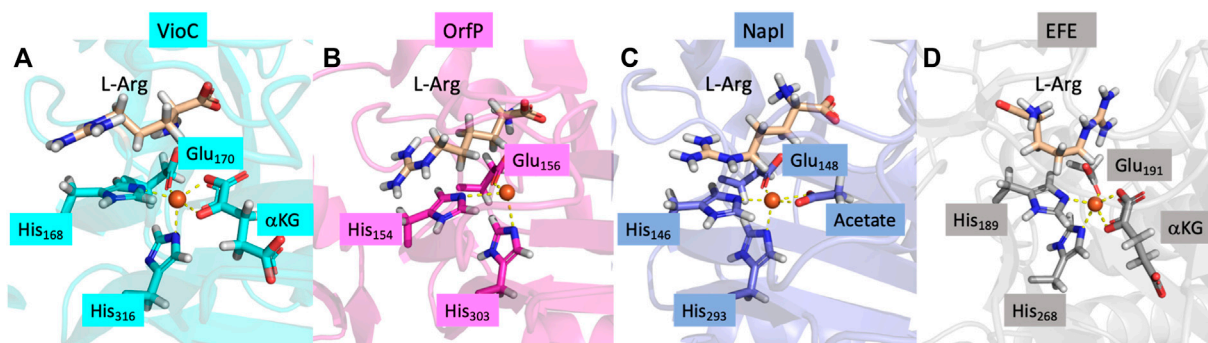
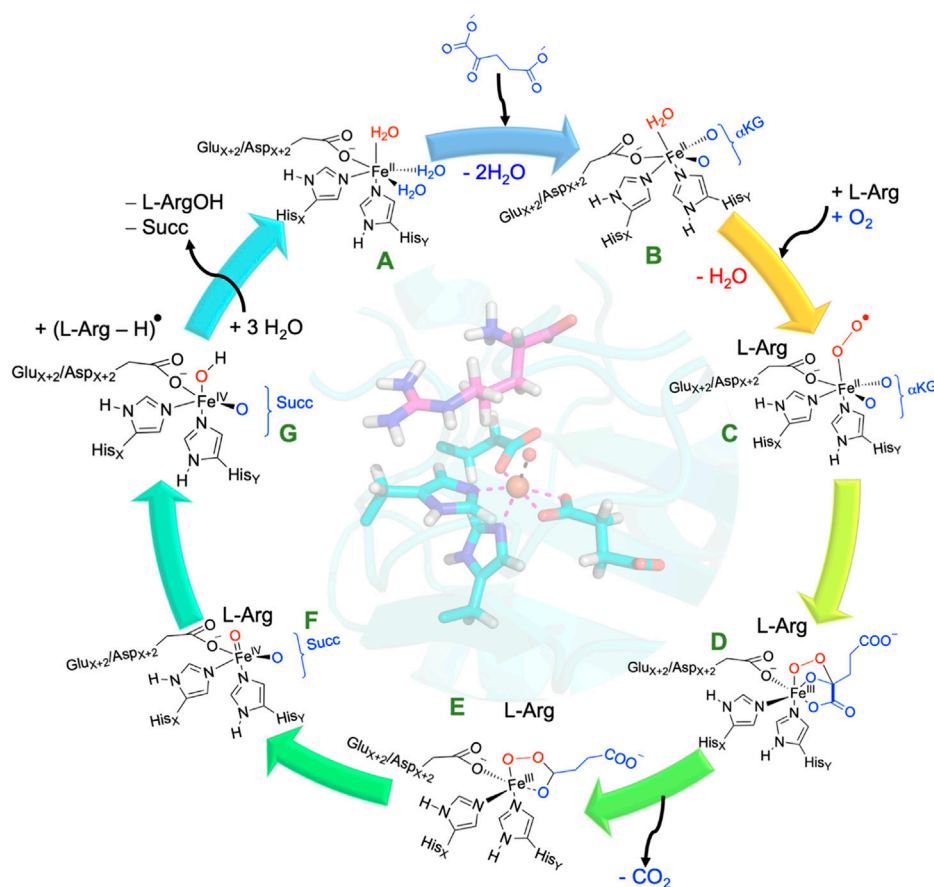


FIGURE 1
Crystal structure coordinates of (A) VioC (PDB ID: 6ALM), (B) OrfP (PDB ID: 4M2E), (C) NapI (PDB ID: 6DAW), and (D) EFE (PDB ID: 6VP4).

Figure 1 (Berman et al., 2000; Chang et al., 2014; Mitchell et al., 2017; Dunham et al., 2018b; Copeland et al., 2021).

All nonheme iron hydroxylases and halogenases follow similar initial catalytic steps, irrespective of their substrate or reaction type, whereby αKG in a reaction with dioxygen is converted into succinate and CO₂ and generates a high-valent iron(IV)-oxo species, as shown in Scheme 2. The catalytic process initiates from the resting state (structure A in Scheme 2), where iron(II) is bound to the protein through the typical 2-His/1-carboxylate motif, and the remaining six ligand sites of the metal are occupied with water molecules. Most of the nonheme iron enzymes commonly feature a conserved, typical facial binding motif of 2-His/1-Glu or 2-His/1-Asp coordination of the iron(II), referred to as the facial triad (Berman et al., 2000; Bruijninx et al., 2008; Kal and Que, 2017; de Visser et al., 2022). In VioC, these ligands are represented by His₁₆₈, Glu₁₇₀, and His₃₁₆, while in NapI, these residues are His₁₄₆, Glu₁₄₈, and His₂₉₃, as shown in Figure 1. Upon αKG binding (structure B), two water molecules are displaced from the metal and leaves only the water molecule trans to the axial histidine group, i.e., His₃₁₆ in VioC. Subsequent binding of the L-Arg substrate results in the release of this remaining water molecule, creating space for O₂ to bind and forming an end-on

iron(III)-superoxo complex (structure C). The iron(III)-superoxo intermediate is transient and has never been directly observed, although there are implications in the ultraviolet-visible (UV-Vis) spectrum of cysteine dioxygenase for its existence (Tchesnokov et al., 2016). Moreover, computational models suggest that the terminal oxygen atom of the superoxo group attacks the α-keto position of αKG (Borowski et al., 2004; de Visser, 2007), thereby forming a bicyclic ring structure (structure D). Additionally, structure D is short-lived and possesses a weak C₁–C₂ bond in the αKG fragment that leads to its rapid disintegration into persuccinate through CO₂ loss (structure E). However, the persuccinate bond is weak, and the O–O cleavage results in a coordinated oxygen atom, i.e., an iron(IV)-oxo (ferryl) intermediate (structure F) and a succinate dianion. The ferryl-oxo group is the active oxidant in the catalytic cycle that targets the substrate. In particular, in the hydroxylases and halogenases, the ferryl complex abstracts a hydrogen atom (H[•]) from the substrate, demonstrating significant reactivity even with very unreactive carbon centers. The resulting state contains a carbon-centered substrate radical (C[•]) and an iron(III)-hydroxo cofactor, which becomes a crucial turning point: its subsequent behavior



SCHEME 2
Consensus catalytic cycle of nonheme iron/αKG-dependent dioxygenases for L-Arg hydroxylation. αKG stands for α-ketoglutarate, Succ represents succinate.

determines the outcome of the reaction (structure G). Different pathways originating from this critical intermediate point result in the diverse and well-documented reaction outcomes within the Fe/αKG superfamily. The iron(IV)-oxo species has been trapped and characterized for various Fe/αKG-dependent dioxygenases through UV-Vis spectroscopy, electron paramagnetic resonance spectrometry, and Mössbauer spectroscopy (Krebs et al., 2007; Tchesnokov et al., 2016; Mitchell et al., 2017; Dunham et al., 2018a; Dunham et al., 2018b; Copeland et al., 2021). For taurine/αKG-dependent dioxygenase, even extended X-ray absorption fine structure (EXAFS) characterization that identified an Fe–O interaction of 1.62 Å has been reported (Riggs-Gelasco et al., 2004). In addition, resonance Raman studies with $^{16}\text{O}_2$ and $^{18}\text{O}_2$ established a difference spectrum and characterized the Fe–O vibration in the iron(IV)-oxo species at 821 cm^{-1} (Proshlyakov et al., 2004).

In hydroxylases after the hydrogen atom abstraction, the C^\bullet radical attacks the hydroxyl group of the iron(III)-hydroxo complex and forms a new C–O bond (Huang and Groves, 2017; Gérard et al., 2022). This OH rebound step creates the alcohol product complex and regenerates the iron(II) cofactor for subsequent cycles. Products (hydroxylated arginine and succinate) are released, and the metal ligand positions filled with water molecules to return to the resting state of the catalytic cycle. The radical coupling step, known as

oxygen rebound, is generally not rate-determining as kinetic isotope effect measurements obtained a large rate constant change when hydrogen atoms in the substrate are replaced by deuterium atoms (Krebs et al., 2007; Dunham et al., 2018a; Dunham et al., 2018b). Indeed, the radical intermediate $\text{C}^\bullet/\text{Fe(III)-OH}$ state has never been characterized experimentally and is transient in Fe/αKG hydroxylases, and hence, its lifetime must be short. However, for some reaction mechanisms (*vide supra*), the radical intermediate leads to bifurcation processes where two reaction channels are possible. Often an intricate balance between the structure, orientation, and local charge distributions determines the ultimate product distributions. In some cases, the oxygen rebound process can be significantly limited, possibly due to certain enzymes having a distinct geometric arrangement in the ferryl complex, allowing for this suppression. For example, the desaturation of L-Arg by NapI enzymes, involving Fe/αKG, is influenced by the orientation of substrate binding and the polarity, along with hydrogen bonding interactions within the substrate-binding pocket (Ali et al., 2023). These factors guide the reaction toward desaturation products rather than hydroxylation by stabilizing the position of the ferryl complex.

All Fe(II)/αKG-dependent dioxygenases are expected to undergo a catalytic cycle, as shown in Scheme 2, where αKG with dioxygen is converted into succinate, CO_2 , and an iron

(IV)-oxo species. However, as many of the proposed intermediates in the cycle remain elusive, most evidence on the catalytic cycle comes from computational modeling. Calculations at various levels of theory (Borowski et al., 2004; de Visser, 2007; Wójcik et al., 2016; Ghafoor et al., 2019; de Visser et al., 2022) reported on the reaction steps leading to the iron(IV)-oxo species and generally give low free energies of activation of approximately 10 kcal mol⁻¹ for the step between structures C and D and lower barriers for all other reaction steps leading to the iron(IV)-oxo species. As such, it is expected that dioxygen binding will rapidly lead to a highly stable iron(IV)-oxo species. The next step of the reaction, therefore, and particularly the second-coordination sphere interaction of the substrate and oxidant, determines the selectivity patterns (de Visser, 2020; Wojdyla and Borowski, 2022). In this review paper, we will summarize and compare substrate activation processes by the iron(IV)-oxo species of Fe(II)/ α KG-dependent dioxygenases and compare several L-Arg-activating enzymes. We ask ourselves how these enzymes direct their chemoselectivity to the required position of the substrate and block alternative reaction products. Our computational studies focused on uncovering how these enzymes activate different C–H bond positions of the same L-Arg substrate and thereby yield a diverse array of hydroxylated and desaturation products. Through a comprehensive analysis of the structures, electronic properties of the substrate, oxidant, and second-coordination sphere, we established the key factors that drive the reactions into a specific direction and unravel the nuances underlying these differences in product formation.

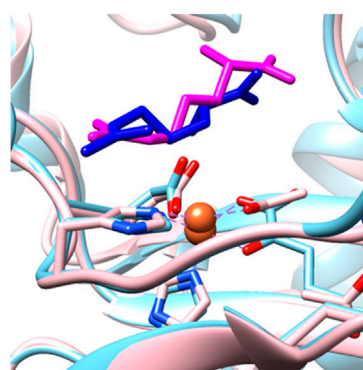
2 Mechanism of L-arginine activation by Fe(II)/ α KG-dependent dioxygenases

Many researchers have investigated the catalytic cycle of iron(II)/ α KG-dependent dioxygenases, and there are reports on spectroscopic characterization including UV-Vis absorption, electron paramagnetic resonance spectrometry, resonance Raman spectroscopy, Mössbauer spectroscopy, and EXAFS measurements on various catalytic cycle intermediates in a range of isozymes (Proshlyakov et al., 2004; Riggs-Gelasco et al., 2004; Krebs et al., 2007; Martinez and Hausinger, 2015). However, since many proposed intermediates are short-lived, experimental work on the catalytic cycle of these enzymes is challenging. Often, insights into reaction pathways and the nature of the short-lived species can be gained only through computational studies. The computational approaches generally range from molecular dynamics studies on full enzymatic systems to quantum mechanics/molecular mechanics (QM/MM) on an enzyme structure. Thus, in QM/MM (Senn and Thiel, 2007a; Senn and Thiel, 2007b; Quesne et al., 2016; Hofer and de Visser, 2018), a complete enzyme with co-factors, substrate, and a water layer is selected, whereby the inner core of the system, i.e., the active site, is calculated with a QM method, and the rest of the protein and solvent, with a MM forcefield. This approach keeps the long-range interactions between the QM and MM regions and restricts motions of the active site atoms during geometry optimization. An alternative approach is using density functional theory (DFT) cluster models of size of up to approximately 500 atoms (Siegbahn and Blomberg, 2010; Sheng et al., 2020; Himo and de Visser, 2022). In DFT cluster models, the active

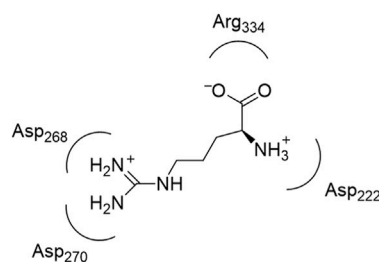
site and second-coordination sphere are calculated with an accurate DFT approach although sometimes some protein atoms are fixed to keep the structure close to the protein model the calculations started from. In Ali and de Visser (2022), we showed that both approaches can reproduce experimentally determined free energies of activation of enzymatic systems to within 2 kcal mol⁻¹; however, either a large QM region in QM/MM or a cluster model with more than 250 atoms is needed to achieve this accuracy. In particular, the second-coordination sphere interactions including hydrogen bonding and dipole moment interactions appear crucial for the correct description of the catalysis reaction. A similar level of accuracy was obtained for the calculations of barrier heights of the oxygen atom transfer of biomimetic models, as compared to the experimental work (Cantú Reinhard et al., 2017; Mukherjee et al., 2019). Using cluster models, our groups also explored regioselectivities and pathways, leading to by-products (Timmins et al., 2017; Lin et al., 2022; Mokkaew and de Visser, 2023), and showed that these bifurcation pathways differ by only a few kcal mol⁻¹ in some cases; hence, modeling will need to predict the correct ordering and able to deal with these small energy differences. The DFT calculations on large cluster models reproduce experimental product distributions very well, and hence, the systematic errors of the DFT approaches do not appear to influence the predictions of reaction mechanisms. Consequently, computational modeling using cluster models is suitable for calculations on complicated reaction channels with small energy differences.

The consensus catalytic mechanism, as described above in Scheme 2, entails dioxygen binding to the iron center, followed by decarboxylation of α KG, resulting in succinate and the creation of an iron(IV)-oxo compound. This iron(IV)-oxo species is considered the primary oxidizing agent but short-lived. Recent computational studies from our group on L-Arg activation by Fe(II)/ α KG dioxygenases show that the L-Arg transformation to hydroxylated or desaturated products is influenced by how the substrate binds, the intrinsic electric field effect in the protein pocket, and the hydrogen bonding interactions between the substrate and its direct environment within the substrate-binding pocket (Ali et al., 2021a; Ali et al., 2021b; Ali et al., 2023).

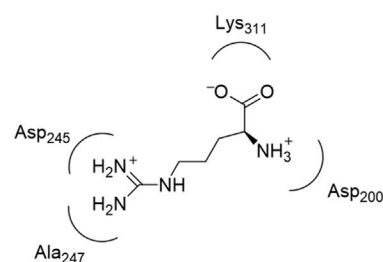
Figure 2 shows an overlay of the crystal structure coordinates of the L-Arg-bound iron(II) complexes of NapI and VioC, as taken from the 6ALM and 6DAW pdb files (Berman et al., 2000; Mitchell et al., 2017; Dunham et al., 2018b). As can be seen, both enzymes display the characteristic 2-His/1-carboxylate iron(II) coordination with the groups in similar positions. In addition, both enzymes bind α KG through the carboxylate and α -keto groups to the iron. Substrate L-Arg is shown in Figure 2 as well, and as can be seen, it is located in a similar orientation and position in NapI and VioC, yet VioC gives substrate C₃-hydroxylation, while NapI reacts through desaturation of the C₄–C₅ bond. As such, the crystal structure coordinates do not give a clear view on the origin of the regioselectivity of these enzymes. The right-hand side of Figure 2 shows nearby residues from the substrate in NapI and VioC. Not surprisingly, the carboxylate group of the substrate interacts with a positively charged amino acid into a salt bridge, namely, with Arg₃₃₄ in VioC and with Lys₃₁₁ in NapI. The positively charged ammonium group of the substrate interacts with a carboxylate side chain of an Asp residue in both enzymes. The major difference in substrate



NapI (pink) vs VioC (blue)

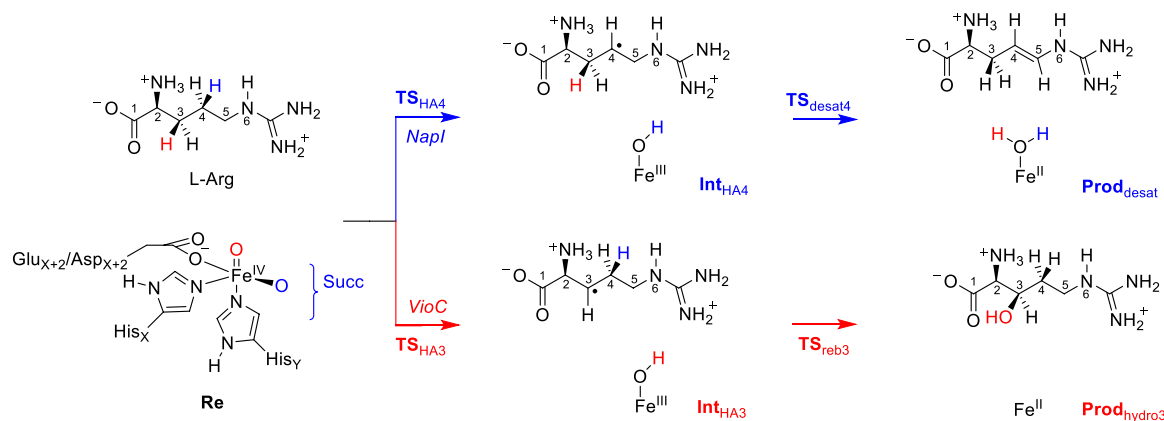


VioC substrate environment



NapI substrate environment

FIGURE 2
Overlay of the crystal structure coordinates of VioC (PDB ID: 6ALM) and NapI (PDB ID: 6DAW).



SCHEME 3
Radical reaction mechanism of L-Arg hydroxylation by VioC and L-Arg desaturation by NapI.

binding between the two enzymes resides in the interactions of the guanidinium group of L-Arg with the protein. Thus, in VioC, it interacts with two carboxylate groups, namely, the side chains of Asp₂₆₈ and Asp₂₇₀. By contrast, NapI only has one carboxylate group in that region, namely, Asp₂₄₅, and the residue with number 247 is not an Asp/Glu amino acid but Ala. Consequently, there are differences in binding interactions of the substrate in the two isozymes, whereby in VioC, the substrate will be more strongly bound with an additional salt bridge from one extra Asp residue. Moreover, since Asp is negatively charged, these differences in the substrate-binding pocket between VioC and NapI will incur changes in the local dipole moment, charge distributions, and local electric field patterns that may influence reactivities. To understand whether these seemingly minor differences in substrate positioning and second-coordination sphere influence catalysis and product distributions, a series of computational studies were performed on the various enzyme models. The mechanisms focused on the reaction pathways starting from an iron(IV)-oxo species with nearby L-Arg bound, i.e., a reactant complex **Re**, as explained in Scheme 3. Thus, the iron(IV)-oxo species abstracts a hydrogen atom from the

substrate to form an iron(III)-hydroxo species. In VioC, this hydrogen atom abstraction is from the C₃–H bond (bottom pathway in Scheme 3), whereas in NapI, the abstraction is from the C₄–H group (top channel in Scheme 3). Normally, hydrogen atom abstraction is followed by OH rebound to form the alcohol product complexes (Latifi et al., 2009; Sahu et al., 2014; Huang and Groves, 2017; Timmins et al., 2018a; Gérard et al., 2022); however, in some cases, a second hydrogen atom abstraction is possible to give desaturation reactions (Kumar et al., 2009), as is the case in NapI.

Let us first start with a description of the calculated reaction mechanism of L-Arg activation by VioC and the possible mechanisms leading to C₃-hydroxylation, C₄-hydroxylation, and C₃–C₄ desaturation. In particular, the viomycin biosynthesis enzyme VioC selectively hydroxylates L-Arg, specifically at the C₃ position during the biosynthesis of its antibiotic, and there is no evidence of C₄-hydroxylation or C₃–C₄ desaturation byproducts (Thomas et al., 2003; Yin and Zabriskie, 2004; Barkei et al., 2009; Helmetag et al., 2009; Mitchell et al., 2017; Dunham et al., 2018a). Figure 3 provides a detailed depiction of the energy landscape for the reaction pathways leading to the various intermediates and products

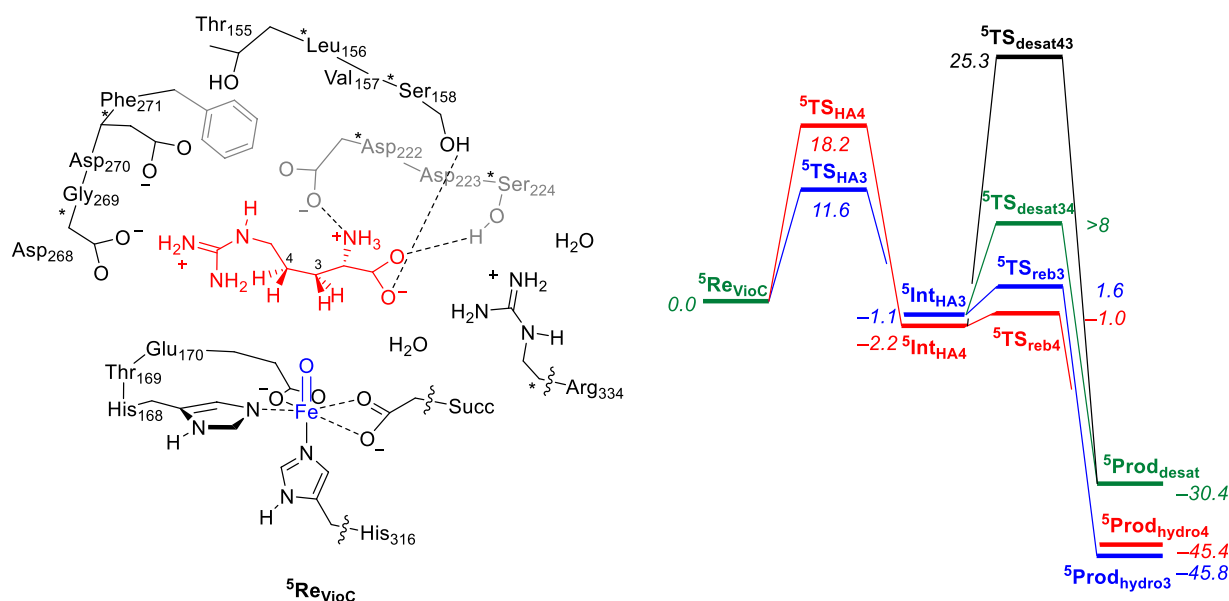


FIGURE 3
Relative free energy (ΔG) landscape for L-Arg hydroxylation at the C₃ and C₄ positions and desaturation across the C₃–C₄ bond by an iron(IV)-oxo species of a VioC model complex using calculations on the cluster model shown on the left. Free energies are expressed in kcal mol⁻¹ and represent energies as obtained with UB3LYP-D3/BS2//UB3LYP/BS1 with solvent, zero-point energies, and thermal and entropic corrections included at 298 K. BS1 refers to LANL2DZ with core potential on iron and 6-31G* on the rest of the atoms, while a BS2 basis set has LACV3P+ with core potential on iron and 6-311+G* on the rest of the atoms. Data can be obtained from Ali et al. (2021a).

in the process. The activation of L-Arg initiates from the iron(IV)-oxo species and commences by abstracting a hydrogen atom either from the C₃ position or an adjacent site, such as the C₄ position of the substrate via the transition states ⁵TS_{HA3} and ⁵TS_{HA4}, respectively. Both of these steps lead to an iron(III)-hydroxo species with a substrate radical on either substrate atom C₃ (⁵Int_{HA3}) or on C₄ (⁵Int_{HA4}). The abstraction of a hydrogen atom from the C₃–H bond necessitates a free energy of activation of $\Delta G^\ddagger = 11.6$ kcal mol⁻¹ within the quintet spin state. By contrast, the abstraction of a hydrogen atom from the C₄–H position of L-Arg by the VioC model presents a notably higher barrier than C₃–H abstraction, registering approximately $\Delta G^\ddagger = 18.2$ kcal mol⁻¹ within the quintet spin state. Interestingly, the formation of the radical intermediates ⁵Int_{HA3} and ⁵Int_{HA4} releases almost the same amount in energy, and ⁵Int_{HA3} was located at $\Delta G = -1.1$ kcal mol⁻¹, while the C₄–H radical intermediate ⁵Int_{HA4} is slightly more stable at $\Delta G = -2.2$ kcal mol⁻¹. Therefore, the calculations predict a different ordering for the thermodynamics of the reaction (⁵Int_{HA3} vs. ⁵Int_{HA4}), as compared to the kinetics (⁵TS_{HA3} vs. ⁵TS_{HA4}). This phenomenon is called negative catalysis and means that the protein disrupts the kinetics through the second-coordination sphere effect so that the Bell–Evans–Polanyi principle does not apply, and the product distribution will not be based on the most thermodynamically favorable pathway (Ghafoor et al., 2019; de Visser et al., 2021). However, despite this, calculations indicate that products primarily originate from C₃–H atom abstraction. This aligns with experimental findings of VioC, showcasing predominant 3-hydroxyarginine products, consistent with the observed dominance of C₃-hydroxylation products for L-Arg as a substrate.

In the catalytic cycle's subsequent phase, the hydroxyl group from the iron(III)-hydroxo species either rebounds to the radical and forms the alcohol products or gathers another hydrogen atom to create water and 3,4-dehydroarginine products (⁵Prod_{desat}). Transition states were characterized for OH rebound to the C₃ and C₄ positions from ⁵Int_{HA3} and ⁵Int_{HA4}, respectively, namely, the structures ⁵TS_{reb3} and ⁵TS_{reb4} that give 3-hydroxyarginine (⁵Prod_{hydro3}) and 4-hydroxyarginine (⁵Prod_{hydro4}) products. In addition, we located a transition state for hydrogen atom abstraction from the C₃–H position from ⁵Int_{HA4}, namely, ⁵TS_{desat43}, but were unsuccessful in fully characterizing the transition state for hydrogen atom abstraction from the C₄–H position from ⁵Int_{HA3}, i.e., ⁵TS_{desat34}. Nevertheless, a constraint geometry scan for this pathway shows that it is well higher in energy than ⁵TS_{reb3}, and consequently, OH rebound should be the dominant pathway. Therefore, for the VioC model, the calculations show that desaturation is unfavorable over the OH rebound, regardless of whether the initial hydrogen atom abstraction proceeds from the C₃–H or C₄–H bonds. In addition, the work indicates a significantly higher free energy of activation for hydrogen atom abstraction from the C₄–H bond than that from the C₃–H group. Overall, the OH rebound to form 3-hydroxyarginine products is dominant, and the calculations predict little or no desaturation products. Similarly, intermediate ⁵Int_{HA4} shows a clear preference for the rebound pathway over desaturation, aligning with experimental product distributions that favor C₃-hydroxylation by VioC. The computational studies highlight that the desaturation pathway faces a notably high second hydrogen atom abstraction barrier that makes it unlikely for VioC to induce L-Arg desaturation. This emphasizes the dominance of the OH rebound mechanism in the enzymatic reaction process.

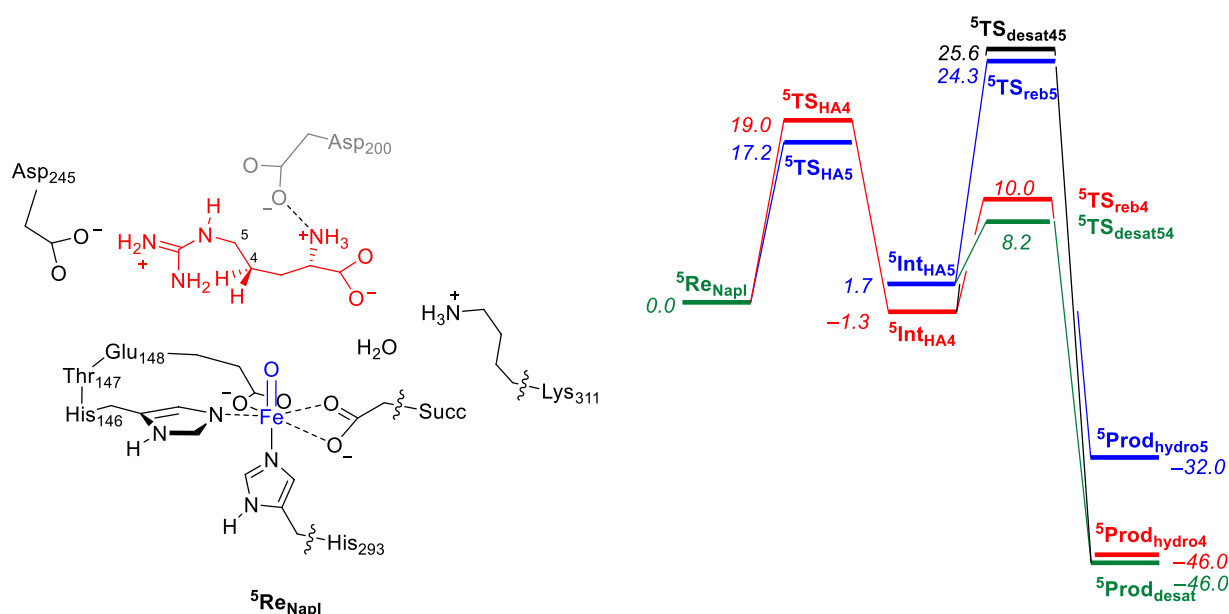


FIGURE 4
QM/MM calculated relative free energy (ΔG) landscape for L-Arg hydroxylation at the C₄ and C₅ positions and desaturation across the C₄–C₅ bond by an iron(IV)-oxo species of a NapI model complex. The QM region is shown on the left. Free energies are expressed in kcal mol⁻¹ and represent energies as obtained with UB3LYP-D3/BS2//UB3LYP/BS1 with solvent, zero-point energies, and thermal and entropic corrections included at 298 K. BS1 refers to LANL2DZ with core potential on iron and 6-31G* on the rest of the atoms, while a BS2 basis set has LACV3P+ with core potential on iron and 6-311+G* on the rest of the atoms. Data can be obtained from Ali et al. (2023).

In a subsequent computational study (Ali et al., 2023), we used the QM/MM approach and set up a full enzyme model of NapI and calculated the L-Arg reaction with the iron(IV)-oxo species to form 4,5-dehydroarginine, 4-hydroxyarginine, and 5-hydroxyarginine products, as shown in Figure 4. A QM region was selected that contains the metal and its first-coordination sphere, the substrate, and its polar second-coordination sphere residues, namely, the side chains of Asp₂₀₀, Asp₂₄₅, and Lys₃₁₁. Subsequently, local minima and transition states were characterized for the mechanism, leading to the various products. Similarly, in line with the work on VioC, the hydrogen atom abstraction step is rate-determining and $\Delta G^\ddagger = 17.2$ kcal mol⁻¹ for abstraction of the C₅–H atom is calculated, while the C₄–H bond requires an activation energy of $\Delta G^\ddagger = 19.0$ kcal mol⁻¹. The latter is close to the value obtained for VioC, and therefore, it appears that the second-coordination sphere does not affect the C₄–H barrier dramatically. Furthermore, for NapI, the reaction proceeds through negative catalysis, whereby the ordering of the radical intermediates is different from that of the transition states. As such, NapI will react dominantly through C₅–H hydrogen atom abstraction to form the iron(III)-hydroxo with C₅ radical (⁵Int_{HA5}). From both radical intermediates, we calculated the desaturation pathway, where a second hydrogen atom abstraction gives a double bond along C₄–C₅, as well as a pathway for the OH rebound. From ⁵Int_{HA5}, the lowest barrier is hydrogen atom abstraction from the C₄–H group with a barrier of $\Delta G = 6.5$ kcal mol⁻¹ above ⁵Int_{HA5}. By contrast, the OH rebound barrier is high in energy and found to be more than 16 kcal mol⁻¹ higher than the hydrogen atom abstraction barrier. Consequently, NapI will react to form 4,5-dehydroarginine

products through sequential hydrogen atom abstraction from the C₅–H and C₄–H bonds. Interestingly, if the reaction starts with hydrogen atom abstraction from the C₄–H bond, then the iron(III)-hydroxo and C₄-radical does not form the desaturated products but will result in C₄-hydroxylation instead due to a lower rebound barrier. To understand the differences between the two isozymes and why they give different product distributions, we analyzed all data in detail and particularly focused on the electron transfer steps and electronic configurations of the various intermediates and the local environment around the substrate and oxidant.

Optimized transition state geometries for hydrogen atom abstraction from the C₄–H and C₅–H bonds of L-arginine by NapI, VioC, and OrfP models are shown in Figure 5 with data taken from Ali et al. (2021a); Ali et al. (2021b); Ali et al. (2023). All transition states have a large imaginary frequency of well over 1000 cm⁻¹, which implies that the reaction will proceed with a large amount of quantum chemical tunneling and will incur a large kinetic isotope effect when the transferring hydrogen atoms are replaced by deuterium atoms (Barman et al., 2019). The three C₄–H hydrogen atom abstraction transition states have similar bonding interactions and the Fe–O distances that range from 1.735 to 1.762 Å. This is the result of the same electronic configuration for all structures due to the same electron transfer patterns; see next section for details. In addition, the C₄–H and O–H distances in the TS_{HA4} transition states are alike, whereby all three transition state structures have a product-like geometry with shorter O–H than C₄–H distances. The only major difference between the three transition state structures for C₄–H abstraction refers to the position of the substrate, which causes a change in the Fe–O–C₄

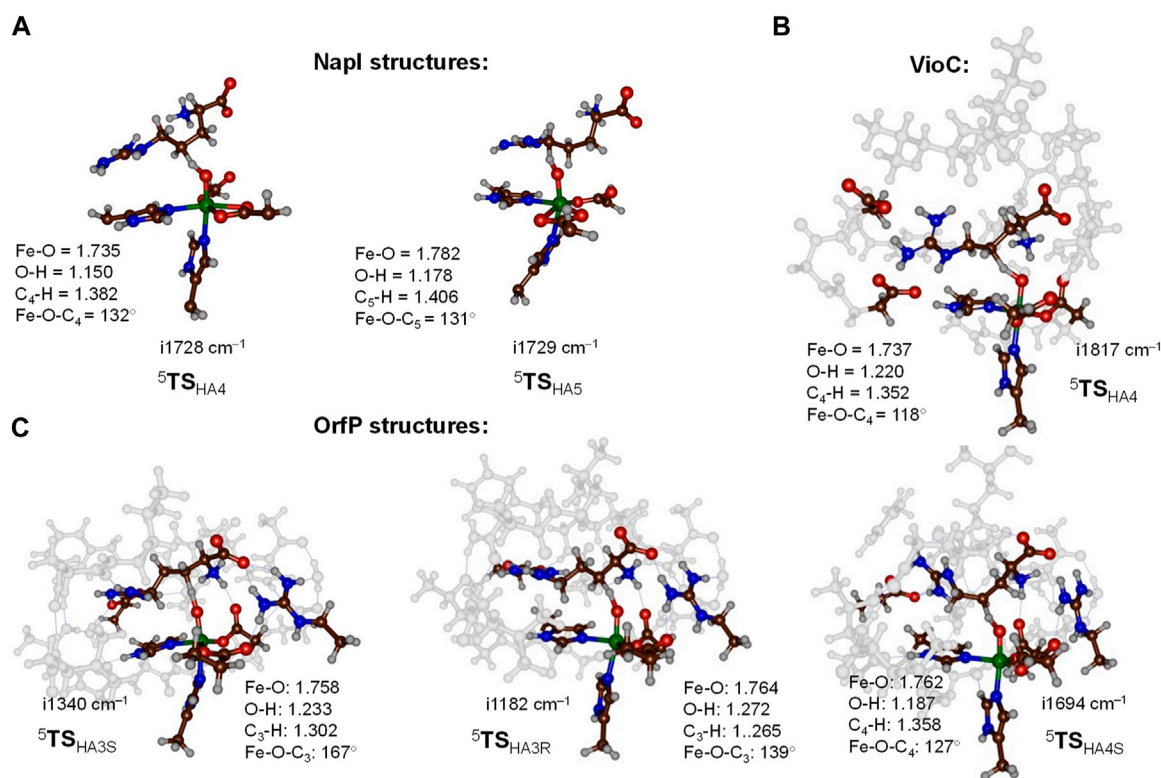


FIGURE 5

Optimized transition state structures for hydrogen atom abstraction steps from L-Arg by NapI (part (A)), VioC (part (B)), and OrfP (part (C)) enzymes with bond lengths in Å and angles in degrees. (A) QM/MM (UB3LYP/BS1:Amber) optimized transition states for NapI. (B, C) DFT cluster model calculated at the UB3LYP/BS1 level of theory.

angle from 118° in the VioC model to 132° in the NapI system. Despite the differences in the angle, the VioC and NapI transition states for hydrogen atom abstraction from the C₄-H position are of similar energy. Interestingly, the optimized transition state structure for C₅-H hydrogen atom abstraction ($^5\text{TS}_{\text{HA5}}$) for NapI is not significantly different from that for C₄-H hydrogen atom abstraction with similar distances and angles. As such, the preference of C₅-H hydrogen atom abstraction does not appear from the optimized geometries, which encouraged us to analyze the environment and the fundamental factors for hydrogen atom abstraction.

The work on L-Arg activation by OrfP investigated the hydrogen atom abstraction of both hydrogen atoms on the C₃-H position, leading to the formation of stereoisomers, namely, the *R*-3-hydroxyarginine and *S*-3-hydroxyarginine products. Both *pro-R* and *pro-S* transition state structures ($^5\text{TS}_{\text{HA3R}}$ and $^5\text{TS}_{\text{HA3S}}$) are displayed alongside each other in Figure 5. Structurally, they are very similar, and the only major difference relates to the Fe-O-C₃ angle that is 167° in the *pro-S* transition state and 139° in the *pro-R* transition state. These differences are related to the position of these hydrogen atoms in the structure, but energetically, the barriers are $\Delta E + \text{ZPE} = 12.1 \text{ kcal mol}^{-1}$ for $^5\text{TS}_{\text{HA3S}}$ and $\Delta E + \text{ZPE} = 15.5 \text{ kcal mol}^{-1}$ for $^5\text{TS}_{\text{HA3R}}$. The calculations show that substrate positioning will drive a stereo- and regioselective reaction mechanism, whereby certain C-H bonds become preferred for cleavage by the iron(IV)-oxo species.

3 Electron transfer during L-arginine activation by Fe(II)/ α KG-dependent dioxygenases

To highlight the electronic configuration changes during the substrate desaturation and hydroxylation mechanisms for L-Arg-activating nonheme iron(IV)-oxo species, we show a valence bond diagram that focuses on the valence states of the substrate and oxidant. We used these valence bond diagrams previously to understand bifurcation pathways and selectivity mechanisms (Faponle et al., 2016; Timmins et al., 2018b; Ali et al., 2020). Thus, as experimentally determined (Krebs et al., 2007), the iron(IV)-oxo species of nonheme iron hydroxylases is in a quintet spin state. Electronically, the metal 3d orbitals mix with first-coordination sphere ligands and split into bonding and antibonding orbitals. The valence orbitals are labeled as π^*_{xy} , π^*_{xz} , π^*_{yz} , σ^*_{x2-y2} , and σ^*_{z2} molecular orbitals and contain a dominant 3d contribution on the metal. The σ^*_{z2} orbital is virtual and represents the antibonding interaction of the 3d_{z2} iron orbital with 2p_z orbitals on the axial nitrogen atom of the His residue and the oxo group. The π^*_{xy} and σ^*_{x2-y2} orbitals are in the xy-plane and represent antibonding interactions of the metal with the equatorial ligands, namely, the His, Asp, and succinate groups. Finally, the π^*_{xz} and π^*_{yz} orbitals are part of two 2-center-3-electron bonds along the Fe-O group for the antibonding interactions between the 3d iron orbitals with 2p orbitals on the oxo group. Overall, the iron(IV)-oxo species has electronic configuration of $\pi^*_{xz}{}^2 \pi^*_{xz}{}^1 \pi^*_{yz}{}^2 \pi^*_{yz}{}^1 \pi^*_{xy}{}^1 \sigma^*_{x2-y2}{}^1$ in

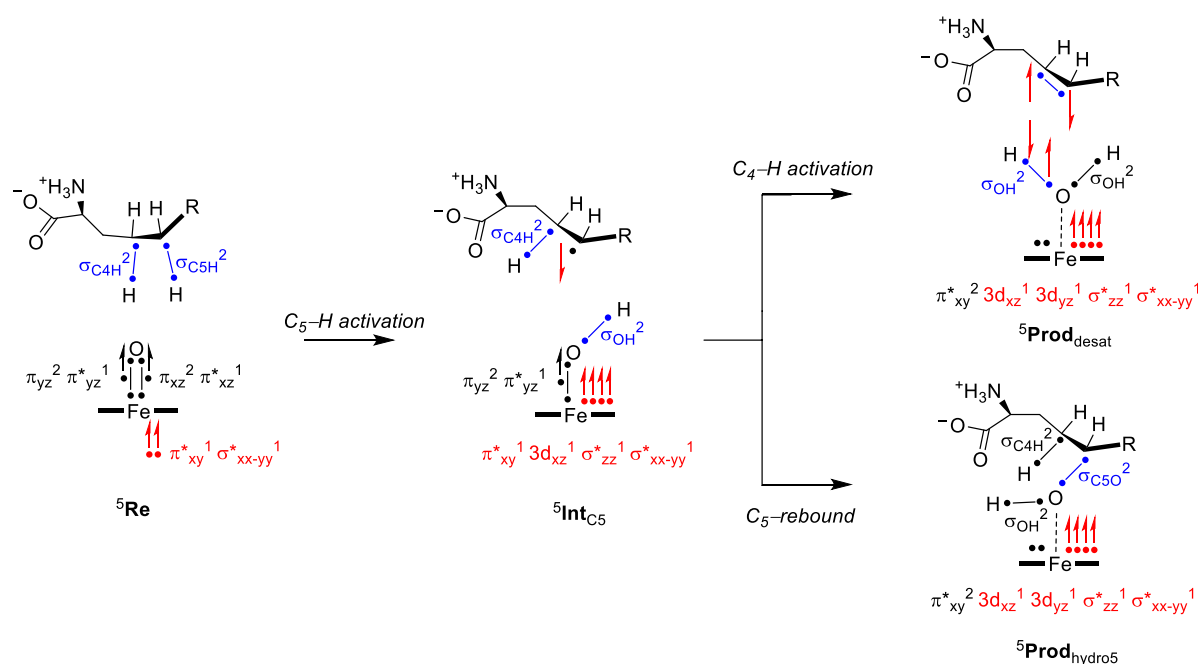


FIGURE 6
Electron transfer pathways and change in electronic configuration and the oxidation state of intermediates during L-Arg desaturation and hydroxylation in NapI.

a quintet spin state. Interestingly, biomimetic models with 6-coordination often give a triplet spin ground state, while the enzymatic structure has 5-coordination and a high-spin state (Latifi et al., 2013). In the valence bond diagram (Figure 6), we identify a chemical bond as two dots with a line in between them, while unpaired electrons are given as a separate dot with the spin direction (α or β -spin) shown with a single-headed arrow.

During the hydrogen atom abstraction, the C–H bond of the substrate is broken, i.e., the C_5 –H orbital (σ_{C_5H}) in Figure 6. The hydrogen then forms a new O–H orbital (σ_{OH}) with the oxo group of the oxidant. This step generally leads to elongation of the Fe–O bond and the cleavage of the π_{xz} and π^*_{xz} molecular orbitals. One of those electrons moves into the σ_{OH} bond, while one stays behind in the nonbonding $3d_{xz}$ orbital with dominant metal contribution. The last electron from the 3-electron π_{xz}/π^*_{xz} set of orbitals is promoted into the virtual σ^*_{zz} orbital. The thus obtained electronic configuration of the radical intermediate with $\sigma_{OH}^2 3d_{xz}^1 \pi_{yz}^2 \pi^*_{yz}^1 \pi^*_{xy}^1 \sigma^*_{x_2-y_2}^1 \sigma^*_{zz}^1$ configuration is called the σ -pathway for hydrogen abstraction. The alternative mechanism is called the π -pathway, where instead of an up-spin electron transfer from substrate into σ^*_{zz} , a down-spin electron is moved into π^*_{xy} . The latter gives an electronic configuration of $\sigma_{OH}^2 3d_{xz}^1 \pi_{yz}^2 \pi^*_{yz}^2 \pi^*_{xy}^2 \sigma^*_{x_2-y_2}^1 \sigma^*_{zz}^0$ and has the radical on the substrate as down-spin, while it is up-spin in the σ -pathway (de Visser, 2006; Hirao et al., 2011; Tang et al., 2012; Bernasconi and Baerends, 2013; Usharani et al., 2013; Ye et al., 2013; Quesne et al., 2014; Mukherjee et al., 2021). Typically, the σ -pathway is energetically and kinetically favored over the π -pathway, but often, they are close in energy. Structurally, the electron transfer into σ^*_{zz} often gives a substrate attack from the top with a large Fe–O–C angle (close to 180°), while in the π -pathway, the substrate attacks more under and angle with typical Fe–O–C angles of approximately 120° (Hirao et al., 2011). The reaction kinetics hinge

on the electron transfer guided by substrate and oxidant positioning, which needs to be accommodated for in the substrate-binding pocket of the enzyme. All transition states for hydrogen atom abstraction in L-Arg-activating nonheme iron dioxygenases, namely, VioC, NapI, and OrfP, were found to proceed through the same electron transfer processes, where a σ -pathway was followed, leading to a radical intermediate. Consequently, the differences in reactivity have no electronic basis but appear to be the result of substrate and oxidant positioning and their second-coordination sphere.

After the radical intermediate, either another hydrogen atom abstraction takes place or OH rebound occurs to form the alcohol product complex. Both product complexes have the same electronic configuration of an iron(II) atom coupled to a closed-shell product. In particular, the product electronic configuration is $\pi^*_{xy}^2 3d_{xz}^1 3d_{yz}^1 \sigma^*_{zz}^1 \sigma^*_{x_2-y_2}^1$ and results from the cleavage of the π_{yz}/π^*_{yz} 3-electron bond into atomic orbitals. The $3d_{yz}$ orbital is now a nonbonding orbital with one electron, while another electron from the π_{yz}/π^*_{yz} orbitals is transferred to σ^*_{zz} (π -pathway) or π^*_{xy} (σ -pathway). The final electron originating from the π_{yz}/π^*_{yz} set of orbitals forms the σ_{OH} orbital (in the desaturation pathway) or the σ_{C_5O} orbital (in the OH rebound).

4 Environmental effects on bifurcation pathways for L-arginine activation

To understand the fundamental factors of the hydrogen atom abstraction process, we took an isolated L-Arg amino acid and calculated the strengths of various C–H and N–H bonds. Thus, the energy for a hydrogen atom abstraction by an iron(IV)-oxo species is equal to the sum of the C–H bond of the substrate that is broken and the O–H bond of the iron(III)-hydroxo species that is formed

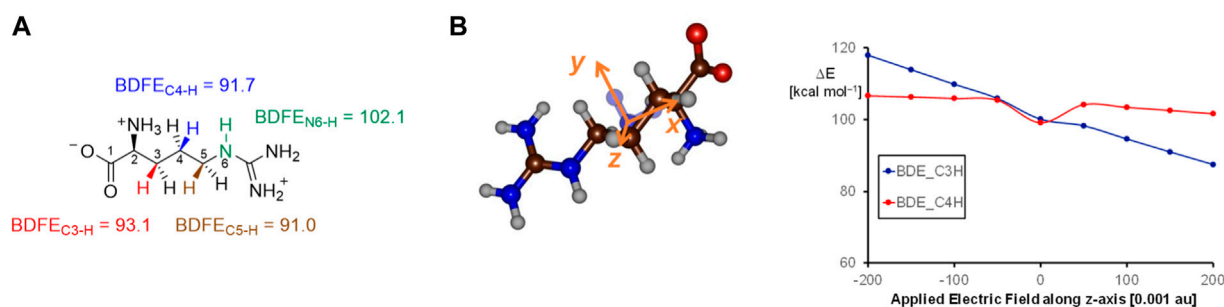


FIGURE 7
 (A) Gas-phase bond dissociation free energies of C–H/N–H bonds in an isolated L-Arg molecule calculated at the UB3LYP/6-311+G* level of theory.
 (B) Electric field effects along the molecular z-axis and the changes in bond dissociation free energies calculated at the UB3LYP/6-311+G* level of theory.

(Bordwell and Cheng, 1991; de Visser, 2010; Pegis et al., 2018). These bond dissociation free energies (BDFEs) were calculated as the difference in the energy between the substrate and the sum of a hydrogen atom and the substrate with a hydrogen atom removed. In the gas phase, the C₄–H and C₅–H BDFE values (Figure 7A) are of similar energy, namely, $\Delta G = 91.7$ kcal mol⁻¹ for the C₄–H bond and $\Delta G = 91.0$ kcal mol⁻¹ for the C₅–H bond. As such, under ideal circumstances, i.e., without external perturbations, arginine hydroxylation should give a mixture of C₄-hydroxylation and C₅-hydroxylation with similar hydrogen atom abstraction barriers. By contrast, the C₃–H bond has a BDFE of $\Delta G = 93.1$ kcal mol⁻¹, and it should be more challenging to cleave the C₃–H bond than the C₄–H or C₅–H bonds. The N₆–H bond strength was also evaluated and found to be well higher in energy than either of the C–H bonds, and hence, activation of the N–H bond will be challenging.

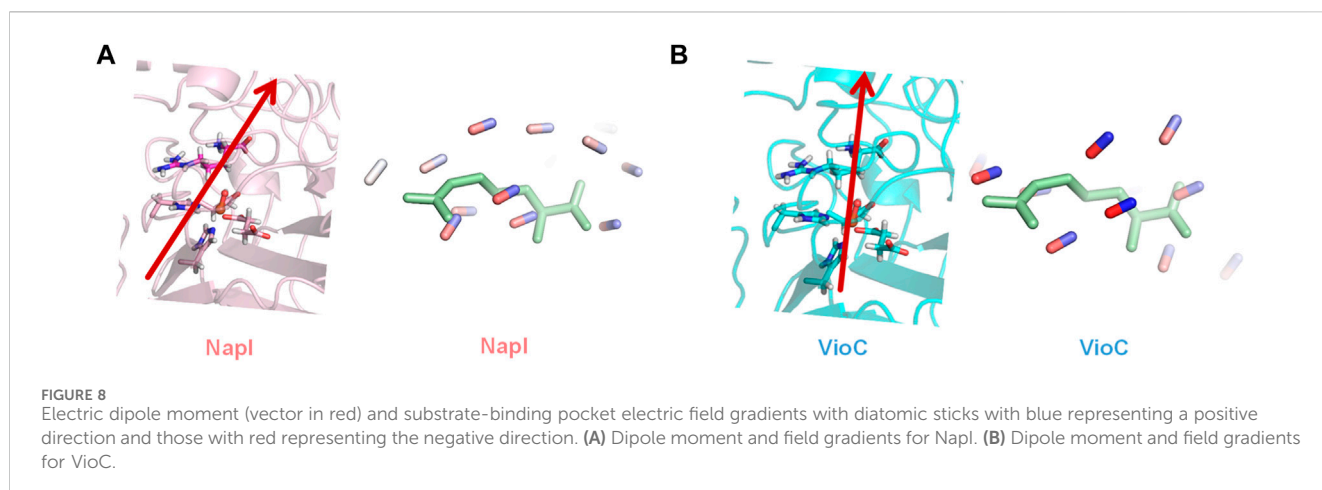
We then explored whether external perturbations could change the order and bond energies of the various C–H bonds in L-Arg. To this end, we applied an external electric field along the molecular x-, y-, or z-axis of the substrate and recalculated the BDFE values for the C₃–H and C₄–H bonds, as shown in Figure 7B. Previously, this approach was shown to change the electronic configuration and reactivity patterns of enzymes (Shaik et al., 2004; Shaik et al., 2018; Lin et al., 2021; Gérard et al., 2023). As can be seen, an electric field along the molecular z-axis of L-Arg affects the C₃–H and C₄–H bond strengths. Thus, this field is along the C–H bonds, but as the hydrogen atoms are on different sides of the substrate, a positive field has a bond-weakening effect for one group and a bond-strengthening effect for the other group. As a result, for large positive electric fields (the field direction is defined as in Gaussian), we observe a weak C₃–H and strong C₄–H bond, while with negative fields, the order is reversed. As a consequence, a local electric field, as appears in a protein, can influence the bond strengths of a substrate and guide the reaction toward the weaker of the two bonds to trigger chemo- or regioselectivity.

As the local environment around L-Arg may affect the C–H bond strengths and thereby the reactivity and selectivity, we decided to analyze the active site charge distributions and polarity. We started with investigating the electric dipole moment of the model. These electric dipole moment vectors are shown in red in Figure 8. In VioC, the electric field vector points along the Fe–O bond and the C₃–H bonds. Therefore, the substrate C–H bond in VioC is aligned with the electric dipole vector and has the C₃–H bond weakened with respect to other C–H bonds in the substrate. The electric dipole

moment in VioC, as a result, guides the reaction to C₃–H hydrogen atom abstraction and C₃-hydroxylation. By contrast, in NapI, the electric dipole vector points along the backbone of the substrate and does not seem to influence C–H bond strengths. Indeed, the lowest energy hydrogen atom abstraction barrier is for the C₅–H hydrogen atom abstraction, which is the weakest C–H bond in the gas phase. Consequently, the environmental effects in NapI do not appear to influence substrate C–H bond strengths, and NapI follows the patterns based on BDFE values of the substrate. An analysis of the electric field gradients of the substrate-bound protein structures comes to the same conclusions, namely, in NapI, the field gradient is along the substrate backbone, while in VioC, it is located along one of the C–H bonds. Overall, these calculations on various L-Arg-activating nonheme iron dioxxygenases show that nature has designed proteins very carefully with specific charge distributions and dipole moments that guide the selectivity and specificity of reaction patterns. Furthermore, the insights obtained from the external electric field perturbations can be utilized in biotechnology to engineer proteins and give them novel functions. For instance, engineering of the VioC protein and mutation of Asp₂₇₀ by an Ala residue may change the dipole moment in the protein and trigger electrostatic changes that will enable substrate desaturation, as is seen in the NapI structure.

5 Conclusion

Computational modeling on enzymatic reaction mechanisms is reviewed with particular emphasis on L-Arg activation by nonheme iron dioxxygenases. Thus, the class of nonheme iron and α KG-dependent dioxxygenases react efficiently with L-Arg as a substrate, but a large variety of products can be obtained, including 3-hydroxyarginine, 4-hydroxyarginine, 5-hydroxyarginine, and 4,5-dehydroarginine. To understand the product distributions and bifurcation pathways, a series of computational studies was performed using either QM/MM or DFT cluster models. Both approaches match the experiment well and predict low-energy barriers, leading to the experimentally determined products. The calculations show that substrate binding and positioning guide the enzyme toward a specific selectivity. However, the intricate bifurcation pathways are determined by charge distributions within the substrate-binding



pocket. Thus, local electric field effects and dipole moments influence the substrate C–H bond strengths and create highly selective enzyme catalysts. It would be interesting to see if proteins can be engineered based on computationally suggested charge distributions and engineered active site structures.

Author contributions

HA: writing–original draft and writing–review and editing. Sd: conceptualization, writing–original draft, and writing–review and editing.

Funding

The author(s) declare that no financial support was received for the research, authorship, and/or publication of this article.

References

- Ali, H. S., and de Visser, S. P. (2022). Electrostatic perturbations in the substrate-binding pocket of taurine/α-ketoglutarate dioxygenase determine its selectivity. *Chem. Eur. J.* 28, e202104167. doi:10.1002/chem.202104167
- Ali, H. S., Henchman, R. H., and de Visser, S. P. (2020). Lignin biodegradation by a cytochrome P450 enzyme: a computational study into syringol activation by GcoA. *Chem. Eur. J.* 26, 13093–13102. doi:10.1002/chem.202002203
- Ali, H. S., Henchman, R. H., and de Visser, S. P. (2021b). What determines the selectivity of arginine dihydroxylation by the nonheme iron enzyme OrfP? *Chem. Eur. J.* 27, 1795–1809. doi:10.1002/chem.202004019
- Ali, H. S., Henchman, R. H., Warwicker, J., and de Visser, S. P. (2021a). How do electrostatic perturbations of the protein affect the bifurcation pathways of substrate hydroxylation versus desaturation in the nonheme iron-dependent viomycin biosynthesis enzyme? *J. Phys. Chem. A* 125, 1720–1737. doi:10.1021/acs.jpca.1c00141
- Ali, H. S., Warwicker, J., and de Visser, S. P. (2023). How does the nonheme iron enzyme NapI react through l-arginine desaturation rather than hydroxylation? A quantum mechanics/molecular mechanics study. *ACS Catal.* 13, 10705–10721. doi:10.1021/acscatal.3c02262
- Barbul, A. (1986). Arginine: biochemistry, physiology, and therapeutic implications. *J. Parenter. Enter. Nutr.* 10, 227–238. doi:10.1177/0148607186010002227
- Barkei, J. J., Kevany, B. M., Felnagle, E. A., and Thomas, M. G. (2009). Investigations into viomycin biosynthesis by using heterologous production in *Streptomyces lividans*. *ChemBioChem* 10, 366–376. doi:10.1002/cbic.200800646
- Barman, P., Cantù Reinhard, F. G., Bagha, U. K., Kumar, D., Sastri, C. V., and de Visser, S. P. (2019). Hydrogen by deuterium substitution in an aldehyde tunes the regioselectivity by a nonheme manganese(III)-peroxo complex. *Angew. Chem. Int. Ed.* 58, 10639–10643. doi:10.1002/anie.201905416
- Beaumier, L., Castillo, L., Yu, Y. M., Ajami, A. M., and Young, V. R. (1996). Arginine: new and exciting developments for an "old" amino acid. *Biomed. Environm. Sc.* 9, 296–315.
- Bérty, J. (2005). Bioactive microbial metabolites. *J. Antibiot.* 58, 1–26. doi:10.1038/ja.2005.1
- Berman, H. M., Westbrook, J., Feng, Z., Gilliland, G., Bhat, T. N., Weissig, H., et al. (2000). The protein data bank. *Nucl. Acids Res.* 28, 235–242. doi:10.1093/nar/28.1.235
- Bernasconi, L., and Baerends, E. J. (2013). A frontier orbital study with *ab initio* molecular dynamics of the effects of solvation on chemical reactivity: solvent-induced orbital control in FeO-activated hydroxylation reactions. *J. Am. Chem. Soc.* 135, 8857–8867. doi:10.1021/ja311144d
- Bordwell, F. G., and Cheng, J.-P. (1991). Substituent effects on the stabilities of phenoxyl radicals and the acidities of phenoxyl radical cations. *J. Am. Chem. Soc.* 113, 1736–1743. doi:10.1021/ja00005a042
- Borowski, T., Bassan, A., and Siegbahn, P. E. M. (2004). Mechanism of dioxygen activation in 2-oxoglutarate-dependent enzymes: a hybrid DFT study. *Chem. Eur. J.* 10, 1031–1041. doi:10.1002/chem.200305306
- Brujinincx, P. C. A., van Koten, G., and Klein Gebbink, R. J. M. (2008). Mononuclear non-heme iron enzymes with the 2-His-1-carboxylate facial triad: recent developments in enzymology and modeling studies. *Chem. Soc. Rev.* 37, 2716–2744. doi:10.1039/b707179p

Conflict of interest

The authors declare that the research was conducted in the absence of any commercial or financial relationships that could be construed as a potential conflict of interest.

The author(s) declare that they were an editorial board member of *Frontiers*, at the time of submission. This had no impact on the peer review process and the final decision.

Publisher's note

All claims expressed in this article are solely those of the authors and do not necessarily represent those of their affiliated organizations, or those of the publisher, the editors, and the reviewers. Any product that may be evaluated in this article, or claim that may be made by its manufacturer, is not guaranteed or endorsed by the publisher.

- Cantú Reinhard, F. G., Barman, P., Mukherjee, G., Kumar, J., Kumar, D., Kumar, D., et al. (2017). Keto-enol tautomerization triggers an electrophilic aldehyde deformylation reaction by a nonheme manganese(III)-peroxo complex. *J. Am. Chem. Soc.* 139, 18328–18338. doi:10.1021/jacs.7b10033
- Chang, C. Y., Lyu, S. Y., Liu, Y. C., Hsu, N. S., Wu, C. C., Tang, C. F., et al. (2014). Biosynthesis of streptolidine involved two unexpected intermediates produced by a dihydroxylase and a cyclase through unusual mechanisms. *Angew. Chem. Int. Ed. Engl.* 53, 1943–1948. doi:10.1002/anie.201307989
- Chaturvedi, S. S., Ramanan, R., Hu, J., Hausinger, R. P., and Christov, C. (2021). Atomic and electronic structure determinants distinguish between ethylene formation and L-arginine hydroxylation reaction mechanisms in the ethylene-forming enzyme. *ACS Catal.* 11, 1578–1592. doi:10.1021/acscatal.0c03349
- Copeland, R. A., Davis, K. M., Shoda, T. K. C., Blaesi, E. J., Boal, A. K., Krebs, C., et al. (2021). An iron(IV)-oxo intermediate initiating l-arginine oxidation but not ethylene production by the 2-oxoglutarate-dependent oxygenase, ethylene-forming enzyme. *J. Am. Chem. Soc.* 143, 2293–2303. doi:10.1021/jacs.0c10923
- de Visser, S. P. (2006). What factors influence the ratio of C–H hydroxylation versus C=C epoxidation by a nonheme cytochrome P450 biomimetic? *J. Am. Chem. Soc.* 128, 15809–15818. doi:10.1021/ja065365j
- de Visser, S. P. (2007). Can the peroxosuccinate complex in the catalytic cycle of taurine/α-ketoglutarate dioxygenase (TauD) act as an alternative oxidant? *Chem. Commun.* 2007, 171–173. doi:10.1039/b611273k
- de Visser, S. P. (2010). Trends in substrate hydroxylation reactions by heme and nonheme iron(IV)-oxo oxidants give correlations between intrinsic properties of the oxidant with barrier height. *J. Am. Chem. Soc.* 132, 1087–1097. doi:10.1021/ja908340j
- de Visser, S. P. (2020). Second-coordination sphere effects on selectivity and specificity of heme and nonheme iron enzymes. *Chem. Eur. J.* 26, 5308–5327. doi:10.1002/chem.201905119
- de Visser, S. P., and Kumar, D. (2011). *Iron-containing enzymes: versatile catalysts of hydroxylation reactions in nature* (Cambridge (UK): Royal Society of Chemistry Publishing).
- de Visser, S. P., Lin, Y.-T., Ali, H. S., Bagha, U. K., Mukherjee, G., and Sastri, C. V. (2021). Negative catalysis/non-Bell-Evans-Polanyi reactivity by metalloenzymes: examples from mononuclear heme and non-heme iron oxygenases. *Coord. Chem. Rev.* 439, 213914. doi:10.1016/j.ccr.2021.213914
- de Visser, S. P., Mukherjee, G., Ali, H. S., and Sastri, C. V. (2022). Local charge distributions, electric dipole moments and local electric fields influence reactivity patterns and guide regioselectivities in α-ketoglutarate-dependent nonheme iron dioxygenases. *Acc. Chem. Res.* 55, 65–74. doi:10.1021/acs.accounts.1c00538
- Dunham, N. P., and Arnold, F. H. (2020). Nature's machinery, repurposed: expanding the repertoire of iron-dependent oxygenases. *ACS Catal.* 10, 12239–12255. doi:10.1021/acscatal.0c03606
- Dunham, N. P., Chang, W.-c., Mitchell, A. J., Martinie, R. J., Zhang, B., Bergman, J. A., et al. (2018b). Two distinct mechanisms for C–C desaturation by iron(II)- and 2-(oxo) glutarate-dependent oxygenases: importance of α-heteroatom assistance. *J. Am. Chem. Soc.* 140, 7116–7126. doi:10.1021/jacs.8b01933
- Dunham, N. P., Mitchell, A. J., Del Río Pantoja, J. M., Krebs, C., Bollinger, J. M., Jr, and Boal, A. K. (2018a). α-Amine desaturation of d-arginine by the iron(II)- and 2-(oxo)glutarate-dependent l-arginine 3-hydroxylase, VioC. *Biochemistry* 57, 6479–6488. doi:10.1021/acs.biochem.8b00901
- Faponle, A. S., Quesne, M. G., and de Visser, S. P. (2016). Origin of the regioselective fatty acid hydroxylation versus decarboxylation by a cytochrome P450 peroxxygenase: what drives the reaction to biofuel production? *Chem. Eur. J.* 22, 5478–5483. doi:10.1002/chem.201600739
- Gérard, E. F., Mokkawas, T., Johannissen, L. O., Warwicker, J., Spiess, R. R., Blanford, C. F., et al. (2023). How is substrate halogenation triggered by the vanadium haloperoxidase from *Curvularia inaequalis*? *ACS Catal.* 13, 8247–8261. doi:10.1021/acscatal.3c00761
- Gérard, E. F., Yadav, Y., Goldberg, D. P., and de Visser, S. P. (2022). What drives radical halogenation versus hydroxylation in mononuclear nonheme iron complexes? A combined experimental and computational study. *J. Am. Chem. Soc.* 144, 10752–10767. doi:10.1021/jacs.2c01375
- Ghafoor, S., Mansha, A., and de Visser, S. P. (2019). Selective hydrogen atom abstraction from dihydroflavonol by a non-heme iron center is the key step in the enzymatic flavonol synthesis and avoids byproducts. *J. Am. Chem. Soc.* 141, 20278–20292. doi:10.1021/jacs.9b10526
- Gorres, K., and Raines, R. T. (2010). Prolyl 4-hydroxylase. *Crit. Rev. Biochem. Mol. Biol.* 45, 106–124. doi:10.3109/10409231003627991
- Groves, J. T., and Wang, C. C.-Y. (2000). Nitric oxide synthase: models and mechanisms. *Curr. Opin. Chem. Biol.* 4, 687–695. doi:10.1016/s1367-5931(00)00146-0
- Helmetag, V., Samel, S. A., Thomas, M. G., Marahiel, M. A., and Essen, L.-O. (2009). Structural basis for the erythro-stereospecificity of the L-arginine oxygenase VioC in viomycin biosynthesis. *FEBS J.* 276, 3669–3682. doi:10.1111/j.1742-4658.2009.07085.x
- Herrise, M., Ishida, K., Porter, J. L., Howden, B., Hertweck, C., Stinear, T. P., et al. (2020). Identification and mobilization of a cryptic antibiotic biosynthesis gene locus from a human-pathogenic nocardia isolate. *ACS Chem. Biol.* 15, 1161–1168. doi:10.1021/acscchembio.9b00763
- Herr, C. Q., and Hausinger, R. P. (2018). Amazing diversity in biochemical roles of Fe(II)/2-oxoglutarate oxygenases. *Trends biochem. Sci.* 43, 517–532. doi:10.1016/j.tibs.2018.04.002
- Himo, F., and de Visser, S. P. (2022). Status report on the quantum chemical cluster approach for modeling enzyme reactions. *Commun. Chem.* 5, 29. doi:10.1038/s42004-022-00642-2
- Hirao, H., Li, F., Que, L., Jr., and Morokuma, K. (2011). Theoretical study of the mechanism of oxoiron (IV) formation from H₂O₂ and a nonheme iron (II) complex: O–O cleavage involving proton-coupled electron transfer. *Inorg. Chem.* 50, 6637–6648. doi:10.1021/ic200522r
- Hofer, T. S., and de Visser, S. P. (2018). Editorial: quantum mechanical/molecular mechanical approaches for the investigation of chemical systems – recent developments and advanced applications. *Front. Chem.* 6, 357. doi:10.3389/fchem.2018.00357
- Höglund, E., Øverli, Ø., and Winberg, S. (2019). Tryptophan metabolic pathways and brain serotonergic activity: a comparative review. *Front. Endocrinol.* 10, 158. doi:10.3389/fendo.2019.00158
- Huang, X., and Groves, J. T. (2017). Beyond ferryl-mediated hydroxylation: 40 years of the rebound mechanism and C–H activation. *J. Biol. Inorg. Chem.* 22, 185–207. doi:10.1007/s00775-016-1414-3
- Kal, S., and Que, L., Jr (2017). Dioxygen activation by nonheme iron enzymes with the 2-His-1-carboxylate facial triad that generate high-valent oxoiron oxidants. *J. Biol. Inorg. Chem.* 22, 339–365. doi:10.1007/s00775-016-1431-2
- Koski, M. K., Hieta, R., Hirsilä, M., Rönkä, A., Myllyharju, J., and Wierenga, R. K. (2009). The crystal structure of an algal prolyl 4-hydroxylase complexed with a proline-rich peptide reveals a novel buried tripeptide binding motif. *J. Biol. Chem.* 284, 25290–25301. doi:10.1074/jbc.m109.014050
- Krebs, C., Fujimori, D. G., Walsh, C. T., and Bollinger, J. M., Jr (2007). Non-heme Fe(IV)-oxo intermediates. *Acc. Chem. Res.* 40, 484–492. doi:10.1021/ar700066p
- Kumar, D., Tahsini, L., de Visser, S. P., Kang, H. Y., Kim, S. J., and Nam, W. (2009). Effect of porphyrin ligands on the regioselective dehydrogenation versus epoxidation of olefins by oxoiron(IV) mimics of cytochrome P450. *J. Phys. Chem. A* 113, 11713–11722. doi:10.1021/jp9028694
- Latifi, R., Bagherzadeh, M., and de Visser, S. P. (2009). Origin of the correlation of the rate constant of substrate hydroxylation by nonheme iron(IV)-oxo complexes with the bond-dissociation energy of the C–H bond of the substrate. *Chem. Eur. J.* 15, 6651–6662. doi:10.1002/chem.200900211
- Latifi, R., Sainna, M. A., Rybak-Akimova, E. V., and de Visser, S. P. (2013). Does hydrogen bonding-donation to manganese(IV)-oxo and iron(IV)-oxo oxidants affect the oxygen atom transfer ability? A computational study. *Chem. Eur. J.* 19, 4058–4068. doi:10.1002/chem.201202811
- Lin, Y.-T., Ali, H. S., and de Visser, S. P. (2021). Electrostatic perturbations from the protein affect C–H bond strengths of the substrate and enable negative catalysis in the TmpA biosynthesis enzyme. *Chem. Eur. J.* 27, 8851–8864. doi:10.1002/chem.202100791
- Lin, Y.-T., Ali, H. S., and de Visser, S. P. (2022). Biodegradation of herbicides by a plant nonheme iron dioxygenase: mechanism and selectivity of substrate analogues. *Chem. Eur. J.* 28, e202103982. doi:10.1002/chem.202103982
- Liu, G., Chater, K. F., Chandra, G., Niu, G., and Tan, H. (2013). Molecular regulation of antibiotic biosynthesis in *Streptomyces*. *Microbiol. Mol. Biol. Rev.* 77, 112–143. doi:10.1128/mmbr.00054-12
- Marsh, E. N., Chang, M. D. T., and Townsend, C. A. (1992). Two isozymes of clavaminase synthase central to clavulanic acid formation: cloning and sequencing of both genes from *Streptomyces clavuligerus*. *Biochemistry* 31, 12648–12657. doi:10.1021/bi00165a015
- Martinez, S., and Hausinger, R. P. (2015). Catalytic mechanisms of Fe(II)- and 2-oxoglutarate-dependent oxygenases. *J. Biol. Chem.* 290, 20702–20711. doi:10.1074/jbc.r115.648691
- Martinez, S., and Hausinger, R. P. (2016). Biochemical and spectroscopic characterization of the non-heme Fe(II)- and 2-oxoglutarate-dependent ethylene-forming enzyme from *Pseudomonas syringae* pv. *phaseolicola* PK2. *Biochemistry* 55, 5989–5999. doi:10.1021/acs.biochem.6b00890
- McDonough, M. A., Li, V., Flashman, E., Chowdhury, R., Mohr, C., Lienard, B. M., et al. (2006). Cellular oxygen sensing: crystal structure of hypoxia-inducible factor prolyl hydroxylase (PHD2). *Proc. Natl. Acad. Sci. U. S. A.* 103, 9814–9819. doi:10.1073/pnas.0601283103
- Mitchell, A. J., Dunham, N. P., Martinie, R. J., Bergman, J. A., Pollock, C. J., Hu, K., et al. (2017). Visualizing the reaction cycle in an iron(II)- and 2-(oxo)-glutarate-dependent hydroxylase. *J. Am. Chem. Soc.* 139, 13830–13836. doi:10.1021/jacs.7b07374
- Mokkawas, T., and de Visser, S. P. (2023). Caffeine biodegradation by cytochrome P450 1A2. What determines the product distributions? *Chem. Eur. J.* 29, e202203875. doi:10.1002/chem.202203875
- Morita, I., Mori, T., and Abe, I. (2021). Enzymatic formation of indolactam scaffold by C–N bond-forming cytochrome P450 oxidases in teleocidin biosynthesis. *Chem. Eur. J.* 27, 2963–2972. doi:10.1002/chem.202003899

- Morris, S. M., Jr (2002). Regulation of enzymes of the urea cycle and arginine metabolism. *Ann. Rev. Nutr.* 22, 87–105. doi:10.1146/annurev.nutr.22.110801.140547
- Morris, S. M., Jr (2009). Recent advances in arginine metabolism: roles and regulation of the arginases. *Brit. J. Pharmacol.* 157, 922–930. doi:10.1111/j.1476-5381.2009.00278.x
- Mukherjee, G., Alili, A., Barman, P., Kumar, D., Sastri, C. V., and de Visser, S. P. (2019). Interplay between steric and electronic effects: a joint spectroscopy and computational study of nonheme iron(IV)-oxo complexes. *Chem. Eur. J.* 25, 5086–5098. doi:10.1002/chem.201806430
- Mukherjee, G., Satpathy, J. K., Bagha, U. K., Mubarak, M. Q. E., Sastri, C. V., and de Visser, S. P. (2021). Inspiration from Nature: influence of engineered ligand scaffolds and auxiliary factors on the reactivity of biomimetic oxidants. *ACS Catal.* 11, 9761–9797. doi:10.1021/acscatal.1c01993
- Pegis, M. L., Wise, C. F., Martin, D. J., and Mayer, J. M. (2018). Oxygen reduction by homogeneous molecular catalysts and electrocatalysts. *Chem. Rev.* 118, 2340–2391. doi:10.1021/acs.chemrev.7b00542
- Proshlyakov, D. A., Henshaw, T. F., Monterosso, G. R., Ryle, M. J., and Hausinger, R. P. (2004). Direct detection of oxygen intermediates in the non-heme Fe enzyme taurine/α-ketoglutarate dioxygenase. *J. Am. Chem. Soc.* 126, 1022–1023. doi:10.1021/ja039113j
- Pu, J.-Y., Peng, C., Tang, M.-C., Zhang, Y., Guo, J.-P., Song, L.-Q., et al. (2013). Naphthylridinomycin biosynthesis revealing the use of leader peptide to guide nonribosomal peptide assembly. *Org. Lett.* 15, 3674–3677. doi:10.1021/ol401549y
- Quesne, M. G., Borowski, T., and de Visser, S. P. (2016). Quantum mechanics/molecular mechanics modeling of enzymatic processes: caveats and breakthroughs. *Chem. Eur. J.* 22, 2562–2581. doi:10.1002/chem.201503802
- Quesne, M. G., Latifi, R., Gonzalez-Ovalle, L. E., Kumar, D., and de Visser, S. P. (2014). Quantum mechanics/molecular mechanics study on the oxygen binding and substrate hydroxylation step in AlkB repair enzymes. *Chem. Eur. J.* 20, 435–446. doi:10.1002/chem.201303282
- Riggs-Gelasco, P. J., Price, J. C., Guyer, R. B., Brehm, J. H., Barr, E. W., Bollinger, J. M., Jr, et al. (2004). EXAFS spectroscopic evidence for an Fe=O unit in the Fe(IV) intermediate observed during oxygen activation by taurine:α-ketoglutarate dioxygenase. *J. Am. Chem. Soc.* 126, 8108–8109. doi:10.1021/ja048255q
- Roberts, K. M., and Fitzpatrick, P. F. (2013). Mechanisms of tryptophan and tyrosine hydroxylase. *Int. Union Biochem. Mol. Biol.* 65, 350–357. doi:10.1002/iub.1144
- Sahu, S., Quesne, M. G., Davies, C. G., Dürr, M., Ivanović-Burmazović, I., Siegler, M. A., et al. (2014). Direct observation of a non-heme iron(IV)-oxo complex that mediates aromatic C-F hydroxylation. *J. Am. Chem. Soc.* 136, 13542–13545. doi:10.1021/ja507346t
- Scott, J. D., and Williams, R. M. (2002). Chemistry and biology of the tetrahydroisoquinoline antitumor antibiotics. *Chem. Rev.* 102, 1669–1730. doi:10.1021/cr010212u
- Senn, H. M., and Thiel, W. (2007a). QM/MM studies of enzymes. *Curr. Opin. Chem. Biol.* 11, 182–187. doi:10.1016/j.cbpa.2007.01.684
- Senn, H. M., and Thiel, W. (2007b). QM/MM methods for biological systems. *Top. Curr. Chem.* 268, 173–290. doi:10.1007/128_2006_084
- Shaik, S., de Visser, S. P., and Kumar, D. (2004). External electric field will control the selectivity of enzymatic-like bond activations. *J. Am. Chem. Soc.* 126, 11746–11749. doi:10.1021/ja047432k
- Shaik, S., Ramanan, R., Danovich, D., and Mandal, D. (2018). Structure and reactivity/selectivity control by oriented-external electric fields. *Chem. Soc. Rev.* 47, 5125–5145. doi:10.1039/c8cs00354h
- Sheng, X., Kazemi, M., Planas, F., and Himo, F. (2020). Modeling enzymatic enantioselectivity using quantum chemical methodology. *ACS Catal.* 10, 6430–6449. doi:10.1021/acscatal.0c00983
- Siegbahn, P. E. M., and Blomberg, M. R. A. (2010). Quantum chemical studies of proton-coupled electron transfer in metalloenzymes. *Chem. Rev.* 110, 7040–7061. doi:10.1021/cr100070p
- Simaan, A. J., and Réglier, M. (2015). In *2-Oxoglutarate-dependent oxygenases*. Editors R. P. Hausinger and C. J. Schofield (Cambridge: Royal Society of Chemistry), 425.
- Stuehr, D. J. (1999). Mammalian nitric oxide synthases. *Biochim. Biophys. Acta (BBA)-Bioenergetics* 1411, 217–230. doi:10.1016/s0005-2728(99)00016-x
- Tang, H., Guan, J., Zhang, L., Liu, H., and Huang, X. (2012). The effect of the axial ligand on distinct reaction tunneling for methane hydroxylation by nonheme iron (iv)-oxo complexes. *Phys. Chem. Chem. Phys.* 14, 12863–12874. doi:10.1039/c2cp42423a
- Tchesnokov, E. P., Paponle, A. S., Davies, C. G., Quesne, M. G., Turner, R., Fellner, M., et al. (2016). An iron-oxygen intermediate formed during the catalytic cycle of cysteine dioxygenase. *Chem. Commun.* 52, 8814–8817. doi:10.1039/c6cc03904a
- Thomas, M. G., Chan, Y. A., and Ozanick, S. G. (2003). Deciphering tuberactinomycin biosynthesis: isolation, sequencing, and annotation of the viomycin biosynthetic gene cluster. *Antimicrob. Agents Chemo* 47, 2823–2830. doi:10.1128/aac.47.9.2823-2830.2003
- Timmins, A., Fowler, N. J., Warwicker, J., Straganz, G. D., and de Visser, S. P. (2018a). Does substrate positioning affect the selectivity and reactivity in the hectorchlorin biosynthesis halogenase? *Front. Chem.* 6, 513. doi:10.3389/fchem.2018.00513
- Timmins, A., Quesne, M. G., Borowski, T., and de Visser, S. P. (2018b). Group transfer to an aliphatic bond: a biomimetic study inspired by nonheme iron halogenases. *ACS Catal.* 8, 8685–8698. doi:10.1021/acscatal.8b01673
- Timmins, A., Saint-André, M., and de Visser, S. P. (2017). Understanding how prolyl-4-hydroxylase structure steers a ferryl oxidant toward scission of a strong C–H bond. *J. Am. Chem. Soc.* 139, 9855–9866. doi:10.1021/jacs.7b02839
- Usharani, D., Janardanan, D., Li, C., and Shaik, S. (2013). A theory for bioinorganic chemical reactivity of oxometal complexes and analogous oxidants: the exchange and orbital-selection rules. *Acc. Chem. Res.* 46, 471–482. doi:10.1021/ar300204y
- Visek, W. J. (1986). Arginine needs, physiological state and usual diets. *A reevaluation. J. Nutr.* 116, 36–46. doi:10.1093/jn/116.1.36
- Walsh, C. T. (2006). *Posttranslational modification of proteins: expanding nature's inventory*. USA: Roberts and Company Publishers, Greenwood Village CO.
- White, M. D., and Flashman, E. (2016). Catalytic strategies of the non-heme iron dependent oxygenases and their roles in plant biology. *Curr. Opin. Chem. Biol.* 31, 126–135. doi:10.1016/j.cbpa.2016.02.017
- Wójcik, A., Radoń, M., and Borowski, T. (2016). Mechanism of O₂ activation by α-ketoglutarate dependent oxygenases revisited. A quantum chemical study. *J. Phys. Chem. A* 120, 1261–1274. doi:10.1021/acs.jpca.5b12311
- Wojdyła, Z., and Borowski, T. (2022). Properties of the reactants and their interactions within and with the enzyme binding cavity determine reaction selectivities. The case of Fe(II)/2-oxoglutarate dependent enzymes. *Chem. Eur. J.* 28, e202104106. doi:10.1002/chem.202104106
- Wu, G., Bazer, F. W., Davis, T. A., Kim, S. W., Li, P., Rhoads, J. M., et al. (2009). Arginine metabolism and nutrition in growth, health and disease. *Amino Acids* 37, 153–168. doi:10.1007/s00726-008-0210-y
- Wu, G., and Morris, S. M., Jr (1998). Arginine metabolism: nitric oxide and beyond. *Biochem. J.* 336, 1–17. doi:10.1042/bj3360001
- Ye, S., Geng, C.-Y., Shaik, S., and Neese, F. (2013). Electronic structure analysis of multistate reactivity in transition metal catalyzed reactions: the case of C–H bond activation by non-heme iron (IV)-oxo cores. *Phys. Chem. Chem. Phys.* 15, 8017–8030. doi:10.1039/c3cp00080j
- Yeh, C.-C. G., Ghafoor, S., Satpathy, J. K., Mokkaew, T., Sastri, C. V., and de Visser, S. P. (2022). Cluster model study into the catalytic mechanism of α-ketoglutarate biodegradation by the ethylene-forming enzyme reveals structural differences with nonheme iron hydroxylases. *ACS Catal.* 12, 3923–3937. doi:10.1021/acscatal.1c04029
- Yin, X., and Zabriskie, T. M. (2004). VioC is a non-heme iron, α-ketoglutarate-dependent oxygenase that catalyzes the formation of 3S-hydroxy-L-arginine during viomycin bio-synthesis. *ChemBioChem* 5, 1274–1277. doi:10.1002/cbic.200400082
- Zwick, C. R., III, Sosa, M. B., and Renata, H. (2019). Characterization of a citrulline 4-hydroxylase from nonribosomal peptide GE81112 biosynthesis and engineering of its substrate specificity for the chemoenzymatic synthesis of enduracididine. *Angew. Chem. Int. Ed.* 58, 18854–18858. doi:10.1002/anie.201910659



OPEN ACCESS

EDITED BY

Steve Suib,
University of Connecticut, United States

REVIEWED BY

Briana Aguila-Ames,
New College of Florida, United States
Bishnu P. Biswal,
National Institute of Science Education and
Research (NISER), India

*CORRESPONDENCE

Raquel Gavara,
✉ raquel.gavara@uam.es
Félix Zamora,
✉ felix.zamora@uam.es

RECEIVED 08 February 2024

ACCEPTED 15 March 2024

PUBLISHED 28 March 2024

CITATION

Gavara R, Royuela S and Zamora F (2024), A
minireview on covalent organic frameworks as
stationary phases in chromatography.
Front. Chem. 12:1384025.
doi: 10.3389/fchem.2024.1384025

COPYRIGHT

© 2024 Gavara, Royuela and Zamora. This is an
open-access article distributed under the terms
of the [Creative Commons Attribution License](#)
(CC BY). The use, distribution or reproduction in
other forums is permitted, provided the original
author(s) and the copyright owner(s) are
credited and that the original publication in this
journal is cited, in accordance with accepted
academic practice. No use, distribution or
reproduction is permitted which does not
comply with these terms.

A minireview on covalent organic frameworks as stationary phases in chromatography

Raquel Gavara^{1,2*}, Sergio Royuela¹ and Félix Zamora^{1,3*}

¹Departamento de Química Inorgánica, Facultad de Ciencias, Universidad Autónoma de Madrid, Madrid, Spain, ²Institute for Advanced Research in Chemical Sciences (IAChem), Universidad Autónoma de Madrid, Madrid, Spain, ³Condensed Matter Physics Center (IFIMAC), Universidad Autónoma de Madrid, Madrid, Spain

Advances in the design of novel porous materials open new avenues for the development of chromatographic solid stationary phases. Covalent organic frameworks (COFs) are promising candidates in this context due to their remarkable structural versatility and exceptional chemical and textural properties. In this minireview, we summarize the main strategies followed in recent years to apply these materials as stationary phases for chromatographic separations. We also comment on the perspectives of this new research field and potential directions to expand the applicability and implementation of COF stationary phases in analytical systems.

KEYWORDS

COF, COF processability, COF composites, COF stationary phase, chromatography

1 Introduction

Covalent organic frameworks (COFs) are highly crystalline organic polymers with large surface area, tunable pore size and geometry, versatile functionalization, and relatively high thermal and chemical stability. Their crystallinity arises from the dynamic nature of the covalent bonds that join the building blocks, which allows the self-healing and error correction of the backbone during the synthesis and gives rise to the most thermodynamically stable structure (Lohse and Bein, 2018; Geng et al., 2020). Due to their outstanding properties, COFs present great potential in several applications such as supercapacitors and batteries (Sun et al., 2023; Tao et al., 2023), gas adsorption (Chen et al., 2022; Li et al., 2023), catalysis (Martínez-Fernández et al., 2022b; Qi et al., 2023), separation (Wang et al., 2020), sensing (Martínez-Fernández et al., 2022a; Yue et al., 2023) and optoelectronics (Keller and Bein, 2021). Moreover, extensive research has been developed on using COFs for membrane-based separations (Burke et al., 2023). Still, the application of these materials in column-based separations has been much less explored. Chromatography is the most widely applied method for accurate analysis and separation in many fields, such as clinical analysis (Kočová Vlčková et al., 2018), pharmaceutical industry (Steinebach et al., 2016), food and beverage testing (Núñez and Lucci, 2020), environmental detection (Yang et al., 2023), and control of industrial chemical processes (Pollo et al., 2018), among others. The most crucial component in a chromatographic system is the stationary phase. In this regard, the separation efficiency depends on establishing several noncovalent interactions between the stationary phase and the analytes. Due to the control on pore size and chemistry, high surface area, and stability, COFs are gaining much attention as stationary phases for chromatographic separations (Zhang et al., 2019;

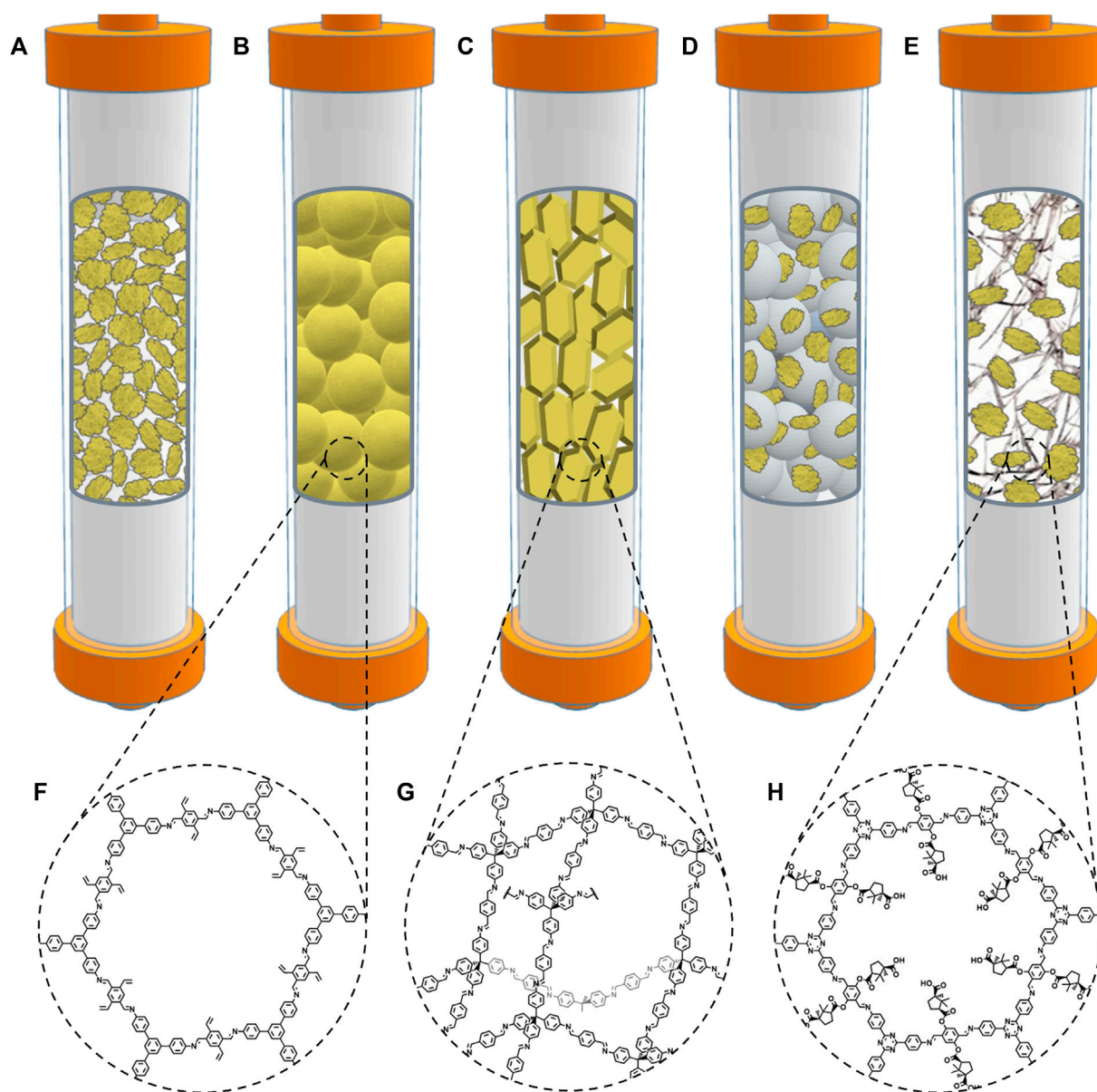


FIGURE 1

Strategies that have been used to prepare stationary phases based on COF powders: (A) polydisperse and irregular COF powders, (B) monodisperse micron-sized spherical COF particles, (C) single-crystal COF particles, (D) physical mixture of irregular and polydisperse COF powder with silica microspheres, and (E) irregular COF powder incorporated into porous polymer monolithic columns. COF-V (F), COF-300 (G), and COF CTzDa (H) are representative examples of COFs employed in strategies (B), (C) and (E), respectively (Zheng Q. et al., 2021; 2022a; Qian H.-L. et al., 2022).

Fikarova et al., 2022). Thus, over the last few years, three main approaches have been developed for the preparation of stationary phases based on COFs: i) direct packing of COF powders in columns, alone or mixed with another material (Figure 1); ii) preparation of composites involving COFs and other materials (Figure 2A); and iii) formation of COF coatings in capillary columns (Figure 2B). This minireview summarizes the recent developments in COF chromatographic stationary phases following these strategies (Table 1). We warn that works that assert the use of COFs as stationary phases without demonstrating their crystallinity and/or porosity have not been included in this revision.

2 Stationary phases based on COF powders

2.1 Pure COF powders

The most straightforward approach to using a COF as a stationary phase involves packing the powder material directly on the chromatographic column (Figure 1). In 2018, Ma et al. designed several chiral stationary phases by immobilizing optically active biomolecules into a new imide-linked COF 1 (Zhang et al., 2018). The pristine material was synthesized under solvothermal conditions and exhibited good crystallinity and high

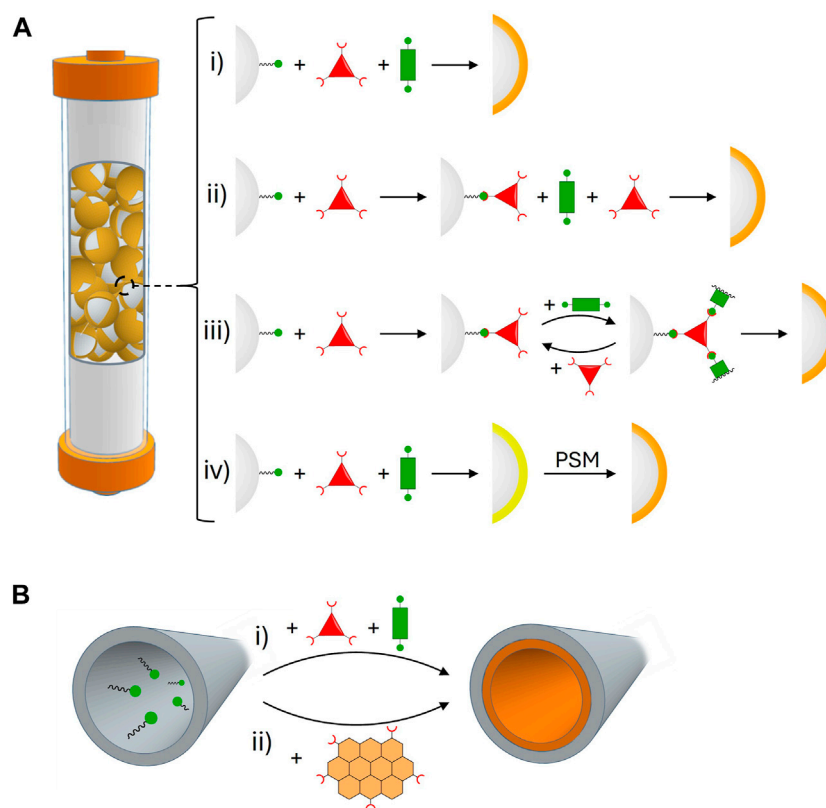


FIGURE 2

(A) Strategies that have been used to prepare stationary phases based on core-shell COF composites with silica microspheres: (i) *in situ* growth, (ii) two-step growth, (iii) layer-by-layer growth, and (iv) *in situ* growth followed by post-synthetic modification. (B) Strategies that have been used to prepare stationary phases based on COF chemical coatings: (i) *in situ* growth on the capillary walls and (ii) physical adsorption/covalent attachment of pre-synthesized COF particles.

Brunauer–Emmett–Teller (BET) surface area. The protein lysozyme, as well as the tripeptide Lys-Val-Phe and the amino acid L-lysine were covalently attached to the material using the -COOH residues accessible on the surface. After functionalization, a remarkable reduction of the surface area was observed. Nevertheless, crystallinity was preserved. The biomolecule-COFs were evaluated as high-performance liquid chromatography (HPLC) stationary phases towards the separation of various racemates. The results showed that Lysozyme-COF exhibited the best chiral separation efficiency for all the tested racemates. Moreover, it was demonstrated that covalent immobilization surpassed the simple adsorption immobilization of the enzyme into the COF.

However, the direct use of COF solvothermal powders is often restricted due to the polydispersity in sizes, irregular shape of COF particles, and their small crystal size. This usually results in high back-pressure and low column efficiency. A way to overcome these issues involves preparing micron-sized COFs with regular spherical shapes. This strategy was employed by Lin and co-workers (Zheng Q. et al., 2021), who prepared micron-sized spherical particles of the imine-linked COF-V (Sun et al., 2017) in a facile synthesis at room temperature. They could synthesize four spherical COFs with tunable sizes of ca. 2, 1.5, 1, and 0.8 μm , by modulating the amount of catalyst used in the synthesis. All the materials showed good monodispersity and high crystallinity. The measured BET surface area was directly related to the amount of

catalyst and decreased with the increase in particle size, ranging from ca. 360–1,170 $\text{m}^2 \text{g}^{-1}$. After packing the materials in short columns for liquid chromatography (LC) separations, the elution of several aromatic compounds and protein digests revealed an excellent chromatographic performance for the 1 μm particle size COF. It was observed that a higher size led to a decreased resolution and retention. However, a decrease in particle size also led to a noticeable increase in column pressure, which made it impossible to test the 0.8 μm particle size COF. The same research group employed a similar approach to prepare a new HPLC stationary phase based on the column packing of a fluoro-functionalized spherical COF. This COF-packed column exhibited superior performance towards the separation of organic halides than commercial C18 and pentafluorophenyl columns (Zheng et al., 2022b).

Another way of controlling particle size and shape relies on developing single-crystalline COF particles. This approach was recently applied to prepare new HPLC stationary phases (Zheng et al., 2022a). The authors were able to obtain, at room temperature, single-crystalline particles of the 3D imine-linked COF-300 (Ma et al., 2018), which exhibited a regular geometric shape and size of around 10 μm . The material presented an excellent diffraction pattern and high BET surface area. The packed HPLC column showed ideal resolution in separating positional isomers of small aromatic compounds, including nitroaniline, dichlorobenzene, and

TABLE 1 Summary of stationary phases based on COFs.

Strategy	Stationary phase	Crystallinity ^a	BET surface area (m ² g ⁻¹)	Application	Performance ^b	References
COF powder	Lysozyme@COF 1	High	103	HPLC separation of racemates of amino acids and chiral drugs	High	Zhang et al. (2018)
	Peptide@COF 1	High	- ^c		Low	
	Lysine@COF 1	High	- ^c		Failed	
COF powder—spherical particles	SCOFs-2.0 μm	High	364	LC separation of PAHs, anilines, alkylbenzenes, halogenated nitrobenzenes, phthalates, BSA tryptic digest	Failed	Zheng et al. (2021a)
	SCOFs-1.5 μm	High	569		Low	
	SCOFs-1.0 μm	High	856		High/Good	
	SCOFs-0.8 μm	High	1,167		Failed ^d	
COF powder—spherical particles	SF-COFs	Moderate	170	HPLC separation of organic halides, organic compounds with different hydrophobicity and aromatic ring structures	High ^e	Zheng et al. (2022b)
COF powder—single crystals	Single-crystalline	High	602	HPLC separation of positional isomers of disubstituted benzenes, alkylbenzenes, monosubstituted aromatics and PAHs	High	Zheng et al. (2022a)
	COF-300					
Mixture with cellulose derivative	CDMPC@SCOF CSP1	High	108	HPLC separation of racemates and chiral fungicides	Low	Yan et al. (2022)
	CDMPC@SCOF CSP2	High	64		Good	
	CDMPC@SCOF CSP3	High	45		High	
Mixture with SiO ₂ particles	CCOF 5	High ^f	655 ^f	HPLC separation of racemic alcohols	Good	Han et al. (2018)
	CCOF 6	High ^f	613 ^f		High	
Mixture with SiO ₂ particles	COF 1	High ^f	666 ^f	HPLC separation of ethylbenzene and xylene isomers and other benzene derivatives	High	Huang et al. (2019a)
	COF 1-Zn	High ^f	460 ^f		Low	
	COF 2	High ^f	701 ^f		High	
	COF 2-Zn	High ^f	535 ^f		Low	
Mixture with SiO ₂ particles	PFPP-COF-1a	High ^f	874 ^f	HPLC separation of PAHs	Low	Wang et al. (2022b)
	PFPP-COF-1b	High ^f	1,027 ^f		Low	
	PFPP-COF-2	High ^f	1,698 ^f		High ^g	
Mixture with SiO ₂ particles—“Wrapped in Net Method”	CSP-1	High ^f	-	HPLC separation of racemates and chiral drugs	High/Good	Yuan et al. (2022)
	CSP-2	High ^f	-		High/Good	
Mixture with SiO ₂ particles—“Wrapped in Net Method”	CD-PlasmaCOF-CSP-1	High ^f	581 ^f	HPLC separation of racemates and chiral drugs	High/Good	Yuan et al. (2023)
	CD-PlasmaCOF-CSP-2	High ^f	335 ^f		High/Good	
Mixture with polymer monolith	3D-IL-COF-1	Low	251	HPLC separation of neutral, acidic, basic, and isomers of organic compounds	High ^h	Liu et al. (2021)
Mixture with polymer monolith	CTzDa-monolith	Moderate	252	HPLC separation of racemic amino acids	High ⁱ	Qian et al. (2022b)
Composites— <i>In situ</i> growth	BtaMth@SiO ₂	High	723 ^f	HPLC separation of nitroaromatics isomers/β-cypermethrin and metconazole cis-trans isomers	Good	Zhang et al. (2017)

(Continued on following page)

TABLE 1 (Continued) Summary of stationary phases based on COFs.

Strategy	Stationary phase	Crystallinity ^a	BET surface area (m ² g ⁻¹)	Application	Performance ^b	References
				HPLC separation of β -cypermethrin and metconazole enantiomers	Failed	
Composites— <i>In situ</i> growth	CTpBD@SiO ₂	Low	260	HPLC enantiomeric separation of 20 different pairs of enantiomers	Good	Guo et al. (2021b)
Composites— <i>In situ</i> growth	β -CD-COF@SiO ₂	Moderate	-	HPLC enantiomeric separation of 24 different pairs of enantiomers	High	Xu et al. (2021a)
Composites— <i>In situ</i> growth	SiO ₂ @COF	- ^j	306	HPLC separation of alkylbenzenes, PAHs, positional isomers, nucleosides, anilines and sulfanilamides	High	Zheng et al. (2021b)
Composites—Two-step growth	TpBD@SiO ₂	Moderate	385	HPLC separation of PAHs, acidic, basic and aromatic compounds, and nucleobases, nucleosides, and deoxynucleosides	High ^h	Wang et al. (2017)
Composites—Two-step growth	COF-300@SiO ₂	High	254	HPLC separation of PAHs, ethers, aldehydes, ketones, photosensitizers, drugs, alkaloids	High	Chen et al. (2019)
				HPLC separation of substituted benzenes, nucleosides and nucleobases	Good	
Composites—Two-step growth	NPS@TPB-DMTP	High	177	HPLC separation of monosubstituted benzenes, PAHs, alkylbenzenes, anilines and phthalates	High	Xie et al. (2023)
Composites—Layer-by-layer reaction	COF-300@SiO ₂	High	431	HPLC separation of benzene homologues, PAHs and substituted aromatics	High	Qian et al. (2018)
Composites—Post-synthetic modification	SiI-COF	Low	328	HPLC separation of alkylbenzenes and PAHs	Good	Wan et al. (2023)
	SiI-COF-CD	Low	-	HPLC separation of 2-phenylpropionic acid and 1-phenyl-1-propanol enantiomers	High	
Composites—Post-synthetic modification	SiO ₂ @rLZU1	Low	194	HPLC separation of PAHs and benzene derivatives	High	Xu et al. (2021b)
				HPLC separation of tar, phenol, ammonia and other substances present in cooking wastewater	Good	
Composites—Post-synthetic modification	COF@CD@SiO ₂	- ^j	298	HPLC separation of enantiomers, positional isomers, alkylbenzenes and PAHs	High	Zheng et al. (2022c)
Dynamic coating	TpBD	Moderate ^k	885 ^f	GC separation of alkanes, cyclohexane and benzene, α - and β -pinene, and alcohols	High ^l	Yang et al. (2015)
Chemical coating— <i>In situ</i> growth	CTpPa-1	Moderate ^m	146 ^f	GC separation of racemates	High ⁿ	Qian et al. (2016)
	CTpPa-2	Moderate ^m	104 ^f		High ⁿ	
	CTpBD	Moderate ^m	317 ^f		High ⁿ	
Chemical coating— <i>In situ</i> growth	BtaMth	Moderate ^k	-	GC separation of alkanes, alcohols, and aromatic positional isomers	High/Good	Huang et al. (2019b)

(Continued on following page)

TABLE 1 (Continued) Summary of stationary phases based on COFs.

Strategy	Stationary phase	Crystallinity ^a	BET surface area (m ² g ⁻¹)	Application	Performance ^b	References
Chemical coating— <i>In situ</i> growth	COF-V	Moderate ^m	-	CEC separation of benzene derivatives, antileptic drugs, herbicides, active ingredients in Chinese medicine	High	Sun et al. (2021)
Chemical coating— <i>In situ</i> growth	TAPB-BPTA	Low	-	CEC separation of benzene derivatives, NSAIDs and parabens	High	He et al. (2022)
Chemical coating— <i>In situ</i> growth	TpTFMB	Moderate	964 ^f	GC separation of isomers of benzene derivatives, alkenes, and acetates	High	Ma et al. (2023)
	TpPa-CF3	Moderate	1,306 ^f		High/Good	
Chemical coating— <i>In situ</i> growth	SCOF-303 (1.6 μm)	High	-	GC separation of isomers of xylene, dichlorobenzene and pinene	High/Good ^o	Wang et al. (2023)
	SCOF-303 (1.2 μm)	Moderate	-		High ^o	
	SCOF-303 (0.8 μm)	Moderate	-		High ^o	
	SCOF-303 (0.4 μm)	Moderate	-		High ^o	
Chemical coating—covalent attachment	Tf-DHzOH	High ^m	82	CEC separation of amino acids, sulfonamides, tetracyclines, and benzene derivatives	High	Wang et al. (2022a)
Chemical coating—covalent attachment	TFA-TAPB	Low ^m	-	CEC separation of fluoroquinolones	High	Zong et al. (2022)
Chemical coating—covalent attachment	JUC-515	Moderate ^m	-	CEC separation of fluoroquinolones	High	Yin et al. (2023)

^aCrystallinity is classified in “High” “Moderate” or “Low” considering the intensity, signal-to-noise ratio, and half-width of the characteristic signals appearing in the XRD diffractograms.

^bPerformance is classified in “High”, “Good”, “Low” and “Failed” according to the resolution of the peaks in the chromatograms.

^cLower than surface area of Lysozyme@COF 1.

^dHigh back-pressure prevented the measurement.

^eBetter than commercial C18 and pentafluorophenyl columns.

^fPristine COF or as-prepared COF.

^gBetter than ZORBAX Eclipse PAH column in resolution.

^hBetter than C18 column.

ⁱBetter than Poroshell 120 chiral-T column.

^jData not available.

^kPristine COF heated up to 250 °C.

^lBetter than HP-5 column.

^mMeasurement was made on a coating analog.

ⁿBetter than β-DEX 225 and Cyclosil B columns.

^oPerformance increases with the decrease of particle size in the coating.

diethylbenzene. The study also found that the single-crystalline COF-300 exhibited higher resolution and selectivity for positional isomers than commercial columns and a polycrystalline COF-300-packed column.

2.2 Mixtures with other materials

The physical mixing of COFs with other materials (Figure 1) can introduce new separation properties in the stationary phases. For example, Cai and co-workers prepared chiral stationary phases by mixing a cellulose derivative with spherical COFs (Yan et al., 2022). Nevertheless, the main goal of physical mixing is usually to overcome the high column back-pressures related to standard COF powders. In that sense, silica is often selected as a co-

packing material due to its availability, stability, and easy preparation as monodisperse particles with regular shapes (Qiu et al., 2011). Thus, Cui and co-workers have implemented this approach in several recent investigations (Han et al., 2018; Huang J. et al., 2019; Wang et al., 2022b; Yuan et al., 2022; Yuan et al., 2023).

In 2018, they reported a new 3D chiral COF, CCOF 5, based on the solvothermal reaction of a TADDOL-derived tetraaldehyde with a tetrafunctionalized amine. The post-synthetic oxidation of the imine linkages gave rise to the amide-linked CCOF 6. Both materials presented good crystallinity and high BET surface area. The HPLC-packed columns were prepared by mixing ~0.3 μm COF particles with silica microspheres with an average size of 5 μm. Several alcohol racemates were selected to evaluate the chromatographic properties of the columns. The experiments revealed superior resolution performance for the amide-linked COF compared to the pristine

material, which was attributed to stronger interactions between the amide groups and alcohol guests in the pore channels (Han et al., 2018).

COFs have also been incorporated into porous polymer monolithic columns to reduce column back-pressure (Svec and Lv, 2015; Song et al., 2023). This strategy was recently employed by Yan and co-workers, who prepared the 3D imine-linked 3D-IL-COF-1 via solvothermal process instead of the previously reported ionothermal synthesis (Guan et al., 2018). The resulting material exhibited a notably high BET surface area and good crystallinity. The COF powder was mixed with the methacrylic precursors of the monolithic polymer and introduced in the HPLC column, where the polymerization reaction was carried out. The characterization of the COF-monolith showed an evident decrease in the BET surface area, which nevertheless was higher than the corresponding blank monolith, pointing out the positive contribution of the COF to the porosity. The efficiency of the HPLC column was tested towards the separation of neutral, acidic, and basic small organic compounds, as well as isomers of disubstituted benzene derivatives and polycyclic aromatic hydrocarbons (PAHs). The chromatographic performance was, in all cases, superior to that found for the blank monolith. Moreover, a comparison with a commercial C18 column revealed that the COF-monolith column was better for separating disubstituted benzene and PAH isomers (Liu et al., 2021). Qian and co-workers developed a HPLC stationary phase using a similar approach based on encapsulating the chiral imine-linked COF CTzDa (Liu et al., 2020) into a methacrylic monolithic polymer. The column gave better enantioseparation of several amino acids than a commercial chiral column (Qian H.-L. et al., 2022).

As the main conclusions of this section, we can say, on the one hand, that the use of pure COF powders with controlled geometry and size alleviates the problems associated with high column back-pressures, although there are still issues when the particle size is small (sub-micrometric range). This could be inconvenient when dealing with samples of difficult separation since decreasing the particle size is usually related to a better resolution performance. On the other hand, using mixtures with other materials, namely silica particles and polymer monoliths, has also been demonstrated to be beneficial in decreasing column back-pressure. However, this improvement is achieved at the expense of losing part or most of the pivotal properties of COFs, i.e., crystallinity and surface area. New research efforts should focus on attaining suitable column back-pressures with minimum loss of these essential attributes of COFs.

3 Stationary phases based on COF composites

As mentioned in the previous section, COF powders as stationary phases for chromatography usually present the drawbacks of their wide particle size distribution and the irregularity of their shape, leading to inefficient packing, high column back-pressure, and poor separation performance. Packing the columns with COF-silica mixtures helps reduce these issues and it uses less active material, but can suffer from COF leaching during column runs. To avoid this problem, covalent COF@SiO₂ core-shell

composites can be prepared to immobilize COFs on the surface of silica microspheres (Figure 2A). This methodology has been successfully accomplished via four different strategies.

3.1 *In situ* growth method

The most straightforward approach to preparing these core-shell composites consists of adding silica microspheres functionalized with amine groups on their surface (SiO₂-NH₂) to the COF synthetic medium. Thus, as the COF forms, it is simultaneously anchored to the surface of the silica microspheres via the same covalent bonds that act as COF linkages. This has been achieved with hydrazone-based (Zhang et al., 2017), imine-based (Xu N. Y. et al., 2021; Guo P. et al., 2021), and imide-based COFs (Zheng Y. et al., 2021).

In a first work, Zhang and co-workers used this approach to immobilize the novel hydrazone-based BtaMth COF on the surface of 5 μm SiO₂-NH₂ microspheres (Zhang et al., 2017). The COF is a variation of COF-42 (Uribe-Romo et al., 2011) endowed with chiral side chains. The microspheres were added directly to the solvothermal reaction mixture, resulting in a core-shell composite that maintained high crystallinity and high porosity. The BtaMth@SiO₂ composite was used to pack HPLC columns, which showed high-resolution performances for separating the positional isomers of nitrotoluene and nitrochlorobenzene in the reverse-phase mode. Moreover, the separation of the *cis-trans* isomers of β-cypermethrin and metconazole in the normal-phase mode could be achieved. However, the separations of the enantiomers of these two analytes on the BtaMth@SiO₂ packed column failed.

This strategy has also been applied to chiral imine-based COFs by Xie and collaborators (Guo P. et al., 2021). They prepared a novel chiral monomer by esterification of 1,3,5-triformylphloroglucinol (Tp) with (+)-diacetyl-L-tartaric anhydride, and this monomer was then reacted with benzidine (BD) in the presence of 5 μm SiO₂-NH₂ microspheres under reflux conditions. The resulting material presents a COF coating of around 250 nm, as determined by scanning electron microscopy (SEM), while slightly improving the BET surface area of the pristine microspheres. The material was used as chiral stationary phase for the HPLC enantioseparation of 20 different pairs of enantiomers, bearing different functional groups, with high enantioselectivity and good reproducibility. Furthermore, the material proved useful for determining enantiomeric excess in commercial reagent samples, obtaining results that agreed with their labeled enantiopurities.

3.2 Two-step growth method

A slightly more sophisticated version of the *in situ* growth approach involves a first reaction of the SiO₂-NH₂ microspheres with the aldehyde monomer of the COF (Wang et al., 2017; Chen et al., 2019; Xie et al., 2023). This way, complete coverage is achieved in the first layer of the shell, reducing the formation of irregular and self-aggregated COF on the surface of the silica microspheres.

The first example of this approach was reported by Yan and co-workers (Wang et al., 2017). They reacted 5 μm SiO₂-NH₂ microspheres with the aldehyde Tp, and the so-formed SiO₂-CHO microspheres were introduced in the reaction under reflux between Tp and the amine BD that gave rise to the COF TpBD (Biswal et al., 2013),

to finally obtain TpBD@SiO₂ composites with COF shell thicknesses between 50 and 150 nm. These materials retained the crystallinity of the COF, and the BET surface area was significantly improved compared to the pristine microspheres. The TpBD@SiO₂ composites were packed as stationary phases for HPLC separation of a variety of analytes, including neutral (toluene from ethylbenzene, PAHs), acidic (hydroquinone, *p*-cresol, and *p*-chlorophenol), and basic (nucleobases, nucleosides, and deoxynucleosides) molecules. They showed good column efficiency, high resolution, and good reproducibility, and in the case of the basic molecules, they outperformed the standard C18 column in separation resolution.

3.3 Layer-by-layer reaction

To ascertain complete control over the coating thickness, Yan and collaborators applied a layer-by-layer approach to preparing COF@SiO₂ composites (Qian et al., 2018). With this strategy, the SiO₂-NH₂ microspheres first react with the aldehyde monomer, then the amine monomer is added, then the aldehyde again, and so on. This sequential addition of the monomers to the reaction medium ensures complete surface coverage in each step, and it allows fine control over the imine-COF coating thickness by changing the number of monomer addition cycles. The authors employed this methodology to prepare COF-300@SiO₂ core-shell composites with high crystallinity and BET surface area, which were successful in the HPLC separation of mixtures of benzene homologs, such as benzyl alcohol, aniline, phenol, and methyl benzoate; substituted aromatics, including nitrophenol, nitroaniline, and aminophenol; and PAHs.

3.4 Post-synthetic modification

Post-synthetic modification (PSM) is a potent approach to introduce functionality into COFs after they have been formed, thus avoiding incompatibilities between the desired functionalities and, for instance, the reaction medium used to obtain the COF (Segura et al., 2019).

This approach has been used by different research groups (Zheng Y. et al., 2022; Wan et al., 2023) to introduce chiral β -cyclodextrin (β -CD) moieties. Thus, Wang and co-workers prepared silica microspheres modified with epoxide groups (Wan et al., 2023), which were used to anchor the imine-linked COF-V (Sun et al., 2017) onto the surface of the microspheres in a one-pot reaction with the COF monomers. Then, they performed a PSM via thiol-ene click chemistry to attach a thiolated β -CD to the vinyl moieties of the COF. The so-obtained chiral material presented low crystallinity and moderate surface area. However, when packed into an HPLC column, it achieved baseline enantiomeric separation of two chiral analytes, 2-phenylpropionic acid and 1-phenyl-1-propanol. In contrast, the composite before the PSM treatment or a commercial β -CD column failed to separate these compounds.

Finally, Li and co-workers reported a different use of the PSM approach; instead of attaching new moieties to the framework, the authors made a post-synthetic imine-to-amine linkage reduction (Xu S. et al., 2021). Hence, they first covered SiO₂-NH₂ microspheres with the imine-based COF LZU1 (Ding et al., 2011) and then reacted them with NaBH₄ to realize the imine-to-amine linkage

transformation. Although the final material exhibited low crystallinity and porosity, it had enhanced stability towards hydrolysis during application as a stationary phase. It showed high performance and good reproducibility in the separation of acidic (phenol, pyrocatechol, and pyrogallol), basic (aniline, 4-chloroaniline, and 4-nitroaniline), and neutral (benzene homologs) compounds, and it was also applied in the separation of real samples, such as tar, phenol, ammonia and other substances present in coking wastewater.

In conclusion, the development of covalent COF@SiO₂ core-shell composites offers a promising approach to overcome the issues associated with COF powders. While straightforward and one-pot, the *in-situ* growth method lacks precise control over the COF coating. In contrast, growing the COFs in steps or employing a PSM affords a finer control of the material and allows tuning of the properties, at the expense of being more complex to implement. Ongoing research aims at a straightforward methodology to control the thickness and functionalization of the COF shell, which would facilitate achieving baseline separation of racemates and complex mixtures.

4 Stationary phases based on COF coatings

Several COFs have also been coated on capillary columns to produce stationary phases for gas chromatography and electrochromatography (CEC) separations (Mao and Chen, 2019; Mametov et al., 2021). The coatings are usually achieved by employing thermal treatments at high temperatures and/or using chemical reactions to anchor the COF to the column surface (Figure 2B). These treatments can affect the crystallinity and porosity of the coated materials; however, in this minireview, we focus on the works where direct or indirect analyses support the preservation of the COF crystalline structure in the coating. For further information on non-crystalline coatings or works in which crystallinity is not reported, we direct the readers to some selected references (Wang et al., 2019; Wang et al., 2022c; Guo J.-X. et al., 2021; Natraj et al., 2022; Yuan et al., 2022; Yuan et al., 2023; Yusuf et al., 2023).

4.1 Dynamic coating

In 2015, Yan and co-workers reported the preparation of the imine-linked COF TpBD as spherical micron-sized particles using a facile synthesis at room temperature (Yang et al., 2015). The material showed moderate crystallinity, although the authors confirmed that it was preserved up to 250°C. Moreover, the as-synthesized COF presented a high BET surface area. The COF coating on the capillary column was achieved by the dynamic coating method, using a final thermal treatment at 150°C, which was well below the limit temperature to preserve the crystallinity of the COF. The dynamic coating is primarily based on the physical adsorption of the stationary phase on the inner walls of the capillary column (Horvath and Dolník, 2001). Nevertheless, given the high temperature used in the final step, the occurrence of some type of covalent attachment of the COF on the column surface cannot be ruled out. The coated column showed good separation properties towards small organic molecules, such as alkanes,

cycloalkanes, benzene, and alcohols. Moreover, it exhibited better performance than a commercial HP-5 column.

4.2 Chemical coating

Chemical coating implies the COF's covalent immobilization to the capillary column's inner surface. This approach can render more stable stationary phases than a dynamic coating, which occasionally may require regeneration of the column (Horvath and Dolník, 2001). To date, two main strategies have been applied to prepare chemical coatings of COFs on capillary columns. The first one is based on the *in situ* growth of the COF on the column walls (Qian et al., 2016; Qian et al., 2022 H. L.; Huang X. L. et al., 2019; Sun et al., 2021; He et al., 2022; Ma et al., 2023; Wang et al., 2023). This methodology was utilized by Yan and co-workers in 2016 to develop chiral COF-bound capillary columns for chiral gas chromatography. The authors first prepared three chiral imine-linked COFs, namely CTpPa-1, CTpPa-2, and CTpBD, as powders outside the columns by reacting a chiral derivative of the aldehyde Tp with several aromatic linear diamines. Characterization of the materials revealed moderate crystallinity and low to moderate BET surface areas. The COF-bound capillary columns were then fabricated by reacting the monomer mixtures in columns modified with 3-aminopropyltriethoxysilane (APTES), to promote the attachment of the aldehyde and subsequent growth of the COF on the column walls. The same type of coating was made in a fused silica plate to confirm the COF structural preservation. The X-ray powder diffraction analysis of the material revealed that crystallinity was maintained. The columns exhibited good chiral separation properties for racemates of small organic compounds, with superior performance to several commercial chiral capillary columns (Qian et al., 2016).

The second strategy to obtain coatings of COFs chemically bound to capillary columns is based on the covalent attachment of the pre-synthesized COF particles (Wang F. et al., 2022; Zong et al., 2022; Yin et al., 2023). Following this approach, Chen and co-workers prepared a stationary phase for open tubular capillary electrochromatography (Wang F. et al., 2022). The stationary phase was based on the hydrazine-linked COF Tf-DHzOH obtained through the reaction of an aromatic linear dihydrazide and 1,3,5-triformylbenzene under solvothermal conditions. The analysis of the as-synthesized material revealed an excellent crystallinity and low BET surface area. Coating of the COF on the capillary column was achieved by reacting a suspension of the COF particles containing residual hydrazide groups with 3-glycidypropyltrimethoxysilane (GLYMO) units attached to the inner surface of the column. Analysis of an analogous coating prepared on a glass surface corroborated that crystallinity is preserved in the coating. The column separation properties were evaluated using as analytes amino acids, sulfonamides, tetracyclines and benzene derivatives, and the results showed a better performance of the COF column as compared to the bare capillary and other reported coated capillary columns.

Therefore, coating COFs on capillary columns opens new opportunities for gas and electrochromatography applications. However, it is still challenging to determine if the crystallinity and surface area of the pristine COFs is preserved in the prepared coatings and under the working conditions of gas chromatography. New research should also focus on optimizing the control of coating thickness and roughness.

5 Conclusion and future outlook

There are various types of porous materials that, due to their properties, can be attractive alternatives to classical stationary phases based on silica and organic polymers. In particular, metal-organic frameworks (MOFs), COFs, and zeolites present excellent designability, which offers a fine control on chemical functionalization and pore size distributions, which are found typically in the micropore and mesopore range (Slater and Cooper, 2015). The control at the molecular level cannot be achieved with other conventional materials, and their application as stationary phases can significantly improve the separation efficiencies for numerous substrates. Comparing MOFs, nitrogen-based COFs, and zeolites, the former present lower chemical stability, while zeolites are challenging to process. In contrast, nitrogen-based COFs are characterized by high chemical and thermal stabilities. Moreover, several methodologies reported in the last years have facilitated their processing for real-world applications (Martín-Illán et al., 2023). Altogether, these properties make COFs excellent candidates for the development of chromatographic stationary phases, and they can bring solutions in enantiomeric separation of bioactive molecules for pharmaceutical applications, extraction and purification of natural products, and fine chemistry.

Current strategies to prepare COF stationary phases, mainly based on the column packing with controlled shape and size particles, mixtures, and composites, and COF-coating on capillary columns, have demonstrated good to excellent results in the chromatographic separation of several substrates, including basic, neutral and acidic small organic molecules, positional isomers, racemates, and PAHs. Therefore, it is worth continuing to investigate these approaches. However, each of these strategies has some drawbacks, such as the usual increase in back-pressure when sub-micron-sized particles are employed, the loss of surface area of the pristine material in mixtures and composites, and the complex and long synthetical procedures associated with the preparation of some composites and coatings. In this regard, work on new processing methodologies can help to overcome some of these disadvantages. Moreover, conducting more research on the separation and purification of added-value compounds would be interesting, which could open new business opportunities and academia-industry collaborations.

Author contributions

RG: Conceptualization, Supervision, Writing—original draft, Writing—review and editing. SR: Writing—original draft, Writing—review and editing. FZ: Conceptualization, Supervision, Writing—original draft, Writing—review and editing, Funding acquisition.

Funding

The author(s) declare that financial support was received for the research, authorship, and/or publication of this article. We thank the financial support to the Spanish MICINN (PID 2022-138908NB-C31, PDC 2022-133498-I00 and TED 2021-129886B-C42) and through the “María de Maeztu” Programme for Units of

Excellence in R&D (CEX 2018-000805-M). This work was also supported by the Comunidad de Madrid (MAD2D-CM) and MICINN (Planes complementarios, Materiales Avanzados). FZ also acknowledges support from the European Innovation Council under grant Agreement 101047081 (EVA).

Conflict of interest

The authors declare that the research was conducted in the absence of any commercial or financial relationships that could be construed as a potential conflict of interest.

References

- Biswal, B. P., Chandra, S., Kandambeth, S., Lukose, B., Heine, T., and Banerjee, R. (2013). Mechanochemical synthesis of chemically stable isorecticular covalent organic frameworks. *J. Am. Chem. Soc.* 135, 5328–5331. doi:10.1021/ja4017842
- Burke, D. W., Jiang, Z., Livingston, A. G., and Dichtel, W. R. (2023). 2D covalent organic framework membranes for liquid-phase molecular separations: state of the field, common pitfalls, and future opportunities. *Adv. Mater.* 36, e2300525. doi:10.1002/adma.202300525
- Chen, L., Gao, J., Wu, Q., Li, H., Dong, S., Shi, X., et al. (2019). Preparation and performance of a novel multi-mode COF-300@SiO₂ chromatographic stationary phase. *Eur. Polym. J.* 116, 9–19. doi:10.1016/j.eurpolymj.2019.04.002
- Chen, Z., Kirlikovali, K. O., Idrees, K. B., Wasson, M. C., and Farha, O. K. (2022). Porous materials for hydrogen storage. *Chem* 8, 693–716. doi:10.1016/j.chempr.2022.01.012
- Ding, S. Y., Gao, J., Wang, Q., Zhang, Y., Song, W. G., Su, C. Y., et al. (2011). Construction of covalent organic framework for catalysis: Pd/COF-LZU1 in Suzuki-Miyaura coupling reaction. *J. Am. Chem. Soc.* 133, 19816–19822. doi:10.1021/ja206846p
- Fikarova, K., Moore, E., Nicolau, A., Horstlotte, B., and Maya, F. (2022). Recent trends on the implementation of reticular materials in column-centered separations. *J. Sep. Sci.* 45, 1411–1424. doi:10.1002/jssc.202100849
- Geng, K., He, T., Liu, R., Dalapati, S., Tan, K. T., Li, Z., et al. (2020). Covalent organic frameworks: design, synthesis, and functions. *Chem. Rev.* 120, 8814–8933. doi:10.1021/acs.chemrev.9b00550
- Guan, X., Ma, Y., Li, H., Yusran, Y., Xue, M., Fang, Q., et al. (2018). Fast, ambient temperature and pressure ionothermal synthesis of three-dimensional covalent organic frameworks. *J. Am. Chem. Soc.* 140, 4494–4498. doi:10.1021/jacs.8b01320
- Guo, J.-X., Yang, C., and Yan, X.-P. (2021a). “Thiol-ene” click synthesis of chiral covalent organic frameworks for gas chromatography. *J. Mater. Chem. A Mater* 9, 21151–21157. doi:10.1039/D1TA04621G
- Guo, P., Yuan, B. Y., Yu, Y. Y., Zhang, J. H., Wang, B. J., Xie, S. M., et al. (2021b). Chiral covalent organic framework core-shell composite CTpBD@SiO₂ used as stationary phase for HPLC enantioseparation. *Microchim. Acta* 188, 292. doi:10.1007/s00604-021-04954-3
- Han, X., Huang, J., Yuan, C., Liu, Y., and Cui, Y. (2018). Chiral 3D covalent organic frameworks for high performance liquid chromatographic enantioseparation. *J. Am. Chem. Soc.* 140, 892–895. doi:10.1021/jacs.7b12110
- He, N., Li, Z., Hu, C., and Chen, Z. (2022). *In situ* synthesis of a spherical covalent organic framework as a stationary phase for capillary electrochromatography. *J. Pharm. Anal.* 12, 610–616. doi:10.1016/j.jpba.2022.06.005
- Horvath, J., and Dolník, V. (2001). Polymer wall coatings for capillary electrophoresis. *Electrophoresis* 22, 644–655. doi:10.1002/1522-2683(200102)22:4<644::AID-ELPS644>3.0.CO;2-3
- Huang, J., Han, X., Yang, S., Cao, Y., Yuan, C., Liu, Y., et al. (2019a). Microporous 3D covalent organic frameworks for liquid chromatographic separation of xylene isomers and ethylbenzene. *J. Am. Chem. Soc.* 141, 8996–9003. doi:10.1021/jacs.9b03075
- Huang, X. L., Lan, H. H., Yan, Y. L., Chen, G., He, Z. H., Zhang, K., et al. (2019b). Fabrication of a hydrazone-linked covalent organic framework-bound capillary column for gas chromatography separation. *Sep. Sci. Plus* 2, 120–128. doi:10.1002/sscp.201800146
- Keller, N., and Bein, T. (2021). Optoelectronic processes in covalent organic frameworks. *Chem. Soc. Rev.* 50, 1813–1845. doi:10.1039/d0cs00793e
- Kočová Vlčková, H., Pilařová, V., Svobodová, P., Plišek, J., Švec, F., and Nováková, L. (2018). Current state of bioanalytical chromatography in clinical analysis. *Analyst* 143, 1305–1325. doi:10.1039/c7an01807j
- Li, H., Dilipkumar, A., Abubakar, S., and Zhao, D. (2023). Covalent organic frameworks for CO₂ capture: from laboratory curiosity to industry implementation. *Chem. Soc. Rev.* 52, 6294–6329. doi:10.1039/d2cs00465h
- Liu, F., Qian, H. L., Yang, C., and Yan, X. P. (2020). Room-temperature preparation of a chiral covalent organic framework for the selective adsorption of amino acid enantiomers. *RSC Adv.* 10, 15383–15386. doi:10.1039/d0ra02647f
- Liu, X., Yang, C., Qian, H. L., and Yan, X. P. (2021). Three-Dimensional nanoporous covalent organic framework-incorporated monolithic columns for high-performance liquid chromatography. *ACS Appl. Nano Mater* 4, 5437–5443. doi:10.1021/acsnm.1c00770
- Lohse, M. S., and Bein, T. (2018). Covalent organic frameworks: structures, synthesis, and applications. *Adv. Funct. Mater.* 28. doi:10.1002/adfm.201705553
- Ma, T., Kapustin, E. A., Yin, S. X., Liang, L., Zhou, Z., Niu, J., et al. (2018). Single-crystal x-ray diffraction structures of covalent organic frameworks. *Science* 361, 48–52. doi:10.1126/science.aat7679
- Ma, T. T., Yang, C., Qian, H. L., Ma, P., Liu, T., and Yan, X. P. (2023). Trifluoromethyl-functionalized 2D covalent organic framework for high-resolution separation of isomers. *ACS Appl. Mater. Interfaces* 15, 32926–32934. doi:10.1021/acsmi.3c05369
- Mametov, R., Ratiu, I.-A., Monedeiro, F., Ligor, T., and Buszewski, B. (2021). Evolution and evaluation of GC columns. *Crit. Rev. Anal. Chem.* 51, 150–173. doi:10.1080/10408347.2019.1699013
- Mao, Z., and Chen, Z. (2019). Advances in capillary electrochromatography. *J. Pharm. Anal.* 9, 227–237. doi:10.1016/j.jpba.2019.05.002
- Martínez-Fernández, M., Gavara, R., Royuela, S., Fernández-Ecija, L., Martínez, J. I., Zamora, F., et al. (2022a). Following the light: 3D-printed COF@poly(2-hydroxyethyl methacrylate) dual emissive composite with response to polarity and acidity. *J. Mater. Chem. A Mater* 10, 4634–4643. doi:10.1039/d1ta09614a
- Martínez-Fernández, M., Martínez-Periñán, E., Royuela, S., Martínez, J. I., Zamora, F., Lorenzo, E., et al. (2022b). Covalent organic frameworks based on electroactive naphthalenediimide as active electrocatalysts toward oxygen reduction reaction. *Appl. Mater. Today* 26, 101384. doi:10.1016/j.apmt.2022.101384
- Martín-Illán, J. Á., Rodríguez-San-Miguel, D., and Zamora, F. (2023). Evolution of covalent organic frameworks: from design to real-world applications. *Coord. Chem. Rev.* 495, 215342. doi:10.1016/j.ccr.2023.215342
- Natraj, A., Ji, W., Xin, J., Castano, I., Burke, D. W., Evans, A. M., et al. (2022). Single-crystalline imine-linked two-dimensional covalent organic frameworks separate benzene and cyclohexane efficiently. *J. Am. Chem. Soc.* 144, 19813–19824. doi:10.1021/jacs.2c07166
- Núñez, O., and Lucci, P. (2020). Application of liquid chromatography in food analysis. *Foods* 9, 1277. doi:10.3390/foods9091277
- Pollo, B. J., Alexandrino, G. L., Augusto, F., and Hantao, L. W. (2018). The impact of comprehensive two-dimensional gas chromatography on oil & gas analysis: recent advances and applications in petroleum industry. *TrAC - Trends Anal. Chem.* 105, 202–217. doi:10.1016/j.trac.2018.05.007
- Qi, S. P., Tang, R., Bi, X., Zhangfan, Z. C., et al. (2023). Recent progress of covalent organic frameworks-based materials in photocatalytic applications: a review. *Small* 19, e2303632. doi:10.1002/sml.202303632
- Qian, H.-L., Liu, F., Liu, X., Yang, C., and Yan, X.-P. (2022b). Chiral covalent organic framework-monolith as stationary phase for high-performance liquid chromatographic enantioseparation of selected amino acids. *Anal. Bioanal. Chem.* 414, 5255–5262. doi:10.1007/s00216-021-03574-3
- Qian, H. L., Wang, Z. H., Yang, J., and Yan, X. P. (2022a). Building-block exchange synthesis of amino-based three-dimensional covalent organic frameworks for gas chromatographic separation of isomers. *Chem. Commun.* 58, 8133–8136. doi:10.1039/d2cc02383k
- Qian, H. L., Yang, C., and Yan, X. P. (2018). Layer-by-layer preparation of 3D covalent organic framework/silica composites for chromatographic separation of position isomers. *Chem. Commun.* 54, 11765–11768. doi:10.1039/c8cc06621c

Publisher's note

All claims expressed in this article are solely those of the authors and do not necessarily represent those of their affiliated organizations, or those of the publisher, the editors and the reviewers. Any product that may be evaluated in this article, or claim that may be made by its manufacturer, is not guaranteed or endorsed by the publisher.

- Qian, H.-L., Yang, C.-X., and Yan, X.-P. (2016). Bottom-up synthesis of chiral covalent organic frameworks and their bound capillaries for chiral separation. *Nat. Commun.* 7, 12104. doi:10.1038/ncomms12104
- Qiu, H., Liang, X., Sun, M., and Jiang, S. (2011). Development of silica-based stationary phases for high-performance liquid chromatography. *Anal. Bioanal. Chem.* 399, 3307–3322. doi:10.1007/s00216-010-4611-x
- Segura, J. L., Royuela, S., and Mar Ramos, M. (2019). Post-synthetic modification of covalent organic frameworks. *Chem. Soc. Rev.* 48, 3903–3945. doi:10.1039/c8cs00978c
- Slater, A. G., and Cooper, A. I. (2015). Porous materials. Function-led design of new porous materials. *Science* 348, aaa8075. doi:10.1126/science.aaa8075
- Song, R., Li, Y., Chen, Y., Qiu, Z., and Huang, L. (2023). Chiral covalent organic framework incorporated organic polymer monolithic capillary column for enantioseparations. *J. Sep. Sci.* 46, e2201039. doi:10.1002/jssc.202201039
- Steinebach, F., Müller-Späh, T., and Morbidelli, M. (2016). Continuous counter-current chromatography for capture and polishing steps in biopharmaceutical production. *Biotechnol. J.* 11, 1126–1141. doi:10.1002/biot.201500354
- Sun, J., Fei, Y., Tang, H., Bao, J., Zhang, Q., and Zhou, X. (2023). Covalent organic frameworks as promising electrode materials for high-valent ion rechargeable batteries. *ACS Appl. Energy Mater.* doi:10.1021/acsaem.3c01892
- Sun, Q., Aguila, B., Perman, J., Earl, L. D., Abney, C. W., Cheng, Y., et al. (2017). Postsynthetically modified covalent organic frameworks for efficient and effective mercury removal. *J. Am. Chem. Soc.* 139, 2786–2793. doi:10.1021/jacs.6b12885
- Sun, W., Liu, Y., Zhou, W., Li, Z., and Chen, Z. (2021). *In-situ* growth of a spherical vinyl-functionalized covalent organic framework as stationary phase for capillary electrochromatography-mass spectrometry analysis. *Talanta* 230, 122330. doi:10.1016/j.talanta.2021.122330
- Svec, F., and Lv, Y. (2015). Advances and recent trends in the field of monolithic columns for chromatography. *Anal. Chem.* 87, 250–273. doi:10.1021/ac504059c
- Tao, R., Yang, T., Wang, Y., Zhang, J., Wu, Z., and Qiu, L. (2023). Design strategies of covalent organic framework-based electrodes for supercapacitor application. *Chem. Commun.* 59, 3175–3192. doi:10.1039/d2cc06573h
- Uribe-Romo, F. J., Doonan, C. J., Furukawa, H., Oisaki, K., and Yaghi, O. M. (2011). Crystalline covalent organic frameworks with hydrazone linkages. *J. Am. Chem. Soc.* 133, 11478–11481. doi:10.1021/ja204728y
- Wan, M., Zheng, Y., Dai, X., Yang, H., Zhou, J., Ou, J., et al. (2023). Click chemistry for the preparation of β -cyclodextrin grafting uniform spherical covalent organic framework materials for chiral separation. *Chem. Mater.* 35, 609–616. doi:10.1021/acs.chemmater.2c03140
- Wang, F., Zhang, Y., Wang, G., Qi, S., Lv, W., Liu, J., et al. (2022a). Synthesis of a covalent organic framework with hydrazine linkages and its application in open-tubular capillary electrochromatography. *J. Chromatogr. A* 1661, 462681. doi:10.1016/j.chroma.2021.462681
- Wang, L. L., Yang, C. X., and Yan, X. P. (2017). *In situ* growth of covalent organic framework shells on silica microspheres for application in liquid chromatography. *Chempluschem* 82, 933–938. doi:10.1002/cplu.201700223
- Wang, X., Han, X., Cheng, C., Kang, X., Liu, Y., and Cui, Y. (2022b). 2D covalent organic frameworks with cem topology. *J. Am. Chem. Soc.* 144, 7366–7373. doi:10.1021/jacs.2c01082
- Wang, X., Wu, J., Liu, X., Qiu, X., Cao, L., and Ji, Y. (2022c). Enhanced chiral recognition abilities of cyclodextrin covalent organic frameworks via chiral/achiral functional modification. *ACS Appl. Mater. Interfaces* 14, 25928–25936. doi:10.1021/acsami.2c05572
- Wang, Y., Zhuo, S., Hou, J., Li, W., and Ji, Y. (2019). Construction of β -cyclodextrin covalent organic framework-modified chiral stationary phase for chiral separation. *ACS Appl. Mater. Interfaces* 11, 48363–48369. doi:10.1021/acsami.9b16720
- Wang, Z., Zhang, S., Chen, Y., Zhang, Z., and Ma, S. (2020). Covalent organic frameworks for separation applications. *Chem. Soc. Rev.* 49, 708–735. doi:10.1039/c9cs00827f
- Wang, Z. H., Yang, C., Liu, T., Qian, H. L., and Yan, X. P. (2023). Particle size regulation of single-crystalline covalent organic frameworks for high performance of gas chromatography. *Anal. Chem.* 95, 8145–8149. doi:10.1021/acs.analchem.3c01550
- Xie, M., Quan, K., Li, H., Liu, B., Chen, J., Yu, Y., et al. (2023). Non-porous silica support covalent organic frameworks as stationary phases for liquid chromatography. *Chem. Commun.* 59, 314–317. doi:10.1039/D2CC005650j
- Xu, N. Y., Guo, P., Chen, J. K., Zhang, J. H., Wang, B. J., Xie, S. M., et al. (2021a). Chiral core-shell microspheres β -CD-COF@SiO₂ used for HPLC enantioseparation. *Talanta* 235, 122754. doi:10.1016/j.talanta.2021.122754
- Xu, S., Li, Z., Zhang, L., Zhang, W., and Li, D. (2021b). *In situ* growth of COF-rLZU1 on the surface of silica sphere as stationary phase for high performance liquid chromatography. *Talanta* 221, 121612. doi:10.1016/j.talanta.2020.121612
- Yan, Y.-L., Guo, D., Wu, J.-L., Tang, X.-H., Luo, J.-J., Li, S.-Q., et al. (2022). Fabrication of cellulose derivative coated spherical covalent organic frameworks as chiral stationary phases for high-performance liquid chromatographic enantioseparation. *J. Chromatogr. A* 1675, 463155. doi:10.1016/j.chroma.2022.463155
- Yang, C. X., Liu, C., Cao, Y. M., and Yan, X. P. (2015). Facile room-temperature solution-phase synthesis of a spherical covalent organic framework for high-resolution chromatographic separation. *Chem. Commun.* 51, 12254–12257. doi:10.1039/c5cc03413b
- Yang, Y., Pan, H., Li, X., Luo, W., and Bharti, B. (2023). Applications of two-dimensional ion chromatography for analytes determination in environmental matrix: a review. *J. Chromatogr. A* 1694, 463908. doi:10.1016/j.chroma.2023.463908
- Yin, H., Zhen, Z., Ning, W., Zhang, L., Xiang, Y., and Ye, N. (2023). Three-dimensional fluorinated covalent organic frameworks coated capillary for the separation of fluoroquinolones by capillary electrochromatography. *J. Chromatogr. A* 1706, 464234. doi:10.1016/j.chroma.2023.464234
- Yuan, C., Jia, W., Yu, Z., Li, Y., Zi, M., Yuan, L. M., et al. (2022). Are highly stable covalent organic frameworks the key to universal chiral stationary phases for liquid and gas chromatographic separations? *J. Am. Chem. Soc.* 144, 891–900. doi:10.1021/jacs.1c11051
- Yuan, C., Wang, Z., Xiong, W., Huang, Z., Lai, Y., Fu, S., et al. (2023). Cyclodextrin incorporation into covalent organic frameworks enables extensive liquid and gas chromatographic enantioseparations. *J. Am. Chem. Soc.* 145, 18956–18967. doi:10.1021/jacs.3c05973
- Yue, Y., Ji, D., Liu, Y., and Wei, D. (2023). Chemical sensors based on covalent organic frameworks. *Chem. – A Eur. J.* 30, e202302474. doi:10.1002/chem.202302474
- Yusuf, K., Natraj, A., Li, K., Ateia, M., Alothman, Z. A., and Dichtel, W. R. (2023). Inverse gas chromatography demonstrates the crystallinity-dependent physicochemical properties of two-dimensional covalent organic framework stationary phases. *Chem. Mater.* 35, 1691–1701. doi:10.1021/acs.chemmater.2c03448
- Zhang, J., Chen, J., Peng, S., Peng, S., Zhang, Z., Tong, Y., et al. (2019). Emerging porous materials in confined spaces: from chromatographic applications to flow chemistry. *Chem. Soc. Rev.* 48, 2566–2595. doi:10.1039/c8cs00657a
- Zhang, K., Cai, S. L., Yan, Y. L., He, Z. H., Lin, H. M., Huang, X. L., et al. (2017). Construction of a hydrazone-linked chiral covalent organic framework–silica composite as the stationary phase for high performance liquid chromatography. *J. Chromatogr. A* 1519, 100–109. doi:10.1016/j.chroma.2017.09.007
- Zhang, S., Zheng, Y., An, H., Aguila, B., Yang, C., Dong, Y., et al. (2018). Covalent organic frameworks with chirality enriched by biomolecules for efficient chiral separation. *Angew. Chem.* 130, 16996–17001. doi:10.1002/ange.201810571
- Zheng, Q., He, Y., Ma, W., Wu, Y., Chen, Z., Wang, R., et al. (2021a). Facile synthesis of spherical covalent organic frameworks as stationary phases for short-column liquid chromatography. *Chem. Commun.* 57, 7501–7504. doi:10.1039/d1cc03182a
- Zheng, Q., Huang, J., He, Y., Huang, H., Ji, Y., Zhang, Y., et al. (2022a). Single-crystalline covalent organic frameworks as high-performance liquid chromatographic stationary phases for positional isomer separation. *ACS Appl. Mater. Interfaces* 14, 9754–9762. doi:10.1021/acsami.1c20989
- Zheng, Q., Liu, J., Wu, Y., Ji, Y., and Lin, Z. (2022b). Fluoro-functionalized spherical covalent organic frameworks as a liquid chromatographic stationary phase for the high-resolution separation of organic halides. *Anal. Chem.* 94, 18067–18073. doi:10.1021/acs.analchem.2c04592
- Zheng, Y., Wan, M., Zhou, J., Dai, X., Yang, H., Xia, Z., et al. (2022c). One-pot method for the synthesis of β -cyclodextrin and covalent organic framework functionalized chiral stationary phase with mixed-mode retention mechanism. *J. Chromatogr. A* 1662, 462731. doi:10.1016/j.chroma.2021.462731
- Zheng, Y., Wan, M., Zhou, J., Luo, Q., Gao, D., Fu, Q., et al. (2021b). Striped covalent organic frameworks modified stationary phase for mixed mode chromatography. *J. Chromatogr. A* 1649, 462186. doi:10.1016/j.chroma.2021.462186
- Zong, R., Yin, H., Xiang, Y., Zhang, L., and Ye, N. (2022). Fluorinated covalent organic frameworks as a stationary phase for separation of fluoroquinolones by capillary electrochromatography. *Microchim. Acta* 189, 237. doi:10.1007/s00604-022-05333-2



OPEN ACCESS

EDITED BY

Steve Suib,
University of Connecticut, United States

REVIEWED BY

Yuichi Kitagawa,
Hokkaido University, Japan
Ashis K. Patra,
Indian Institute of Technology Kanpur, India

*CORRESPONDENCE

Joulia Larionova,
✉ joulia.larionova@umontpellier.fr
Alexey N. Bilyachenko,
✉ bilyachenko@ineos.ac.ru
Albano N. Carneiro Neto,
✉ albanoneto@ua.pt

RECEIVED 31 January 2024

ACCEPTED 07 March 2024

PUBLISHED 03 April 2024

CITATION

Félix G, Kulakova AN, Sene S, Khrustalev VN, Hernández-Rodríguez MA, Shubina ES, Pelluau T, Carlos LD, Guari Y, Carneiro Neto AN, Bilyachenko AN and Larionova J (2024), Luminescent Ln³⁺-based silsesquioxanes with a β-diketonate antenna ligand: toward the design of efficient temperature sensors. *Front. Chem.* 12:1379587. doi: 10.3389/fchem.2024.1379587

COPYRIGHT

© 2024 Félix, Kulakova, Sene, Khrustalev, Hernández-Rodríguez, Shubina, Pelluau, Carlos, Guari, Carneiro Neto, Bilyachenko and Larionova. This is an open-access article distributed under the terms of the [Creative Commons Attribution License \(CC BY\)](#). The use, distribution or reproduction in other forums is permitted, provided the original author(s) and the copyright owner(s) are credited and that the original publication in this journal is cited, in accordance with accepted academic practice. No use, distribution or reproduction is permitted which does not comply with these terms.

Luminescent Ln³⁺-based silsesquioxanes with a β-diketonate antenna ligand: toward the design of efficient temperature sensors

Gautier Félix¹, Alena N. Kulakova^{1,2}, Saad Sene¹, Victor N. Khrustalev^{3,4}, Miguel A. Hernández-Rodríguez^{5,6}, Elena S. Shubina², Tristan Pelluau¹, Luís D. Carlos⁵, Yannick Guari¹, Albano N. Carneiro Neto^{5*}, Alexey N. Bilyachenko^{2,3*} and Joulia Larionova^{1*}

¹CNRS, ENSCM, University Montpellier, Montpellier, France, ²Nesmeyanov Institute of Organoelement Compounds, Russian Academy of Sciences, Moscow, Russia, ³Peoples' Friendship University of Russia (RUDN University), Moscow, Russia, ⁴Zelinsky Institute of Organic Chemistry, Russian Academy of Sciences, Moscow, Russia, ⁵Phantom-g, Physics Department and CICECO—Aveiro Institute of Materials, University of Aveiro, Aveiro, Portugal, ⁶Departamento de Física, Universidad de La Laguna San Cristóbal de La Laguna, Santa Cruz de Tenerife, Spain

We report the synthesis and single-crystal X-ray diffraction, magnetic, and luminescence measurements of a novel family of luminescent cage-like tetranuclear silsesquioxanes (PhSiO_{1.5})₈(LnO_{1.5})₄(O)(C₅H₈O₂)₆(EtOH)₂(CH₃CN)₂·2CH₃CN (where Ln = Tb, **1**; Tb/Eu, **2**; and Gd, **3**), featuring seven-coordinated lanthanide ions arranged in a one-capped trigonal prism geometry. Compounds **1** and **2** exhibit characteristic Tb³⁺ and Tb³⁺/Eu³⁺-related emissions, respectively, sensitized by the chelating antenna acetylacetonate (acac) ligands upon excitation in the UV and visible spectral regions. Compound **3** is used to assess the energies of the triplet states of the acac ligand. For compound **1**, theoretical calculations on the intramolecular energy transfer and multiphonon rates indicate a thermal balance between the ⁵D₄ Stark components, while the mixed Tb³⁺/Eu³⁺ analog **2**, with a Tb:Eu ratio of 3:1, showcases intra-cluster Tb³⁺-to-Eu³⁺ energy transfer, calculated theoretically as a function of temperature. By utilizing the intensity ratio between the ⁵D₄→⁷F₅ (Tb³⁺) and ⁵D₀→⁷F₂ (Eu³⁺) transitions in the range 11–373 K, we demonstrate the realization of a ratiometric luminescent thermometer with compound **2**, operating in the range 11–373 K with a maximum relative sensitivity of 2.0% K⁻¹ at 373 K. These findings highlight the potential of cage-like silsesquioxanes as versatile materials for optical sensing-enabled applications.

KEYWORDS

thermometry, silsesquioxanes, lanthanides, luminescence, magnetism, energy transfer

1 Introduction

Luminescent coordination complexes containing trivalent lanthanide ions (Ln³⁺) have attracted significant attention over several decades due to tremendous perspectives in different applications, including bioimaging and biosensing (Eliseeva and Bünzli, 2009; Ning et al., 2019), light-emitting technology (Bünzli, 2019; Costa et al., 2024), smart

windows (Choi et al., 2017; Fernandes et al., 2018; Costa et al., 2024), nano-thermometry (Allison, 2019; Brites et al., 2019; Brites et al., 2023), detection of molecules and ions (Eliseeva and Bünzli, 2009; Allison, 2019; Brites et al., 2023), cell labeling (Aulsebrook et al., 2018; Bodman and Butler, 2021). These compounds exhibit distinctive photophysical characteristics, manifesting as prolonged emission with lifetimes extending up to milliseconds. This extended emission attributed to the $4f-4f$ transitions occurs in the visible and/or near-infrared (NIR) spectral domains depending on the nature of the Ln^{3+} ion. Moreover, it usually includes narrow emission lines, significant ligand-induced Stokes shifts, and high quantum yields. For these reasons, the coordination chemistry of Ln^{3+} ions employed in association with various ligands to design mono- and polynuclear compounds of various topologies with optimized optical properties has been the subject of huge development during recent decades (Bünzli, 2010; Bünzli, 2015; Seethalakshmi et al., 2017; Liu et al., 2020; Monteiro, 2020; Bernot et al., 2021). In particular, extensive effort has been focused on the synthesis of highly luminescent, photo- and thermostable complexes valuable for the above-mentioned applications (Kaczmarek et al., 2019).

However, directly exciting the $4f$ levels poses a challenge as the majority of the $f-f$ transitions are prohibited by the Laporte rule, resulting in low molar absorption coefficients. This constraint can be surmounted by the tune of organic chromophores as ligands to generate the well-known “antenna effect,” yielding highly emissive complexes. In these systems, chromophore ligands, typically excited in the UV or, less frequently, in the visible spectral domains, allow the energy transfer from the ligand triplet excited state to the emitting level of the Ln^{3+} ion. Consequently, this process induces a radiative decay in the visible or NIR spectral regions depending on the Ln^{3+} ion used (Bünzli, 2015). Note that an alternative mechanism has been documented, which entails the energy transfer from the first excited singlet state of the ligand to the $4f$ levels (Alaoui, 1995; Yang et al., 2004; Kasprzycka et al., 2017; Gregório et al., 2019; Moura Jr. et al., 2021a; Manzur et al., 2023). Hence, achieving efficient energy transfer requires a meticulous alignment of energy levels and adherence to selection rules among various excited states. This optimization can be accomplished through a careful selection of ligands and Ln^{3+} ions, coupled with the strategic design of the metal center geometry within a suitable ligand environment (Carneiro Neto et al., 2019). Furthermore, note that improved luminescence has been documented in complexes featuring an asymmetric Ln^{3+} coordination environment, notably in a seven-coordinated geometry (Miyata et al., 2009; Miyata et al., 2012; Yanagisawa et al., 2015; Ferreira da Rosa et al., 2020; Aquino LE do et al., 2021).

A significant breakthrough in Ln^{3+} -based luminescent coordination compounds lies in their application as temperature sensors, enabling remote temperature measurements through emission monitoring. This approach offers temperature sensing with high spatial precision (below $10\ \mu\text{m}$), temporal (time scale) and thermal resolutions ($0.1\ \text{K}$) within short acquisition times (less than $10\ \mu\text{s}$), and high relative thermal sensitivity ($S_r > 1\% \text{ K}^{-1}$) (Brites et al., 2012; Jaque and Vetrone, 2012; Brites et al., 2016; Brites et al., 2019; Brites et al., 2023). It shows enormous potential in a wide range of applications ranging from biology and medicine to cryogenics (Cui et al., 2012; Bettinelli et al., 2015; Dramićanin, 2020). Starting from the first example showing the possibility of the

real-time observation of thermogenesis in a single HeLa cell using the simple mononuclear $\text{Eu}(\text{tta})_3$ complex (where tta^- is 3-thenoyltrifluoroacetate) (Suzuki et al., 2007), numerous Ln^{3+} -based compounds have been investigated for this purpose. A particular emphasis in this field has been placed on the design of ratiometric thermometers, in which a luminescence intensity ratio (LIR) of two constituent Ln^{3+} ions is used as a signal permitting a self-referencing emissive system (Brites et al., 2010). The most used complexes contain a $\text{Tb}^{3+}/\text{Eu}^{3+}$ pair due to the high quantum yield of these ions, for which different parameters can be optimized to increase the performance of the luminescent thermometers (Cui et al., 2012; Rocha et al., 2016; Lyubov et al., 2022). In particular, molecular cluster-aggregates have shown high potential for this purpose, attributed to a rigid metal core of high nuclearity, precise coordination environment, and tunable energy transfer. This is achieved through the precise control of the ratio of the ions and the distance between them, as well as their structural organization, ion environment, and the nature of ligands (Calado et al., 2023; Gállico et al., 2023). A particular family of these molecular cluster-aggregates, luminescent Ln^{3+} -based silsesquioxanes, provides a compelling alternative to coordination complexes, offering high photothermal and chemical stabilities, particularly pertinent with increasing temperature for thermometry applications.

Cage-like Ln^{3+} -based metallasilsesquioxanes are an exciting family of compounds presenting the combination of Ln^{3+} ions with the silsesquioxane repeating subunits, $(\text{RSiO}_{1.5})_n$ (where $n = 6, 8, 10, 12, \dots$). The latter permits the construction of inorganic Si-O-Si skeletons as a basic structural unit, realizing cyclic and polycyclic types of matrixes, which offer these architectures the chemical stability, mechanical robustness, thermal stability, and possibility to form cage-like topology. Moreover, they possess oxygen atoms able to coordinate Ln^{3+} ions and, therefore, integrate and specially organize them inside the cage-like rigid framework. Moreover, terminal ligands may also be coordinated with the metal ions to complete their coordination environment, bringing additional functionalities. These architectures have mainly been investigated as molecule-based models for catalysis (Herrmann et al., 1994; Shchegolikhina et al., 1996; Annand et al., 1999; Annand and Aspinall H, 2000; Arnold et al., 2001; Lorenz et al., 2002; Lorenz et al., 2004; Wu et al., 2009; Marchesi et al., 2014; Davies et al., 2017; Sheng et al., 2022a; Sheng et al., 2022b), but recently, their magnetic (Sheng et al., 2022b) and optical properties (Sheng et al., 2022a) have also been investigated. Recently, we reported the first examples of luminescent Tb^{3+} , Eu^{3+} , and Dy^{3+} -based metallasilsesquioxanes presenting unusual (for metallasilsesquioxanes) anionic prism-like structures. These structures encompass four Ln^{3+} ions linked through oxygen atoms and situated between two cyclic tetraphenylcyclotetrasiloxanolate moieties (Kulakova et al., 2020; Kulakova et al., 2021; Nigoghossian et al., 2021; Félix et al., 2023a; Félix et al., 2023b). They present Ln^{3+} characteristic luminescence and interesting magnetic properties, depending on the nature of the ion, chemical robustness, and thermal stability. Moreover, we demonstrated that anionic cages containing mixed $\text{Tb}^{3+}/\text{Eu}^{3+}$ exhibited a tunable thermosensitive Tb^{3+} -to- Eu^{3+} energy transfer and proposed them as an efficient temperature sensor operating in the range $300\text{--}373\ \text{K}$ with good linearity and repeatability. Remarkably, these compounds presented an important stability

to photobleaching at a relatively high working temperature (100°C) due to the presence of the siloxane matrix, which played a protective role. However, the Ln^{3+} ions in these structures are not coordinated with antenna ligands, and the excitation was performed directly in the 4f levels, which is not optimal to achieve highly luminescent materials.

A major objective of the present work consists of the sensitization of Ln^{3+} luminescence in the silsesquioxane cages through the coordination of an antenna ligand. The most popular chelating acetylacetonate (*acac*) antenna has been used as a terminal ligand for this purpose (de Sá et al., 2000; Arnold et al., 2001; Eliseeva and Bünzli, 2009; Bünzli and Eliseeva, 2013; Gállico et al., 2023). Here, we report the synthesis, crystal structures, magnetic properties, and luminescence investigations of three new tetranuclear complexes ($\text{PhSiO}_{1.5}$)₈($\text{LnO}_{1.5}$)₄(O)(C₅H₈O₂)₆(EtOH)₂(CH₃CN)₂·2CH₃CN (where Ln = Tb (**1**), Tb/Eu (**2**), and Gd (**3**)) by introducing a terminal chelating ligand *acac* coordinated with the Ln^{3+} ions. Notably, this not only permits to afford an antenna effect and sensitizes the characteristic 4f luminescence but also induces an important change in the geometry of the ions from distorted antiprism (octa-coordinated) to a pentagonal bipyramidal geometry (seven-coordinated), which can positively impact their photophysical properties (Ferreira da Rosa et al., 2020). Complexes **1** and **2** present high Tb³⁺ or Tb³⁺/Eu³⁺ characteristic emissions and paramagnetic properties, while complex **3** has been used to assess the energies of the triplet states of the *acac* ligand. Theoretical calculations on the intramolecular energy transfer and multiphonon rates for the Tb³⁺-based compound indicate a thermal balance between Stark components of the ⁵D₄ level. The mixed Tb³⁺/Eu³⁺ analog showcases intra-cluster Tb³⁺-to-Eu³⁺ energy transfer and may be used for efficient temperature sensing with good stability, sensibility ($S_r = 2.0\%$ K⁻¹ at 373 K), and repeatability after several heating/cooling cycles.

2 Materials and methods

Phenyltrimethoxysilane (98%), Et₄NCl (≥98%), Eu(NO₃)₃·6H₂O (99.9% trace metal basis), Tb(NO₃)₃·6H₂O (99.9% trace metal basis), ethanol, acetylacetonate, and acetonitrile were purchased from Merck and used as received.

2.1 Synthesis

Compounds **1–3** were synthesized in a similar way. A mixture of PhSi(OMe)₃ and NaOH was dissolved in 30 mL of ethanol. The resulting solution was heated to reflux for 1.0 h. Afterward, Tb(NO₃)₃·6H₂O for compound **1** (or the mixture of Tb(NO₃)₃·6H₂O and Eu(NO₃)₃·6H₂O, in a 3:1 ratio, for compound **2**, or Gd(NO₃)₃·5H₂O for compound **3**) and sodium acetylacetonate dissolved in 30 mL of CH₃CN were added at once. The resulting mixture was heated to reflux for 3.0 h. Filtration of the mixture from the insoluble part provided a non-colored solution. Slow evaporation of solvents (ethanol/CH₃CN) provided, in 5–10 days, many crystalline materials. The single crystals suitable for single-crystal X-ray diffraction were collected. The crystal products were dried in a vacuum to perform elemental analysis and calculate the yield.

(PhSiO_{1.5})₈(TbO_{1.5})₄(O)(C₅H₈O₂)₆(EtOH)₂(CH₃CN)₂·2CH₃CN **1**. Reactant loadings: PhSi(OMe)₃ (0.186 g, 0.8 mmol), NaOH (0.032 g, 0.8 mmol), Tb(NO₃)₃·6H₂O (0.174 g, 0.4 mmol), and sodium acetylacetonate (0.049 g, 0.4 mmol). Yield = 30% (0.068 g).

Anal. calcd for C₇₈H₈₈Tb₄O₃₀Si₈: % C 39.60, % H 3.75. Found: % C 39.54, % H 3.71. IR in KBr pellets (cm⁻¹): 3443 (w), 3071 (s), 3048 (s), 1592 (s), 1519 (s), 1384 (w), 1129 (s), 1051 (w), 1027 (w), 952 (s), 945 (w), 835 (s), 745 (s), 700 (s), 676 (s), 576 (s), 547 (s), and 494 (s). (PhSiO_{1.5})₈(TbO_{1.5})₃(EuO_{1.5})₁(O)(C₅H₈O₂)₆(EtOH)₂(CH₃CN)₂·2CH₃CN **2**. Reactant loadings: PhSi(OMe)₃ (0.186 g, 0.8 mmol), NaOH (0.032 g, 0.8 mmol), Tb(NO₃)₃·6H₂O (0.131 g, 0.3 mmol), Eu(NO₃)₃·5H₂O (0.043 g, 0.1 mmol), and sodium acetylacetonate (0.049 g, 0.4 mmol). Yield = 25% (0.057 g).

Anal. calcd for C₇₈H₈₈Eu₃O₃₀Si₈Tb: % C 39.95, % H 3.78. Found: % C 39.89, % H 3.73. EDS analysis: Tb/Eu ratio 22.1/7.4. IR in KBr pellets (cm⁻¹): 3619 (s), 3365 (w), 3071 (s), 3048 (s), 1592 (s), 1518 (s), 1429 (s), 1384 (w), 1266 (s), 1129 (s), 1052 (m), 950 (s), 745 (s), 701 (s), 676 (s), 576 (s), and 494 (s).

(PhSiO_{1.5})₈(GdO_{1.5})₄(O)(C₅H₈O₂)₆(EtOH)₂(CH₃CN)₂·2CH₃CN **3**. Reactant loadings: PhSi(OMe)₃ (0.186 g, 0.8 mmol), NaOH (0.032 g, 0.8 mmol), Gd(NO₃)₃·5H₂O (0.173 g, 0.4 mmol), and sodium acetylacetonate (0.049 g, 0.4 mmol). Yield = 39% (0.092 g).

Anal. calcd for C₇₈H₈₈Gd₄O₃₀Si₈: % C 39.71, % H 3.76. Found: % C 39.63, % H 3.72. IR in KBr pellets (cm⁻¹): 3439 (w), 3066 (s), 3045 (s), 1596 (s), 1517 (s), 1390 (w), 1121 (s), 1060 (w), 1025 (w), 950 (s), 940 (w), 833 (s), 741 (s), 690 (s), 674 (s), 579 (s), 544 (s), and 491 (s).

2.2 Characterization

IR spectra (KBr pellets) were recorded using a PerkinElmer Spectrum Two FT-IR spectrometer. The quantification of Eu, Tb, and Si was performed using a scanning electron microscope and energy-dispersive X-ray analysis (SEM-EDX) on a FEI Quanta FEG 200 instrument. The powders were deposited on an adhesive carbon film and analyzed under vacuum. The heavy elements were quantified using INCA software, with a dwell time of 3 μs.

The emission and excitation spectra were at first evaluated at room (298 K) and low (77 K) temperatures using an Edinburgh FLS-920 spectrofluorimeter. The excitation source was a 450-W Xe arc lamp. The spectra were corrected for the detection and optical spectral response of the spectrofluorimeter. In the second step, the emission spectra were measured as a function of the temperature. The temperature setup included a thermal element (Heidolph, MR Hei-Tec [EU], 825 W, plate diameter 145 mm), a thermal camera (Optris PI 450i, accuracy ± 0.01°C), an excitation source, and a detector. The powder sample was placed on a cover glass (14 mm diameter) at the center of the heating source. The thermal camera was positioned at an angle of 30° relative to the sample to work as a temperature standard controller. A UV LED operating at 365 nm (Thorlabs M365L2) was used to excite the samples ($I = 0.7\text{ A}$) by irradiating at 15 mm from the sample surface.

The spectrometric detector and the excitation source were coupled using a multimode fiber. The fiber excitation output and detector were located at the top of the sample. A long-pass filter (in-line fiber optic filter mount, Thorlabs, FOFMS/M, 450 nm, 20 μm) was placed in the light path between the sample and detector to avoid artifacts arising from the excitation source. The emission

spectra were recorded in the temperature range from 300 to 376 K. At each temperature step, 10 min was provided to allow the temperature to stabilize, and then, 10 emission spectra were recorded from an average of 10 consecutive spectra with an integration time of 100 ms.

The UV-visible-NIR absorption spectrum was measured using a Specord 210 Plus spectrophotometer (Analytik Jena AG, Germany). Magnetic susceptibility data were collected using a Quantum Design MPMS-XL SQUID magnetometer working between 1.8 and 350 K with a magnetic field up to 7 T. The sample was prepared under an ambient condition. The data were corrected for the sample holder, and the diamagnetic contributions were calculated from Pascal's constants.

2.3 Crystal structure determination

X-ray diffraction data for compounds **1–3** were collected using a three-circle Bruker D8 QUEST PHOTON-III CCD diffractometer ($\lambda(\text{MoK}\alpha)$ radiation, graphite monochromator, and φ and ω scan modes) and corrected for absorption using the SADABS program. The data were indexed and integrated using the SAINT program. Details are given in [Supplementary Table S1](#). The structures were solved by direct methods and refined by the full-matrix least squares technique on F^2 with anisotropic displacement parameters for non-hydrogen atoms. The hydrogen atoms of the OH groups were localized in difference Fourier maps and refined isotropically with fixed-displacement parameters [$U_{\text{iso}}(\text{H}) = 1.5U_{\text{eq}}(\text{O})$]. The other hydrogen atoms were placed in calculated positions and refined within the riding model with fixed isotropic displacement parameters [$U_{\text{iso}}(\text{H}) = 1.5U_{\text{eq}}(\text{C})$ for the CH_3 groups and $1.2U_{\text{eq}}(\text{C})$ for the other groups]. All calculations were carried out using the SHELXTL program suite.

Crystallographic data have been deposited in the Cambridge Crystallographic Data Center, CCDC 2189837 (**1**), CCDC 2189838 (**2**), and CCDC 2189839 (**3**). Copies of this information may be obtained free of charge from the Director, CCDC, 12 Union Road, Cambridge CB2 1EZ, United Kingdom (Fax: +44 1223 336033; e-mail: deposit@ccdc.cam.ac.uk or www.ccdc.cam.ac.uk).

The crystal structure was determined in the Department of Structural Studies of Zelinsky Institute of Organic Chemistry, Moscow, Russia.

3 Results and discussion

3.1 Synthesis and crystal structures

The synthesis of Ln^{3+} -based silsesquioxanes ($\text{PhSiO}_{1.5}$)₈($\text{LnO}_{1.5}$)₄($\text{O}(\text{C}_5\text{H}_8\text{O}_2)_6(\text{EtOH})_2(\text{CH}_3\text{CN})_2 \cdot 2\text{CH}_3\text{CN}$ (where $\text{Ln} = \text{Tb}$ **1**, Tb/Eu **2**, and Gd **3**) with an antenna ligand was performed using a two-step approach involving conventional alkaline hydrolysis ([Prigyi et al., 2019](#); [Laird et al., 2021](#)) with the *in situ* formation of phenylsiloxanolate [$\text{PhSi}(\text{O})\text{ONa}$]_x species, following a self-assembling reaction with the *acac* ligand and the corresponding Ln^{3+} salts for compounds **1** (Tb^{3+}) and **3** (Gd^{3+}) or mixed Tb^{3+} and Eu^{3+} salts (with a $\text{Tb}^{3+}/\text{Eu}^{3+}$ ratio of 3/1) for compound **2**. The crystallization from an acetonitrile/ethanol

mixture affords the formation of single crystals suitable for crystallographic analysis. Single-crystal X-ray diffraction performed on compounds **1–3** indicates that they are isostructural and crystallize in the $P2_1/n$ space group ([Supplementary Table S1](#), Electronic Supplementary Material (ESI)). Their crystal packing may be viewed as an assembly of neutral tetranuclear lanthanide-based cages directed almost toward $[-1\ 1\ -1]$ ([Figure 1A](#) for compound **1**; [Supplementary Figures S1,S2](#), ESI for compounds **2–3**). In all compounds, the cages form layers parallel to $(1\ 0\ -1)$. Within the layers, the cages are arranged perpendicular to each other. Two acetonitrile molecules were also crystallized in the unit cell and situated between the tetranuclear cages. The shortest intermolecular Ln–Ln distances are equal to 10.0765, 10.0709, and 10.0981 Å for compounds **1**, **2**, and **3**, respectively.

The molecular structure of the neutral tetranuclear lanthanide-based cages of compound **1** may be described as a prism-like polyhedron in the form of a New Year paper lantern. It is formed by a $(\text{TbO}_2)_4$ core wedged between two tetraphenylcyclotetrasiloxanolate moieties ([Figure 1B, C](#) for compound **1**).

For compound **2**, the prism-like polyhedron is formed by a $(\text{Tb}_{1-x}\text{Eu}_x\text{O}_2)_4$ core, where $x = 0.25$, with statistically distributed Tb/Eu ions linked through oxygen atoms, forming a distorted square ([Supplementary Figure S1](#), ESI). In both compounds, there are two slightly different seven-coordinated Tb (for compound **1**) or Tb/Eu sites (for compound **2**), which adopt a one-capped trigonal prism geometry. Each Ln^{3+} ion is coordinated by four bridging oxygens, two oxygens from terminal acetylacetonate, and one ethanol or acetonitrile molecule. The Tb (or Tb/Eu)–O distances involving bridging oxygens are in the range 2.3121(1)–2.3471(1) Å for compound **1** and 2.3013(2)–2.3789(2) Å for compound **2**, while those involving terminal acetylacetonate and ethanol molecules are larger and situated in the range 2.2884(1)–2.3966(1) Å for compound **1** and 2.2822(6)–2.4401(6) Å for compound **2**. The Tb (or Tb/Eu)–N distances involving terminal acetonitrile are 2.5358 (2) Å for compound **1** and in the range 2.4564–2.5691 Å for compound **2**. The O–Ln–O angles in the square are in the range 70.322(3)–81.654(3)° for compounds **1** and **2**. Compound **3** presents crystal structures similar to those of compound **1** ([Supplementary Figure S2](#), ESI). The main distances and angles are given in ESI ([Supplementary Table S2](#)). The atomic Tb/Eu ratio in compound **2** determined by SEM-EDX analysis is equal to 3/1, as expected.

3.2 Magnetic properties

The magnetic measurements were determined for all compounds using a SQUID MPMS-XL magnetometer working between 1.8 and 300 K and up to 7 T.

The temperature dependence of the magnetic susceptibility performed in the direct current (dc) mode has been performed under an applied magnetic field of 1,000 Oe. The room temperature χT values of 48.40 and 31.30 $\text{cm}^3 \cdot \text{K} \cdot \text{mol}^{-1}$ for compounds **1** and **2**, respectively, are coherent with the theoretical values of 47.28 and 35.46 $\text{cm}^3 \cdot \text{K} \cdot \text{mol}^{-1}$ expected for four (compound **1**) and three Tb^{3+} ions (compound **2**), using the free-ion approximation (7F_6 , $S = 3$, $L = 3$, $g = 3/2$, $\chi T =$

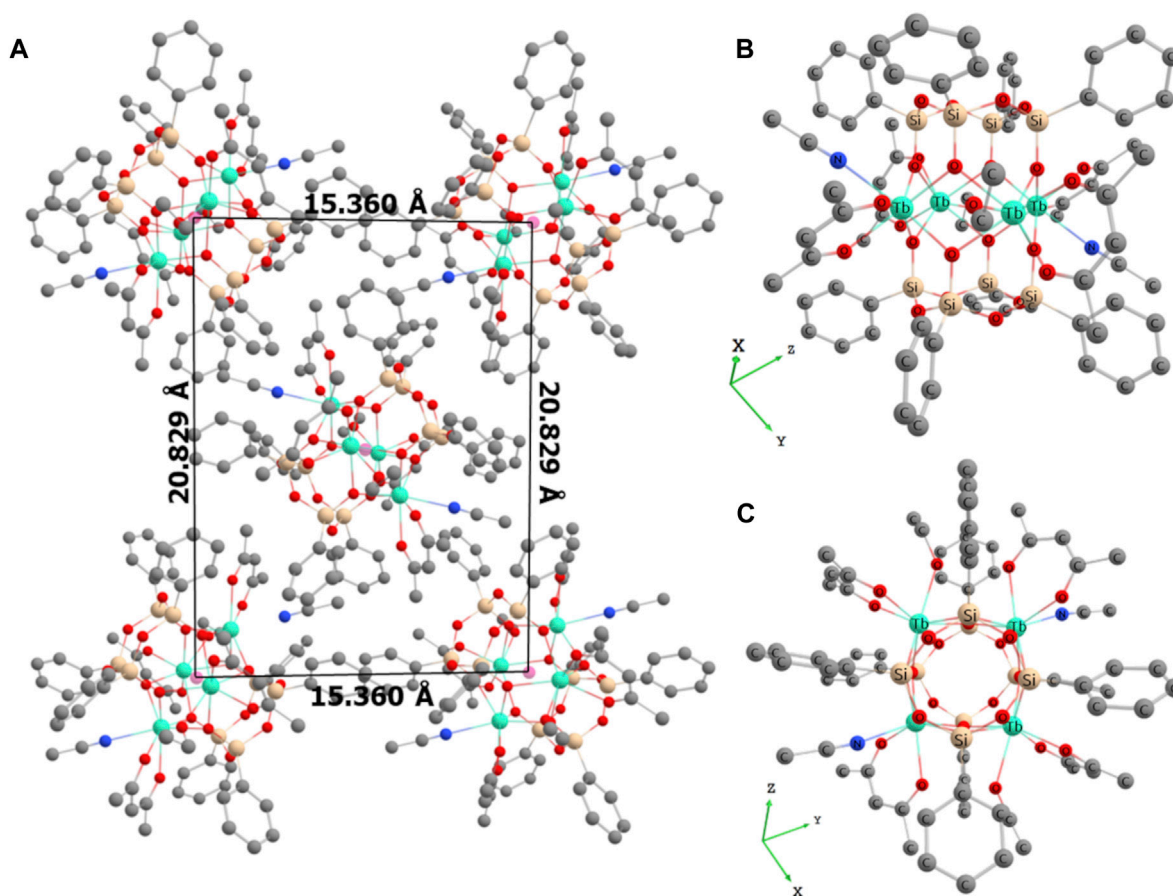


FIGURE 1

(A) Perspective view of crystal packing for compound **1** along the crystallographic axis *a*. Hydrogen atoms and crystallized acetonitrile molecules have been omitted for clarity; (B) molecular structure of compound **1** showing the prism-like polyhedron; (C) molecular structure of compound **1** showing the square arrangement of the Tb atoms in the $(\text{TbO}_2)_4\text{O}$ core. Color code: green, Tb; beige, Si; red, O; blue, N; and gray, C.

$11.82 \text{ cm}^3 \cdot \text{K} \cdot \text{mol}^{-1}$) (Long et al., 2011). Upon cooling, the compounds exhibit a typical decrease in χT caused by the thermal depopulation of the Stark sublevels and/or the presence of antiferromagnetic interactions between the Tb^{3+} centers (Figure 2A). The field dependence of magnetization performed at 1.8 K shows a rapid linear increase in the magnetization with the field for both compounds (Figure 2B). The curves do not reach the saturation and magnetization values of 22.9 and 14.95 $N\beta$ under 7 T for compounds **1** and **2**, respectively, indicating the presence of significant magnetic anisotropy. This behavior is perfectly coherent with the previously published cage-like compounds containing Tb^{3+} ions. Note that no slow relaxation of the magnetization has been observed by investigation of the dynamic magnetic behaviors of these compounds by alternating current (ac) magnetic measurements.

The magnetic behavior of Gd^{3+} -based silsesquioxane **3** is coherent with the presence of four isotropic Gd^{3+} ions. The room temperature χT value of $34.4 \text{ cm}^3 \cdot \text{K} \cdot \text{mol}^{-1}$ is in agreement with the expected value ($31.52 \text{ cm}^3 \cdot \text{K} \cdot \text{mol}^{-1}$) calculated for four Gd^{3+} ions in a free-ion approximation ($^8S_{7/2}$, $g = 2$) (Long et al., 2011). As the temperature decreases, the χT vs. T curve almost remains constant up to 20 K and then sharply declines at low temperatures, indicating the presence of

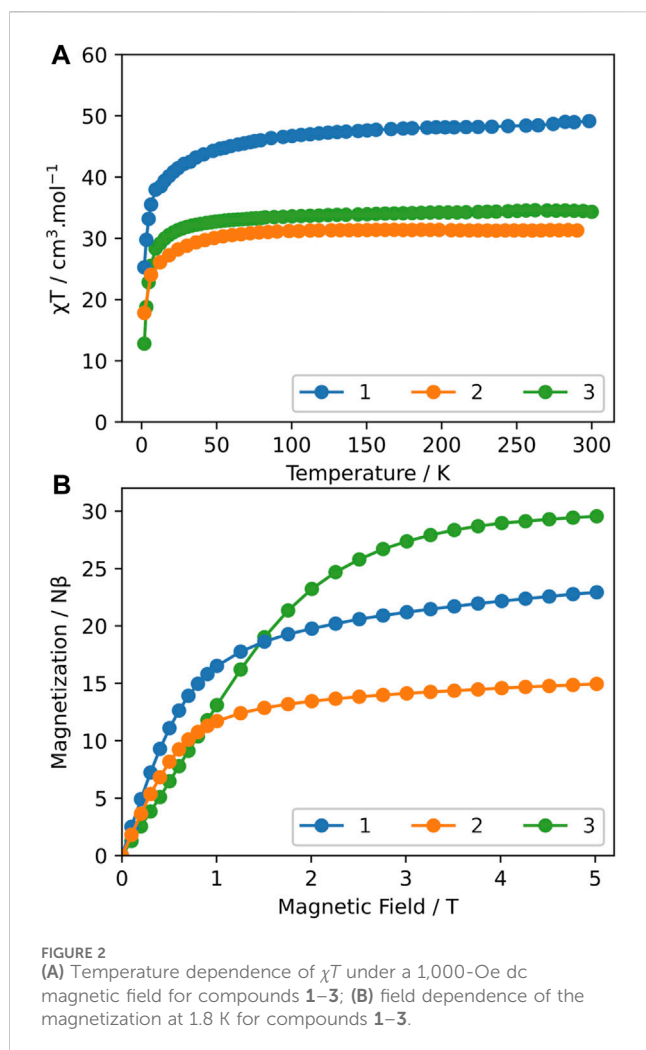
weak antiferromagnetic interactions between adjacent Gd^{3+} ions (Figure 2A). The M vs. H curve performed at 1.8 K is coherent with the presence of four Gd^{3+} ions (28 $N\beta$) (Figure 2B).

3.3 Experimental and theoretical photoluminescence studies

The excitation and emission spectra of all compounds were investigated in the solid state at different temperatures ranging from 11 to 378 K.

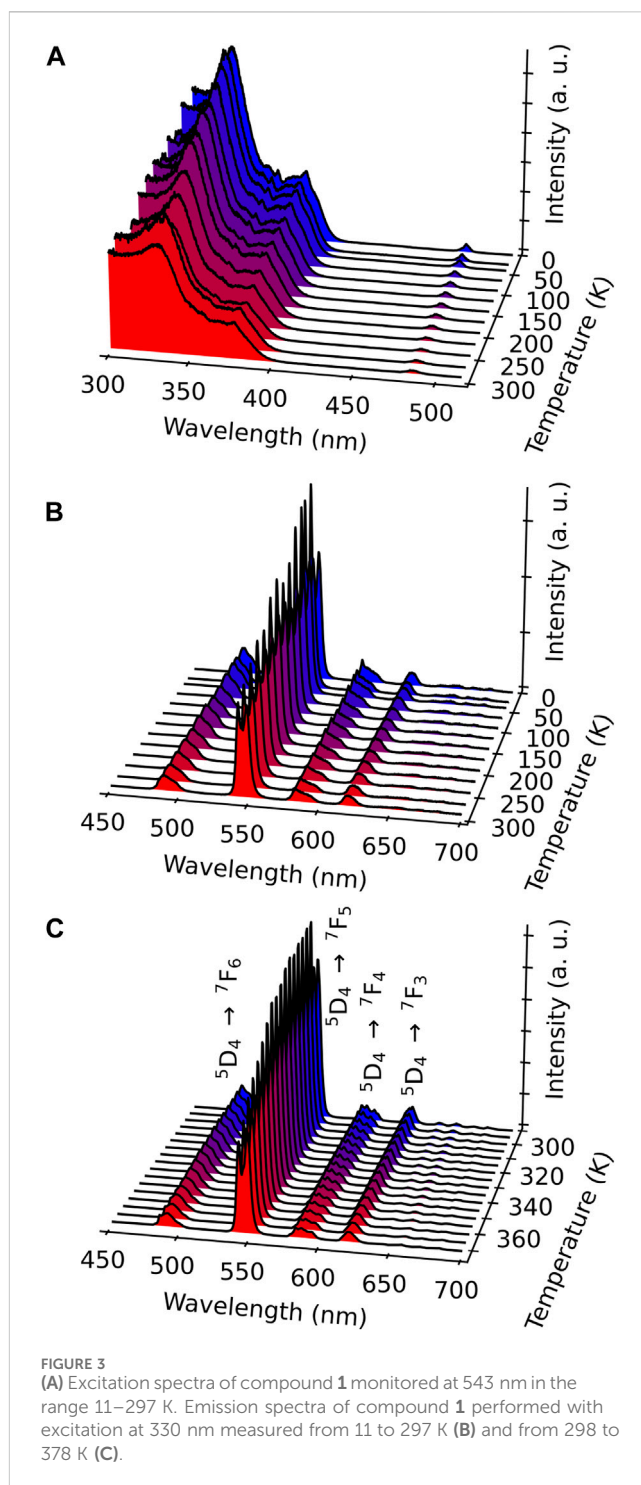
3.3.1 Gd^{3+} compound **3**

The photoluminescence of Gd^{3+} -containing compound **3** has been used to assess the energies of the triplet states located on the terminal *acac* ligand since Gd^{3+} has a high energy-accepting electronic level, which prevents any population through the energy transfer from the electronic level of the antenna ligand. Supplementary Figure S3, ESI, shows the emission spectrum of compound **3** obtained upon excitation at 246 nm at 77 K. The energy of the triplet state is $25,316 \text{ cm}^{-1}$ (corresponding to an emission peak at 395 nm).



3.3.2 Tb^{3+} compound 1

The excitation spectra of Tb^{3+} -containing compound 1 monitored within the main $^5\text{D}_4 \rightarrow ^7\text{F}_5$ transition (543 nm) in the range 11–300 K exhibit large broadband, with a main component at *ca.* 330 nm attributed to the *acac* ligand excited state (Figure 3A). A series of low-intensity narrow lines attributed to transitions between $^7\text{F}_6$ and the $^5\text{G}_5$, $^5\text{G}_6$, and $^5\text{D}_3$ excited states indicates that Tb^{3+} is mainly populated through antenna-assisted sensitization rather than by a direct excitation into the intra- $4f^8$ lines. The emission spectra of compound 1 recorded under excitation at 330 nm in the 11–297-K and 298–378-K intervals (Figures 3B,C) exhibit the classical Tb^{3+} $^5\text{D}_4 \rightarrow ^7\text{F}_{6-0}$ characteristic emission lines. The profile of the emission spectra is similar under direct $4f^8$ excitation at 485 nm (Supplementary Figures S4A, B, ESI). The most intense emission, centered at 543 nm, corresponds to the $^5\text{D}_4 \rightarrow ^7\text{F}_5$ transition, displaying a gradual decrease with increasing temperature, as shown in Figure 4 and Supplementary Figures S4C, S5 (ESI). The emission decay curve of compound 1 was monitored at room temperature within $^5\text{D}_4 \rightarrow ^7\text{F}_5$. The curve is well-reproduced by a single exponential function, yielding a $^5\text{D}_4$ lifetime of 0.851 ± 0.002 ms, which is a rather typical value for Tb^{3+} complexes (Supplementary Figure S6). The presence of two maxima in the $^5\text{D}_4 \rightarrow ^7\text{F}_5$ transition, I_1 and I_2 in Figure 4, is associated with two



distinct Stark components. Although the maximum number of $^5\text{D}_4$ and $^7\text{F}_5$ Stark levels can lead to 99 components in the $^5\text{D}_4 \rightarrow ^7\text{F}_5$ transition, once the majority is degenerate, only a few can be observed (Figure 4). A question can be raised concerning whether some of these transitions between Stark levels could be attributed to vibronic transitions (or sidebands). This can be answered with the emission spectrum recorded at 11 K (Figure 5A), where vibrational modes that could couple in this spectral region can be suppressed. As the emission intensity is directly proportional to the population of the emitting level, the

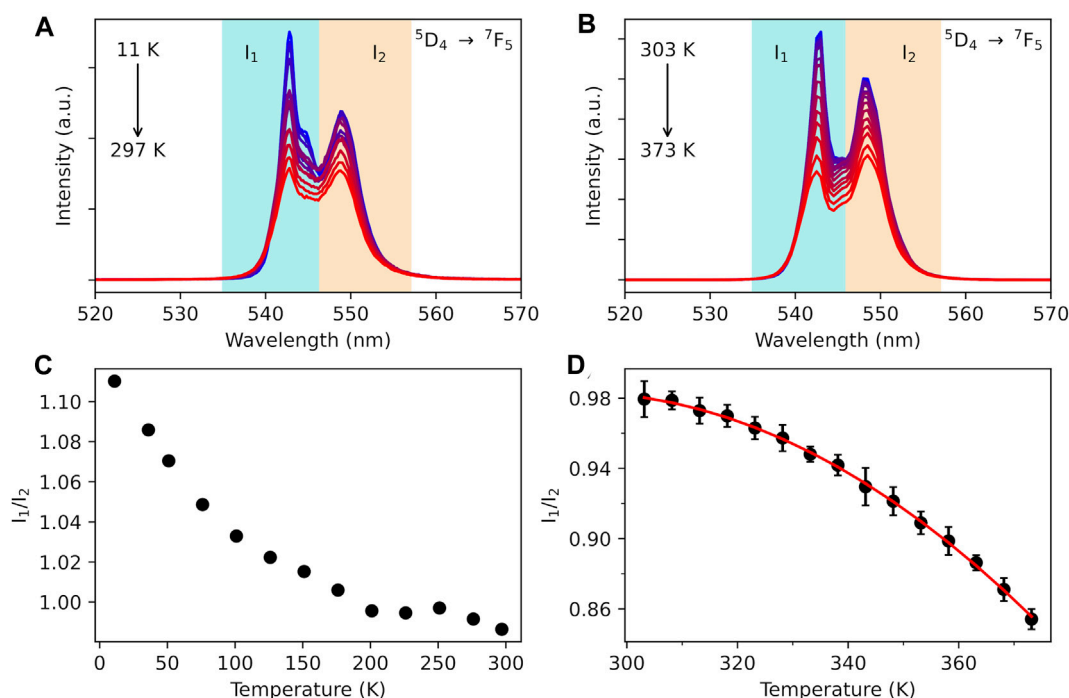


FIGURE 4
 $^5D_4 \rightarrow ^7F_5$ transition emission band for compound **1** upon the excitation at 330 nm in the ranges 11–297 K (A) and 303–378 K (B). The shadowed blue and orange regions represent the integration ranges for the I_1 and I_2 Stark components, respectively. Temperature dependence of the I_1/I_2 ratio in the intervals 11–297 K (C) and 303–378 K (D). The red curves represent a single exponential function as the best fit to the experimental data ($r^2 > 0.99$).

model suggests that emission I_1 originates from a Stark component ($|1\rangle$ in Figure 5B) associated with the lower Stark level of 5D_4 . In contrast, emission I_2 comprises the emission from a Stark level with higher energy ($|2\rangle$ in Figure 5B). It is important to note that the high-energy emission is not always attributed to a Stark level with higher energy as the energy of the transition also depends on the energy of the ending level (7F_5), as shown in Figure 5B.

The model assumes that the high-energy emission stems from a lower-energy Stark component of 5D_4 . This assumption is relevant because, at 11 K, there would be no thermal population arising from $|1\rangle$ to $|2\rangle$, and the emission I_2 should vanish at low-temperature ranges because $W_{2 \rightarrow 1} \gg W_{1 \rightarrow 2}$ (Figure 5C), where $W_{2 \rightarrow 1}$ and $W_{1 \rightarrow 2}$ are the multiphonon decay rate (creation of phonons) and absorption (annihilation of phonons) rates, respectively, between $|1\rangle$ and $|2\rangle$ Stark components of the 5D_4 level. The decay rate $W_{2 \rightarrow 1}$ was calculated from the energy gap law (Moos, 1970; Reisfeld et al., 1977; Riseberg et al., 1977; Malkin et al., 2005) in the Miyakawa–Dexter approach (Supplementary Eqs S1,S2) (Miyakawa and Dexter, 1970). The intramolecular energy transfer (IET) rates from T_1 to 5D_4 levels were calculated using Supplementary Eqs S5–S7 (Carneiro Neto et al., 2019) (details given in ESI) using the JOYSpectra web platform (Moura Jr. et al., 2021b).

Based on the obtained IET and multiphonon rates (Figure 5C; Supplementary Table S3), together with the energy level diagram shown in Figures 5A,B, a three-level rate equation model can be considered as follows:

$$\frac{d\eta_1(t)}{dt} = W_{2 \rightarrow 1}\eta_2(t) - \left(W_{1 \rightarrow 2} + \frac{1}{\tau}\right)\eta_1(t) \quad (1)$$

$$\frac{d\eta_2(t)}{dt} = W_{1 \rightarrow 2}\eta_1(t) + \phi\eta_3(t) - \left(W_{2 \rightarrow 1} + \frac{1}{\tau}\right)\eta_2(t) \quad (2)$$

$$\frac{d\eta_3(t)}{dt} = \frac{1}{\tau}[\eta_1(t) + \eta_2(t)] - \phi\eta_3(t) \quad (3)$$

where η_1 , η_2 , and η_3 are the populations of $|1\rangle$, $|2\rangle$, and 7F_5 , respectively, with initial conditions (when $t = 0$) of $\eta_1(0) = \eta_2(0) = 0$ and $\eta_3(0) = 1$. $\tau = 0.851$ ms is the measured decay lifetime of the 5D_4 level, and ϕ is the feeding rate of the emitting level 5D_4 that comes mainly from the energy transfer rates involving the 7F_6 and 7F_5 levels as the starting level (e.g., IET rates from ligand states to Tb^{3+} $^7F_6 \rightarrow ^5D_4$ and $^7F_5 \rightarrow ^5D_4$) (Kasprzycka et al., 2020; Carneiro Neto et al., 2022).

One premise of the present model is that the ϕ feeding rate is attributed to the direct energy transfer from the T_1 state to the 5D_4 level, following the pathways $[T_1 \rightarrow S_0] \rightarrow Tb^{3+}[^7F_6 \rightarrow ^5D_4]$ and $[T_1 \rightarrow S_0] \rightarrow Tb^{3+}[^7F_5 \rightarrow ^5D_4]$ (Supplementary Table S3). It is noteworthy that the last pathway dominates the direct energy transfer process with a rate of 1.9×10^6 s $^{-1}$, and the exchange mechanism (Supplementary Eq. S7) has the most significant contribution (Supplementary Table S3).

Although the energy transfer from the S_1 state has been a recent topic of debate in the literature (Alaoui, 1995; Rodríguez-Cortinas et al., 2002; Yang et al., 2004; Kasprzycka et al., 2017; Moura Jr. et al., 2021a; Aquino LE do et al., 2021; Manzur et al., 2023), as certain levels of Tb^{3+} may serve as better acceptors due to the high values of matrix elements involved in the IET process (e.g., $^7F_6 \rightarrow ^5G_6$ and $^7F_5 \rightarrow ^5G_6$) (Moura Jr. et al., 2021a), the population in the upper levels

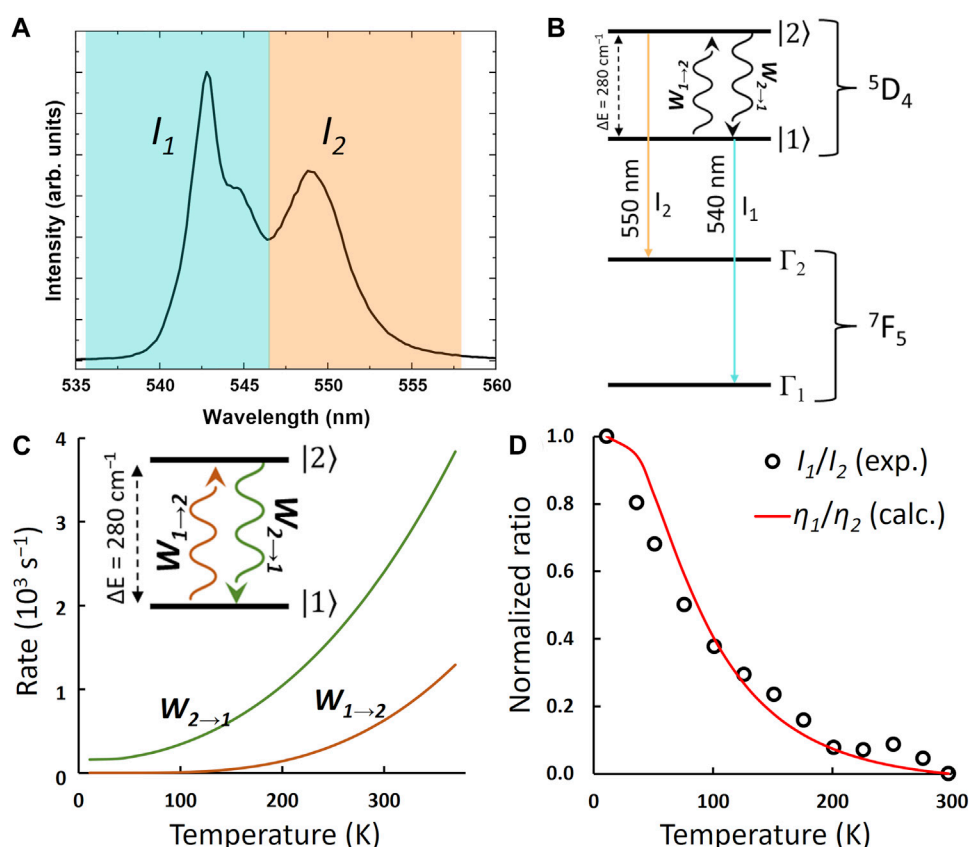


FIGURE 5

(A) Low-temperature (11 K) emission spectrum, recorded with excitation at 322 nm, showing the two main Stark levels of the $5D_4 \rightarrow 7F_5$ transition. (B) Illustration of the emission process between different Stark components of the $5D_4$ level to different Stark components of the $7F_5$ level. (C) Calculated multiphonon rates, as a function of temperature, exchanged by $5D_4$ Stark levels $|1\rangle$ and $|2\rangle$. (D) Normalized intensity ratio (I_1/I_2) vs temperature.

essentially decays not as quickly to the $5D_4$ level compared to the rising of the population from the $7F_6$ and $7F_5$ to the $5D_4$ level in the direct energy transfer process. Thus, this premise can be justified by the subsequent multiphonon decay between adjacent levels of Tb^{3+} , forming a ladder-like decay process. These decays are generally slower than direct energy transfer, and consequently, decay steps like $5G_6 \rightarrow 5D_3 \rightarrow 5D_4$ can be neglected in the present model.

For comparison, the decay from $5D_3 \rightarrow 5D_4$ involves a large energy gap of $\Delta(5D_3 \rightarrow 5D_4) \approx 5,792 \text{ cm}^{-1}$ (Carnall et al., 1978), leading to a decay rate of $W_{mp} = 7.4 \times 10^3 \text{ s}^{-1}$ if two optical phonons with $\hbar\omega = 2,896 \text{ cm}^{-1}$ each are considered to bridge the $\Delta(5D_3 \rightarrow 5D_4)$ gap. This calculation is based on the application of Supplementary Eqs S1, S2 within the energy gap law framework. If a three-phonon process is required to bridge the gap, the multiphonon rate will be even lower ($W_{mp} \sim 60 \text{ s}^{-1}$), as expected when the number of phonons is increased. This underscores that the direct IET rates from the T_1 state are more than two orders of magnitudes higher (see Supplementary Table S3) than the multiphonon decay in the $5D_4$ sensitization process.

The rate equation model (Supplementary Eqs S1–S3) was numerically propagated using the Radau method, a numerical approach belonging to the class of fully implicit Runge–Kutta methods (Hairer et al., 2015), over a time span of 0–10 ms with a step size of 10 ns. This implies that 1,000,000 points were

calculated for each temperature, ranging from 11 to 297 K in steps of 2 K.

As the intensity is directly proportional to the population of the emitting level, the experimental intensity ratio (I_1/I_2 in Figure 4) and the calculated population ratio (η_1/η_2) in the steady-state regime can be compared. Figure 5D illustrates this comparison, and it can be concluded that the calculated trend is similar to the experimental trend. This observation suggests that the Stark components of the $5D_4$ are governed by an equilibrium between non-radiative decay and rising among these components ($|1\rangle$ and $|2\rangle$), driven by a Boltzmann distribution between $W_{2\rightarrow 1}$ and $W_{1\rightarrow 2}$.

Suta and Meijerink (2020) reported that there is potential temperature dependence in the use of crystal field splitting (Stark levels) for trivalent lanthanides at low temperatures. However, at higher temperatures, where the product $k_B T$ is significantly greater than the crystal splitting energy, a thermodynamic equilibrium among Stark levels could be established, allowing for their treatment as an effectively thermally averaged single level with an average radiative decay rate. In our model, this implies that the non-radiative decays and absorptions between two Stark levels are approximately equal, rendering the model inapplicable. In other words, Boltzmann statistics between Stark levels become ineffective at higher temperatures, resulting in a shift in the trend for temperatures exceeding 250 K, as shown in Supplementary Figure

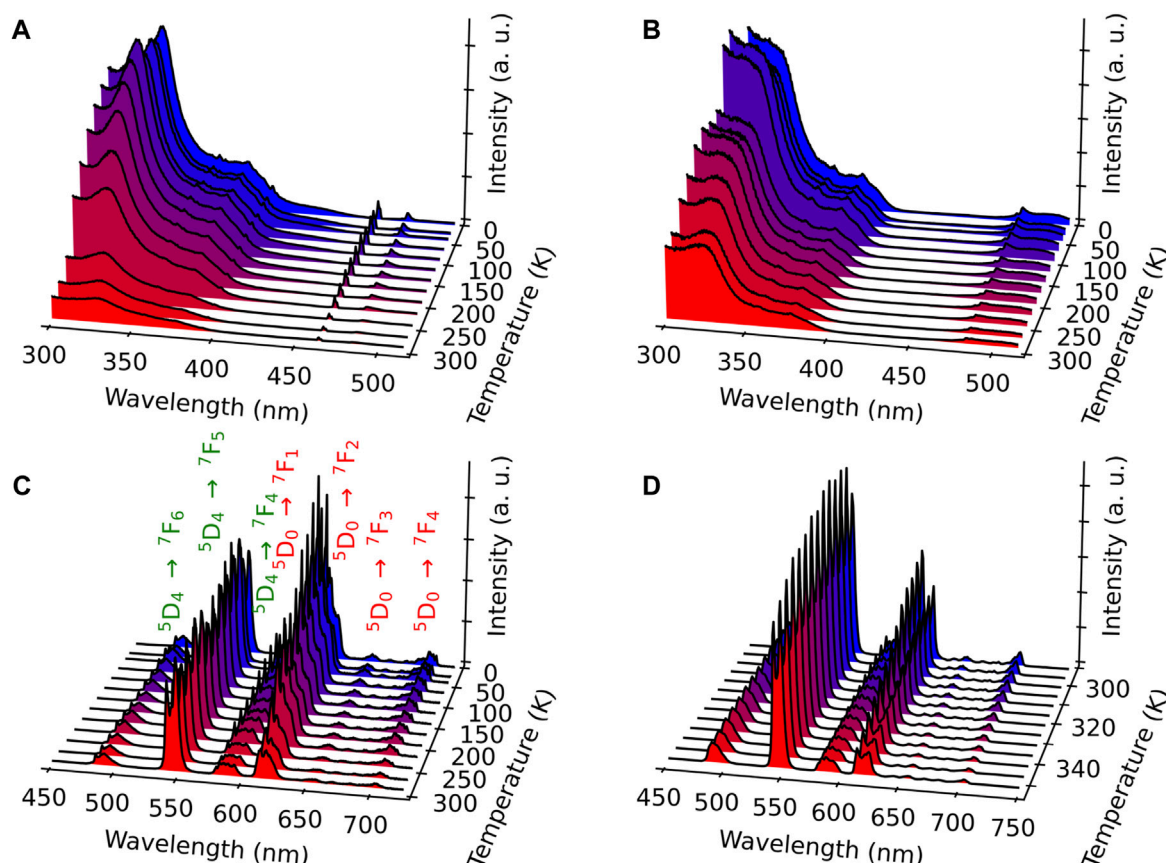


FIGURE 6
Excitation spectra of compound **2** monitored at 615 nm (Eu^{3+}) (A) and 543 nm (Tb^{3+}) (B) in the range 11–297 K. Emission spectra of compound **2** excited at 330 nm in the ranges 11–297 K (C) and 298–378 K (D). The transitions ascribed to Eu^{3+} and Tb^{3+} are indicated in red and green, respectively.

S5A (ESI), and consistent with the behavior shown in Supplementary Figure S5B (ESI).

3.3.3 Mixed $\text{Eu}^{3+}/\text{Tb}^{3+}$ compound **2**

To provide a self-calibrated ratiometric luminescent thermometer, the Eu^{3+} ion was introduced in the structure to obtain compound **2**, as previously demonstrated in different MOF materials and Ln^{3+} -based complexes (Brites et al., 2019). The excitation spectra at different temperatures were recorded by monitoring the main emissions of both Eu^{3+} at 615 nm ($^5\text{D}_0 \rightarrow ^7\text{F}_2$) and Tb^{3+} at 543 nm ($^5\text{D}_4 \rightarrow ^7\text{F}_5$) (Figures 6A,B). The spectra are relatively similar and, as in the case of compound **1**, present main broadband (at 330 nm) attributed to the *acac* ligand excited states, confirming the excitation through antenna sensitization. Low-intensity intra-4f transitions of both Ln^{3+} ions can also be visible in the spectra, e.g., $^7\text{F}_{0,1} \rightarrow ^5\text{D}_2$ (Figure 6A) and $^7\text{F}_6 \rightarrow ^5\text{D}_4$ (Figures 6A,B). The observation of this latter Tb^{3+} line when monitoring Eu^{3+} emission at 615 nm points out the occurrence of Tb^{3+} -to- Eu^{3+} energy transfer.

The emission spectra were measured upon excitation at 330 nm, which is operational for both Ln^{3+} ions, in the ranges 11–297 K (Figure 6C) and 298–378 K (Figure 6D). Compared with the emission spectra of compound **1**, the Eu^{3+} -characteristic transitions from $^5\text{D}_0$ to $^7\text{F}_j$ ($j = 0-4$) appear besides the Tb^{3+} transitions. Note that the emission spectra obtained under a

direct excitation at 484 nm ($\text{Tb}^{3+} \ ^7\text{F}_6 \rightarrow ^5\text{D}_4$ transition) show, besides the main Tb^{3+} transition $^5\text{D}_4 \rightarrow ^7\text{F}_5$ (indicated in green), a series of the Eu^{3+} -related transitions $^5\text{D}_0 \rightarrow ^7\text{F}_{1,2,3,4}$ (indicated in red, Supplementary Figure S7, ESI). This fact points out the presence of the Tb^{3+} -to- Eu^{3+} energy transfer, as already inferred from the excitation spectra shown in Figure 6B. This is not surprising considering that the shortest Ln^{3+} - Ln^{3+} distance in compound **2** is equal to 3.728 Å. As expected, the emission spectra performed with direct excitation in the Eu^{3+} -related band at 464 nm display only the Eu^{3+} transitions (Supplementary Figure S8, ESI).

To estimate the energy transfer rates, in addition to the calculations of pairwise interactions (Malta, 2008; Carneiro Neto et al., 2020), the distribution of donor-acceptor distances, where Tb^{3+} is the donor and Eu^{3+} is the acceptor, was calculated from the crystallographic structure using a custom program written in C. The simulations of the $\text{Tb}^{3+}/\text{Eu}^{3+}$ ratio (3:1) in the structure of an expanded $20 \times 20 \times 20$ crystal, consisting of 64,000 Ln^{3+} sites, were conducted. The sites could be occupied by either Tb^{3+} or Eu^{3+} ions. The program performed 100 simulations while maintaining the 3:1 ratio to provide statistically reliable donor-acceptor distance results. Thus, the occurrence of the formation of a Tb-Eu pair with a given distance is given by (Trannoy et al., 2021)

$$O_i = \frac{\mathcal{N}_i}{s \cdot x} \quad (4)$$

where \mathcal{N}_i is the counting of a donor–acceptor pair with distance $R(i)$, $s = 64,000$ is the number of total host sites (i.e., Ln^{3+} sites) available for Eu^{3+} and Tb^{3+} substitution, and x is the fraction of Eu^{3+} ($x = 0.25$ for forward energy transfer) or Tb^{3+} ($x = 0.75$ for backward energy transfer).

Figure 1A and Supplementary Figure S1, ESI, show that the shortest distance between two $\{\text{Ln}_4\}$ clusters of Ln^{3+} is in the order of 15 Å. This results in a weak interaction concerning Tb–Eu energy transfer between different $\{\text{Ln}_4\}$ clusters. Thus, the Tb–Eu interaction is restricted to intra-cluster energy transfer, which can lead to highly effective energy transfer rates, as discussed in the literature (Wang et al., 2014; Calado et al., 2023; Gállico et al., 2023; Pelluau et al., 2023).

Using the calculated Tb–Eu pairwise energy transfer rates (see Supplementary Table S4 and the theoretical section in the ESI for further details) and the O_i coefficients (Supplementary Table S5; Eq. 4) obtained from doping simulations of Tb^{3+} and Eu^{3+} , the average (or effective) energy transfer rates from Tb-to-Eu can be estimated as (Trannoy et al., 2021)

$$\langle W \rangle = \sum_{i=1}^4 \langle W \rangle_i = (1-x)x \sum_{i=1}^4 O_i \cdot W_i \quad (5)$$

where $x = 0.25$ is the fraction of Eu^{3+} in the compound and W_i represents the pairwise Tb–Eu energy transfer for the i th distance (Supplementary Table S5).

Supplementary Figure S9 illustrates the temperature behavior of W_i and $\langle W \rangle$. Although the temperature increase provides high Eu^{3+} sensitization, the emission of Eu^{3+} undergoes quenching (Figures 6C,D), probably due to high-energy phonons that may couple with the $^5\text{D}_0$ level. Thus, although intra-cluster Tb^{3+} -to- Eu^{3+} energy transfer can provide high rates in contrast to non-clustering systems (Carneiro Neto et al., 2020; Trannoy et al., 2021), there are other factors in the chemical environment around Ln^{3+} that may act as a quenching channel, in this case, selectively affecting the Eu^{3+} ion, while the decrease in the intensity of the Tb^{3+} emissions may be related to the increase in the Tb^{3+} -to- Eu^{3+} rates with temperature.

To demonstrate the possibility of using compound 2 as a self-referenced luminescent thermometer, temperature dependence of the normalized integrated intensity area related with the two main transitions $\text{Tb}^{3+} \ ^5\text{D}_4 \rightarrow ^7\text{F}_5$ (in green) and $\text{Eu}^{3+} \ ^5\text{D}_0 \rightarrow ^7\text{F}_2$ (in red) was extracted for both emission spectra obtained upon excitations at 330 nm (antenna) and 484 nm (intra- $4f^8$). The temperature-dependent variation in the corresponding thermometric parameter ($I_{5\text{D}_4 \rightarrow 7\text{F}_5} / I_{5\text{D}_0 \rightarrow 7\text{F}_2}$, LIR) in the ranges 11–297 K (Figure 7A) and 298–378 K (Figure 7B) shows exponential correlations, which can be used for temperature measurements. The relative thermal sensitivity (S_r) is the main parameter, allowing the comparison of the performance among different types of thermometers (Bednarkiewicz et al., 2020). The S_r value represents the variation in the experimental thermometric parameter (LIR in the present case) per degree of temperature, which is expressed as

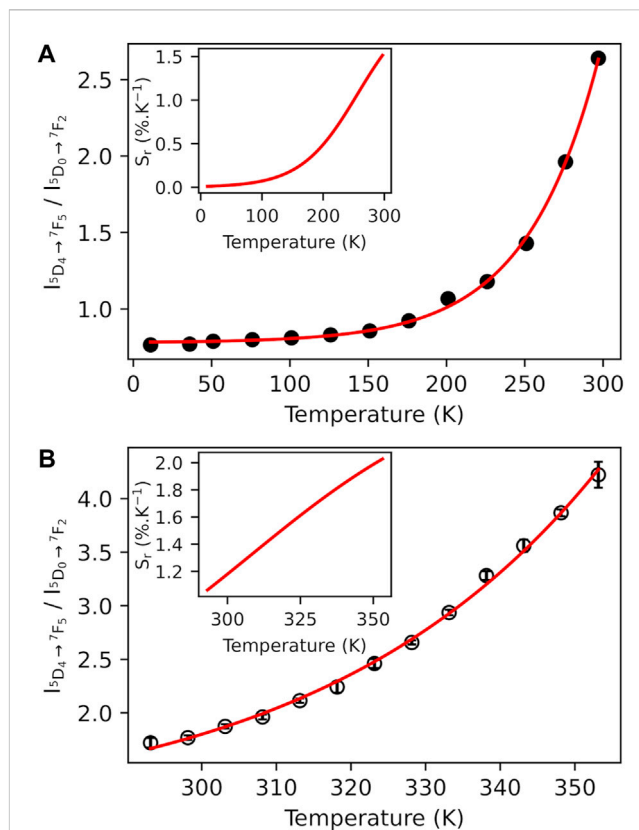


FIGURE 7 Temperature dependence of the normalized luminescence intensity ($I_{5\text{D}_4 \rightarrow 7\text{F}_5} / I_{5\text{D}_0 \rightarrow 7\text{F}_2}$) performed for the emission spectra of compound 2 under the excitation at 330 nm in the ranges 11–297 K (A) and 298–378 K (B) with several experimental cycles (circles) and the associated fit (red curve) with a single exponential function (full line) ($r^2 > 0.99$). Inset: S_r , temperature dependence.

$$S_r(T) = \frac{1}{\text{LIR}(T)} \left| \frac{\partial \text{LIR}(T)}{\partial T} \right| \quad (6)$$

The temperature dependences of S_r are shown in the insets of Figures 7A,B. The maximum S_r value is equal to $1.5\% \cdot \text{K}^{-1}$ at 297 K, for 11–297 K, and $2.0\% \cdot \text{K}^{-1}$ at 373 K, for 298–378 K. Both values are close to a frequently considered high relative thermal sensitivity ($\sim 1\% \cdot \text{K}^{-1}$) (Brites et al., 2019) and are close to the best S_r values reported for mixed $\text{Eu}^{3+}/\text{Tb}^{3+}$ compounds (Trannoy et al., 2021). Temperature uncertainty (or thermal resolution, δT) is the smallest temperature change that can be detected (Brites et al., 2016). This value is related to S_r as follows:

$$\delta T = \frac{1}{S_r(T)} \left| \frac{\delta \text{LIR}(T)}{\text{LIR}(T)} \right| \quad (7)$$

where $\delta \text{LIR}(T)$ is the standard deviation in the $\text{LIR}(T)$ obtained upon several temperature cycles. According to this, the minimal thermal resolution is 0.2 K. Note that the use of emission spectra upon excitation at 484 nm for thermometry is also possible. Supplementary Figures S10A, B, ESI show the corresponding temperature dependences of LIR and the maximal value of S_r of $1.3\% \cdot \text{K}^{-1}$ at 297 K. Therefore, the

temperature sensor **2** proposed here works reliably in the operating range 11–378 K.

The emission decay curves of compound **2** were monitored at room temperature upon excitation at 330 nm within the $^5D_4 \rightarrow ^7F_6$ (Tb^{3+}) and $^5D_0 \rightarrow ^7F_4$ (Eu^{3+}) transitions (Supplementary Figure S11, ESI). The curves are well-reproduced by double-exponential functions as the best fits to the experimental data ($r^2 > 0.99$), yielding lifetimes of 0.126 ± 0.002 and 0.668 ± 0.002 ms for the former and 0.110 ± 0.002 and 0.406 ± 0.002 ms for the latter transitions. The occurrence of two lifetimes is under investigation and will be addressed later.

4 Conclusion

In summary, here, we reported three new luminescent cage-like silsesquioxanes containing a tetranuclear Tb^{3+} , Tb^{3+}/Eu^{3+} , or Gd^{3+} core, where each Ln^{3+} ion is coordinated by an antenna acetylacetonate ligand. The crystal structures indicate that the introduction of chelating acetylacetonate changes the coordination environment of the Ln^{3+} ions conducting to seven-coordination geometry close to the one-capped trigonal prism.

Lanthanide-based silsesquioxanes **1** and **2** present solid-state characteristic Tb^{3+} and Tb^{3+}/Eu^{3+} -related emissions between 11 and 373 K sensitized by acetylacetonate antenna upon excitation in the UV region, while the direct excitation in the visible domain is also possible.

Theoretical calculations were conducted to elucidate the primary characteristics of the thermal behavior between the Stark levels of the 5D_4 level in compound **1**. The results demonstrated good agreement between experiment and theory, enabling the extraction of the main effect, which is the balance between multiphonon decays and absorptions between these two Stark levels as a function of temperature.

For compound **2**, where intra-cluster energy transfer can be highly efficient and even surpass the ligand-to- Ln^{3+} transfer, simulations were performed to obtain the average Tb^{3+} -to- Eu^{3+} energy transfer rates within the $\{Ln_4\}$ cluster structure. The analysis revealed that the average energy transfer increases with temperature, consistent with the low quenching observed for Tb^{3+} emissions. Conversely, the abrupt quenching of Eu^{3+} emissions with increasing temperature suggests a strong electron–phonon coupling for this ion.

Mixed Tb^{3+}/Eu^{3+} (Tb/Eu ration 3/1) compound **2** exhibits a tunable thermosensitive Tb^{3+} -to- Eu^{3+} energy transfer driven by Tb^{3+} and Eu^{3+} emissions. The corresponding temperature dependence allows the verification of the use of this compound for a ratiometric self-reference luminescent thermometer. It was realized by using a fluorescence intensity ratio between the two main components of the spectra ($Tb^{3+} \ ^5D_4 \rightarrow ^7F_5$ and $Eu^{3+} \ ^5D_0 \rightarrow ^7F_2$ transitions) in the range 11–373 K, demonstrating the maximum relative thermal sensitivity referred above 2.0 % K^{-1} at 373 K.

Data availability statement

The original contributions presented in the study are included in the article/Supplementary Material; further inquiries can be directed to the corresponding authors.

Author contributions

GF: data curation, investigation, methodology, supervision, validation, and writing–original draft. AK: data curation, formal analysis, investigation, methodology, and writing–original draft. SS: data curation, formal analysis, investigation, supervision, validation, and writing–original draft. VK: data curation, formal analysis, investigation, software, and writing–original draft. MH-R: data curation, formal analysis, investigation, and writing–original draft. ES: supervision, writing–original draft, and funding acquisition. TP: writing–original draft, data curation, formal analysis, and investigation. LC: conceptualization, funding acquisition, project administration, resources, supervision, validation, writing–original draft, and writing–review and editing. YG: conceptualization, funding acquisition, supervision, validation, writing–original draft, writing–review and editing, and investigation. AC: investigation, validation, writing–original draft, writing–review and editing, data curation, formal analysis, software, and visualization. AB: validation, writing–original draft, writing–review and editing, conceptualization, funding acquisition, methodology, and supervision. JL: conceptualization, methodology, supervision, validation, writing–original draft, writing–review and editing, funding acquisition, project administration, and visualization.

Funding

The author(s) declare that financial support was received for the research, authorship, and/or publication of this article. This work was financially supported by the Russian Science Foundation (project No. 22-13-00250, synthetic and luminescent studies), the University of Montpellier and CNRS, and the project PRC2287 Premium 2019–2021. Elemental analysis data were collected using the equipment of the Center for Molecular Composition Studies of INEOS RAS with support from the Ministry of Science and Higher Education of the Russian Federation. JL acknowledges the Vernadsky program of the Embassy of France in the Russian Federation (2019–2021). This project was developed within the scope of the national program ANR (Project Hotspot), France. MAHR acknowledges the Beatriz Galindo Fellowship (BG22/00061). This work was also developed within the scope of the projects CICECO, Aveiro Institute of Materials, UIDB/50011/2020, UIDP/50011/2020, and LA/P/0006/2020 financed by Portuguese funds through the FCT/MCTES (PIDDAC).

Acknowledgments

The authors acknowledge the Platform of Analysis and Characterization (PAC) of ICGM for providing magnetic and X-ray diffraction measurements.

Conflict of interest

The authors declare that the research was conducted in the absence of any commercial or financial relationships that could be construed as a potential conflict of interest.

The author(s) declared that they were an editorial board member of Frontiers, at the time of submission. This had no impact on the peer review process and the final decision.

Publisher's note

All claims expressed in this article are solely those of the authors and do not necessarily represent those of their affiliated organizations, or those of the publisher, the editors, and the

reviewers. Any product that may be evaluated in this article, or claim that may be made by its manufacturer, is not guaranteed or endorsed by the publisher.

Supplementary material

The Supplementary Material for this article can be found online at: <https://www.frontiersin.org/articles/10.3389/fchem.2024.1379587/full#supplementary-material>

References

- Alaoui, I. M. (1995). Nonparticipation of the ligand's first triplet state in intramolecular energy transfer in Eu^{3+} and Tb^{3+} ruthmann's purple complexes. *J. Phys. Chem.* 99 (35), 13280–13282. doi:10.1021/j100035a036
- Allison, S. W. (2019). A brief history of phosphor thermometry. *Meas. Sci. Technol.* 30 (7), 072001. doi:10.1088/1361-6501/ab1d02
- Annand, J., Aspinall, H. C., and Steiner, A. (1999). Novel heterometallic lanthanide silsesquioxane. *Inorg. Chem.* 38 (17), 3941–3943. doi:10.1021/ic990208p
- Annand, J., and Aspinall, H. C. (2000). Lanthanide silsesquioxanes: monomeric and functionalised complexes. *J. Chem. Soc. Dalton Trans.* 0 (12), 1867–1871. doi:10.1039/b000659i
- Aquino Le do, N., Barbosa, G. A., Ramos, J. de L., Giese S, O. K., Santana, F. S., Hughes, D. L., et al. (2021). Seven-coordinate Tb^{3+} complexes with 90% quantum yields: high-performance examples of combined singlet- and triplet-to- Tb^{3+} energy-transfer pathways. *Inorg. Chem.* 60 (2), 892–907. doi:10.1021/acs.inorgchem.0c03020
- Arnold, P. L., Blake, A. J., Hall, S. N., Ward, B. D., and Wilson, C. (2001). A functional model for lanthanide doped silicate materials: synthesis of an apically substituted samarium silsesquioxane complex. *J. Chem. Soc. Dalton Trans.* 0 (4), 488–491. doi:10.1039/b009123p
- Aulsebrook, M. L., Graham, B., Grace, M. R., and Tuck, K. L. (2018). Lanthanide complexes for luminescence-based sensing of low molecular weight analytes. *Coord. Chem. Rev.* 375, 191–220. doi:10.1016/j.ccr.2017.11.018
- Bednarkiewicz, A., Marciniak, L., Carlos, L. D., and Jaque, D. (2020). Standardizing luminescence nanothermometry for biomedical applications. *Nanoscale* 12 (27), 14405–14421. doi:10.1039/d0nr03568h
- Bernot, K., Daigebonne, C., Calvez, G., Suffren, Y., and Guillou, O. (2021). A journey in lanthanide coordination chemistry: from evaporable dimers to magnetic materials and luminescent devices. *Acc. Chem. Res.* 54 (2), 427–440. doi:10.1021/acs.accounts.0c00684
- Bettinelli, M., Carlos, L., and Liu, X. (2015). Lanthanide-doped upconversion nanoparticles. *Phys. Today* 68 (9), 38–44. doi:10.1063/pt.3.2913
- Bodman, S. E., and Butler, S. J. (2021). Advances in anion binding and sensing using luminescent lanthanide complexes. *Chem. Sci.* 12 (8), 2716–2734. doi:10.1039/d0sc05419d
- Brites, C. D. S., Balabhadra, S., and Carlos, L. D. (2019). Lanthanide-based thermometers: at the cutting-edge of luminescence thermometry. *Adv. Opt. Mater.* 7 (5), 1801239. doi:10.1002/adom.201801239
- Brites, C. D. S., Lima, P. P., Silva, N. J. O., Millán, A., Amaral, V. S., Palacio, F., et al. (2010). A luminescent molecular thermometer for long-term absolute temperature measurements at the nanoscale. *Adv. Mater.* 22 (40), 4499–4504. doi:10.1002/adma.201001780
- Brites, C. D. S., Lima, P. P., Silva, N. J. O., Millán, A., Amaral, V. S., Palacio, F., et al. (2012). Thermometry at the nanoscale. *Nanoscale* 4 (16), 4799–4829. doi:10.1039/c2nr30663h
- Brites, C. D. S., Marin, R., Suta, M., Carneiro Neto, A. N., Ximenes, E., Jaque, D., et al. (2023). Spotlight on luminescence thermometry: basics, challenges, and cutting-edge applications. *Adv. Mater.* 35, 2302749. doi:10.1002/adma.202302749
- Brites, C. D. S., Millán, A., and Carlos, L. D. (2016). "Chapter 281 - lanthanides in luminescent thermometry," in *Handbook on the physics and chemistry of rare earths*. Editors B. Jean-Claude and K. P. Vitalij (Elsevier), 339–427. doi:10.1016/bs.hcre.2016.03.005
- Bünzli, J. C. G. (2010). Lanthanide luminescence for biomedical analyses and imaging. *Chem. Rev.* 110 (5), 2729–2755. doi:10.1021/cr900362e
- Bünzli, J. C. G. (2015). On the design of highly luminescent lanthanide complexes. *Coord. Chem. Rev.* 293–294, 19–47. doi:10.1016/j.ccr.2014.10.013
- Bünzli, J. C. G. (2019). Lanthanide photonics: shaping the nanoworld. *TRECHEM.* 1 (8), 751–762. doi:10.1016/j.trechm.2019.05.012
- Bünzli, J. C. G., and Eliseeva, S. V. (2013). Intriguing aspects of lanthanide luminescence. *Chem. Sci.* 4 (5), 1939–1949. doi:10.1039/c3sc22126a
- Calado, C. M. S., Gálico, D. A., and Murugesu, M. (2023). Intra-cluster energy transfer editing in a dual-emitting system to tap into lifetime thermometry. *Chem. Commun.* 59 (92), 13715–13718. doi:10.1039/d3cc03658h
- Carnall, W. T., Crosswhite, H., and Crosswhite, H. M. (1978). "Energy level structure and transition probabilities in the spectra of the trivalent lanthanides in LaF_3 ." Report No.: ANL-78-XX-95. Available at: <https://www.osti.gov/biblio/6417825> (Accessed December 12, 2023).
- Carneiro Neto, A. N., Kasprzycka, E., Souza, A. S., Gawryszewska, P., Suta, M., Carlos, L. D., et al. (2022). On the long decay time of the $^7\text{F}_5$ level of Tb^{3+} . *J. Luminescence* 248, 118933. doi:10.1016/j.jlumin.2022.118933
- Carneiro Neto, A. N., Moura, R. T., Jr., Shyichuk, A., Paterlini, V., Piccinelli, F., Bettinelli, M., et al. (2020). Theoretical and experimental investigation of the $\text{Tb}^{3+} \rightarrow \text{Eu}^{3+}$ energy transfer mechanisms in cubic $\text{A}_3\text{Tb}_{0.90}\text{Eu}_{0.10}(\text{PO}_4)_3$ (A = Sr, Ba) materials. *J. Phys. Chem. C* 124 (18), 10105–10116. doi:10.1021/acs.jpcc.0c00759
- Carneiro Neto, A. N., Teotonio, E. E. S., de Sá, G. F., Brito, H. F., Legendziewicz, J., Carlos, L. D., et al. (2019). "Chapter 310 - modeling intramolecular energy transfer in lanthanide chelates: a critical review and recent advances," in *Handbook on the physics and chemistry of rare earths*. Editors J. C. G. Bünzli and V. K. Pecharsky (Elsevier), 55–162.
- Choi, S. H., Duzik, A. J., Kim, H. J., Park, Y., Kim, J., Ko, H. U., et al. (2017). Perspective and potential of smart optical materials. *Smart Mater. Struct.* a0126 (9), 093001. doi:10.1088/1361-665x/aa7c32
- Costa, I. F., Blois, L., Paolini, T. B., Assunção, I. P., Teotonio, E. E. S., Felinto, MCFC, et al. (2024). Luminescence properties of lanthanide tetrakis complexes as molecular light emitters. *Coord. Chem. Rev.* 502, 215590. doi:10.1016/j.ccr.2023.215590
- Cui, Y., Xu, H., Yue, Y., Guo, Z., Yu, J., Chen, Z., et al. (2012). A luminescent mixed-lanthanide metal-organic framework thermometer. *J. Am. Chem. Soc.* 134 (9), 3979–3982. doi:10.1021/ja2108036
- Davies, G. L., O'Brien, J., and Gun'ko, Y. K. (2017). Rare earth doped silica nanoparticles via thermolysis of a single source metallasilsesquioxane precursor. *Sci. Rep.* 7 (1), 45862. doi:10.1038/srep45862
- de Sá, G. F., Malta, O. L., de Mello Donegá, C., Simas, A. M., Longo, R. L., Santa-Cruz, P. A., et al. (2000). Spectroscopic properties and design of highly luminescent lanthanide coordination complexes. *Coord. Chem. Rev.* 196 (1), 165–195. doi:10.1016/s0010-8545(99)00054-5
- Dramićanin, M. D. (2020). Trends in luminescence thermometry. *J. Appl. Phys.* 128 (4), 040902. doi:10.1063/5.0014825
- Eliseeva, S. V., and Bünzli, J. C. G. (2009). Lanthanide luminescence for functional materials and bio-sciences. *Chem. Soc. Rev.* 39 (1), 189–227. doi:10.1039/b905604c
- Félix, G., Kulakova, A., Sene, S., Charlot, C., Bilyachenko, A. N., Korlyukov, A. A., et al. (2023a). Tetranuclear lanthanide-based silsesquioxanes: towards a combination of germesquioxanes: luminescence and temperature sensing. *Organometallics* 42 (18), 2613–2622. doi:10.1021/acs.organomet.3c00009
- Félix, G., Sene, S., Kulakova, A., Bilyachenko, A. N., Khrustalev V, N., Shubina E, S., et al. (2023b). Tetranuclear lanthanide-based silsesquioxanes: towards a combination of a slow relaxation of the magnetization and a luminescent thermometry. *RSC Adv.* 13 (37), 26302–26312. doi:10.1039/d3ra04901a
- Fernandes, M., Freitas, V., Pereira, S., Leones, R., Silva, M. M., Carlos, L. D., et al. (2018). Luminescent electrochromic devices for smart windows of energy-efficient buildings. *Energies* 11 (12), 3513. doi:10.3390/en11123513

- Ferreira da Rosa, P. P., Kitagawa, Y., and Hasegawa, Y. (2020). Luminescent lanthanide complex with seven-coordination geometry. *Coord. Chem. Rev.* 406, 213153. doi:10.1016/j.ccr.2019.213153
- Gállico, D. A., Calado, C. M. S., and Murugesu, M. (2023). Lanthanide molecular cluster-aggregates as the next generation of optical materials. *Chem. Sci.* 14 (22), 5827–5841. doi:10.1039/d3sc01088k
- Gregório, T., Leão, J. D. M., Barbosa, G. A., Ramos, J. de L., Kumar Giese, O. S., Briganti, M., et al. (2019). Promoting a significant increase in the photoluminescence quantum yield of terbium(III) complexes by ligand modification. *Inorg. Chem.* 58 (18), 12099–12111. doi:10.1021/acs.inorgchem.9b01397
- Hairer, E., and Wanner, G. (2015). “Radau methods,” in *Encyclopedia of applied and computational mathematics*. Editor B. Engquist (Berlin, Heidelberg: Springer), 1213–1216. doi:10.1007/978-3-540-70529-1_139
- Herrmann, W. A., Anwender, R., Dufaud, V., and Scherer, W. (1994). Molecular siloxane complexes of rare earth metals—model systems for silicate-supported catalysts? *Angewandte Chemie Int. Ed. Engl.* 33 (12), 1285–1286. doi:10.1002/anie.199412851
- Jaque, D., and Vetrone, F. (2012). Luminescence nanothermometry. *Nanoscale* 4 (15), 4301–4326. doi:10.1039/c2nr30764b
- Kaczmarek, A. M., Deun, R. V., and Voort, P. V. D. (2019). Nanothermometers based on lanthanide incorporated periodic mesoporous organosilica. *J. Mater. Chem. C* 7 (14), 4222–4229. doi:10.1039/c8tc06353b
- Kasprzycka, E., Carneiro Neto, A. N., Trush, V. A., Jerzykiewicz, L., Amirkhanov, V. M., Malta, O. L., et al. (2020). How minor structural changes generate major consequences in photophysical properties of RE coordination compounds; resonance energy, LMCT state. *J. Rare Earths* 38 (5), 552–563. doi:10.1016/j.jre.2020.02.001
- Kasprzycka, E., Trush, V. A., Amirkhanov, V. M., Jerzykiewicz, L., Malta, O. L., Legendziewicz, J., et al. (2017). Contribution of energy transfer from the singlet state to the sensitization of Eu^{3+} and Tb^{3+} luminescence by sulfonamidophosphates. *Chem. – A Eur. J.* 23 (6), 1318–1330. doi:10.1002/chem.201603767
- Kulakova, A. N., Bilyachenko, A. N., Levitsky, M. M., Khrustalev, V. N., Shubina, E. S., Félix, G., et al. (2020). New luminescent tetranuclear lanthanide-based silsesquioxane cage-like architectures. *Chem. – A Eur. J.* 26 (70), 16567–16568. doi:10.1002/chem.202004207
- Kulakova, A. N., Nigoghossian, K., Félix, G., Khrustalev, V. N., Shubina, E. S., Long, J., et al. (2021). New magnetic and luminescent Dy(III) and Dy(III)/Y(III) based tetranuclear silsesquioxane cages. *Eur. J. Inorg. Chem.* 2021 (27), 2696–2701. doi:10.1002/ejic.202100308
- Laird, M., Totée, C., Gaveau, P., Silly, G., Lee, A. V. D., Carcel, C., et al. (2021). Functionalised polyhedral oligomeric silsesquioxane with encapsulated fluoride – first observation of fluxional Si...F interactions in POSS. *Dalton Trans.* 50 (1), 81–89. doi:10.1039/d0dt03057k
- Liu, J. Q., Luo, Z. D., Pan, Y., Kumar Singh, A., Trivedi, M., and Kumar, A. (2020). Recent developments in luminescent coordination polymers: designing strategies, sensing application and theoretical evidences. *Coord. Chem. Rev.* 406, 213145. doi:10.1016/j.ccr.2019.213145
- Long, J., Habib, F., Lin, P. H., Korobkov, I., Enright, G., Ungur, L., et al. (2011). Single-molecule magnet behavior for an antiferromagnetically superexchange-coupled dinuclear dysprosium(III) complex. *J. Am. Chem. Soc.* 133 (14), 5319–5328. doi:10.1021/ja109706y
- Lorenz, V., Fischer, A., and Edelman, F. T. (2002). Silsesquioxane chemistry: Part 10. Silsesquioxane silanolate complexes of samarium and scandium. *J. Organomet. Chem.* 647 (1), 245–249. doi:10.1016/s0022-328x(01)01434-6
- Lorenz, V., Gießmann, S., Gun'ko, Y. K., Fischer, A. K., Gilje, J. W., and Edelman, F. T. (2004). Fully metalated silsesquioxanes: building blocks for the construction of catalytic models. *Angew. Chem. Int. Ed.* 43 (35), 4603–4606. doi:10.1002/anie.200454094
- Lyubov, D. M., Neto, A. N. C., Fayoumi, A., Lyssenko, K. A., Korshunov, V. M., Taydakov, I. V., et al. (2022). Employing three-blade propeller lanthanide complexes as molecular luminescent thermometers: study of temperature sensing through a concerted experimental/theory approach. *J. Mater. Chem. C* 10 (18), 7176–7188. doi:10.1039/d2tc01289h
- Malkin, B. Z. (2005). “Ion-phonon interactions,” in *Spectroscopic properties of rare earths in optical materials*. Editors R. Hull, J. Parisi, R. M. Osgood, H. Warlimont, G. Liu, and B. Jacquier (Berlin, Heidelberg: Springer), 130–190. doi:10.1007/3-540-28209-2_3
- Malta, O. L. (2008). Mechanisms of non-radiative energy transfer involving lanthanide ions revisited. *J. Non-Crystalline Solids* 354 (42), 4770–4776. doi:10.1016/j.jnoncrysol.2008.04.023
- Manzur, J., Fuentealba, P., Gil, Y., Pérez-Obando, J., Morales Alfaro, J., Vega Carvallo, A. I., et al. (2023). Tuning the emission of homometallic Dy^{III} , Tb^{III} , and Eu^{III} 1-D coordination polymers with 2,6-di(1H-1,2,4-triazole-1-yl-methyl)-4-R-phenoxy ligands: sensitization through the singlet state. *Inorg. Chem.* 62 (47), 19195–19207. doi:10.1021/acs.inorgchem.3c02201
- Marchesi, S., Carniato, F., and Boccaleri, E. (2014). Synthesis and characterisation of a novel europium(III)-containing heptaisobutyl-POSS. *New J. Chem.* 38 (6), 2480–2485. doi:10.1039/c4nj00157e
- Miyakawa, T., and Dexter, D. L. (1970). Phonon sidebands, multiphonon relaxation of excited states, and phonon-assisted energy transfer between ions in solids. *Phys. Rev. B* 1 (7), 2961–2969. doi:10.1103/physrevb.1.2961
- Miyata, K., Hasegawa, Y., Kuramochi, Y., Nakagawa, T., Yokoo, T., and Kawai, T. (2009). Characteristic structures and photophysical properties of nine-coordinate europium(III) complexes with tandem-connected tridentate phosphine oxide ligands. *Eur. J. Inorg. Chem.* 2009 (32), 4777–4785. doi:10.1002/ejic.200900598
- Miyata, K., Nakanishi, T., Fushimi, K., and Hasegawa, Y. (2012). Solvent-dependent luminescence of eight-coordinated Eu(III) complexes with bidentate phosphine oxide. *J. Photochem. Photobiol. A Chem.* 235, 35–39. doi:10.1016/j.jphotochem.2012.03.005
- Monteiro, JHSK (2020). Recent advances in luminescence imaging of biological systems using lanthanide(III) luminescent complexes. *Molecules* 25 (9), 2089. doi:10.3390/molecules25092089
- Moos, H. W. (1970). Spectroscopic relaxation processes of rare earth ions in crystals. *J. Luminescence* 1–2, 106–121. doi:10.1016/0022-2313(70)90027-x
- Moura Jr., R. T., Carneiro Neto, A. N., Aguiar, E. C., Santos-Jr., C. V., de Lima, E. M., Faustino, W. M., et al. (2021b). (INVITED) JOYSpectra: a web platform for luminescence of lanthanides. *Opt. Mater. X* 11, 100080. doi:10.1016/j.omx.2021.100080
- Moura Jr., R. T., Oliveira, J. A., Santos, I. A., de Lima, E. M., Carlos, L. D., Aguiar, E. C., et al. (2021a). Theoretical evidence of the singlet predominance in the intramolecular energy transfer in Ruhemann's purple Tb(III) complexes. *Adv. Theory Simulations* 4 (3), 2000304. doi:10.1002/adts.202000304
- Nigoghossian, K., Kulakova, A. N., Félix, G., Khrustalev, V. N., Shubina, E. S., Long, J., et al. (2021). Temperature sensing in $\text{Tb}^{3+}/\text{Eu}^{3+}$ -based tetranuclear silsesquioxane cages with tunable emission. *RSC Adv.* 11 (55), 34735–34741. doi:10.1039/d1ra06755a
- Ning, Y., Zhu, M., and Zhang, J. L. (2019). Near-infrared (NIR) lanthanide molecular probes for bioimaging and biosensing. *Coord. Chem. Rev.* 399, 213028. doi:10.1016/j.ccr.2019.213028
- Pelluau, T., Sene, S., Ali, L. M. A., Félix, G., Neto, A. N. C., Carlos, L. D., et al. (2023). Hybrid multifunctionalized mesostructured stellate silica nanoparticles loaded with β -diketonate $\text{Tb}^{3+}/\text{Eu}^{3+}$ complexes as efficient ratiometric emissive thermometers working in water. *Nanoscale* 15, 14409–14422. doi:10.1039/d3nr01851b
- Prigay, N., Channungkalakul, S., Ervithayasuporn, V., Yodsins, N., Jungsuttiwong, S., Takeda, N., et al. (2019). Lithium-templated formation of polyhedral oligomeric silsesquioxanes (POSS). *Inorg. Chem.* 58 (22), 15110–15117. doi:10.1021/acs.inorgchem.9b01836
- Reisfeld, R., and Jørgensen, C. K. (1977). “Lasers and excited states of rare earths,” in *Inorganic chemistry concepts*. Editors M. Becke, M. F. Lippert, J. L. Margrave, R. W. Parry, C. K. Jørgensen, S. J. Lippard, et al. (Berlin, Heidelberg: Springer). doi:10.1007/978-3-642-66696-4
- Riseberg, L. A., and Weber, M. J., III (1977). “Relaxation phenomena in rare-earth luminescence,” in *Progress in optics*. Editor E. Wolf (Elsevier).
- Rocha, J., Brites, C. D. S., and Carlos, L. D. (2016). Lanthanide organic framework luminescent thermometers. *Chem. – A Eur. J.* 22 (42), 14782–14795. doi:10.1002/chem.201600860
- Rodríguez-Cortinas, R., Avecilla, F., Platas-Iglesias, C., Imbert, D., Bünzli, J. C. G., de Blas, A., et al. (2002). Structural and photophysical properties of heterobimetallic 4f-Zn iminophenolate cryptates. *Inorg. Chem.* 41 (21), 5336–5349. doi:10.1021/ic025587s
- Seethalakshmi, S., Ramya, A. R., Reddy, M. L. P., and Varughese, S. (2017). Lanthanide complex-derived white-light emitting solids: a survey on design strategies. *J. Photochem. Photobiol. C Photochem. Rev.* 33, 109–131. doi:10.1016/j.jphotochemrev.2017.11.001
- Shchegolikina, O. I., Pozdniakova, Y. A., Lindeman, S. V., Zhdanov, A. A., Psaro, R., Ugo, R., et al. (1996). Cyclosiloxane sandwich complexes of a lanthanide metal: $\text{Na}_6\{[(\text{C}_6\text{H}_5\text{SiO}_2)_8]_2\text{Nd}_4(\mu_4\text{-O})\}$. *J. Organomet. Chem.* 514 (1), 29–35. doi:10.1016/0022-328x(95)06005-h
- Sheng, K., Si, W. D., Wang, R., Wang, W. Z., Dou, J., Gao, Z. Y., et al. (2022a). Keggin-type tridecanuclear europium-oxo nanocluster protected by silsesquioxanes. *Chem. Mater.* 34 (9), 4186–4194. doi:10.1021/acs.chemmater.2c00627
- Sheng, K., Wang, R., Bilyachenko, A., Khrustalev, V., Jagodić, M., Jagličić, Z., et al. (2022b). Tridecanuclear Gd(III)-silsesquioxane: synthesis, structure, and magnetic property. *Chem. Phys. Mater.* 1 (4), 247–251. doi:10.1016/j.chphma.2022.04.008
- Suta, M., and Meijerink, A. (2020). A theoretical framework for ratiometric single ion luminescent thermometers—thermodynamic and kinetic guidelines for

optimized performance. *Adv. Theory Simulations* 3 (12), 2000176. doi:10.1002/adts.202000176

Suzuki, M., Tseeb, V., Oyama, K., and Ishiwata, S. (2007). Microscopic detection of thermogenesis in a single HeLa cell. *Biophysical J.* 92 (6), L46–L48. doi:10.1529/biophysj.106.098673

Trannoy, V., Carneiro Neto, A. N., Brites, C. D. S., Carlos, L. D., and Serier-Brault, H. (2021). Engineering of mixed $\text{Eu}^{3+}/\text{Tb}^{3+}$ metal-organic frameworks luminescent thermometers with tunable sensitivity. *Adv. Opt. Mater.* 9 (6), 2001938. doi:10.1002/adom.202001938

Wang, J., Deng, R., MacDonald, M. A., Chen, B., Yuan, J., Wang, F., et al. (2014). Enhancing multiphoton upconversion through energy clustering at sublattice level. *Nat. Mater.* 13 (2), 157–162. doi:10.1038/nmat3804

Wu, G., Chen, Y., Xu, D. J., Liu, J. C., Sun, W., and Shen, Z. (2009). Synthesis and molecular structure of a tetrameric neodymium-silsesquioxane cage complex: $\{[(\text{i-C}_4\text{H}_9)_7(\text{Si}_7\text{O}_{12})\text{Nd}]_4\text{NaCl}\}$. *J. Organomet. Chem.* 694 (9), 1571–1574. doi:10.1016/j.jorganchem.2009.01.042

Yanagisawa, K., Nakanishi, T., Kitagawa, Y., Seki, T., Akama, T., Kobayashi, M., et al. (2015). Seven-coordinate luminophores: brilliant luminescence of lanthanide complexes with C_{3v} geometrical structures. *Eur. J. Inorg. Chem.* 2015 (28), 4769–4774. doi:10.1002/ejic.201500820

Yang, C., Fu, L. M., Wang, Y., Zhang, J. P., Wong, W. T., Ai, X. C., et al. (2004). A highly luminescent europium complex showing visible-light-sensitized red emission: direct observation of the singlet pathway. *Angew. Chem. Int. Ed.* 43 (38), 5010–5013. doi:10.1002/anie.200454141



OPEN ACCESS

EDITED BY

Marko Jukic,
University of Maribor, Slovenia

REVIEWED BY

Piia Bartos,
University of Eastern Finland, Finland
Bekim Bajrami,
Biogen Idec, United States
Xiang Ma,
Taiyuan Institute of Technology, China

*CORRESPONDENCE

Michael Kassiou,
✉ michael.kassiou@sydney.edu.au

RECEIVED 31 January 2024

ACCEPTED 12 March 2024

PUBLISHED 18 April 2024

CITATION

Chan BWGL, Lynch NB, Tran W, Joyce JM,
Savage GP, Meutermans W, Montgomery AP
and Kassiou M (2024), Fragment-based drug
discovery for disorders of the central nervous
system: designing better drugs piece by piece.
Front. Chem. 12:1379518.
doi: 10.3389/fchem.2024.1379518

COPYRIGHT

© 2024 Chan, Lynch, Tran, Joyce, Savage,
Meutermans, Montgomery and Kassiou. This is
an open-access article distributed under the
terms of the [Creative Commons Attribution
License \(CC BY\)](#). The use, distribution or
reproduction in other forums is permitted,
provided the original author(s) and the
copyright owner(s) are credited and that the
original publication in this journal is cited, in
accordance with accepted academic practice.
No use, distribution or reproduction is
permitted which does not comply with these
terms.

Fragment-based drug discovery for disorders of the central nervous system: designing better drugs piece by piece

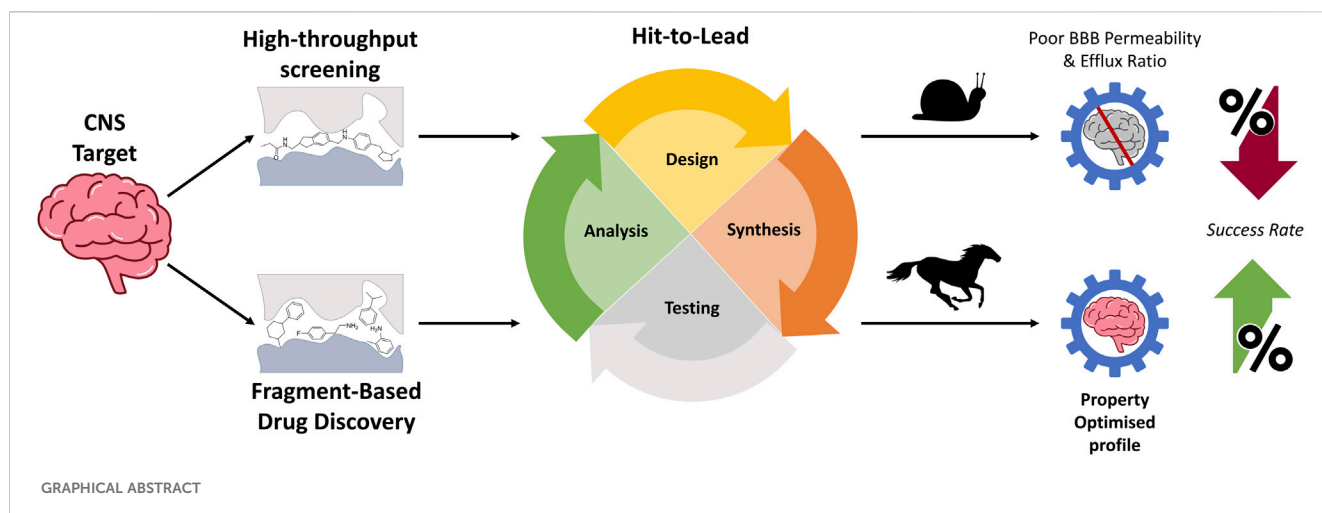
Bill W. G. L. Chan¹, Nicholas B. Lynch¹, Wendy Tran¹,
Jack M. Joyce¹, G. Paul Savage², Wim Meutermans³,
Andrew P. Montgomery¹ and Michael Kassiou^{1*}

¹School of Chemistry, The University of Sydney, Sydney, NSW, Australia, ²CSIRO Manufacturing, Clayton South, VIC, Australia, ³Vast Bioscience, Brisbane, QLD, Australia

Fragment-based drug discovery (FBDD) has emerged as a powerful strategy to confront the challenges faced by conventional drug development approaches, particularly in the context of central nervous system (CNS) disorders. FBDD involves the screening of libraries that comprise thousands of small molecular fragments, each no greater than 300 Da in size. Unlike the generally larger molecules from high-throughput screening that limit customisation, fragments offer a more strategic starting point. These fragments are inherently compact, providing a strong foundation with good binding affinity for the development of drug candidates. The minimal elaboration required to transition the hit into a drug-like molecule is not only accelerated, but also it allows for precise modifications to enhance both their activity and pharmacokinetic properties. This shift towards a fragment-centric approach has seen commercial success and holds considerable promise in the continued streamlining of the drug discovery and development process. In this review, we highlight how FBDD can be integrated into the CNS drug discovery process to enhance the exploration of a target. Furthermore, we provide recent examples where FBDD has been an integral component in CNS drug discovery programs, enabling the improvement of pharmacokinetic properties that have previously proven challenging. The FBDD optimisation process provides a systematic approach to explore this vast chemical space, facilitating the discovery and design of compounds piece by piece that are capable of modulating crucial CNS targets.

KEYWORDS

fragment-based drug discovery, central nervous system, Alzheimer's disease, Parkinson's disease, schizophrenia, Huntington's disease, neuroinflammation, glioblastoma



1 Introduction

1.1 CNS drug discovery

Drug discovery is an extremely expensive process, both in terms of the time and money invested. From target discovery to regulatory approval, an FDA-approved drug will take an average of 12–15 years (Brown et al., 2022) and up to US\$ 3.2 billion (DiMasi et al., 2016). Whilst drug discovery is a high-risk venture with no guarantee of producing a return on any resources invested, it is still a necessary investment for improving our quality of life. Drug discovery is increasingly more important, given the ageing global population and an increasing prevalence of neurodegenerative and neuropsychiatric diseases as well as brain cancers. There are currently no cures, and the limited therapeutics available are largely ineffective; new treatments are, therefore, urgently needed. Drug developments that target disorders associated with the central nervous system (CNS) are considerably more difficult than diseases of the periphery. The CNS is protected by the blood–brain barrier (BBB), which dictates the necessary pharmacokinetic (PK) properties a drug must possess in order to enter the brain. As most CNS drug leads fail to pass through the BBB, identifying a high-quality hit with a favourable PK profile may potentially save both time and resources, making it one of the most vital steps in a drug design process. Traditional hit identification strategies have varied but ultimately see limited success in tackling issues faced in CNS drug development (Gribkoff and Kaczmarek, 2017). Therefore, exploring alternative approaches to drug development should be considered to improve the development of effective therapeutics for these diseases.

1.2 Challenges with conventional hit discovery and lead optimisation

Many drug discovery campaigns aim to develop orally administered drugs as they are non-invasive, convenient, and generally meet high patient acceptance (Alqahtani et al., 2021). A standard drug development program begins with the identification of “hits”. A hit molecule is a compound that has the desired activity

at the target of interest; a good hit is considered one that generally obeys Lipinski’s Rule of Five (Ro5) for oral bioavailability (Hughes et al., 2011). The Ro5 advises that a molecule should have no more than five hydrogen bond donors (HBD), no more than ten hydrogen bond acceptors (HBA), a molecular weight (MW) less than 500 Daltons, and a LogP less than 5 (Lipinski et al., 2001). Although this “rule” has successfully provided guidance to many drug discovery campaigns, strictly following these could limit the design of small-molecule drugs for easily druggable targets (Hartung et al., 2023). This is emphasised by the oral drugs that had been approved between 2018 and 2022, where many of these molecules possessed high MW and number of HBA. Furthermore, the recent discovery of PROTACs also highlights that MW does not always directly correlate with oral delivery as these molecules possess MW as high as 1,000 Da and are orally bioavailable.

The most common strategy for identifying these hit molecules is through high-throughput screening (HTS), which is often used by big pharmaceutical companies for small-molecule drug development (Blay et al., 2020). A standard HTS campaign will screen a compound library (comprising hundreds of thousands of molecules) in a series of biochemical assays to identify hits (Ver Donck et al., 2020). Large libraries that contain a broad variety of structural types are necessary to explore diverse chemical space. Despite the extensive number of molecules screened, the hit rates are generally low, and the few compounds that are identified can possess suboptimal physiochemical properties. Even with a judicious selection of compound libraries that are Ro5-compliant, optimisation of the resulting hit can still be difficult. One of the major challenges when commencing a drug discovery campaign based on a hit molecule derived from conventional screening methods is that they are often complex and possess a high molecular weight (MW) (Volochnyuk et al., 2019). A standard HTS library can comprise compounds with average MWs of 400 Da. Optimising hits often involves introducing desirable functionalities which generally only adds further to the already large MW (Bienstock, 2011). Consequently, this increase in MW may compromise the oral bioavailability of the hit, as molecules larger than 400 Da typically do not undergo passive diffusion through the BBB and are also more susceptible to efflux processes (Mikitsh and Chacko, 2014; Pardridge, 2020).

TABLE 1 Various parameters for an ideal fragment.

Rule-of-three (Ro3)	Parameters
Original	MW \leq 300 Da; cLogP \leq 3; HBD \leq 3 HBA \leq 3
Updated	150 \leq MW \leq 230 Da; 9–16 non hydrogen atoms; cLogP \leq 2

Furthermore, the high complexity of the initial hit poses synthetic challenges and can make further elaboration difficult. As such, HTS hits may not offer the most ideal starting point for lead optimisation. These challenges drive the difficulty and cost of developing CNS drugs, culminating in the high failure rates of CNS drug discovery programs (Gribkoff and Kaczmarek, 2017). Therefore, incorporating alternative methods of identifying lead compounds that can accommodate the unique design challenges inherent in CNS drug discovery may ameliorate the high failure rates of CNS campaigns.

1.3 Fragment-based drug design

Fragment-based drug discovery (FBDD) is a method that utilises smaller, less complex, and non-specific structures known as “fragments.” These molecules can be thought of as building blocks to obtain a more customised, target-specific molecule. Fragments possess a specified degree of complexity as a proxy for the number of ligand–target binding interactions and are generally structurally guided by the “rule-of-three” (Ro3) (Table 1). (Congreve et al., 2003) Fragments obeying these criteria efficiently probe the structural morphology of a biological target, allowing key binding interactions to be deduced, which are in turn utilised to design a lead. More recent guidelines have fine-tuned the optimum molecular parameters which describe ideal fragments (Table 1). (Keserü et al., 2016) As a consequence of the lower complexity of the fragment-like molecules, their binding affinities are typically in the millimolar range, thereby necessitating biophysical screening techniques with a higher sensitivity than traditional methods. A chemically diverse fragment library of a few thousand, lower-complexity fragments can probe chemical space just as efficiently, if not more, than traditional large screening libraries whilst providing the same chemical space coverage. Furthermore, the smaller size of these FBDD-sourced leads will generally lead to higher ligand efficiency structures (which is a measure of how important each atom in a molecule is in establishing a strong binding interaction with the target). This may provide a means of resolving the issues of underperforming parameters during lead optimisation (Abad-Zapatero and Metz, 2005).

1.3.1 Fragment-based screening methods

FBDD programs utilise several biophysical methods for hit validation as a part of their screening process. Commonly, these techniques are used in tandem to verify the validity of a fragment hit. These screening methods have been reviewed in detail (Kirsch et al., 2019; Li, 2020; Togle et al., 2022); this section therefore serves as a

brief summary of techniques that have been prominent in recent CNS drug discovery programs highlighted in this review.

Nuclear magnetic resonance (NMR) is an essential technique in FBDD to identify target binders, especially with weak interactions between the ligand and target, in a non-destructive manner. NMR screening can be categorised into two separate techniques: target-based and ligand-based screening. Target-based NMR utilises an isotopically labelled protein in two-dimensional (2D) experiments to identify binding mechanisms of the ligand with the protein (Singh et al., 2018). It is capable of determining if a ligand binds, and, if it does, where it binds by observing the chemical shifts experienced by the protein. This does, however, require high concentrations ($>50\ \mu\text{M}$) of isotopically labelled proteins to produce examinable spectra (Stark and Powers, 2011). Comparatively, ligand-based methods rely on the change in NMR parameters between the proteins bound and ligand-free state in one-dimensional (1D) data (Di Carluccio et al., 2021). This technique does not observe changes in chemical shift in the protein but in the ligands instead; isotopic labelling of the protein is thus not required. Therefore, ligand-based NMR is ideal for proteins that can be difficult to express as it allows for the protein's concentration to be as low as $10\ \mu\text{M}$ (Stark and Powers, 2011). Although this method can determine ligand binding, it is unable to deduce specific binding sites of the ligand. Furthermore, it has a higher chance of producing false negatives for medium-to high-binding affinity ligands with slow binding kinetics (Di Carluccio et al., 2021).

X-ray crystallography is a powerful tool that provides high-resolution structural information about the binding modality of the fragment to the protein. This binding modality can be determined regardless of the binding affinity of the fragment or the size of the protein (Hartshorn et al., 2005). This method is generally utilised in tandem with others as it does not provide a quantitative value for comparison, is limited by its low-medium throughput due to the time and effort in solving ligand-binding, and heavily relies on the solubility of the fragment and protein. Furthermore, this method is also limited to crystallisable proteins, which can make it challenging for targets such as membrane-bound proteins. Alternatively, cryogenic electron microscopy (cryo-EM) has become an increasingly popular technique for reconstructing the 3D structure of a molecule with the protein as protein crystals are not necessary (Callaway, 2020). However, for cases where experimental 3D structures of the protein are not available, predicted protein structures, using programs such as AlphaFold, can be generated for virtual screening purposes (Shi et al., 2023).

Surface plasmon resonance (SPR) is both a rapid and cost-effective method, utilising a high-throughput strategy to identify hits by measuring the kinetics of protein–ligand interactions (Navratilova and Hopkins, 2010). This screening method can be more advantageous than other current biophysical screening techniques, particularly due to its 10- to 100-fold lower protein consumption. Like ligand-based NMR, SPR can only identify whether a ligand will bind; it cannot verify the binding location. Furthermore, as fragments are typically tested in cocktails, SPR is unable to discriminate between structures that bind and those that do not. As such, a subsequent study is required with the individual fragments from cocktail mixtures to identify hit fragments (Farid E. Ahmed et al., 2010).

There are also a variety of auxiliary techniques that are used in FBDD campaigns. Thermal shift assays (TSA) are commonly used to measure the thermal stability of a purified recombinant protein or an isolated protein domain by measuring the change in the protein's melting temperature when bound with a molecule (Jafari et al., 2014). Alternatively, cellular TSA (CETSA) can be performed if the whole cell or the cell lysates are available. Mass spectrometry (MS) is a rapid, autonomous, and highly sensitive method for identifying the binding of a fragment to a protein. The mass of the ligand-protein adduct can be observed to indicate successful binding (Dueñas et al., 2022). More recently, high-throughput affinity selection MS (HT-ASMS) introduced a cost-effective evaluation of large libraries by separating non-bound ligands from the protein through affinity enrichment or size exclusion chromatography. The bound ligands are then separated from the target protein, and their masses are accurately measured using MS. Liquid chromatographic-MS (LC-MS) can detect a reaction product within a mixture, requiring no substrate modifications, and is a label-free technique. In order to produce quantitative data, trypsin digestion is generally conducted to cleave proteins down into peptide fragments between 700 and 1,500 Da to ensure a readable mass (Laskay et al., 2013). By looking for the particular residue adduct, bound fragments could be distinguished from unbound. However, MS unfortunately limits the size of the protein due to the upper limit of the mass resolution (Chan et al., 2017). The protein sample must also be pure, as heterogeneity can increase the number of m/z signals in the spectra, resulting in increased complexity during analysis. Furthermore, MS and biochemical assays are also incompatible due to poor assay reproducibility and ion suppression from the high concentrations of salt, detergents, and buffering agents (Dueñas et al., 2022).

Unfortunately, there are difficulties faced by an FBDD campaign during its screening process. The fragments' small size can limit the number of protein interactions, resulting in weak binding affinity (Shraga et al., 2021). Furthermore, biophysical screening requires higher concentrations of the fragments due to their weak binding, which can be a challenge for those with poor solubility. To circumvent this, the use of fragments with electrophilic moieties known as covalent fragments has started to emerge. These fragments allow covalent binding with the protein, alleviating the need for higher concentrations of fragments, as these interactions typically enhance a fragment's activity. This technique is based on disulfide tethering, which allows for a reversible disulfide bond exchange between a molecule and the target protein containing a cysteine residue near the binding site as they are the most nucleophilic residues (Kathman and Statsyuk, 2016). However, this is not limited to the use of disulfides, as it is possible with other groups such as acrylamide and vinylsulfone, which the fragment may already contain. It can also be site-directing by introducing a fabricated cystine on the target protein that does not have one available. The screening process of these covalent fragments is typically done on LC-MS, which allows mixtures of fragments to be evaluated. Once covalent hits are identified, they can be reverted to their non-covalent counterpart

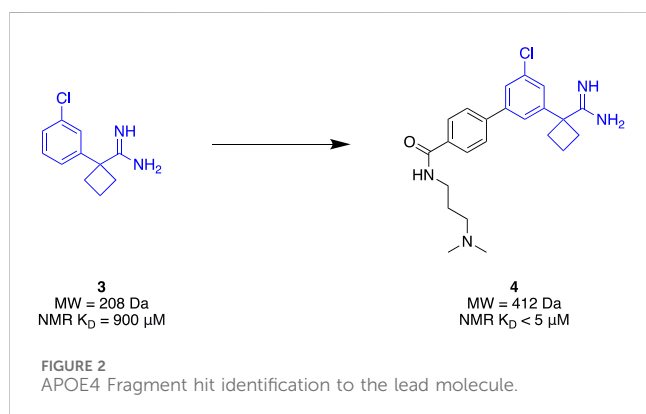
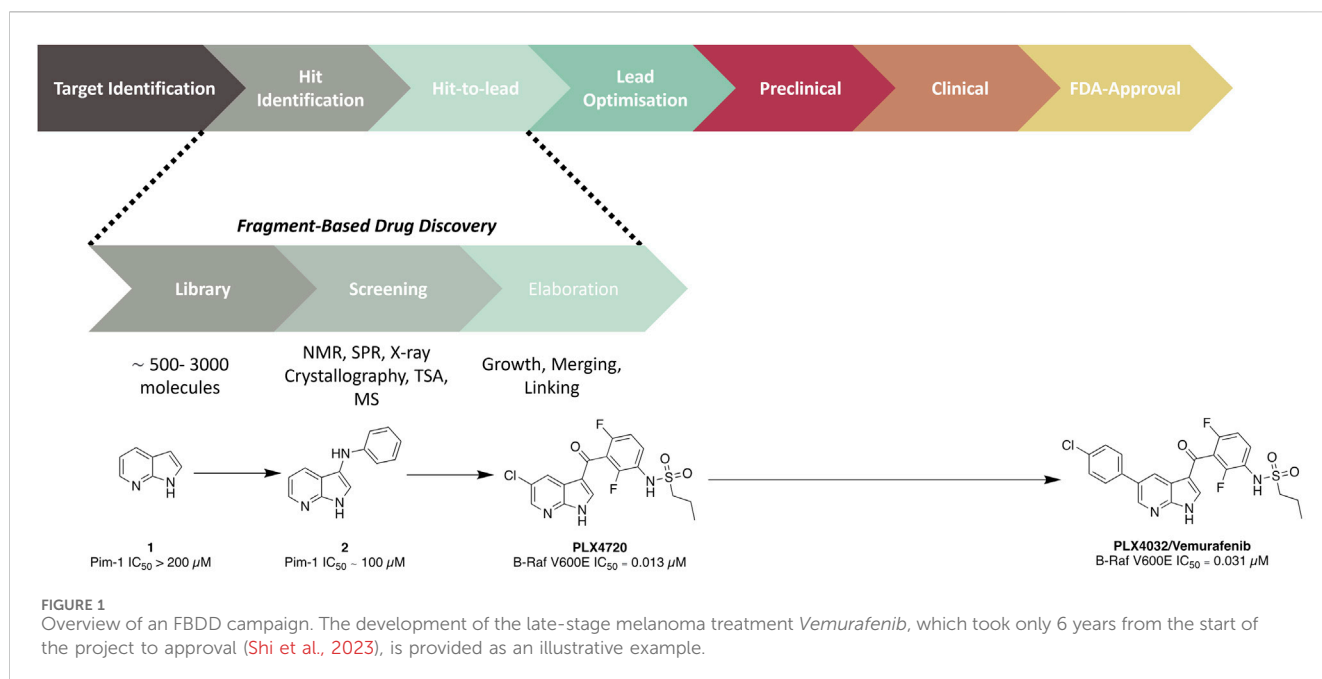
to be assessed at the same binding site. However, it has become increasingly popular to use these as a starting point for covalent inhibitors. The benefits of these fragments is their increased potency, improved selectivity, and prolonged duration of activity and exposure. Regardless, once a fragment hit is identified, a subsequent elaboration process will develop these building blocks into a drug-like lead.

1.3.2 Fragment elaboration

Fragment hits generally possess weak millimolar binding affinities and little to no potency effects on the target. Therefore, guided structural modifications are required to advance these fragments from a hit to a lead compound. The aim in this procedure is to improve the binding affinity/activity of the structure whilst transitioning to a drug-like molecule. This process can be achieved through either fragment growth, linking, or merging. Fragment growth is the most common method, where a hit is taken through a structure-activity relationship (SAR) study to add structural motifs. This is possible even without binding data; however, it is crucial that some form of biochemical or biophysical assay is conducted to direct the SAR study. Fragment linking involves the joining of two or more fragments which recess in different subdomains of the protein. This process is generally undertaken for targets with large binding sites so that there are clear identifications of fragments binding in different regions of the pocket. This method relies on data provided through NMR or x-ray crystallography to understand the binding mode of individual fragments and the combined compounds. However, one of the challenges with this strategy is developing a linker that connects fragments that have no negative effect on the overall activity of the molecule. Finally, fragment merging, which also relies on understanding binding modes, is an alternative strategy to identify more drug-like core structures or molecules. This method aims to merge hit fragments that occupy overlapping space in the binding site to generate an optimised pharmacophore. With the successful elaboration of a fragment hit to a lead molecule, further optimisation is undertaken to advance a lead along the drug discovery pipeline. To date, there have been six FBDD derived drugs that are FDA-approved: *Vemurafenib* (Figure 1) (Bollag et al., 2012), *Erdaftinib* (Murray et al., 2019), *Sotorasib* (Lanman et al., 2020), *Venetoclax* (Souers et al., 2013), *Pexidartinib* (Benner et al., 2020), and *Asciminib* (Schoepfer et al., 2018).

2 Applications and advances of CNS studies with FBDD

This section highlights CNS drug discovery programs that have utilised FBDD since 2015, when the last review in this field was published by Wasko et al. (2015). Each of the studies will be categorised by indications and the specific targets of interest. For each study, we explore the various screening techniques and libraries used to obtain a hit and how this hit was elaborated to an improved lead. Where possible, we also compare the FBDD-derived molecules to those identified via other methodologies.



2.1 Alzheimer's disease

Alzheimer's disease (AD) is commonly characterised by dementia, which includes cognitive deterioration, memory loss, and personality and behavioural abnormalities. Although there are treatments that temporarily alleviate symptoms, there are no disease-modifying treatments currently available. The number of people living with dementia (60%–70% attributed to AD) globally has reached over 55 million (Greenblat, 2023), which is more than double the 20.3 million reported in 1990 (Li et al., 2022).

2.1.1 Apolipoprotein E (apoE)

One of the theoretical causes of AD is the accumulation and deposition of amyloid-beta (Aβ) peptides in the brain. This increase of Aβ peptides is most commonly associated with the gene, *apolipoprotein E* (apoE). ApoE has roles in brain homeostasis, and there is emerging evidence that it mediates one of the many pathways for the clearance of Aβ, although the precise mechanisms are currently unclear (Yamazaki et al., 2019). There are several isoforms of apoE which each possess varying degrees of efficiency in

Aβ clearance, with apoE4 the slowest. ApoE4 also appears to promote Aβ aggregation due to its lower stability profile than other isoforms. As such, individuals possessing a pair of apoE4 alleles have the strongest genetic risk factor for AD (Yamazaki et al., 2019).

Given its clinical relevance, apoE4 has become a therapeutic target of interest. It has been theorised that increasing the stability of apoE4 will improve Aβ clearance as well as minimise aggregation (Petros et al., 2019). The N-terminal domain of apoE4 was seen as a suitable target due to its small, stable nature. Due to its small binding site and the limited number of molecules associated with apoE4, an FBDD strategy is well-suited to efficiently explore the target for novel chemotypes. Petros et al. (2019) utilised a combination of ¹³C-HSQC fragment screening, SPR, and TSA to identify a suitable apoE4 stabiliser. A library of 4068 fragments was first screened using ¹³C-HSQC NMR against the N-terminal domain of apoE4 that was ¹³C-labelled. Each fragment complied with Ro3, and they were assayed as a cocktail mixture of 12. A genuine hit was considered to cause a minimum shift of 0.05 ppm and 0.5 ppm in the proton and carbon spectra, respectively. The hits then underwent NMR titration to determine binding affinity, which identified amidine **3** (Figure 2) as the highest affinity binder (K_D = 900 μM) at the apoE4 N-terminal domain. Amidine **3** was further subjected to SPR to obtain its binding affinity of K_D = 205 μM at the N-terminal domain of apoE4. In addition, the binding affinity with the full length of apoE4 from mammalian cell expression, and the full length apoE3 (isoform) resulting in K_D = 233 μM and K_D = 890 μM, respectively, represented good selectivity towards apoE4. Furthermore, stabilisation of the protein was observed with the addition of 5 nM of the fragment, improving thermal stability by approximately 4°C in comparison with the lone protein. With excellent preliminary results, fragment growth was conducted to transform the fragment into lead **4** that exhibited NMR-derived affinity of K_D < 5 μM whilst retaining the same thermal stability amount through TSA of initial fragment **3** at a five-fold lower

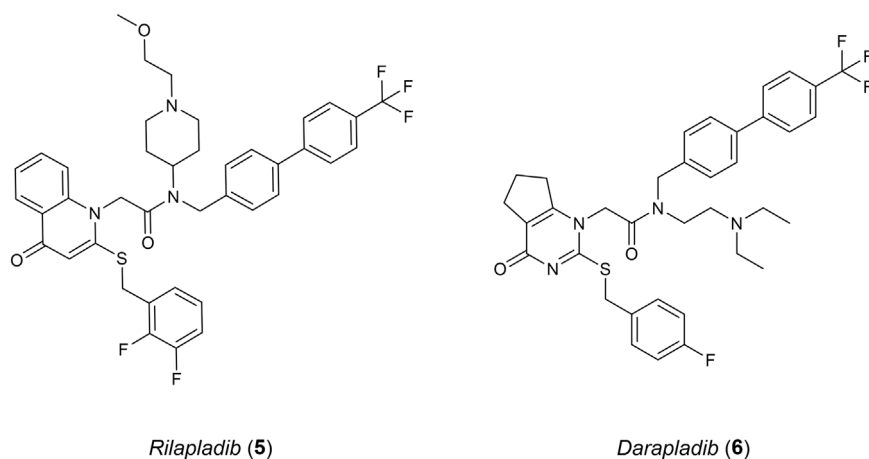


FIGURE 3
Known Lp-PLA₂ inhibitors.

concentration. The conclusion of this study demonstrated a successful identification of a stabiliser for apoE4 through a streamlined elaboration that was enabled through a comprehensive FBDD campaign.

2.1.2 Lipoprotein-associated phospholipase A2 (Lp-PLA₂)

Studies surrounding lipoprotein-associated phospholipase A2 (Lp-PLA₂) have linked an increased expression of this protein in humans to AD and atherosclerosis (Woolford et al., 2016). Lp-PLA₂ belongs to a group of the phospholipase A2 superfamily, cleaving *sn*-2 ester bonds of glycerophospholipids such as platelet activating factor (PAF). Elevated levels of Lp-PLA₂ cause oxidised modifications of phospholipids into various pro-inflammatory stimuli which include lysophosphatidylcholine and oxidised non-esterified fatty acids. Oxidative stress and inflammation occur as a result. Lp-PLA₂ has become a suitable inflammatory biomarker for cardiovascular disease (CVD) and heart disease (Doody et al., 2015). However, understanding the relationship between Lp-PLA₂ and AD is still difficult, as risk factors such as CVD could have an influence in its progression. *Rilapladib* (5), a known Lp-PLA₂ inhibitor (Figure 3), was able to provide initial evidence supporting Lp-PLA₂ as a treatment for AD (Maher-Edwards et al., 2015). Among the class for Lp-PLA₂ inhibitors, *Darapladib* (6) has been the most promising, advancing into phase III clinical trials originally as a therapeutic for atherosclerosis but failing to meet efficacy requirements (Woolford et al., 2016).

Initially, 6 presented itself as a promising molecule to Chen et al. (2015), where its high potency prompted SAR studies to improve oral efficacy, allowing it to be repurposed as an AD therapeutic. Unfortunately, improving the oral bioavailability of these analogues proved to be challenging, mainly due to their already large molecular size and high lipophilicity. Liu et al. (2017) followed up this study with an FBDD campaign with the aim of identifying a novel scaffold that could improve the physicochemical properties of 6 whilst maintaining a comparable potency and selectivity profile. Virtual screening was initially conducted with a library of 500 in-house fragments utilising a co-crystal structure of a recombinant human

Lp-PLA₂ (rhLp-PLA₂). This allowed for observations of each fragment's occupancy in the binding pocket and led to fragment 7 (IC₅₀ = 1 mM, LE = 0.30) that exhibited similar interactions to 6. Utilising the SPECS database, molecules that contained the structural moiety of 7 underwent molecular docking studies using the co-crystal structure of the sulfonamide with rhLp-PLA₂ to grow the fragment to fill the binding site. The 500 highest ranked compounds were filtered, prioritising those that had dissimilar binding modes to the original small fragment. This was followed by cluster analysis using a leader-follower method to obtain 100 structures. Finally, a PAF enzymatic assay was conducted with the remaining molecules, obtained either commercially or in-house, which identified potent structure 8 (IC₅₀ = 3.43 μM) as a hit (Figure 4A). Structure 8 was subsequently elaborated, resulting in sulfonamide 9. Compound 9 demonstrated good *in vivo* clearance in male rat hepatocytes (CL = 4.9 mL/min/kg), favourable AUC value (3.4 μg h/mL), and good oral bioavailability (*F* = 35.5%). Furthermore, it maintained inhibitory activity 24 h after oral administration, which is superior to 6 exhibiting inhibitory activity for only 8 h. With the success of this campaign, 9 is currently under further optimization, which illustrates that a successful fragment-based campaign allowed for an accelerated hit-to-lead transition.

Huang et al. (2020) also had success with an FBDD campaign which aimed to create covalent ligands as a drug for AD or biochemical tool for Lp-PLA₂. Serine and cysteine residues are most often exploited to form covalent interactions with small molecules, given their nucleophilicity under physiological conditions. As serine (Ser273) was located deep within the binding pocket of Lp-PLA₂, it was chosen as the ideal residue to investigate through a fragment-based approach. Ideally, a small molecule that covalently binds to the Ser273 residue would be grown into a drug-like molecule, without sacrificing binding efficiency. Through a deconvolution study of three known inhibitors that bound to Lp-PLA₂, 10 was chosen as the covalent binding moiety as it possessed good selectivity for Lp-PLA₂ over other serine hydrolases. Elaboration of 10 began with hybridisation with 11 to form 12, a molecule strikingly similar to the previous gold

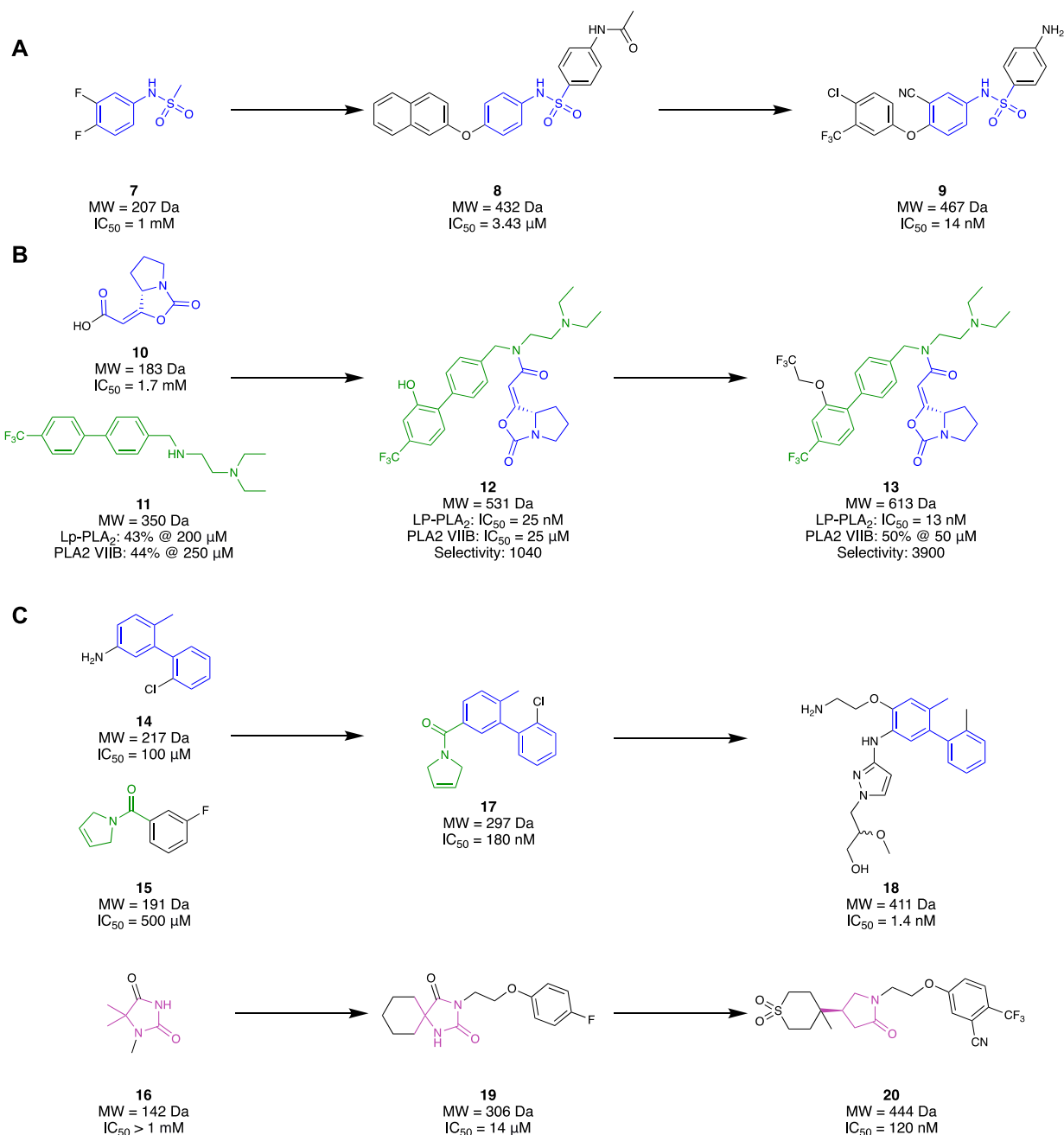


FIGURE 4
Lp-PLA₂ fragment hit identification to the lead molecule. (A) Liu and co, (B) Huang and co development of a covalent ligand, (C) GlaxoSmithKline.

standard, **6**. Both individual fragments **10** and **11** showed millimolar potency with no selectivity towards Lp-PLA₂ over PLABVIIB. However, their hybrid, **12**, exhibited a 68000-fold improvement in IC₅₀ (IC₅₀ = 25 nM) and 1000-fold improvement in selectivity for Lp-PLA₂ (Figure 4B). Comparison of the co-crystal structures of hybrid **12** and **10** illustrated that the binding conformation of the small fragment was highly conserved. Similarly, the comparison of the co-crystal structure of **12** with **6** illustrated the conserved binding pose of the biphenyl group, recessed in a hydrophobic sub-pocket. Therefore, minimal changes were made to enhance the synergistic behaviour of the fragments, only filling the unoccupied

sub-pockets regions to obtain their lead molecule **13**. The addition of a linear 1,1,1-trifluoroethoxy group on the *meta*-position of the second biphenyl ring exhibited a two-fold increase in the inhibitory response (IC₅₀ = 13 nM) and a four-fold increase in selectivity for Lp-PLA₂ compared to hybrid **12**. Furthermore, it exhibited exceptional selectivity over a wide selection of serine hydrolases and a three-fold improvement in selectivity compared to **6** for Lp-PLA₂. Such exemplary results illustrate that a covalent fragment-based campaign can be a promising alternative to conventional approaches where directly probing an inhibitor to introduce covalent properties may not be feasible.

Researchers from GlaxoSmithKline (GSK) also chose to explore novel chemical space for Lp-PLA₂ utilising an FBDD strategy (A. J. A. Woolford et al., 2016). Unlike the previous research discussed, GSK utilised a commercialised fragment screening platform from Astex Pharmaceuticals against Lp-PLA₂. This platform utilised a combination of TSA, NMR, and x-ray crystallography experiments to identify a desirable fragment hit. An in-house crystal system was also developed to facilitate the fragment soaking and data collection. A library of 1,360 small fragments was screened in cocktail mixtures of four, where a subset of 150 fragments was subjected to x-ray crystallography. The fragment hits that were identified from TSA or ligand-detected NMR (LD-NMR) were only pursued if they could be validated *via* x-ray crystallography. This resulted in a total of 34 fragments, with an additional 16 identified from a substructure search around the x-ray-validated fragments. Interestingly, superimposing the crystal structures of a select group of five fragment hits illustrated a collective binding surface comparable to **6**. However, a collection of bis-aryl fragments such as **14** (IC₅₀ = ~100 µM, LE = ~0.36) was found to bind in a novel binding site. Superimposing the binding mode of one of the other five fragment groups, an amide **15** (IC₅₀ = ~500 µM) with **14** saw similar binding behaviours in the pocket. Both fragments harboured interactions in different areas of the pocket, leading to the design of their hybrid fragment **17** (IC₅₀ = 180 nM, LE = 0.44). Subsequent growth of fragment **17** resulted in compound **18** (IC₅₀ = 1.4 nM) with over 1000-fold selectivity over PLA₂-VIIB. Although it possessed improved physicochemical properties (cLogP = 3.4, aqueous solubility = 302 µM) compared to **6** (cLogP = 8.2, solubility = 8 µM), it did not possess a suitable PK profile (Cl_{int} = 10.2 mL/hr/mg) required for once-daily dosing in humans, highlighting a major challenge in drug development and subsequently putting a halt to this study (Figure 4C).

In conjunction with the previously discussed study, GSK also pursued a selection of fragments with the aim of designing an inhibitor capable of matching the activity of **6** in a plasma assay (Woolford et al., 2016). They hypothesised that a lead molecule might not need to possess picomolar activity if the discrepancy between Lp-PLA₂ biochemical and plasma assays could be reduced. Such an approach could potentially lead to a reduction in MW, resulting in a more favourable level of lipophilicity than **5**. Sharing the same fragment-based screening output as above, 50 fragments were prepared for x-ray crystallography to observe their binding at the target. This resulted in three distinct fragment hits that occupied different regions of the binding pocket. Specifically, a hydantoin fragment **16** (IC₅₀ > 1 mM, cLogP = 0.03) represented a good starting point due to its small size and convenient synthetic accessibility for exploring the binding pocket through different growth vectors (Figure 4C). Hydantoin **16** occupied the oxyanion hole with two hydrogen bonds to the NH of the amide junction between Leu153 and Phe274. However, due to its significantly reduced activity than the other hit fragments, a virtual screening strategy was implemented to combine motifs of hydantoin **16** with the other hit fragments that occupy adjacent sites of the binding pocket with notable activity. Approximately 16,000 hydantoin fragments commercially obtained or prepared in-house were screened against an in-house Lp-PLA₂ crystal structure utilising the Astex proprietary version of Gold software to grow the fragment, resulting in structure **19** (IC₅₀ = 14 µM, LE = 0.30) as the favourable

hit molecule. Further structural elaboration of **19**, which included the replacement of the hydantoin with a γ-lactam, resulted in lactam **20** (IC₅₀ = 0.12 µM, LE = 0.35, and cLogP = 0.75) —a low MW, potent inhibitor with favourable lipophilicity which exhibited selectivity against PLA₂-VIIB and no significant inhibition of CYP enzymes. The design of lactam **20** demonstrates an alternative potent and selective inhibitor that possesses favourable PK properties and low MW.

These studies surrounding Lp-PLA₂ present great examples of the benefits and shortcomings of FBDD. Previous rational drug design has seen challenges in obtaining a potent molecule that retains desirable lipophilicity when working with larger drug-like molecules. However, the fragment-based strategy allows for the constructive identification of fragment binders possessing desirable qualities, followed by the coherent optimisation of the molecule to improve its potency whilst retaining desirable parameters.

2.1.3 Notum

The wingless-related integration site (Wnt) signalling pathway regulates important factors associated with cell fate determination, migration, polarity, and neural patterning. However, the carboxylesterase Notum has been implicated in the suppression of Wnt signalling through the deacylation of essential palmitoleate groups on Wnt proteins. As Wnt signalling contributes to healthy brain function and synaptic plasticity, its suppression has been implicated in AD (Palomer et al., 2019). Wnt signalling has been considered a challenging target for the medicinal chemist as many targets are not considered “classically druggable” (Mahy et al., 2020b).

Mahy et al. (2020a) utilised an FBDD approach to investigate a novel class of Notum inhibitors to gain new insight into Wnt signalling. A library of 4,350 fragments sourced from the Enamine Carboxylic Acids Fragment library was used due to its novelty and diversity. A subsequent collection of 250 fragments was made through a selection process based on molecular properties, structural parameters, physicochemical property space, and structural diversity. Through a Notum 8-octanoyloxypyrene-1,3,6-trisulfonate (OPTS) biochemical assay which measured suppressed fluorescence with binding to Notum and crystallography study, 14 fragments were selected. These were found to bind in the palmitoleate pocket of Notum, revealing interactions with the Phe268 and Trp128—favourable for inhibitory activity. A set of pyrrole-3-carboxylic acid **21** and pyrrolidine-3-carboxylic acid **22** motifs were subsequently selected as their leads, whilst the remaining hits were used to help guide the SAR investigation (Figure 5A). These two lead motifs were grown to better fill the binding pocket, revealing four lead-like molecules, such as **23** and **24**, with low to sub-micromolar potency. Unfortunately, even though these fragment-derived molecules were able to inhibit Notum, they remained inferior to other lead molecules identified through traditional screening strategies.

Following this study, Mahy et al. (2020a) then published another investigation revealing a class of potent inhibitors of Notum. An x-ray crystallography fragment screening method was performed at the XChem platform of Diamond Light Source using 768 compounds from the DSPL fragment library. This library of

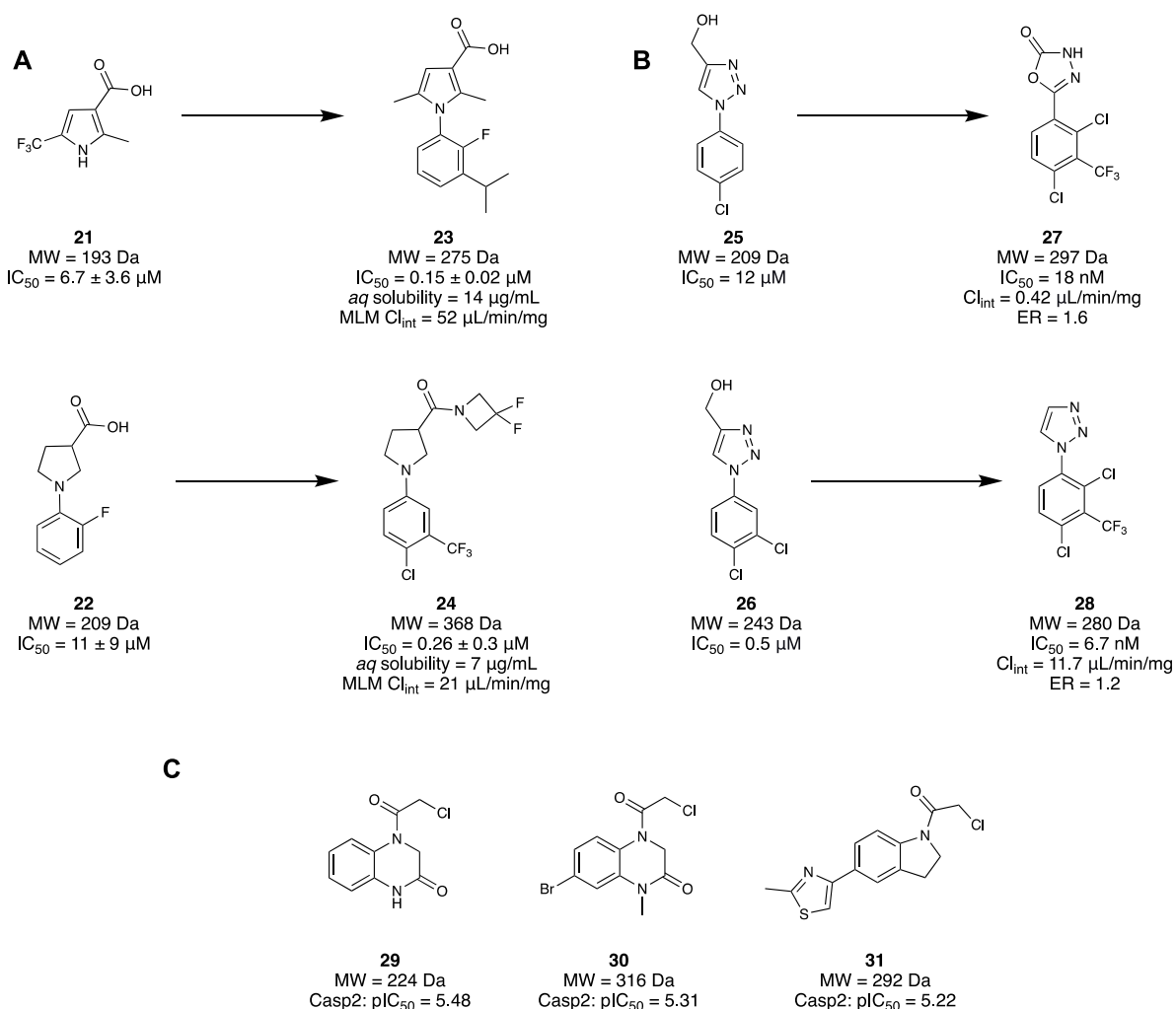


FIGURE 5
(A) Examples of the set of pyrrole-3-carboxylic acid **21** and pyrrolidine-3-carboxylic acid **22** structural motifs. (B) Identification of two fragment hits for Notum and their subsequent lead molecule for Notum. (C) Final fragment hits with potential to become Casp2 inhibitors.

768 fragments was assessed in a crystallographic fragment screen using the XChem platform to seek fragments that bind in the palmitoleate pocket. A diverse group of 60 fragments were identified, including **25** and **26**. Molecule **25** demonstrated an exemplary binding mode, with modest potency (IC₅₀ = 11.5 μM). Hence, subsequent efforts were made to elaborate both ring systems of **25**, wherein the triazole ring was hypothesized to participate in crucial H-bonding interactions. As a result, the triazole ring was replaced with an oxadiazole to improve H bonding capabilities, yielding compound **27**. Compound **27** maintained a fragment-like size and a nanomolar potency (IC₅₀ = 18 nM), good metabolic stability (Cl_{int} = 0.42 μL/min/mg), and high cell permeability with a low efflux ratio (ER = 1.6) (Figure 5B).

A subsequent study from Willis and colleagues examined the same compound library using the same screening method, this time examining compound **26** as the lead compound. Fragments **25** and **26** differ only by a meta-chloro group on the phenyl ring. However, fragment **26** possessed slightly better potency (IC₅₀ = 0.5 μM), good aqueous solubility (100 μg/mL), moderate stability in mouse liver microsomes (MLM) protein

(Cl_{int} = 88 μL/min/mg), and excellent cell permeability (ER = 1.0), consistent with a lead-like molecule. Unsurprisingly, both compounds bind in the same pocket and conformation. Efforts to optimise compound **26** aimed to maintain the vital triazole interactions, instead focusing on functionalising the phenol ring in the southern portion of the molecule. Minimal elaboration was required to access their lead molecule **28** with nanomolar inhibitory activity (IC₅₀ = 6.7 nM), involving the removal of the alcohol group on the triazole and an additional CF₃ group on the phenyl. X-ray crystallography of **28** demonstrated retention of the H-bonding interaction of the triazole with Trp128. Furthermore, with a trisubstituted phenyl ring, the palmitoleate pocket was nearly completely occupied. In addition to the high potency, the physicochemical properties were consistent with a drug-like molecule, displaying good aqueous solubility (solubility = 240 μM), MLM stability (Cl_{int} = 11.7 μL/min/mg), and high permeability (ER = 1.2) (Figure 5B). *In vitro* studies of **28** demonstrated restored Wnt signalling in the presence of Notum, and subsequent *in vivo* results illustrated good oral bioavailability and brain penetration as drug concentrations

in the brain and plasma were similar. The collective result of these studies demonstrates the identification of a novel class of inhibitor for Notum through a successful FBDD campaign, and a new chemical probe to further support the implications of Notum and AD.

2.1.4 Caspase-2

Caspase-2 (Casp2) is a cysteine protease that has generally been targeted using peptidic and peptidomimetic ligands. Casp2 cleaves neuronal scaffold-protein tau, leading to neurofibrillary tangles resulting in reversible synaptic dysfunction, thus making it a potential target for AD *via* synaptic function restoration (Vigneswara and Ahmed, 2020). Focus has recently been drawn to developing inhibitors with covalent reversible and irreversible binding modes (Cuellar et al., 2023). This form of binding is possible through electrophilic moieties and has demonstrated validity in both reversible and irreversible cysteine protease inhibitors.

Cuellar et al. (2023) have tried to develop a small-molecule inhibitor through a fragment scaffold which utilises an electrophilic screening strategy to overcome the CNS drug challenges faced by pentapeptides and peptidomimetics. These generally have several H-bond donors and a molecular weight that are incompatible with passive diffusion into the brain, and therefore suffer from poor brain bioavailability. Incorporating an α -chloroacetamide library from Enamine, 1,920 compounds were tested for the inhibitory effects on Casp2 and Casp3 due to their similar substrate recognition sequence using a fluorometric enzyme assay. α -chloroacetamides were chosen as there is precedent in the literature for these groups to undergo covalent bonding against cysteine proteases (Resnick et al., 2019; Gao et al., 2022). The screening of the compounds was conducted at two concentrations for both Casp2 (12.5 and 6.25 μ M) and Casp3 (125 and 62.5 μ M). A three-sigma rule ($\mu + 3\sigma$) was used to determine molecules that were at least three standard deviations (σ) greater in inhibition activity from the mean (μ) and class them as hits. The results from the 12.5 μ M concentration screen provided better differentiation between the molecule and baseline, resulting in 64 hits that could yield an inhibition greater than 60% with Casp2. Five compounds stood out, with inhibition values $\geq 90\%$. An identical method was used to identify compounds with inhibitory activity at Casp3, resulting in 72 hits. However, significantly lower values were obtained when the experiment was repeated at 12.5 μ M to align with values obtained for Casp2. Comparing the data and calculations of pIC_{50} values to determine selectivity profiles, a select group of compounds were found to have the highest affinities and single digit micromolar activity. To investigate the covalent binding of the fragments to Casp2, mass spectroscopy peptide sequencing using LC-MS was conducted for a target engagement study. To illustrate the irreversibility of these fragments to the active site of Cys320, the fragments and other reference molecules were incubated with Casp2. Trypsin digestion of the protein/fragment adduct was performed, ensuring observation of the protein fragment MFFIQAC₃₂₀R, as this contained the active site Cys320. The results confirmed the covalent irreversibility binding of all the electrophilic fragments to Cys320. Hit validation was then conducted with three of the promising hits, fragments 29–31 (Figure 5C), and resubjecting them to another

fluorometric enzyme assay. All hits demonstrated affinity to Casp2 in a single-digit micromolar range with no significant Casp3 inhibition. Overall, it was demonstrated that a selection of electrophilic fragments with promising affinity and selectivity for Casp2 could create a diverse fragment scaffold. As they all observed low micromolar inhibitory concentrations, they could provide a great foundation for developing a selective small-molecule Casp2 inhibitor.

2.1.5 Sortilin

Sortilin is a membrane protein that mediates several physiological functions through trafficking and signalling with different protein partners. It has become a promising therapeutic target due to its implication with several disease states, including AD. Andersen et al. (2017) aimed to identify a modulator for Sortilin as a possible therapeutic intervention. Previously, Schröder et al. (2014) had reported an orally bioavailable small molecule AF38469 (32) developed through HTS screening; however, it exhibited poor CNS exposure, making it unsuitable as a tool for *in vivo* studies. As the carboxylic acid of 32 was deemed responsible for the low CNS exposure, an FBDD campaign exploring suitable chemotype replacements for this moiety was undertaken. Utilising the Lundbeck Fragment Library, 1,600 compounds were screened using a previously reported neurotensin binding scintillation proximity assay (Schröder et al., 2014). Among the four fragments identified, 33 and 34 both demonstrated adequate potency to produce a concentration response curve and calculative IC_{50} , while 35 and 36 could not but still demonstrated a reproducible specific inhibition at the highest assay concentration (Figure 6). Taking these initial hits (33–36), the first round of modifications led to fragment 37 with max. inhibition of 69%. Subsequent elaborations aimed to improve potency by expanding the fragment to occupy similar regions demonstrated by 32, which afforded the lead compound 38 ($pIC_{50} = 5.4$, $cLogP = 2.2$, MDCK cell line permeability $2.9 \text{ cm/s} \times 10^{-6}$). Overall, a novel cell-permeable sortilin inhibitor was successfully identified with good potency. It was found that further elaboration of 38 could yield a better optimised interaction with sortilin, resulting in improved potency, permeability, and possible CNS exposure.

2.2 Parkinson's disease

Parkinson's disease (Parkinson's) is a brain disorder diagnosed by uncontrollable movements that manifest symptomatically as tremors, shaking, stiffness, and slow movements as well as a loss of unconscious movements, sense of smell, and fatigue. Typical homeostatic function normally mediates the production of dopamine, which acts as a neurotransmitter between the body and brain to regulate body movements and emotions. In cases of Parkinson's, the basal ganglia become impaired and/or die, resulting in a reduced production of dopamine. Dopaminergic loss is one of the pathological indicators of Parkinson's. Monoamine oxidase-B (MAO-B) is an enzyme associated with Parkinson's and has been classed as a pharmacological target for its treatment, as its inhibition increases dopamine levels (Tan et al., 2022). There have been a variety of inhibitors developed for MAO-B, such as *tranylcypromine* and *phenelzine*—two nonselective, irreversible inhibitors. These can,

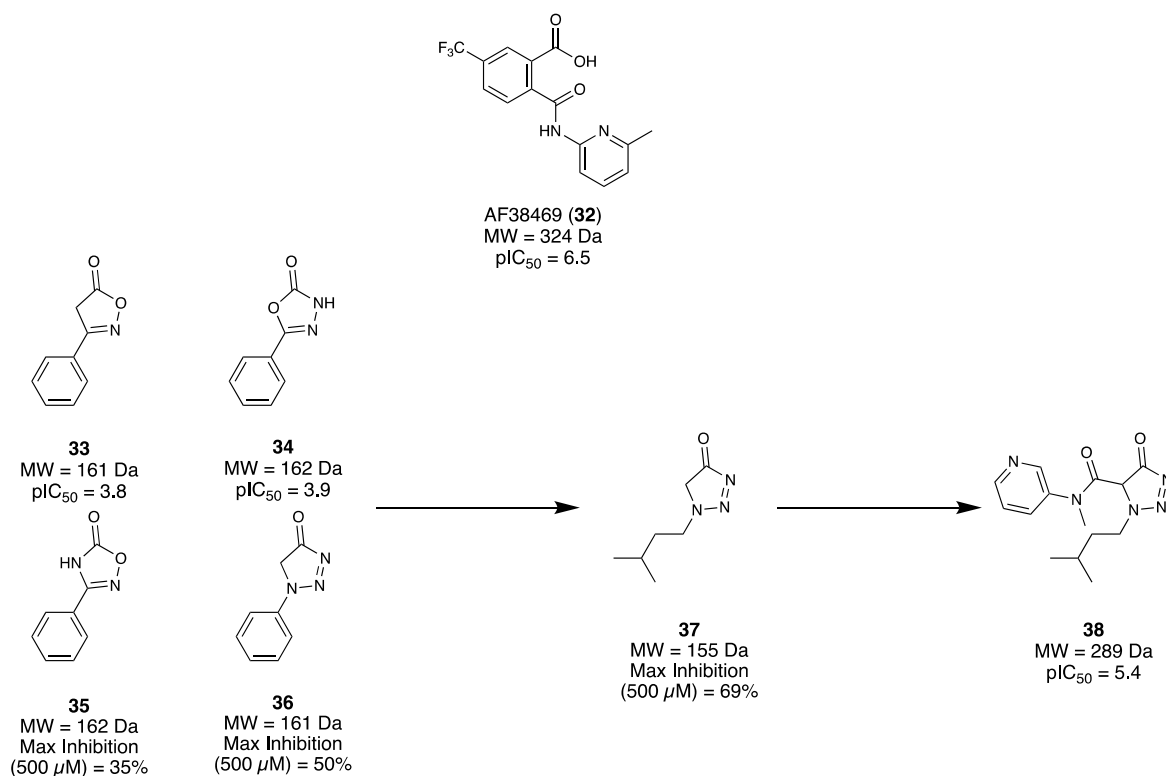


FIGURE 6
Fragment hit identification to the lead molecule for sortilin.

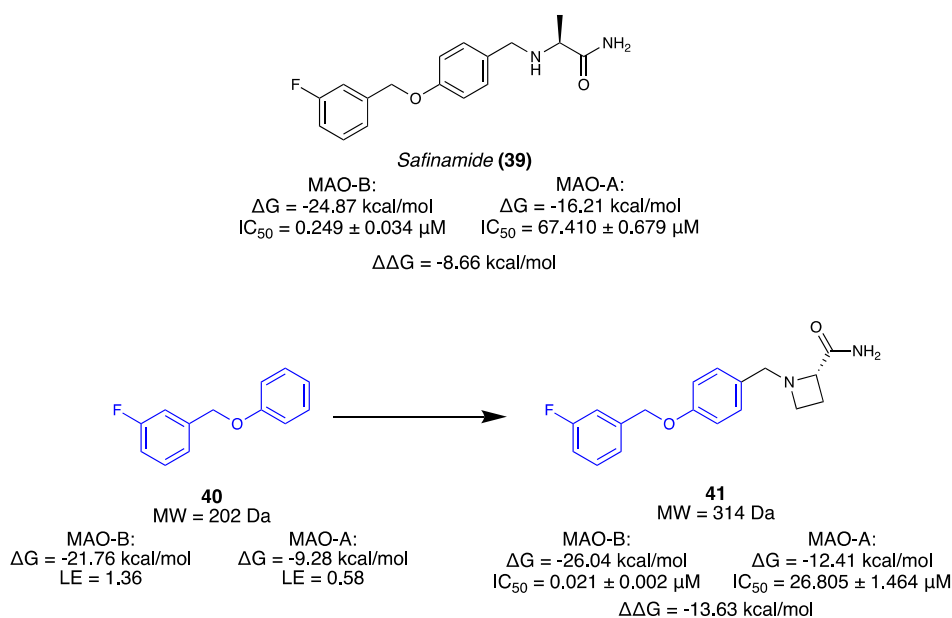


FIGURE 7
Known inhibitor of MAO-B. Fragment selection through steric stress to lead molecule for MAO-B.

however, lead to tyramine build-up due to the consumption of tyramine-rich foods, resulting in a hypertensive crisis called the “cheese effect.”

Jin et al. (2020) aimed to isolate a selective, reversible inhibitor for MAO-B by incorporating a novel computational strategy called steric clash-induced binding allosterity (SCIBA). MAO-A and

MAO-B share a highly conserved protein sequence, except for a pair of residues (MAO-B has Ile199 in place of Phe208 and MAO-A has the inverse). The residue variation was considered the reason for the favourable binding mode of the linear-type *Safinamide* (**39**) in MAO-B whilst being unsuited for the curved binding site of MAO-A (Figure 7). SCIBA was used to identify fragments with steric clashes with MAO-A proteins and select them as fragments that possess favourable PK properties at MAO-B. Borne from the west half of **39**, fragment **40** observed steric clashing with the sub-pocket of MAO-A due to the residue difference. It was thought to result in a conformational change of **39**, weakening the binding affinity. A deconvolution study of **39** was conducted, calculating the binding free energy (ΔG) and ligand efficiency (LE) of each fragment. A fragment library was assembled using a database of FDA-approved drugs, and fragments were sorted based on the ΔG value towards MAO-B. Using **40** as the hit fragment, only minimal growth was required to fill the unoccupied sub-pocket where flavin adenine dinucleotide (FAD) cofactor resided, resulting in a series of (S)-2-(benzylamino)propanamides (Figure 7). Subsequent *in vitro* results indicated that all the derivatives had no inhibitory activity at MAO-A. Compound **41** ($IC_{50} = 0.021 \mu M$) was selected as the lead as it exhibited high inhibitory activity at MAO-B and no activity at MAO-A. Reversibility as 100% recovery of MAO-B was observed after 24 h, whilst also exhibiting similar increases of dopamine levels compared to **39** (Figure 7). Overall, Jin et al. (2020) demonstrate a novel fragment approach for identifying favourable motifs of a target by observing steric clashing at an off-target site, resulting in a successful hit campaign and a potential lead compound for the treatment of Parkinson's through minimal optimisation.

2.3 Schizophrenia

Schizophrenia is a chronic, debilitating disorder that impairs the psyche and motor function of the brain. Schizophrenia is characterised by positive, negative, and cognitive symptoms that manifest as delusions and hallucinations, amotivation and apathy, and deficits in memory and learning ability (McCutcheon et al., 2020). The current understanding of its pathology is that there is no singular target that can be drugged to cure the disease. Current therapies focus on antagonism of the dopamine 2 (D2) receptor to treat positive symptoms, whilst there are little to no effective therapies for negative symptoms or cognitive impairments (McCutcheon et al., 2020).

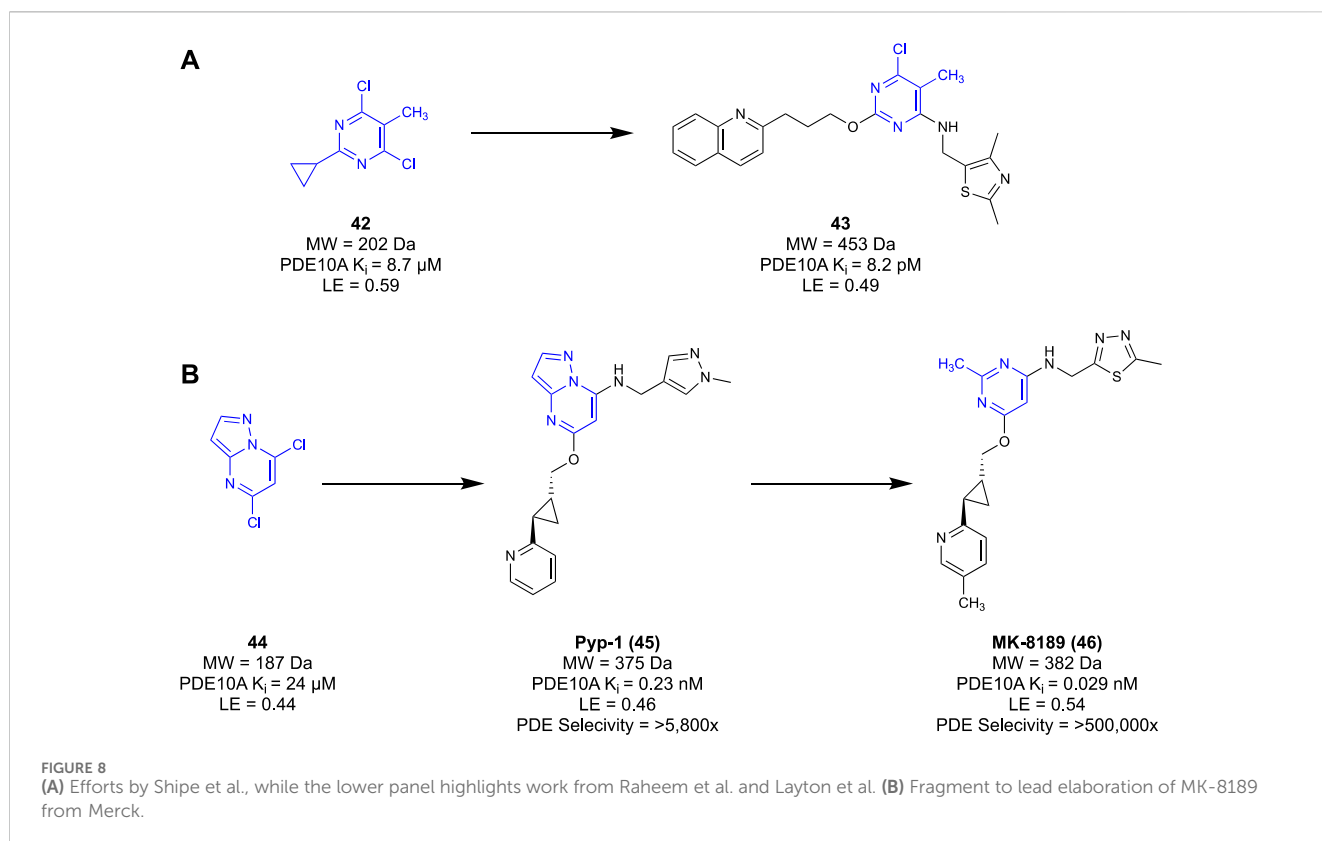
2.3.1 Phosphodiesterase 10A

Phosphodiesterases (PDEs) are a family of enzymes that control the hydrolysis of signal messengers, cyclic adenosine monophosphate (cAMP), and cyclic guanosine monophosphate (cGMP). This family of enzymes regulates the concentration of cAMP and cGMP to maintain healthy signalling in the brain (Zagorska et al., 2018). Inhibition of the PDE isoform 10A (PDE10A) is considered effective in the treatment of a range of psychological, neurological, and movement disorders associated with schizophrenia (Zagorska et al., 2018; Amin et al., 2021).

Researchers from Merck discovered a novel chemotype of PDE10A antagonists through a dual fragment and conventional drug discovery campaign (Shipe et al., 2015). HTS was conducted

using the proprietary Merck compound library, yielding hit and subsequent lead compounds that would ultimately suffer from poor physicochemical characteristics. Compounds from this series were used as PET tracers (Cox et al., 2015) or benchmark compounds for biochemical assays (Raheem et al., 2012) but were never utilised as candidates for further development. A subsequent fragment screen of the Merck fragment libraries against an *in vitro* PDE10A2 inhibition assay delivered a pyrimidine-based fragment hit **42**. The compounds developed from this fragment were synthesised in parallel, with SAR decisions informed by an *in silico* structure-based study. The pyrimidine fragment was elaborated into candidate **43**, showing an over 1-million-fold improvement in potency relative to the initial fragment hit **42** ($K_i = 8.2 \text{ pM}$ vs $8.7 \mu M$, respectively). Unfortunately, like the series identified in HTS, this generation of compounds suffered low oral bioavailability and high clearance, amongst other issues, ceasing development. The next generation of antagonists was reported by Raheem et al. (2016) using the fragment hits discarded from the initial fragment screen. In an attempt to address the unfavourable PK profile that ceased development of candidate **42**, fragment core **44** was selected. This had a lower LE and potency, but it did not suffer from the clearance, bioavailability, and selectivity issues seen in the previous generation. The next-generation core was rapidly optimised, utilising data from the *in silico* study as well as knowledge gained from the initial fragment screen. This development led to compound PYP-1 (**45**), with similar potency to the previous generation of compounds but with less metabolic liabilities. A subsequent study by Layton et al. (2023) refined both the east and west wings of **45**, resulting in slight potency gains. They then re-examined the pyrazolopyrimidine core of the molecule to investigate nitrogen placement in the heterocyclic ring. Subsequent SAR studies concluded that a 2-methyl-pyridimidine core was the most favourable moiety. This research culminated in 2020, when MK-8189 (**46**) (Figure 8B), a lead compound borne of **45**, entered phase I clinical trials and was well-tolerated by patients (Layton et al., 2023).

AstraZeneca developed a PDE10A inhibitor borne of a dual fragment and conventional drug discovery campaign (Varnes et al., 2016). A HTS of the AstraZeneca corporate compound library against a PDE10A inhibition assay at $100 \mu M$ yielded 11,000 hits, at a high hit rate of 5%. Hits from this library that had structural similarities to known PDE inhibitors were discounted to ensure that any novel hits had a favourable selectivity profile for the PDE10A receptor. They identified 5,328 compounds as possible starting points for lead development. To sift through the hits identified, a low molecular weight fragment screen was initiated to narrow down the possible HTS leads. Some 3,000 fragments from the corporate compound library were screened, yielding 414 hits at a high hit rate of 14% at $100 \mu M$. From this screen, an atypical group of fragment hits were identified, exemplified by **47** and **48**, which had different structural features from other hits. These unique fragment hits were then evaluated in an *in silico* docking study to indicate binding modalities unique to these structures. This *in silico* study highlighted a key scaffold, a five-membered ring core connected to a heterocycle and aromatic/hydrophobic group (Figure 9A). This key scaffold was believed to be essential to the novel binding modality. Compounds from the HTS campaign were then compared to this key scaffold in the hopes of maintaining the novel binding modalities discovered. This filtered the potential leads from



5,328 to just 14 compounds and was even further refined to only one after structures with unfavourable physicochemical characteristics and false positives were discarded. Having narrowed the HTS hits down to the lead compound **49**, the scaffold was rapidly optimised to compounds **50** and **51** (IC_{50} = 0.12 μ M and IC_{50} = 0.49 μ M, respectively). Ultimately, the fragment screen used by AstraZeneca acted as a filter in their drug discovery program term “fragment-assisted drug discovery” (FADD). Their FADD campaign identified lead compound **49**, which would have been overlooked if the initial screening had only been undertaken through HTS. Compounds **50** and **51** serve as a starting point for the next generation of PD10A antagonists from AstraZeneca.

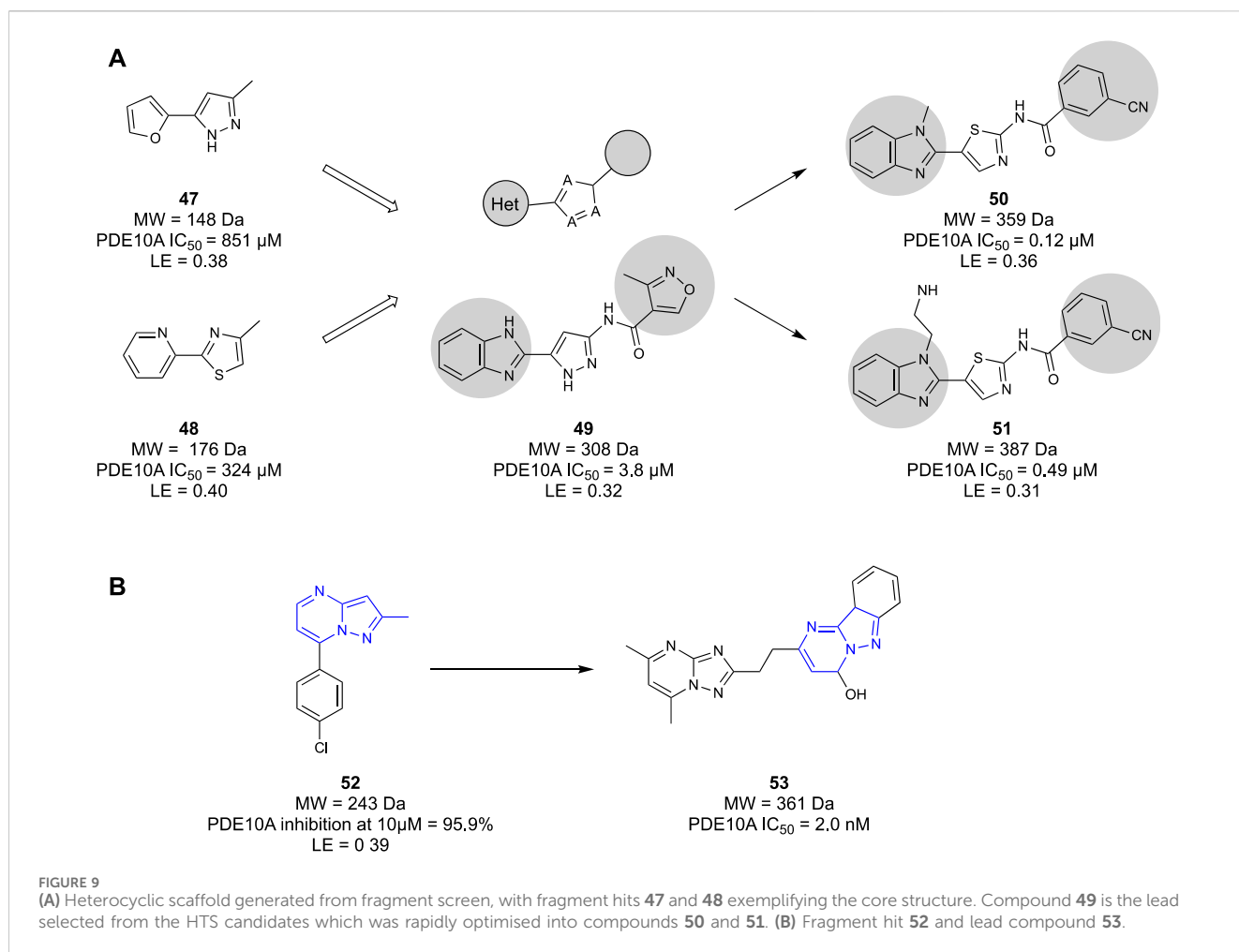
Chino et al. (2018) utilised a fragment-based technique to generate a novel pyrimido[1,2-*b*]indazole chemotype of PDE10A inhibitors. Fragments from an undisclosed in-house fragment library were screened in an x-ray crystallography assay, identifying fragments that co-crystallised in the receptor. A pyrazolopyrimidine core **52** (Figure 9B) was selected as a starting point from the screen as it was identified as interacting with a key Gln726 residue within the binding pocket. However, it was seen that the fragment did not interact with a crucial Tyr693 residue that dictated PDE10A selectivity identified in previous studies (Chappie et al., 2009; Verhoest et al., 2009). To remedy this, the fragment was grown to increase its synthetic tractability to make screening heterocycles to interact with the Tyr693 residue easier. The co-crystal structure of **52** bound to the PDE10A receptor showed that the 4-chlorophenol moiety had no valuable interactions in the binding pocket. Thus, SAR studies investigating substitution at the 7-position showed that substitution with a hydroxyl group had the greatest increase in

potency. The desired Tyr693 residue interaction was then created through substitution at the 5-position of the pyrazolopyrimidine with heterocycles and alkyl chains of various sizes. Compound **53** showed the desired interaction with Tyr693, as well as no inhibition of CYP enzymes, low PGP efflux (net efflux ratio = 1.8), and high metabolic stability (0 mL/min/kg). Therefore, compound **53** was identified as a lead compound for future work in a new series of PDE10A inhibitors from Astellas Pharma.

2.3.2 Catechol O-methyltransferase

Catechol O-methyltransferase (COMT) catalyses the degradation of neurotransmitters such as dopamine and epinephrine, stopping their natural biological activity. In regions of the brain that have low concentrations of these neurotransmitters, COMT activation can prevent effective communication between cells. Therefore, in disease states characterised by low concentrations of neurotransmitters, such as dopamine and epinephrine, COMT inhibition shows promise as a therapeutic target to alleviate symptoms. The inhibition of COMT is theorised to abate some of the cognitive impairments and negative symptoms seen in schizophrenia patients (Apud and Weinberger, 2007; Akhtar et al., 2020).

COMT inhibitors have been successfully used in neurodegenerative disease as a therapeutic agent for treating Parkinson's disease (Kiss and Soares-da-Silva, 2014). However, these COMT inhibitors were rapidly metabolised and peripherally restricted, serving to protect the liver, rather than permeating into the CNS. Similarly, previous generations of COMT inhibitors also suffered from poor pharmacokinetic properties, generally resultant of phenolic metabolism in the



body (Tangphao et al., 1999; Wu et al., 2011). To distance themselves from these unfavourable molecules, Lerner et al. (2016) opted to take a fragment-based approach to identify a novel scaffold of COMT inhibitors. They set out to design competitive inhibitors of the co-factor S-adenosyl-L-methionine (SAM) binding pocket, thereby inhibiting COMT function. Initially, a fragment screen of 6000 Ro3 compliant molecules from an undisclosed library were screened in an SPR assay, yielding 600 hits. The identified fragment hits were then confirmed in a ten-point SPR concentration-response measurement, identifying 200 confirmed binders. The confirmed fragment binders were then reconfirmed again in a 1D ^1H -NMR study before being characterised in a 2D $^1\text{H}/^{15}\text{N}$ HSQC study to validate the binding interactions. The IC_{50} of all 600 hits was then determined in an enzymatic fluorescence-based assay. The results of all four assays were combined and considered, yielding four compounds that performed well in all assays. Of these four hits, compounds **54–56** were selected as lead compounds with a high LE (Figure 10A) and moderate potencies with IC_{50} ranging from 69 μ M to 85 μ M. It was noted that one of the four fragments was similar to known COMT inhibitors, so a co-crystallisation study was undertaken to confirm that the identified fragments bound in the SAM pocket. Furthermore, the co-crystallisation study provided detailed binding interactions that would inform the SAR, aiding in

the optimization process. Optimisation efforts produced compound **57** with a potent COMT inhibitor (IC_{50} = 0.075 μ M) Ro3-compliant lead molecule for future work. Ultimately, Lerner et al. (2016) developed a novel chemotype and subsequent lead molecules to target the SAM pocket of the COMT enzyme. Their fragment-based approach ensured that they could tailor their molecules to increase affinity for the SAM pocket whilst avoiding the metabolism that had plagued previous generations of COMT inhibitors.

2.3.3 Kynurenine aminotransferase

Kynurenine aminotransferase-II (KAT-II) is an enzyme involved in the metabolism of tryptophan. KAT-II converts kynurenine into kynurenic acid (KYNA), the latter being both an antagonist of N-methyl-D-aspartic acid (NMDA) and acetylcholine receptors (Plitman et al., 2017). The antagonism of both receptors, a result of KYNA, is linked to the cognitive impairments seen in schizophrenia (Koshy Cherian et al., 2014). Previous generations of KAT-II antagonists have demonstrated reduction in KYNA levels, whilst increasing levels of neurotransmitter signalling exhibited the potential to ameliorate cognitive impairments seen in schizophrenia (Pellicciari et al., 2006; Wu et al., 2014; Nematollahi et al., 2016).

Jayawickrama et al. (2018) utilised a fragment-based approach to identify a new class of KAT-II inhibitors and gain a new

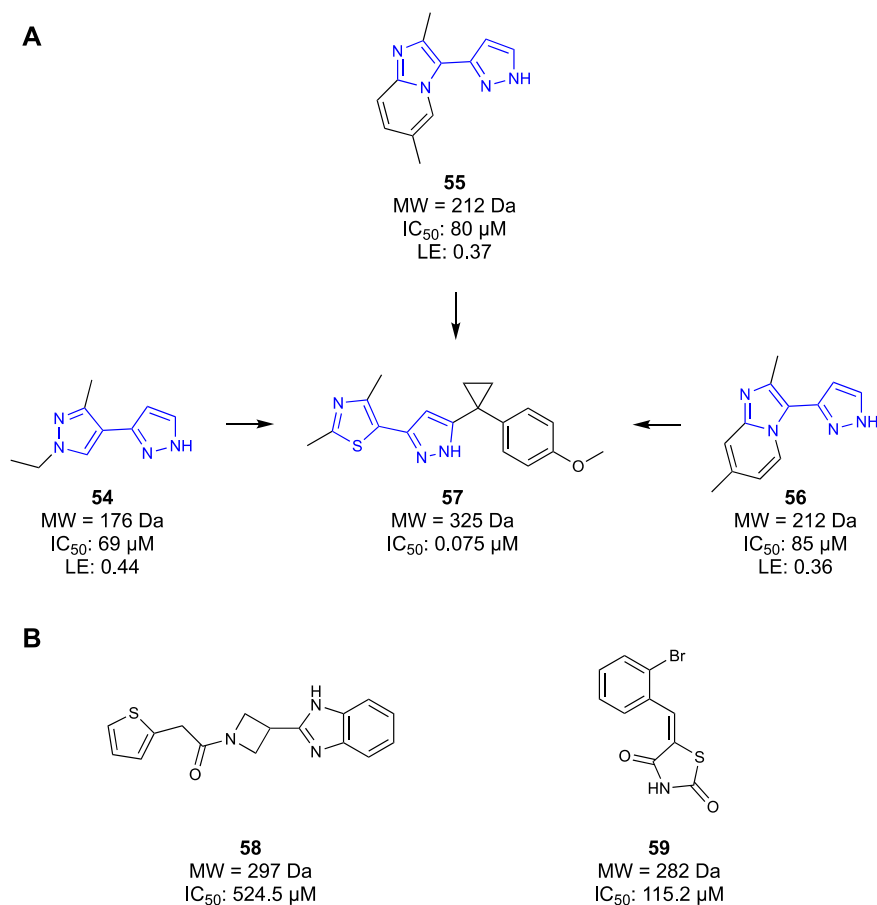


FIGURE 10

(A) COMT Fragments hits identified by Lerner et al. and the eventual lead compound synthesised. (B) KAT-II lead compounds identified by Jayawickrama et al.

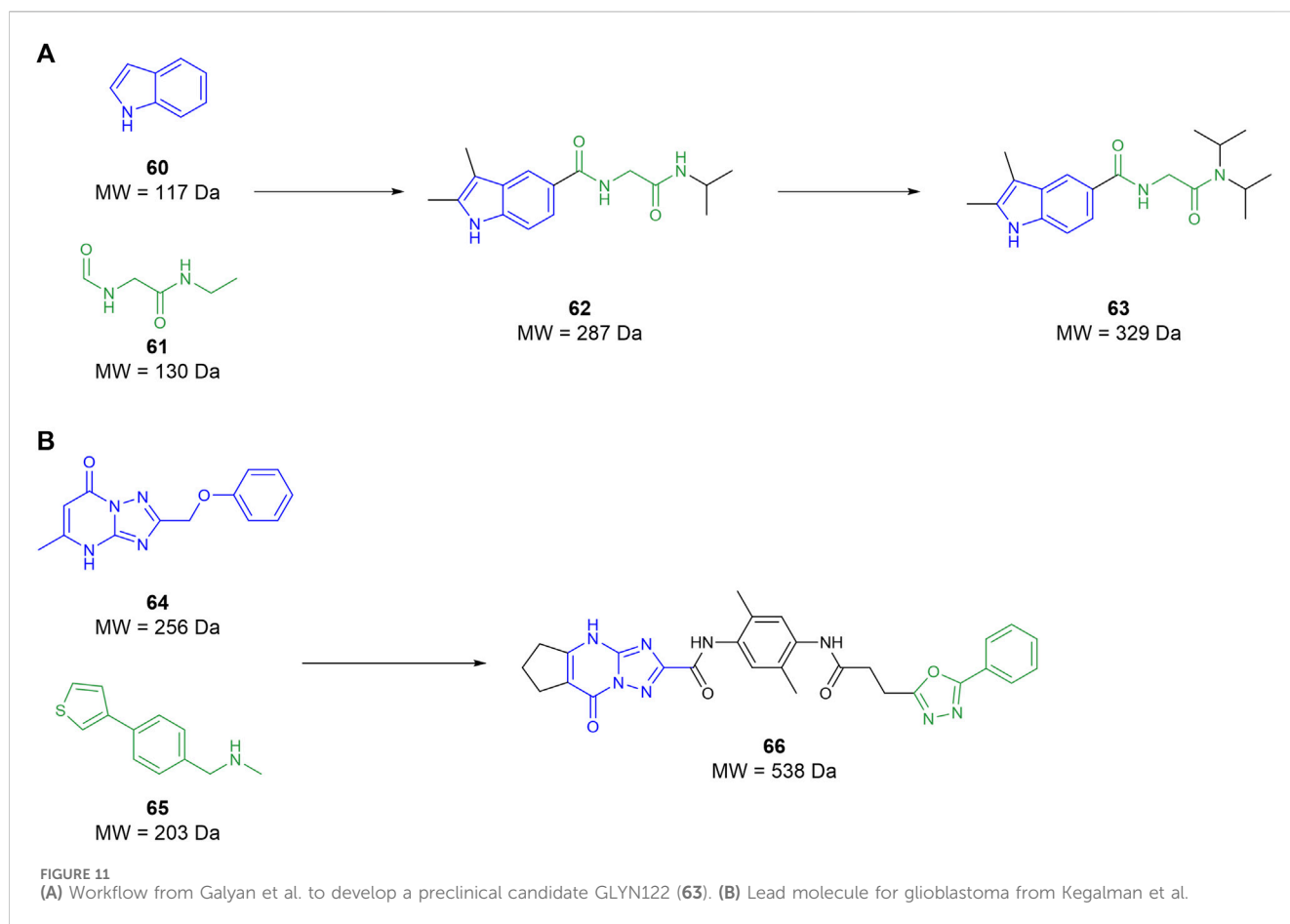
understanding of KAT-II inhibition. Initially, 1,000 compounds were screened from a structurally diverse in-house library, with an average molecular weight of 223 Da. Fragments were evaluated in an SPR assay, yielding 41 promising compounds that would undergo a concentration–response SPR to eliminate false positives. Only 18 compounds remained after the assay, all having confirmed affinity for the KAT-II binding site. The 18 compounds were screened in an HPLC inhibition assay wherein only three compounds had inhibitory effects. One of the three compounds was discarded due to similarities to another fragment, ultimately yielding two fragments as a base for further optimisation—**58** and **59** (Figure 10B). These two fragments also served as benchmarks for a computational study, evaluating the key binding interactions needed for potent KAT-II receptors. Jayawickrama et al. (2018) successfully discovered two new chemotypes of KAT-II inhibitors, serving as leads for the development of novel therapeutics.

2.4 Huntington's disease

Huntington's disease (Huntington's) is a neurodegenerative disease that causes the progressive decline of both cognitive and motor function, amongst other psychiatric and behavioural issues

(Bates et al., 2015). Huntington's is characterised by the expansion of a cytosine–adenine–guanosine repeat on the huntingtin gene (HTT). Huntington's is pathologically defined by this mutant huntingtin (mHTT) gene (Bates et al., 2015). Following the onset of symptoms, the progression of the disease is ultimately fatal, with a median survival time of 15–18 years (Caron et al., 1993). Currently, there are no therapies available to alleviate the symptoms or slow the progression of Huntington's. Ko et al. (2001) identified that antibody MW1 effectively binds to both HTT and mHTT. They suggested that MW1 binding to mHTT may prevent protein aggregation and serve as a therapeutic target for Huntington's (Ko et al., 2001). In 2007, a crystal structure of MW1 bound to mHTT was isolated by Li (2007) that would serve as the basis of future FBDD campaigns.

In 2022, Galyan et al. (2022) conducted an FBDD campaign informed by the crystal structure previously identified Li (2007). Initially, the known mHTT crystal structure was simplified down to a collection of surface feature points. This simplified structure was then compared to the protein-database bind (PDBbind) containing the crystal structures of 240,013 interactions between chemical fragments and protein environments. When a surface from the PDBbind database matched the surface feature points from the mHTT structure, the fragment from the former was mapped onto



the latter. This yielded 82 fragments that covered a reasonable portion of the protein–protein interaction between the MW1 antibody and the mHTT protein. These fragments were then used to screen 12 million compounds *in silico* from catalogues of unnamed commercial vendors. Compounds identified from the chemical vendors were considered compatible if they contained a substructure with atoms matching at least two-thirds of the atoms of the 82 selected fragments. Compounds that contained the same fragment substructure were selected based on size, with the larger molecules being discarded. This filter identified 2,937 suitable compounds to be examined, of which fragments **60** and **61** were notable upon re-examination as they comprise compound **62** (Figure 11A). The compounds that passed were then docked against the mHTT structure and ranked based on predicted binding energy. Compounds that shared a surface overlap with another fragment of over 66% were filtered out, keeping only the fragment with the best predicted binding ability. This reduced the suitable compounds from 2,937 to 67, wherein 40 compounds were purchased from vendors to begin testing. The purchased compounds were screened using SPR, identifying four compound hits that showed a concentration-response of binding, among which compound **62** was identified. Commercially available derivatives of the four initial hits that comply with Lipinski's Ro5 and a Tanimoto similarity score of 80% were purchased and screened using SPR. The SPR screen showed that two derivatives had improved potency relative to the initial four hits identified. The two second-round

hits were then used to identify similar analogues using the same similarity metrics defined above. However, this time, the filter included a polarity metric (TPSA < 75 Å) to improve BBB permeability, identifying 56 more candidates. The third-round SPR screen identified 20 compounds with improved affinity relative to the initial first-round hits. These compounds were then screened in a PAMPA BBB permeability assay in which all compounds were seen to be BBB-permeable. The top eight compounds from the PAMPA assay were then tested in an mHTT clearance assay, selecting compound **63** as a hit for further *in vivo* testing. This showed that **63** attenuated motor deficits and reduced mHTT expression in transgenic mice. However, the doses required to do so were too high for translation into human trials. These studies suggest that **63** is a good preclinical candidate for the treatment of Huntington's, but its potency must be improved to reduce the dose needed for human administration. Galyan et al. (2022) effectively demonstrate that fragment-assisted drug discovery and SAR by catalogue can rapidly improve the potency of drug candidates without the need for synthetic medicinal chemists.

2.5 Glioblastoma

Glioblastoma multiforme (GBM) is currently an incurable disease with an average survival time of 15 months and only

5.5% of patients surviving 5 years post-diagnosis. GBM is a fast-growing, aggressive brain tumour that affects the brain and spine and generally develops from glial cells. Melanoma differentiation-associated gene 9 (*mda-9*) is implicated in the invasion and metastatic signalling of GBM, amongst other cancers (Das et al., 2019). MDA-9 stimulates the invasion, angiogenesis, and tumour progression of GBM. Consequently, the inhibition of MDA-9 expression is theorised to decrease GBM invasion and improve patient outcomes (Das et al., 2019). A key characteristic of MDA-9 is the presence of two tandem PDZ domains (PDZ1 and PDZ2). These PDZ domains enable protein–protein interactions that stimulate pro-invasive signalling in GBM (Kegelman et al., 2017).

Kegelman et al. (2017) aimed to develop an MDA-9 inhibitor to prevent invasion by and metastasis of GBM as a supplement to radiotherapy. Utilising a ^{15}N NMR-based screening, 5,000 fragments were tested with a ^{15}N -labelled PDZ1/2 tandem domain from MDA-9. The screening yielded two fragment hits, **64** and **65**, which both interacted at the PDZ1 domain, while no suitable fragments interacted at the PDZ2 domain. A subsequent docking campaign suggested that both fragments needed substantial elaboration to effectively fill the binding pocket. The two fragments were linked, and the resulting compound was optimised through subsequent SAR studies yielding compound **66** (Figure 11B). This compound possesses micromolar affinity for PDZ1, with very slow clearance ($T_{1/2} \geq 9\text{ h}$) and, surprisingly, the ability to cross the BBB. Patients suffering from GBM have a defective blood–brain barrier, meaning that antigens that do not typically permeate the BBB can still pass through. As compound **66** is not traditionally CNS permeable, ($\text{MW} > 450$), it can exploit the imperfect BBB to exert its therapeutic effect. Subsequent *in vivo* assays suggest that **66** is a radiosensitizer and is useful as an adjunct to radiotherapy. Ultimately, Kegelman et al. (2017) utilised FBDD to create a new class of small molecule drugs to target GBM and other advanced, targeted brain cancers.

2.6 Neuroinflammation

Neuroinflammation is an incredibly complex phenomenon that can be attributed to a variety of stimuli. As neuroinflammation can be due to so many causes, the context of the inflammation must be considered. Acute neuroinflammation can be neuroprotective, repairing or rebuilding the brain post injury (DiSabato et al., 2016). However, chronic neuroinflammation is almost always detrimental to the brain (DiSabato et al., 2016). Given the delicate environment of the CNS, developing effective therapeutics for the treatment of neuroinflammation is extremely challenging.

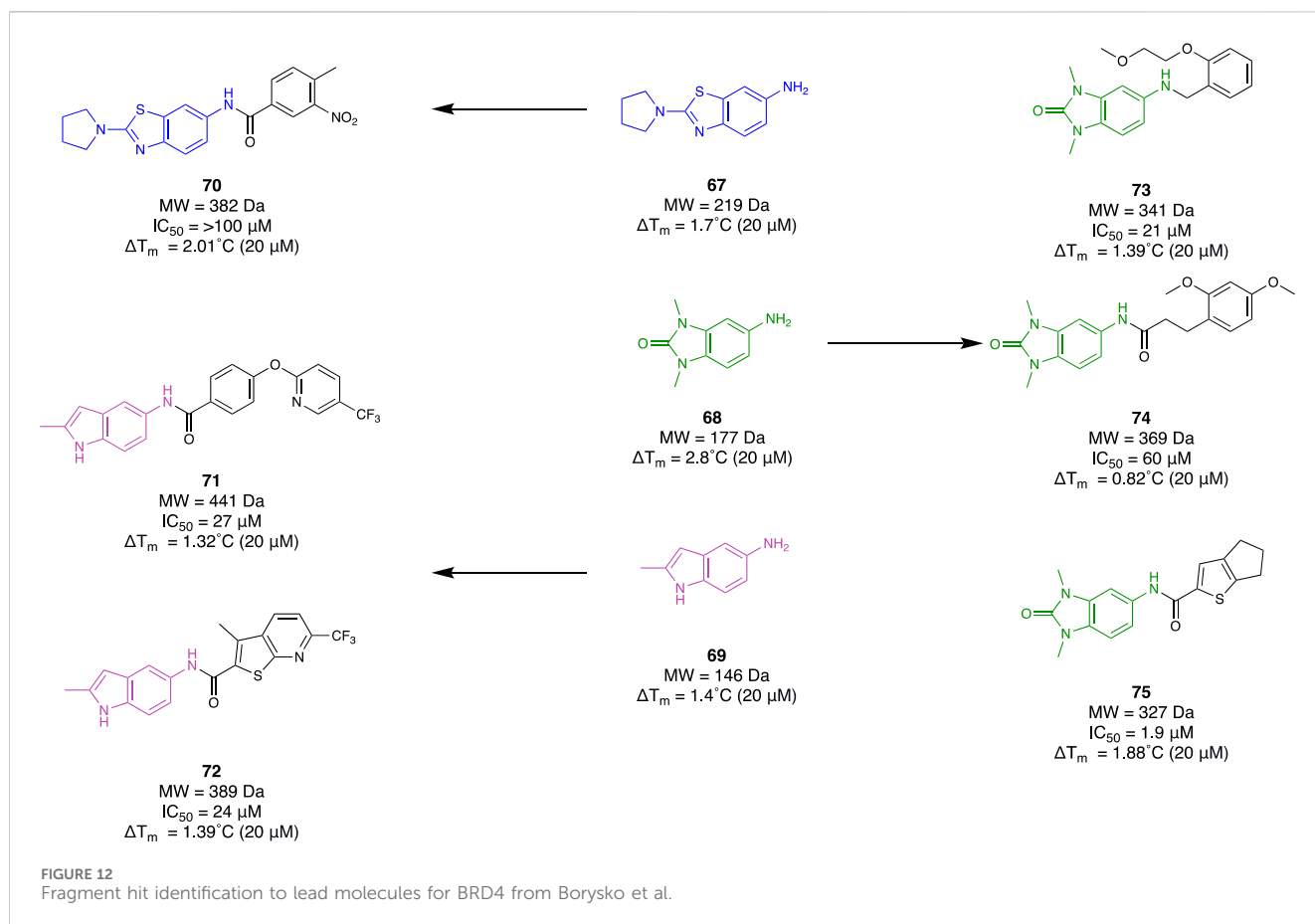
Bromodomain and extra-terminal domain (BET) protein has been implicated as playing a major role in the transcriptional regulation of the inflammatory response. There are four mammalian members (BRD2, BRD3, BRD4, and BRDT). Understanding the mechanistic behaviour of BET proteins has been of great importance in revealing potential novel therapeutics for neuroinflammation. Borysko et al. (2018) demonstrated a fragment-based approach by using “SAR by catalogue” for BRD4. They employed an Enamine Ro3-compliant fragment collection for 7450 compounds. These underwent solubility confirmation with

DMSO at 200 mM, a 2D fingerprint-based diversity filtering followed by visual inspection, resulting in a group of 3,695 fragments. Subsequent TSA was conducted to determine their mean thermal shifting value (ΔT_m) using a recombinant, truncated His-tagged bromodomain 1 of BRD4. Observing fragments exhibiting positive thermal shifting and negative thermal shifting, 79 primary hits were selected (48 positive and 31 negative) which included fragments **67–69** (Figure 12). Utilising this set of fragments, a substructure search was completed within the Enamine REAL database to identify hit molecules that could be synthetically accessed within 3–4 weeks to improve time efficiency for their SAR study. Through physicochemical evaluation, fingerprint-based diversity selection, and visual inspection, 3,200 compounds derived from the group of hit fragments were selected for screening and classed as “active” compounds. The same process was repeated with the class of “non-hit” fragments to also obtain a collection of 3,200 compounds that were grouped as “non-active” compounds. Following this, a random selection of 3,200 compounds was made within Enamine’s stock screening collection with MW and cLogP comparable to the “active” compounds. TSA was conducted with these three groups to obtain 61 hits (39 from the “active” group, 10 from the “non-active” group, and 12 from the “random” group). Subsequently, a fluorescence resonance energy transfer assay against BRD4 found 18 compounds that exhibited at least 50% inhibitory activity. Six molecules, **70–75**, derived from the group of “active” fragments saw greater than 60% inhibitory activity whilst also having a positive mean thermal shift value (Figure 12). The workflow of this study demonstrated how a fragment-based campaign with SAR by catalogue can be an efficient pipeline for early drug discovery. Not only was a group of active molecules for BRD4 identified, but it demonstrated the enhanced efficiency of utilising FBDD to first identify suitable scaffolds.

3 Perspective

FBDD has been effectively utilised to develop hit and lead molecules, both independently and as an adjunct to traditional drug design methods. Each of the examples discussed follows the workflow of identifying a hit/lead molecule and subsequent optimisation using knowledge gained throughout the FBDD process. This results in a more streamlined process of fragment elaboration and, therefore, a quicker turnaround time in drug development.

However, like all methods, FBDD is still bound by limitations that prevent it from being the gold standard of the drug discovery process. As demonstrated through these studies, FBDD relies heavily on x-ray crystallography to provide data on the binding modes of the fragment to subsequently direct synthetic elaboration towards a lead molecule. Understanding where each fragment binds and what type of interaction is responsible for the binding event is crucial to constructing a molecule that complements the domain of the binding pocket. Unfortunately, this poses a disadvantage to certain targets that are “un-crystallisable” or difficult to crystallise, such as membrane-bound receptors (Carpenter et al., 2008). The flexibility and instability of these proteins lead to issues with expression, solubility, purification, and subsequent



crystallisation. As a result, membrane-bound targets that cannot be crystallized must use predicted structures rather than the actual target, effectively eliminating the advantages of FBDD.

It is also challenging to employ FBDD to target protein misfolding-derived neurodegenerative diseases. As FBDD relies on a target with a known morphology, processes that have an unknown or ever-changing morphology are not suitable in fragment-based campaigns (Sweeney et al., 2017). For these cases, a traditional target-specific screen may be a more appropriate approach for developing therapeutics. This is highlighted in Aβ, where the pathogenic species initially proposed in AD was fibrils and plaques but now is believed to be aggregation intermediates such as oligomers and soluble protofibrils (Hampel et al., 2021). Chaperones, such as heat shock proteins (Hsp), and particularly Hsp70, are a popular alternative target class for therapeutic intervention in protein misfolding diseases. Although Hsps are considered “druggable” targets, their binding pockets are generally located at a protein–protein interface (PPI), which is extremely challenging to drug. PPIs comprise many small interactions called “hot spots”, wherein a small molecule can bind. Fortunately, FBDD is inherently good at identifying and mapping these hot spots. For this reason, fragment-based approaches have achieved success in regulating PPIs for human disease therapy, with examples such as *venetoclax* and *sotorasib* as FDA-approved PPI modulators.

Furthermore, fragment-based studies have consistently been limited to target-based studies. Unfortunately, the last 150 years has demonstrated that only 9.4% of small-molecule drugs have been identified through a target-based approach (Sadri, 2023). When exploring the list of FDA-approved drugs, many exhibit activity at more than one target, suggesting that the therapeutic effect may be the result of more than just the modulation of one key target. For example, physical changes to the brain which lead to AD include amyloid plaques, neurofibrillary tangles, and inflammation (Selkoe, 1991). Targeting the genesis of these physical changes by inhibiting Aβ generation, promoting Aβ clearance from the brain, or inhibiting the formation of tau tangles all aim to slow the inflammatory response (Yoon and AhnJo, 2012). However, we now know that these are all examples of treating a manifestation of the disease, rather than the underlying cause. This is not to say that target-based approaches cannot yield a drug. Such approaches are hypothesis-driven; however, phenotypic studies rely on measures of responses (Swinney, 2013). Nevertheless, the ambiguity of where to target and the nature of the target creates a challenge during hit identification and optimisation when utilising FBDD. Although conventional studies such as HTS suffer from similar limitations, they excel in this area, such as the HTS library of drug-like molecules which can produce a tangible response in a phenotypic screening which, unfortunately, is impossible for fragments.

Most FBDD campaigns utilise a combination of various biophysical screenings to determine and validate fragment hits. These methods generally provide a binding affinity value which is improved as the hits are elaborated. However, binding affinity and binding mode are properties that do not always correlate linearly with a target response. Unfortunately, due to the small size of the fragment, biochemical data may be difficult to obtain. To identify any correlation between binding affinity value and activity, some studies, such as the examples discussed earlier, utilise a biochemical assay as soon as possible to obtain values in the milli- to micromolar range, or to identify maximum inhibition at a particular concentration. This will not only probe the target more efficiently but could potentially improve the physicochemical properties of the molecule by omitting unnecessary customisation.

The well-considered curation of fragment libraries is advantageous for efficiently sampling chemical space. Many libraries, especially those highlighted earlier, demonstrate a lack of sp^3 -rich compounds. Drug discovery has long had issues with tackling the spatial arrangement of a pharmacophore group to enhance the properties of the molecule (Meutermans et al., 2006). Sp^3 fragments are frequently omitted from libraries to prevent synthetic inaccessibility from being a barrier to efficient lead compound development (Caplin and Foley, 2021). Therefore, the utilisation of sp^3 fragments can build greater diversity into libraries whilst also exploring new and potentially chiral chemical space. Consequently, sp^3 -rich molecules are generally considered less rigid, being able to cover a broader chemical space than their typically planar aromatic counterparts. This lack of rigidity and planarity can be advantageous in drug design, allowing a molecule to more broadly fill out a binding pocket, exemplified by carbohydrates and spirocycles (Meutermans et al., 2006; Svecizer et al., 2019). Limiting the scope of potential fragments can hinder the development of superior lead molecules.

FBDD represents growth towards a new age of drug discovery. More than a complementary approach, it has emerged as a pivotal tool to overcome limitations that have proven difficult with more conventional methods. By identifying optimal scaffolds followed by a promising lead with minimal elaboration, FBDD is capable of fulfilling the stringent criteria for developing CNS-tailored small molecules. It reveals optimal interactions to offer crucial insights for designing superior molecules. FBDD has the potential to reshape the drug discovery landscape, setting new standards for pharmaceutical development.

References

- Abad-Zapatero, C., and Metz, J. T. (2005). Ligand efficiency indices as guideposts for drug discovery. *Drug Discov. Today* 10, 464–469. doi:10.1016/S1359-6446(05)03386-6
- Ahmed, F. E., Wiley, J. E., Weider, D. A., Bonnerup, C., and Mota, H. (2010). Surface plasmon resonance (SPR) spectrometry as a tool to analyze nucleic acid–protein interactions in crude cellular extracts. *Cancer Genomics - Proteomics* 7, 303–309.
- Akhtar, M. J., Yar, M. S., Grover, G., and Nath, R. (2020). Neurological and psychiatric management using COMT inhibitors: a review. *Bioorg. Chem.* 94, 103418. doi:10.1016/j.bioorg.2019.103418
- Alqahtani, M. S., Kazi, M., Alsenaidy, M. A., and Ahmad, M. Z. (2021). Advances in oral drug delivery. *Front. Pharmacol.* 12, 618411. doi:10.3389/fphar.2021.618411
- Amin, H. S., Parikh, P. K., and Ghate, M. D. (2021). Medicinal chemistry strategies for the development of phosphodiesterase 10A (PDE10A) inhibitors - an update of recent progress. *Eur. J. Med. Chem.* 214, 113155. doi:10.1016/j.ejmech.2021.113155
- Andersen, J. L., Lindberg, S., Langgård, M., Maltas, P. J., Rønn, L. C. B., Bundgaard, C., et al. (2017). The identification of novel acid isostere based inhibitors of the VPS10P family sorting receptor Sortilin. *Bioorg. Med. Chem. Lett.* 27, 2629–2633. doi:10.1016/j.bmcl.2017.02.028
- Apud, J. A., and Weinberger, D. R. (2007). Treatment of cognitive deficits associated with schizophrenia. *CNS Drugs* 21, 535–557. doi:10.2165/00023210-200721070-00002
- Bates, G. P., Dorsey, R., Gusella, J. F., Hayden, M. R., Kay, C., Leavitt, B. R., et al. (2015). Huntington disease. *Nat. Rev. Dis. Primer* 1, 15005–15021. doi:10.1038/nrdp.2015.5
- Benner, B., Good, L., Quiroga, D., Schultz, T. E., Kassem, M., Carson, W. E., et al. (2020). Pexidartinib, a novel small molecule CSF-1R inhibitor in use for tenosynovial giant cell tumor: a systematic review of pre-clinical and clinical development. *Drug Des. devel. Ther.* 14, 1693–1704. doi:10.2147/DDDT.S253232
- Bienstock, R. J. (2011). "Overview: fragment-based drug design," in *Library design, search methods, and applications of fragment-based drug design, ACS symposium series* (American Chemical Society), 1–26. doi:10.1021/bk-2011-1076.ch001

Author contributions

BC: Conceptualization, writing–original draft, review and editing. NL: writing–original draft, review and editing. WT: writing–review and editing. JJ: writing–review and editing. GS: writing–review and editing. WM: writing–review and editing. AM: writing–review and editing. MK: conceptualization, supervision, and writing–review and editing.

Funding

The author(s) declare that financial support was received for the research, authorship, and/or publication of this article. This work was supported by the ARC Industrial Transformation Training Centre for Fragment-Based Design (Project ID IC180100021). NL is a recipient of an Australian Government Research Training Program Award scholarship. We also wish to acknowledge the University of Sydney's Drug Discovery Initiative for supporting a Postdoctoral Research Fellowship for AM.

Conflict of interest

Author GS was employed by CSIRO Manufacturing. Author WM was employed by Vast Bioscience.

The remaining authors declare that the research was conducted in the absence of any commercial or financial relationships that could be construed as a potential conflict of interest.

The author(s) declared that they were an editorial board member of Frontiers at the time of submission. This had no impact on the peer review process and the final decision.

Publisher's note

All claims expressed in this article are solely those of the authors and do not necessarily represent those of their affiliated organizations, or those of the publisher, the editors, and the reviewers. Any product that may be evaluated in this article, or claim that may be made by its manufacturer, is not guaranteed or endorsed by the publisher.

- Blay, V., Tolani, B., Ho, S. P., and Arkin, M. R. (2020). High-Throughput Screening: today's biochemical and cell-based approaches. *Drug Discov. Today* 25, 1807–1821. doi:10.1016/j.drudis.2020.07.024
- Bollag, G., Tsai, J., Zhang, J., Zhang, C., Ibrahim, P., Nolop, K., et al. (2012). Vemurafenib: the first drug approved for BRAF-mutant cancer. *Nat. Rev. Drug Discov.* 11, 873–886. doi:10.1038/nrd3847
- Borysko, P., Moroz, Y. S., Vasylychenko, O. V., Hurmach, V. V., Starodubtseva, A., Stefanishena, N., et al. (2018). Straightforward hit identification approach in fragment-based discovery of bromodomain-containing protein 4 (BRD4) inhibitors. *Bioorg. Med. Chem.* 26, 3399–3405. doi:10.1016/j.bmc.2018.05.010
- Brown, D. G., Wobst, H. J., Kapoor, A., Kenna, L. A., and Southall, N. (2022). Clinical development times for innovative drugs. *Nat. Rev. Drug Discov.* 21, 793–794. doi:10.1038/d41573-021-00190-9
- Callaway, E. (2020). Revolutionary cryo-EM is taking over structural biology. *Nature* 578, 201. doi:10.1038/d41586-020-00341-9
- Caplin, M. J., and Foley, D. J. (2021). Emergent synthetic methods for the modular advancement of sp³-rich fragments. *Chem. Sci.* 12, 4646–4660. doi:10.1039/D1SC00161B
- Caron, N. S., Wright, G. E., and Hayden, M. R. (1993). "Huntington disease," in *GeneReviews*®. Editors M. P. Adam, J. Feldman, G. M. Mirzaa, R. A. Pagon, S. E. Wallace, L. J. Bean, et al. (Seattle, Seattle (WA): University of Washington).
- Carpenter, E. P., Beis, K., Cameron, A. D., and Iwata, S. (2008). Overcoming the challenges of membrane protein crystallography. *Curr. Opin. Struct. Biol.* 18, 581–586. doi:10.1016/j.sbi.2008.07.001
- Chan, D. S.-H., Whitehouse, A. J., Coyne, A. G., and Abell, C. (2017). Mass spectrometry for fragment screening. *Essays Biochem.* 61, 465–473. doi:10.1042/EBC20170071
- Chappie, T., Humphrey, J., Menniti, F., and Schmidt, C. (2009). PDE10A inhibitors: an assessment of the current CNS drug discovery landscape. *Curr. Opin. Drug Discov. Dev.* 12, 458–467.
- Chen, X., Xu, W., Wang, K., Mo, M., Zhang, W., Du, L., et al. (2015). Discovery of a novel series of imidazo[1,2-a]pyrimidine derivatives as potent and orally bioavailable lipoprotein-associated phospholipase A2 inhibitors. *J. Med. Chem.* 58, 8529–8541. doi:10.1021/acs.jmedchem.5b01024
- Chino, A., Seo, R., Amano, Y., Namatame, I., Hamaguchi, W., Honbou, K., et al. (2018). Fragment-based discovery of pyrimido[1,2-B]indazole PDE10A inhibitors. *Chem. Pharm. Bull. (Tokyo)* 66, 286–294. doi:10.1248/cpb.c17-00836
- Congreve, M., Carr, R., Murray, C., and Jhoti, H. (2003). A 'Rule of Three' for fragment-based lead discovery? *Drug Discov. Today* 8, 876–877. doi:10.1016/S1359-6446(03)02831-9
- Cox, C. D., Hostettler, E. D., Flores, B. A., Evelhoch, J. L., Fan, H., Gantert, L., et al. (2015). Discovery of [11C]MK-8193 as a PET tracer to measure target engagement of phosphodiesterase 10A (PDE10A) inhibitors. *Bioorg. Med. Chem. Lett.* 25, 4893–4898. doi:10.1016/j.bmcl.2015.05.080
- Cuellar, M. E., Yang, M., Karavadi, S., Zhang, Y.-Q., Zhu, H., Sun, H., et al. (2023). An electrophilic fragment screening for the development of small molecules targeting caspase-2. *Eur. J. Med. Chem.* 259, 115632. doi:10.1016/j.ejmech.2023.115632
- Das, S. K., Sarkar, D., Cavenee, W. K., Emdad, L., and Fisher, P. B. (2019). Rethinking glioblastoma therapy: MDA-9/Syntenin targeted small molecule. *ACS Chem. Neurosci.* 10, 1121–1123. doi:10.1021/acschemneuro.9b00016
- Di Carluccio, C., Forgione, M. C., Martini, S., Berti, F., Molinaro, A., Marchetti, R., et al. (2021). Investigation of protein-ligand complexes by ligand-based NMR methods. *Carbohydr. Res.* 503, 108313. doi:10.1016/j.carres.2021.108313
- DiMasi, J. A., Grabowski, H. G., and Hansen, R. W. (2016). Innovation in the pharmaceutical industry: new estimates of R&D costs. *J. Health Econ.* 47, 20–33. doi:10.1016/j.jhealeco.2016.01.012
- DiSabato, D., Quan, N., and Godbout, J. P. (2016). Neuroinflammation: the devil is in the details. *J. Neurochem.* 139, 136–153. doi:10.1111/jnc.13607
- Doody, R. S., Demirovic, J., Ballantyne, C. M., Chan, W., Barber, R., Powell, S., et al. (2015). Lipoprotein-associated phospholipase A2, homocysteine, and Alzheimer's disease. *Alzheimers Dement. Diagn. Assess. Dis. Monit.* 1, 464–471. doi:10.1016/j.dadm.2015.08.001
- Dueñas, M. E., Peltier-Heap, R. E., Leveridge, M., Annan, R. S., Büttner, F. H., and Trost, M. (2022). Advances in high-throughput mass spectrometry in drug discovery. *EMBO Mol. Med.* 15, e14850. doi:10.15252/emmm.202114850
- Galyan, S. M., Ewald, C. Y., Jalencas, X., Masrani, S., Meral, S., and Mestres, J. (2022). Fragment-based virtual screening identifies a first-in-class preclinical drug candidate for Huntington's disease. *Sci. Rep.* 12, 19642. doi:10.1038/s41598-022-21900-2
- Gao, S., Song, L., Claff, T., Woodson, M., Sylvester, K., Jing, L., et al. (2022). Discovery and crystallographic studies of nonpeptidic piperazine derivatives as covalent SARS-CoV-2 main protease inhibitors. *J. Med. Chem.* 65, 16902–16917. doi:10.1021/acs.jmedchem.2c01716
- Greenblat, C. (2023). Dementia [WWW document]. URL <https://www.who.int/news-room/fact-sheets/detail/dementia> (Accessed 1.31.24).
- Gribkoff, V. K., and Kaczmarek, L. K. (2017). The need for new approaches in CNS drug discovery: why drugs have failed, and what can be done to improve outcomes. *Neuropharmacology* 120, 11–19. doi:10.1016/j.neuropharm.2016.03.021
- Hampel, H., Hardy, J., Blennow, K., Chen, C., Perry, G., Kim, S. H., et al. (2021). The amyloid- β pathway in Alzheimer's disease. *Mol. Psychiatry* 26, 5481–5503. doi:10.1038/s41380-021-01249-0
- Hartshorn, M. J., Murray, C. W., Cleasby, A., Frederickson, M., Tickle, I. J., and Jhoti, H. (2005). Fragment-based lead discovery using X-ray crystallography. *J. Med. Chem.* 48, 403–413. doi:10.1021/jm0495778
- Hartung, I. V., Huck, B. R., and Crespo, A. (2023). Rules were made to be broken. *Nat. Rev. Chem.* 7, 3–4. doi:10.1038/s41570-022-00451-0
- Huang, F., Wang, K., and Shen, J. (2020). Lipoprotein-associated phospholipase A2: the story continues. *Med. Res. Rev.* 40, 79–134. doi:10.1002/med.21597
- Hughes, J., Rees, S., Kalindjian, S., and Philpott, K. (2011). Principles of early drug discovery. *Br. J. Pharmacol.* 162, 1239–1249. doi:10.1111/j.1476-5381.2010.01127.x
- Jafari, R., Almqvist, H., Axelsson, H., Ignatushchenko, M., Lundbäck, T., Nordlund, P., et al. (2014). The cellular thermal shift assay for evaluating drug target interactions in cells. *Nat. Protoc.* 9, 2100–2122. doi:10.1038/nprot.2014.138
- Jayawickrama, G. S., Nematollahi, A., Sun, G., and Church, W. B. (2018). Fragment screening of human kynurenine aminotransferase-II. *SLAS Discov.* 23, 511–519. doi:10.1177/2472555218764620
- Jin, C. F., Wang, Z. Z., Chen, K. Z., Xu, T. F., and Hao, G. F. (2020). Computational fragment-based design facilitates discovery of potent and selective monoamine oxidase-B (MAO-B) inhibitor. *J. Med. Chem.* 63, 15021–15036. doi:10.1021/acs.jmedchem.0c01663
- Kathman, S. G., and Statsyuk, A. V. (2016). Covalent tethering of fragments for covalent probe discovery. *MedChemComm* 7, 576–585. doi:10.1039/c5md00518c
- Kegelman, T. P., Wu, B., Das, S. K., Talukdar, S., Beckta, J. M., Hu, B., et al. (2017). Inhibition of radiation-induced glioblastoma invasion by genetic and pharmacological targeting of MDA-9/Syntenin. *Proc. Natl. Acad. Sci. U. S. A.* 114, 370–375. doi:10.1073/pnas.1616100114
- Keserü, G. M., Erlanson, D. A., Ferenczy, G. G., Hann, M. M., Murray, C. W., and Pickett, S. D. (2016). Design principles for fragment libraries: maximizing the value of learnings from pharma fragment-based drug discovery (FBDD) programs for use in academia. *J. Med. Chem.* 59, 8189–8206. doi:10.1021/acs.jmedchem.6b00197
- Kirsch, P., Hartman, A. M., Hirsch, A. K. H., and Empting, M. (2019). Concepts and core principles of fragment-based drug design. *Molecules* 24, 4309. doi:10.3390/molecules24234309
- Kiss, L. E., and Soares-da-Silva, P. (2014). Medicinal chemistry of catechol O-methyltransferase (COMT) inhibitors and their therapeutic utility. *J. Med. Chem.* 57, 8692–8717. doi:10.1021/jm500572b
- Ko, J., Ou, S., and Patterson, P. H. (2001). New anti-huntingtin monoclonal antibodies: implications for huntingtin conformation and its binding proteins. *Brain Res. Bull. Triple Repeat Dis.* 56, 319–329. doi:10.1016/S0361-9230(01)00599-8
- Koshy Cherian, A., Gritton, H., Johnson, D. E., Young, D., Kozak, R., and Sarter, M. (2014). A systemically-available kynurenine aminotransferase II (KAT II) inhibitor restores nicotine-evoked glutamatergic activity in the cortex of rats. *Neuropharmacology* 82, 41–48. doi:10.1016/j.neuropharm.2014.03.004
- Lanman, B. A., Allen, J. R., Allen, J. G., Amegadzie, A. K., Ashton, K. S., Booker, S. K., et al. (2020). Discovery of a covalent inhibitor of KRAS^{G12C} (AMG 510) for the treatment of solid tumors. *J. Med. Chem.* 63, 52–65. doi:10.1021/acs.jmedchem.9b01180
- Laskay, Ü. A., Lobas, A. A., Szrentić, K., Gorshkov, M. V., and Tsybin, Y. O. (2013). Proteome digestion specificity analysis for rational design of extended bottom-up and middle-down proteomics experiments. *J. Proteome Res.* 12, 5558–5569. doi:10.1021/pr400522h
- Layton, M. E., Kern, J. C., Harting, T. J., Shipe, W. D., Raheem, I., Kandebo, M., et al. (2023). Discovery of MK-8189, a highly potent and selective PDE10A inhibitor for the treatment of schizophrenia. *J. Med. Chem.* 66, 1157–1171. doi:10.1021/acs.jmedchem.2c01521
- Lerner, C., Jakob-Roetne, R., Buettelmann, B., Ehler, A., Rudolph, M., and Sarmiento, R. M. R. (2016). Design of potent and druglike nonphenolic inhibitors for catechol O-methyltransferase derived from a fragment screening approach targeting the S-adenosyl-1-methionine pocket. *J. Med. Chem.* 59, 10163–10175. doi:10.1021/acs.jmedchem.6b00927
- Li, P. (2007). Crystal structure of Fv polyglutamine complex. *Protein Data Bank*, <https://doi.org/doi:10.2210/pdb2otu/pdb>
- Li, Q. (2020). Application of fragment-based drug discovery to versatile targets. *Front. Mol. Biosci.* 7, 180–213. doi:10.3389/fmolb.2020.00180
- Li, X., Feng, X., Sun, X., Hou, N., Han, F., and Liu, Y. (2022). Global, regional, and national burden of Alzheimer's disease and other dementias, 1990–2019. *Front. Aging Neurosci.* 14, 937486. doi:10.3389/fnagi.2022.937486
- Lipinski, C. A., Lombardo, F., Dominy, B. W., and Feeney, P. J. (2001). Experimental and computational approaches to estimate solubility and permeability in drug discovery and development settings. *Adv. Drug Deliv. Rev.* 64, 4–17. doi:10.1016/j.addr.2012.09.019
- Liu, Q., Huang, F., Yuan, X., Wang, K., Zou, Y., Shen, J., et al. (2017). Structure-guided discovery of novel, potent, and orally bioavailable inhibitors of lipoprotein-associated phospholipase A2. *J. Med. Chem.* 60, 10231–10244. doi:10.1021/acs.jmedchem.7b01530

- Maher-Edwards, G., De'Ath, J., Barnett, C., Lavrov, A., and Lockhart, A. (2015). A 24-week study to evaluate the effect of rilapladib on cognition and cerebrospinal fluid biomarkers of Alzheimer's disease. *Alzheimers Dement. Transl. Res. Clin. Interv.* 1, 131–140. doi:10.1016/j.trci.2015.06.003
- Mahy, W., Patel, M., Steadman, D., Woodward, H. L., Atkinson, B. N., Svensson, F., et al. (2020a). Screening of a custom-designed acid fragment library identifies 1-phenylpyrroles and 1-phenylpyrrolidines as inhibitors of Notum carboxylesterase activity. *J. Med. Chem.* 63, 9464–9483. doi:10.1021/acs.jmedchem.0c00660
- Mahy, W., Willis, N. J., Zhao, Y., Woodward, H. L., Svensson, F., Siphthorp, J., et al. (2020b). 5-Phenyl-1,3,4-oxadiazol-2(3-H)-ones are potent inhibitors of Notum carboxylesterase activity identified by the optimization of a crystallographic fragment screening hit. *J. Med. Chem.* 63, 12942–12956. doi:10.1021/acs.jmedchem.0c01391
- McCutcheon, R. A., Reis Marques, T., and Howes, O. D. (2020). Schizophrenia - an overview. *JAMA Psychiatry* 77, 201–210. doi:10.1001/jamapsychiatry.2019.3360
- Meutermans, W., Le, G. T., and Becker, B. (2006). Carbohydrates as scaffolds in drug discovery. *ChemMedChem* 1, 1164–1194. doi:10.1002/cmdc.200600150
- Mikitsh, J. L., and Chacko, A.-M. (2014). Pathways for small molecule delivery to the central nervous system across the blood-brain barrier. *Perspect. Med. Chem.* 6, PMC.S13384–24. doi:10.4137/PMC.S13384
- Murray, C. W., Newell, D. R., and Angibaud, P. (2019). A successful collaboration between academia, biotech and pharma led to discovery of erdafitinib, a selective FGFR inhibitor recently approved by the FDA. *MedChemComm* 10, 1509–1511. doi:10.1039/C9MD90044F
- Navratilova, I., and Hopkins, A. L. (2010). Fragment screening by surface plasmon resonance. *ACS Med. Chem. Lett.* 1, 44–48. doi:10.1021/ml900002k
- Nematollahi, A., Sun, G., Jayawickrama, G., Hanrahan, J., and Church, W. (2016). Study of the activity and possible mechanism of action of a reversible inhibitor of recombinant human KAT-2: a promising lead in neurodegenerative and cognitive disorders. *Molecules* 21, 856. doi:10.3390/molecules21070856
- Palomer, E., Buechler, J., and Salinas, P. C. (2019). Wnt signaling deregulation in the aging and Alzheimer's brain. *Front. Cell. Neurosci.* 13, 227. doi:10.3389/fncel.2019.00227
- Pardridge, W. M. (2020). Treatment of Alzheimer's disease and blood-brain barrier drug delivery. *Pharmaceuticals* 13, 394. doi:10.3390/ph13110394
- Pellicciari, R., Rizzo, R. C., Costantino, G., Marinozzi, M., Amori, L., Guidetti, P., et al. (2006). Modulators of the kynurenine pathway of tryptophan metabolism: synthesis and preliminary biological evaluation of (S)-4-(Ethylsulfonyl)benzoylalanine, a potent and selective kynurenine aminotransferase II (KAT II) inhibitor. *ChemMedChem* 1, 528–531. doi:10.1002/cmdc.200500095
- Petros, A. M., Korepanova, A., Jakob, C. G., Qiu, W., Panchal, S. C., Wang, J., et al. (2019). Fragment-based discovery of an apolipoprotein E4 (apoE4) stabilizer. *J. Med. Chem.* 62, 4120–4130. doi:10.1021/acs.jmedchem.9b00178
- Plitman, E., Iwata, Y., Caravaggio, F., Nakajima, S., Chung, J. K., Gerretsen, P., et al. (2017). Kynurenine acid in schizophrenia: a systematic review and meta-analysis. *Schizophr. Bull.* 43, 764–777. doi:10.1093/schbul/sbw221
- Raheem, I. T., Breslin, M. J., Fandozzi, C., Fuerst, J., Hill, N., Huszar, S., et al. (2012). Discovery of tetrahydropyridopyrimidine phosphodiesterase 10A inhibitors for the treatment of schizophrenia. *Bioorg. Med. Chem. Lett.* 22, 5903–5908. doi:10.1016/j.bmcl.2012.07.072
- Raheem, I. T., Schreier, J. D., Fuerst, J., Gantert, L., Hostetler, E. D., Huszar, S., et al. (2016). Discovery of pyrazolopyrimidine phosphodiesterase 10A inhibitors for the treatment of schizophrenia. *Bioorg. Med. Chem. Lett.* 26, 126–132. doi:10.1016/j.bmcl.2015.11.013
- Resnick, E., Bradley, A., Gan, J., Douangamath, A., Krojer, T., Sethi, R., et al. (2019). Rapid covalent-probe discovery by electrophile-fragment screening. *J. Am. Chem. Soc.* 141, 8951–8968. doi:10.1021/jacs.9b02822
- Sadri, A. (2023). Is target-based drug discovery efficient? Discovery and “off-target” mechanisms of all drugs. *J. Med. Chem.* 66, 12651–12677. doi:10.1021/acs.jmedchem.2c01737
- Schoepfer, J., Jahnke, W., Berellini, G., Buonamici, S., Cotesta, S., Cowan-Jacob, S. W., et al. (2018). Discovery of Asciminib (ABL001), an allosteric inhibitor of the tyrosine kinase activity of BCR-ABL1. *J. Med. Chem.* 61, 8120–8135. doi:10.1021/acs.jmedchem.8b01040
- Schröder, T. J., Christensen, S., Lindberg, S., Langgård, M., David, L., Maltas, P. J., et al. (2014). The identification of AF38469: an orally bioavailable inhibitor of the VPS10P family sorting receptor Sortilin. *Bioorg. Med. Chem. Lett.* 24, 177–180. doi:10.1016/j.bmcl.2013.11.046
- Selkoe, D. J. (1991). The molecular pathology of Alzheimer's disease. *Neuron* 6, 487–498. doi:10.1016/0896-6273(91)90052-2
- Shi, X.-X., Wang, Z.-Z., Wang, F., Hao, G.-F., and Yang, G.-F. (2023). ACFIS 2.0: an improved web-server for fragment-based drug discovery via a dynamic screening strategy. *Nucleic Acids Res.* 51, W25–W32. doi:10.1093/nar/gkad348
- Shipe, W. D., Sharik, S. S., Barrow, J. C., McGaughey, G. B., Theberge, C. R., Uslander, J. M., et al. (2015). Discovery and optimization of a series of pyrimidine-based phosphodiesterase 10A (PDE10A) inhibitors through fragment screening, structure-based design, and parallel synthesis. *J. Med. Chem.* 58, 7888–7894. doi:10.1021/acs.jmedchem.5b00983
- Shraga, A., Resnick, E., Gabizon, R., and London, N. (2021). “Chapter eight - covalent fragment screening,” in *Annual reports in medicinal Chemistry, the design of covalent-based inhibitors*. Editors R. A. Ward, and N. P. Grimster (Academic Press), 243–265. doi:10.1016/bs.armac.2021.04.001
- Singh, M., Tam, B., and Akabayov, B. (2018). NMR-fragment based virtual screening: a brief overview. *Molecules* 23, 233. doi:10.3390/molecules23020233
- Souers, A. J., Levenson, J. D., Boghaert, E. R., Ackler, S. L., Catron, N. D., Chen, J., et al. (2013). ABT-199, a potent and selective BCL-2 inhibitor, achieves antitumor activity while sparing platelets. *Nat. Med.* 19, 202–208. doi:10.1038/nm.3048
- Stark, J. L., and Powers, R. (2011). “Application of NMR and molecular docking in structure-based drug discovery,” in *NMR of proteins and small biomolecules, topics in current Chemistry*. Editor G. Zhu (Berlin, Heidelberg: Springer Berlin Heidelberg), 1–34. doi:10.1007/128_2011_213
- Svecizer, A., North, A. J. P., Mateu, N., Kidd, S. L., Sore, H. F., and Spring, D. R. (2019). Spirocycles as rigidified sp³-rich scaffolds for a fragment collection. *Org. Lett.* 21, 4600–4604. doi:10.1021/acs.orglett.9b01499
- Sweeney, P., Park, H., Baumann, M., Dunlop, J., Frydman, J., Kopito, R., et al. (2017). Protein misfolding in neurodegenerative diseases: implications and strategies. *Transl. Neurodegener.* 6, 6. doi:10.1186/s40035-017-0077-5
- Swinney, D. C. (2013). Phenotypic vs target-based drug discovery for first-in-class medicines. *Clin. Pharmacol. Ther.* 93, 299–301. doi:10.1038/clpt.2012.236
- Tan, Y.-Y., Jenner, P., and Chen, S.-D. (2022). Monoamine oxidase-B inhibitors for the treatment of Parkinson's disease: past, present, and future. *J. Park. Dis.* 12, 477–493. doi:10.3233/JPD-212976
- Tangphao, O., Grossmann, M., Chalon, S., Hoffman, B. B., and Blaschke, T. F. (1999). Pharmacokinetics of intravenous and oral L-arginine in normal volunteers. *Br. J. Clin. Pharmacol.* 47, 261–266. doi:10.1046/j.1365-2125.1999.00883.x
- Togre, N. S., Vargas, A. M., Bhargavi, G., Mallakuntla, M. K., and Tiwari, S. (2022). Fragment-based drug discovery against mycobacteria: the success and challenges. *Int. J. Mol. Sci.* 23, 10669. doi:10.3390/ijms231810669
- Varnes, J. G., Geschwindner, S., Holmquist, C. R., Forst, J., Wang, X., Dekker, N., et al. (2016). Fragment-assisted hit investigation involving integrated HTS and fragment screening: application to the identification of phosphodiesterase 10A (PDE10A) inhibitors. *Bioorg. Med. Chem. Lett.* 26, 197–202. doi:10.1016/j.bmcl.2015.10.100
- Ver Donck, F., Downes, K., and Freson, K. (2020). Strengths and limitations of high-throughput sequencing for the diagnosis of inherited bleeding and platelet disorders. *J. Thromb. Haemost.* 18, 1839–1845. doi:10.1111/jth.14945
- Verhoest, P. R., Chapin, D. S., Corman, M., Fonseca, K., Harms, J. F., Hou, X., et al. (2009). Discovery of a novel class of phosphodiesterase 10A inhibitors and identification of clinical candidate 2-[4-(1-Methyl-4-pyridin-4-yl-1H-pyrazol-3-yl)-phenoxy]methyl-quinoline (PF-2545920) for the treatment of Schizophrenia†Coordinates of the PDE10A crystal structures have been deposited in the protein data bank for compound 1 (3HQW), 2 (3HQY), 3 (3HQV) and 9 (3HR1). *J. Med. Chem.* 52, 5188–5196. doi:10.1021/jm900521k
- Vigneswara, V., and Ahmed, Z. (2020). The role of caspase-2 in regulating cell fate. *Cells* 9, 1259. doi:10.3390/cells9051259
- Volochnyuk, D. M., Ryabukhin, S. V., Moroz, Y. S., Savych, O., Chuprina, A., Horvath, D., et al. (2019). Evolution of commercially available compounds for HTS. *Drug Discov. Today* 24, 390–402. doi:10.1016/j.drudis.2018.10.016
- Wasko, M. J., Pellegrine, K. A., Madura, J. D., and Surratt, C. K. (2015). A role for fragment-based drug design in developing novel lead compounds for central nervous system targets. *Front. Neurol.* 6, 197–211. doi:10.3389/fneur.2015.00197
- Woolford, A. J. A., Day, P. J., Bénét, V., Berdini, V., Coyle, J. E., Dudit, Y., et al. (2016). Fragment-based approach to the development of an orally bioavailable lactam inhibitor of lipoprotein-associated phospholipase A2 (Lp-PLA₂). *J. Med. Chem.* 59, 10738–10749. doi:10.1021/acs.jmedchem.6b01427
- Woolford, A. J. A., Pero, J. E., Aravapalli, S., Berdini, V., Coyle, J. E., Day, P. J., et al. (2016). Exploitation of a novel binding pocket in human lipoprotein-associated phospholipase A2 (Lp-PLA₂) discovered through X-ray fragment screening. *J. Med. Chem.* 59, 5356–5367. doi:10.1021/acs.jmedchem.6b00212
- Wu, B., Kulkarni, K., Basu, S., Zhang, S., and Hu, M. (2011). First-pass metabolism via UDP-glucuronosyltransferase: a barrier to oral bioavailability of phenolics. *J. Pharm. Sci.* 100, 3655–3681. doi:10.1002/jps.22568
- Wu, H.-Q., Okuyama, M., Kajii, Y., Pocivavsek, A., Bruno, J. P., and Schwarcz, R. (2014). Targeting kynurenine aminotransferase II in psychiatric diseases: promising effects of an orally active enzyme inhibitor. *Schizophr. Bull.* 40, S152–S158. doi:10.1093/schbul/sbt157
- Yamazaki, Y., Zhao, N., Caulfield, T. R., Liu, C. C., and Bu, G. (2019). Apolipoprotein E and Alzheimer disease: pathobiology and targeting strategies. *Nat. Rev. Neurol.* 15, 501–518. doi:10.1038/s41582-019-0228-7
- Yoon, S.-S., and AhnJo, S.-M. (2012). Mechanisms of amyloid- β peptide clearance: potential therapeutic targets for Alzheimer's disease. *Biomol. Ther.* 20, 245–255. doi:10.4062/biomolther.2012.20.3.245
- Zagorska, A., Partyka, A., Bucki, A., Gawalskax, A., Czopek, A., and Pawlowski, M. (2018). Phosphodiesterase 10 inhibitors - novel perspectives for psychiatric and neurodegenerative drug discovery. *Curr. Med. Chem.* 25, 3455–3481. doi:10.2174/0929867325666180309110629



OPEN ACCESS

EDITED BY

Steve Suib,
University of Connecticut, United States

REVIEWED BY

Nan Zheng,
University of Arkansas, United States
Manabu Hatano,
Kobe Pharmaceutical University, Japan

*CORRESPONDENCE

Iwao Ojima,
✉ iwao.ojima@stonybrook.edu

RECEIVED 09 March 2024

ACCEPTED 22 April 2024

PUBLISHED 09 May 2024

CITATION

Garg A, Rendina D, Bendale H, Akiyama T and Ojima I (2024), Recent advances in catalytic asymmetric synthesis.
Front. Chem. 12:1398397.
doi: 10.3389/fchem.2024.1398397

COPYRIGHT

© 2024 Garg, Rendina, Bendale, Akiyama and Ojima. This is an open-access article distributed under the terms of the [Creative Commons Attribution License \(CC BY\)](#). The use, distribution or reproduction in other forums is permitted, provided the original author(s) and the copyright owner(s) are credited and that the original publication in this journal is cited, in accordance with accepted academic practice. No use, distribution or reproduction is permitted which does not comply with these terms.

Recent advances in catalytic asymmetric synthesis

Ashna Garg¹, Dominick Rendina¹, Hersh Bendale¹,
Takahiko Akiyama² and Iwao Ojima^{1,3*}

¹Stony Brook University, Department of Chemistry, Stony Brook, NY, United States, ²Gakushuin University, Department of Chemistry, Tokyo, Japan, ³Stony Brook University, Institute of Chemical Biology and Drug Discovery, Stony Brook, NY, United States

Asymmetric catalysis stands at the forefront of modern chemistry, serving as a cornerstone for the efficient creation of enantiopure chiral molecules characterized by their high selectivity. In this review, we delve into the realm of asymmetric catalytic reactions, which spans various methodologies, each contributing to the broader landscape of the enantioselective synthesis of chiral molecules. Transition metals play a central role as catalysts for a wide range of transformations with chiral ligands such as phosphines, *N*-heterocyclic carbenes (NHCs), etc., facilitating the formation of chiral C-C and C-X bonds, enabling precise control over stereochemistry. Enantioselective photocatalytic reactions leverage the power of light as a driving force for the synthesis of chiral molecules. Asymmetric electrocatalysis has emerged as a sustainable approach, being both atom-efficient and environmentally friendly, while offering a versatile toolkit for enantioselective reductions and oxidations. Biocatalysis relies on nature's most efficient catalysts, i.e., enzymes, to provide exquisite selectivity, as well as a high tolerance for diverse functional groups under mild conditions. Thus, enzymatic optical resolution, kinetic resolution and dynamic kinetic resolution have revolutionized the production of enantiopure compounds. Enantioselective organocatalysis uses metal-free organocatalysts, consisting of modular chiral phosphorus, sulfur and nitrogen components, facilitating remarkably efficient and diverse enantioselective transformations. Additionally, unlocking traditionally unreactive C-H bonds through selective functionalization has expanded the arsenal of catalytic asymmetric synthesis, enabling the efficient and atom-economical construction of enantiopure chiral molecules. Incorporating flow chemistry into asymmetric catalysis has been transformative, as continuous flow systems provide precise control over reaction conditions, enhancing the efficiency and facilitating optimization. Researchers are increasingly adopting hybrid approaches that combine multiple strategies synergistically to tackle complex synthetic challenges. This convergence holds great promise, propelling the field of asymmetric catalysis forward and facilitating the efficient construction of complex molecules in enantiopure form. As these methodologies evolve and complement one another, they push the boundaries of what can be accomplished in catalytic asymmetric synthesis, leading to the discovery of novel, highly selective transformations which may lead to groundbreaking applications across various industries.

KEYWORDS

asymmetric catalytic synthesis, asymmetric organocatalysis, asymmetric photocatalysis, asymmetric electrocatalysis, biocatalysis, C-H activation, flow chemistry

1 Introduction

One of the fundamental challenges in organic synthesis is the creation of molecules with specific chirality. The synthesis of enantiopure compounds remains a significant focus in pharmaceutical research, due to the fact that each enantiomer may well have distinct metabolic and toxicological characteristics and only specific enantiomer possesses desirable pharmacological properties, while the other enantiomer may cause undesirable side effects. Thus, the use of racemic compounds as pharmaceutical drugs may impose serious risks (Ceramella et al., 2022). The production of enantiomerically pure drugs is often time-consuming, costly, and environmentally deleterious (Meggers, 2015). The use of chiral auxiliaries or enantiomerically pure starting materials from natural sources is costly in general and inefficient. Therefore, the development of highly efficient methods and processes in catalytic asymmetric synthesis has profound significance in the pharmaceutical industry, which needs to develop efficacious and safe chiral drugs with high target specificity (Betz et al., 2023).

In 2022, a book, "Catalytic Asymmetric Synthesis, fourth Edition" edited by Akiyama and Ojima, was published, which provided a comprehensive overview of the advances in the field between 2010 to early 2020 (Akiyama and Ojima, 2022). Since the advancement in this field of research is continuous, very fast and highly robust, numerous publications emerged since early 2020. Accordingly, the purpose of this review article is to focus on the most significant advances in catalytic asymmetric synthesis in the last 5 years (2018–2023) in specific areas, i.e., organocatalysis, photocatalysis, electrochemical catalysis, biocatalytic transformations, and applications of these catalytic processes in continuous flow system.

This review also intends to showcase how different chiral catalysts can be synergistically used in addressing complex synthetic challenges (Emmanuel et al., 2023; Malakar et al., 2023). The development of these protocols has been spearheading the development of sophisticated, but cost-friendly and environmentally benign processes in catalytic asymmetric synthesis (Guo et al., 2022; Nagib, 2022; Wang et al., 2023). Judicious combination of various chiral catalysts and catalytic asymmetric processes would substantially expand chemist's toolbox for the design and synthesis of target molecules with chiral centers bearing required absolute configurations.

Where a drug's efficacy and safety hinges on its purity and stereochemical integrity, continuous flow processes can provide precise control over the quality of products (Tsubogo et al., 2015). There has been a substantial advancement in continuous flow processes since Kobayashi and coworkers demonstrated the potential of these systems in practical catalytic asymmetric synthesis in 2013 (Tsubogo et al., 2013). This area of research involves chemistry, chemical engineering and computer science, aiming at rendering chemical manufacturing processes more efficient, safe and eco-friendly (Plutschack et al., 2017).

Catalytic asymmetric synthesis appears to have a bright future not only for the productions of pharmaceuticals, diagnostics and materials, but also for the advancement of chemical sciences through new discoveries and innovative applications (Yamamoto and Ishihara, 2008; Reyes et al., 2022).

2 Asymmetric organocatalysis

2.1 Enamine/iminium catalysis

Enamine species are prevalent in literature as a key intermediate for a diverse array of asymmetric organocatalytic transformations. In 2000, List, Lerner, and Barbas reported their proline-catalyzed intermolecular aldol condensation with an enamine species as a key intermediate (Bahmanyar and Houk, 2001; Sakthivel et al., 2001; Mukherjee et al., 2007) and in the same year MacMillan reported a Diels–Alder cyclization catalyzed by a chiral imidazolidinone via an iminium ion intermediate (Sakthivel et al., 2001; Erkkilä et al., 2007; Mukherjee et al., 2007). Since initial discoveries in 1970s (Hajos ZGP and Parrish, 1974), proline-derived organocatalysts have been indispensable tools in asymmetric catalytic transformations with some advantages associated with their usage, e.g., reactions proceed under mild and aerobic conditions, wherein moisture is tolerated. In 2021, the Nobel Prize in Chemistry was awarded jointly to Benjamin List and David MacMillan, highlighting the importance of asymmetric enamine/iminium organocatalysis as a versatile and environmentally benign chemical process, effective for complex organic transformations in laboratories and industry (Mukerjee, 2021).

In 2022, Jørgensen and coworkers succeeded in synthesizing atropisomeric cyclizine cores with a conformationally stable C (sp²)-C (sp³) stereogenic axis for the first time, via enantioselective cyclization (Bertuzzi et al., 2022). This reaction took place between 5*H*-benzo [a]pyrrolizine-3-carbaldehydes and nitroolefins, α,β-unsaturated ketoesters or α,β-unsaturated aldehydes, and represents the first example of highly enantioselective synthesis of cyclazine cores. For the reaction of **1-A1** with **1-A2**, a modified amine catalyst **A2** was found to be optimal, which gave cyclizine **1A** in 54% yield and 95% e. e. As Figure 1A shows, the condensation of aldehyde **1-A2** with organocatalyst **A2**, produces enamine **1-A3**, followed by C-C bond formation with nitroolefin **1-A1** to afford **1-A4**. Then, **1-A4** cyclizes to give **1-A5**, and the subsequent elimination of organocatalyst **A2** yields **1A**. This reaction tolerated a diverse scope of aldehydes, nitroolefins with different *O*-protecting groups, and naphthalene substitutions, giving the corresponding cyclizine products **1A** in 32–68% yields with 92–99% e. e. and 10:1~>20:1 d. r.

In 2021, Anderson and coworkers reported a multi-catalytic strategy, incorporating organo-, photo- and hydrogen atom transfer (HAT) catalysis to synthesize α-chiral bicyclo [1.1.1]pentanes (BCPs) **1B**, which are important bioisosteres for 1,4-disubstituted arenes, alkynes, and *tert*-butyl groups (Figure 1B) (Wong et al., 2021). The three catalytic cycles operate in unison without side reactions. During the optimization of reaction conditions, it was confirmed that iridium photocatalyst, Jørgensen-Hayashi's catalyst **A3** and HAT catalyst were essential to obtain BCPs in 29–99% yield and 64–98% e. e. This multi-catalyst process is applicable to the asymmetric synthesis of various α-chiral BCPs bearing various functional groups at the α-position. For example, α-chiral BCP aldehydes were further derived into carboxylic acids, secondary amines, secondary alcohols, and homologated to alkynes without erosion of enantiomeric purity.

In 2019, Guo and coworkers reported a bifunctional enamine catalyst in the course of the total synthesis of naucleoficine I and II (Figure 1C) (Yuan et al., 2019). A trifluoromethanesulfonamide group was introduced into a spirobicyclic pyrrolidine to enhance enantioselectivity. Through the optimization of this process, catalyst

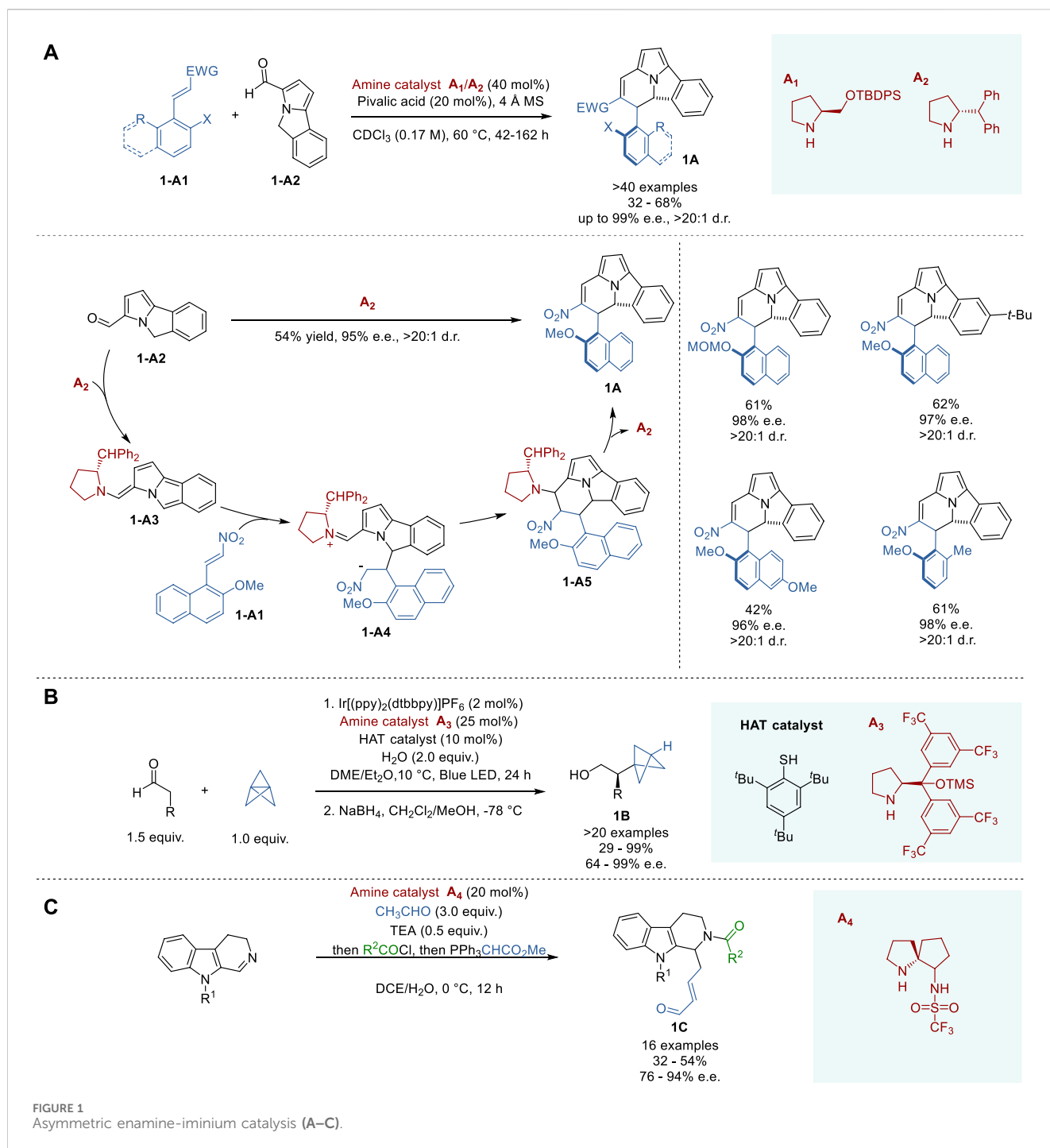


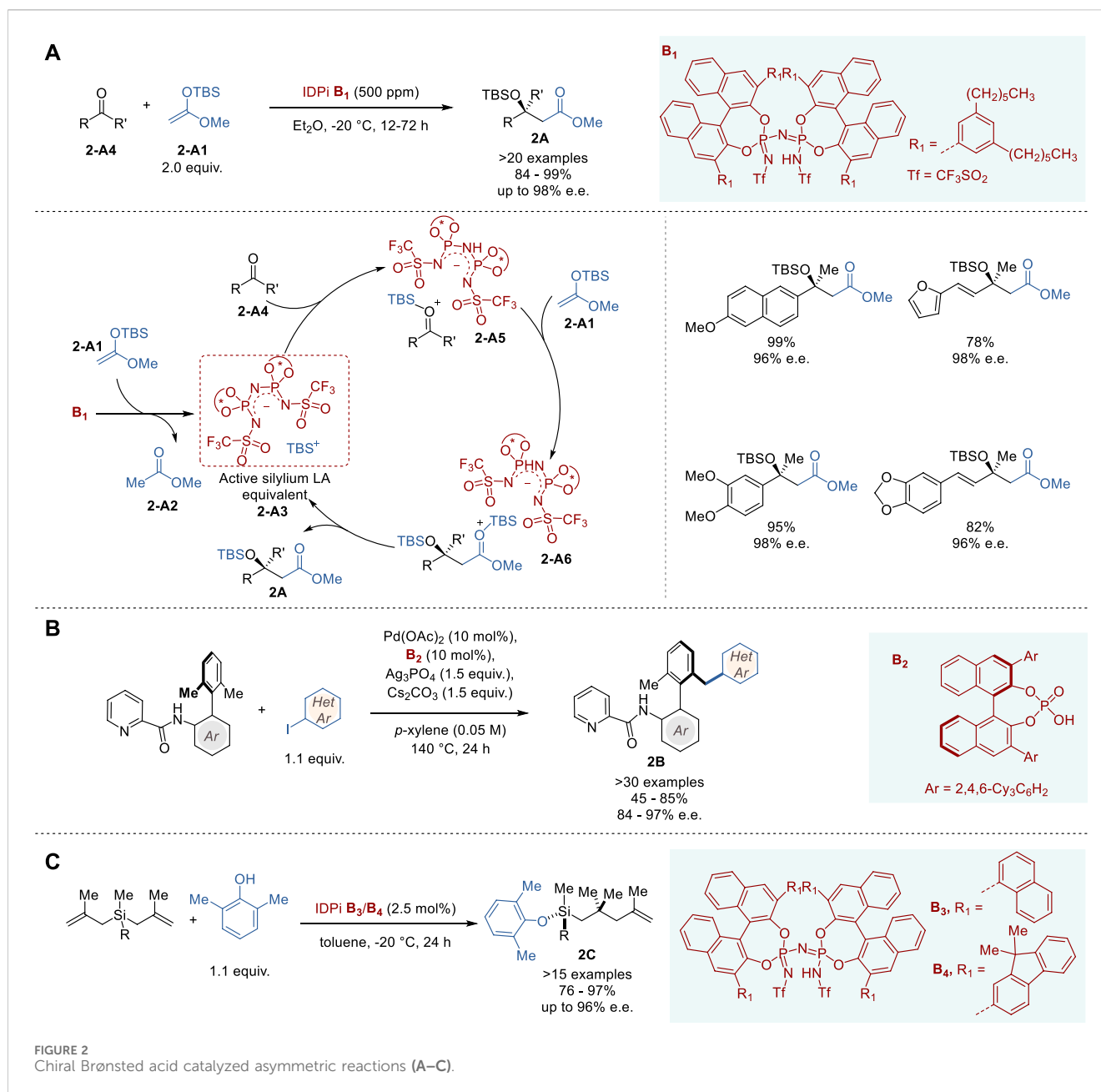
FIGURE 1
Asymmetric enamine-iminium catalysis (A–C).

\mathbf{A}_4 was identified as optimal, which gave the key intermediate **1C** ($R^2 = t\text{-Boc}$, $R^3 = \text{Ac}$) in 51% yield with 91% e. e. This asymmetric catalysis was applied to the enantioselective synthesis of a variety of substituted 3,4-dihydro- β -carbolines and indoles in 32–54% yield and 76–94% e. e.

2.2 Asymmetric Brønsted acid catalysis

Chiral Brønsted acid catalysts have been playing an important role in various asymmetric transformations since early 2000s

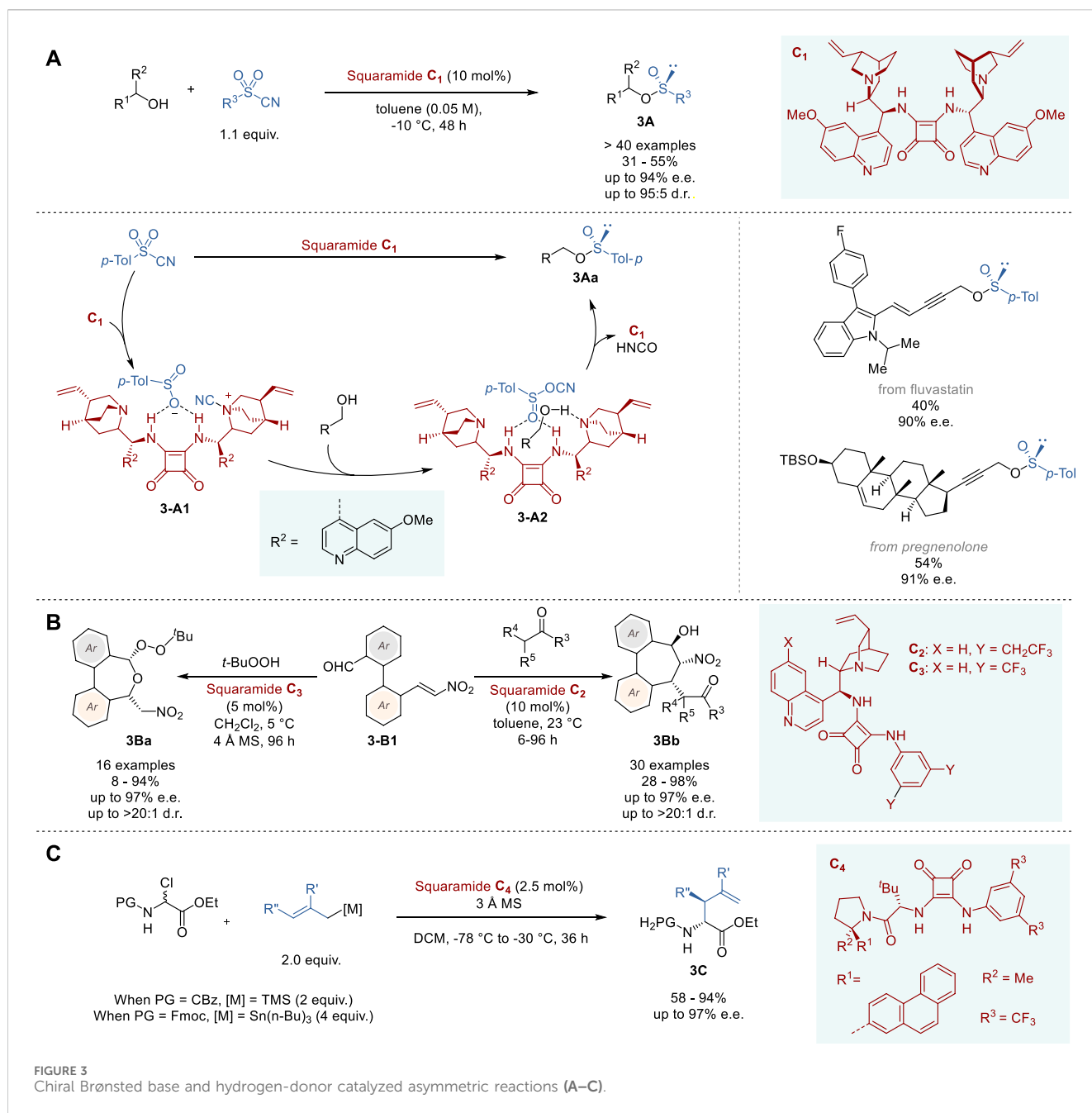
(Yamamoto and Ishihara, 2008). Chiral Brønsted acids are tunable by varying the pK_a, steric environment and mode of activation to produce effective catalysts for different asymmetric transformations (Akiyama and Ojima, 2022). Among a variety of chiral Brønsted acid catalysts, chiral phosphoric acids (CPAs) have been extensively studied and developed as one of the most versatile chiral catalysts. CPA is a bifunctional catalyst that functions as a Brønsted acid, as well as a Brønsted base, to form a hydrogen bonding network, involving a nucleophile and electrophile to promote asymmetric transformations (Faisca Phillips and Pombeiro, 2023). In 2004, Akiyama and Terada reported a



successful application of CPAs to enantioselective Mannich-type reactions, achieving high yields and excellent enantioselectivity (Akiyama et al., 2004; Uraguchi and Terada, 2004). Chiral Brønsted acids were also designed for asymmetric counter-anion directed catalysis (ACDC), as demonstrated by the works of List, wherein chiral imidodiphosphorimidates (IDPis) were successfully used as catalysts in a variety of asymmetric transformations (Schreyer et al., 2019).

In 2018, List and coworkers reported highly efficient silylium-based ACDC, using IDPi-based catalysts in Mukaiyama-type aldol condensation, which proceeded with a sub-ppm quantity of the catalyst in a 10 g scale reaction (Figure 2A) (Bae et al., 2018). The aldol reaction of TBS-ketene acetal 2-A1 with a variety of ketones 2-A4 using catalyst B₁ gave the corresponding cross-aldol products 2A in 84–99% yield and 68–>98% e.e.

In 2023, Akiyama and coworkers reported the first example of axially chiral biaryl desymmetrization by directing group-assisted atroposelective C (sp³)-H activation using a CPA-Pd(II) catalyst (Figure 2B) (Uchikura et al., 2023). The reaction of biaryls bearing a picolinamido moiety at the 2'-position as the directing group with aryl iodides catalyzed by Pd(OAc)₂-B₂ with Ag₃PO₄ as an additive, afforded chiral biaryl products 2B in 45–85% yield and 84–97% e.e. However, 2-methoxyiodobenzene was an exception, resulting in poor yield with enantioselectivity, due to its steric constraints. The picolinoyl directing group can be removed with zinc/HCl quantitatively to give the corresponding amine without loss of enantiopurity. The catalytic cycle, involving Pd^{II}- and Pd^{IV}-phosphate species, and the mechanism of enantioselection based on DFT analysis of TS-models were presented, which nicely accommodate the experimental results.



In 2022, List and coworkers reported the first organocatalytic enantioselective synthesis of tertiary silyl ethers with “central chirality” on silicon using IDPi catalysts (Figure 2C) (Zhou et al., 2022). This novel reaction involves an asymmetric desymmetrization of symmetrical bis(methallyl)silanes via carbon–carbon bond formation and silicon–hydrogen exchange reaction with phenols. The reaction of benzylbis(methallyl)silane with 2,6-dimethylphenol to give 2C (R = Bn) was used for optimization of IDPi catalysts and found that B₃ and B₄ were optimal, giving 2C with 90% e.e. and 94% e.e., respectively, in >95% yield. The reactions of substituted benzylbis(methallyl)silanes and arylbis(methallyl)silanes catalyzed by B₃ or B₄ gave the corresponding Si-stereogenic aryloxysilanes 2C in 76–97% yield with 92–96% e.e. The absolute configuration of 2C (R = 4-

methylbenzyl) was determined by Fujita’s crystalline sponge method (Zigon et al., 2021). Aryloxysilanes 2C with high enantiopurity can serve as key building blocks for a variety of applications, since 2C can be derived to various organosilanes through functionalizations of the olefin moiety and substitutions at the aryloxy-Si bond.

2.3 Asymmetric Brønsted base and hydrogen-donor catalysis

In a manner similar to that of proline-derived organocatalysts, chiral Brønsted bases function as catalyst for a variety of asymmetric transformations under mild conditions. Chiral Brønsted bases

typically consist of chiral amine moieties as essential components by design. This asymmetric catalysis involves rather complex hydrogen-bonding networks among the substrate, chiral catalyst and nucleophile. This multi-component process also requires a delicate balance between the basicity of the catalyst and the acidity of the nucleophile. Since a variety of chiral Brønsted bases can be rationally designed, a large number of chiral catalysts have been invented and developed (Denmark and Beutner, 2008; Ishikawa et al., 2017), which are impossible to cover comprehensively. Accordingly, only a few selected examples, including hydrogen-donor catalysis are discussed here.

In 2023, Yan and coworkers reported the successful transformation of achiral hexavalent sulfonyl cyanides to the corresponding tetravalent chiral organosulfonates **3A** through asymmetric deoxygenation catalyzed by novel squaramide catalyst **C₁** (Figure 3A) (Huang et al., 2023). This unique catalysis involves the activation of tosyl cyanide through hydrogen bonding to the two NH groups of **C₁**, which promotes the stereoselective cleavage of the S-CN bond and the migration of the CN group to the quinuclidine nitrogen (**3-A1**), followed by addition of alcohol and another migration of the CN group to the sulfinyl oxygen to form sulfinyl cyanate complexed to (**3-A2**). Then, alcohol undergoes S_N² substitution at sulfur to give chiral sulfinate **3Aa**, liberating HNCO/HOCN and catalyst **C₁**. The mechanism of this catalysis was elucidated by FT-IR spectroscopy, ¹⁸O labeling experiment and DFT calculations. A broad range of alcohols and sulfonyl cyanides were used to demonstrate the versatility of this enantioselective catalytic process, with emphasis on the use of a variety of functionalized propargylic alcohols, which gave the corresponding sulfonates **3A** in 31–55% yield with 80–94% e. e. This process was also applied to late-stage modifications of drugs and bioactive natural products such as carbazoles, citral, β-ionone, fluvastatin, D-glucose, and pregnenolone.

In 2023, Chauhan and coworkers reported the catalytic asymmetric synthesis of 5,7-dihydrobenzo [*c,e*]oxepines (**3Ba**) bearing two stereogenic centers, as well as dibenzocycloheptanes (**3Bb**) bearing three stereogenic centers, using bifunctional quinuclidine-squaramide catalysts (Figure 3B) (Kotwal et al., 2023). The bifunctional catalyst was designed to bear two different reaction sites, i.e., aldehyde and nitrovinyl groups, at the two *ortho* positions of the biaryl ring system (**3-B1**). After complexation of **3-B1** to bifunctional catalyst **C₂** or **C₃**, a soft nucleophile, a β-keto ester, β-diketone or amide, undergoes a domino 1,4/1,2-addition to afford dibenzocycloheptanes **3Bb**, while a hard nucleophile, *t*-BuOOH, proceeds with a tandem 1,2/oxa-Michael addition to give dihydrobenzooxepines **3Ba**. An optimization study initially identified bifunctional Brønsted base catalyst **C₂** as optimal for the domino 1,4/1,2 addition to give dibenzocycloheptanes in 28–98% yields with 93–97% e. e. and >20:1 d. r. Further tuning of **C₂** for tandem 1,2/oxa-Michael addition led to **C₃**, which was found to be the optimal catalyst for this process, affording various oxepines **3Ba** in 8–94% with 83–97% e. e. and 4:1~>20:1 d.r. The relative and absolute configuration of **3Ba** and **3Bb** were determined by X-ray crystallography and DFT analysis revealed that these reactions are thermodynamically controlled processes.

In 2018, Jacobsen and coworkers reported the enantio- and diastereoselective synthesis of α-allyl amino esters **3C** through allylation of *N*-Cbz- or *N*-Fmoc- α-chloroglycinates by hydrogen-

donor catalysis of squaramides (Figure 3C) (Bendelsmith et al., 2019). The reaction of ethyl *N*-Cbz-α-chloroglycinate with 2-methallyltrimethylsilane was used to screen squaramide catalysts, which identified **C₄** as the optimal catalyst. A variety of allylsilanes and allylstannanes were employed as allylating agents, wherein ethyl *N*-Fmoc-α-chloroglycinate was used for the reaction with allylstannanes, to give the corresponding *N*-Cbz-/N-Fmoc-α-allylglycinates **3C** in 58–94% yield with 90–97% e. e. and >10:1 d. r. A mechanistic study, including kinetics experiments and DFT calculations, suggests a concerted S_N2 process with dynamic kinetic resolution.

2.4 Asymmetric *N*-heterocyclic carbene catalysis

N-Heterocyclic carbenes (NHC) can be generated *in situ* through the deprotonation of the corresponding various “azolium” salts (Flanigan et al., 2015). Since Ukai's pioneering work on an NHC generated from a thiazolium salt in benzoin condensation 80 years ago (Ukai et al., 1943) and Breslow's work on the mechanism in 1958 (Breslow, 1958), chiral NHCs appeared already in 1960–1970s and have been contributing to the advancement of catalytic asymmetric synthesis (Flanigan et al., 2015). The field of chiral NHC catalysis appears to be still expanding its boundaries in asymmetric organocatalysis.

In 2022, Chi and coworkers reported the enantioselective sulfonylation of 2-(substituted acryloyl)benzaldehydes catalyzed by chiral NHC species generated from triazolium pre-catalyst **D₁** to give the corresponding sulfonylethylideneisobenzofuranones **4A** in 20–95% yield and 87–98% e.e. (Figure 4A) (Deng et al., 2022). Since chiral sulfones are unique functional groups found in pharmaceuticals and natural products, this process may provide an efficient access to biologically active sulfone-containing compounds. In this NHC catalysis, sulfonyl chloride functions as both an oxidant and a nucleophile via its reduced form. The chiral NHC species generated from pre-catalyst **D₁** reacts with the aldehyde moiety to initiate the activation of sulfonyl chloride, generating a sulfinate species that undergoes Michael addition to a remote enone moiety stereoselectively, triggering the cascade cyclization to give the product **4A** and regenerate the chiral NHC catalyst. Mechanistic studies, including DFT calculations, suggest the involvement of an unprecedented Breslow intermediate and a novel mode of oxidation.

Although successful chiral NHC catalyzed asymmetric reactions typically involve aldehydes, enals and esters as substrates, the reactions involving amides are still challenging. Nevertheless, in 2022, Huang and coworkers reported a successful protocol for the enantioselective desymmetrization of 4-substituted and 4,4-disubstituted *N*-Cbz-glutarimides (**4-B1**) with alcohols under mild conditions in the presence of triazolium pre-catalyst **D₂** (Figure 4B) (Hu et al., 2022). This process includes the enantioselective cleavage of the imide C-N bond by chiral NHC species generated from **D₂**, followed by ester formation with an alcohol to give the corresponding glutarate-*N*-Cbz-amide **4B**. A structurally diverse 3-substituted and 3,3-disubstituted glutarate-*N*-Cbz-amides **4B** were synthesized by this process in 40–97% yield and 46–98% e. e. Furthermore, this process was successfully applied

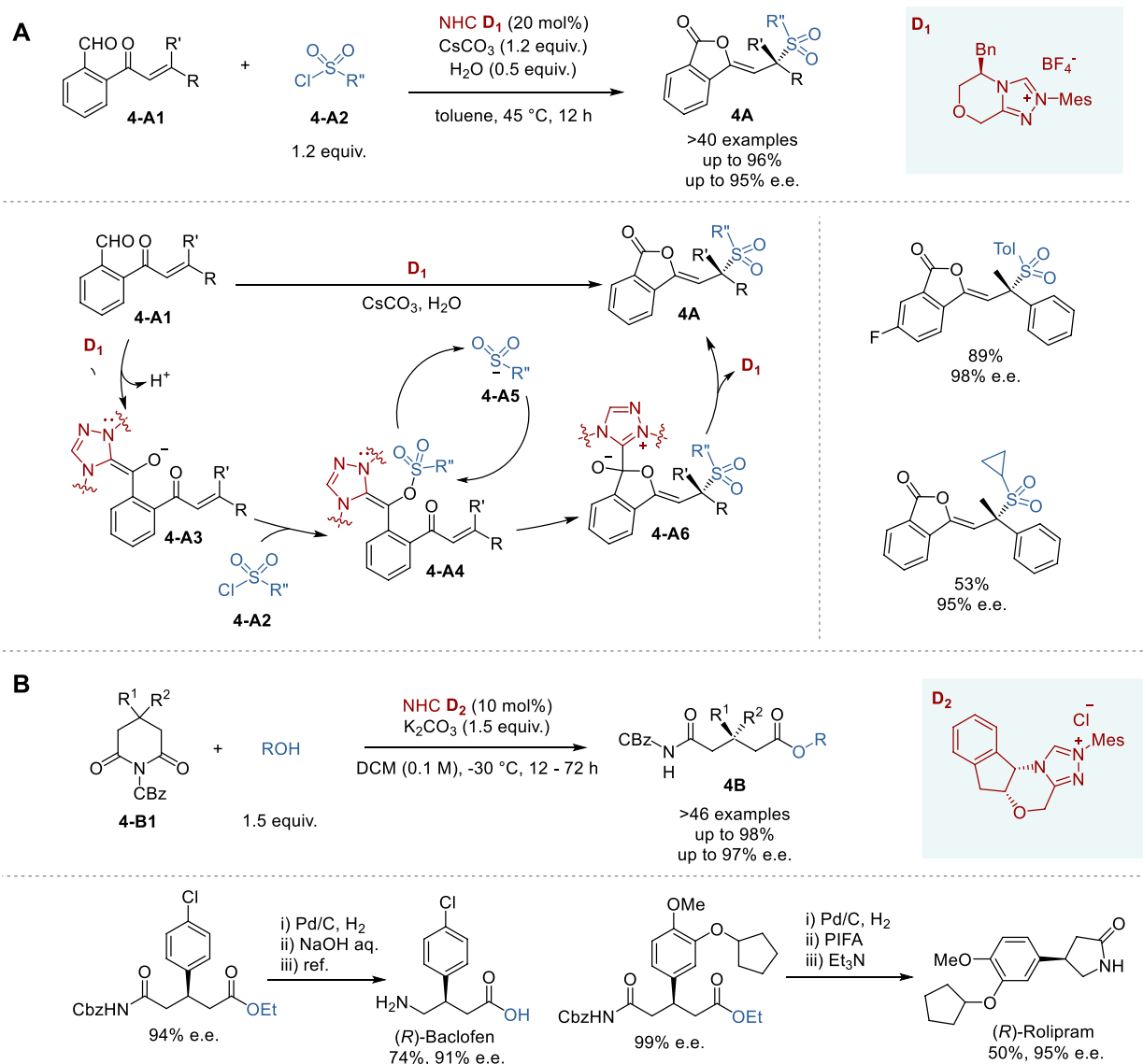


FIGURE 4
Chiral NHC catalyzed asymmetric synthesis (A,B).

to the synthesis of the key intermediates of (*R*)-Baclofen (skeletal muscular relaxant) in 74% yield and 91% e. e., and (*R*)-Rolipram (antidepressant) in 50% yield and 95% e. e.

2.5 Hypervalent iodine catalysts in asymmetric synthesis

In 2018, Jacobsen and coworkers reported the synthesis of *syn*- β -fluoroaziridines **5A** through diastereo- and enantioselective fluorination-aziridination of *N*-tosyl-3-arylprop-2-enylamines (**5-A1**) with *m*CPBA (stoichiometric oxidant) and HF-pyridine (nucleophilic fluoride source) promoted by chiral aryl iodide catalyst **E₁**, which generates hypervalent iodine species (Figure 5A) (Mennie et al., 2018). A variety of allylamines **5-A1** bearing substituted aryl and fused hetero-bicyclic aryl groups were employed as substrates in this reaction to give the corresponding

fluoroaziridines **5A** in 44–93% yield and 61–97% e. e. with perfect diastereoselectivity.

Since the catalyst-controlled diastereoselectivity in this process is extremely high, the fluorination of chiral 1-substituted *N*-tosyl-3-arylprop-2-enylamines afforded the corresponding 1,3-difluoro-2-amines bearing three contiguous stereocenters with very high diastereoselectivity (>20:1). This process was also successfully applied to the fluoroamination of *N*-tosyl-3-nitrophenylpent-4-ylamine to give the corresponding *anti*- β -fluoropyrrolidine in 82% yield with 86% e. e. and >20:1 d. r. Furthermore, variants of this process were applied to allyl benzyl ether, allyl carbamate and allyl acetate to give the corresponding 1,2-oxyfluorinated products in 64–77% yield and 92–94% e. e.

Inspired by the pioneering works of Fujita (Fujita et al., 2010) and Ishihara (Uyanik et al., 2010) on chiral hypervalent iodine catalysts, and the work of List and Corić on confined Brønsted acids with BINOL-derived CPAs (C et al., 2012), Zhang and coworkers

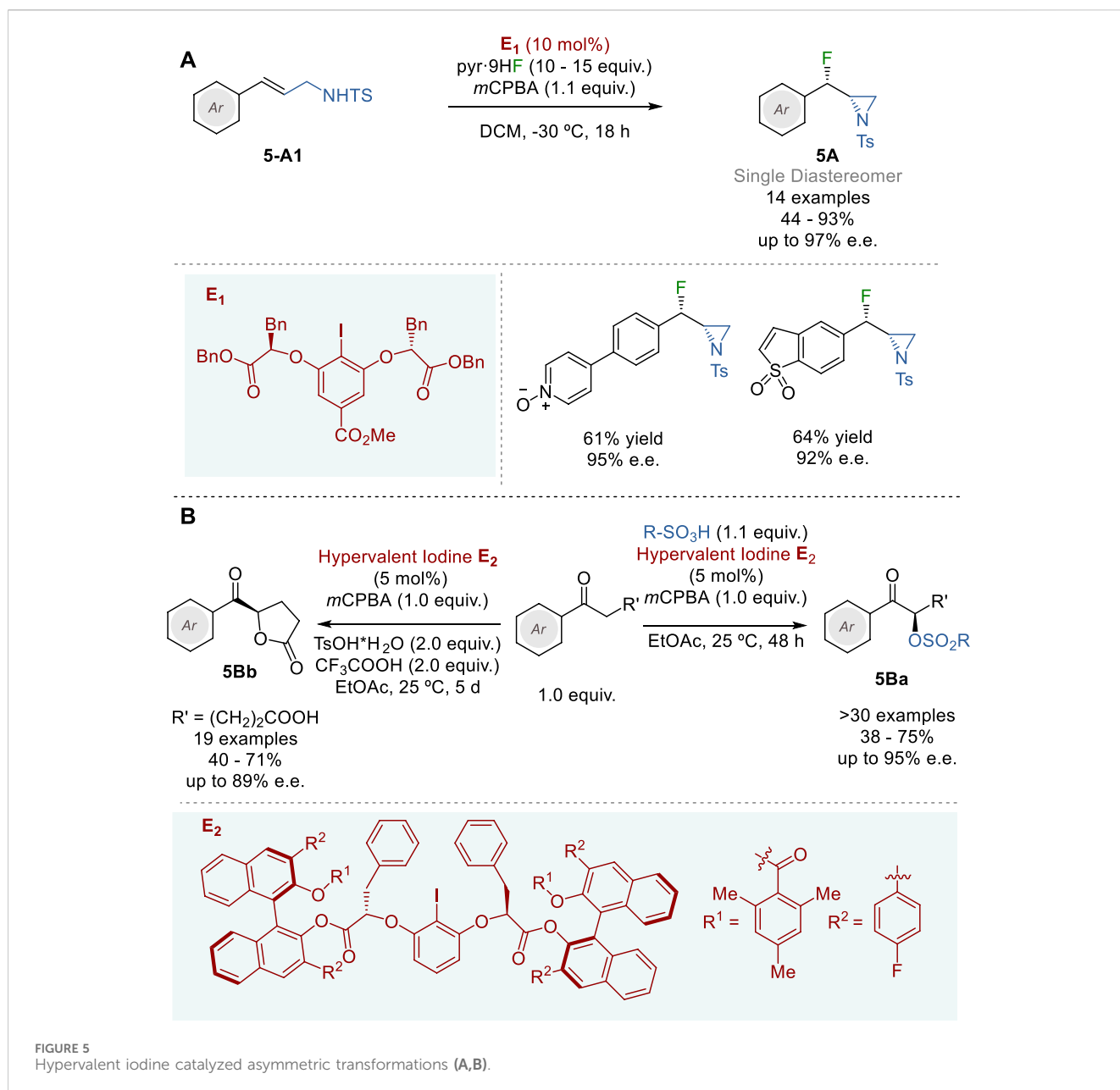


FIGURE 5
Hypervalent iodine catalyzed asymmetric transformations (A,B).

developed novel two-layer chiral aryl iodide catalysts (**E₂** and variants) in 2023 (Figure 5B) (Zhang et al., 2023a). The salient feature of this catalyst design includes the highly confined 2-iodoresorcinol core, which is linked to two sterically demanding BINOL derivatives by two chiral α -benzylglycolate arms. The first layer, consisting of 2-iodoresorcinol core linked to two chiral α -benzylglycolate moiety serves as the chiral environment for hypervalent iodine catalysis and the second layer, consisting of the finely tuned BINOL-derivatives drastically restricts the flexibility of the first layer, locking the highly demanding chiral environment at the iodine site. Through tuning of various BINOL derivatives the catalyst **E₂** was identified as optimal and used in the asymmetric α -oxysulfonylation of alkyl aryl ketones to give the corresponding α -sulfonyloxyketones **5Ba** in 38–75% yield and 73–95% e.e. Catalyst **E₂** was also applied to the oxidative enantioselective lactonization of various 5-oxo-5-arylpentanoic

acids to afford various arenecarbonyl- and 5-heteroarene carbonyl- γ -butyrolactones **5Bb** in 40–71% yield and 71–89% e. e.

3 Asymmetric visible-light photoredox catalysis

Visible-light photoredox catalysis represents a fundamental departure from traditional methods of activating chemical reactions. Visible light, which is abundant and non-destructive, is an ideal energy source for these processes. The process involves a catalyst that absorbs visible light, triggering an electron transition from HOMO to LUMO (Li et al., 2020). Then, the excited catalyst species thus formed can undergo intersystem crossing to reach a triplet excited state (T_1), which is more stable than the singlet excited

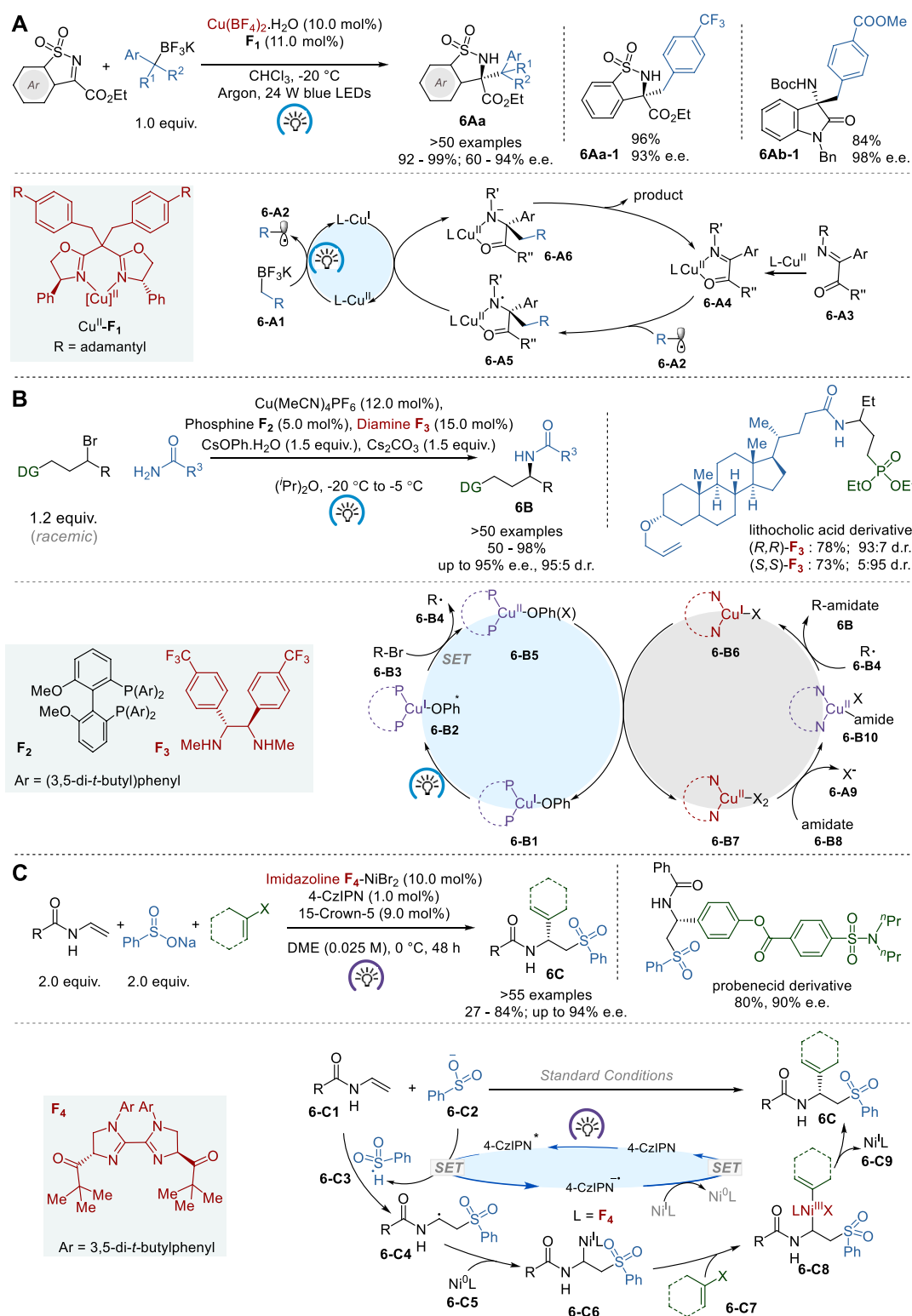


FIGURE 6
Metallaphotoredox asymmetric catalysis (A–C).

state (*S*₁). This approach offers several appealing and complementary advantages over conventional ground-state catalysis. It facilitates the generation of reactive radical species under mild reaction conditions, thereby enabling unique

transformations that can rapidly generate molecular complexity and the late-stage functionalization of intricate molecules (Albini and Fagnoni, 2004; Prier et al., 2013; Schultz and Yoon, 2014). Establishing enantioselective photoredox-catalyzed processes is

challenging in organic synthesis, given that intermediate radicals are highly reactive and reactions involving these species have low energy barriers (Shaw et al., 2016). This eventually leads to side reactions that are not enantioselective. Even with these problems, new ways of controlling the stereochemistry in photoredox processes have emerged in the last 10 years, facilitating the efficient synthesis of chiral molecules (Yoon, 2016; Saha, 2020; Yao et al., 2022).

A key to the successful asymmetric photoredox catalysis is the selection of an appropriate catalyst. A typical photoredox catalyst is a transition metal complex or an organic dye that facilitates electron transfer processes, generating radical intermediates (Prior et al., 2013). This activation has enabled countless synthetic transformations. Merging photocatalysis with either a transition metal or an organocatalyst leads to reactions that neither catalyst could achieve alone (Prior et al., 2013). Transition metal complexes, such as those based on noble metals, e.g., platinum, rhodium, ruthenium and iridium, have demonstrated remarkable efficiency in a wide range of transformations (Lee and Lo, 2022). However, this section will focus on the potential of economically favorable transition metals such as copper and nickel, which mediate organic transformations, achieving high enantioselectivity.

In addition to examples that demonstrate how photoredox catalysis has been effectively combined with traditional metal catalysis, the synergism between photocatalysis and organocatalysis will be highlighted in this section.

3.1 Asymmetric metallaphotoredox catalysis

In 2018, Gong and coworkers reported an enantioselective light-induced alkylation of *N*-sulfonylimines with benzyl trifluoroborates catalyzed by copper (II)-bisoxazoline complexes (Cu^{II}-BOX), which was generated *in situ* from Cu(BF₄)₂ and BOX ligands (Figure 6A) (Li et al., 2018). The Cu^{II}-BOX complexes (e.g., Cu^{II}-F₁) act as chiral photoredox bifunctional catalysts in this process to give various chiral *N*-sulfonylamines **6Aa** with tetrasubstituted carbon stereocenters in 92–99% yield and 60–94% e. e. This reaction was also successfully applied to the asymmetric alkylation of isatin-derived ketimines to afford the corresponding 3-*N*-*t*-Boc-amino-3-alkyloxindoles **6Ab** in 69–84% yield and 96–98% e.e.

Transition-metal catalysis in the asymmetric synthesis of chiral alkylamines, involving alkyl electrophiles and nitrogen nucleophiles, is gaining traction as a promising synthetic approach to higher-order amines (Trowbridge et al., 2020). However, the progress has been rather limited except for asymmetric allylic aminations (Grange et al., 2016). In 2021, Fu and coworkers reported a novel enantioconvergent amidation of unactivated racemic alkyl electrophiles using a photoinduced copper catalyst system (Figure 6B) (Chen et al., 2021). The process relies on three distinct ligands, i.e., bisphosphine **F₂**, phenoxide and chiral diamine **F₃**, and these ligands form two distinct catalysts, i.e., (i) a copper/bisphosphine/phenoxide complex that acts as a photocatalyst **6-B1** and (ii) a chiral copper/diamine complex **6-B6** that catalyzes enantioselective C-N bond formation. This novel process gives a variety of chiral secondary amides **6B** with high enantiopurity up to 95% e. e. through coupling of primary amides with unactivated racemic electrophiles, expanding enantioselective *N*-substitution by alkyl electrophiles beyond activated electrophiles.

Traditional S_N2 reactions have limited utility when dealing with less reactive electrophiles, particularly those that are sterically hindered. Also, it is noteworthy that conventional substitution methods seldom provide the ability to manipulate the stereochemistry at the carbon atom of the newly formed C-N bond when using a readily accessible racemic electrophile. Thus, this process marks a significant breakthrough in synthetic methodology.

In 2023, Nevado and coworkers reported a novel asymmetric three-component carbosulfonylation of *N*-vinyl amides and *N*-vinyl carbamates (**6-C1**) with sodium benzenesulfinate and aryl/vinyl halides, using a dual nickel/photoredox catalyst system, to give the corresponding chiral 2-aryl/alkenyl-2-amidoethylsulfones **6C** in 27–84% yield and 76–94% e.e. (Figure 6C) (Du et al., 2023). This process allows for the concurrent formation of C-C and C-S bonds across the alkene's π-system with enantiocontrol. With a broad substrate scope and high functional group tolerance, this process has been proven effective for the synthesis of pharmacologically pertinent 2-aryl-2-amidoethylsulfones. The mechanism of this dual catalysis includes a chiral biimidazoline (BiIM) **F₄**-NiBr₂ catalyst cycle for asymmetric cross-coupling and 4-CzIPN for photoredox catalyst cycle. BiIM **F₄** was selected over several ligands screened for this process as the best chiral ligand so far. The proposed mechanism involves the formation of a secondary alkyl radical **6-C4**, which is captured by Ni⁰L (L = **F₄**) **6-C5** to generate Ni^I complex **6-C6**. Then, aryl/alkenyl halide **6-C7** undergoes oxidative addition to generate Ni^{III} complex **6-C8**, which subsequently undergoes reductive elimination to give the product **6C** and Ni^I-L species, **6-C9**. Finally, **6-C9** is reduced to Ni⁰-L by photoredox catalysis to regenerate Ni⁰-L catalyst **6-C5**. The proposed Ni⁰/Ni^I/Ni^{III} catalytic cycle is supported by various control experiments, including radical scavengers, cross-over and control experiments.

3.2 Asymmetric photoredox organocatalysis

The advancement of asymmetric photoredox catalysis has gained utmost recognition in recent years (Shaw et al., 2016). Asymmetric organocatalysis, including enamine, iminium-ion, Brønsted acid/base, and *N*-heterocyclic carbene catalysis, has been used to induce chirality transfer in photocatalytic reactions (Yoon, 2016; Zou et al., 2018). In general, asymmetric photoredox catalysis needs a second activation mode to facilitate asymmetric induction, due to the absence of general methods to control the stereochemistry of radical ion species (Nicewicz and MacMillan, 2008; Proctor et al., 2018; Huan et al., 2021; Sherbrook et al., 2021). However, in 2023, List and coworkers reported a single-catalyst solution for enantioselective [2 + 2] cross-cycloaddition of styrenes using a chiral organic salt **G₁** with confined imidodiphosphorimidate (IDPi) counteranions as the catalyst (Figure 7A) (Das et al., 2023). A broad range of mono/di-substituted styrenes with different electronic properties were employed in the reaction with *trans*-anethole derivatives to give the corresponding chiral cyclobutanes **7A** in 31–91% yield and 76–96% e.e., wherein various functionalities, including alcohol, silyl ether, aldehyde, ester, and terminal olefin, were well tolerated. Mechanistic investigations suggest that the first step in the catalytic cycle,

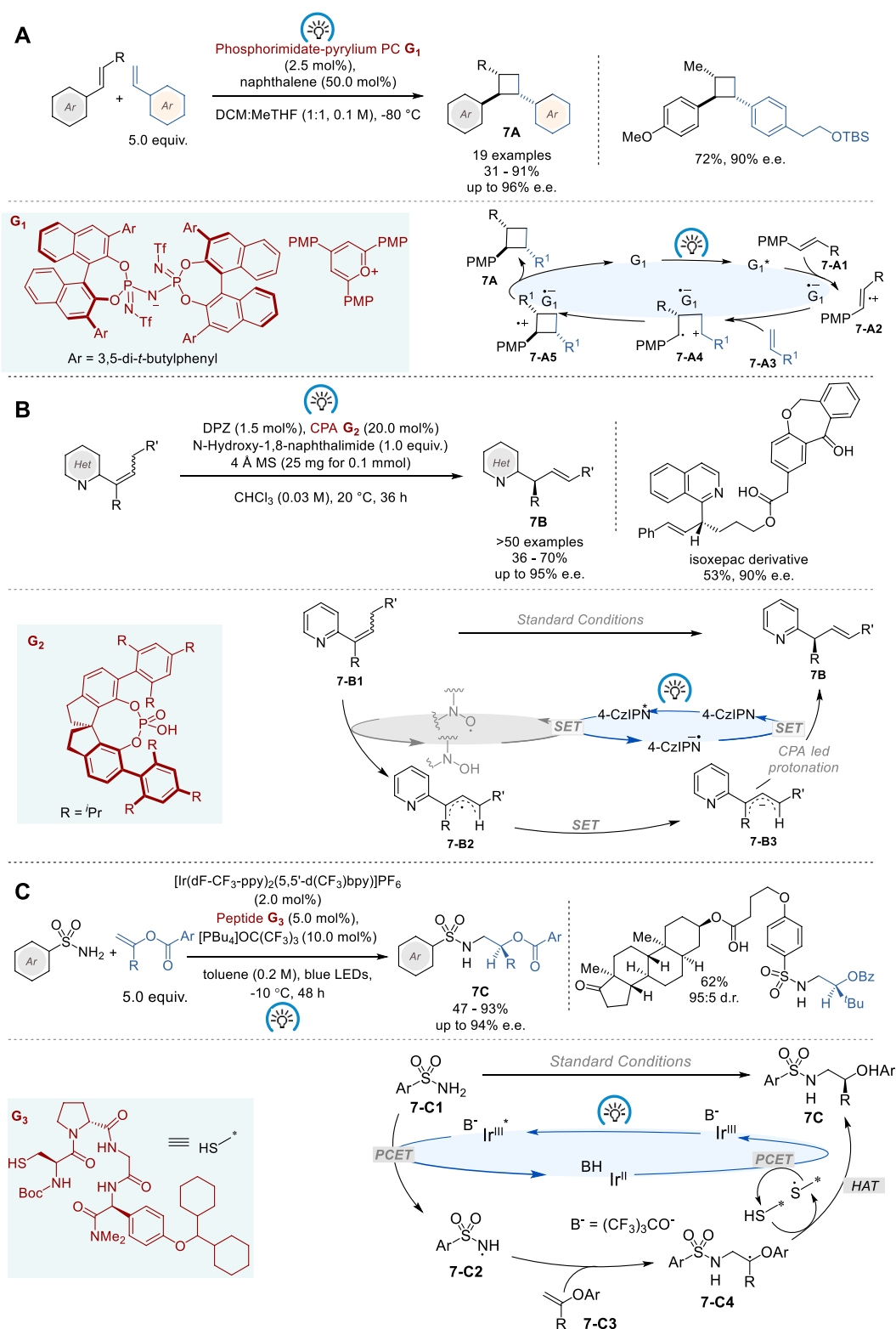


FIGURE 7
Photoredox organocatalysis for asymmetric synthesis (A–C).

generating cation radical intermediate complexed to **G₁** (**7-A4**), determines the enantioselectivity, and the second step, forming the cyclobutane cation radical complexed to **G₁** (**7-A5**), determines the diastereoselectivity, resulting in

thermodynamically and kinetically favored C-C bond formation between two benzylic sites in a *trans*-configuration. Finally, single electron transfer from the counter anion radical of **G₁**[•] to the cyclobutane cation radical gives product **7A**.

The catalytic asymmetric olefin isomerization to create a chiral tertiary carbon stereocenter is a highly atom economical process to produce chiral alkenes that are versatile intermediates in organic synthesis. Thus, this process has attracted considerable interest over the past couple of decades, wherein asymmetric hydride transfer catalysis (Tani et al., 1982; Tani et al., 1984; Tanaka and Fu, 2001) and bio-inspired enantioselective proton-transfer catalysis (Wu et al., 2011; Lee and Deng, 2012; Morack et al., 2021) are found to be effective. However, thermodynamic advantage of the product over the starting alkene is naturally required for this process to proceed, and thus the substrate type is structurally limited. Accordingly, it is necessary to overcome thermodynamic barrier to expand this process.

In 2023, Jiang and coworkers provided a partial solution to this challenge by applying a dual catalyst system, comprising visible light photosensitizer 5,6-bis(5-methoxythiophen-2-yl)pyrazine-2,3-dicarbonitrile (DPZ) as photoredox catalyst, chiral phosphoric acid (CPA) **G**₂ and *N*-hydroxyimide as the hydrogen atom transfer (HAT) catalyst (Figure 7B) (Liu et al., 2023). A wide range of conjugated α -substituted γ -arylalkenylazaarenes (*E/Z*-mixture) were successfully isomerized by this dual catalyst system to give the corresponding chiral γ -arylallylazaarenes **7B** bearing α -tertiary carbon stereocenters in 36–70% yield and 66–95% e. e. This process was also applied to the synthesis of α -deuterio- γ -arylallylazaarenes using D₂O as the deuterium source with 95% deuterium incorporation and 90–94% e. e, although 21–32% of the starting material was recovered. The proposed mechanism suggests that this transformation is triggered by the reductive quenching of DPZ*, which allows the generation of the crucial imide-*N*-oxyl radical (PINO) from *N*-hydroxynaphthalimide through single-electron oxidation. Following the abstraction of γ -H from **7-B1** by PINO, the resulting neutral radical intermediate **7-B2** is reduced by DPZ- \bullet , to generate anion **7-B3**. Then, anion **7-B3** undergoes a highly α -regioselective and enantioselective protonation to give product **7B** catalyzed by CPA **G**₂. The proposed mechanism also explains the reason why this process does not achieve full conversion, due to the regioselectivity issue at the protonation of **7-B3**.

In 2023, Knowles and coworkers reported enantioselective radical-based hydroamination of enol esters with sulfonamides, using a triple catalyst system consisting of an Ir photocatalyst, a Brønsted base, and a tetrapeptide thiol catalyst for asymmetric HAT (Figure 7C) (Hejna et al., 2023). This reaction provides easy access to a variety of chiral β -amino alcohol derivatives, i.e., α -substituted β -arylsulfonamidoethyl benzoates **7C**, in 47–93% yield and 73–94% e. e. In this catalysis, the absolute configuration of the product **7C** is determined by enantioselective HAT from the chiral peptide thiol catalyst to a prochiral C-centered radical **7-C4**. The optimization of tetrapeptide thiol HAT catalyst identified Boc-Cys-^DPro-Acpc-^XPhg-NMe₂ (X = *p*-Cy₂CH-O) **G**₃ to be optimal. Computational and experimental mechanistic study on this triple catalysis revealed that hydrogen-bonding, π - π stacking, and London dispersion interactions play key roles for substrate recognition and induction of chirality by chiral tetrapeptide HAT catalyst in this process.

4 Asymmetric electrochemical catalysis

The coupling of electrochemistry with chiral transition metal catalysis or organocatalysis has been recognized as a powerful

strategy for asymmetric electrochemical catalysis, leveraging precise control over redox processes to drive enantioselective reactions.

Electrosynthesis uses electricity instead of chemical reagents to transform organic molecules, which involves oxidation at the anode and reduction at the cathode in a conductive medium and is executed at either constant current or potential. Electrosynthesis can be carried out in a cell with or without a membrane, separating the anodic and cathodic spaces. The electrochemical transformations can be conducted directly at the electrode or indirectly using a redox mediator in the solution, and the latter can enhance efficiency and selectivity under milder conditions. Thus, catalytic asymmetric electrosynthesis can be realized by the combination of a chiral catalysts and a redox mediator (Yan et al., 2017; Shah and Ngai, 2022). This approach is more economically feasible and versatile than the use of specialized chiral electrodes, electrolytes, solvents or pre-modified chiral substrates (Arnaboldi et al., 2018). Moreover, electrochemical synthesis can be effectively combined with various asymmetric catalyst systems, such as transition metal-catalysts and organocatalysts, as well as photochemical and bioelectrochemical asymmetric synthesis (Kärkäs, 2018; Kingston et al., 2019; Zhu et al., 2021).

4.1 Asymmetric electrochemical organocatalysis

Shono oxidation is an effective electrochemical process for α -functionalization of amines with a variety of nucleophiles to capture the *in situ* formed iminium ion species (Jones and Banks, 2014; Zhu et al., 2021). This oxidation process is significant in organic synthesis to construct complex nitrogen-containing molecules.

In 2021, Mei and coworkers reported an electrochemical asymmetric coupling of secondary acyclic amines **8-A1** with ketones **8-A2** via Shono-type oxidation for the formation of amino acid derivatives **8A** (Figure 8A) (Wang et al., 2021). In this process, an *N*-oxyl radical TEMPO was used as the redox mediator for anodic oxidation, which enables selective oxidation of *N*-arylglycinate substrates, but not α -substituted products **8A** by exploiting a slight potential difference between the two. The use of TEMPO provided better functional group tolerance, as compared to the use of stoichiometric additives such as metals, electrolytes, and oxidants. For the substrate scope of this process, a variety of *N*-anisylglycinate derivatives, as well as cyclohexanone, cycloheptanone, tetrahydro-4-pyranone and tetrahydro-4-thiopyranone were employed to give the corresponding *N*-aryl- α -cycloalkylglycinates in 33–80% yield with diastereoselectivity up to >99:1 d.r. and enantioselectivity up to 99% e.e.

The proposed catalytic cycle commences with the oxidation of TEMPO at the anode, forming oxoammonium species **8-A3**, which reacts with a glycine ester to produce TEMPO-H (**8-A4**) and iminoester **8-A6**. On the other hand, enamine **8-A5**, formed from ketone **8-A2** and amine catalyst **H**₁, reacts with **8-A6** to generate iminium **8-A7**. Hydrolysis of **8-A7** gives the product **8A** and regenerates catalyst **H**₁. In the meantime, protons at the cathode are reduced to hydrogen, preventing them from interfering with the catalytic cycle.

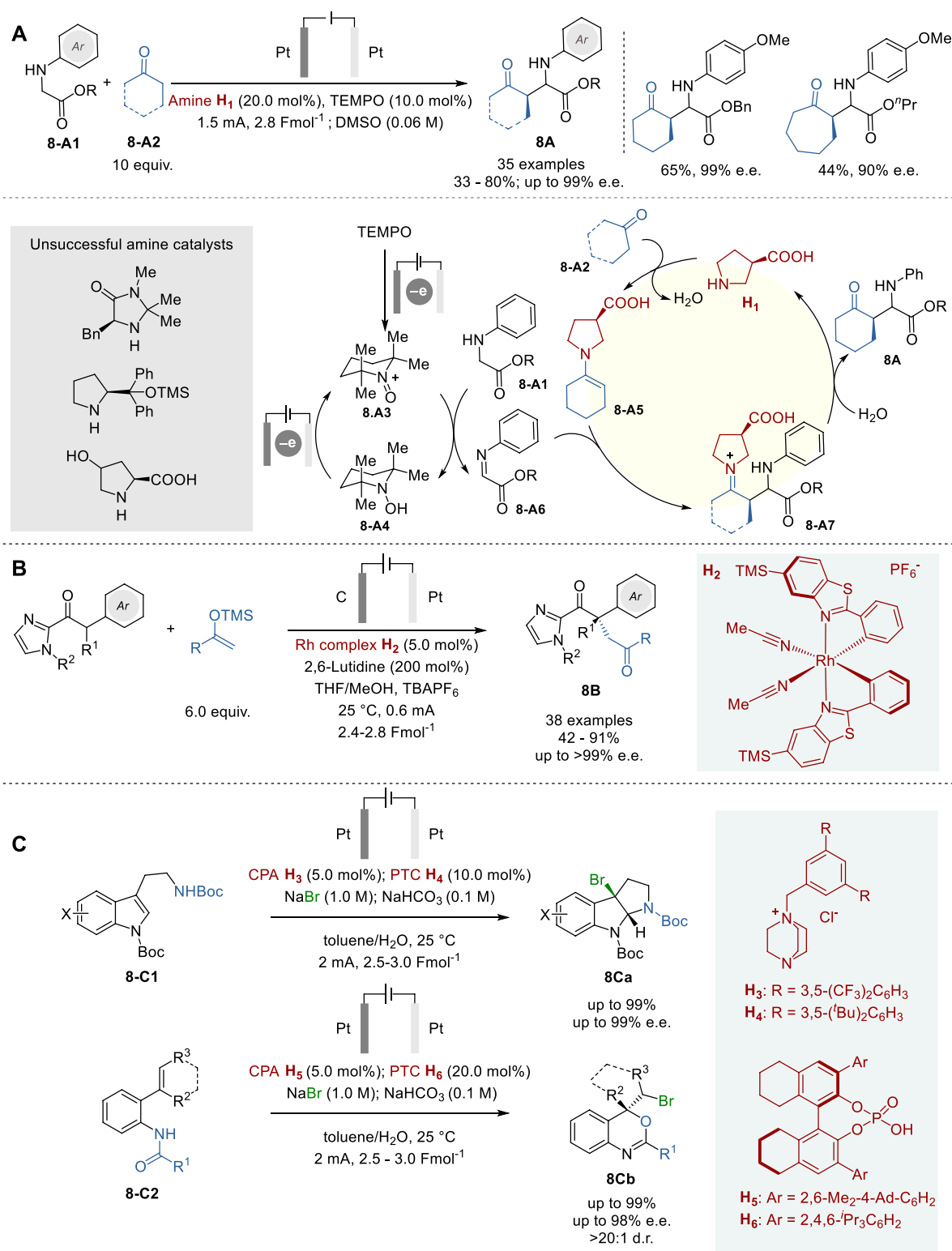


FIGURE 8
Electrochemical organocatalysis for asymmetric synthesis (A–C).

Although combining organic electrosynthesis with asymmetric catalysis is a highly promising strategy, there are challenging issues that impede its progress. For instance, the radical or ion intermediates, generated via oxidation or reduction electrochemically, need to be

connected to an enantioselective catalyst cycle. Otherwise, it will lead to non-catalyzed side reactions, impacting yield and enantioselectivity. Furthermore, certain chiral catalysts may have limited compatibility with an electrochemical cell conditions.

In 2019, Meggers and coworkers introduced a simplified strategy to overcome these challenges, which is termed “electricity-driven chiral Lewis acid catalysis”, using a cationic chiral-at-metal rhodium catalyst **H₂** for the oxidative cross-coupling of 2-acyl imidazoles with silyl enol ethers, producing 1,4-dicarbonyl compounds **8B** (Figure 8B) (Huang et al., 2019). A broad substrate scope was shown with 38 examples to give the corresponding 1,4-dicarbonyl compounds **8B**, including those bearing all-carbon quaternary stereocenters, in 42–91% yields and 90–>99% e. e. A novel chiral cationic Rh complex **H₂** acts as a Lewis acid to activate 2-acyl imidazole substrate toward anodic oxidation by raising the HOMO on Rh enolate formation, which enables mild redox conditions to avoid undesirable side reactions, leading to high levels of chemo- and enantioselectivities, as well as high functional group tolerance.

In 2023, Sun and coworkers reported a combinatory catalysis approach for asymmetric bromocyclizations of tryptamines (**8-C1**) and 2-benzamidostyrenes (**8-C2**) to give the corresponding products **8Ca** and **8Cb** with excellent enantiopurity, using a phase transfer catalyst (PTC), CPA, and electrochemical oxidation (Figure 8C) (Tan et al., 2023). Bromine anion from NaBr is converted to Br₂ by anodic oxidation in aqueous phase, which is captured by PTC catalyst (**H₃** or **H₄**) to form PTC-Br₂ species. Then, the PTC-Br₂ species interacts with lipophilic CPA catalyst (**H₅** or **H₆**) to form an organic-soluble CPA/PTC-Br₂ ion pair, which is transferred to the organic layer to trigger the asymmetric bromination of **8-C1** or **8-C2** without interference from the electrochemical system in the aqueous layer. After bromination, organic product remains in the organic layer, but HBr generated and the ionic PTC catalyst move back to the aqueous layer, where HBr is neutralized by NaHCO₃ and converted to H₂ (cathode) and Br₂ (anode) which is captured by PTC, forming PTC-Br₂ to complete the catalytic cycle. This process is applicable to a good number of tryptamines (**8-C1**) and 2-benzamidostyrenes (**8-C2**) to give the corresponding 3-bromotetrahydropyrroloindoles **8Ca** (90–99% yield and 76–99% e.e.) and 4-bromomethyl-2-phenylbenzooxazines **8Cb** (93–99% yield 89–98% e.e.). This process was also successfully applied to tryptophol derivatives and tryptophan derivatives, as well as the synthesis of a key intermediate (99.5% yield and 90% e.e.) in the total synthesis of (–)-chimonanthine and (–)-hodgkinsine.

4.2 Asymmetric metallaelectrocatalysis

Asymmetric metallaelectrocatalysis is another successful combination of transition-metal catalyzed asymmetric synthesis with electrochemistry, which has proven to be highly effective, as evidenced by its growing use in organic synthesis (Chakraborty et al., 2021). Although the use of heterogeneous metal reductants such as Mn⁰ and Zn⁰ is a common practice to generate and maintain the active catalyst species in transition-metal catalyzed processes, it is associated with some major issues, such as variability in activity due to different sources, batches, storage conditions, stirring conditions, production of excess waste, etc. Thus, more environmentally friendly and efficient alternative to heterogeneous metal reductants is desirable.

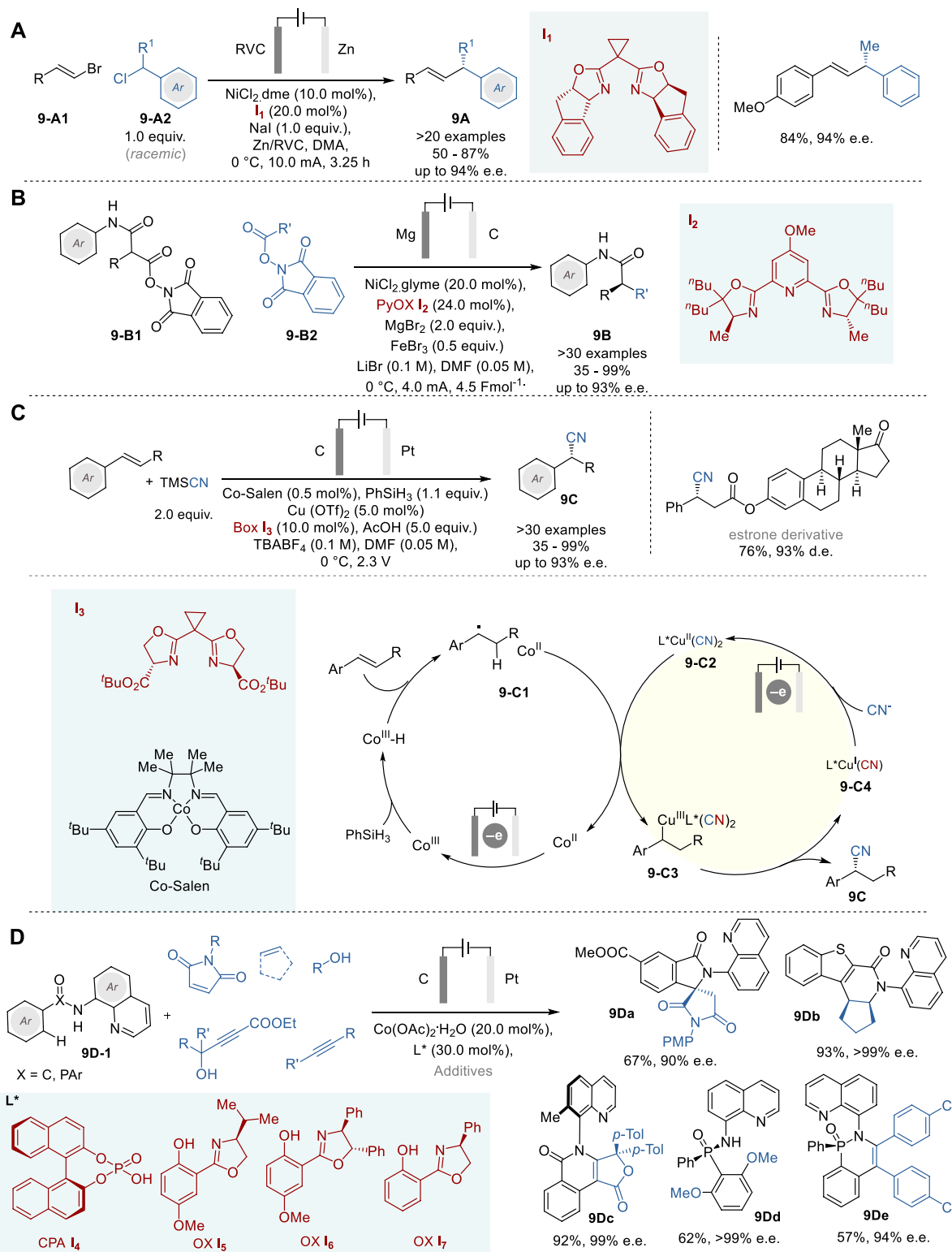
In 2019, DeLano and Reisman reported a novel nickel complex-catalyzed enantioselective electroreductive cross-coupling of alkenyl

bromides **9-A1** and racemic α -substituted benzyl chlorides **9-A2** to give the corresponding α -substituted allylbenzenes **9A** with good structural diversity in 50–87% yield and 80–94% e. e. (Figure 9A) (DeLano and Reisman, 2019). This Ni catalysis includes NiCl₂dme complex with an indanyl-substituted bis(oxazoline) ligand **I₁** as the precursor of the active chiral Ni⁰ catalyst, which is generated by effective electrolysis using a cell equipped with an RVC cathode, a sacrificial Zn anode, and NaBr as an effective additive, as well as an electrolyte.

In 2023, Baran and coworkers reported enantioselective doubly decarboxylative C(sp³)–C(sp³) cross-coupling of the redox-active esters (i.e., *N*-hydroxyphthalimide esters) of malonic acid half amide (**9-B1**) and those of primary carboxylic acids (**9-B2**) by means of Ni-electrocatalysis to give the corresponding amides with α -alkylated stereocenters **9B** (Figure 9B) (Gao et al., 2023). This novel process includes a NiCl₂-glyme complex with a new PyBox-based chiral ligand **I₂** as the chiral metal catalyst, MgBr₂, FeBr₃, and LiBr as electrolytes, Mg anode and RVC cathode. A broad scope of redox-active substrates was used to give the corresponding α -alkylated amides **9B** in 35–99% yield with up to 80–93% e.e. Furthermore, notable advantages of this process were demonstrated by the highly efficient short synthesis of medicinally relevant key intermediates in the total synthesis of natural products through simplification of synthetic pathways, e.g., from 10 to 15 steps to 3–5 steps and elimination of numerous functional group manipulations.

Chiral nitriles are versatile motifs and often serve as key intermediates in the synthesis of pharmaceuticals and bioactive compounds (Fleming et al., 2010). While asymmetric transformations of C=O and C=N bonds into cyanohydrins and α -aminonitriles are well known, the asymmetric hydrocyanation of alkenes is still a challenging reaction. In 2020, Lin and coworkers reported an efficient enantioselective hydrocyanation of conjugated alkenes by means of dual electrocatalysis without stoichiometric oxidants, involving Co-catalyzed HAT and Cu-catalyzed radical cyanation, to give the corresponding α -cyanoalkylarenes (**9C**) and α -cyanoalkylalkenes/alkynes in 32–95% yield and 76–95% e. e. (Figure 9C) (Song et al., 2020). In this process, dual catalytic cycles comprise a Co^{III}-Salen catalyst for HAT with PhSiH₃ and chiral bisoxazoline-Cu(OTf)₂ complex (**I₃**-Cu) for enantioselective cyanation with trimethylsilyl cyanide (TMSCN). In the Co catalyst cycle, H radical is generated from Co^{III}-Salen and hydrosilane to form Co^{III}-H species via HAT, which reacts with the alkene substrate to form a carbon-centered radical **9-C1**. On the other hand, bisoxazoline-Cu(OTf)₂ complex is converted to bisoxazoline-Cu(CN)₂ complex by reacting with cyanide anion generated from TMSCN in the Cu catalyst cycle. Then, radical **9-C1** is captured by L^{*}Cu^{II}(CN)₂ (L^{*} = bisoxazoline **I₃**) (**9-C2**) to generate chiral Cu^{III} species **9-C3**, followed by reductive elimination to form the cyanation product **9C** and releases L^{*}Cu^I(CN) catalyst **9-C4**, which is converted to **9-C2** via single electron oxidation to complete the Cu catalyst cycle.

In 2023, Ackermann and coworkers reported a novel enantioselective electrochemical Co-catalyzed dehydrogenative aryl C-H activation reaction and its applications to the enantioselective C-H/N-H annulations of carboxylic amides, affording various nitrogen heterocycles bearing point and axial chirality, as well as enantioselective desymmetrization of



phosphinic amides by dehydrogenative C–H activation, yielding various P-stereogenic compounds with high enantiopurity (Figure 9D) (von Münchow et al., 2023). This work demonstrated the versatility of electro-oxidative cobalt catalysis

for the synthesis of a range of complex molecules, including spirolactams (e.g., 9Da), dihydroisoquinolinones (e.g., 9Db), atropisomeric furoisoquinolinones (e.g., 9Dc), and phosphinic amides (e.g., 9Dd and 9De). This process shows a broad

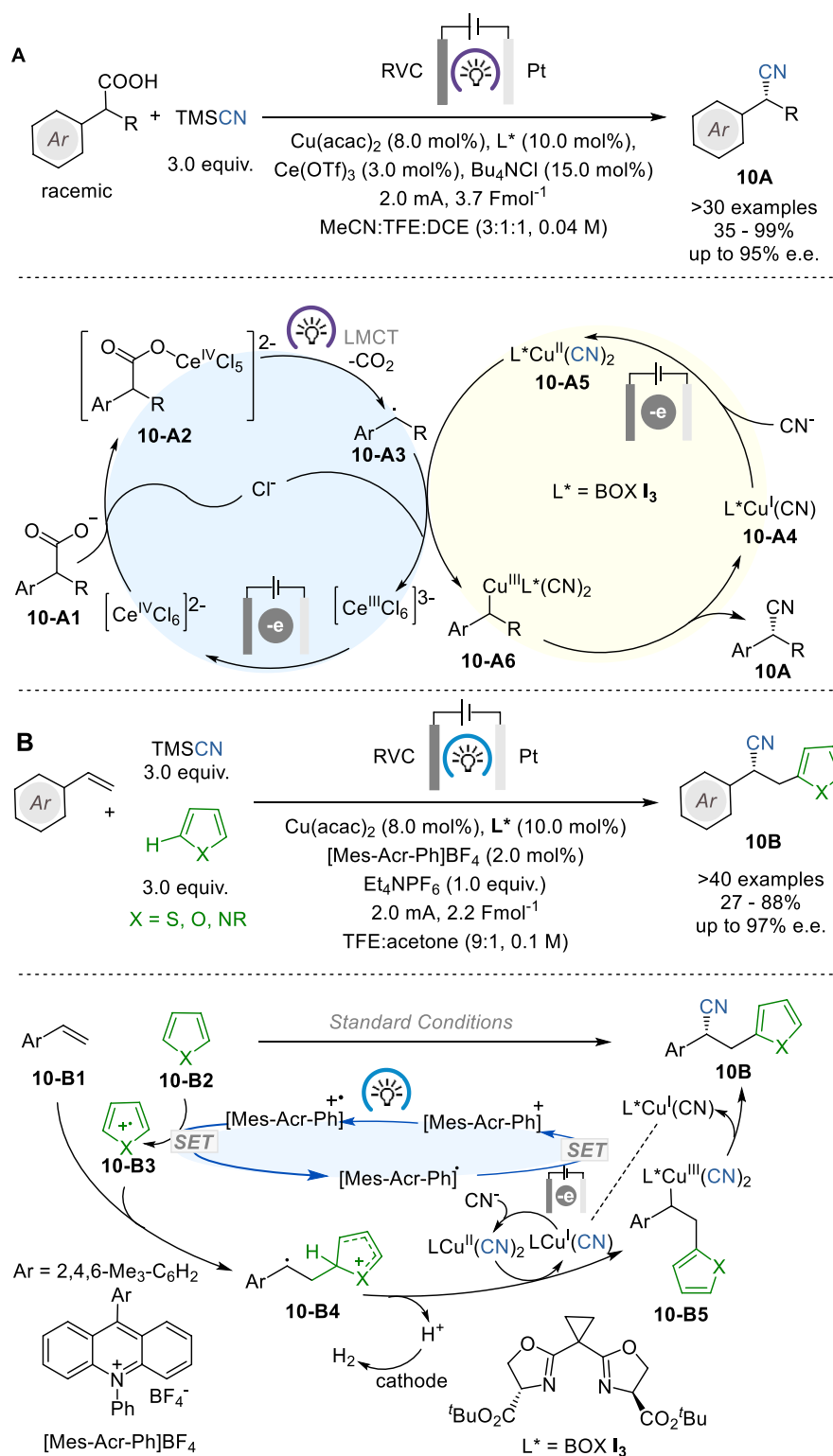


FIGURE 10
 Photoelectrocatalysis for asymmetric cyanations (A,B).

functional group compatibility and uses readily available chiral ligands $\text{I}_4\sim\text{I}_7$ directly accessible from BINOL or amino alcohols, which achieved high enantioselectivity to give those products with up to 99% e.e. Also, this process is scalable to decagram-scale

without any loss of efficiency and enantioselectivity. Since this process generates molecular hydrogen as the sole by-product, it has a high potential to serve as a widely useful electro-oxidative transformation with excellent sustainability.

4.3 Asymmetric photoelectrochemical catalysis

Molecular photoelectrocatalysis has been under rapid development, allowing access to a broad range of redox potentials, enabling oxidative transformations with mild electrode potentials (Barham and König, 2020; Wu et al., 2022). Asymmetric photoelectrochemical catalysis (PEAC) combines photoredox catalysis with asymmetric electrocatalysis to facilitate enantioselective reactions without the need for external chemical oxidants.

In 2022, Xu and coworkers reported a photoelectrocatalytic reaction that enables direct and enantioselective decarboxylative cyanation of racemic α -alkylarylacetic acids (**10-A1**) with TMSCN to give the corresponding enantioenriched α -cyanoalkylarenes (**10A**) by means of Ce/Cu relay catalysis with a Ce salt for catalytic decarboxylation and a chiral Cu complex for stereoselective C–CN formation (Figure 10A) (Lai et al., 2022). The reactions were conducted in an undivided cell equipped with a RVC anode and a Pt plate cathode and the reaction mixture was illuminated with 395 nm LEDs during electrolysis, using Ce(OTf)₃ and Cu(acac)₂ as pre-catalysts and chiral bisoxazoline (BOX) ligand (see **I**₃ in Figure 9C) to give a variety of nitriles **10A** in 35–99% yield and 66–95% e.e.

The proposed mechanism indicates that Ce^{III}(OTf)₃ is converted to Ce^{III}Cl₆^{3–} which is oxidized to Ce^{IV}Cl₆^{2–} at the anode in the presence of chloride ion. The coordination of the carboxylate, followed by photoinduced ligand to metal charge transfer (LMCT) to regenerate the Ce^{III} species and produce a benzylic radical **10-A3** through decarboxylation. This radical **10-A3** then reacts with L^{*}Cu^{II}(CN)₂ (**10-A4**) to produce Ar(R)CH–Cu^{III} complex (**10-A5**), which undergoes reductive elimination to give the chiral nitrile product **10A** and releases L^{*}Cu^I(CN) (**10-A3**). Then, **10-A3** is either anodically oxidized back to the Cu^{II} complex **10-A4** to complete the Cu catalyst cycle.

In 2023, Lai and Xu reported a photoelectrocatalytic protocol for the enantioselective heteroarylcyanation of styrene congeners with unactivated heteroarenes and TMSCN through C–H functionalization, which simultaneously introduces a heteroaryl group and a cyano group across the alkene moiety to give the corresponding α -cyano- β -heteroarylethylarenes **10B** (Figure 10B) (Lai and Xu, 2023). This process employs acridinium salt [Mes-Acr-Ph]BF₄ as photoredox catalyst, Cu(CN)₂ with a bisoxazoline ligand BOX **I**₃ as chiral electrocatalyst, 456 nm LEDs, and TMSCN as the CN source. This novel enantioselective heteroarylcyanation reaction is scalable to gram-scale synthesis of various α -cyano- β -heteroarylethylarenes **10B** in 27–88% yield and 72–97% e. e. The chiral Cu catalyst cycle includes radical cation **10-B4** and chiral Cu^{III} species **10-B5** as key intermediates.

5 Asymmetric biocatalysis

By leveraging the inherent selectivity and efficiency of enzymes and other biological catalysts, biocatalytic asymmetric reactions offer a powerful tool for sustainable and efficient chemical synthesis (Hauer, 2020). In recent years, significant advances have been made in the evolution of biocatalysis (Bornscheuer

et al., 2012; Bell et al., 2021). The exploration of biocatalysts underwent a transformative transition from the extraction of compounds from natural sources to the sophisticated approach of gene mining, facilitated by bioinformatics (Yi et al., 2021).

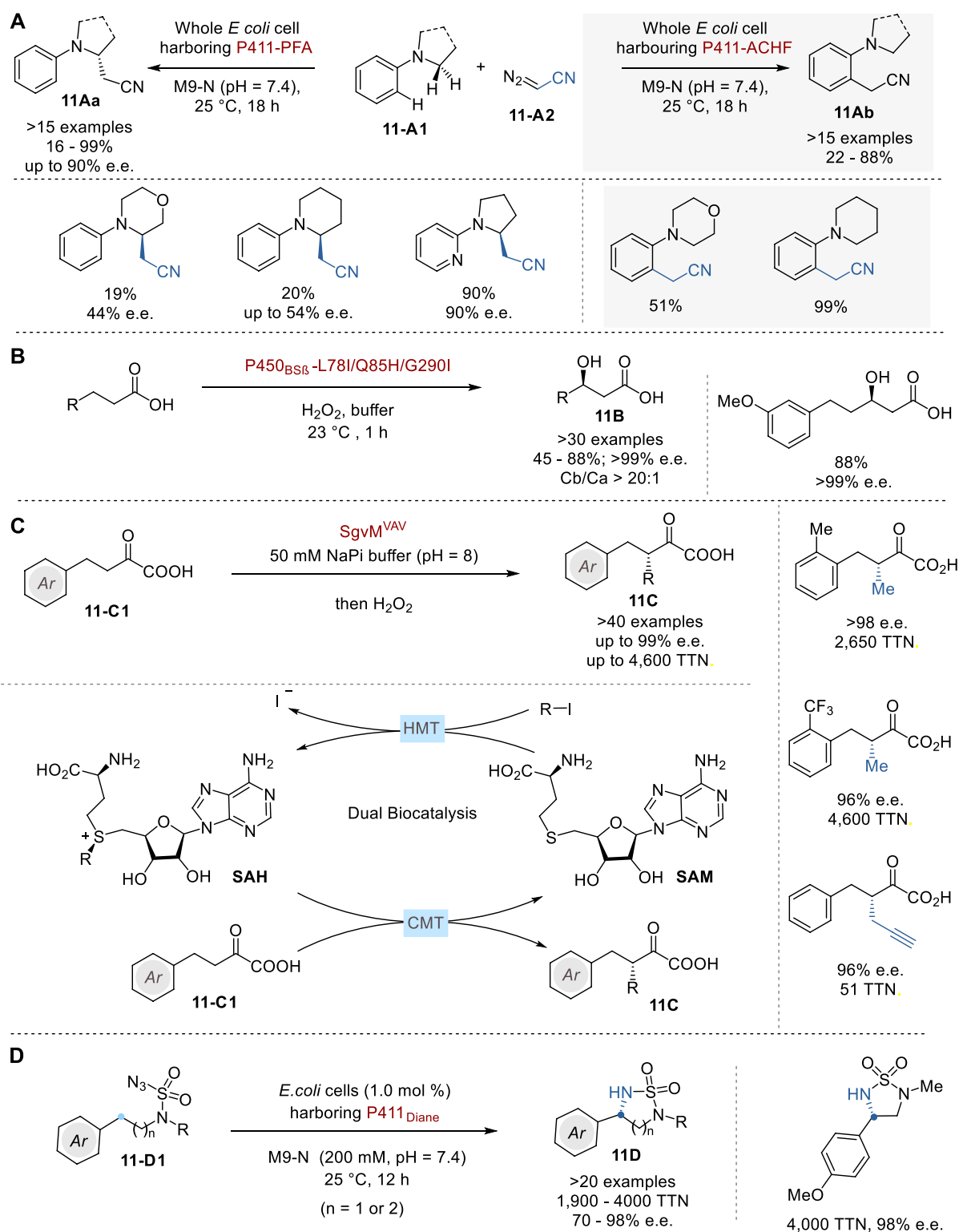
Enzymes are highly efficient as they possess a directing group, which controls selectivity, and a catalytic domain in one molecule. Moreover, an enzyme can be combined with other enzymes in a single process, augmenting their adaptability and effectiveness. Broadly, three distinct approaches have been pursued to enhance enantioselective reactions: (i) the generation of whole-cell biocatalysts by crafting designer organisms, (ii) the refinement of existing enzymes with inherent enantioselectivity for a specific process, and (iii) the evolution of novel enantioselective biocatalysts, starting from non-selective wild-type enzymes (Jaeger and Eggert, 2004).

5.1 Asymmetric enzymatic biocatalysis

In 2023, Arnold and coworkers reported the selective α -cyanocarbene insertion into α -aminoalkyl C (sp³)-H bonds of *N,N*-dialkylaniline congeners **11-A1** via cytochrome P450 enzymes from *Bacillus megaterium* through minimal protein modifications to give enantioenriched α -cyanomethylamines **11Aa** in 16–99% yield with up to 90% e. e. (Figure 11A) (Zhang et al., 2023b). Following comprehensive crystallographic structural analysis, P411-PFA and P411-ACHF were selected as two distinct cyanomethylases. Fluoroalkylase P411-PFA effectively introduces a cyanomethyl group into the α -aminoalkyl C (sp³)-H bond of **11-A1** with notable chemo-, regio-, and enantioselectivity. In sharp contrast, P411-ACHF catalyzes an alkylation of the *ortho*-C (sp²)-H bonds of **11-A1**. This approach represents a significant advancement in the field of biocatalysis, demonstrating the enzyme's ability to perform highly selective and efficient chemical transformations that are challenging to achieve through chemical catalysis.

The selective catalytic hydroxylation of aliphatic C (sp³)-H bonds in the absence of a directing group poses a significant challenge for synthetic chemists (Zhang et al., 2022). In 2022, Wang and coworkers reported an oxy functionalization of inactive C–H bonds in several aliphatic carboxylic acids by using directed evolution of P450_{BSP} hydroxylase. This process exhibited excellent selectivity in terms of chemo-, regio-, and enantioselectivity (>30 examples, C β /C α >20:1, >99% e. e.) (Figure 11B). The X-ray crystal structure analysis of the engineered variant P450_{BSP}-L78I/Q85H/G290I, in conjunction with palmitic acid, provided a comprehensive rationale for the experimentally discerned regio- and enantioselectivity. Furthermore, the structural data revealed that a diminished catalytic pocket volume is responsible for the augmented reactivity with smaller substrates (Ma et al., 2023).

Addition of a methyl group to medicinally active molecules often greatly enhances their biological activity, a notable phenomenon commonly referred to as the “magic methyl effect” (Barreiro et al., 2011; Schönherr and Cernak, 2013). The incorporation of the smallest alkyl group into the α -position of carbonyl compounds with high enantioselectivity presents a considerable challenge for synthetic chemists. In 2023, Yang and



coworkers reported a comprehensive biocatalytic framework comprising an engineered *S*-adenosylmethionine-dependent carbon methyltransferase (CMT) and a remarkably efficient halogen methyltransferase (HMT) to facilitate asymmetric β -

alkylation of α -ketoalkanoic acids **11-C1** to give β -alkyl- α -ketoalkanoic acids **11C** (Ju et al., 2023). CMT SgvM^{VAV} was successfully designed and implemented as a versatile biocatalyst for the enantioselective methylation,

ethylation, allylation, and propargylation of a diverse array of α -keto acids, achieving total turnover numbers (TTNs) of up to 4,600 with high enantioselectivity as high as 99% e.e. The detailed analysis of crystal structures of the engineered biocatalyst unveiled two key catalytic elements, i.e., a Lewis acidic Zn site for substrate enolization and an adjacent chemical co-factor, S-adenosylmethionine (SAM), for stereoselective methyl transfer. Furthermore, HMTs from *Pseudomonas* bacteria, especially those from *P. aeruginosa*, were examined, which showed high efficiency in asymmetric methylation, highlighting the excellent potential of this biocatalytic approach (with HMT turnover up to 7,700 and SAM turnover up to 1,000). β -Alkyl- α -ketoalkanoic acids **11A** thus obtained were further transformed to various α -alkyl carboxylic acids, β -alkyl- α -hydroxy acids, and β -alkyl- α -amino acids.

In the realm of naturally occurring enzymatic C–H functionalization processes, the cytochrome P450-catalyzed C(sp³)–H hydroxylation stands out for its remarkable stereocontrol. Recently, various research groups have put together their efforts on reengineering these enzymes and other heme proteins and employing them to catalyze synthetically valuable reactions previously unknown to nature (Key et al., 2016; Dydio et al., 2017). Along this line, Arnold and coworkers reported a universal cytochrome P450-derived biocatalysts tailored for the enantioselective amination of primary, secondary, and tertiary C(sp³)–H bonds of azidosulfonyl amines **11-D1** to give the chiral cyclic sulfonylimides **11D** (Figure 11D) (Yang et al., 2019). The sulfonylimides **11D** can be deprotected through treatment with 1,3-propanediamine to afford the corresponding chiral 1,2- and 1,3-diamines.

Several cytochromes, including cytochromes P450, cytochromes P411, cytochromes C, and globins, were introduced into intact *Escherichia coli* cells of which P411_{Dianel} (P411 variant lacking the FAD domain) displayed at least ten times higher activity compared to the other heme proteins, providing a TTN of 450. Under the optimized conditions, a variety of chiral cyclic sulfonylimides were obtained with TTN between 1,900–4,000 with enantioselectivity up to 98% e.e. Introduction of beneficial mutations I327P, Y263W and Q437F led to a ten-fold improvement in activity and enhanced the enantioselectivity. This best variant under optimized conditions afforded a C(sp³)–H amination product **11D** with 72,000 TTN and 99.9% e.e.

5.2 Asymmetric photoredox enzymatic biocatalysis

Nature is the best example to showcase how enzymes like fatty acid photodecarboxylase, DNA photolyase, etc., use light to facilitate biologically essential transformations (Schmermund et al., 2019). Asymmetric photoredox enzymatic biocatalysis has recently emerged as an innovative and highly promising synthetic methodology (Schmermund et al., 2019; Emmanuel et al., 2023). Merging biocatalysis with photocatalysis enables selective, light-driven transformations that offer novel reactivity, high selectivity, and better yields under environmentally benign conditions (Emmanuel et al., 2023).

The conventional methods for synthesizing non-canonical amino acids (ncAAs) includes the laborious process of installation and subsequent removal of protecting groups for

amine and carboxylic acid moieties (Najera and Sansano, 2007). In 2023, Yang and coworkers reported a novel approach to the diastereo- and enantioselective synthesis of ncAAs by merging photoredox catalysis with pyridoxal 5'-phosphate (PLP) biocatalysis (Figure 12A) (Cheng et al., 2023). This synergistic photoredox-pyridoxal radical biocatalysis made it possible to synthesize a variety of ncAAs in 24–73% yield with 12–96% e.e. and 10:1~>20:1 d.r. without using any protecting groups. This dual catalysis involves the generation of carbon-centered radical **12-A3** from achiral or racemic alkylborate **12-A2** by photoredox catalyst rhodamine B (RhB) in the photoredox catalyst cycle, while free β -hydroxy- α -amino acid **12-A1** reacts with the pyridoxal-alimine of Lys88 **12-A4** through amine exchange to form the corresponding pyridoxal-alimine of the amino acid **12-A5**, which is dehydrated via quinonoid intermediate to form pyridoxal-alimine of aminoacrylic acid **12-A6** in the P/PLP⁶ enzyme biocatalyst cycle. Then, the radical **12-A3** is captured by **12-A6** to form the stereo-defined pyridoxal-alimine of α -alkylated α -amino acid **12-A7**, which undergoes amine exchange with Lys88 of the enzyme to give the α -alkylated α -amino acid product **12A** and regenerate **12-A4** to complete the biocatalyst cycle.

Stereo-convergent processes offer a streamlined and simplified approach to synthetic routes, but they are often limited by the restricted range of dynamically inducible stereocenters that can be easily epimerized. In 2020, MacMillan, Hyster and their coworkers reported the successful combination of photoredox catalysis, organocatalysis and biocatalysis for the stereoconvergent synthesis of 3-substituted cyclohexanol (X = O) and cyclohexylamines (X = NH) (**12B**) from 3-substituted cyclohexanones (**12-B1**) in 68–92% yield with >98% e.e., and 4:1~>20:1 d.r. via enzymatic dynamic kinetic resolution (DKR) of the substrates bearing traditionally static, unreactive stereocenters (Figure 12B) (DeHovitz et al., 2020). This protocol employs [Ir(dF(CF₃)ppy)₂(dtbbpy)]⁺ PF₆[−] as the photocatalyst, racemic 2-(*tert*-butyldiphenylsilyloxymethyl)pyrrolidine as the amine organocatalyst, and 4-methoxythiophenol as the hydrogen atom transfer (HAT) catalyst for efficient racemization. A ketoreductase *Lactobacillus kefir* alcohol dehydrogenase (LK-ADH) was used for the DKR and reduction to 3-substituted cyclohexanol (**12B**, X = O), while aminotransferases, ATA-256 and ATA-013, were employed for DKR and amination to 3-substituted cyclohexylamine (**12B**, X = NH).

6 Asymmetric catalysis in continuous flow system

Continuous flow reactions and processes have been continuously developed, which encompass a diverse chemical transformations. The advancement in the engineering of continuous flow reactors and precise control of reaction conditions will lead to more productive and energy-efficient systems. While continuous flow processes are not always a replacement for batch processes, there are many advantages that flow chemistry can offer, including safe handling of gaseous reagents, high-pressure reactions, better mixing and heat transfer for very rapid exothermic reactions, and full-automation for higher efficiency (Plutschack et al., 2017). Flow chemistry has attracted much attention from chemists and engineers both in academia and

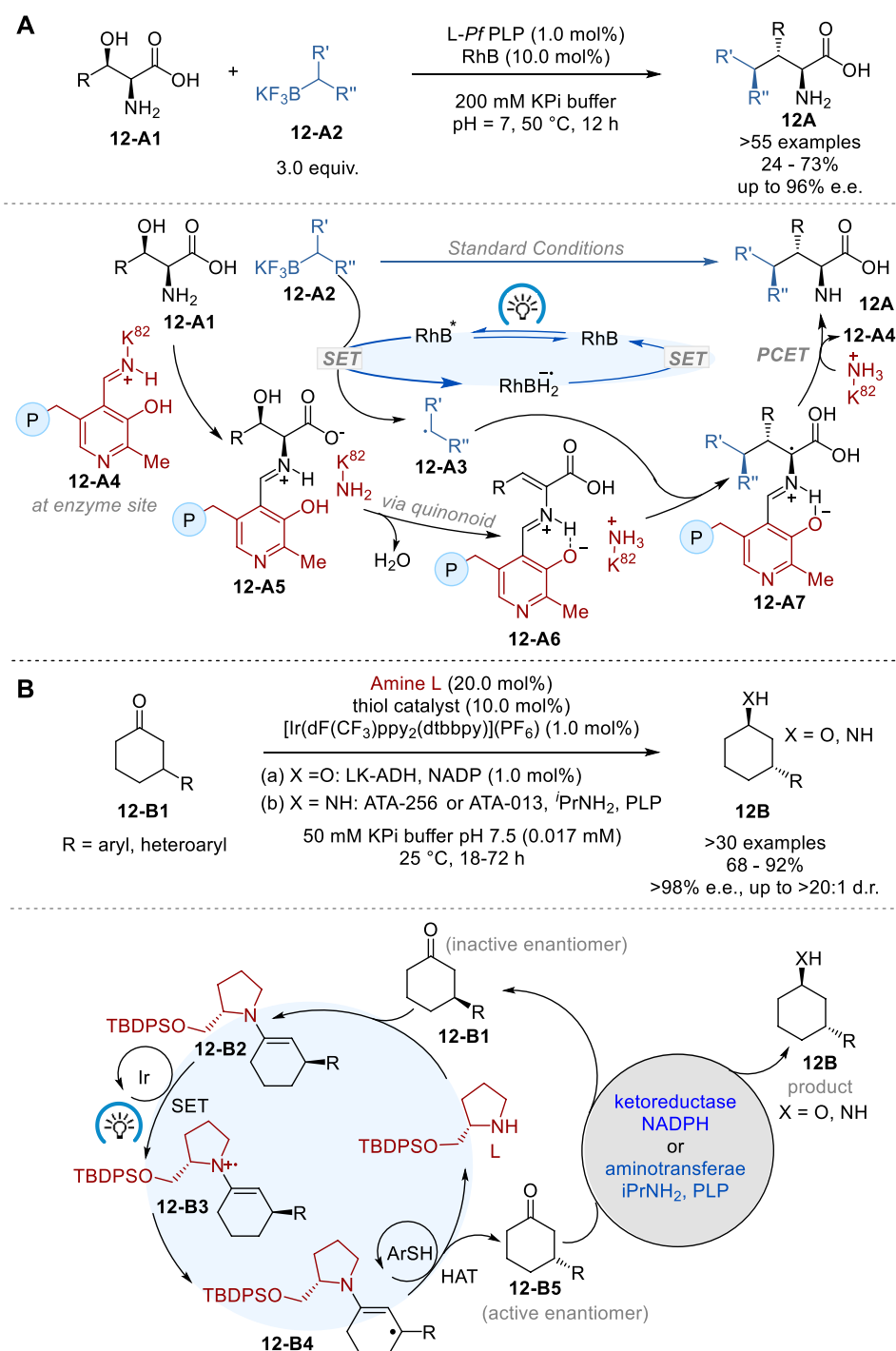


FIGURE 12
Asymmetric photoredox enzymatic biocatalysis (A,B).

industry, since the continuous flow systems can produce a large quantity of fine chemicals and commodity chemicals through continuous operation. As the research on continuous flow reactions has progressed (Ingham et al., 2015), naturally the applications of the continuous flow system to catalytic asymmetric transformations have attracted substantial interest among synthetic chemistry communities in the last decade, and significant advances have been made (Pastre et al., 2013).

6.1 Enantioselective C–C bond-formation through 1,4-addition reactions in continuous flow system

In 2023, Kobayashi and coworkers reported an enantioselective 1,4-addition of malonates to nitroolefins in a continuous flow system, using a mesoporous silica loaded with Ni salts as pre-catalyst, followed by co-feeding of chiral diamine ligand **M**₁ to

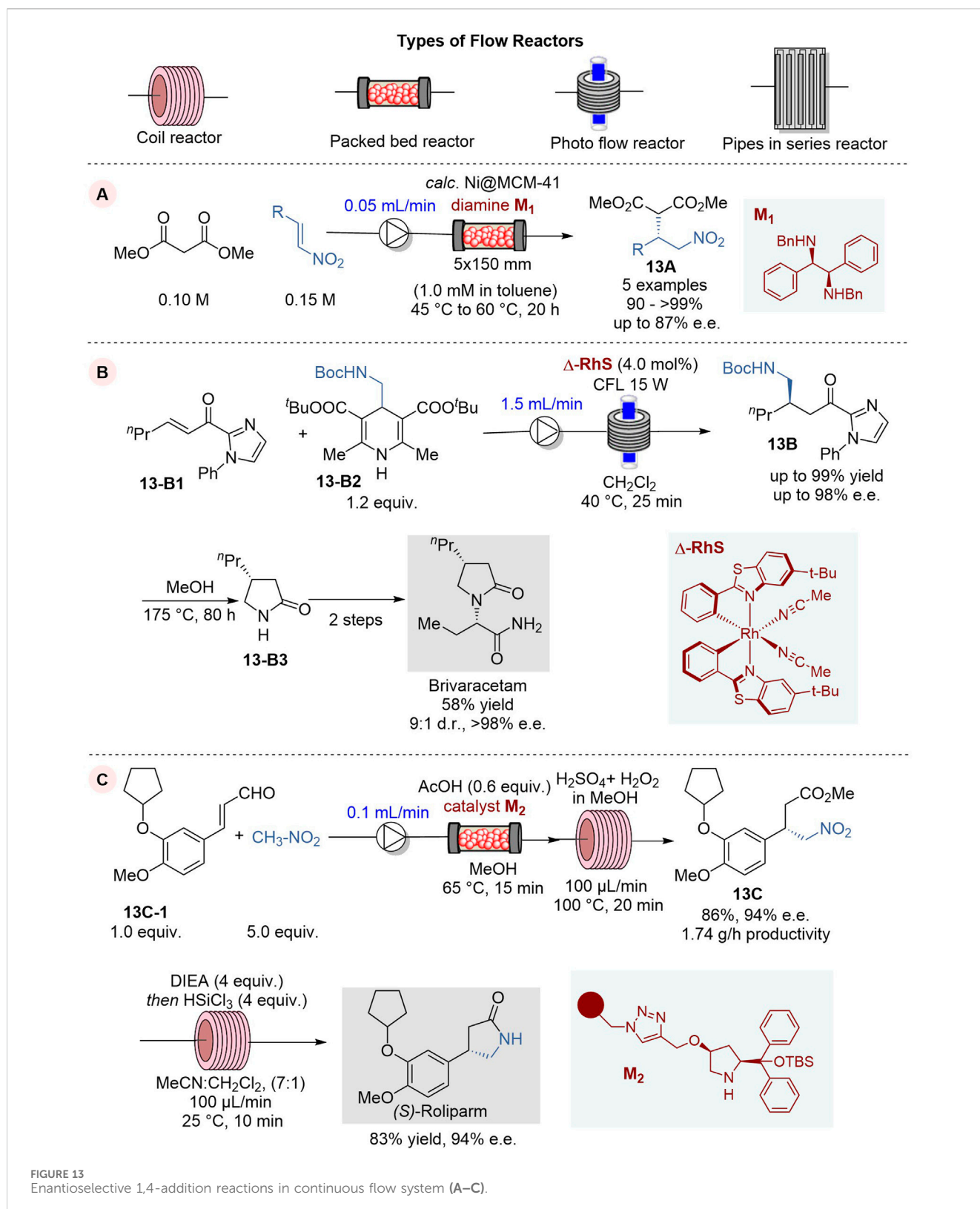


FIGURE 13
Enantioselective 1,4-addition reactions in continuous flow system (A–C).

induce enantioselectivity to give the corresponding 1,4-addition product **13A** (Figure 13A) (Ishitani et al., 2023). This continuous flow process used a column reactor loaded with calcinated Ni pre-catalyst *calc.* Ni@MCM-41 with co-feeding of chiral ligand **M₁** and

run at 45–60°C for 20 h to give 1,4-addition product **13A** in 90–>99% yield and 73–87% e.e. (5 examples). It was found that the enantiopurity of **13A** does not change with extended operation so far up to 90 h with turnover frequency (TOF) of 3.1 h⁻¹ based on

Ni and a turnover number (TON) of 257, and the leaching of Ni was 1.6% after 89 h of operation.

The use of Brivaracetam as an antiepileptic drug for the treatment of drug-resistant epilepsy was approved in Europe and US in 2016 (Markham, 2016). Accordingly, the development of a practical synthetic process for Brivaracetam has been in demand and attracting considerable interest. In 2023, de Assis and coworkers reported the first application of asymmetric photocatalysis in continuous flow for the enantioselective synthesis of Brivaracetam (Figure 13B) (Franco et al., 2023). The key step in this synthesis is the enantioselective photochemical Giese 1,4-addition of BocNHCH₂ radical, generated from Hantzsch ester **13-B2**, to *n*-hex-2-enoylimidazole **13-B1**, promoted by visible-light and chiral bifunctional Rh photocatalyst Δ -RhS, to give the key intermediate **13B** (de Assis et al., 2018). The key parameters for this photocatalysis were investigated and optimized in batch reactions to afford the key intermediate **13B** with 99% yield and 96% e. e. The reaction conditions were further tuned for the continuous flow process and the reaction with a flow rate of 1.0 mL/min and 4% catalytic loading of photocatalyst Δ -RhS at 40°C afforded **13B** in 95% yield and 95% e.e. When a blue LED lamp was substituted by a CFL lamp for better photon emission stability, the reaction gave **13B** in 94% yield and 94% e.e. in just 75 min, while the reaction in a batch reactor required 24 h to achieve a comparable result. The key intermediate **13B** was converted to another key intermediate lactam **13-B3**, followed by *N*-alkylation with (*R*)-2-bromobutanoic acid and subsequent amidation to give Brivaracetam in 58% conversion yield with 98% e. e. and 9:1 d.r.

(*S*)-Rolipram, a selective inhibitor of cAMP-specific phosphodiesterase PDE4, is an anti-inflammatory/antidepressant agent, which is often employed as a racemic mixture in biological studies. However, the pharmaceutical activity of its enantiomers was found to be divergent in many cases and thus its enantioselective synthesis needs to be developed.

In 2022, Kappe, Ötvös and their coworkers reported an efficient and green asymmetric synthesis of (*S*)-Rolipram by means of a telescoped enantioselective conjugate addition-oxidative esterification sequence followed by metal-free nitro reduction and lactamization process under continuous flow conditions (Figure 13C) (Nagy et al., 2022). The asymmetric 1,4-addition of nitromethane to cinnamaldehyde derivative **13-C1** was effectively promoted by a diphenylproline-based organocatalyst on a cross-linked polystyrene-support **M₂** in an Omnifit glass column reactor at 65°C at the flow rate of 0.075 mL/min to give the corresponding chiral γ -nitro aldehyde. This aldehyde was directly delivered to a column reactor for oxidative esterification with persulfuric acid and methanol at 100°C to afford the key intermediate, γ -nitro ester **13C**, in 84% yield and 94% e. e. in a 3-h operation. In this process, hazardous and explosive persulfuric acid is safely generated in a highly controlled manner by mixing concentrated sulfuric acid and hydrogen peroxide, which is fed to the reactor with ease in a flow system. The nitro reduction and spontaneous lactamization of **13C** was carried with trichlorosilane and diisopropylethylamine (DIEA) in acetonitrile/dichloromethane, using a coil reactor under continuous flow conditions to give (*S*)-Rolipram in 83% yield and 94% e.e.

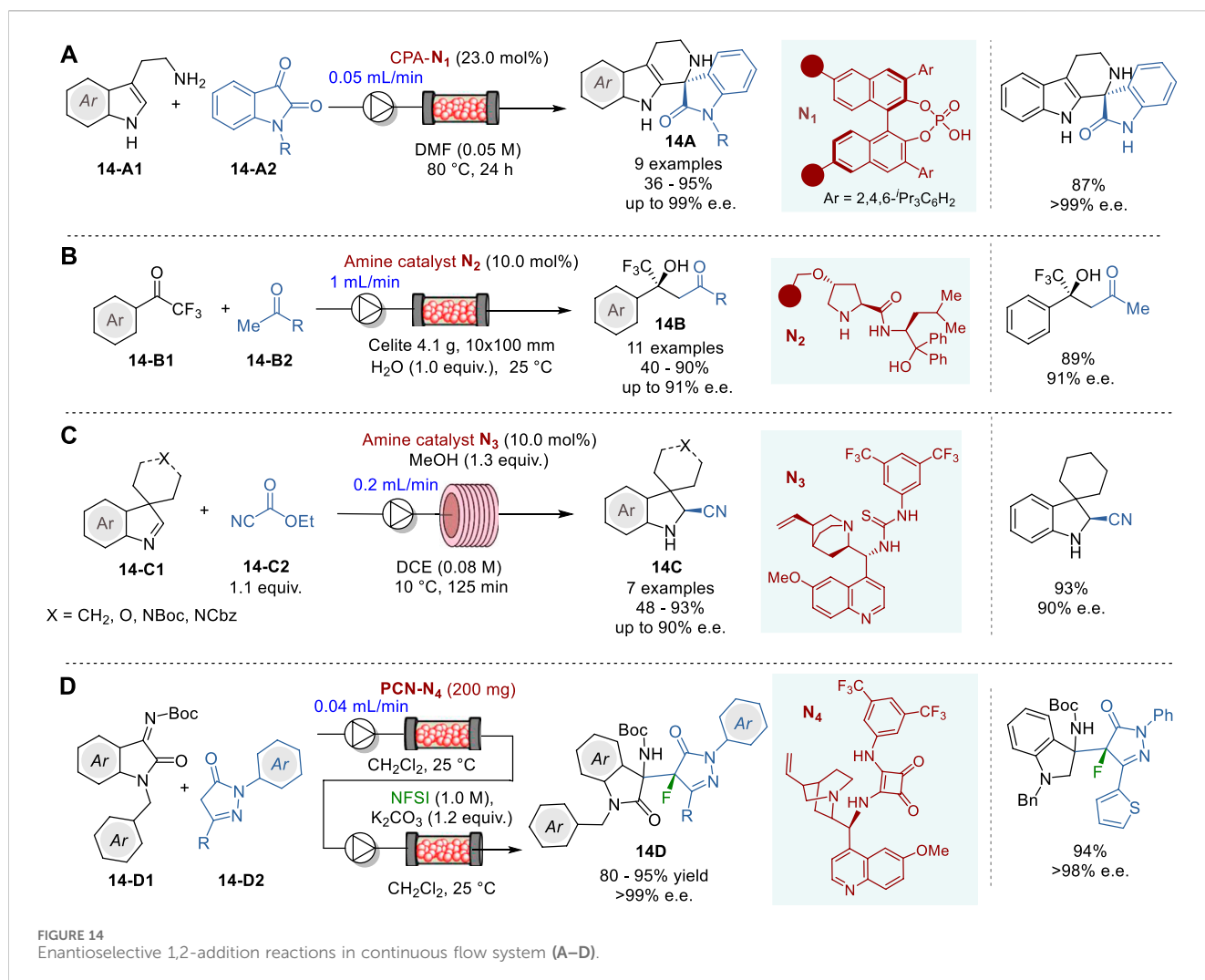
6.2 Enantioselective C-C bond-formation through 1,2-addition in continuous flow system

One of the most widely used methods for the synthesis of chiral tetrahydro- β -carboline is the asymmetric Pictet–Spengler reaction. Thus, over the years many enantioselective Pictet–Spengler reactions of tryptamines with aldehydes using chiral organo/metal catalysts have been reported, however limited to only batch operations (Wanner et al., 2007; Stöckigt et al., 2011). In 2023, Pericàs and coworkers reported the first enantioselective Pictet–Spengler reaction of tryptamines **14-A1** and isatins **14-A2** under continuous flow conditions, using a polymer-supported CPA (*R*)-TRIP **N₁** in a packed bed reactor, to give the corresponding quarternary tetrahydro- β -carboline (TH β C) **14A** in 36–95% yield and 39–99% e.e. (Figure 14A) (Chaudhari et al., 2023). This continuous flow system was successfully applied to the synthesis of the chiral precursors of Tadalafil, the Iboga-type alkaloid (+)-Tabertingine, and antimalarial spiroindolines.

The use of chiral secondary amines as catalysts in asymmetric aldol reactions has been developed as a powerful method for the synthesis of optically active secondary or tertiary alcohols through asymmetric carbon-carbon bond formation. Thus, a few catalytic processes have been developed for the enantioselective synthesis of tertiary trifluoromethyl carbinols, but there are certain issues, such as long reaction time, high catalyst loading and racemization of the product, which needs to be addressed for practical use (Trost and Brindle, 2010; Pluta et al., 2019). In 2021, Kobayashi and coworkers reported the first catalytic enantioselective aldol reactions of trifluoroacetophenones **14-B1** with methyl ketones **14-B2** under continuous flow conditions, using a polystyrene-supported prolinamide catalyst **N₂** in a column reactor to give trifluoromethyl carbinols **14B** in 40–90% yield and 83–91% e.e. (Figure 14B) (Yue et al., 2021). It was found that a proper feeding of water facilitated the hydrolysis of the iminium intermediates on the polymer, which enabled unusually long life times (>195 h) of prolinamide catalyst **N₂** in this continuous flow system. A mechanistic study revealed that the continuous flow system suppressed the racemization of the product **14B** observed under batch conditions. The salient feature of this continuous flow process was demonstrated by its application to the formal synthesis of a chiral fepentadiol analog.

In 2023, Brindisi and coworkers reported the first continuous flow asymmetric Strecker synthesis of spiroindolenines **14C** through enantioselective cyanation of cyclic (*Z*)-aldimines **14-C1** promoted by cinchona alkaloid-based organocatalyst using ethyl cyanofornate as the cyanide source (Figure 14C) (Alfano et al., 2023). Under optimized continuous flow conditions with the quinine-derived catalyst **N₃** using 0.08 M solution of reactants at a flow rate of 0.2 mL/min, several spiroindolenines **14C** were obtained in 48–93% yield and 50–90% e.e. Regarding sustainability, the reaction time was drastically reduced from 72 h under batch conditions to 125 min under continuous flow conditions, showing a far greater space-time-yield (STY) (0.24 g L⁻¹h⁻¹) in the flow system than that in batch system (0.0208 g L⁻¹h⁻¹).

In 2018, Zhao and coworkers reported the first successful use of porous carbon nanosheet (PCN) as a support for immobilizing chiral quinine-squaramide **N₄**, and its application to the

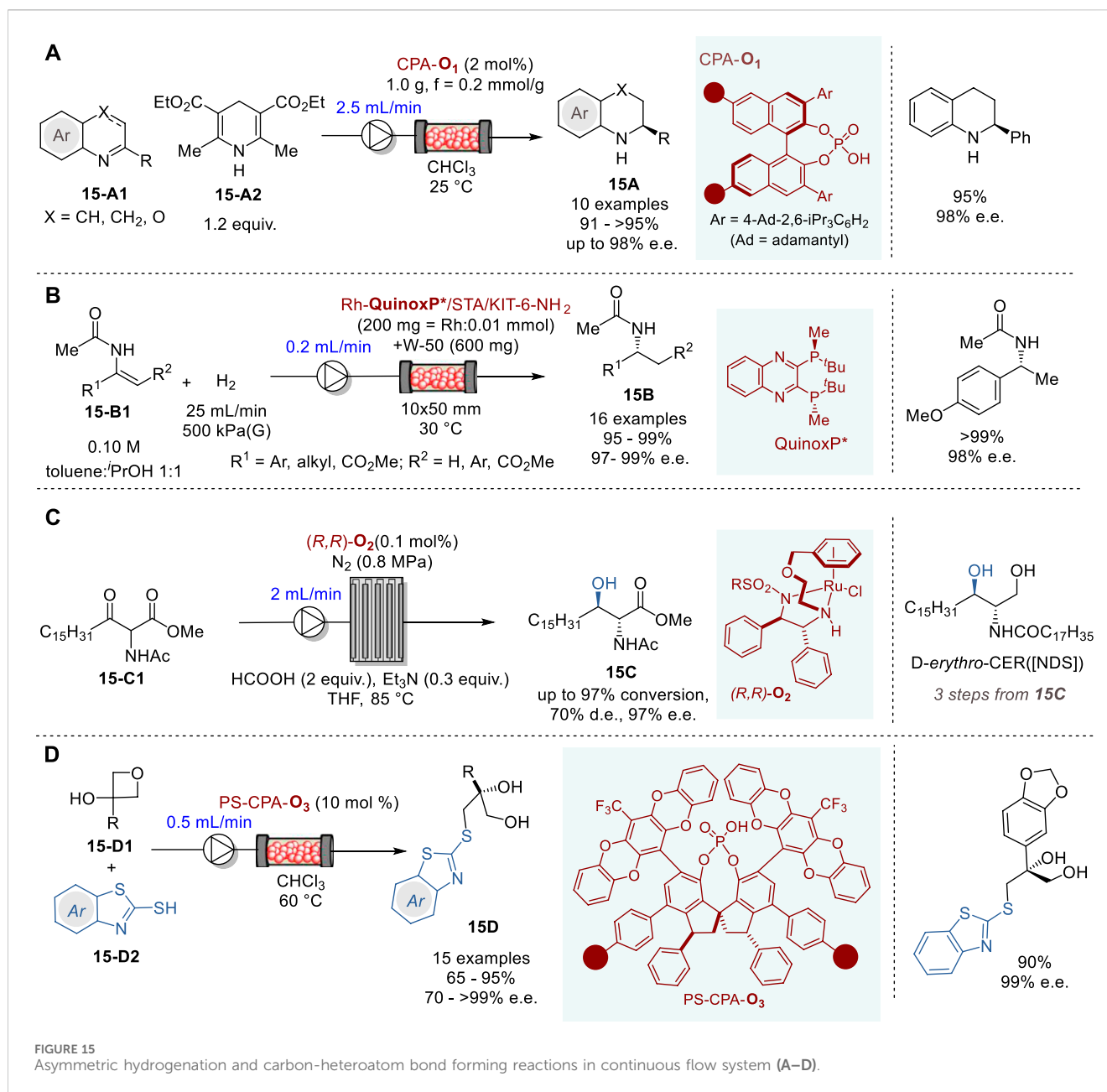


continuous flow synthesis of fluoropyrazolonylaminoxyindoles **14D** through asymmetric Friedel–Crafts addition of pyrazolones **14-D2** to isatin ketimines **14-D1** with *N*-fluoro-benzene-sulfonimide (NFSI) (Figure 14D) (Zhao et al., 2018). The 3-substituted-3-aminooxindoles motifs constitute the core structure of numerous natural products and drug candidates (Kaur et al., 2015). The PCN-quinine-squaramide catalyst PCN-**N**₄ was prepared by immobilizing quinine-squaramide **N**₄ on the vinylated PCN surface through free-radical co-polymerization of **N**₄, bearing a vinyl group, using divinylbenzene (DVB) as a linker. For the surface modification, PCN was first reacted with diazonium salt generated *in situ* from 4-aminobenzyl alcohol and sodium nitrate to give 4-hydroxymethylphenyl-PCN. The subsequent acylation with acryloyl chloride afforded the vinyl-functionalized PCN intermediate (PCN-vinyl), which was ready for co-polymerization with **N**₄ and DVB to give polymer-coated PCN-**N**₄. The continuous flow reaction of **14-D1** with **14-D2** was performed, using a packed-bed reactor with PCN-**N**₄ and the product solution was directly delivered to a column reactor with K₂CO₃ with NFSI feeding to give **14D** in 80–90% yield and >99% e.e. (5 examples). Throughout the continuous flow operation, no decline in the catalytic efficiency of PCN-**N**₄ was

observed, which indicates that **N**₄ attached to PCN is fully exposed to the reaction medium, resulting in a homogeneous catalytic environment for the active sites.

6.3 Asymmetric hydrogenation and carbon-heteroatom bond forming reactions in continuous flow system

Recently, transfer hydrogenation for the synthesis of chiral nitrogen-containing heterocycles has been attracting considerable attention (Parmar et al., 2014; Pálvölgyi et al., 2021; Faisca Phillips and Pombeiro, 2023). In 2023, Nagorny and coworkers reported an efficient transfer hydrogenation of 2-substituted quinolines (X = CH or CH₂) and 3-substituted 1,4-benzooxazines (X = O) (**15-A1**) with a Hantzsch ester **15-A2** promoted by an immobilized chiral phosphoric acid catalyst CPA-**O**₁ in a fluidized bed reactor under continuous flow conditions to give the corresponding tetrahydroquinolines (X = CH₂) and dihydrobenzooxazines (X = O) **15A** in 91–>95% yield and 86–98% e. e. (Figure 15A) (Zhelavskiy and Jhang, 2023). The immobilized CPA-**O**₁ catalyst can be recovered and recycled by filtration and washing. In this



reactor, the flow rate of 2.0–2.5 mL/min was optimal, yielding the product **15A** at 1.5 g (7.5 mmol) per hour.

In 2020, Kobayashi and coworkers reported a highly efficient continuous flow asymmetric hydrogenation of enamides and dehydroamino esters **15-B1** promoted by the immobilized chiral Rh-QuinoxP* catalyst on KIT-6 mesoporous silica to give the corresponding amides, α - and β -amino acid esters **15B** in excellent yield and enantiopurity (Figure 15B) (Saito and Kobayashi, 2020). Preparation of the chiral heterogeneous Rh catalyst involved three steps, i.e., (i) the surface amine functionalization of KIT-6 with 3-aminopropyl-Si(OEt)₃ coupling reagent to form KIT-6-NH₂, (ii) salt formation with silicotungstic acid (STA) to form STA/KIT-6-NH₂, and (iii) immobilization of chiral Rh complex Rh-QuinoxP*, which was prepared *in situ* from [Rh(nbd)₂]⁺BF₄[−] and QuinoxP* to give Rh-QuinoxP*/STA/KIT-6-

NH₂ catalyst. Then, a fixed-bed reactor was packed with the chiral heterogeneous catalyst and used for the continuous flow reaction under hydrogen gas flow. Various enamides, α - and β -dehydroamino esters were converted to the corresponding amides, α - and β -dehydroamino acid esters **15B** in 95–>99% yield and 97–99% e.e. The chiral catalyst activity did not change for 90 h with a turnover number (TON) of 10,800.

The optically active ceramide *N*-((2S,3R)-1,3-dihydroxyoctadecan-2-yl)stearamide (D-erythro-CER [NDS]) is clinically used for the treatment of prominent skin diseases such as psoriasis and atopic dermatitis. In 2019, Touge and coworkers reported an efficient continuous flow asymmetric transfer hydrogenation process through dynamic kinetic resolution of methyl 2-acetamido-3-oxooctadecanoate (**15-C1**) catalyzed by a chiral diamine-Ru complex (*R,R*)-O₂ to produce methyl (2R,3R)-

2-acetamido-3-hydroxyoctadecanoate (**15C**) (Figure 15C) (Touge et al., 2018). The continuous flow reaction was executed by introducing **15-C1**, HCO_2H , NEt_3 , and Ru-diamine catalyst (R,R)-**O₂** in THF into a pipes-in-series reactor. The reaction, conducted in a 100 L reactor, comprising 19 stainless steel pipes connected to 18 smaller diameter jumper tubes with 0.1 mol% catalyst (R,R)-**O₂** for 36 h, produced 77.4 kg of **15C** in 96% yield with 97% e. e. and 69% d. e. This product **15C** was converted to ceramide D-erythro-CER [NDS] in three steps, i.e., NaBH_4 reduction, deacetylation with NaOH and amidation with methyl stearate, followed by recrystallization, wherein 58 kg of D-erythro-CER [NDS] with >99% d. e. and >99% e.e.

In 2020, Pericàs and coworkers reported the enantioselective desymmetrization of 3-substituted 3-hydroxyoxetanes **15-D1** with benzothiazole-2-thiols **15-D2** promoted by immobilized CPAs with very bulky 3,3'-diphenyl-SPINOLs (e.g., CPA-**O₃**) to give the corresponding 3-benzothiazol-2-ylthiopropene-1,2-diol (**15D**) in high yield and enantiopurity (Figure 15D) (Lai et al., 2020). C2-symmetrical 1,1-spirobiindane-7,7-diol (SPINOL) derivatives containing polymerizable styryl units were prepared and subjected to radical co-polymerization with styrene to form the corresponding polystyrene anchored SPINOLs, which were reacted with POCl_3 /pyridine to give polymer anchored PS-CPAs. Six chiral PS-CPAs were screened for optimization and PS-CPA-**O₄** was identified as the best catalyst, giving a product **15D** in 90% yield and 98% e. e. in the model reaction for optimization. The excellent results achieved by PS-CPA-**O₃** could be attributed to the very bulky pentacyclic heteroaryl substituents at the 6 and 6' positions and their rotational mobility which plays a crucial role in achieving excellent enantioselectivity. The continuous flow reactions were carried out in a size-adjustable jacketed tubular reactor to give various 3-benzothiazol-2-ylthiopropene-1,2-diols (**15D**) in 65–95% yield and 70~>99% e. e.

7 Conclusion and future perspective

Development of catalytic asymmetric reactions continues to be an important research topic in organic chemistry, partly because it will contribute significantly to the pharmaceutical sciences and production of therapeutic drugs. The ideal catalytic reactions would proceed in 100% yield with complete chemoselectivity, regioselectivity, and stereoselectivity. From the standpoint of green chemistry, highly efficient (i.e., high turnover number) and safe reagents are desirable. We have highlighted the most significant works on the catalytic asymmetric reactions from 2018 to 2023 in this review article, which clearly shows that significant advances have been made in this field in the last 5 years. In addition to metal catalysis and biocatalysis, organocatalysis has also proven to be a valuable tool for the construction of optically active compounds as evidenced by the Nobel Prize in Chemistry awarded jointly to Benjamin List and David MacMillan in 2021. Recently, electrocatalysis and photoredox catalysis have emerged as powerful tools for the development of new and valuable transformations for construction of organic molecules in enantiomerically pure form.

In addition to single catalyst systems, dual catalyst systems have significantly contributed to the development of novel enantioselective catalytic reactions. For example, hybrid catalyst systems, consisting of a transition metal catalyst and an organocatalyst are quite effective and efficient. Cooperative catalyst systems such as photoredox catalyst with transition metal catalyst, biocatalyst with electrocatalyst, and organocatalyst with photoredox catalyst, have also flourished. Furthermore, continuous flow system has made rapid advancement and will potentially lead the industrial production of chiral pharmaceutical drugs in the near future. Continuous flow system has an advantage over classical batch system such as ease of precise control of reaction conditions, and ease of scale-up for production. The future of catalytic asymmetric synthesis is highly promising, because of the continuous emergence of novel catalytic systems, while multi-catalyst systems will further expand their horizon. We hope this review article will help readers update and appreciate the remarkable recent progress in catalytic asymmetric synthesis and its bright future.

Author contributions

AG: Conceptualization, Writing–original draft, Writing–review and editing. DR: Conceptualization, Writing–original draft, Writing–review and editing. HB: Conceptualization, Writing–original draft, Writing–review and editing. TA: Conceptualization, Writing–original draft, Writing–review and editing. IO: Conceptualization, Funding acquisition, Supervision, Writing–original draft, Writing–review and editing.

Funding

The author(s) declare that financial support was received for the research, authorship, and/or publication of this article. This work was supported in part by grants from the National Institutes of Health, U. S. A. (CA237154 and AI116420).

Conflict of interest

The authors declare that the research was conducted in the absence of any commercial or financial relationships that could be construed as a potential conflict of interest.

The author(s) declared that they were an editorial board member of Frontiers, at the time of submission. This had no impact on the peer review process and the final decision.

Publisher's note

All claims expressed in this article are solely those of the authors and do not necessarily represent those of their affiliated organizations, or those of the publisher, the editors and the reviewers. Any product that may be evaluated in this article, or claim that may be made by its manufacturer, is not guaranteed or endorsed by the publisher.

References

- Akiyama, T., Itoh, J., Yokota, K., and Fuchibe, K. (2004). Enantioselective Mannich-type reaction catalyzed by a chiral Brønsted acid. *Angew. Chem. Int. Ed.* 43 (12), 1566–1568. doi:10.1002/anie.200353240
- Akiyama, T., and Ojima, I. (2022). *Catalytic asymmetric synthesis*. 4th Edition. USA: John Wiley and Sons.
- Albini, A., and Fagnoni, M. (2004). Green chemistry and photochemistry were born at the same time. *Green Chem.* 6 (1), 1–6. doi:10.1039/b309592d
- Alfano, A. I., Sorato, A., Ciogli, A., Lange, H., and Brindisi, M. (2023). Enantioselective catalytic Strecker reaction on cyclic (Z)-aldimines in flow: reaction optimization and sustainability aspects. *J. Flow Chem.* 14, 197–210. doi:10.1007/s41981-023-00279-9
- Arnaboldi, S., Magni, M., and Mussini, P. R. (2018). Enantioselective selectors for chiral electrochemistry and electroanalysis: stereogenic elements and enantioselection performance. *Curr. Opin. Electrochem.* 8, 60–72. doi:10.1016/j.coelec.2018.01.002
- Bae, H. Y., Höfler, D., Kaib, P. S., Kasaplar, P., De, C. K., Döhring, A., et al. (2018). Approaching sub-ppm-level asymmetric organocatalysis of a highly challenging and scalable carbon-carbon bond forming reaction. *Nat. Chem.* 10 (8), 888–894. doi:10.1038/s41557-018-0065-0
- Bahmanyar, S., and Houk, K. (2001). The origin of stereoselectivity in proline-catalyzed intramolecular aldol reactions. *J. Am. Chem. Soc.* 123 (51), 12911–12912. doi:10.1021/ja011714s
- Barham, J. P., and König, B. (2020). Synthetic photoelectrochemistry. *Angew. Chem. Int. Ed.* 59 (29), 11732–11747. doi:10.1002/anie.201913767
- Barreiro, E. J., Kümmerle, A. E., and Fraga, C. A. (2011). The methylation effect in medicinal chemistry in medicinal chemistry. *Chem. Rev.* 111, 5215–5246. doi:10.1021/cr200060g
- Bell, E. L., Finnigan, W., France, S. P., Green, A. P., Hayes, M. A., Hepworth, L. J., et al. (2021). Biocatalysis. *Nat. Rev. Methods Prim.* 1 (1), 46. doi:10.1038/s43586-021-00044-z
- Bendelsmith, A. J., Kim, S. C., Wasa, M., Roche, S. P., and Jacobsen, E. N. (2019). Enantioselective synthesis of α -allyl amino esters via hydrogen-bond-donor catalysis. *J. Am. Chem. Soc.* 141 (29), 11414–11419. doi:10.1021/jacs.9b05556
- Bertuzzi, G., Corti, V., Izzo, J. A., Ricko, S., Jessen, N. I., and Jørgensen, K. A. (2022). Organocatalytic enantioselective construction of conformationally stable C (sp²)-C (sp³) atropisomers. *J. Am. Chem. Soc.* 144 (2), 1056–1065. doi:10.1021/jacs.1c12619
- Betz, U. A., Arora, L., Assal, R. A., Azevedo, H., Baldwin, J., Becker, M. S., et al. (2023). Game changers in science and technology-now and beyond. *Technol. Forecast. Soc. Change* 193, 122588. doi:10.1016/j.techfore.2023.122588
- Bornscheuer, U. T., Huisman, G., Kazlauskas, R., Lutz, S., Moore, J., and Robins, K. (2012). Engineering the third wave of biocatalysis. *Nature* 485 (7397), 185–194. doi:10.1038/nature11117
- Breslow, R. (1958). On the mechanism of thiamine action. IV. 1 Evidence from studies on model systems. *J. Am. Chem. Soc.* 80 (14), 3719–3726. doi:10.1021/ja01547a064
- Ceramella, J., Iacopetta, D., Franchini, A., De Luca, M., Saturnino, C., Andreu, I., et al. (2022). A look at the importance of chirality in drug activity: some significative examples. *Appl. Sci.* 12 (21), 10909. doi:10.3390/app122110909
- Chakraborty, P., Mandal, R., Garg, N., and Sundararaju, B. (2021). Recent advances in transition metal-catalyzed asymmetric electrocatalysis. *Coord. Chem. Rev.* 444, 214065. doi:10.1016/j.ccr.2021.214065
- Chaudhari, M. B., Gupta, P., Llanes, P., and Pericàs, M. A. (2023). Polymer-supported phosphoric-acid catalyzed enantioselective pictet-spengler cyclisation for the synthesis of quaternary tryptolines in batch/continuous flow. *Adv. Synthesis Catal.* 365 (4), 527–534. doi:10.1002/adsc.202201275
- Chen, C., Peters, J. C., and Fu, G. C. (2021). Photoinduced copper-catalysed asymmetric amidation via ligand cooperativity. *Nature* 596 (7871), 250–256. doi:10.1038/s41586-021-03730-w
- Cheng, L., Li, D., Mai, B. K., Bo, Z., Cheng, L., Liu, P., et al. (2023). Stereoselective amino acid synthesis by synergistic photoredox-pyridoxal radical biocatalysis. *Science* 381 (6656), 444–451. doi:10.1126/science.adg2420
- Corić, I., and List, B. (2012). Asymmetric spiroacetalization catalysed by confined brønsted acids. *Nature* 483, 315–319. doi:10.1038/nature10932
- Das, S., Zhu, C., Demirbas, D., Bill, E., De, C. K., and List, B. (2023). Asymmetric counteranion-directed photoredox catalysis. *Science* 379 (6631), 494–499. doi:10.1126/science.adc8190
- de Assis, F. F., Huang, X., Akiyama, M., Pilli, R. A., and Meggers, E. (2018). Visible-light-activated catalytic enantioselective β -alkylation of α,β -unsaturated 2-acyl imidazoles using Hantzsch esters as radical reservoirs. *J. Org. Chem.* 83 (18), 10922–10932. doi:10.1021/acs.joc.8b01588
- DeHovitz, J. S., Loh, Y. Y., Kautzky, J. A., Nagao, K., Meichan, A. J., Yamauchi, M., et al. (2020). Static to inducibly dynamic stereocontrol: the convergent use of racemic β -substituted ketones. *Science* 369 (6507), 1113–1118. doi:10.1126/science.abc9909
- DeLano, T. J., and Reisman, S. E. (2019). Enantioselective electroreductive coupling of alkenyl and benzyl halides via nickel catalysis. *ACS Catal.* 9 (8), 6751–6754. doi:10.1021/acscatal.9b01785
- Deng, R., Wu, S., Mou, C., Liu, J., Zheng, P., Zhang, X., et al. (2022). Carbene-catalyzed enantioselective sulfonylation of enone aryl aldehydes: a new mode of Breslow intermediate oxidation. *J. Am. Chem. Soc.* 144 (12), 5441–5449. doi:10.1021/jacs.1c13384
- Denmark, S. E., and Beutner, G. L. (2008). Lewis base catalysis in organic synthesis. *Angew. Chem. Int. Ed.* 47 (9), 1560–1638. doi:10.1002/anie.200604943
- Du, X., Cheng-Sánchez, I., and Nevado, C. (2023). Dual nickel/photoredox-catalyzed asymmetric carbosulfonylation of alkenes. *J. Am. Chem. Soc.* 145 (23), 12532–12540. doi:10.1021/jacs.3c00744
- Dydie, P., Key, H. M., Hayashi, H., Clark, D. S., and Hartwig, J. F. (2017). Chemoselective, enzymatic C–H bond amination catalyzed by a cytochrome P450 containing an Ir (Me)-PIX cofactor. *J. Am. Chem. Soc.* 139 (5), 1750–1753. doi:10.1021/jacs.6b11410
- Emmanuel, M. A., Bender, S. G., Bilodeau, C., Carceller, J. M., DeHovitz, J. S., Fu, H., et al. (2023). Photobiocatalytic strategies for organic synthesis. *Chem. Rev.* 123 (9), 5459–5520. doi:10.1021/acs.chemrev.2c00767
- Erkkilä, A., Majander, I., and Pihko, P. M. (2007). Iminium catalysis. *Chem. Rev.* 107 (12), 5416–5470. doi:10.1021/cr068388p
- Faisca Phillips, A. M., and Pombeiro, A. J. (2023). Applications of Hantzsch esters in organocatalytic enantioselective synthesis. *Catalysts* 13 (2), 419. doi:10.3390/catal13020419
- Flanigan, D. M., Romanov-Michailidis, F., White, N. A., and Rovis, T. (2015). Organocatalytic reactions enabled by N-heterocyclic carbenes. *Chem. Rev.* 115 (17), 9307–9387. doi:10.1021/acs.chemrev.5b00060
- Fleming, F. F., Yao, L., Ravikumar, P., Funk, L., and Shook, B. C. (2010). Nitrile-containing pharmaceuticals: efficacious roles of the nitrile pharmacophore. *J. Med. Chem.* 53 (22), 7902–7917. doi:10.1021/jm100762r
- Franco, M. S., Silva, R. C., Rosa, G. H., Flores, L. M., de Oliveira, K. T., and de Assis, F. F. (2023). Synthesis of the Brivaracetam employing asymmetric photocatalysis and continuous flow conditions. *ACS Omega* 8, 23008–23016. doi:10.1021/acsomega.3c02134
- Fujita, M. Y. Y., Miyata, K., Wakisaka, A., and Sugimura, T. (2010). Enantiodifferentiating endo-selective oxylactonization of ortho-alk-1-Enylbenzoate with a lactate-derived aryl- λ 3-iodane. *Angew. Chem. Int. Ed.* 49, 7068–7071. doi:10.1002/anie.201003503
- Gao, Y., Zhang, B., He, J., and Baran, P. S. (2023). Ni-electrocatalytic enantioselective doubly decarboxylative C(sp³)-C(sp³) cross coupling. *J. Am. Chem. Soc.* 145, 11518–11523. doi:10.1021/jacs.3c03337
- Grange, R. L., Clizbe, E. A., and Evans, P. A. (2016). Recent developments in asymmetric allylic amination reactions. *Synthesis* 48 (18), 2911–2968. doi:10.1055/s-0035-1562090
- Guo, J., Lian, Y., Li, F., Duan, Y., Xue, X., Long, C., et al. (2022). Metal-organic frameworks' tricks in asymmetric catalysis. *Chem. Catal.* 2, 2986–3018. doi:10.1016/j.cheat.2022.09.024
- Hajos Zgp, D. R., and Parrish, D. R. (1974). Asymmetric synthesis of bicyclic intermediates of naturalproduct chemistry. *J. Org. Chem.* 39 (12), 1615–1621. doi:10.1021/jo00925a003
- Hauer, B. (2020). Embracing nature's catalysts: a viewpoint on the future of biocatalysis. *ACS Catal.* 10 (15), 8418–8427. doi:10.1021/acscatal.0c01708
- Hejna, B. G., Ganley, J. M., Shao, H., Tian, H., Ellefsen, J. D., Fastuca, N. J., et al. (2023). Catalytic asymmetric hydrogen atom transfer: enantioselective hydroamination of alkenes. *J. Am. Chem. Soc.* 145 (29), 16118–16129. doi:10.1021/jacs.3c04591
- Hu, Z., Wei, C., Shi, Q., Hong, X., Liu, J., Zhou, X., et al. (2022). Desymmetrization of N-Cbz glutarimides through N-heterocyclic carbene organocatalysis. *Nat. Commun.* 13 (1), 4042. doi:10.1038/s41467-022-31760-z
- Huan, L., Shu, X., Zu, W., Zhong, D., and Huo, H. (2021). Asymmetric benzylic C (sp³)-H acylation via dual nickel and photoredox catalysis. *Nat. Commun.* 12 (1), 3536. doi:10.1038/s41467-021-23887-2
- Huang, S., Zeng, Z., Zhang, N., Qin, W., Lan, Y., and Yan, H. (2023). Organocatalytic asymmetric deoxygenation of sulfones to access chiral sulfinyl compounds. *Nat. Chem.* 15 (2), 185–193. doi:10.1038/s41557-022-01120-x
- Huang, X., Zhang, Q., Lin, J., Harms, K., and Meggers, E. (2019). Electricity-driven asymmetric Lewis acid catalysis. *Nat. Catal.* 2 (1), 34–40. doi:10.1038/s41929-018-0198-y
- Ingham, R. J., Battilocchio, C., Fitzpatrick, D. E., Sliwinski, E., Hawkins, J. M., and Ley, S. V. (2015). A systems approach towards an intelligent and self-controlling platform for integrated continuous reaction sequences. *Angew. Chem.* 127 (1), 146–150. doi:10.1002/ange.201409356

- Ishikawa, T., Palomo, C., Oiarbide, M., Lopez, R., Ooi, T., Maruoka, K., et al. (2017). Recent advances in enantioselective brønsted base organocatalytic reactions. *Synlett* 28 (11), 1272–1277. doi:10.1055/s-0036-1588847
- Ishitani, H., Kanai, K., and Kobayashi, S. (2023). Continuous-flow enantioselective 1,4-addition reactions of malonates with nitroolefins on Ni-supported mesoporous silica materials with Co-feeding of a chiral ligand. *Adv. Synthesis Catal.* 365 (9), 1526–1530. doi:10.1002/adsc.202300024
- Jaeger, K.-E., and Eggert, T. (2004). Enantioselective biocatalysis optimized by directed evolution. *Curr. Opin. Biotechnol.* 15 (4), 305–313. doi:10.1016/j.copbio.2004.06.007
- Jones, A. M., and Banks, C. E. (2014). The Shono-type electroorganic oxidation of unfunctionalised amides. Carbon-carbon bond formation via electrogenerated N-acyliminium ions. *Beilstein J. Org. Chem.* 10 (1), 3056–3072. doi:10.3762/bjoc.10.323
- Ju, S., Kuzelka, K. P., Guo, R., Krohn-Hansen, B., Wu, J., Nair, S. K., et al. (2023). A biocatalytic platform for asymmetric alkylation of α -keto acids by mining and engineering of methyltransferases. *Nat. Commun.* 14 (1), 5704. doi:10.1038/s41467-023-40980-w
- Kärkäs, M. D. (2018). Electrochemical strategies for C–H functionalization and C–N bond formation. *Chem. Soc. Rev.* 47 (15), 5786–5865. doi:10.1039/c7cs00619e
- Kaur, J., Chimni, S. S., Mahajana, S., and Kumar, A. (2015). Stereoselective synthesis of 3-amino-2-oxindoles from isatin imines: new scaffolds for bioactivity evaluation. *RSC Adv.* 5, 52481–52496. doi:10.1039/c5ra06969f
- Key, H. M., Dydio, P., Clark, D. S., and Hartwig, J. F. (2016). Abiological catalysis by artificial haem proteins containing noble metals in place of iron. *Nature* 534 (7608), 534–537. doi:10.1038/nature17968
- Kingston, C., Palkowitz, M. D., Takahira, Y., Vantourout, J. C., Peters, B. K., Kawamata, Y., et al. (2019). A survival guide for the “electro-curious”. *Accounts Chem. Res.* 53 (1), 72–83. doi:10.1021/acs.accounts.9b00539
- Kotwal, N., Tamanna, C. A., and Chauhan, P. (2023). Organocatalytic asymmetric synthesis of carbo-and oxacyclic seven-membered bridged biaryls via nucleophile-dependent switchable domino processes. *Org. Lett.* 25 (41), 7523–7528. doi:10.1021/acs.orglett.3c02832
- Lai, J., Fianchini, M., and Pericàs, M. A. (2020). Development of immobilized SPINOL-derived chiral phosphoric acids for catalytic continuous flow processes. Use in the catalytic desymmetrization of 3,3-disubstituted oxetanes. *ACS Catal.* 10 (24), 14971–14983. doi:10.1021/acscatal.0c04497
- Lai, X.-L., Chen, M., Wang, Y., Song, J., and Xu, H.-C. (2022). Photoelectrochemical asymmetric catalysis enables direct and enantioselective decarboxylative cyanation. *J. Am. Chem. Soc.* 144 (44), 20201–20206. doi:10.1021/jacs.2c09050
- Lai, X.-L., and Xu, H.-C. (2023). Photoelectrochemical asymmetric catalysis enables enantioselective heteroarylcyanation of alkenes via C–H functionalization. *J. Am. Chem. Soc.* 145 (34), 18753–18759. doi:10.1021/jacs.3c07146
- Lee, J. H., and Deng, L. (2012). Asymmetric approach toward chiral cyclohex-2-enones from anisoles via an enantioselective isomerization by a new chiral diamine catalyst. *J. Am. Chem. Soc.* 134 (44), 18209–18212. doi:10.1021/ja308623n
- Lee, L. C.-C., and Lo, K. K.-W. (2022). Luminescent and photofunctional transition metal complexes: from molecular design to diagnostic and therapeutic applications. *J. Am. Chem. Soc.* 144 (32), 14420–14440. doi:10.1021/jacs.2c03437
- Li, P., Terrett, J. A., and Zbieg, J. R. (2020). Visible-light photocatalysis as an enabling technology for drug discovery: a paradigm shift for chemical reactivity. *ACS Med. Chem. Lett.* 11 (11), 2120–2130. doi:10.1021/acsmchemlett.0c00436
- Li, Y., Zhou, K., Wen, Z., Cao, S., Shen, X., Lei, M., et al. (2018). Copper (II)-catalyzed asymmetric photoredox reactions: enantioselective alkylation of imines driven by visible light. *J. Am. Chem. Soc.* 140 (46), 15850–15858. doi:10.1021/jacs.8b09251
- Liu, Y., Zhang, L., Zhang, Y., Cao, S., Ban, X., Yin, Y., et al. (2023). Asymmetric olefin isomerization via photoredox catalytic hydrogen atom transfer and enantioselective protonation. *J. Am. Chem. Soc.* 145 (33), 18307–18315. doi:10.1021/jacs.3c03732
- Ma, Q., Shan, W., Chu, X., Xu, H., Chen, Z., Li, F., et al. (2023). Biocatalytic enantioselective γ -C–H lactonization of aliphatic carboxylic acids. *Nat. Synth.* 3, 123–130. doi:10.1038/s44160-023-00427-y
- Malakar, C. C., Dell’Amico, L., and Zhang, W. (2023). Dual catalysis in organic synthesis: current challenges and new trends. *Eur. J. Org. Chem.* 26 (1), e202201114. doi:10.1002/ejoc.202201114
- Markham, A. (2016). Brivaracetam: first global approval. *Drugs* 76 (4), 517–522. doi:10.1007/s40265-016-0555-6
- Meggers, E. (2015). Asymmetric catalysis activated by visible light. *Chem. Commun.* 51 (16), 3290–3301. doi:10.1039/c4cc09268f
- Mennie, K. M., Banik, S. M., Reichert, E. C., and Jacobsen, E. N. (2018). Catalytic diastereo- and enantioselective fluorination of alkenes. *J. Am. Chem. Soc.* 140 (14), 4797–4802. doi:10.1021/jacs.8b02143
- Morack, T., Onneken, C., Nakahara, H., Muck-Lichtenfeld, C., and Gilmour, R. (2021). Enantiodivergent prenylation via deconjugative isomerization. *ACS Catal.* 11 (19), 11929–11937. doi:10.1021/acscatal.1c03089
- Mukerjee, S. (2021). The 2021 Nobel Prize in Chemistry: asymmetric catalysis with small organic molecules. *Curr. Sci.* 121 (9), 1148.
- Mukherjee, S., Yang, J. W., Hoffmann, S., and List, B. (2007). Asymmetric enamine catalysis. *Chem. Rev.* 107 (12), 5471–5569. doi:10.1021/cr0684016
- Nagib, D. A. (2022). Asymmetric catalysis in radical chemistry. *Chem. Rev.* 122 (21), 15989–15992. doi:10.1021/acs.chemrev.2c00622
- Nagy, B. S., Llanes, P., Pericas, M. A., Kappe, C. O., and Otvos, S. B. (2022). Enantioselective flow synthesis of rolipram enabled by a telescoped asymmetric conjugate addition–oxidative aldehyde esterification sequence using *in situ*-generated persulfuric acid as oxidant. *Org. Lett.* 24 (4), 1066–1071. doi:10.1021/acs.orglett.1c04300
- Najera, C., and Sansano, J. M. (2007). Catalytic asymmetric synthesis of α -amino acids. *Chem. Rev.* 107 (11), 4584–4671. doi:10.1021/cr050580o
- Nicewicz, D. A., and MacMillan, D. W. (2008). Merging photoredox catalysis with organocatalysis: the direct asymmetric alkylation of aldehydes. *Science* 322 (5898), 77–80. doi:10.1126/science.1161976
- Pálvölgyi, Á. M., Scharinger, F., Schnürch, M., and Bica-Schröder, K. (2021). Chiral phosphoric acids as versatile tools for organocatalytic asymmetric transfer hydrogenations. *Eur. J. Org. Chem.* 2021 (38), 5367–5381. doi:10.1002/ejoc.202100894
- Parmar, D., Sugiono, E., Raja, S., and Rueping, M. (2014). Complete field guide to asymmetric BINOL-phosphate derived brønsted acid and metal catalysis: history and classification by mode of activation; brønsted acidity, hydrogen bonding, ion pairing, and metal phosphates. *Chem. Rev.* 114 (18), 9047–9153. doi:10.1021/cr5001496
- Pastre, J. C., Browne, D. L., and Ley, S. V. (2013). Flow chemistry syntheses of natural products. *Chem. Soc. Rev.* 42, 8849–8869. doi:10.1039/c3cs60246j
- Pluta, R., Kumagai, N., and Shibasaki, M. (2019). Direct catalytic asymmetric aldol reaction of α -alkoxyamides to α -fluorinated ketones. *Angew. Chem. Int. Ed.* 58 (8), 2459–2463. doi:10.1002/anie.201814607
- Plutschack, M. B., Bu, P., Gilmore, K., and Seeberger, P. H. The hitchhiker’s guide to flow chemistry. *Chem. Rev.* 2017;117(18):11796–11893. doi:10.1021/acs.chemrev.7b00183
- Prier, C. K., Rankic, D. A., and MacMillan, D. W. (2013). Visible light photoredox catalysis with transition metal complexes: applications in organic synthesis. *Chem. Rev.* 113 (7), 5322–5363. doi:10.1021/cr300503r
- Proctor, R. S., Davis, H. J., and Phipps, R. J. (2018). Catalytic enantioselective Minisci-type addition to heteroarenes. *Science* 360 (6387), 419–422. doi:10.1126/science.aar6376
- Reyes, E., Prieto, L., and Milelli, A. (2022). Asymmetric organocatalysis: a survival guide to medicinal chemists. *Molecules* 28 (1), 271. doi:10.3390/molecules28010271
- Saha, D. (2020). Catalytic enantioselective radical transformations enabled by visible light. *Chemistry–An Asian J.* 15 (14), 2129–2152. doi:10.1002/asia.202000525
- Saito, Y., and Kobayashi, S. (2020). Development of robust heterogeneous chiral rhodium catalysts utilizing acid–base and electrostatic interactions for efficient continuous-flow asymmetric hydrogenations. *J. Am. Chem. Soc.* 142 (39), 16546–16551. doi:10.1021/jacs.0c08109
- Sakthivel, K., Notz, W., Bui, T., and Barbas, C. F. (2001). Amino acid catalyzed direct asymmetric aldol reactions: a bioorganic approach to catalytic asymmetric carbon–carbon bond-forming reactions. *J. Am. Chem. Soc.* 123 (22), 5260–5267. doi:10.1021/ja010037z
- Schmermund, L., Jurkas, V., Ozgen, F. F., Barone, G. D., Buchsenschutz, H. C., Winkler, C. K., et al. (2019). Photo-biocatalysis: biotransformations in the presence of light. *ACS Catal.* 9 (5), 4115–4144. doi:10.1021/acscatal.9b00656
- Schönherr, H., and Cernak, T. (2013). Profound methyl effects in drug discovery and a call for new C–H methylation reactions. *Angew. Chem. Int. Ed.* 52 (52), 12256–12267. doi:10.1002/anie.201303207
- Schreyer, L., Properzi, R., and List, B. (2019). IDPi catalysis. *Angew. Chem. Int. Ed.* 58 (37), 12761–12777. doi:10.1002/anie.201900932
- Schultz, D. M., and Yoon, T. P. (2014). Solar synthesis: prospects in visible light photocatalysis. *Science* 343 (6174), 1239176. doi:10.1126/science.1239176
- Shah, J. A., and Ngai, M. Y. (2022). (Hetero) aryl C–H amination via organic electrochemistry. *Handb. CH-Functionalization*, 1–46. doi:10.1002/9783527834242.chf0066
- Shaw, M. H., Twilton, J., and MacMillan, D. W. (2016). Photoredox catalysis in organic chemistry. *J. Org. Chem.* 81 (16), 6898–6926. doi:10.1021/acs.joc.6b01449
- Sherbrook, E. M., Genzink, M. J., Park, B., Guzei, I. A., Baik, M.-H., and Yoon, T. P. (2021). Chiral Brønsted acid-controlled intermolecular asymmetric [2+2] photocycloadditions. *Nat. Commun.* 12 (1), 5735. doi:10.1038/s41467-021-25878-9
- Song, L., Fu, N., Ernst, B. G., Lee, W. H., Frederick, M. O., DiStasio, Jr R. A., et al. (2020). Dual electrocatalysis enables enantioselective hydrocyanation of conjugated alkenes. *Nat. Chem.* 12 (8), 747–754. doi:10.1038/s41557-020-0469-5
- Stöckigt, J., Antonchick, A. P., Wu, F., and Waldmann, H. (2011). The Pictet–Spengler reaction in nature and in organic chemistry. *Angew. Chem. Int. Ed.* 50 (37), 8538–8564. doi:10.1002/anie.201008071
- Tan, X., Wang, Q., and Sun, J. (2023). Electricity-driven asymmetric bromocyclization enabled by chiral phosphate anion phase-transfer catalysis. *Nat. Commun.* 14 (1), 357. doi:10.1038/s41467-023-36000-6

- Tanaka, K., and Fu, G. C. (2001). A versatile new catalyst for the enantioselective isomerization of allylic alcohols to aldehydes: scope and mechanistic studies. *J. Org. Chem.* 66 (24), 8177–8186. doi:10.1021/jo010792v
- Tani, K., Yamagata, T., Akutagawa, S., Kumobayashi, H., Taketomi, T., Takaya, H., et al. (1984). Metal-assisted terpenoid synthesis. 7. Highly enantioselective isomerization of prochiral allylamines catalyzed by chiral diphosphine rhodium (I) complexes. Preparation of optically active enamines. *J. Am. Chem. Soc.* 106 (18), 5208–5217. doi:10.1021/ja00330a029
- Tani, K., Yamagata, T., Otsuka, S., Akutagawa, S., Kumobayashi, H., Taketomi, T., et al. (1982). Cationic rhodium (I) complex-catalyzed asymmetric isomerization of allylamines to optically active enamines. *J. Chem. Soc. Chem. Commun.* (11), 600–601. doi:10.1039/c39820000600
- Touge, T., Kuwana, M., Komatsuki, Y., Tanaka, S., Nara, H., Matsumura, K., et al. (2018). Development of asymmetric transfer hydrogenation with a bifunctional oxo-ethered ruthenium catalyst in flow for the synthesis of a ceramide (d-erythro-CER [NDS]). *Org. Process Res. Dev.* 23 (4), 452–461. doi:10.1021/acs.oprd.8b00338
- Trost, B. M., and Brindle, C. S. (2010). The direct catalytic asymmetric aldol reaction. *Chem. Soc. Rev.* 39 (5), 1600–1632. doi:10.1039/b923537j
- Trowbridge, A., Walton, S. M., and Gaunt, M. J. (2020). New strategies for the transition-metal catalyzed synthesis of aliphatic amines. *Chem. Rev.* 120 (5), 2613–2692. doi:10.1021/acs.chemrev.9b00462
- Tsubogo, T., Ishiwata, T., and Kobayashi, S. (2013). Asymmetric carbon–carbon bond formation under continuous-flow conditions with chiral heterogeneous catalysts. *Angew. Chem. Int. Ed.* 52 (26), 6590–6604. doi:10.1002/anie.201210066
- Tsubogo, T., Oyamada, H., and Kobayashi, S. (2015). Multistep continuous-flow synthesis of (R)- and (S)-rolipram using heterogeneous catalysts. *Nature* 520 (7547), 329–332. doi:10.1038/nature14343
- Uchikura, T., Kato, S., Makino, Y., Fujikawa, M. J., Yamanaka, M., and Akiyama, T. (2023). Chiral phosphoric acid–palladium (II) complex catalyzed asymmetric desymmetrization of biaryl compounds by C (sp³)–H activation. *J. Am. Chem. Soc.* 145 (29), 15906–15911. doi:10.1021/jacs.3c03552
- Ukai, T., Tanaka, R., and Dokawa, T. (1943). A new catalyst for the acyloin condensation. *Yakugaku Zasshi* 63, 296–304.
- Uraguchi, D., and Terada, M. (2004). Chiral Brønsted acid-catalyzed direct Mannich reactions via electrophilic activation. *J. Am. Chem. Soc.* 126 (17), 5356–5357. doi:10.1021/ja0491533
- Uyanik, M., Yasui, T., and Ishihara, K. (2010). Enantioselective Kita oxidative spirocyclization catalyzed by *in situ* generated chiral hypervalent iodine (III) species. *Angew. Chem. Int. Ed.* 49 (12), 2175–2177. doi:10.1002/anie.200907352
- von Münchow, T., Dana, S., Xu, Y., Yuan, B., and Ackermann, L. (2023). Enantioselective electrochemical cobalt-catalyzed aryl C–H activation reactions. *Science* 379 (6636), 1036–1042. doi:10.1126/science.adg2866
- Wang, Q., Qi, Y., Gao, X., Gong, L., Wan, R., Lei, W., et al. (2023). Recent trends and developments in the asymmetric synthesis of profens. *Green Synthesis Catal.* 4, 89–103. doi:10.1016/j.gresc.2023.02.002
- Wang, Z.-H., Gao, P.-S., Wang, X., Gao, J.-Q., Xu, X.-T., He, Z., et al. (2021). TEMPO-enabled electrochemical enantioselective oxidative coupling of secondary acyclic amines with ketones. *J. Am. Chem. Soc.* 143 (38), 15599–15605. doi:10.1021/jacs.1c08671
- Wanner, M. J., van der Haas, R. N., de Cuba, K. R., van Maarseveen, J. H., and Hiemstra, H. (2007). Catalytic asymmetric Pictet–Spengler reactions via sulfonyliminium ions. *Angew. Chem. Int. Ed.* 46 (39), 7485–7487. doi:10.1002/anie.200701808
- Wong, M. L., Sterling, A. J., Mousseau, J. J., Duarte, F., and Anderson, E. A. (2021). Direct catalytic asymmetric synthesis of α -chiral bicyclo [1.1. 1] pentanes. *Nat. Commun.* 12 (1), 1644. doi:10.1038/s41467-021-21936-4
- Wu, S., Kaur, J., Karl, T. A., Tian, X., and Barham, J. P. (2022). Synthetic molecular photoelectrochemistry: new frontiers in synthetic applications, mechanistic insights and scalability. *Angew. Chem. Int. Ed.* 61 (12), e202107811. doi:10.1002/anie.202107811
- Wu, Y., Singh, R. P., and Deng, L. (2011). Asymmetric olefin isomerization of butenolides via proton transfer catalysis by an organic molecule. *J. Am. Chem. Soc.* 133 (32), 15219–15261. doi:10.1021/ja206996p
- Yamamoto, H., and Ishihara, K. (2008). *Acid catalysis in modern organic synthesis*. China: Wiley-VCH Weinheim.
- Yan, M., Kawamata, Y., and Baran, P. S. (2017). Synthetic organic electrochemical methods since 2000: on the verge of a renaissance. *Chem. Rev.* 117 (21), 13230–13319. doi:10.1021/acs.chemrev.7b00397
- Yang, Y., Cho, I., Qi, X., Liu, P., and Arnold, F. H. (2019). An enzymatic platform for the asymmetric amination of primary, secondary and tertiary C (sp³)–H bonds. *Nat. Chem.* 11 (11), 987–993. doi:10.1038/s41557-019-0343-5
- Yao, W., Bazan-Bergamino, E. A., and Ngai, M. Y. (2022). Asymmetric photocatalysis enabled by chiral organocatalysts. *ChemCatChem* 14 (1), e202101292. doi:10.1002/cctc.202101292
- Yi, D., Bayer, T., Badenhorst, C. P., Wu, S., Doerr, M., Höhne, M., et al. (2021). Recent trends in biocatalysis. *Chem. Soc. Rev.* 50 (14), 8003–8049. doi:10.1039/d0cs01575j
- Yoon, T. P. (2016). Photochemical stereocontrol using tandem photoredox–chiral Lewis acid catalysis. *Accounts Chem. Res.* 49 (10), 2307–2315. doi:10.1021/acs.accounts.6b00280
- Yuan, Y.-H., Han, X., Zhu, F.-P., Tian, J.-M., Zhang, F.-M., Zhang, X.-M., et al. (2019). Development of bifunctional organocatalysts and application to asymmetric total synthesis of naucleoficine I and II. *Nat. Commun.* 10 (1), 3394. doi:10.1038/s41467-019-11382-8
- Yue, C., Yamashita, Y., and Kobayashi, S. (2021). Highly enantioselective immobilized prolinamide-catalyzed aldol reactions in continuous-flow systems: effect of water on the catalyst lifetime and application in the synthesis of a chiral fepentadiol analogue. *Green Chem.* 23 (5), 1989–1994. doi:10.1039/d0gc04202a
- Zhang, J., Maggiolo, A. O., Alfonzo, E., Mao, R., Porter, N. J., Abney, N. M., et al. (2023b). Chemodivergent C (sp³)–H and C (sp²)–H cyanomethylation using engineered carbene transferases. *Nat. Catal.* 6 (2), 152–160. doi:10.1038/s41929-022-00908-x
- Zhang, K., Yu, A., Chu, X., Li, F., Liu, J., Liu, L., et al. (2022). Biocatalytic enantioselective β -hydroxylation of unactivated C–H bonds in aliphatic carboxylic acids. *Angew. Chem. Int. Ed.* 61 (28), e202204290. doi:10.1002/anie.202204290
- Zhang, X., Liu, M., Ge, H., and Zhang, Z. (2023a). Second-layer chiral environment-induced steric hindrance enables catalyst conformation lockdown in enantioselective hypervalent iodine organocatalysis. *ACS Catal.* 13, 8273–8280. doi:10.1021/acscatal.3c02018
- Zhao, L., Bao, X., Hu, Q., Wang, B., and Lu, A. H. (2018). Porous carbon nanosheet-supported chiral squaramide for highly enantioselective friedel–crafts reaction. *ChemCatChem* 10 (6), 1248–1252. doi:10.1002/cctc.201701897
- Zhelavskiy, O., and Jhang, Y.-J. (2023). Asymmetric transfer hydrogenation of heterocyclic compounds in continuous flow using an immobilized chiral phosphoric acid as the catalyst. *Synthesis* 55 (15), 2361–2369. doi:10.1055/a-2085-5256
- Zhou, H., Han, J. T., Nothling, N., Lindner, M. M., Jenniches, J., Kuhn, C., et al. (2022). Organocatalytic asymmetric synthesis of Si-stereogenic silyl ethers. *J. Am. Chem. Soc.* 144 (23), 10156–10161. doi:10.1021/jacs.2c04261
- Zhu, C., Ang, N. W., Meyer, T. H., Qiu, Y., and Ackermann, L. (2021). Organic electrochemistry: molecular syntheses with potential. *ACS central Sci.* 7 (3), 415–431. doi:10.1021/acscentsci.0c01532
- Zigon, N., Duplan, V., Wada, N., and Fujita, M. (2021). Crystalline sponge method: X-ray structure analysis of small molecules by post-orientation within porous crystals - principle and proof-of-concept studies. *Angew. Chem. Int. Ed.* 60, 25204–25222. doi:10.1002/anie.202106265
- Zou, Y.-Q., Hörmann, F. M., and Bach, T. (2018). Iminium and enamine catalysis in enantioselective photochemical reactions. *Chem. Soc. Rev.* 47 (2), 278–290. doi:10.1039/c7cs00509a



OPEN ACCESS

EDITED BY

Ruguang Ma,
Suzhou University of Science and Technology,
China

REVIEWED BY

Xiaomin Xu,
Curtin University, Australia
Shiliu Yang,
Huainan Normal University, China
Kuikui Wang,
Qingdao University, China

*CORRESPONDENCE

Sanjubala Sahoo,
✉ sanjubala.sahoo@uconn.edu
Steven L. Suib,
✉ steven.suib@uconn.edu

RECEIVED 29 March 2024

ACCEPTED 06 May 2024

PUBLISHED 17 May 2024

CITATION

Sahoo S, Wickramathilaka KY, Njeri E, Silva D and
Suib SL (2024), A review on transition metal
oxides in catalysis.
Front. Chem. 12:1374878.
doi: 10.3389/fchem.2024.1374878

COPYRIGHT

© 2024 Sahoo, Wickramathilaka, Njeri, Silva and
Suib. This is an open-access article distributed
under the terms of the [Creative Commons
Attribution License \(CC BY\)](#). The use,
distribution or reproduction in other forums is
permitted, provided the original author(s) and
the copyright owner(s) are credited and that the
original publication in this journal is cited, in
accordance with accepted academic practice.
No use, distribution or reproduction is
permitted which does not comply with these
terms.

A review on transition metal oxides in catalysis

Sanjubala Sahoo^{1*}, Kaveendra Y. Wickramathilaka², Elsa Njeri²,
Dilshan Silva² and Steven L. Suib^{1,2*}

¹Department of Materials Science and Engineering, Institute of Materials Science, University of Connecticut, Storrs, CT, United States, ²Department of Chemistry, University of Connecticut, Storrs, CT, United States

Transition Metal Oxides (TMOs) have drawn significant attention due to their diverse range of properties and applications. The partially filled *d* orbitals of the transition metal ions, with highly electronegative oxygen atoms, give rise to unique electronic structures that lead to multiple applications due to their magnetic, optical, and structural properties. These properties have a direct influence on chemical reactions that enable tailoring materials for specific applications in catalysis, such as electrocatalysis and photocatalysis. While the potential of TMOs is promising, their development for enhanced functional properties poses numerous challenges. Among these challenges, identifying the appropriate synthesis processes and employing optimal characterization techniques are crucial. In this comprehensive review, an overview of recent trends and challenges in the synthesis and characterization of highly functional TMOs as well as ceramics will be covered with emphasis on catalytic applications. Mesoporous materials play a key role in augmenting their functionality for various applications and will be covered. Ab-initio modeling aspects for the design and development of novel TMO will be also discussed.

KEYWORDS

porous transition metal oxides, high temperature ceramic composites, coating, photocatalysis, electrocatalysis, density functional theory

1 Introduction

Materials play a crucial role in the realms of chemistry, physics, and materials science, serving as the foundation for understanding the properties, behaviors, and applications of substances across these interdisciplinary fields. Transition metal oxides (TMOs) are one of the technologically important materials with wide ranges of applications such as in the chemical, energy storage and electronics industries where these are used as catalysts for the conversion of feedstocks to valuable chemicals and sensors, actuators (Nova, 2014). They are also used as electrode materials in electrochemical processes. In the electronics industry, TMOs are used as thin film conductors. Their use as catalysts is the most technologically advanced and economically important of all applications. Much progress has been made recently in the field of catalysis for the understanding of fundamental processes due to the development of advanced experimental and theoretical techniques which has made it possible to study the chemistry of the interface between the transition metal oxide and the fluid and gaseous phase.

The surface properties of TMOs, including acidity, basicity, and redox behavior, can be finely tuned through compositional modifications and surface functionalization (Cox, 2010). These tunable surface properties play an important role in modulation of catalytic activity, selectivity, and stability. For instance, the Lewis acid-base properties of

TMOs facilitate the adsorption and activation of reactant molecules, while redox-active sites enable facile electron transfer processes during catalytic reactions. TMOs as supports have several advantages specifically for catalytic applications. Their thermal stability, chemical robustness, and resistance to sintering make them ideal candidates for high-temperature catalytic processes (Xu et al., 2020). TMO supports can provide redox-active sites that participate in catalytic cycles, promote oxygen activation, or stabilize reactive intermediates, thereby influencing reaction pathways and product distributions. By tailoring the surface chemistry of TMO supports, it is possible to optimize the interactions between the support and catalytic species thereby enhancing the overall performance of heterogeneous catalysts.

Recent developments in surface science techniques have provided more insight about the surface structures, chemical compositions, and electronic properties of the surfaces (Cox, 2010). Surface characterization probes include Low Energy Electron Diffraction (LEED) and Electron Energy Loss Spectroscopy (EELS) for investigating geometry and structure of surfaces, X-ray fluorescence (XRF) and X-ray photoelectron spectroscopy (XPS) for elemental compositions, chemical states, binding energies, and the electronic structures of surfaces. TMOs are projected as ideal candidates for single atom catalysis where the optimal efficiency could be gained by tuning catalyst support interactions along with quantum confinement effects of precious metal particles (Wang et al., 2018; Beniya and Higashi, 2019; Elsevier, 2019). The structure, thermal stability and wide range of surface functionalities provide highly stable supports for anchoring and stabilizing isolated metal atoms and fine dispersion. Moreover, the tunable electronic structures of TMOs lead to the precise control over the coordination environment and electronic properties of single metal atoms, facilitating the high catalytic activity and enhanced selectivity. A number of SACs have been synthesized using TMOs as supports for CO oxidation and methane conversion reactions (Qiao et al., 2011; Guo et al., 2014; Sahoo et al., 2016; Zuo et al., 2018). Among these, FeO_x , Fe_2O_3 , CeO_x , TiO_2 and zeolites supports together with Pt/Pd/Rh precious metal atoms are important (Bayram et al., 2015; Tang et al., 2019; Chen et al., 2022). TMOs are also used as precursors for catalysts besides being used as catalysts and support materials. For example, cobalt-molybdenum sulfide catalysts are used in hydrodesulfurization reactions where the catalyst is prepared by sulfiding cobalt-molybdenum oxide. Another example is chromium-based catalysts for ethylene polymerization. The catalyst can be made from supported chromium oxide as a precursor. Additionally, noble metal catalysts are prepared by reduction of the corresponding oxides, where the structures, morphologies, and properties of the TMO precursors have an influence on the properties of the final catalysts.

This review covers a combined experimental and theoretical overview of TMOs with emphasis on several synthetic processes, characterization methods, theoretical modeling approaches, and potential applications in photocatalysis, electrocatalysis and a variety of TMO catalyzed chemical reactions other than those related to photo and electrocatalysis. TMOs exhibit numerous structures, spanning from simple oxides to intricate mixed-metal oxides and nanostructured materials. Such structural diversity enables the precise control of surface morphology, porosity, and

surface area, which have significant influence on catalytic performance. In this review, the primary focus will be on mesoporous TMOs due to their several advantages such as large surface areas, controlled pore sizes and structures, facile adsorption, and separation (Suib, 2017).

2 Synthesis and characterization of TMOs

Porous metal oxide materials are grouped into three classes based on pore size: microporous (less than 2 nm pore diameter), mesoporous (2–50 nm pore diameter), and macroporous with a pore diameter greater than 50 nm (Adegoke and Maxakato, 2022). Excellent reviews on porous TMOs and their applications have been published (Suib, 2017; Wang et al., 2017; Yang et al., 2017; Okonye et al., 2021). The seminal work on mesoporous materials by Mobil Corporation (Kresge et al., 1992) pioneered extensive research in the synthesis and utilization of porous TMOs. Nano-size mixed valent mesoporous oxides have received much attention in catalysis, electrochemistry, and adsorption due to their high surface areas and improved mass transfer within pores (Wang et al., 2017; Achola et al., 2022). Our lab has done considerable research on synthesizing mesoporous TMOs in recent years (Dang et al., 2021; Achola et al., 2022; Zhao et al., 2022a; Tabassum et al., 2022).

The synthesis methods of porous TMOs influence their crystallinity and porosity and thus their surface and bulk characteristics (Lermusiaux et al., 2022). Crystalline porous TMOs have different physicochemical properties compared to their amorphous counterparts. The presence of multiple crystalline phases in some oxides leads to distinct properties (Lermusiaux et al., 2022). In a study on the toxicity of TiO_2 nanoparticles, Uboldi et al. (2016) confirmed that the rutile phase was slightly more toxic to cells than the anatase phase. The exposure of high energy crystal facets in TMOs results in improved gas sensing, photocatalytic activity, and selectivity in reactions (Zhou and Li, 2012). Crystal facet engineering can be accomplished during synthesis by selectively controlling the nucleation rate during crystal growth and utilizing capping agents (Liu et al., 2011; Zhou and Li, 2012). An example is the facet-controlled synthesis of h- WO_3 for ppb level acetone detection via a fluorinated hydrothermal method. The highly active (002) facets and high density of oxygen vacancies resulted in superior sensing properties of acetone for the h- WO_3 material mentioned above (Wang et al., 2019). Amorphous oxides present unique catalytic, optical, and electrochemical activity due to structural disorder and defects in these complex systems (Zhou and Fan, 2021). Nonetheless, a limitation in characterization techniques makes studying the structures of amorphous porous TMOs challenging.

While designing the porous materials, depending on the type of synthesis (top-down or bottom-up approach) and desired product, it is critical to have proper control over factors such as pH, temperature, solvents, precursors, type of surfactant, solubility in the reaction matrix, reaction time, scalability and so forth (Suib, 2017; Drummer et al., 2021). The environmental impact of these synthetic processes should also be evaluated since clean systems are essential to design intrinsically less hazardous systems that take advantage of greener technologies (Bandeira et al., 2020; Drummer

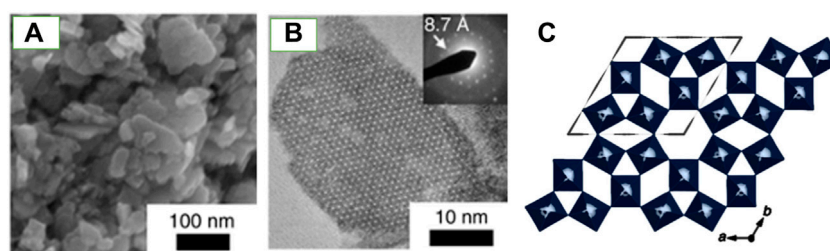


FIGURE 1
Structure and nanostructure of the h' - WO_3 framework. (A) SEM and (B) HRTEM images showing nanosized platelets. (C) The tungsten octahedra along the c axis. Figure adapted from Ref. Lin et al. (2021).

et al., 2021; Zhao et al., 2022b). Reactions on the surface of TMOs are affected by their pore sizes. Thus, pore size control should be a key consideration for countless synthetic methods. Recent studies on hierarchically porous materials have shown that having multimodal pore size distribution (micropores, mesopores, and macropores) in TMOs improves catalytic and photocatalytic activity (Yang et al., 2017). Macroporous systems can enable better mass transportation of reactants to the active sites of porous TMOs in cases where mesoporous materials are limited by a smaller pore size (Li et al., 2015; Yang et al., 2017; Cai et al., 2021). Incorporating the strengths of different pore sizes into one material is a solution for improved mass transfer. Below are some recent examples of synthetic methods used to make porous TMOs.

Octahedral molecular sieves (OMS) are microporous oxide materials preferred for their mixed valent states and tunnel structures, facilitating superior redox chemistry. Incorporating several types of cations into transition metal OMS results in properties such as improved thermal stability and conductivity. The stability of OMS tunnel structures is dependent on water molecules or cations (Suib, 2008; Suib et al., 2020). These cations or water cannot be removed without collapsing the tunnels. A novel photosensitive h' - WO_3 OMS was synthesized by Besnardiere et al. (2019) via a “chimie douce” (soft chemistry) route. The synthesis initially yielded a mixed valent (W^V , W^{VI}) hexagonal hydrogen bronze h' - $H_{0.07}WO_3$, which converted to h' - WO_3 OMS with framework retention. In this case, the cations could be extracted reversibly via gentle annealing without collapsing the tunnels of the h' - WO_3 . Characterization using powder X-Ray Diffraction (XRD), Scanning Electron Microscope (SEM), and high-resolution Scanning Transmission Electron Microscope (STEM) were utilized to identify the structure, crystal phase, and morphology of these OMS catalysts. Crystal defects were observed via STEM. The thermal stability of the materials was studied via thermogravimetric analysis (TGA) suggesting that the synthesized h' - WO_3 OMS have better thermal stability compared to h' - WO_3 previously reported in the literature. UV/Visible spectroscopy was used to analyze the optical properties of the OMS. Figures 1A–C illustrates the structure of the synthesized h' - WO_3 framework (Besnardiere et al., 2019).

Mesoporous TMOs of Fe, Cu, Co and Zr were synthesized using a simple and fast solvent free mechanochemical nanocasting procedure (Xiao et al., 2018). The metal oxide precursors and silica template were ball milled in a stainless steel reactor. After calcination the powder was stirred in 2.5 M NaOH, at room temperature to remove the silica template to obtain a porous

oxide. The surface areas and pore size distributions were investigated using N_2 sorption studies and calculated via BET/BJH models, with reported surface areas as high as 293 m^2/g . Surface morphology was studied using SEM, and the crystal structures were analyzed using powder XRD. The surface chemical state of ZrO_2 analyzed through XPS confirmed the presence of oxygen vacancies and the primary oxidation state of Zr in the metal oxide (Zr^{4+}). The materials were calcined at different temperatures and retained their porosity and high surface area at high calcination temperatures. In most cases, pores collapse under exposure to high calcination temperatures (Thalgaspitiya et al., 2020). Mechanical nanocasting can be a great alternative to traditional wet nanocasting syntheses, which are plagued with prolonged reaction times (hours) and restricted solubility of metal oxide precursors in solvents (Xiao et al., 2018). A comprehensive review of mechanical nanocasting discusses reaction mechanisms, choice of parameters and comparison to other synthesis methods (Tsuzuki, 2021). Figure 2 represents a schematic of the synthetic procedure (Xiao et al., 2018). By using co-solvents in a wet synthesis procedure, one can easily tune the pore sizes and crystal phases of porous TMOs. An example is the synthesis of Zr doped TiO_2 by a modified inverse micelle route (Owalude et al., 2023). Both 1-butanol and hydrogen peroxide were used as solvents to synthesize a mixed phase (85% rutile and 15% anatase) TiO_2 with mesopores and a small amount of macropores. The pore size distribution was determined by N_2 sorption studies. Powder XRD studies confirmed that the anatase phase proportion increased to 36.8% upon Zr doping. The anatase/rutile phase % was determined from the XRD data. The crystalline phase was also confirmed using Raman spectroscopy. The catalysts were calcined at 450°C, a preferably low temperature for rutile formation. Optical studies were conducted using UV/Vis and photoluminescence spectroscopy (Owalude et al., 2023). Due to the poor solubility of precursors in a previously developed inverse micelle route (Poyraz et al., 2013), Thalgaspitiya et al. developed a metal dissolution synthetic procedure that involves dissolving metals in hydrogen peroxide to form peroxo complexes, followed by reacting the complexes with nitric acid and Pluronic P-123 surfactant in a one-pot synthesis. This approach led to the synthesis of multiple mixed valent mesoporous TMOs of Ti, Mn, Fe, Ni, Cu, and Zn, focusing on W and Mo oxides (Thalgaspitiya et al., 2020). A follow-up of this soft templating synthesis was done by using dual surfactants or solvent systems to form hierarchically porous TMOs (Yang et al., 2017). Photo-assisted synthetic methods such

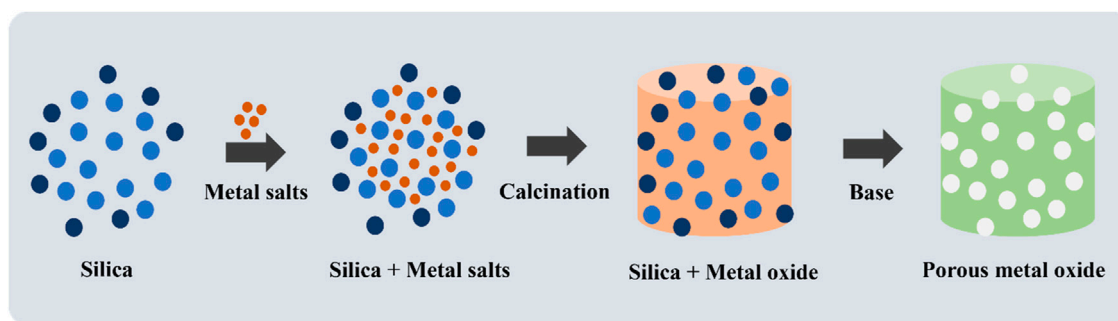


FIGURE 2
Mechanochemical nano casting route for the synthesis of porous metal oxide.

as photo-assisted sol gel syntheses or biodegradable templates were further explored to create more efficient and cleaner processes (Liu et al., 2003; Drummer et al., 2021). Some synthesis methods are sensitive to contamination from foreign particles, which could lead to undesirable materials. These syntheses could be done in a clean room to solve this issue. These reactions are typically done on an industrial scale but can also be applied to laboratory scale synthesis.

Some of the common challenges faced by synthetic chemists in metal oxide synthesis are precise control of particle size, scalability and reproducibility. Additionally, retention of framework structures while doping and phase identification via characterization play a major role in their performance as catalysts. To thoroughly investigate these features, *in-situ* techniques such as XRD and TEM are used. Phase changes along with varying temperature profiles have been studied. These methods are advantageous for correlating structure function relationships and studying mechanisms. The challenge of scalability and reproducibility is addressed by Besenhard et al. (2023) who used a high temperature flow reactor with varying temperature profiles to investigate the self-seeded growth mechanism of particle sizes <20 nm with temperature $T < 200^{\circ}\text{C}$. They tried to keep the residence time to a minimum, which is a challenge to be performed under batch synthetic conditions. The goal of the synthesis is to use these materials as Magnetic Resonance Imaging (MRI) contrast agents or similar applications requiring high surface to volume ratios of iron oxide particles.

3 TMOs as photocatalysts

Photocatalytic water splitting reactions are widely researched due to their potential for providing clean and sustainable hydrogen. The process involves splitting water into its constituent elements (H_2 and O_2) in the presence of light and a photocatalyst, typically a semiconductor. To achieve maximum water splitting efficiency, the semiconductor valence band should be more positive than the water oxidation potential ($\text{O}_2/\text{H}_2\text{O}$, 1.23 eV), while the conduction band should be more negative than the hydrogen evolution potential (H^+/H_2 , 0 eV). In addition, the photocatalyst should have an ideal band gap of >1.23 eV to facilitate efficient photon absorption (Lin et al., 2021; Bie et al., 2022). Nanoparticles are preferred due to their high surface area and faster diffusion (which occurs in the pico to

nanosecond range) of photogenerated charges from the bulk to the surface of photocatalysts (Takanabe, 2017). Oxygen vacancies (Ov) enhance charge carrier separation, thus improving overall water splitting efficiency (Bie et al., 2022). Wei et al. synthesized tungsten oxides and Pt tungsten oxides with oxygen vacancies ($\text{O}_v\text{-WO}_3$ and $\text{O}_v\text{-WO}_3\text{-Pt}$, respectively) for photocatalytic oxygen evolution.

These samples were compared to pure WO_3 . XPS analysis indicated the presence of Ov due to the presence of W^{5+} in the W 4f core level spectra. An intense signal at $g = 2.002$ was observed for Ov-WO_3 via Electron Paramagnetic Resonance (EPR) studies, confirming the XPS results. The charge carrier separation was investigated using femtosecond transient absorption spectroscopy and photoluminescence measurements. Photocatalytic oxygen evolution levels reached $683 \mu\text{mol h}^{-1} \text{g}^{-1}$, which is 4.3 times higher than pure WO_3 . The Pt cocatalyst further improved the photocatalytic performance of the $\text{O}_v\text{-WO}_3$ material. Figures 3A–C illustrates the mechanism of photoinduced electron transfer and charge recombination routes of WO_3 , Ov-WO_3 , and $\text{Ov-WO}_3\text{-Pt}$ (Wei et al., 2021).

Solar fuels such as methanol and methane can be produced through photocatalytic CO_2 reduction. Forming composite materials through heterojunction engineering can drastically improve the reduction process (Li et al., 2021). An example is the enhanced redox and photon absorption efficiency achieved via Z-scheme heterojunctions. A TiO_2/CdS direct Z-scheme thin film composite was successfully utilized for photocatalytic CO_2 reduction and compared to TiO_2 and CdS. Higher performance for methane production was observed for TiO_2/CdS . Lesser amounts of methanol and formaldehyde were also detected using *in situ* Fourier Transform Infrared (FTIR) Spectroscopy. Electron transfer via a Z-scheme mechanism was confirmed using *in situ* irradiated XPS by observing the shifts in binding energy on the Ti 2p and Cd 3d spectra. ROS detection methods further confirmed the formation of a direct Z-scheme (Low J. et al., 2019).

An et al. (2022) report a direct photo oxidation approach to convert methane to methanol by using mono-iron hydroxyl sites. These iron hydroxyl sites are immobilized in a porous metal organic framework which can act as sites to promote C-H bond activation. Fe is incorporated into the framework by post synthetic metalation using $\text{FeCl}_3 \cdot 6\text{H}_2\text{O}$ precursor and the loadings determined by ICP-OES to be 2.6 wt%.

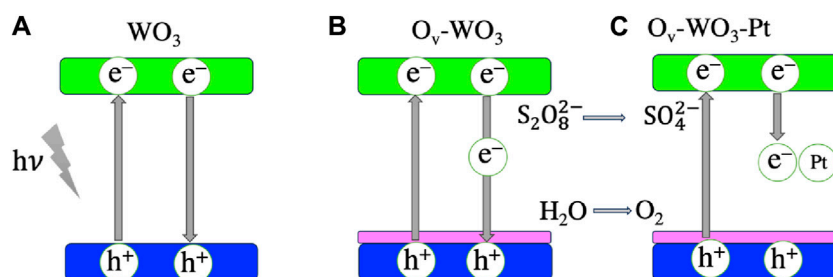


FIGURE 3
Mechanism of photoinduced electron transfer and charge recombination routes of (A) WO_3 , (B) Ov-WO_3 , and (C) $\text{Ov-WO}_3\text{-Pt}$. The blue, green and magenta colors indicate the valence band, conduction band and surface oxygen-vacancy states, respectively. The figure is adapted from Ref. Zhang et al. (2018).

4 TMOs as electrocatalysts

Electrocatalysts are key components in energy storage and conversion devices such as fuel cells, where they facilitate the conversion of chemical energy into electrical energy through the oxidation of fuel such as hydrogen or methanol. In the electrolysis processes, electrocatalysts lead to the production of hydrogen or other valuable chemicals via water splitting. TMO-based electrocatalysis are of immense interest due to their diverse chemical compositions, tunable electronic structures, and catalytic activities. TMOs exhibit unique electrochemical properties that make them suitable for various applications, including oxygen reduction reactions (ORR) in fuel cells, oxygen evolution reactions (OER) in water-splitting devices, and carbon dioxide reduction reaction for sustainable fuel production.

The steam reforming of hydrocarbons still accounts for 50% of global hydrogen production, leading to global warming due to CO_2 emissions. Electrochemical seawater splitting could be an abundant source of hydrogen, which is used as a fuel and chemical feedstock in various synthetic processes. The reaction involves hydrogen and oxygen evolution from the cathode and anode, respectively. However, the presence of chlorine ions and other impurities in seawater leads to electrode corrosion. A high overpotential is required for the OER thus limiting the efficiency of this process (Xiao et al., 2022). $\text{RuO}_2/\text{NiO}_2$ composite nanosheets were fabricated on nickel foam ($\text{RuO}_2\text{-NiO NSs/NF}$) for seawater splitting to produce hydrogen through hydrogen evolution reaction (HER) under acidic and alkaline conditions. $\text{RuO}_2\text{-NiO NSs/NF}$ calcined at 300°C showed the best HER activity, higher than commercial Pt. The RuO_2 was amorphous up to 300°C . During HER, the RuO_2 formed an Ru/RuO_2 interface, contributing to the performance of the catalysts. Dang et al. also hypothesized that the improved water adsorption and dissociation capabilities accelerated the Volmer step, subsequently leading to the production of H_2 . The stability of the catalysts was assessed through cycling experiments, resulting in excellent cycling durability compared to commercial Pt/C and Pt electrodes (Dang et al., 2021).

Fe containing oxides have been a primary candidate for electrochemical applications recently. Due to their low cost, non-toxicity and long-term stability, Iron containing compounds are preferred over expensive benchmark materials consisting of Platinum, Ruthenium, and Iridium. Wang et al. have reported

the synthesis of partially amorphous, CoFeO_x by a facile ion exchange followed by an etching method (Wang et al., 2023a). Using a ZIF-67 framework as a structural template this method is developed and finally decorated with SO_4^{2-} ions to enhance adsorption of reactants to the catalyst surface. The optimized nanosheets thus formed have proven to be effective OER catalyst with a greater stability (62 h) and an overpotential of 268 mV at 10 mA cm^{-2} . On a similar note, NiFe_2O_4 synthesized using microwave assisted hydrothermal synthesis by Suib (Achola et al., 2022) has shown low overpotential of 278 mV at 10 mA cm^{-2} as an OER catalyst.

Among the TMOs, layered perovskites from the ABX_3 family are reported to exhibit enhanced OER activities (Xu et al., 2020; Tang et al., 2022; Abdelghafar et al., 2024). Specifically, the layered Ruddleson-Popper perovskites such as $\text{Ba}_{0.5}\text{Sr}_{0.5}\text{Co}_{0.8}\text{Fe}_{0.2}\text{O}_{3-\delta}$ and $\text{LaSr}_{2.7}\text{Co}_{1.5}\text{Fe}_{1.5}\text{O}_{10}$ have demonstrated high OER activity with an overall high water splitting current density value 2.01 A cm^{-2} at 2 V at high temperature. The high OER activity is attributed due to the enhanced participation of lattice oxygen at high temperature.

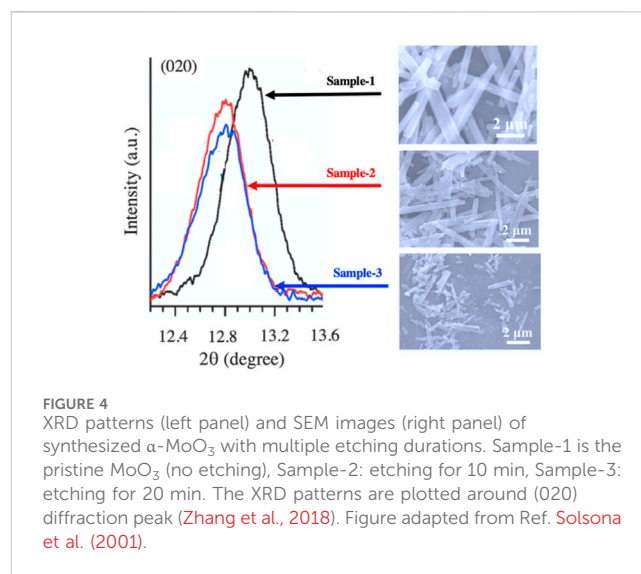
Honeycomb like open edge reduced graphene oxide nanosheets (HORGONSs) and TMO hybrids can be used as supercapacitors. NiO and Co_3O_4 are promising due to good electrochemical capacitance behavior, low cost, and ease of accessibility (Low W. H. et al., 2019). Kumar et al. synthesized a hybrid reduced graphene oxide/TMO system via a microwave method (HORGO/TMO) for studies as electrode materials for supercapacitors. The TMO in this case was $\text{NiO/Co}_3\text{O}_4$. Reduced graphene oxide has exceptional electrical and thermal conductivity and a high specific surface area. Hybrid systems are expected to have superior conductivity and electrochemical capacitance behavior. The hybrid nanoparticles exhibited high electrochemical performance based on the electrochemical results. These data were influenced by the high surface area of the nanoparticles as well as the interaction between HORGONSs and $\text{NiO/Co}_3\text{O}_4$ (Kumar et al., 2020).

Mesoporous Iron oxide synthesized using waste wood powder as a template has been successful in providing a high efficiency catalyst for the slurry phase hydrocracking of heavy oil. Ping et al. (2023) presents that by varying the NaOH content during synthesis both $\alpha\text{-Fe}_2\text{O}_3$ and $\gamma\text{-Fe}_2\text{O}_3$ can be obtained. Furthermore, the crystal size of the iron oxide reduces with increasing NaOH amounts. Larger surface areas close to $134 \text{ m}^2/\text{g}$ are recorded which provide more

exposure of Fe active sites. These have proven to have improved hydrogenation activity with a conversion close to 80%. The mesoporous nature can enhance the diffusion of molecules in vacuum, allowing them to come into contact with the active sites. This promotes the conversion process, leading to a higher yield of gasoline and diesel distillates.

5 TMOs as general catalysts

Besides their application as photocatalysts and electrocatalysts, TMOs play a crucial role for catalyzing many other chemical reactions such as oxidations, selective oxidations, selective reductions, oxidative and non-oxidative dehydrogenations, water-gas shift reaction (WGS), CO₂ hydrogenation, and many others. For example, FeO/Pt(111) and Cu₂O/Ag(111) catalysts have demonstrated high reactivity for gas-phase aerobic oxidation of benzyl alcohol and other primary alcohols where the metal-oxide interface is identified as the active site (Zhao et al., 2017). Mixed valent manganese oxides have superior redox chemistry. They form layered, spinel, perovskite, bixbyite, and other structures with oxidation states ranging from 2⁺ to 4⁺ (Risch et al., 2017). MnO₂@FeOOH catalysts were prepared for oxidation of indoor air containing formaldehyde by Wang C. et al. (2022) Reactive oxygen species (ROS) formed on the catalyst surfaces were responsible for formaldehyde oxidation. *In situ* and *ex situ* aqueous and gaseous ROS quenching experiments confirmed the crucial role of the superoxide anion in this oxidation. An ultrathin coating of MnO₂ on FeOOH decreased electron transfer resistance while increasing the amount of oxygen vacancies on the surface of these materials. These oxygen vacancies facilitated the absorption of molecular oxygen, which was subsequently activated to generate ROS (Wang C. et al., 2022). Lithium promoted mesoporous manganese oxides were utilized for the mild partial oxidation of allyl ethers. Dutta et al. hypothesized that the reaction proceeded via a radical mediated route. Introducing lithium increased the surface activity, which improved catalytic activity. Excellent conversion (95%) to allyl acrylate and a selectivity of >99% were achieved for this reaction (Dutta et al., 2019). Al₂O₃ supported vanadia (VO_x) and MoO₃-Fe₂O₃ catalysts are reported to be highly active for the ODH of alkanes such as ethane and propane (Solsona et al., 2001; Kondratenko et al., 2005). Furthermore, the MoO₃-Fe₂O₃ and ZnO_x catalysts are also reported to be highly active for the ODH of propane (Zhao et al., 2021; Wang et al., 2023b). IrO₂-based catalysts have been highly effective for ethane oxidative dehydrogenation (Ping et al., 2023). In a recent study, the CeO_{2-x}/CoO_{1-x}/Co dual-interfaces are structurally active for catalyzing the WGS reaction, where the kinetic evidence and *in-situ* characterization results revealed that CeO_{2-x} modulates the oxidized state of Co species and consequently generates the dual active CeO_{2-x}/CoO_{1-x}/Co interface during the WGS reaction. The CeO_{2-x}/CoO_{1-x} interface alleviates the CO poisoning effect, and the CoO_{1-x}/Co interface promotes H₂ formation (Fu et al., 2023). A combined Ni-NiO_x-Y₂O₃ is reported to show high WGS activity when compared to pure Ni catalysts where the presence of Y₂O₃ tremendously improved the catalytic activity and stability, enabling efficient WGS reactivity at a medium temperature range (Xu et al., 2022). Many of the processes require high selectivity for specific



products and oxidation of the reactant molecules. The multiple oxidation states of the oxide materials control the selectivity in catalytic oxidations using oxides. Some TMOs can also catalyze selective hydrogenation. For example, copper-zinc oxide-based catalysts are used as the primary catalyst rather than copper metal for the conversion of CO or CO₂ via hydrogenation for methanol production (Martin and Pérez-Ramírez, 2013; Kattel et al., 2017a). Silica accelerates the selective hydrogenation of CO₂ to methanol on cobalt catalysts (Wang et al., 2020).

Molybdenum based oxide materials are highly preferred in electrochemical applications due to their tunable crystal structures, variability in Mo oxidation states, and the ability to modify the composition by introducing dopants. Defect engineering also involves morphology and oxygen vacancies. Synthesizing a highly mesoporous MoO_x catalyst via an inverse micelle molybdenum peroxo cluster formation method has been reported (Shubhashish et al., 2022) where a high surface area of 157 m²/g is found. These systems have shown high catalytic activity towards electrophilic aromatic substitution of benzyl alcohol with a higher conversion and selectivity towards methyl diphenylmethane. Ammonia chemisorption has shown that these materials are highly acidic in nature which could be attributed to the higher electrophilicity of the material. The diffraction obtained from X-ray powder diffraction suggests that the material is orthorhombic phase MoO₃.

α-MoO₃ has been used as a cathode material in lithium-ion batteries due to its high specific capacity (<1.6 Li⁺ per one transition metal) where cycling causes irreversible phase changes in the material, resulting in lower performance. However, a synthetic route via controllable plasma etching of α-MoO₃ has been performed by Zhang et al. (2018), which generates oxygen vacancies in the structure. The SEM image and XRD patterns of the synthesized pristine sample with varying etching times are demonstrated in Figure 4. Oxygen vacancies play a vital role in enhancing the electronic properties of these materials electronically through the band gap reduction which in turn affects the electron transfer resistance and effective Li⁺ diffusion. An incipient wet impregnation method has been used to synthesize crystalline

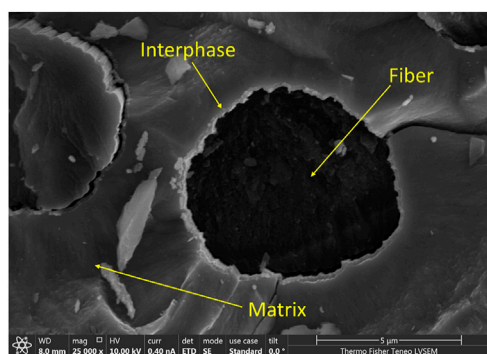


FIGURE 5
Cross sectional SEM image of carbon fiber with SiC coating of CMC.

MoO₃ catalysts on Al₂O₃ supports by Yao et al. (2020). This material has proven to be effective in conversion of ethane into ethylene in the presence of oxygen as well as other mild oxidants. Ethylene selectivity is reported to be 80%–85% in the presence of CO₂ and H₂O as oxidants in place of O₂. Mechanistic studies have shown that oxygen vacancies play an important role in the catalysis and regeneration process as the reaction progresses. Understanding the structures of these oxides is as important as their syntheses to obtain an understanding of the active sites of these materials and to correlate them with respective performances.

6 TMOs-based ceramics in high-temperature applications

Materials that have the capability to withstand high temperatures are in high demand in the aerospace industry. These materials are used in various applications such as the hot section of the gas turbine engine, brake pads, and as heat shields in space vehicles (Bakan et al., 2020; Binner et al., 2020; Borawski, 2020). Apart from being able to operate at high temperatures, these materials should also be resistant to extreme mechanical and oxidative stresses. A single material that adheres to all these criteria has not been invented yet. Instead, ceramic materials which have high temperature resistance are formed into composite materials known as Ceramic Matrix Composites (CMCs) to overcome the high mechanical and temperature stresses (Sato et al., 1999). A protective coating is added on top of the surface to protect these composites and nickel based superalloy structural parts from oxidation. This protective layer is known as Environmental Barrier Coatings (EBCs) for CMCs or Thermal Barrier Coatings (TBCs) for Nickel based superalloy structural parts (Lee, 2000; Vaßen et al., 2010). TMOs are promising candidates for making these protective coatings due to their low thermal conductivity, high thermal stability, and high corrosion resistance (Fang et al., 2023).

6.1 Ceramic Matrix Composites

CMCs consist of a three-part system namely Matrix, Interface, and Reinforcing Fiber. Bulk ceramic material is considered as the matrix. The matrix could be nonoxide ceramics like silicon carbide

or oxide ceramics like aluminum oxide. Monolithic refractory ceramics which are used as the matrix are usually brittle. Reinforcing fibers are incorporated into the bulk ceramic material to increase the mechanical strength of the ceramic. Commonly used fibers are carbon fibers or silicon carbide fibers (Gottlieb et al., 2016). These fibers increase the strength of the final composite by carrying the mechanical load applied upon the composite. Figure 5 shows a cross sectional SEM image of a carbon fiber/SiC CMC which, is synthesized using chemical vapor deposition methods. It is imperative to protect these fibers from oxidation at high temperatures to avoid ultimate composite failure due to oxidation or crack propagation through fibers (Li, 2020). Prior to densifying the bulk matrix, fibers are coated with a thin layer of ceramic to overcome this scenario, and this thin layer is known as the interphase layer. Such interphases act as barriers to oxidation and stop failure of fibers by crack deflection or by facilitating fiber debonding (Kerans et al., 2002).

Oxidation under high temperatures is a major drawback in CMCs. Most nonoxide ceramics decompose into their respective oxides under high thermal stress leading to investigations of making CMCs using metal oxides (Coons et al., 2013). Poges et al. studied the effect of a transition metal zinc oxide as the interface coating in oxide/oxide CMCs by comparing the flexural strength of a CMC system containing Nextel 610 reinforcing fibers and an alpha alumina matrix with a ZnO interphase coating to the same CMC system without a ZnO interphase layer. From their data, adding the ZnO interphase layer increased the flexural strength by 30% for the CMC by introducing toughening mechanisms such as interphase debonding and crack deflection (Poges et al., 2017).

6.2 TMO ceramics as thermal/environmental barrier coatings

In the aerospace industry thermal barrier coatings are applied on top of Nickel based superalloys for protection from high thermal stresses. TBCs consist of two layers, namely, the bond coat and the top coat as shown in Figure 6 (Mehta et al., 2022). Ytria stabilized Zirconia (YSZ) is the most used transition metal oxide ceramic in the aerospace industry which provides thermal resistivity due to its low thermal conductivity.

The behavior of YSZ under the cycling of thermal and oxidative stresses has been widely studied over the past couple of decades (Weng et al., 2020). With the emergence of more powerful next-generation gas turbine engines, the operating temperature of the hot section has risen considerably over the years. There have been various recent attempts to develop novel transition metal oxide systems that can outperform current YSZ systems.

Sang et al. developed a novel high entropy ceramic system (Sm_{0.2}Lu_{0.2}Dy_{0.2}Yb_{0.2}Y_{0.2})₃TaO₇ using a sol gel and sintering hybrid method with high crystallinity and increased phase stability. This transition metal oxide system has the single fluorite crystal system, and exhibits lower thermal conductivity than the YSZ system. The low thermal conductivity is due to the complexity of the elemental composition, oxygen vacancies, and lattice distortion which ultimately resulted in higher phonon scattering (Sang et al., 2023).

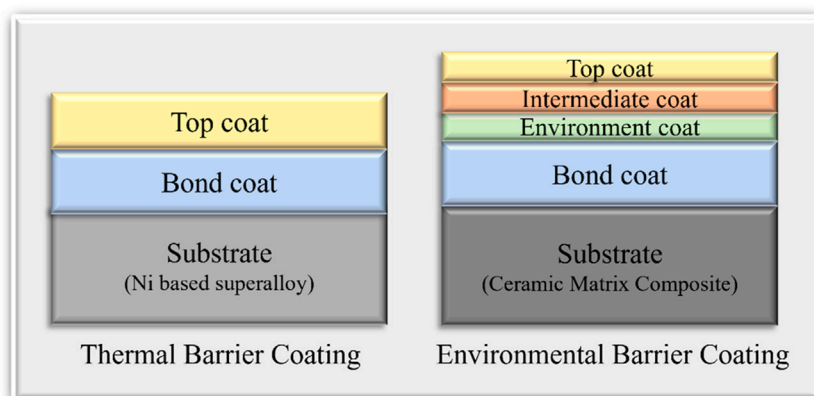


FIGURE 6
Schematic diagram of TBCs and EBCs (Thickness of the layers are not depicted in correct proportions).

A recent study by Dang et al. suggested a novel candidate for the TBC top coat. They produced yttria doped hafnia ($\text{Y}_4\text{Hf}_3\text{O}_{12}$) using an atmospheric plasma spray method. This material showed promising results for phase stability after 200 h at $1,300^\circ\text{C}$ and thermal stability after 459 cycles. Phonon thermal conductivity measurements portrayed lower thermal conductivity than YSZ and authors attributed this lower thermal conductivity to the high concentration of Y cations in the fluorite crystal system. Even though this material has promising results, the low Coefficient of Thermal Expansion (CTE) is a downside. $\text{Y}_4\text{Hf}_3\text{O}_{12}$ was suggested as coating with a YSZ buffer coat to overcome that problem (Dang et al., 2023).

Environmental barrier coatings are more complex when compared to thermal barrier coatings. Typically, third generation EBCs have four layers on top of the CMC substrate namely Topcoat, Intermediate Coat, Environment Coat, and Bond Coat. Oxide ceramics like mullite and BSAS ($1-x\text{BaO} \cdot x\text{SrO} \cdot \text{Al}_2\text{O}_3 \cdot 2\text{SiO}_2, 0 < x < 1$) are widely used in top coats (Chen et al., 2023). In recent years there have been new developments of a new type of ceramic coating which involves transition metal elements. These are called rare earth monosilicates (RE_2SiO_5) or rare earth disilicates (RESi_2O_7) (Tejero-Martin et al., 2021).

Among the available rare earth silicates, Ytterbium disilicates ($\text{Yb}_2\text{Si}_2\text{O}_7$) have caught the attention of the researchers due to their close CTE match with SiC substrates and the relatively high oxidation corrosion in Ytterbium monosilicates (YbSiO_5). Wang et al. hypothesized that combining a mixture of these two Ytterbium silicates would be more successful as an EBC topcoat and studied the protection effects of the Atmospheric Plasma Spray deposited mix coating on SiC_f/SiC composites. After exposing the system to a mixture of water vapor and oxygen at $1,300^\circ\text{C}$ for 200 h the protected CMC systems retained their original strength by 90% when compared to the non-protected ones only retaining 10%–15% (Wang Y. et al., 2022).

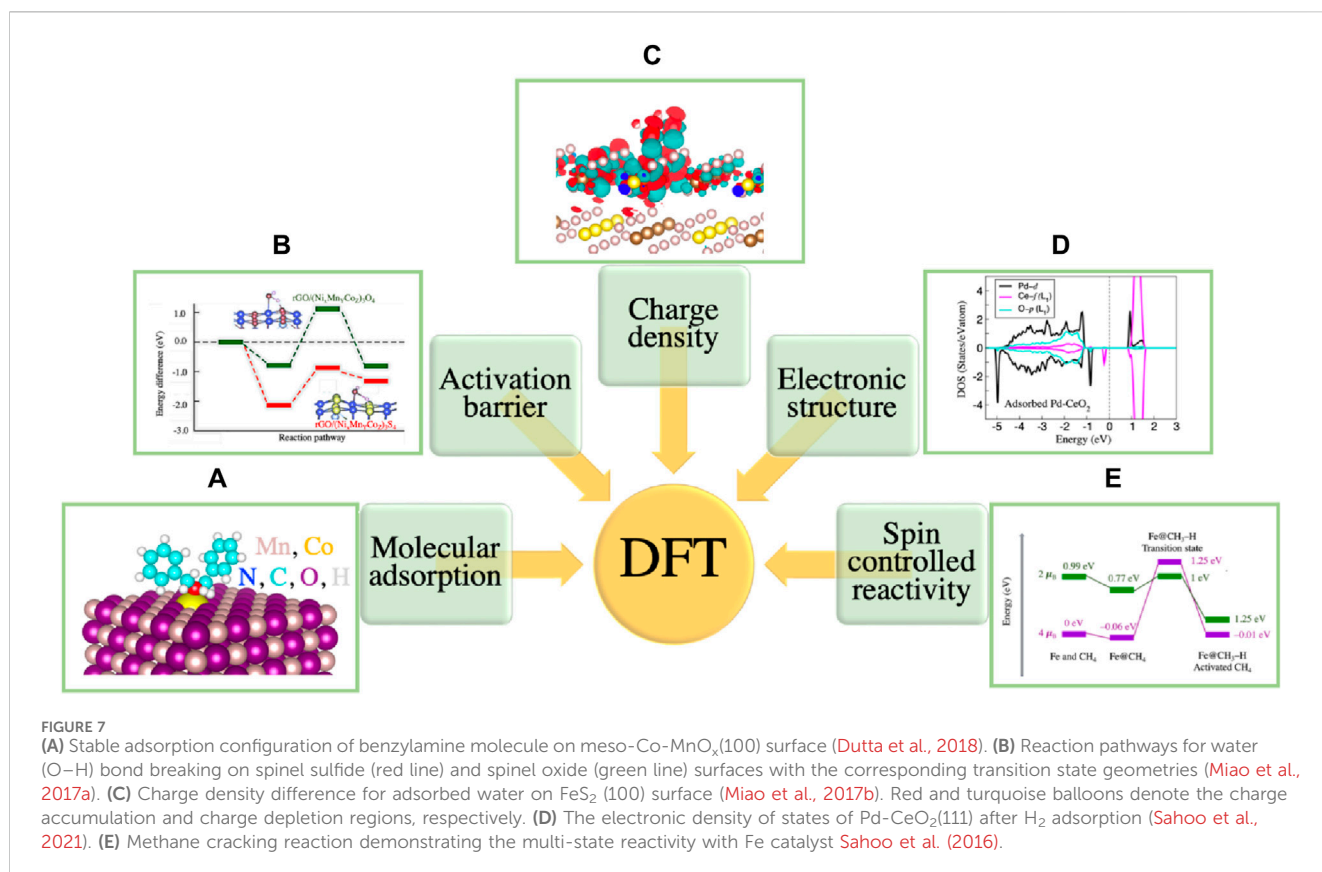
Transition metal oxides are mostly used as protective coatings in the aerospace industry. For example, fabricating CMCs involves depositing a thin film coating on the reinforcing fibers, or making a TBC/EBC involves depositing a multilayer coating on substrates leading to the utilization of thin film deposition techniques. The

most common thin film fabrication technique is chemical vapor deposition (CVD). In CVD the substrate is heated to the desired deposition temperature and then the precursors are flown over the substrate. When the precursors meet the heated substrate, they react and form a thin film (Morosanu, 1990). CVD is a very useful technique, but is also a highly inefficient technique. Most of the reactants will not react and form a thin film. The other problem is finding the proper precursor. Reactants must be either in gaseous form or should be able to be converted into gaseous forms by evaporation or sublimation. This limits the number of compounds that can be formed by CVD.

Various thin film coating techniques like electron beam physical vapor deposition, plasma spray, and magnetron sputtering are used to make TBC/EBCs. Among these methods, Atmospheric Plasma Spray (APS) is commonly used to make these complex multilayer protective coatings due to low cost, flexibility of the process, and higher deposition rates. In this method precursors are heated using plasmas and then mixed with carrier gas. Then the mixture is bombarded onto the pretreated substrate (Thakare et al., 2021). Due to the nature of the process, the coating is formed in a lamellar structure which induces the formation of amorphous phases and undesirable microstructures such as porosity. Post process annealing is required to overcome these challenges. This will allow the amorphous phases to crystallize and heal the microcracks and pores present in the coating (Arhami et al., 2023).

7 Challenges from theory in modeling TMOs

The bonding and interaction of reactants with the surface and the influence of surfaces on the bonding and interactions between reactants are the key factors that significantly contribute to catalytic processes. The TMO surface imposes several complexities for both theoretical modeling and experimental characterization. Some of the important descriptors that must be taken into account for surface characterization and surface reactions are: the stoichiometric ratios of cations and anions, the covalent and ionic bonding, the charges of adsorbed species, the surface acidity and basicity, the cation and



anion vacancies, oxygen mobility, and the surface reconstruction due to the presence of dangling bond. These complexities make TMOs one of the most complicated systems for experimental and theoretical investigations. While recent experimental techniques can synthesize and characterize TMO surfaces, understanding the atomic level interactions in the TMOs is extremely challenging from an experimental viewpoint. For instance, obtaining information about processes related to the diffusion and mobility of impurities and oxygen, the locations and the amounts of oxygen vacancies, the charge transfer mechanism, the exact electronic structures, and the surface reconstruction processes are extremely challenging. Furthermore, contamination of the surface with light-weight elements (below the atomic number of Na) that can easily interfere with surface reactions and influence efficiency, is hard to track in laboratories without the application of numerous special techniques. Electronic structure methods have been proven to be highly effective to address these issues. The accuracy and efficiency of these methods has led to a paradigm shift in coupling experiments and theoretical research together with the aim of tangible understanding, predicting, and designing properties of materials. Several quantum chemical methodologies, such as wavefunction-based Hartree–Fock (HF), and post-Hartree–Fock approaches ranging from Møller–Plesset (MP) perturbation theory (Møller and Plesset, 1934) to coupled cluster (CC), configuration interaction (CI) (David Sherrill et al., 1999), and many body Green’s function methods have been applied to study catalysis (Mandaliya and Gudi, 2023). The focus of our modeling has been the total charge-density based density functional theory (DFT) which helps to track chemical reactions with a larger size

of model that is representative of the actual experiments (Kohn and Sham, 1965; Jones, 2015). The quantities related to chemical reactivity and catalysis such as the molecular adsorption sites on surfaces, the binding energies between adsorbates and surfaces, the reaction pathways and activation barriers, the charge distribution and charge transfer are also reliably predicted using DFT methods (Sahoo et al., 2018a; Sahoo et al., 2021; Bamonte et al., 2022). Figures 7A–E demonstrates examples of systems with such properties. More details are explained in the caption.

Although DFT is limited to zero temperature and pressure, it has a major role for investigating the thermal stability and composition of transition metal surfaces under realistic conditions. One such approach is the *ab initio* thermodynamics method where the total energies obtained from DFT are used as input for determining the thermodynamic phase stability as well as the surface structure and composition (Reuter et al., 2005; Stampfl, 2005; Sahoo et al., 2018b).

For example, when transition metal surfaces are exposed to high oxygen pressures, thin oxide-like structures are reported to form with little similarity to the bulk oxides (Stampfl, 2005). Among these, oxygen interaction with Ag(111), Pd(111), Ru(0001) and Rh(111) surfaces are important. For O/Ag(111) and O/Pd(111), the free energy phase-diagrams as a function of (*T*, *p*) show high stability for thin surface-oxide-like configurations whereas, the O/Rh(111) and O/Ru(0001) are metastable with respect to bulk oxide formation. In many of these cases, formation of surface-oxides leads to significant geometrical changes with little similarity to the corresponding bulk oxide (Stampfl, 2005). Using a similar approach, the interaction of oxygen, nitrogen and hydrogen with Ti(0001) surfaces under varying gas partial pressure and temperature is studied, where

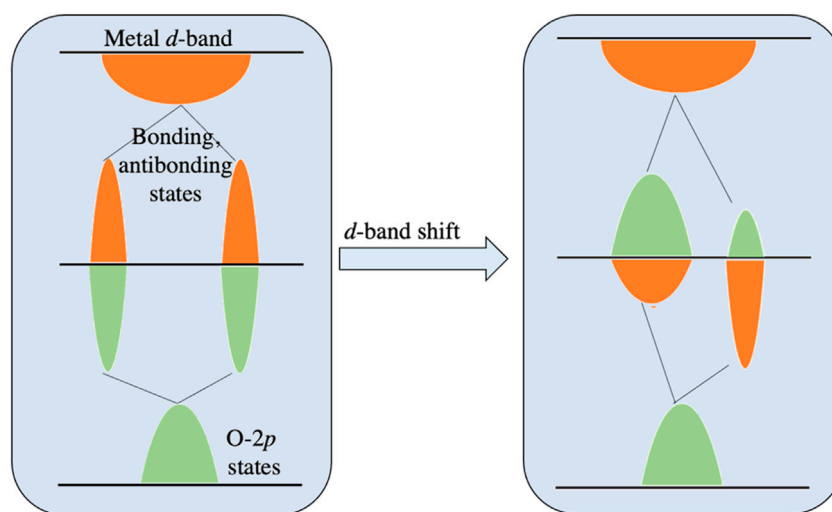


FIGURE 8

The energy diagram demonstrating the change in metal d -band in the $2p$ -states of adsorbed oxygen at a transition metal surface. As shown in the left panel, prior to the mixing with metal d -band, the O $2p$ -states hybridize with the metal sp -band, resulting in the O $2p$ -state. These states interact with the metal d -band as shown in the right panel, to form bonding and antibonding states, which are projected onto the O $2p$ -states or metal d -states as indicated by the green peaks and orange peaks, respectively.

the Ti(0001) surface was reported to have the high affinity for oxygen with a strong surface passivation tendency compared to nitrogen and hydrogen (Sahoo et al., 2018b). Apart from *ab initio* thermodynamics, there are other methods such as the Kinetic Monte Carlo (KMC) and microkinetic modeling where the DFT total energies could be used as inputs for investigating the reaction kinetics under realistic conditions (Kattel et al., 2017b).

In TM catalysis, spin controlled reactivity is an important characteristic. DFT offers a versatile framework for investigating the multistate reactivity via providing detailed description of electronic transitions between different molecular states and insights into the electronic structure as well as energetics of complex chemical processes. For instance, during a reaction the reactants in a given spin state could convert into products with the same spin state, but the intermediates could have a different spin state. One such example is shown in Figure 7E where the interaction of methane with Fe catalyst has demonstrated a multi-state reactivity for the methane cracking reaction (Sahoo et al., 2016). The minimum energy pathway for methane activation is characterized by two spin states, a high spin state of $4 \mu_B$, and a low spin state of $2 \mu_B$. The high spin state is more stable for the reactant complex by 0.99 eV, as the reaction progresses, a spin-crossover takes place at the transition state with methane C-H bond distance (1.58 Å). The low spin state becomes favorable followed by a high spin state as energetically stable for the product (the cracked methane with C-H bond distance 2.93 Å). With the evolution of computational methodologies, DFT is expected to play a key role in unraveling the intricate mechanisms of multistate reactions, guiding experimental efforts, and contributing to the design of novel materials and catalysts for applications in diverse fields of chemistry and materials science.

Given certain limitations of DFT pertaining to strong electron correlation effects that describe the properties of

TMOs, one needs certain technical improvements in DFT to accurately capture the properties. The most used approach is the Hubbard U treatment to DFT Hamiltonian, called the DFT+ U . The parameter U is either calculated theoretically or determined from experiments by matching the electronic density of states. The DFT + U has been found to yield accurate and robust results (Adeagbo et al., 2014; Nayak et al., 2015; Miao et al., 2017a; Miao et al., 2017b).

Catalysis studies have been done through a hybrid-functional approach to the DFT, where while the correlation interactions are kept at the generalized-gradient approximation level, the exchange interaction is supplemented by screened Hartree-Fock exchange constructed from the Kohn-Sham orbitals. Such an approach has shown to improve the band gap description of bulk semiconductors and strong-correlation of the TMO almost simultaneously. The hybrid functional scheme has been applied to study surface reactions (Getsoian and Bell, 2013). However, owing to their intense computational resource requirements, this method is not the most applied method in the community. Furthermore, questions about how to treat the reference energies in the formation energy calculations (Nayak et al., 2015; Nayak et al., 2018; Reid et al., 2020), and reliable modeling of electronic structures for more sophisticated quantum properties, suggest that the hybrid functional approach may be redundant for high-Z TMOs. As shown in the literature, spin orbit coupling is more important to describe these delicate properties.

The optimal choice of the functional in DFT ultimately depends on the target properties and requires validation with experiments. However, the analogy is not universal across all materials. Identifying and understanding relationships between the electronic and atomic structure of surfaces and their catalytic activity is an essential step towards the rational design of heterogeneous catalysts. One successful example is the d -band

model for transition metals, which has provided rational trends in surface reactivity with compositional changes, lattice constants, and facets. The *d*-band model has also provided a physical basis for the widely used descriptor-based analyses and scaling relationships between adsorbate binding energies and transition state energies (Dahl et al., 2001; Xin et al., 2014).

Recently, for TMOs, a direct relationship is established between electronic structure and catalytic properties, where the correlations between adsorbate binding energies and the metal *d*-states or oxygen 2*p*-states have been made for rutile, perovskite, and rock-salt TMOs (Dickens et al., 2019). The oxygen electrochemical rates of perovskite catalysts, have been shown to correlate with the electron occupancies and other electronic structural properties such as the oxygen 2*p*-band center and charge transfer energy obtained from DFT and X-ray spectroscopy measurements. A description in this regard is given in Figure 8.

8 Conclusion

The review provides an overview of designing TMOs and their functional applications using state-of-the-art synthetic and characterization techniques, with specific emphasis on mesoporous oxides. The primary focus on the applications side includes utilizing TMOs as effective materials for clean energy and sustainability, especially involving their usage in photocatalysis, electrocatalysis. Another usage includes their application in high-temperature thermal barrier coatings that is important in aerospace industry. Despite numerous studies, the characterization and investigation of TMOs, both from experimental and theoretical perspectives, have not yet reached an optimum level. There are still many important issues and open questions that require attention for a complete understanding of TMOs. A key research focus pertains to the development of theoretical methods capable of providing reliable energies and an accurate description of the electronic structure of TMOs. In this regard, DFT, has become an important tool for supporting the interpretation of experimental data such as providing structural insights, analyzing spectroscopic data, and testing mechanistic hypotheses through the microscopic insights into the relationships between atomic and electronic structures. The review addresses the major pros and cons of DFT as well as those issues that need to be overcome in modeling TMOs to

achieve the desired functionalities and optimization of TMO-based catalysts.

Author contributions

SS: Conceptualization, Investigation, Supervision, Visualization, Writing—original draft, Writing—review and editing, Formal Analysis, Methodology. KW: Data curation, Methodology, Writing—original draft, Writing—review and editing, Formal Analysis. EN: Data curation, Methodology, Writing—original draft, Writing—review and editing. DS: Data curation, Methodology, Writing—original draft. SLS: Conceptualization, Data curation, Funding acquisition, Investigation, Methodology, Supervision, Writing—original draft, Writing—review and editing, Formal Analysis, Project administration, Resources.

Funding

The author(s) declare that no financial support was received for the research, authorship, and/or publication of this article.

Acknowledgments

We appreciate the support of NEUCORSE for this research.

Conflict of interest

The authors declare that the research was conducted in the absence of any commercial or financial relationships that could be construed as a potential conflict of interest.

Publisher's note

All claims expressed in this article are solely those of the authors and do not necessarily represent those of their affiliated organizations, or those of the publisher, the editors and the reviewers. Any product that may be evaluated in this article, or claim that may be made by its manufacturer, is not guaranteed or endorsed by the publisher.

References

- Abdelghafar, F., Xu, X., Jiang, S. P., and Shao, Z. (2024). Perovskite for electrocatalytic oxygen evolution at elevated temperatures. *ChemSusChem* n/a (n/a), e202301534. doi:10.1002/cssc.202301534
- Achola, L. A., Shubhashish, S., Tobin, Z., Su, Y., Posada, L. F., Dang, Y., et al. (2022). Microwave hydrothermal synthesis of mesoporous first-row transition metal ferrites. *Chem. Mat.* 34, 7692–7704. doi:10.1021/acs.chemmater.2c00684
- Adeagbo, W. A., Thomas, S., Nayak, S. K., Ernst, A., and Hergert, W. (2014). First-principles study of uniaxial strained and bent ZnO wires. *Phys. Rev. B* 89 (19), 195135. doi:10.1103/physrevb.89.195135
- Adegoke, K. A., and Maxakato, N. W. (2022). Porous metal oxide electrocatalytic nanomaterials for energy conversion: oxygen defects and selection techniques. *Coord. Chem. Rev.* 457, 214389. doi:10.1016/j.ccr.2021.214389
- An, B., Li, Z., Wang, Z., Zeng, X., Han, X., Cheng, Y., et al. (2022). Direct photo-oxidation of methane to methanol over a mono-iron hydroxyl site. *Nat. Mat.* 21 (8), 932–938. doi:10.1038/s41563-022-01279-1
- Arhami, F., Ben Ettouil, F., and Moreau, C. (2023). As-Sprayed highly crystalline Yb₂Si₂O₇ environmental barrier coatings (EBCs) by atmospheric plasma spray (APS). *J. Therm. Spray. Technol.* 32 (2), 706–718. doi:10.1007/s11666-022-01526-6
- Bakan, E., Mack, D. E., Mauer, G., Vafsen, R., Lamon, J., and Pature, N. P. (2020) *Elsevier series on advanced ceramic materials*. Amsterdam, Netherlands: Elsevier, 3–62.
- Bamonte, S., Shubhashish, S., Khanna, H., Shuster, S., Rubio, S. J. B., Suib, S. L., et al. (2022). Magnetically doped molybdenum disulfide layers for enhanced carbon dioxide capture. *ACS Appl. Mat. Interfaces* 14 (24), 27799–27813. doi:10.1021/acsami.2c01820

- Bandeira, M., Giovanela, M., Roesch-Ely, M., Devine, D. M., and da Silva Crespo, J. (2020). Green synthesis of zinc oxide nanoparticles: a review of the synthesis methodology and mechanism of formation. *Sustain. Chem. Pharm.* 15, 100223. doi:10.1016/j.scp.2020.100223
- Bayram, E., Lu, J., Aydin, C., Browning, N. D., Özkaz, S., Finney, E., et al. (2015). Agglomerative sintering of an atomically dispersed Ir₁/zeolite Y catalyst: compelling evidence against ostwald ripening but for bimolecular and autocatalytic agglomeration catalyst sintering steps. *ACS Catal.* 5 (6), 3514–3527. doi:10.1021/acscatal.5b00321
- Bellini, M., Pagliaro, M. V., Lenarda, A., Fornasiero, P., Marelli, M., Evangelisti, C., et al. (2019). Palladium–ceria catalysts with enhanced alkaline hydrogen oxidation activity for anion exchange membrane fuel cells. *ACS Appl. Energy Mat.* 2 (7), 4999–5008. doi:10.1021/acsaem.9b00657
- Beniya, A., and Higashi, S. (2019). Nature catalysis. *Nat. Res. July* 1, 590–602. doi:10.1038/s41467-020-15850-4
- Besenhard, M. O., Storozhuk, L., LaGrow, A. P., Panariello, L., Maney, A., Pal, S., et al. (2023). High temperature flow synthesis of iron oxide nanoparticles: size tuning via reactor engineering. *Chem. Eng. J.* 473, 144542. doi:10.1016/j.cej.2023.144542
- Besnardiere, J., Ma, B., Torres-Pardo, A., Wallez, G., Kabbour, H., González-Calbet, J. M., et al. (2019). Structure and electrochromism of two-dimensional octahedral molecular sieve h'-WO₃. *Nat. Commun.* 10 (1), 327. doi:10.1038/s41467-018-07774-x
- Bie, C., Wang, L., and Yu, J. (2022). Challenges for photocatalytic overall water splitting. *Chem* 8 (6), 1567–1574. doi:10.1016/j.chempr.2022.04.013
- Binner, J., Porter, M., Baker, B., Zou, J., Venkatachalam, V., Diaz, V. R., et al. (2020). Selection, processing, properties and applications of ultra-high temperature ceramic matrix composites, UHTCMCs – a review. *Int. Mat. Rev.* 65 (7), 389–444. doi:10.1080/09506608.2019.1652006
- Borawski, A. (2020). Conventional and unconventional materials used in the production of brake pads – review. *Sci. Eng. Compos. Mater.* 27 (1), 374–396. doi:10.1515/secm-2020-0041
- Cai, G., Yan, P., Zhang, L., Zhou, H.-C., and Jiang, H.-L. (2021). Metal–organic framework-based hierarchically porous materials: synthesis and applications. *Chem. Rev.* 121 (20), 12278–12326. doi:10.1021/acs.chemrev.1c00243
- Chen, H.-Y., Lu, J., Fedeyko, J. M., and Raj, A. (2022). Zeolite supported Pd catalysts for the complete oxidation of methane: a critical review. *Appl. Catal. A Gen.* 633, 118534. doi:10.1016/j.apcata.2022.118534
- Chen, W., He, J., Zhou, D., and Guo, H. (2023). *Woodhead publishing series in metals and surface engineering*. Sawston, United Kingdom: Woodhead Publishing, 433–465.
- Coons, T. P., Reutenauer, J. W., Mercado, A., Kmetz, M. A., and Suib, S. L. (2013). The characterization of an oxide interfacial coating for ceramic matrix composites. *Mat. Sci. Eng. A* 573, 190–196. doi:10.1016/j.msea.2013.02.060
- Cox, P. A. (2010). *Transition metal oxides an introduction to their electronic structure and properties*. Oxford, United Kingdom: Oxford University Press.
- Dahl, S., Logadottir, A., Jacobsen, C. J. H., and Nørskov, J. K. (2001). Electronic factors in catalysis: the volcano curve and the effect of promotion in catalytic ammonia synthesis. *Appl. Catal. A Gen.* 222 (1–2), 19–29. doi:10.1016/S0926-860X(01)00826-2
- Dang, X., Yuan, J., Li, X., Huang, Z., Hu, X., Li, Y., et al. (2023). Properties evaluation and failure behaviour of plasma sprayed Y4Hf3O12 for thermal barrier coating applications. *Surf. Coatings Technol.* 454, 129162. doi:10.1016/j.surfcoat.2022.129162
- Dang, Y., Wu, T., Tan, H., Wang, J., Cui, C., Kerns, P., et al. (2021). Partially reduced Ru/RuO₂ composites as efficient and pH-universal electrocatalysts for hydrogen evolution. *Energy Environ. Sci.* 14 (10), 5433–5443. doi:10.1039/d1ee02380b
- David Sherrill, C., Schaefer, H. F., Löwdin, P.-O., Sabin, J. R., Zerner, M. C., and Brändas, E. B. T.-A. (1999), 34. Academic Press, 143–269.
- Dickens, C. F., Montoya, J. H., Kulkarni, A. R., Bajdich, M., and Nørskov, J. K. (2019). An electronic structure descriptor for oxygen reactivity at metal and metal-oxide surfaces. *Surf. Sci.* 681, 122–129. doi:10.1016/j.susc.2018.11.019
- Drummer, S., Madzimbamuto, T., and Chowdhury, M. (2021). Green synthesis of transition-metal nanoparticles and their oxides: a review. *Materials* 14, 2700. doi:10.3390/ma14112700
- Dutta, B., Clarke, R., Raman, S., Shaffer, T. D., Achola, L., Nandi, P., et al. (2019). Lithium promoted mesoporous manganese oxide catalyzed oxidation of allyl ethers. *Nat. Commun.* 10 (1), 655. doi:10.1038/s41467-019-08619-x
- Dutta, B., March, S., Achola, L., Sahoo, S., He, J., Shirazi Amin, A., et al. (2018). Mesoporous cobalt/manganese oxide: a highly selective bifunctional catalyst for amine–imine transformations. *Green Chem.* 20 (14), 3180–3185. doi:10.1039/c8gc00862k
- Elsevier (2019). *Single-atom catalysis*. Amsterdam, Netherlands: Elsevier.
- Fang, G., Gao, X., and Song, Y. (2023). A review on ceramic matrix composites and environmental barrier coatings for aero-engine: material development and failure analysis. *Coatings* 13, 357. doi:10.3390/coatings13020357
- Fu, X.-P., Wu, C.-P., Wang, W.-W., Jin, Z., Liu, J.-C., Ma, C., et al. (2023). Boosting reactivity of water-gas shift reaction by synergistic function over CeO₂-x/CoO₁-x/Co dual interfacial structures. *Nat. Commun.* 14 (1), 6851. doi:10.1038/s41467-023-42577-9
- Getsoian, A., and Bell, A. T. (2013). The influence of functionals on density functional theory calculations of the properties of reducible transition metal oxide catalysts. *J. Phys. Chem. C* 117 (48), 25562–25578. doi:10.1021/jp409479h
- Gottlieb, R., Poges, S., Monteleone, C., Suib, S. L., and Suib, S. L. (2016). “Continuous fiber-reinforced ceramic matrix composites,” in *Advanced ceramic materials* (Hoboken, New Jersey, United States: Wiley), 146–199.
- Guo, X., Fang, G., Li, G., Ma, H., Fan, H., Yu, L., et al. (2014). Direct, nonoxidative conversion of methane to ethylene, aromatics, and hydrogen. *Science* 344 (6184), 616–619. doi:10.1126/science.1253150
- Jones, R. O. (2015). Density functional theory: its origins, rise to prominence, and future. *Rev. Mod. Phys.* 87 (3), 897–923. doi:10.1103/revmodphys.87.897
- Kattel, S., Liu, P., and Chen, J. G. (2017b). Tuning selectivity of CO₂ hydrogenation reactions at the metal/oxide interface. *J. Am. Chem. Soc.* 139 (29), 9739–9754. doi:10.1021/jacs.7b05362
- Kattel, S., Ramírez, P. J., Chen, J. G., Rodriguez, J. A., and Liu, P. (2017a). Active sites for CO₂ hydrogenation to methanol on Cu/ZnO catalysts. *Science* 355 (6331), 1296–1299. doi:10.1126/science.aal3573
- Kerans, R. J., Hay, R. S., Parthasarathy, T. A., and Cinibulk, M. K. (2002). Interface design for oxidation-resistant ceramic composites. *J. Am. Ceram. Soc.* 85 (11), 2599–2632. doi:10.1111/j.1151-2916.2002.tb00505.x
- Kohn, W., and Sham, L. (1965). Self-consistent equations including exchange and correlation effects. *Phys. Rev.* 140 (4A), 1133–A1138. doi:10.1103/physrev.140.a1133
- Kondratenko, E. V., Cherian, M., Baerns, M., Su, D., Schlögl, R., Wang, X., et al. (2005). Oxidative dehydrogenation of propane over V/MCM-41 catalysts: comparison of O₂ and N₂O as oxidants. *J. Catal.* 234 (1), 131–142. doi:10.1016/j.jcat.2005.05.025
- Kresge, C. T., Leonowicz, M. E., Roth, W. J., Vartuli, J. C., and Beck, J. S. (1992). Ordered mesoporous molecular sieves synthesized by a liquid-crystal template mechanism. *Nature* 359 (6397), 710–712. doi:10.1038/359710a0
- Kumar, R., Youssry, S. M., Soe, H. M., Abdel-Galeil, M. M., Kawamura, G., and Matsuda, A. J. (2020). Honeycomb-like open-edged reduced-graphene-oxide-enclosed transition metal oxides (NiO/Co₃O₄) as improved electrode materials for high-performance supercapacitor. *Energy Storage* 30, 101539. doi:10.1016/j.est.2020.101539
- Lee, K. N. (2000). Current status of environmental barrier coatings for Si-Based ceramics. *Surf. Coatings Technol.* 133–134, 1–7. doi:10.1016/S0257-8972(00)00889-6
- Lermusiaux, L., Mazel, A., Carretero-Genevri, A., Sanchez, C., and Drisko, G. L. (2022). Metal-induced crystallization in metal oxides. *Acc. Chem. Res.* 55 (2), 171–185. doi:10.1021/acs.accounts.1c00592
- Li, B., Hao, Y., Shao, X., Tang, H., Wang, T., Zhu, J., et al. (2015). Synthesis of hierarchically porous metal oxides and Au/TiO₂ nanohybrids for photodegradation of organic dye and catalytic reduction of 4-nitrophenol. *J. Catal.* 329, 368–378. doi:10.1016/j.jcat.2015.05.015
- Li, L. (2020). *Durability of ceramic-matrix composites*. Amsterdam, Netherlands: Elsevier Science.
- Li, X., Garlisi, C., Guan, Q., Anwer, S., Al-Ali, K., Palmisano, G., et al. (2021). A review of material aspects in developing direct Z-scheme photocatalysts. *Mat. Today* 47, 75–107. doi:10.1016/j.mat.2021.02.017
- Lin, S., Huang, H., Ma, T., and Zhang, Y. (2021). Photocatalytic oxygen evolution from water splitting. *Adv. Sci.* 8 (1), 2002458.
- Liu, H., Yang, W., Ma, Y., Cao, Y., Yao, J., Zhang, J., et al. (2003). Synthesis and characterization of titania prepared by a photoassisted Sol–Gel method. *Langmuir* 19 (7), 3001–3005. doi:10.1021/la026600o
- Liu, S., Yu, J., and Jaroniec, M. (2011). Anatase TiO₂ with dominant high-energy {001} facets: synthesis, properties, and applications. *Chem. Mat.* 23 (18), 4085–4093. doi:10.1021/cm200597m
- Low, J., Dai, B., Tong, T., Jiang, C., and Yu, J. (2019a). *In situ* irradiated X-ray photoelectron spectroscopy investigation on a direct Z-scheme TiO₂/CdS composite film photocatalyst. *Adv. Mat.* 31 (6), e1807920. doi:10.1002/adma.201807920
- Low, W. H., Khiew, P. S., Lim, S. S., Siong, C. W., and Ezeigwe, E. R. (2019b). Recent development of mixed transition metal oxide and graphene/mixed transition metal oxide based hybrid nanostructures for advanced supercapacitors. *J. Alloys Compd.* 775, 1324–1356. doi:10.1016/j.jallcom.2018.10.102
- Mandaliya, D. D., and Gudi, R. D. (2023). A Green's Function Method based approach for effectiveness factor evaluation in two-dimensional spherical catalyst geometries with non-linear kinetics and partial wetting. *Chem. Eng. Sci.* 275, 118714. doi:10.1016/j.ces.2023.118714
- Martin, O., and Pérez-Ramírez, J. (2013). New and revisited insights into the promotion of methanol synthesis catalysts by CO₂. *Catal. Sci. Technol.* 3 (12), 3343–3352. doi:10.1039/c3cy00573a
- Mehta, A., Vasudev, H., Singh, S., Prakash, C., Saxena, K. K., Linul, E., et al. (2022). Processing and advancements in the development of thermal barrier coatings: a review. *Coatings* 12, 1318. doi:10.3390/coatings12091318
- Miao, R., Dutta, B., Sahoo, S., He, J., Zhong, W., Cetegen, S. A., et al. (2017b). Mesoporous iron sulfide for highly efficient electrocatalytic hydrogen evolution. *J. Am. Chem. Soc.* 139 (39), 13604–13607. doi:10.1021/jacs.7b07044

- Miao, R., He, J., Sahoo, S., Luo, Z., Zhong, W., Chen, S.-Y., et al. (2017a). Reduced graphene oxide supported nickel-manganese-cobalt spinel ternary oxide nanocomposites and their chemically converted sulfide nanocomposites as efficient electrocatalysts for alkaline water splitting. *ACS Catal.* 7 (1), 819–832. doi:10.1021/acscatal.6b02650
- Møller, C., and Plesset, M. S. (1934). Note on an approximation treatment for many-electron systems. *Phys. Rev.* 46 (7), 618–622. doi:10.1103/physrev.46.618
- Morosanu, C. E. (1990). *Thin films by chemical vapour deposition*. Amsterdam, Netherlands: Elsevier Science.
- Nayak, S. K., Hung, C. J., Sharma, V., Alpay, S. P., Dongare, A. M., Brindley, W. J., et al. (2018). Insight into point defects and impurities in titanium from first principles. *npj Comput. Mat.* 4 (1), 11. doi:10.1038/s41524-018-0068-9
- Nayak, S. K., Langhammer, H. T., Adeagbo, W. A., Hergert, W., Müller, T., and Böttcher, R. (2015). Chromium point defects in hexagonalBaTiO₃: a comparative study of first-principles calculations and experiments. *Phys. Rev. B* 91 (15), 155105. doi:10.1103/physrevb.91.155105
- Nova (2014). *Oxide electronics and functional properties of transition metal oxides*. Hauppauge, New York, United States: Nova.
- Okonye, L. U., Yao, Y., Hildebrandt, D., and Meijboom, R. (2021). Contributing to energy sustainability: a review of mesoporous material supported catalysts for Fischer–Tropsch synthesis. *Sustain. Energy Fuels* 5 (1), 79–107. doi:10.1039/d0se01442g
- Owale, S. O., Olowookere, I. T., Perera, I., Khanna, H. S., Njeri, E., Huang, X., et al. (2023). Photocatalytic degradation of orange II dye via high pore volume polymorph zirconium-doped titania under visible light irradiation. *Appl. Surf. Sci.* 616, 156452. doi:10.1016/j.apsusc.2023.156452
- Ping, L., Zhang, Y., Wang, B., Fan, M., Ling, L., and Zhang, R. (2023). Unraveling the surface state evolution of IrO₂ in ethane chemical looping oxidative dehydrogenation. *ACS Catal.* 13 (2), 1381–1399. doi:10.1021/acscatal.2c05770
- Poges, S., Monteleone, C., Petroski, K., Richards, G., and Suib, S. L. (2017). Preparation and characterization of an oxide-oxide continuous fiber reinforced ceramic matrix composite with a zinc oxide interphase. *Ceram. Int.* 43 (18), 17121–17127. doi:10.1016/j.ceramint.2017.09.133
- Poyraz, A. S., Kuo, C.-H., Biswas, S., King'ondou, C. K., and Suib, S. L. (2013). A general approach to crystalline and monomodal pore size mesoporous materials. *Nat. Commun.* 4 (1), 2952. doi:10.1038/ncomms3952
- Qiao, B., Wang, A., Yang, X., Allard, L. F., Jiang, Z., Cui, Y., et al. (2011). Single-atom catalysis of CO oxidation using Pt1/FeOx. *Nat. Chem.* 3 (8), 634–641. doi:10.1038/nchem.1095
- Reid, T. K., Pamir Alpay, S., Balatsky, A. V., and Nayak, S. K. (2020). First-principles modeling of binary layered topological insulators: structural optimization and exchange-correlation functionals. *Phys. Rev. B* 101 (8), 085140. doi:10.1103/physrevb.101.085140
- Reuter, K., Stampf, C., and Scheffler, M. (2005). “Ab initio atomistic thermodynamics and statistical mechanics of surface properties and functions,” in *Handbook of materials modeling* (Dordrecht: Springer Netherlands), 149–194.
- Risch, M., Stoerzinger, K. A., Han, B., Regier, T. Z., Peak, D., Sayed, S. Y., et al. (2017). Redox processes of manganese oxide in catalyzing oxygen evolution and reduction: an *in situ* soft X-ray absorption spectroscopy study. *J. Phys. Chem. C* 121 (33), 17682–17692. doi:10.1021/acs.jpcc.7b05592
- Sahoo, S., Alpay, S. P., and Hebert, R. J. (2018b). Surface phase diagrams of titanium in Oxygen, Nitrogen and Hydrogen environments: a first principles analysis. *Surf. Sci.* 677, 18–25. doi:10.1016/j.susc.2018.05.007
- Sahoo, S., Dekel, D. R., Maric, R., and Alpay, S. P. (2021). Atomistic insights into the hydrogen oxidation reaction of palladium-ceria bifunctional catalysts for anion-exchange membrane fuel cells. *ACS Catal.* 11 (5), 2561–2571. doi:10.1021/acscatal.0c04646
- Sahoo, S., Reber, A. C., and Khanna, S. N. (2016). Effect of location and filling of d-states on methane activation in single site Fe-based catalysts. *Chem. Phys. Lett.* 660, 48–54. doi:10.1016/j.cplett.2016.07.053
- Sahoo, S., Suib, S. L., and Alpay, S. P. (2018a). Graphene supported single atom transition metal catalysts for methane activation. *ChemCatChem* 10 (15), 3229–3235. doi:10.1002/cctc.201800465
- Sang, W., Zhang, H., Zhang, H., Liu, X., Chen, X., Xie, W., et al. (2023). Novel (Sm_{0.2}Lu_{0.2}Yb_{0.2}Y_{0.2}Dy_{0.2})₃TaO₇ high-entropy ceramic for thermal barrier coatings. *Ceram. Int.* 49 (6), 9052–9059. doi:10.1016/j.ceramint.2022.11.061
- Sato, K., Morozumi, H., Funayama, O., and Isoda, T. (1999). Mechanical properties and oxidation resistance of C–B–Si coated silicon nitride fiber reinforced Si–N–C composites with cross-ply structure. *Compos. Part A Appl. Sci. Manuf.* 30 (4), 577–581. doi:10.1016/s1359-835x(98)00152-3
- Shubhashish, S., Wijanayake, S., Huang, X., Posada, L. F., Rubio, S. J. B., Khanna, H. S., et al. (2022). Highly mesoporous MoO₃ catalysts for electrophilic aromatic substitution. *ACS Appl. Mat. Interfaces* 14 (45), 51041–51052. doi:10.1021/acsmi.2c16891
- Solsona, B., Blasco, T., López Nieto, J. M., Peña, M. L., Rey, F., and Vidal-Moya, A. (2001). Vanadium oxide supported on mesoporous MCM-41 as selective catalysts in the oxidative dehydrogenation of alkanes. *J. Catal.* 203 (2), 443–452. doi:10.1006/jcat.2001.3326
- Stampf, C. (2005). Surface processes and phase transitions from *ab initio* atomistic thermodynamics and statistical mechanics. *Catal. Today* 105 (1), 17–35. doi:10.1016/j.cattod.2005.04.015
- Suib, S. L. (2008). Porous manganese oxide octahedral molecular sieves and octahedral layered materials. *Acc. Chem. Res.* 41 (4), 479–487. doi:10.1021/ar7001667
- Suib, S. L. (2017). A review of recent developments of mesoporous materials. *Chem. Rec.* 17 (12), 1169–1183. doi:10.1002/tcr.201700025
- Suib, S. L., Přech, J., Čejka, J., Kuwahara, Y., Mori, K., and Yamashita, H. (2020). Some novel porous materials for selective catalytic oxidations. *Mat. Today* 32, 244–259. doi:10.1016/j.mattod.2019.06.008
- Tabassum, L., Tasnim, H., Shubhashish, S., Perera, I., Bhosale, T., Li, M., et al. (2022). Selenium-doped copper oxide nanoarrays: robust electrocatalyst for the oxygen evolution reaction with ultralow overpotential. *Appl. Mat. Today* 27, 101485. doi:10.1016/j.apmt.2022.101485
- Takanabe, K. (2017). Photocatalytic water splitting: quantitative approaches toward photocatalyst by design. *ACS Catal.* 7 (11), 8006–8022. doi:10.1021/acscatal.7b02662
- Tang, J., Xu, X., Tang, T., Zhong, Y., and Shao, Z. (2022). Perovskite-based electrocatalysts for cost-effective ultrahigh-current-density water splitting in anion exchange membrane electrolyzer cell. *Small Methods* 6 (11), 2201099. doi:10.1002/smt.202201099
- Tang, Y., Asokan, C., Xu, M., Graham, G. W., Pan, X., Christopher, P., et al. (2019). Rh single atoms on TiO₂ dynamically respond to reaction conditions by adapting their site. *Nat. Commun.* 10 (1), 4488. doi:10.1038/s41467-019-12461-6
- Tejero-Martin, D., Bennett, C., and Hussain, T. (2021). A review on environmental barrier coatings: history, current state of the art and future developments. *J. Eur. Ceram. Soc.* 41 (3), 1747–1768. doi:10.1016/j.jeurceramsoc.2020.10.057
- Thakare, J. G., Pandey, C., Mahapatra, M. M., and Mulik, R. S. (2021). Thermal barrier coatings—a state of the art review. *Mater. Mat. Int.* 27 (7), 1947–1968. doi:10.1007/s12540-020-00705-w
- Thalgasipitiya, W. R. K., Kapuge, T. K., Rathnayake, D., He, J., Willis, W. S., and Suib, S. L. (2020). A novel generalized metal dissolution approach for the synthesis of mixed valent mesoporous metal oxides. *Mat. Today* 35, 50–68. doi:10.1016/j.mattod.2019.10.024
- Tsuzuki, T. (2021). Mechanochemical synthesis of metal oxide nanoparticles. *Commun. Chem.* 4 (1), 143. doi:10.1038/s42004-021-00582-3
- Uboldi, C., Urbán, P., Gilliland, D., Bajak, E., Valsami-Jones, E., Ponti, J., et al. (2016). Role of the crystalline form of titanium dioxide nanoparticles: rutile, and not anatase, induces toxic effects in Balb/3T3 mouse fibroblasts. *Toxicol. Vitro* 31, 137–145. doi:10.1016/j.tiv.2015.11.005
- Vaßen, R., Jarligo, M. O., Steinke, T., Mack, D. E., and Stöver, D. (2010). Overview on advanced thermal barrier coatings. *Surf. Coatings Technol.* 205 (4), 938–942. doi:10.1016/j.surfcoat.2010.08.151
- Wang, A., Li, J., and Zhang, T. (2018). *Nature reviews chemistry*. Berlin, Germany: Nature Publishing Group, 65–81.
- Wang, C., Han, Z., Zou, X., Liu, H., Wang, H., Shu, D., et al. (2022a). Ultrathin MnO₂-coated FeOOH catalyst for indoor formaldehyde oxidation at ambient temperature: new insight into surface reactive oxygen species and in-field testing in an air cleaner. *Environ. Sci. Technol.* 56 (15), 10963–10976. doi:10.1021/acs.est.2c02663
- Wang, L., Guan, E., Wang, Y., Wang, L., Gong, Z., Cui, Y., et al. (2020). Author Correction: silica accelerates the selective hydrogenation of CO₂ to methanol on cobalt catalysts. *Nat. Commun.* 11 (1), 1722. doi:10.1038/s41467-020-15385-8
- Wang, S., Liu, G., and Wang, L. (2019). Crystal facet engineering of photoelectrodes for photoelectrochemical water splitting. *Chem. Rev.* 119 (8), 5192–5247. doi:10.1021/acs.chemrev.8b00584
- Wang, X., Li, J., Xue, Q., Han, X., Xing, C., Liang, Z., et al. (2023a). Sulfate-decorated amorphous-crystalline cobalt-iron oxide nanosheets to enhance O–O coupling in the oxygen evolution reaction. *ACS Nano* 17 (1), 825–836. doi:10.1021/acsnano.2c12029
- Wang, X., Pei, C., Zhao, Z.-J., Chen, S., Li, X., Sun, J., et al. (2023b). Coupling acid catalysis and selective oxidation over MoO₃-Fe₂O₃ for chemical looping oxidative dehydrogenation of propane. *Nat. Commun.* 14 (1), 2039. doi:10.1038/s41467-023-37818-w
- Wang, Y., Arandiyán, H., Scott, J., Bagheri, A., Dai, H., and Amal, R. (2017). Recent advances in ordered meso/macroporous metal oxides for heterogeneous catalysis: a review. *J. Mat. Chem. A* 5 (19), 8825–8846. doi:10.1039/c6ta10896b
- Wang, Y., Zhang, J., Chen, X., Wan, F., Jian, Y., and Liu, R. (2022b). The excellent protection effects of silicon/yttrium silicate bilayer environmental barrier coatings on SiC/SiC composites. *Int. J. Appl. Ceram. Technol.* 19 (6), 2950–2956. doi:10.1111/ijac.14129
- Wei, Z., Wang, W., Li, W., Bai, X., Zhao, J., Tse, E. C. M., et al. (2021). Steering electron-hole migration pathways using oxygen vacancies in tungsten oxides to enhance their photocatalytic oxygen evolution performance. *Angew. Chem. Int. Ed.* 60 (15), 8236–8242. doi:10.1002/anie.202016170
- Weng, W.-X., Zheng, Z.-H., and Li, Q. (2020). Cracking evolution of atmospheric plasma-sprayed YSZ thermal barrier coatings subjected to isothermal heat treatment. *Surf. Coatings Technol.* 402, 125924. doi:10.1016/j.surfcoat.2020.125924

- Xiao, W., Yang, S., Zhang, P., Li, P., Wu, P., Li, M., et al. (2018). Facile synthesis of highly porous metal oxides by mechanochemical nanocasting. *Chem. Mat.* 30 (9), 2924–2929. doi:10.1021/acs.chemmater.7b05405
- Xiao, X., Yang, L., Sun, W., Chen, Y., Yu, H., Li, K., et al. (2022). Electrocatalytic water splitting: from harsh and mild conditions to natural seawater. *Small* 18 (11), 2105830. doi:10.1002/smll.202105830
- Xin, H., Vojvodic, A., Voss, J., Nørskov, J. K., and Abild-Pedersen, F. (2014). Effects of d-band shape on the surface reactivity of transition-metal alloys. *Phys. Rev. B - Condens. Matter Mat. Phys.* 89 (11), 15114. doi:10.1103/PhysRevB.89.115114
- Xu, K., Ma, C., Yan, H., Gu, H., Wang, W.-W., Li, S.-Q., et al. (2022). Catalytically efficient Ni-NiOx-Y2O3 interface for medium temperature water-gas shift reaction. *Nat. Commun.* 13 (1), 2443. doi:10.1038/s41467-022-30138-5
- Xu, X., Pan, Y., Zhong, Y., Ran, R., and Shao, Z. (2020). Ruddlesden-Popper perovskites in electrocatalysis. *Mat. Horizons* 7 (10), 2519–2565. doi:10.1039/d0mh00477d
- Yang, X.-Y., Chen, L.-H., Li, Y., Rooke, J. C., Sanchez, C., and Su, B.-L. (2017). Hierarchically porous materials: synthesis strategies and structure design. *Chem. Soc. Rev.* 46 (2), 481–558. doi:10.1039/c6cs00829a
- Yao, R., Herrera, J. E., Chen, L., and Chin, Y. H. C. (2020). Generalized mechanistic framework for ethane dehydrogenation and oxidative dehydrogenation on molybdenum oxide catalysts. *ACS Catal.* 10 (12), 6952–6968. doi:10.1021/acscatal.0c01073
- Zhang, G., Xiong, T., Yan, M., He, L., Liao, X., He, C., et al. (2018). α -MoO₃- by plasma etching with improved capacity and stabilized structure for lithium storage. *Nano Energy* 49, 555–563. doi:10.1016/j.nanoen.2018.04.075
- Zhao, D., Tian, X., Doronkin, D. E., Han, S., Kondratenko, V. A., Grunwaldt, J.-D., et al. (2021). *In situ* formation of ZnOx species for efficient propane dehydrogenation. *Nature* 599 (7884), 234–238. doi:10.1038/s41586-021-03923-3
- Zhao, G., Yang, F., Chen, Z., Liu, Q., Ji, Y., Zhang, Y., et al. (2017). Metal/oxide interfacial effects on the selective oxidation of primary alcohols. *Nat. Commun.* 8 (1), 14039. doi:10.1038/ncomms14039
- Zhao, W., Fee, J., Khanna, H., March, S., Nisly, N., Rubio, S. J. B., et al. (2022a). A two-electron transfer mechanism of the Zn-doped δ -MnO₂ cathode toward aqueous Zn-ion batteries with ultrahigh capacity. *J. Mat. Chem. A* 10 (12), 6762–6771. doi:10.1039/d1ta10864f
- Zhao, W., Rubio, S. J. B., Dang, Y., and Suib, S. L. (2022b). Green electrochemical energy storage devices based on sustainable manganese dioxides. *ACS ES&T Eng.* 2 (1), 20–42. doi:10.1021/acsestengg.1c00317
- Zhou, K., and Li, Y. (2012). Catalysis based on nanocrystals with well-defined facets. *Angew. Chem. Int. Ed.* 51 (3), 602–613. doi:10.1002/anie.201102619
- Zhou, Y., and Fan, H. J. (2021). Progress and challenge of amorphous catalysts for electrochemical water splitting. *ACS Mat. Lett.* 3 (1), 136–147. doi:10.1021/acsmaterialslett.0c00502
- Zuo, Z., Liu, S., Wang, Z., Liu, C., Huang, W., Huang, J., et al. (2018). Dry reforming of methane on single-site Ni/MgO catalysts: importance of site confinement. *ACS Catal.* 8 (10), 9821–9835. doi:10.1021/acscatal.8b02277



OPEN ACCESS

EDITED BY

Steve Suib,
University of Connecticut, United States

REVIEWED BY

Federico Palazzetti,
University of Perugia, Italy
Ryan C. Fortenberry,
University of Mississippi, United States
Giuseppe Cassone,
National Research Council (CNR), Italy

*CORRESPONDENCE

Mohamad Akbar Ali,
✉ akbar.mohamad@ku.ac.ae

RECEIVED 26 March 2024

ACCEPTED 08 May 2024

PUBLISHED 30 May 2024

CITATION

Nulakani NVR and Ali MA (2024), Unveiling the chemical kinetics of aminomethanol ($\text{NH}_2\text{CH}_2\text{OH}$): insights into $\dot{\text{O}}\text{H}$ and O_2 photo-oxidation reactions and formamide dominance. *Front. Chem.* 12:1407355. doi: 10.3389/fchem.2024.1407355

COPYRIGHT

© 2024 Nulakani and Ali. This is an open-access article distributed under the terms of the [Creative Commons Attribution License \(CC BY\)](#). The use, distribution or reproduction in other forums is permitted, provided the original author(s) and the copyright owner(s) are credited and that the original publication in this journal is cited, in accordance with accepted academic practice. No use, distribution or reproduction is permitted which does not comply with these terms.

Unveiling the chemical kinetics of aminomethanol ($\text{NH}_2\text{CH}_2\text{OH}$): insights into $\dot{\text{O}}\text{H}$ and O_2 photo-oxidation reactions and formamide dominance

Naga Venkateswara Rao Nulakani¹ and Mohamad Akbar Ali^{1,2*}

¹Department of Chemistry, Khalifa University of Science and Technology, Abu Dhabi, United Arab Emirates, ²Center for the Catalyst and Separations, Khalifa University of Science and Technology, Abu Dhabi, United Arab Emirates

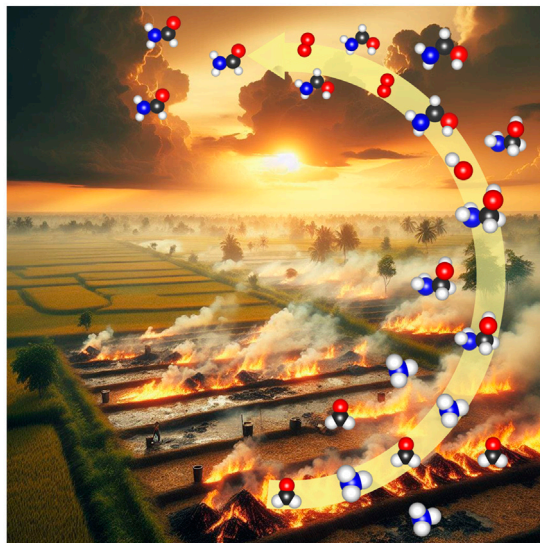
Aminomethanol is released into the atmosphere through various sources, including biomass burning. In this study, we have expounded the chemical kinetics of aminomethanol in the reaction pathways initiated by the hydroxyl radical ($\dot{\text{O}}\text{H}$) with the aid of *ab initio*//density functional theory (DFT) *i.e.*, coupled-cluster theory (CCSD(T))//hybrid-DFT (M06-2X/6-311++G (3df, 3pd)). We have explored various possible directions of the $\dot{\text{O}}\text{H}$ radical on aminomethanol, as well as the formation of distinct pre-reactive complexes. Our computational findings reveal that the H transfer necessitates activation energies ranging from 4.1 to 6.5 kcal/mol from the $-\text{CH}_2$ group, 3.5–6.5 kcal/mol from the $-\text{NH}_2$ group and 7–9.3 kcal/mol from the $-\text{OH}$ group of three rotational conformers. The H transfer from $-\text{CH}_2$, $-\text{NH}_2$ and $-\text{OH}$ exhibits an estimated total rate constant (k_{OH}) of approximately $1.97 \times 10^{-11} \text{ cm}^3 \text{ molecule}^{-1} \text{ s}^{-1}$ at 300 K. The branching fraction analysis indicates a pronounced dominance of C-centered $\text{NH}_2\dot{\text{C}}\text{HOH}$ radicals with a favorability of 77%, surpassing the N-centered $\dot{\text{N}}\text{HCH}_2\text{OH}$ (20%) and O-centered $\text{NH}_2\text{CH}_2\dot{\text{O}}$ (3%) radicals. Moreover, our investigation delves into the oxidation of the prominently favored carbon-centered $\text{NH}_2\dot{\text{C}}\text{HOH}$ radical through its interaction with atmospheric oxygen molecules. Intriguingly, our findings reveal that formamide (NH_2CHO) emerges as the predominant product in the $\text{NH}_2\dot{\text{C}}\text{HOH} + {}^3\text{O}_2$ reaction, eclipsing alternative outcomes such as amino formic acid (NH_2COOH) and formimidic acid ($\text{HN} = \text{C}(\text{H})-\text{OH}$). At atmospheric conditions pertinent to the troposphere, the branching fraction value for the formation of formamide is about 99%, coupled with a rate constant of $5.5 \times 10^{-12} \text{ cm}^3 \text{ molecule}^{-1} \text{ s}^{-1}$. Finally, we have scrutinized the detrimental impact of formamide on the atmosphere. Interaction of formamide with atmospheric hydroxyl radicals could give rise to the production of potentially perilous compounds such as HNCO . Further, unreacted $\dot{\text{N}}\text{HCH}_2\text{OH}$ radicals may initiate the formation of carcinogenic nitrosamines when reacting with trace N-oxides (namely, NO and NO_2). This, in turn, escalates the environmental risk factors.

KEYWORDS

aminomethanol, photooxidation, DFT, transition state theory, formamide, rate constant

Table of Contents

Formation of Aminomethanol from Biomass Burning



GRAPHICAL ABSTRACT

1 Introduction

Amines, especially those bearing the -NH_2 functional group (RNH_2), find extensive applications in the chemical industry, including uses in solvents, catalysis, surfactants, pharmaceuticals, adhesives, dyes and pigments, etc. (Ge et al., 2011a). For instance, carbon capture and storage (CCS) technology utilizes amine solvents to separate the CO_2 emission from the acid gas treatment of natural gas and fossil fuel power plants (Dai et al., 2012; Yamada, 2021). The rapid development of CCS technology consequently leads to a significant increase in alkanolamines emissions into the atmosphere due to their high vapor pressure (Kapteina et al., 2005). Additionally, the amines are also released into the atmosphere by various other sources such as thorough industrial emission, wastewater treatment, animal husbandry and automotive activities, emissions from ocean organisms, biomass combustion and the degradation of proteins, etc. (Ge et al., 2011b). These amines undergo degradation and participate in conversion reactions both in gas and aqueous phase (clouds, raindrops, fog) in the atmosphere. As a result, they have detrimental effects on air quality, leading to issues like acid rain, urban smog and tropospheric ozone. Also, the amines and alkanolamines have the potential to contribute to greenhouse gas formation, notably nitrous oxide (N_2O) and the production of highly carcinogenic compounds and nitrosamines (Schade and Crutzen, 1995; Ge et al., 2011a; Ge et al., 2011b). Hence, elucidating the transformation, mechanisms and kinetics of amines is of potential importance.

The Strecker synthesis, involving a series of chemical reactions, has received great scholarly attention as a potential technique to synthesize chiral α -amino acids using ammonia (NH_3), hydrogen cyanide (HCN) and aldehyde (RCHO) (Strecker, 1850; Gröger, 2003; Nájera and Sansano, 2007; Wang et al., 2011). However, aminomethanol ($\text{NH}_2\text{CH}_2\text{OH}$), a pivotal intermediate for the

synthesis of the simplest amino acid namely, glycine, has not been observed in the laboratories (Nielsen et al., 1979; Schutte et al., 1993). This is may be due to the decomposition of aminomethanol to methanimine (CH_2NH) and water (H_2O). Previous theoretical investigations have indicated that aminomethanol is kinetically stable in the gas phase with a substantial barrier of 230 kJ/mol toward dehydration to methanimine (Feldmann et al., 2005). Our recent study also supports that the formation of methanimine and water from aminomethanol is negligibly small and forbidden by an energy barrier of 234 kJ/mol (Ali, 2019). Bossa et al., have observed aminomethanol at low temperatures through the thermal reaction between ammonia and formaldehyde (Bossa et al., 2009). They have also pointed out that aminomethanol may exist in hot corinos in gas phase. The recent experimental study on aminomethanol in astrophysical-like conditions also validates that aminomethanol could be generated from amines on ice grains in proto-stellar cores or protoplanetary disks (Singh et al., 2022). These studies strongly corroborate the existence of aminomethanol in the atmosphere.

In our recent study (Ali, 2019), the calculated rate constant of $\text{CH}_2\text{O} + \text{NH}_3$ has suggested that aminomethanol could potentially form at higher temperatures rather than under atmospheric conditions, as illustrated in Figure 1. Additionally, the significant lifetime (~ 4 days) of aminomethanol could facilitate the initiation of various chemical reactions with other atmospheric species (Ali, 2019). Nevertheless, the atmospheric chemistry of aminomethanol remains largely unexplored to date, primarily due to the considerable challenges associated with experimental synthesis. Therefore, it is crucial to delve into the reaction mechanisms and kinetics of aminomethanol to evaluate the potential formation of various compounds, including toxicants or carcinogenic byproducts. However, there has been a lack of experimental studies specifically examining the reaction kinetics of the photo-oxidation of aminomethanol. In light of this gap, theoretical approaches,

coupled with state-of-the-art computational methodologies and advanced statistical rate theories, are essential for exploring the intricate atmospheric chemistry of aminomethanol, particularly in extreme environmental conditions.

The fate of aminomethanol, in general, is greatly influenced by its gas-phase oxidation by various oxidizing agents. Hydroxyl radicals ($\dot{\text{O}}\text{H}$) are widely present in the atmosphere and the reactions initiated by them are of significant importance among with by various other potential oxidizing agents. It is noteworthy to mention that the higher-order analogue of aminomethanol, namely, monoethanolamine (MEA) ($\text{NH}_2\text{CH}_2\text{CH}_2\text{OH}$), is commercially available and the corresponding gas-phase species are easily formed. Numerous experimental studies have been conducted to characterize MEA and to determine its rate constants (k_{OH}) with the $\dot{\text{O}}\text{H}$ radical, along with the resulting products. For example, Murphy and co-workers have evaluated the rate constant, k_{OH} of MEA by reacting with the $\dot{\text{O}}\text{H}$ radical at room temperature. They determined the rate constant to be $7.02 \pm 0.46 \times 10^{-11} \text{ cm}^3 \text{ molecule}^{-1} \text{ s}^{-1}$ (Borduas et al., 2013). Similarly, Onel et al., reported the k_{OH} of MEA reacting with $\dot{\text{O}}\text{H}$ as $7.61 \pm 0.76 \times 10^{-11}$, while Karl et al., obtained a value of $9.2 \pm 1.1 \times 10^{-11} \text{ cm}^3 \text{ molecule}^{-1} \text{ s}^{-1}$ (Karl et al., 2012; Onel et al., 2012). These studies demonstrate a rapid reaction between MEA and the $\dot{\text{O}}\text{H}$ radical, resulting in formamide and formaldehyde as major products, along with the potential formation of hazardous HNCO species. These experimental findings suggest that the initial reaction of MEA with the $\dot{\text{O}}\text{H}$, followed by MEA radicals reacting with O_2 , plays a crucial role in determining the atmospheric fate of MEA. In a parallel fashion, the abstraction of a hydrogen atom from $\text{NH}_2\text{CH}_2\text{OH}$ by the $\dot{\text{O}}\text{H}$ radical leads to the formation of three different aminomethanol radicals, including a carbon-centered $\text{NH}_2\dot{\text{C}}\text{HOH}$ radical, a nitrogen-centered $\dot{\text{N}}\text{HCH}_2\text{OH}$ radical and an oxygen-centered $\text{NH}_2\text{CH}_2\dot{\text{O}}$ radical as well as H_2O , as depicted in Figure 1. It is evident from previous studies on analogous electronic systems that carbon-centered radicals are more prevalent than nitrogen- and oxygen-centered radicals (Xie et al., 2014; Franco et al., 2021). These carbon-centered radicals are subsequently targeted by atmospheric oxygen, leading to the formation of

$\dot{\text{O}}\text{H}$ radical initiated products of aminomethanol namely, formamide (NH_2CHO), formimidic acid ($\text{HN}=\text{C}(\text{H})\text{-OH}$) and amino formic acid (NH_2COOH) in the atmosphere.

Among these product species, formamide is simplest and naturally occurring amide molecule. It is a potential precursor for the synthesis of a broad range of organic molecules (Saladino et al., 2012a; Saitta and Saija, 2014), which are vital for life as it poses all the important elements including carbon C), hydrogen H), oxygen O) and nitrogen N) except the heavy elements like sulphur S) and phosphorus P) (Saladino et al., 2005; 2007; 2012b). Additionally, formamide has an amide functional ($-\text{N}-\text{C}(=\text{O})-$) group, which is essential for the formation of the chains of amino acids in order to build up proteins. It promotes the synthesis of four nucleobases namely, adenine, guanine, cytosine and uracil of ribonucleic acid (RNA) (Saladino et al., 2005; Ferus et al., 2015). It also serves as the pre-cursor for carboxylic acids, amino acids and sugars (Botta et al., 2018). These points clearly demonstrating the potential role of formamide in biochemical processes, that are essential for life's sustenance and evolution.

Also, formamide is a highly ubiquitous molecule in the Universe. It was first detected in space dates back to 1971 when Rubin et al., utilized the 140-foot telescope at the National Radio Astronomy Observatory (NRAO) to scrutinize the Sagittarius B2 region (Sgr B2), situated proximate to the Galactic center (Rubin et al., 1971). Their observations distinctly revealed the three hyperfine components ($\Delta F = 0$) of the $2_{1,1}-2_{1,2}$ rotational transition of NH_2CHO , resonating at 4.62 GHz (6.5 cm). Sgr B2, renowned as the most prodigious star formation region within our Milky Way and marked the maiden identification of an interstellar compound harboring carbon C), hydrogen H), oxygen O), and nitrogen N). Subsequent detections of formamide have been made in diverse astronomical locales, including the vicinity of the young stellar entity W33A (Schutte et al., 1999), within cometary bodies such as C/1995 O1 (Bockelée-Morvan et al., 2000) and C/1996 B2 (Lis et al., 1997) and within the broader expanse of the interstellar medium (Solomon, 1973).

A plethora of experimental and theoretical inquiries have been undertaken to elucidate the formation of formamide along with other organic compounds in the interstellar medium (ISM) by different methods (Woon, 2002; Navarro-González and Raulin, 2004; Pastorek

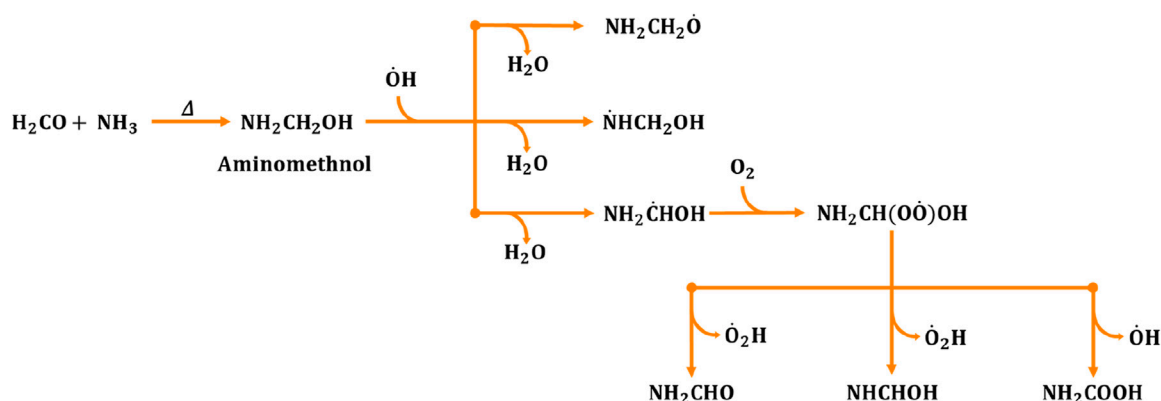


FIGURE 1
Generalized reaction mechanism for the formation of formamide (NH_2CHO), formimidic acid (NHCHOH) and amino formic acid (NH_2COOH) during the aminomethanol + $\dot{\text{O}}\text{H}$ radical reaction (Ali, 2019).

et al., 2019; Ferus et al., 2023). These investigations spanning from the proton irradiation (PI) of gas mixtures containing methane and nitrogen (Koike et al., 2003), ultraviolet irradiation (UV) of ice mixtures containing hydrogen cyanide (HCN), water (H₂O) and ammonia (NH₃) (Gerakines et al., 2004), pyrolysis of mixtures comprising carbon monoxide (CO), NH₃, and H₂O (Takano et al., 2004) and the photolysis of ices (Bernstein et al., 1997). Similarly, under terrestrial conditions, formamide (NH₂CHO) can be synthesized from combinations of low molecular weight compounds such as NH₃, formic acid (HCOOH), formic ester derivatives (HCOOR), CO and alcohols, under both catalyzed and uncatalyzed experimental setups (Deschamps, 1931).

In the current investigation, our focus lies in exploring the intricate mechanistic aspects and branching ratios corresponding to the pivotal stages of the $\dot{\text{O}}\text{H}$ -initiated oxidation reactions of aminomethanol. The primary objectives of this study are described as follows, 1) unveiling the intricate details about the reaction pathways, energetics and kinetics involved in the interaction of aminomethanol with $\dot{\text{O}}\text{H}$ radicals and identifying the potential aminomethanol-derived radicals, 2) exploring the reaction pathways, energetics and kinetics involved in the further reactions of aminomethanol-derived radicals with molecular oxygen (O₂). 3) analyzing the atmospheric implications arising from the exclusive product molecules resulting from the reactions of aminomethanol with OH and O₂ and 4) conducting a comparative analysis of the pre-reactive complexes, transition states, intermediates, other reactive species and rate constants derived from this study with those reported in previous investigations involving the atmospheric reactions of analogous electronic systems to validate our methodology.

2 Theoretical methodology

2.1 Electronic structure calculations

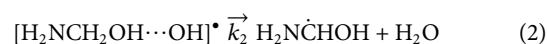
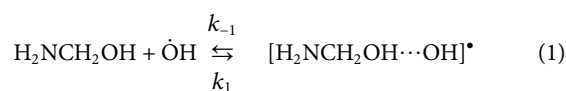
All gas-phase *ab initio*/density functional theory (DFT) calculations were performed using the Gaussian 16 suite of programs (Frisch et al., 2019). The stationary points of all molecular systems, including reactants, products, intermediates and transition states on the potential energy surface (PES) were optimized using the Minnesota 2006 exchange correlation functional such as M06-2X, in conjunction with the Pople's split-valence 6-311++G (3df, 3pd) basis set (Frisch et al., 1984; Zhao and Truhlar, 2008). The long-range van der Waals interactions between the reactive species were accounted using Grimme's empirical dispersion (GD3) corrections (Grimme et al., 2010). Previous studies have demonstrated that the current level of theory exhibits a reliable performance in addressing noncovalent interactions between gaseous molecules and in locating the transition states of atmospheric and combustion reactions (Ali et al., 2016; 2018; 2022; Ali, 2019; 2020; Dash and Ali, 2022; 2023; Ali and Balaganesh, 2023). Tight convergence criteria were applied during the wave function optimization of the reactive species, complexes, products and transition states. Unscaled vibrational frequencies at the same level of theory (M06-2X/6-311++G (3df, 3pd)) were utilized to compute zero-point energy (ZPE) corrections to the total energies of all molecular systems, to

characterize the stationary points on the PES and for rate-constant calculations. Vibrational frequency analysis confirmed all positive frequencies for the reactants, complexes, intermediates and products, while a single imaginary frequency was observed for the transition states.

Additionally, single-point energy calculations were conducted at a higher-level of theory on the molecular structures optimized at a lower-level of theory to ensure an accurate description of the energetic parameters. Specifically, the CCSD(T)/6-311++G (3df, 3pd) level of theory was utilized to estimate the single-point energies of the gas-phase molecular geometries, which were initially optimized at the M06-2X/6-311++G (3df, 3pd) level of theory (Raghavachari et al., 1989). The basis set superposition error (BSSE) calculations were also performed using the counterpoise (CP) corrected method (Boys and Bernardi, 1970; Simon et al., 1996). The $\langle \hat{S}^2 \rangle$ eigenvalues were monitored to evaluate the spin contamination for the wavefunction of the open-shell radicals. The T1-diagnostic values obtained at the CCSD(T)/6-311++G (3df, 3pd) level of theory were analyzed to validate the single-reference method and were found to be within the acceptable range (i.e., ≤ 0.02) for all important species (Lee and Taylor, 1989). Overall, the combination of CCSD(T)//M06-2X functionals has been employed in numerous research studies, providing a reasonably accurate description of the thermochemistry and chemical kinetics of many atmospheric reactions (Ali et al., 2016; Ali et al., 2018; Ali, 2019; Ali, 2020; Ali et al., 2022; Dash and Ali, 2022; Ali and Balaganesh, 2023; Dash and Ali, 2023).

2.2 Chemical kinetic analysis

Comprehensive chemical kinetic calculations for the $\dot{\text{O}}\text{H}$ initiated oxidation reaction of aminomethanol (AM) using MultiWell suite of codes (Barker, 2001; Barker, 2009; Barker et al., 2023) were performed. This oxidation reaction involves a fast pre-equilibrium between the reactive species such as H₂NCH₂OH + $\dot{\text{O}}\text{H}$ and the pre-reactive complex [H₂NCH₂OH...OH][•] stabilized by the van der Waals forces followed by a second step leading to the respective products as follows,



where, k_1 and k_{-1} are the forward and reverse rate constant for the first bimolecular reaction and the k_2 is the rate constant for the second unimolecular reaction. The kinetic rate constants for these bimolecular (k , in cm³ molecule⁻¹ s⁻¹) and unimolecular (k_{uni} , s⁻¹) reactions in the high-pressure limit defined by transition state theory are represented as follows,

$$k_2 = \Gamma(T) \times \frac{\sigma k_B T}{h} \times \frac{Q_{\text{TS}}}{Q_{\text{IM}}} \times \exp\left(-\frac{\Delta E_0}{RT}\right) \quad (3)$$

Assuming that the pre-reactive complex was in equilibrium with the reactants and was at a steady state, then the overall rate constants is expressed as;

$$k = \frac{k_1}{k_{-1} + k_2} k_2 \quad (4)$$

If $k_{-1} \gg k_2$, the rate constant is rewritten as

$$k = \frac{k_1}{k_{-1}} k_2 \quad (5)$$

$$k = K_e k_2 \quad (6)$$

This kinetic model is reasonably correct at the high-pressure limit, where the pre-reactive complex can be stabilized by collisions with other atmospheric species. This approach was widely used in literature for the water-assisted reaction and the predicted rate coefficients are in reasonably good agreement with the experimental values (Ali, 2019; Ali et al., 2022; Ali and Balaganesh 2023).

The different parameters of Eqs 3, 6 were breakdown and elaborately discussed the specifics of each component in [Supplementary Material](#) to prevent redundancy from earlier research. The k and k_2 for the other plausible oxidation reactions of $\dot{\text{O}}\text{H}$ initiated oxidation reaction of AM such as for $\text{H}_2\text{NCH}_2\text{OH} + \dot{\text{O}}\text{H} \rightarrow \text{HNCH}_2\text{OH} + \text{H}_2\text{O}$ and $\text{H}_2\text{NCH}_2\text{OH} + \dot{\text{O}}\text{H} \rightarrow \text{H}_2\text{NCH}_2\dot{\text{O}}\text{H} + \text{H}_2\text{O}$ were also computed.

The temperature- and pressure-dependent microscopic rate constants $k(E)$ have also been computed for the O_2 addition reaction to the aminomethanol radicals generated in Eq. 2. This was accomplished using the Rice–Ramsperger–Kassel–Marcus (RRKM)/master equation (ME) theory, implemented in the MultiWell suite of programs. The MultiWell code facilitates the computation of non-steady-state effects including unimolecular decomposition processes, isomerization, collision energy transfer and chemical activation for the complex rate-constant calculations. To perform these calculations, molecular and energetic parameters such as vibrational frequencies, moments of inertia and reaction barriers are required as input data. Using this data, the MultiWell suite computes sum and density-of-states, followed by the evaluation of microscopic rate-constant $k(E)$. The RRKM/ME microscopic rate-constant $k(E)$ is defined as follows,

$$k(E) = \left[\frac{m^\ddagger}{m} \frac{\sigma_{\text{ext}}}{\sigma_{\text{ext}}^\ddagger} \right] \frac{g_e^\ddagger}{g_e} \frac{1}{h} \frac{G^\ddagger(E - E_0)}{\rho(E)}. \quad (7)$$

The details of each term can be found in the [Supplementary Material](#). Temperature and pressure-dependent rate constants and branching ratios of the products were evaluated by incorporating N_2 gas as the bath gas. The collisional energy transfer process was addressed using the conventional temperature-dependent exponential-down model with a $\langle \Delta E \rangle_{\text{down}}$ parameter (which represents the average energy loss per the collision of the active compound with the bath gas molecule), with an approximate value of $\sim 200 \cdot (T/300)^{0.85} \text{ cm}^{-1}$ (Goldsmith et al., 2012). Lennard-Jones (L-J) parameters were employed to account for the frequency of collisions between the active compound and the bath gas (N_2) collider. The L-J parameters for N_2 gas, specifically $\sigma(\text{N}_2) = 3.74 \text{ \AA}$ and $\epsilon/k_B(\text{N}_2) = 82 \text{ K}$, were sourced from the literature, while the same parameters for all wells were adopted from our previous study (Dash and Ali, 2022).

For the barrierless reactions i.e., $\dot{\text{A}}\text{M} + \text{O}_2 \rightarrow \text{AM} - \text{O}\dot{\text{O}}$ and product complexes to individual product molecules Inverse Laplace Transform (ILT) method was incorporated to determine the rate-coefficients (Robertson et al., 1995). Consistent with studies on numerous analogous reactions, this method has proven effective, with the Arrhenius's activation energy equating to the critical energy of the reaction (E_0) (Firaha et al., 2018). Additionally, statistical rate theories that neglect non-statistical effects were applied, including slow intramolecular vibrational energy redistribution (IVR) as discussed in previous study (Mazarei and Barker, 2022).

The pressure-dependent total rate constants $k^{\text{bimol}}(T, M)$ for aminomethanol radical ($\dot{\text{A}}\text{M}$) + O_2 have been computed using,

$$k^{\text{bimol}}(T, M) = \Gamma K_{\text{eq}} \times k_{\text{co}}^{\text{uni}} (1 - f_{\dot{\text{A}}\text{M} + \text{O}_2}) \quad (8)$$

where, Γ represents the quantum mechanical tunneling corrections, $f_{\dot{\text{A}}\text{M} + \text{O}_2}$ is the branching fraction (f) of the chemical reaction returning to the respective reactive species and $k_{\text{co}}^{\text{uni}}$ is the rate constant at the high-pressure limit. The tunneling was incorporated for the chemical activation distribution in all our chemical kinetic calculations using the keywords “CHEMACT” and “TUN”.

Finally, the calculated rate constants were fitted at the high-pressure limit (k_{co}) in the temperature range of 200–400 K to the modified Arrhenius expression, which is as follows,

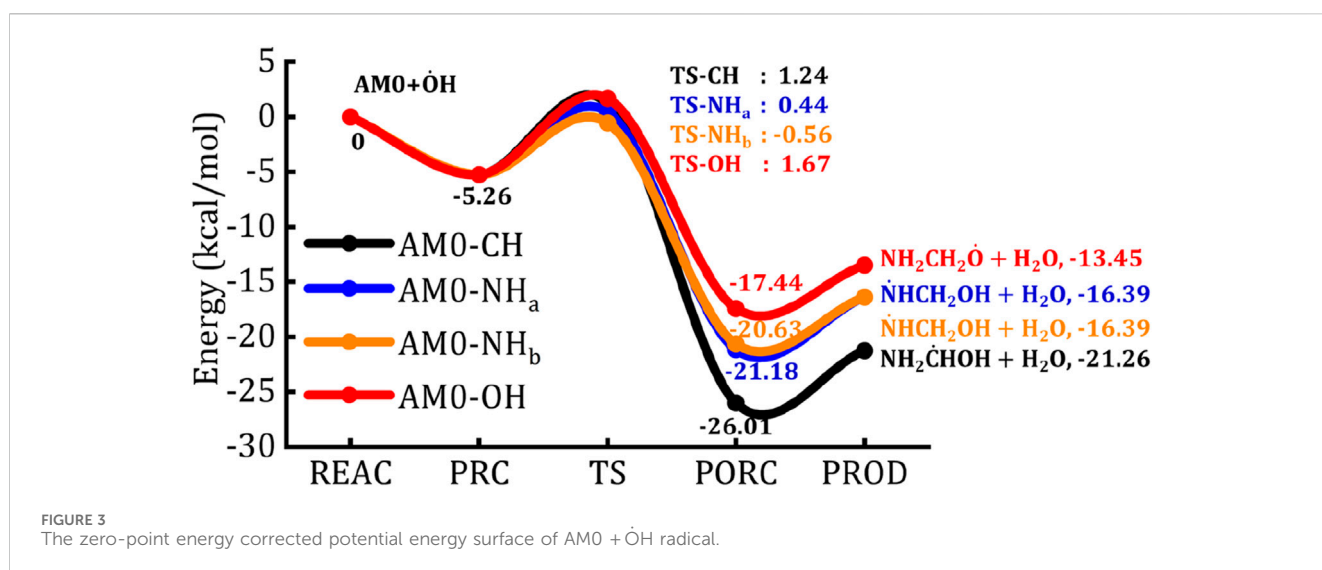
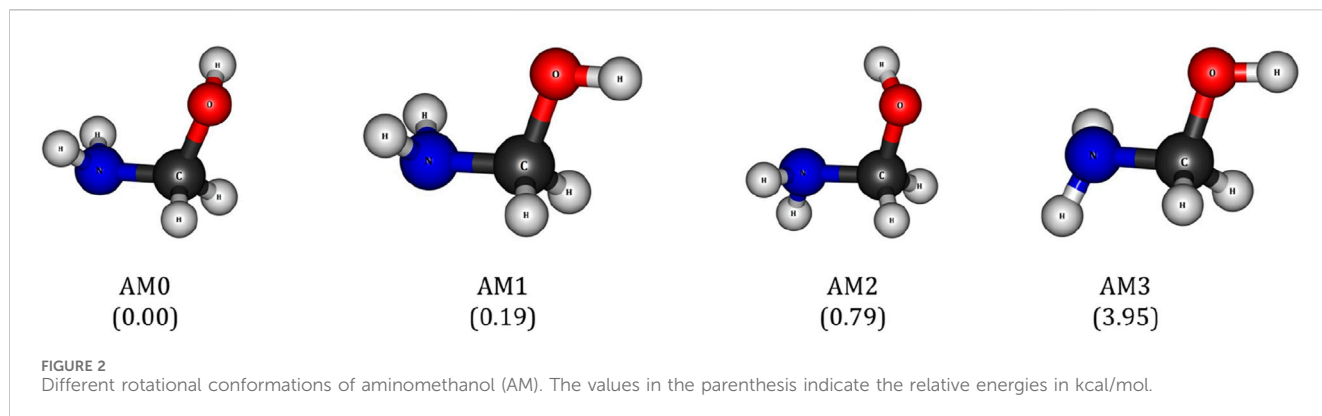
$$k_{\text{co}}(T) = A \times T^n \times \exp\left(\frac{-E_a}{RT}\right) \quad (9)$$

where A is the pre-exponential factor, T is the temperature, n is the temperature exponent and E_a is the activation energy. The coordinates of equilibrium geometries, vibrational harmonic frequencies and rotational constants of all important species involved in the $\dot{\text{O}}\text{H}$ initiated oxidation reaction of AM are listed in the [Supplementary Material](#).

3 Results and discussion

3.1 Rotational conformers of aminomethanol

The oxidation reaction between the aminomethanol (AM) and $\dot{\text{O}}\text{H}$ radical occur through the abstraction of H-atom from three different H-bearing functional groups (i.e., $-\text{CH}_2$, $-\text{NH}_2$ and $-\text{OH}$) of AM. Generally, the H atom of $-\text{CH}_2$, $-\text{NH}_2$ and $-\text{OH}$ groups along with the presence of lone pair of electrons on the N and O atoms facilitate the hydrogen bonding (H-bonding) between the AM and the $\dot{\text{O}}\text{H}$ radical. Interestingly, the $-\text{NH}_2$ and $-\text{OH}$ groups of AM can freely rotate around the single bonds to form the inter molecular H-bonding with the $\dot{\text{O}}\text{H}$ radical based on its attacking direction. It leads to different rotational conformations for the AM- $\dot{\text{O}}\text{H}$ radical complex. In addition, formation of such intermolecular H-bonding in the pre-reactive and the transition state (TS) structures has a great effect on the energetics of the reaction. Hence, we have comprehensively explored the different reaction pathways and the corresponding energy barriers using different rotational conformations of AM. It is evident from previous studies that the AM exhibits four different rotational conformations, which we



named as AM0, AM1, AM2 and AM3 as presented in Figure 2 (Hays et al., 2013). It shows that the AM0 is energetically more stable and can be considered as ground state conformation of AM. The geometrical features of ground state conformation of AM are in good agreement with that of previous study (Hays et al., 2013). Other rotational conformations such as AM1, AM2 and AM3 exhibit ~0.2, 0.8 and 4 kcal/mol higher energy compared to the AM0, respectively. The trend in the conformational stabilities of AM is in accordance with the study of Weaver and co-workers (Hays et al., 2013). Hence, the AM0 is used as a reference to provide the further intricate details about the mechanistic pathways of the AM oxidation reaction with the OH radical.

3.2 Potential energy surface of aminomethanol + OH

The zero-point energy (ZPE) corrected potential energy surface (PES) for the H-abstraction reaction of the most stable conformation of aminomethanol (AM0) by the OH radical is depicted in Figure 3. In this reaction, the OH radical abstracts the H-atom from three different H-bearing moieties (*i.e.*, -CH₂, -NH₂ and -OH) of AM0, leading to the formation of three distinct

AM0 radicals, namely, the carbon-centered NH₂CHOH radical, nitrogen-centered NHCH₂OH radical and oxygen-centered NH₂CH₂O radical. These radicals are obtained through an energetically favorable pre-reactive complex (PRC), followed by the transition states (TSs) for the transfer of the H-atom. The optimized geometries of AM0, OH radical, PRC, TSs, post-reactive complexes (PORCs) and the final radical species of OH initiated AM oxidation reaction are presented in Figure 4. In detail, the OH radical attacks the AM0 and forms a PRC, which is stabilized by the formation of H-bonding between the H atom of OH radical and the O atom of AM0 as shown in Figure 4. The PRC is stabilized with respect to the reactants by -5.26 kcal/mol. Subsequently, the H-bonding stabilized OH radical rearranges in the reactive space of AM0 in a way to form a bond angle between the H-atom of -CH₂, -NH₂ and -OH groups and the OH radical close to that of H₂O molecule, to viably eliminate as a H₂O molecule through a transition state.

For example, the bond angle between the H atom of the -CH₂ group and OH is found to be 94.6° (*i.e.*, ∠HC-H...OH = 94.6°) in the TS-CH (see Figure 4). The presence of two inequivalent H-atoms on -NH₂ group form two different TSs. The TSs associated with the back and front H-atoms are designated as TS-NH_a and TS-NH_b, respectively. The bond angles are found to be ∠H_bN-H_a...OH =

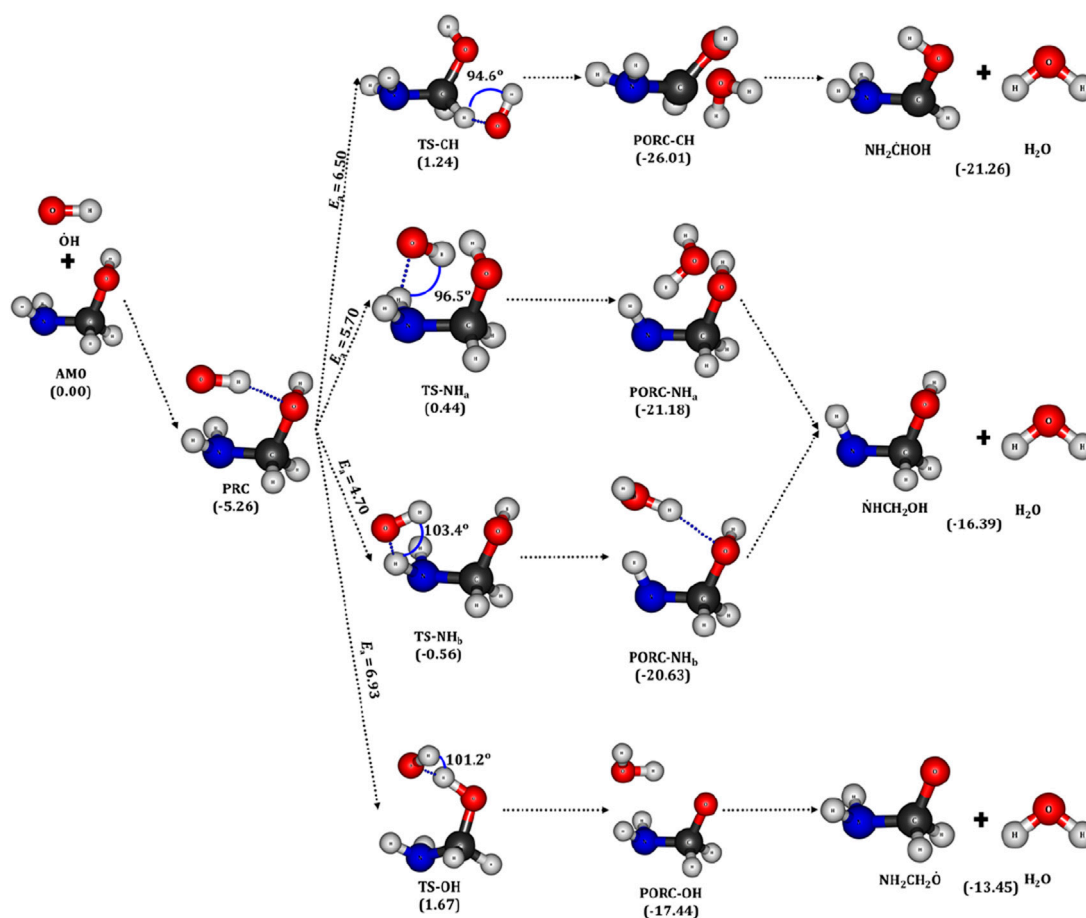


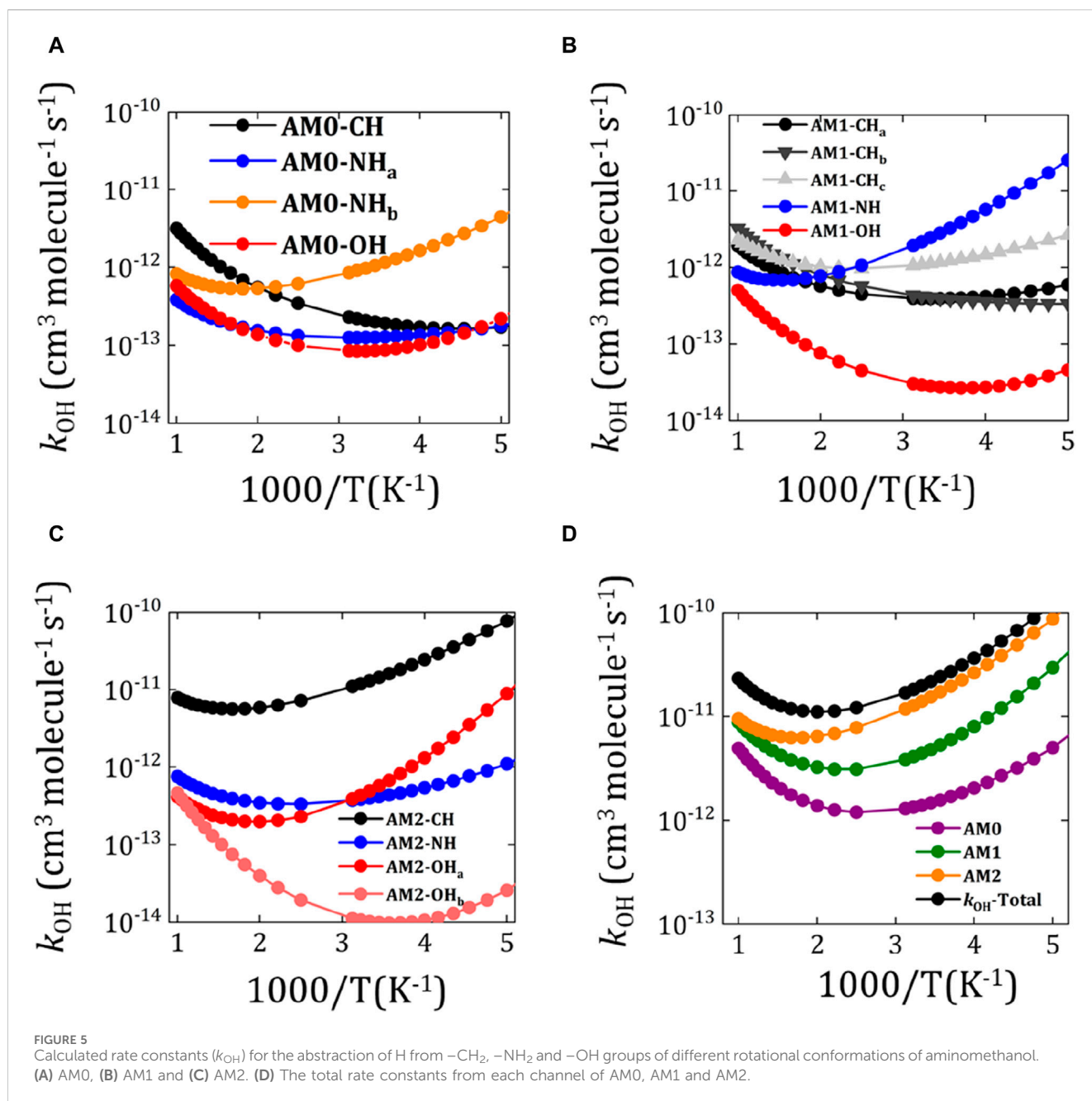
FIGURE 4
Optimized geometries of aminomethanol (AM0), PRC, TSs, PORCs and the radicals of $\dot{\text{O}}\text{H}$ initiated AM0 oxidation reaction. All the values in the parenthesis are in kcal/mol.

96.5°, $\angle \text{H}_a\text{N}-\text{H}_b\cdots\dot{\text{O}}\text{H} = 103.4^\circ$ and $\angle \text{O}-\text{H}\cdots\dot{\text{O}}\text{H} = 101.2^\circ$ in the TS- NH_a , TS- NH_b and TS-OH, respectively. Computed results reveal that the abstraction of H-atom from the $-\text{NH}_2$ group through the transition state, TS- NH_b (TS- NH_a) is more favorable with an energy barrier of 4.7 (5.7) kcal/mol followed by the abstraction from the $-\text{CH}_2$ (6.5 kcal/mol) and $-\text{OH}$ (6.93 kcal/mol) groups. The H transfer through the transition states namely, TS-CH, TS- NH_a , TS- NH_b and TS-OH forms the corresponding post-reactive complexes of water molecule and AM0 radicals, which are stabilized by -26 , -21 , -21 and -17 kcal/mol with respect to the reactants, respectively. Finally, these post-reactive complexes separate into the AM0 radical and water molecules in each reaction pathway.

To account for the effect of other rotational conformers on the oxidation reaction, the energies of PRCs, TSs and PORCs have been computed for the abstraction of H atom from $-\text{CH}_2$, $-\text{NH}_2$ and $-\text{OH}$ groups of other rotational conformations of AM (*i.e.*, AM1 and AM2). The complete reaction profile for the H-abstraction reaction of AM1 along with the energies is presented [Supplementary Figure S1](#). The H abstraction from the $-\text{CH}_2$ group of AM1 proceeds via three TSs such as TS- CH_a , TS- CH_b and TS- CH_c . Among these TSs, TS- CH_a is linked to the PRC1 while TS- CH_b and TS- CH_c are linked to the PRC2 (see [Supplementary Figure S2](#)). However, all these-CH

TSs are linked to the same product complex and lead to the formation of a single $\text{NH}_2\dot{\text{C}}\text{HOH}$ radical conformation. On the other hand, the abstraction of H from $-\text{NH}$ and $-\text{OH}$ groups of AM1 occurs *via* the TSs namely, TS-NH and TS-OH, which are linked to the pre-reactive complex, PRC1. These TSs of AM1 subsequently form the N- and O-centered radicals similar to that of AM0+ $\dot{\text{O}}\text{H}$ radical reaction. Similarly, we evaluated the energetics of all important species of AM2+ $\dot{\text{O}}\text{H}$ oxidation reaction and the reaction profile is shown in [Supplementary Figure S3](#). The optimized geometries of the reactive species, intermediates, TSs, post-reactive complexes and C-, N-, O-centered radicals of AM2+ $\dot{\text{O}}\text{H}$ reactions are presented in [Supplementary Figure S4](#).

Finally, the energetics and the barrier height values of H abstraction reactions from AM0, AM1 and AM2 by $\dot{\text{O}}\text{H}$ radical have been compared and presented in [Supplementary Table S1](#). It shows that the energies of PRCs of AM0, AM1 and AM2 are in the range of -4.6 to -5.8 kcal/mol. These values are in good agreement with the PRC energies of similar electronic systems. For example, Franco et al., have investigated the abstraction of H atom from the different conformers of methanediol (Franco et al., 2021). They showed that, the PRC between OHCH_2OH and $\dot{\text{O}}\text{H}$ is stabilized by -5.22 kcal/mol with respect to the reactants in the most stable conformation of methanediol. Ali et al., have studied the $\dot{\text{O}}\text{H} +$



CH_3OH reaction profile under tropospheric conditions (Ali et al., 2021). They showed that the H abstraction occurred through a hydrogen bond stabilized PRC, which exhibits a relative energy of -4.97 kcal/mol. Du and co-workers have explored the gas-phase reaction of ethanol with $\dot{O}H$ radical (Xu et al., 2019). Results of this study reveal that the PRC between $\dot{O}H$ radical and CH_3CH_2OH is stabilized by the H-bonding. It exhibits a relative energy of -5.2 kcal/mol. On the other hand, González et al. have explored the rate constants for the $\dot{O}H$ radical reaction with CH_3NH_2 using experimental and theoretical methods (González et al., 2022). They have found that the PRC between $\dot{O}H$ radical and CH_3NH_2 is stabilized through formation of H-bond between the $N(CH_3NH_2)$ and $H(OH)$. It exhibits a relative energy of -6.69 kcal/mol similar to that of PRC1 (-5.8 kcal/mol) formed with the conformer AM1.

Clearly, the energies of PRCs formed between $\dot{O}H$ radical and different rotational conformers of AM are in close agreement with those of previous studies. The computed barrier height values for the abstraction of H-atom from the different moieties of AM by $\dot{O}H$ radical are closely corroborating with that of abstraction of H from the respective moieties of similar electronic systems. For example, Franco et al., have reported the barrier height values in the range of 6.03 – 6.95 and 8.25 – 10.22 kcal/mol for the abstraction hydrogen from the $-CH_2$ and $-OH$ groups of methanediol, respectively (Franco et al., 2021). Similarly, Ali et al., and Xu et al., have reported the barrier height values around 5.8 (7.5) and 5.8 (6.8) kcal/mol for H abstraction from $-CH$ ($-OH$) groups of methanol and ethanol, respectively (Xu et al., 2019; Ali et al., 2021). Onel et al., and Tian et al., have reported the barrier height values for

TABLE 1 Calculated temperature dependent rate constants (k_{OH} , $\text{cm}^3 \text{ molecule}^{-1} \text{ s}^{-1}$) for the O H initiated oxidation reaction of aminomethanol using the rotational conformations, AM0, AM1 and AM2. $k_{\text{OH}}\text{-Total}$ is the total rate constant using all the conformations.

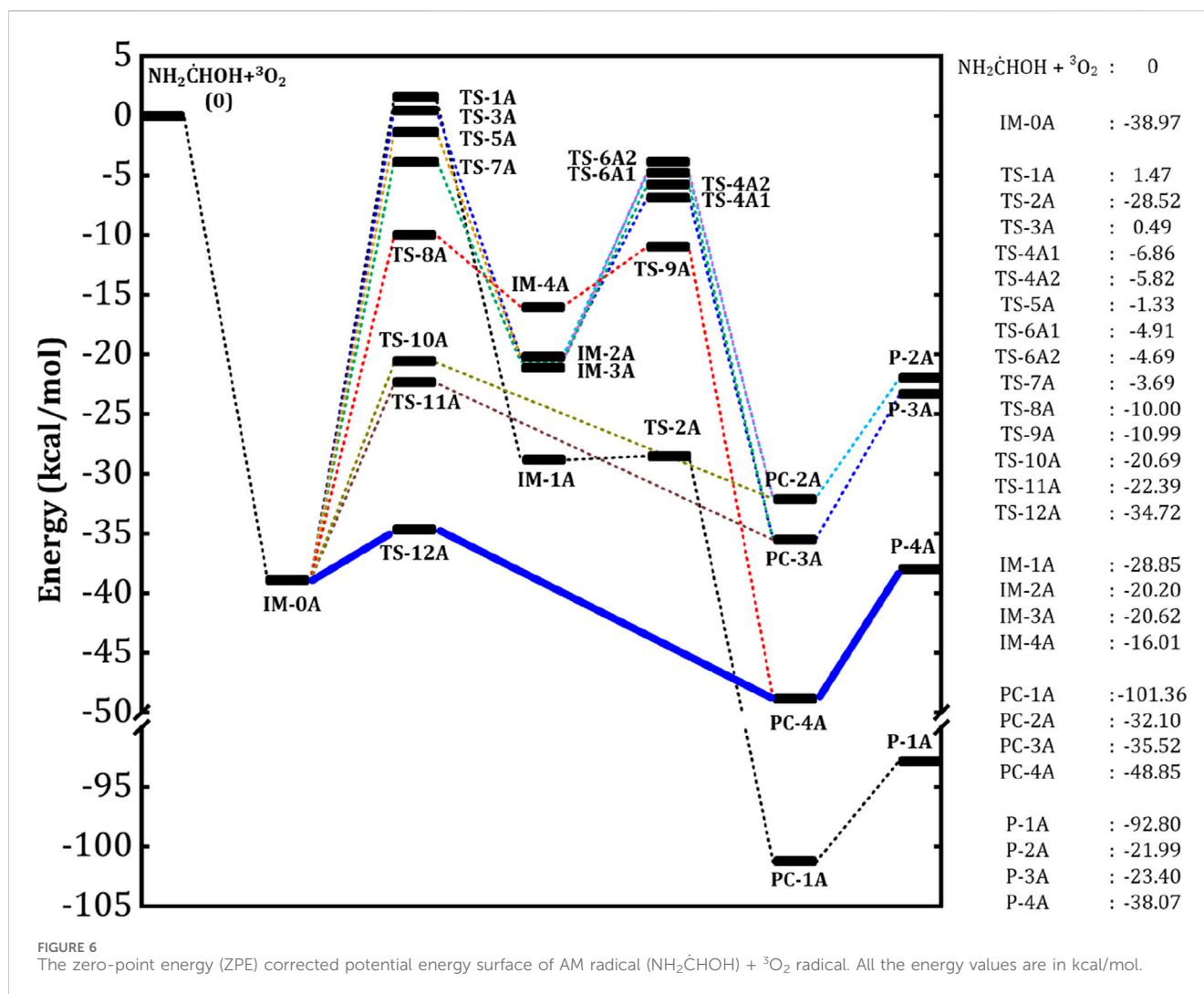
Temp	$k_{\text{OH}}\text{-AM0}$	$k_{\text{OH}}\text{-AM1}$	$k_{\text{OH}}\text{-AM2}$	$k_{\text{OH}}\text{-total}$
200	5.00×10^{-12}	2.95×10^{-11}	8.70×10^{-11}	1.22×10^{-10}
210	3.92×10^{-12}	2.08×10^{-11}	6.37×10^{-11}	8.85×10^{-11}
220	3.19×10^{-12}	1.55×10^{-11}	4.87×10^{-11}	6.74×10^{-11}
230	2.68×10^{-12}	1.20×10^{-11}	3.86×10^{-11}	5.33×10^{-11}
240	2.32×10^{-12}	9.62×10^{-12}	3.15×10^{-11}	4.34×10^{-11}
250	2.04×10^{-12}	7.99×10^{-12}	2.63×10^{-11}	3.64×10^{-11}
260	1.84×10^{-12}	6.81×10^{-12}	2.25×10^{-11}	3.11×10^{-11}
270	1.69×10^{-12}	5.94×10^{-12}	1.95×10^{-11}	2.71×10^{-11}
280	1.56×10^{-12}	5.29×10^{-12}	1.72×10^{-11}	2.41×10^{-11}
290	1.47×10^{-12}	4.79×10^{-12}	1.54×10^{-11}	2.17×10^{-11}
300	1.40×10^{-12}	4.40×10^{-12}	1.39×10^{-11}	1.97×10^{-11}
310	1.34×10^{-12}	4.10×10^{-12}	1.27×10^{-11}	1.82×10^{-11}
320	1.29×10^{-12}	3.86×10^{-12}	1.18×10^{-11}	1.69×10^{-11}
400	1.19×10^{-12}	3.10×10^{-12}	7.78×10^{-12}	1.21×10^{-11}
450	1.26×10^{-12}	3.09×10^{-12}	6.86×10^{-12}	1.12×10^{-11}
500	1.38×10^{-12}	3.24×10^{-12}	6.43×10^{-12}	1.10×10^{-11}
550	1.55×10^{-12}	3.49×10^{-12}	6.26×10^{-12}	1.13×10^{-11}
600	1.76×10^{-12}	3.82×10^{-12}	6.27×10^{-12}	1.18×10^{-11}
650	2.01×10^{-12}	4.22×10^{-12}	6.40×10^{-12}	1.26×10^{-11}
700	2.30×10^{-12}	4.68×10^{-12}	6.63×10^{-12}	1.36×10^{-11}
750	2.63×10^{-12}	5.21×10^{-12}	6.94×10^{-12}	1.48×10^{-11}
800	3.00×10^{-12}	5.80×10^{-12}	7.32×10^{-12}	1.61×10^{-11}
850	3.41×10^{-12}	6.45×10^{-12}	7.77×10^{-12}	1.76×10^{-11}
900	3.87×10^{-12}	7.17×10^{-12}	8.27×10^{-12}	1.93×10^{-11}
950	4.38×10^{-12}	7.95×10^{-12}	8.83×10^{-12}	2.12×10^{-11}
1000	4.93×10^{-12}	8.80×10^{-12}	9.45×10^{-12}	2.32×10^{-11}

–NH abstraction of alkylamines around 4.4–9.5 kcal/mol (Tian et al., 2009; Onel et al., 2013). Our computed results show that the barrier height values for the abstraction of H from –CH₂, –NH₂ and –OH groups are in the range of 4.12–6.50, 3.76–5.50 and 6.5–9.25 kcal/mol, respectively. These results also corroborate that the barrier heights are good in agreement with the previous studies. This analysis not only provides more confidence but also substantiate our choice of *ab initio* and DFT methods.

It is worth to mention here that, the TS energies for the major H-abstraction pathways i.e., from the –CH₂ and –NH₂ channels of NH₂CH₂OH + $\dot{\text{O}}\text{H}$ radical reaction are found to be around 1–2 kcal/mol. Previous studies show that the $\dot{\text{O}}\text{H}$ radical initiated H-abstraction reactions from different reactants are favorable even with the slight positive TS energies. For example, Nguyen et al., have studied the H-abstraction from the CH₃OH using *ab*

initio/RRKM methods (Nguyen et al., 2019). They reported the TS energies for H-abstraction around 2.3 and 0.5 kcal/mol. Further, they satisfactorily reproduced the experimental rate constants using these TS energies. Baidya et al., have explored the H-abstraction reaction of CHF₂CH₂OH with $\dot{\text{O}}\text{H}$ radical to unveil the atmospheric implications of chlorofluorocarbons (Baidya et al., 2018). All the TSs reported in this study exhibit positive energies in the range of 0.8–3.1 kcal/mol. However, they reported that their calculated k_{OH} value is in good agreement with the experimental value. Rahbar et al., have investigated the kinetics and mechanism of the $\dot{\text{O}}\text{H}$ radical initiated atmospheric oxidation of catechol over the temperature range 200–400 K (Rahbar et al., 2021). However, catechol shows high positive TS values (1.27–8.8 kcal/mol) for the H-abstraction reaction. The authors pointed out that the computed rate constants are close to that of experimental value. In light of these analogous studies, we believe that the slight positive energies (~1–2 kcal/mol) for the TSs are acceptable within the troposphere, which is the focal point of interest in our present investigation.

The rate constant (k_{OH}) and the branching fraction values have been computed for the hydrogen abstraction reactions at 300 K using all possible conformations. The k_{OH} values for the abstraction of H from different channels (–CH₂, –NH₂ and –OH) of AM0 are plotted in Figure 5A and listed in Supplementary Table S2. The sum of the rate constant values from different channels of AM0 (i.e., $k_{\text{OH}}\text{-AM0}$) are presented in Table 1. This data indicates that the rate constants for H abstraction from different channels gradually decrease within the temperature range 200–400 K. The $k_{\text{OH}}\text{-AM0}$ value for $\dot{\text{O}}\text{H}$ radical reaction with AM0 rotational conformation is found to be $1.40 \times 10^{-12} \text{ cm}^3 \text{ molecule}^{-1} \text{ s}^{-1}$ at 300 K. Similarly, the k_{OH} for each H abstraction channel of AM1 and AM2 has been computed and plotted in Figures 5B, C and the numerical values are presented in Supplementary Tables S3, S4. The sum of the rate constant values from different channels of AM1 and AM2 (i.e., $k_{\text{OH}}\text{-AM1}$ and $k_{\text{OH}}\text{-AM2}$) has been found to be 4.40×10^{-12} and $1.39 \times 10^{-11} \text{ cm}^3 \text{ molecule}^{-1} \text{ s}^{-1}$, respectively at 300 K (see Table 1). This results in an overall rate constant for the hydrogen abstraction from the all AM conformations to be around $1.97 \times 10^{-11} \text{ cm}^3 \text{ molecule}^{-1} \text{ s}^{-1}$ (see Figure 5D; Table 1). The computed total k_{OH} value of AM is closely aligns with that of CH₃NH₂ ($1.97 \times 10^{-11} \text{ cm}^3 \text{ molecule}^{-1} \text{ s}^{-1}$) (Onel et al., 2013), CH₃NHCH₃ ($6.27 \times 10^{-11} \text{ cm}^3 \text{ molecule}^{-1} \text{ s}^{-1}$) (Onel et al., 2013), CH₃CH₂NH₂ ($2.50 \times 10^{-11} \text{ cm}^3 \text{ molecule}^{-1} \text{ s}^{-1}$) (Onel et al., 2013), NH₂CH₂CH₂OH ($7.27 \times 10^{-11} \text{ cm}^3 \text{ molecule}^{-1} \text{ s}^{-1}$) (Xie et al., 2014), CH₃CH₂OH ($9.06 \times 10^{-11} \text{ cm}^3 \text{ molecule}^{-1} \text{ s}^{-1}$) at 300 K. The k_{OH} values are also computed using basis set super position error (BSSE) corrections. It is evident from Supplementary Table S5 that the BSSE corrections does not altered the rate constants appreciably. Overall, a negative temperature dependence in the k_{OH} of AM has been observed over the temperature range 200–400 K as can be seen from Figure 5D, similar to that of amines and alcohol reactions. The energetic values coupled with the computed rate constant results clearly align with those of previous studies, which further corroborating the reliability of the computational methodology and the scheme adopted in this study. Additionally, the branching fraction values for the abstraction of H from –CH₂, –NH₂ and –OH groups to successively form product radicals NH₂ $\dot{\text{C}}\text{HOH}$, $\dot{\text{N}}\text{HCH}_2\text{OH}$ and NH₂CH₂ $\dot{\text{O}}$ are estimated to be around 77%, 20% and 3%, respectively. Xie et al., have shown that the branching ratio is



around 82%, 17% and 1% for the abstraction of H from -CH₂, -NH₂ and -OH groups of monoethanolamine (MEA) (Xie et al., 2014). The computed branching fraction values of AM are in good agreement with that of MEA (Xie et al., 2014). The branching fraction values clearly suggest a strong preference for the C-centered H-abstraction over N- and O- centered H-abstraction. Interestingly, the computed branching fraction values also strongly adhere to the Evans–Polanyi relationship bond enthalpy of O–H > N–H > CH relationship (Evans and Polanyi, 1938).

The bimolecular reactions between the aminomethanol (NH₂CH₂OH) + $\dot{\text{O}}\text{H}$ radical and the NH₂CHOH + O₂ would also be possible in their excited electronic states. It is evident from previous studies that, the computationally characterized potential energy surface (PES) and the corresponding rate constants of (for example, ethyl alcohol (H₃C-CH₂-OH) (Xu et al., 2019), monoethanolamine (NH₂CH₂CH₂OH) (Xie et al., 2014), methanediol (OH-CH₂-OH) (Franco et al., 2021)) similar electronic systems agrees well with that of experimental studies. However, these studies not included any excited state photochemical interactions to obtain the rate constants. Further, Al-Hashimi and co-workers reported that the interactions between the O-Anisidine and $\dot{\text{O}}\text{H}$ radical occurs in the ground state rather than in the excited

state (Abdel-Rahman et al., 2021). Priya et al., have explored the abstraction reaction mechanism of $\dot{\text{O}}\text{H}$ radical with 2-methoxyphenol (Priya and Lakshmipathi, 2017). They showed that the H-abstraction reaction can occur in ground state than the in the excited state. Similar to these studies, we believe that the interactions between the aminomethanol and the gaseous species could be corresponding to ground state rather than to excited state.

In recent decades, significant advances in atmospheric chemistry have spurred the development of new theoretical approaches for exploring intricate details of ground-state chemical reactions and their underlying mechanisms. Nevertheless, an equivalent synergy between theory and experimentation remains absent in the realm of atmospheric photochemistry involving electronically excited states. The modeling of molecular photochemistry necessitates a meticulous consideration of non-adiabatic effects, specifically, the coupling between electronic states and molecular motion. This presents formidable challenges, as it contradicts several conventional approximations in theoretical chemistry. Notably, non-adiabatic effects challenge the venerable Born-Oppenheimer approximation, while classical treatments of nuclear dynamics may prove inadequate and non-equilibrium phenomena can challenge established reaction rate theories.

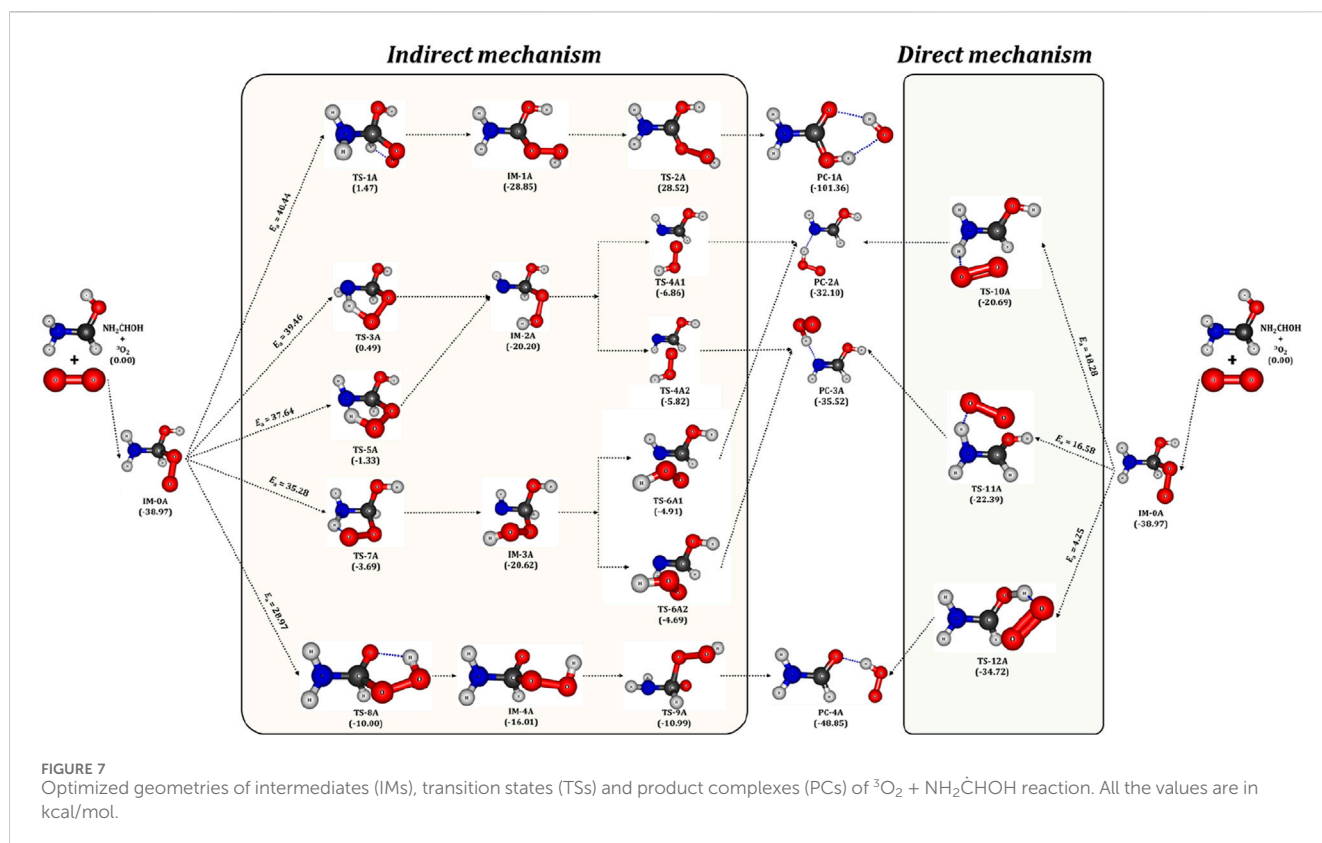


FIGURE 7
Optimized geometries of intermediates (IMs), transition states (TSs) and product complexes (PCs) of $^3\text{O}_2 + \text{NH}_2\dot{\text{C}}\text{HOH}$ reaction. All the values are in kcal/mol.

A plethora of methodologies have emerged to address these challenges, including MCTDH (Multi Configuration Time Dependent Hartree) (Manthe et al., 1992; Beck, 2000; Meyer, 2012), trajectory surface hopping (TSH) (Tully and Preston, 1971; Hammes-Schiffer and Tully, 1994; Fabiano et al., 2008) and *ab initio* multiple spawning (AIMS) (Ben-Nun et al., 2000; Ben-Nun and Martinez, 2002; Yang and Martinez, 2011). However, the application of these techniques to investigate atmospheric photochemistry encounters various challenges. These encompass complexities in simulating spectroscopically relevant choices and atmospheric modeling interests, the intricate electronic architecture of multichromophoric volatile organic compounds (VOCs), the diverse excited-state dynamics triggered by solar irradiation, the protracted dynamics of excited VOCs, the prominence of intersystem crossings or collisional processes and the modulating influence of aqueous environments such as those found in atmospheric aerosols and clouds. Given that non-adiabatic dynamic approaches demand considerable computational resources beyond our current capacity and each method carries its own limitations, we envision these studies as prospects for future exploration.

3.3 Potential energy surface of $\text{NH}_2\dot{\text{C}}\text{HOH}$ radical + $^3\text{O}_2$

The aminomethanol radicals produced in the initial reactions of aminomethanol + $\dot{\text{O}}\text{H}$ are highly reactive and undergoes subsequent reactions with atmospheric O_2 . The $\text{NH}_2\dot{\text{C}}\text{HOH}$ has been

considered for further reactions with atmospheric oxygen due to its large branching fraction. The zero-point energy (ZPE) corrected potential energy surface of $\text{NH}_2\dot{\text{C}}\text{HOH} + \text{O}_2$ reaction has been computed and shown in Figure 6, while the optimized geometries of intermediates, transition state structures and the product complexes (PCs) are depicted in Figure 7. The triplet oxygen molecule ($^3\text{O}_2$) reacts with $\text{NH}_2\dot{\text{C}}\text{HOH}$ radical and barrierlessly added to the C-site to form a peroxy radical (IM-0A) intermediate, as shown in Figure 6. However, the attacking direction of O_2 molecule on $\text{NH}_2\dot{\text{C}}\text{HOH}$ and the feasibility for the rotation of $-\text{NH}_2$ and $-\text{OH}$ groups around the CO and CN single bonds lead to the formation of different peroxy radical intermediate rotational conformers. Similar to aminomethanol, the IM-0A also exhibits other rotational conformations, for example, IM-0B and IM-0C as presented in Supplementary Figure S5. Previous studies have shown that the rotational conformations of the peroxy radical have a negligible effect on the formation of the end products (Xie et al., 2014). Hence, we have chosen the highly stable $\text{NH}_2\text{C}(\text{OO})\text{HOH}$ radical (IM-0A) for further studies and the reactions between other rotational conformations and O_2 have been excluded. The IM-0A strongly stabilized and located well below the reactants with a relative energy of -39 kcal/mol with respect to the reactants. The transfer of H occurred from $-\text{CH}$, $-\text{NH}_2$ and $-\text{OH}$ groups to the O-site within the peroxy radical intermediate (IM-0A). We consider the H transfer followed by the breaking of CO or OO bonds occurs through two consecutive steps as an indirect mechanism while the same occurs in a single step as a direct mechanism. Overall, five indirect (*via* TS-1A, TS-3A, TS-5A, TS-7A and TS-8A) and three direct reaction paths (*via* TS-10A, TS-11A and TS-12A) have been studied for the $\text{NH}_2\dot{\text{C}}\text{HOH} + \text{O}_2$ reaction as shown in Figure 7.

In detail, the transfer of H atom from $-CH$ and $-OH$ groups to the O-site of peroxy radical (IM-0A) is favored through the transition states TS-1A and TS-8A. On the other hand, the presence of two different H atoms in $-NH_2$ group and different attacking directions of 3O_2 lead to three different reaction pathways, which proceed through the TSs, TS-3A, TS-5A and TS-7A for the H abstraction from $-NH_2$ group. Among all these TSs, the TS-1A and TS-3A are situated above the reactants with an energy of 1.5 and 0.5 kcal/mol followed by TS-5A, TS-7A and TS-8A (-1.3 , -3.7 and -10.0 kcal/mol). It indicates that the H-transfer from $-CH$ group to O-site of IM-0A requires a high energy of ~ 40 kcal/mol to form the intermediate IM-1A. The transfer of two different H atoms from $-NH_2$ group respectively requires 40 (*via* TS-3A) and 35 (*via* TS-7A) kcal/mol to form the intermediates, IM-2A and IM-3A. Further, different spatial arrangement of O_2 also facilitates a distinct transition state, TS-5A for the H transfer from $-NH_2$ group and it leads to the previous intermediate, IM-2A. The reaction proceed through TS-5A shows a barrier height more than 35 kcal/mol. The H transfer process from that of $-OH$ group requires a relatively low energy of 29 kcal/mol *via* the TS-8A to form IM-4A. The barrier heights for these H-transfer reactions strongly comply with that of H transfer from the similar functional groups. The intermediates IM-1A to IM-4A are stabilized by ~ -29 , -20.2 , -20.6 and -16 kcal/mol with respect to the reactants, respectively. The breaking of O-O and C-O bond in IM-1A and IM-4A through the transition states TS-2A and TS-9A form the product complexes, PC-1A and PC-4A, respectively. While, PC-2A and PC-3A can be formed by the breaking of C-O bond of IM-2A *via* the TSs, TS-4A1 and TS-4A2. The IM-3A also leads to the same product complexes, PC-2A and PC-4A *via* the TSs, TS-6A1 and TS-6A2. Figure 6 shows that, the IM-1A is almost barrierlessly (0.3 kcal/mol) dissociated into the product complex PC-1A, which is composed of hydrogen bonded amino formic acid (H_2NCOOH) and $\dot{O}H$ radical (see Figure 7). The PC-1A is a highly stable product complex with an energy of ~ -101 kcal/mol, which eventually separates into amino formic acid (NH_2COOH) and $\dot{O}H$ radical. While, the IM-2A, IM-3A and IM-4A exhibit a barrier height of ~ 13 , 16 and 13 kcal/mol for the conversion into PC-2A, PC-3A and PC-4A, which are the hydrogen bond stabilized product complexes of formimidic acid ($HN = C(H)-OH$), formamide (H_2N-CHO) and \dot{O}_2H radical. The formimidic acid and formamide product complexes (PC-2A, PC-3A and PC-4A) located above than that of amino formic acid (PC-1A) with an energy of -32 , -36 and -49 kcal/mol, respectively (see Figure 6). Finally, these product complexes dissociate into the final products of the $^3O_2 + NH_2\dot{C}HOH$ reaction, P-2A ($HN = C(H)-OH + \dot{O}_2H$), P-3A ($HN = C(H)-OH + \dot{O}_2H$) and P-4A ($H_2N-CHO + \dot{O}_2H$) with the energies of -22 , 23.5 and -38 kcal/mol, respectively.

On the other hand, the reactions proceed *via* the transition states, TS-10A, TS-11A and TS-12A directly form the product complexes. In detail, these TSs initiates the simultaneous transfer of H atom from $-NH_2$ and $-OH$ groups to the O-site of peroxy radical and the breaking of C-O bond to form the post-reactive product complexes, PC-2A, PC-3A and PC-4A, respectively. Similar to TS-3A and TS-7A, the TS-10A and TS-11A involve the transfer of inequivalent H atoms of $-NH_2$ to the O-site. The energy barriers have been found to be 18, 17 and 4.3 kcal/mol for the transfer of H atom from $-NH_2$ (*via* TS-10A, TS-11A) and $-OH$ (*via* TS-12A) groups to the O-site of peroxy radical. Overall, it is evident from

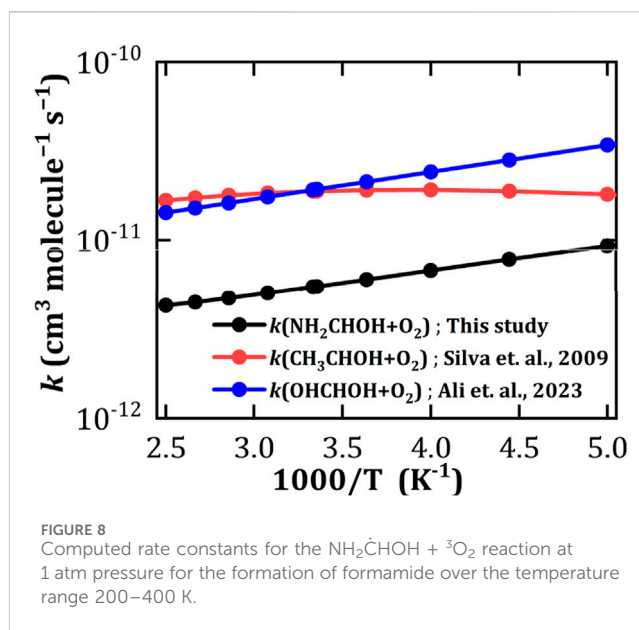
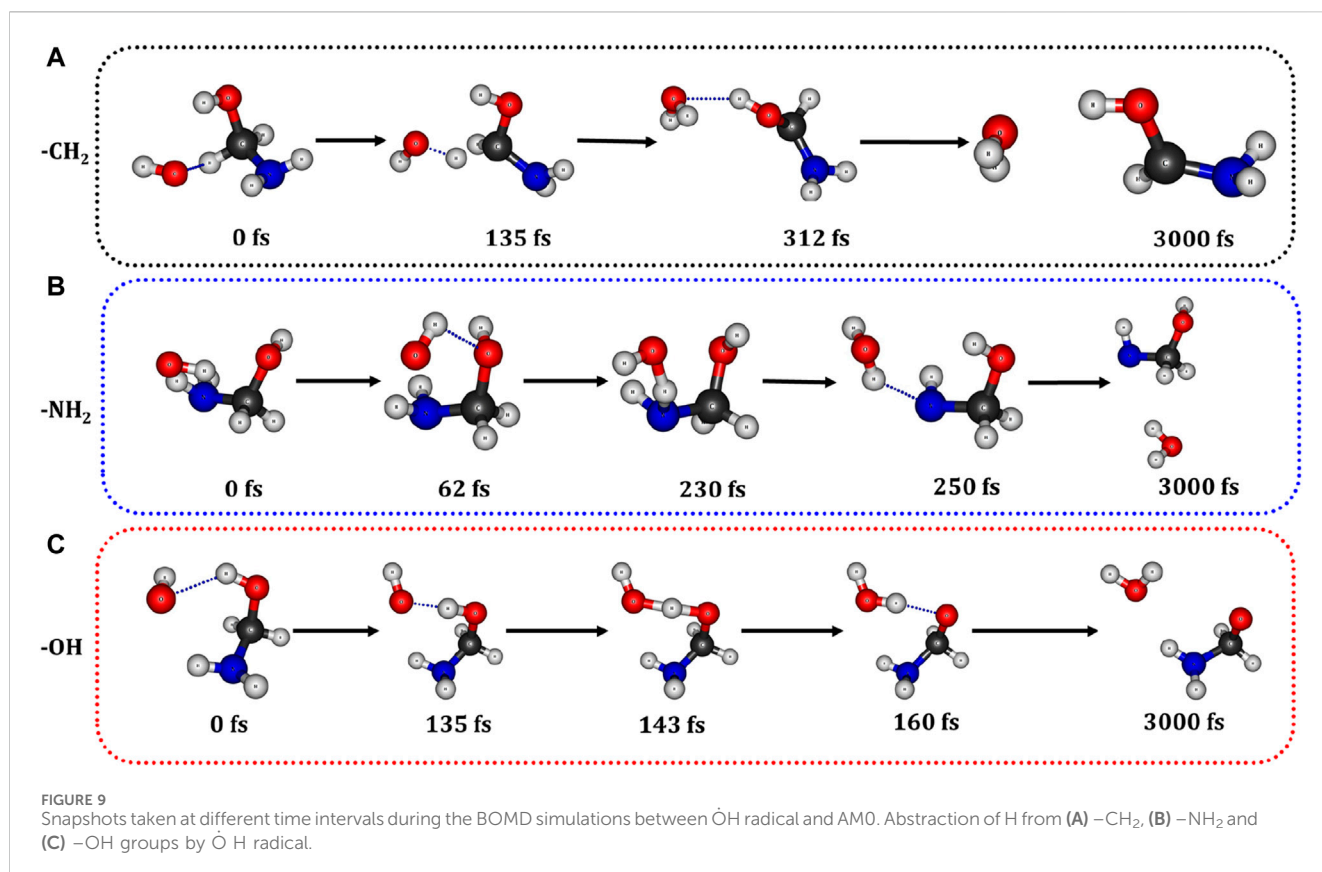


Figure 8
Computed rate constants for the $NH_2\dot{C}HOH + ^3O_2$ reaction at 1 atm pressure for the formation of formamide over the temperature range 200–400 K.

Figure 6 that, the reaction pathway proceeding through the transition state, TS-12A to form P-4A (NH_2CHO) is energetically more favorable followed by that proceeding through TS-10A and TS-11A to form P-2A and P-3A ($NHCHOH$) by the simultaneous H transfer and CO bond breaking process rather than reaction pathways that proceeding through TS-1A, TS-3A, TS-5A, TS-7A and TS-8A.

We have compared the energetics of important reactive species of $NH_2\dot{C}HOH + O_2$ reaction with that of similar species of previous studies. For example, the relative energy of IM-0A (-39 kcal/mol) is comparable to that of $OH\dot{C}HOH + O_2$ (-39.4 kcal/mol) (Franco et al., 2021), $CH_3\dot{C}HNH_2 + O_2$ (-36 kcal/mol) (Rissanen et al., 2014). Similarly, the barrier height values for the H transfer from $-CH$ (40.5 kcal/mol) *via* indirect mechanism closely match with that of $CH_3\dot{C}HNH_2 + O_2$ (38 kcal/mol) (Rissanen et al., 2014), $CH_2NH_2 + O_2$ (39.5 kcal/mol) (Rissanen et al., 2014) and $CH_2OH + O_2$ (40.5 kcal/mol) reactions (Dash and Ali, 2022). On the other hand, the barrier height values for transfer of $-NH$ hydrogen *via* an indirect mechanism (35–39 kcal/mol) are close to that of $CH_2NH_2 + O_2$ (35.8 kcal/mol) (Rissanen et al., 2014) reaction whereas *via* direct mechanism (16–18 kcal/mol) are well in agreement with the $NH_2\dot{C}HCH_2OH + O_2$ (16.3–18.6 kcal/mol) (Silva, 2012; Xie et al., 2014) mechanistic studies. On the other hand, the direct (4.5 kcal/mol) and indirect (29 kcal/mol) $-OH$ hydrogen transfer energy barrier values are also in similar range of $OH\dot{C}HOH + O_2$ (6.7 kcal/mol) (Franco et al., 2021) and $CH_2OH + O_2$ (25 kcal/mol) (Dash and Ali, 2022) reactions, respectively. These results strongly authenticate the close resemblance of energy parameters of the current study with that of previous studies.

Overall, the computed results suggest that the reaction pathways, which proceed through the TS-1A, TS-3A, TS-5A, TS-7A and TS-8A from the intermediate IM0-A exhibit high energy barriers. These energy barriers are in the range of (30–40 kcal/mol) as shown in Figure 7. Hence, these reaction pathways are excluded from the further studies of reaction kinetics and branching ratio analysis due to the high energy barriers. Relatively low energy barrier pathways which occurred *via* the transition states TS-10A, TS-11A and TS-12A were adopted for further kinetics and branching ratio calculations.



The rate constants and the branching ratio values of $^3\text{O}_2 + \text{NH}_2\dot{\text{C}}\text{HOH}$ reaction have been computed for the most favorable reaction pathways (*via* TS-10A, TS-11A and TS-12A), which form the product compounds P-2A, P-3A and P-4A. We have treated all these reaction pathways in a master equation to evaluate the temperature and pressure-dependent rate constants. The computed rate constants at the atmospheric conditions relevant to the troposphere, *i.e.*, at 1 atm pressure and 298 K for the overall reaction is $5.5 \times 10^{-12} \text{ cm}^3 \text{ molecule}^{-1} \text{ s}^{-1}$. The rate constant of $\text{O}_2 + \text{NH}_2\dot{\text{C}}\text{HOH}$ was compared with those of isoelectronic systems, namely, $\text{CH}_3\dot{\text{C}}\text{HOH} + \text{O}_2$ (Silva et al., 2009) and $\text{OH}\dot{\text{C}}\text{HOH} + \text{O}_2$ (Ali and Balaganesh, 2023) reactions. We have found that the overall rate constant of $\text{O}_2 + \text{NH}_2\dot{\text{C}}\text{HOH}$ decreases with the temperature similar to that of $\text{OH}\dot{\text{C}}\text{HOH} + \text{O}_2$ as shown in Figure 8. The total rate constant of $\text{NH}_2\dot{\text{C}}\text{HOH} + \text{O}_2$ reaction is mainly contributed from the rate constant of P-4A reaction rather than that of P-2A and P-3A (see Supplementary Figure S6). Further, branching ratio analysis suggests that $^3\text{O}_2 + \text{NH}_2\dot{\text{C}}\text{HOH}$ reaction predominantly leads to the formation of P-4A (NH_2CHO) with the branching fraction of $\sim 99\%$ over the temperature range 200–400 K, which is akin to the previous analysis on similar reaction system (Ali et al., 2021). The branching fraction values for the other products are negligibly small and independent of temperature and pressure.

We have also computed the ZPE corrected PES of nitrogen centered radical, namely, $\dot{\text{N}}\text{HCH}_2\text{OH} + \text{O}_2$ reaction and presented in Supplementary Figure S8. The CH-direct, CH-indirect and OH-indirect reaction pathways shows the high positive energies for the TSs around 8.9 (TS5), 27.6 (TS1) and 19.5 (TS2) kcal/mol and

hindered by the strong positive energy barriers, which are around 10.5, 29.2 and 22.9 kcal/mol, respectively. The large positive energies for the TSs are not encouraging and the corresponding reaction pathways will likely not be traversed in the upper atmosphere.

3.4 Molecular dynamics simulations

We have conducted Born-Oppenheimer molecular dynamics (BOMD) simulations to investigate the formation of formamide at 300 K through the reactions involving the reactive species ($\dot{\text{O}}\text{H} + \text{AM}$ and $\text{NH}_2\dot{\text{C}}\text{HOH}$ radical + O_2) using the CP2K code (VandeVondele et al., 2005). The computational methodology details are provided in the Supplementary Material. The snapshots captured at different time intervals from the trajectory of the 3ps BOMD simulation for the H abstraction from each channel of AM are shown in Figure 9. These snapshots clearly demonstrate that the abstraction of H from $-\text{CH}_2$, $-\text{NH}_2$ and $-\text{OH}$ groups during the $\dot{\text{O}}\text{H} + \text{AM}$ reaction follows the similar paths as discussed in Section 3.2. For example, the initial geometry for the H abstraction by the $\dot{\text{O}}\text{H}$ radical from $-\text{NH}_2$ group is depicted in Figure 9 at 0 femtoseconds (fs). During the BOMD simulation, a pre-reactive complex like geometry formed between the AM and $\dot{\text{O}}\text{H}$ radical at 62 fs. Subsequently, we have observed the transfer of H from $-\text{NH}_2$ to $\dot{\text{O}}\text{H}$ radical occurring through a transition state-like geometry at 230 fs. Further, this forms a $\dot{\text{N}}\text{HCH}_2\text{OH} + \text{H}_2\text{O}$ complex at 250 fs. Similar mechanisms are also observed in the cases of H abstraction from $-\text{CH}_2$ and $-\text{OH}$ groups of AM as illustrated in Figure 9. Additionally, BOMD simulations have

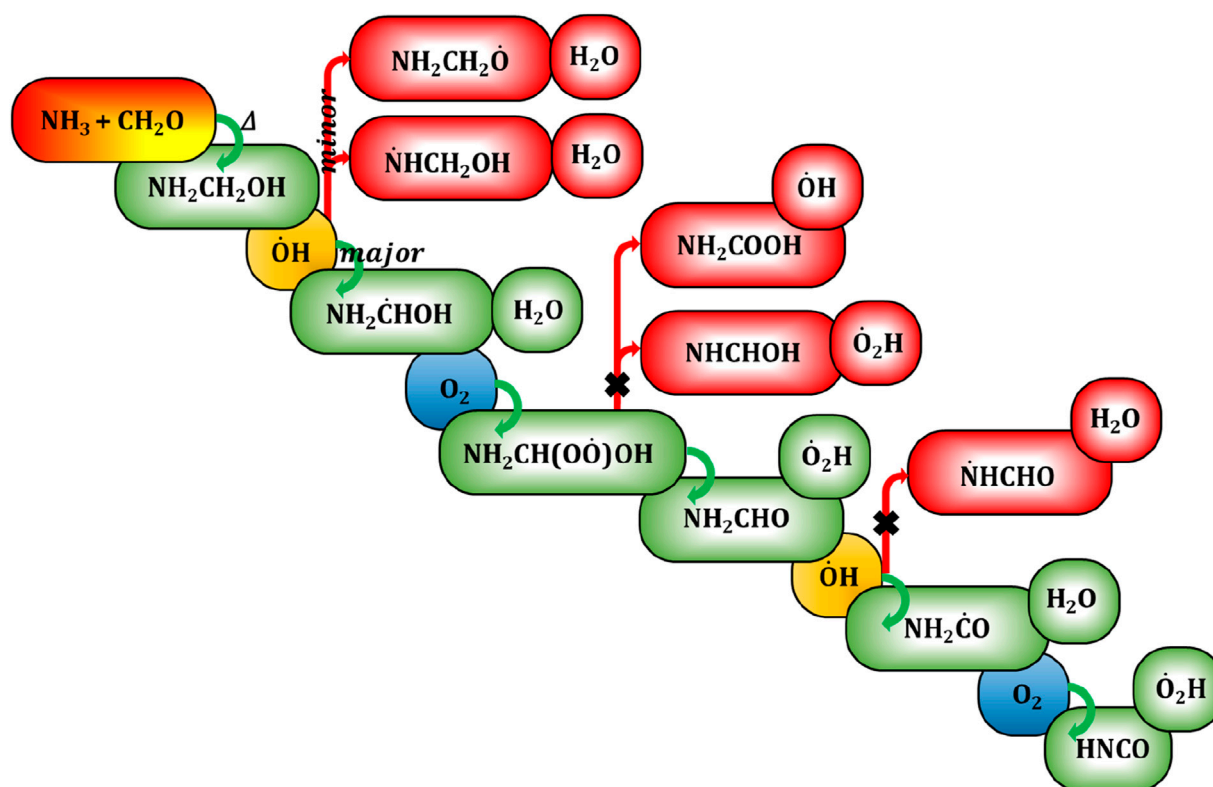


FIGURE 10
Generalized reaction mechanism for the formation of aminomethanol from ammonia and formaldehyde and its subsequent decomposition reaction pathways to potentially hazardous isocyanic acid.

been employed to simulate the reaction between $\text{NH}_2\dot{\text{C}}\text{HOH}$ radical and O_2 . Snapshots captured at different time intervals during the BOMD simulations between $\text{NH}_2\dot{\text{C}}\text{HOH}$ and O_2 are presented in **Supplementary Figure S7**, which are consistent with the earlier formamide formation reaction through TS-12A. These BOMD simulations strongly substantiate the predominant formation of formamide during the $\text{NH}_2\text{CH}_2\text{OH} + \dot{\text{O}}\text{H}/\text{O}_2$ reactions.

3.5 Atmospheric implications

Our previous investigation (Ali, 2019) has demonstrated the occurrence of a high-temperature reaction between ammonia (NH_3) and formaldehyde (H_2CO) during biomass burning, resulting in the formation of aminomethanol ($\text{NH}_2\text{CH}_2\text{OH}$). This prompts a keen interest in elucidating the oxidation reaction mechanism and kinetics of aminomethanol, leading to the formation of various compounds, including potentially hazardous or carcinogenic byproducts. The possible atmospheric decomposition pathway resulting from $\dot{\text{O}}\text{H}$ radical initiated oxidation of $\text{NH}_2\text{CH}_2\text{OH}$ is portrayed in **Figure 10**. We have computed the atmospheric lifetime (τ) of $\text{NH}_2\text{CH}_2\text{OH}$ due to its interactions with $\dot{\text{O}}\text{H}$ radicals using the following equation,

$$\tau = \frac{1}{k \times [\dot{\text{O}}\text{H}]} \quad (10)$$

where, k denotes the rate constant of $\text{NH}_2\text{CH}_2\text{OH} + \dot{\text{O}}\text{H}$ radical reaction ($5.33 \times 10^{-11} \text{ cm}^3 \text{ molecule}^{-1} \text{ s}^{-1}$) at 230 K, relevant to an altitude of 12 km.

The averaged concentration of $\dot{\text{O}}\text{H}$ radicals in the upper troposphere is denoted by $[\dot{\text{O}}\text{H}]$ and has been taken as $1.0 \times 10^6 \text{ molecule cm}^{-3}$ akin to that of earlier studies (Ali and Balaganesh, 2023). Computed results reveal that, the aminomethanol has a lifetime of 5 h in the presence of $\dot{\text{O}}\text{H}$ radicals and produce the $\text{NH}_2\dot{\text{C}}\text{HOH}$ radicals as the major product when compared to $\dot{\text{N}}\text{HCH}_2\text{OH}$ and $\text{NH}_2\text{CH}_2\dot{\text{O}}$ radicals. Under tropospheric conditions, the major radical product, i.e., $\text{NH}_2\dot{\text{C}}\text{HOH}$ undergoes further reaction with molecular oxygen ($^3\text{O}_2$) to yield formamide (NH_2CHO). We have employed k of $7.80 \times 10^{-12} \text{ cm}^3 \text{ molecule}^{-1} \text{ s}^{-1}$ at 225 K to calculate the atmospheric lifetime of the $\text{NH}_2\dot{\text{C}}\text{HOH}$ radicals. Our results show that, the lifetime of $\text{NH}_2\dot{\text{C}}\text{HOH}$ is approximately 13 microseconds (μs), indicating a rapid formation of formamide under atmospheric conditions. The current study also suggests that the formations of amino formic acid (NH_2COOH) and formimidic acid (NHCHOH) are unfavorable. It is important to mention here that the formation of formamide involves the reaction of aminomethanol with $\dot{\text{O}}\text{H}$ and O_2 . Analysis of $\text{NH}_2\text{CH}_2\text{OH} + \dot{\text{O}}\text{H}$ reactions indicates that the transition states (TSs) tend to exhibit a slight positive value for the H-abstraction reactions. Consequently, these reactions pose challenges under astrochemical conditions, where temperatures typically remain below 100 K. Nevertheless, the reactions involving the carbon-centred $\text{NH}_2\dot{\text{C}}\text{HOH}$ radical with O_2 may be viable in such conditions, as the corresponding aminomethanol-based peroxy radical intermediate, $\text{NH}_2\text{CH}(\text{OO}\dot{\text{O}})\text{OH}$ required less than 5 kcal/mol for the formamide formation. Therefore, investigating the comprehensive reaction pathways for the formamide formation from aminomethanol under astrochemical conditions holds significant promise for future studies in this field.

Barnes et al., have reviewed the mechanistic details and atmospheric chemistry of amides (Barnes et al., 2010). They showed that the formamide could further react with $\dot{\text{O}}\text{H}$ radicals and produce C- and N-centered formamide radicals as shown in Figure 10. However, Zhu and co-workers have revealed that the C-centered formamide radicals have exclusively been formed and rule out the possibility for the formation of N-centered radicals using the combination of experimental and theoretical studies (Bunkan et al., 2016). They have also found that the isocyanic acid (HNCO), which is known to be a potentially hazardous compound for the human health, is only the product formed during the $\text{NH}_2\text{CHO} + \text{OH}$ and O_2 reaction.

On the other hand, the branching fraction (20%) of N-centered radicals indicates the formation of $\dot{\text{N}}\text{HCH}_2\text{OH}$ in significant quantities. It suggests that the N-centered radicals are also prone to further reactions with atmospheric gaseous compounds. However, N-centered radicals usually react slowly with the atmospheric oxygen and potentially leads to the formation of carcinogenic nitrosamines or nitramines through the bi-molecular reactions with the other trace compounds of the atmosphere (NO and NO_2).

Overall, investigating the branching fraction and ensuing rate constants associated with the hydrogen abstraction from $-\text{CH}_2$, $-\text{NH}_2$, and $-\text{OH}$ groups of aminomethanol by hydroxyl radicals offers initial insights into the predominant formation of formamide. Additionally, this study provides additional insights into the formation of N-centered radicals in significant quantities. Nevertheless, conducting further investigations on the reactions of O_2 , NO and NO_2 with N-centered radicals would undoubtedly contribute to significantly understand their impact on the atmosphere.

4 Conclusion

In this study, we have comprehensively explored the mechanistic details of aminomethanol oxidation reaction initiated by atmospheric $\dot{\text{O}}\text{H}/\text{O}_2$ using CCSD(T)/M06-2X level of theory. The $\text{NH}_2\text{CH}_2\text{OH} + \dot{\text{O}}\text{H}$ reaction predominantly yields the C-centered $\text{NH}_2\dot{\text{C}}\text{HOH}$ radicals when compared to the N- and O-centered $\dot{\text{N}}\text{HCH}_2\text{OH}$ and $\text{NH}_2\dot{\text{C}}\text{HO}$ radicals. Our findings reveal that, the total rate constants (k_{OH}) for the H transfer from aminomethanol is approximately $1.97 \times 10^{-11} \text{ cm}^3 \text{ molecule}^{-1} \text{ s}^{-1}$ at 300 K. This k_{OH} value closely matches with that of CH_3NH_2 ($1.97 \times 10^{-11} \text{ cm}^3 \text{ molecule}^{-1} \text{ s}^{-1}$), CH_3NHCH_3 ($6.27 \times 10^{-11} \text{ cm}^3 \text{ molecule}^{-1} \text{ s}^{-1}$), $\text{CH}_3\text{CH}_2\text{NH}_2$ ($2.50 \times 10^{-11} \text{ cm}^3 \text{ molecule}^{-1} \text{ s}^{-1}$), $\text{NH}_2\text{CH}_2\text{CH}_2\text{OH}$ ($7.27 \times 10^{-11} \text{ cm}^3 \text{ molecule}^{-1} \text{ s}^{-1}$), indicating the accuracy of our findings. Moreover, the computed atmospheric lifetime of $\text{NH}_2\dot{\text{C}}\text{HOH}$ radicals is remarkably short, estimated at 13 μs , suggesting rapid reactions with atmospheric oxygen. We observed that the reaction between $\text{NH}_2\dot{\text{C}}\text{HOH}$ radicals and O_2 exclusively forms formamide (NH_2CHO) as the product, with a branching fraction of approximately 99% and a rate constant of $5.5 \times 10^{-12} \text{ cm}^3 \text{ molecule}^{-1} \text{ s}^{-1}$ under the tropospheric conditions. The rate constant of $\text{NH}_2\dot{\text{C}}\text{HOH} + \text{O}_2$ reaction aligns well with that of $\text{HOCHOH} + \text{O}_2$ and $\text{CH}_3\text{CHOH} + \text{O}_2$ reactions. Our Born-Oppenheimer molecular dynamics (BOMD) simulations also substantiate the formation of formamide as the prime product. Finally, we have addressed the environmental implications of exclusively formed formamide. The formamide can lead to formation of potentially hazardous compounds like HNCO on further reactions with atmospheric hydroxyl radicals. The unreacted aminomethanol $\dot{\text{N}}\text{HCH}_2\text{OH}$ radicals may form the carcinogenic nitrosamines on

reacting with trace N-oxides (*viz.*, NO and NO_2). Consequently, it leads to increase the environmental risk factors.

Data availability statement

The original contributions presented in the study are included in the article/Supplementary Material, further inquiries can be directed to the corresponding author.

Author contributions

NN: Conceptualization, Data curation, Formal Analysis, Methodology, Writing—original draft, Writing—review and editing. MA: Conceptualization, Formal Analysis, Funding acquisition, Investigation, Software, Supervision, Validation, Writing—original draft, Writing—review and editing.

Funding

The author(s) declare that financial support was received for the research, authorship, and/or publication of this article. The work is supported by the faculty startup grant #8474000461 at Khalifa University of Science and Technology, Abu Dhabi, UAE.

Acknowledgments

NN and MA thank the supercomputer facility and Department of Chemistry at the College of Engineering and Physical Sciences at Khalifa University of Science and Technology, at Abu Dhabi UAE for their support. MA thanks Khalifa University of Science and Technology, at Abu Dhabi UAE for Faculty Start-up grant #8474000461.

Conflict of interest

The authors declare that the research was conducted in the absence of any commercial or financial relationships that could be construed as a potential conflict of interest.

Publisher's note

All claims expressed in this article are solely those of the authors and do not necessarily represent those of their affiliated organizations, or those of the publisher, the editors and the reviewers. Any product that may be evaluated in this article, or claim that may be made by its manufacturer, is not guaranteed or endorsed by the publisher.

Supplementary material

The Supplementary Material for this article can be found online at: <https://www.frontiersin.org/articles/10.3389/fchem.2024.1407355/full#supplementary-material>

References

- Abdel-Rahman, M. A., Shibl, M. F., El-Nahas, A. M., Abdel-Azeim, S., El-demerdash, S. H., and Al-Hashimi, N. (2021). Mechanistic insights of the degradation of an O-anisidine carcinogenic pollutant initiated by OH radical attack: theoretical investigations. *New J. Chem.* 45, 5907–5924. doi:10.1039/D0NJ06248K
- Ali, M. A. (2019). Theoretical study on the gas phase reaction of $\text{CH}_2\text{O} + \text{NH}_3$: the formation of $\text{CH}_2\text{O} \cdots \text{NH}_3$, $\text{NH}_2\text{CH}_2\text{OH}$, or $\text{CH}_2\text{NH} + \text{H}_2\text{O}$. *Phys. Chem. Chem. Phys.* 21, 19242–19251. doi:10.1039/C9CP02777G
- Ali, M. A. (2020). Computational studies on the gas phase reaction of methylenimine (CH_2NH) with water molecules. *Sci. Rep.* 10, 10995. doi:10.1038/s41598-020-67515-3
- Ali, M. A., and Balaganesh, M. (2023). Effect of formic acid on $\text{O}_2 + \text{OHCHOH} \rightarrow \text{HCOOH} + \text{HO}_2$ reaction under tropospheric condition: kinetics of *cis* and *trans* isomers. *Phys. Chem. Chem. Phys.* 25, 9965–9978. doi:10.1039/D2CP05874J
- Ali, M. A., Balaganesh, M., Al-Odail, F. A., and Lin, K. C. (2021). Effect of ammonia and water molecule on $\text{OH} + \text{CH}_3\text{OH}$ reaction under tropospheric condition. *Sci. Rep.* 11, 12185. doi:10.1038/s41598-021-90640-6
- Ali, M. A., Balaganesh, M., and Lin, K. C. (2018). Catalytic effect of a single water molecule on the $\text{OH} + \text{CH}_2\text{NH}$ reaction. *Phys. Chem. Chem. Phys.* 20, 4297–4307. doi:10.1039/C7CP07091H
- Ali, M. A., Dash, M. R., and Al Maieli, L. M. (2022). Catalytic effect of CO_2 and H_2O molecules on $\bullet\text{CH}_3 + {}^3\text{O}_2$ reaction. *Catalysts* 12, 699. doi:10.3390/catal12070699
- Ali, M. A., Sonk, J. A., and Barker, J. R. (2016). Predicted chemical activation rate constants for $\text{HO}_2 + \text{CH}_2\text{NH}$: the dominant role of a hydrogen-bonded pre-reactive complex. *J. Phys. Chem. A* 120, 7060–7070. doi:10.1021/acs.jpca.6b06531
- Baidya, B., Lily, M., and Chandra, A. K. (2018). Theoretical insight into the kinetics of H-abstraction reaction of $\text{CHF}_2\text{CH}_2\text{OH}$ with OH radical, atmospheric lifetime and global warming potential. *ChemistrySelect* 3, 6136–6144. doi:10.1002/slct.201800491
- Barker, J. R. (2001). Multiple-Well, multiple-path unimolecular reaction systems. I. MultiWell computer program suite. *Int. J. Chem. Kinet.* 33, 232–245. doi:10.1002/kin.1017
- Barker, J. R. (2009). Energy transfer in master equation simulations: a new approach. *Int. J. Chem. Kinet.* 41, 748–763. doi:10.1002/kin.20447
- Barker, J. R., Nguyen, T. L., Stanton, J. F., Aieta, C., Ceotto, M., Gabas, F., et al. (2023). *MultiWell-2023 software Suite*. Ann Arbor, Michigan, USA: J. R. University of Michigan. Available at: <https://multiwell.engin.umich.edu>.
- Barnes, I., Solignac, G., Mellouki, A., and Becker, K. H. (2010). Aspects of the atmospheric chemistry of amides. *ChemPhysChem* 11, 3844–3857. doi:10.1002/cphc.201000374
- Beck, M. (2000). The multiconfiguration time-dependent Hartree (MCTDH) method: a highly efficient algorithm for propagating wavepackets. *Phys. Rep.* 324, 1–105. doi:10.1016/S0370-1573(99)00047-2
- Ben-Nun, M., and Martínez, T. J. (2002). *Ab initio* quantum molecular dynamics. *Adv. Chem. Phys.* 121, 439–512. doi:10.1002/0471264318.ch7
- Ben-Nun, M., Quenneville, J., and Martínez, T. J. (2000). *Ab initio* multiple spawning: photochemistry from first principles quantum molecular dynamics. *J. Phys. Chem. A* 104, 5161–5175. doi:10.1021/jp994174i
- Bernstein, M. P., Allamandola, L. J., and Sandford, S. A. (1997). Complex organics in laboratory simulations of interstellar/cometary ices. *Adv. Space Res.* 19, 991–998. doi:10.1016/S0273-1177(97)00340-2
- Bockelée-Morvan, D., Lis, D. C., Wink, J. E., Despois, D., Crovisier, J., Bachiller, R., et al. (2000). New molecules found in comet C/1995 O1 (Hale-Bopp). Investigating the link between cometary and interstellar material. *Astron Astrophys.* 353, 1101–1114.
- Borduas, N., Abbatt, J. P. D., and Murphy, J. G. (2013). Gas phase oxidation of monoethanolamine (MEA) with OH radical and ozone: kinetics, products, and particles. *Environ. Sci. Technol.* 47, 6377–6383. doi:10.1021/es401282j
- Bossa, J. B., Theule, P., Duvernay, F., and Chiavassa, T. (2009). $\text{NH}_2\text{CH}_2\text{OH}$ thermal formation in interstellar ices contribution to the 5–8 μm region toward embedded protostars. *Astrophys. J.* 707, 1524–1532. doi:10.1088/0004-637X/707/2/1524
- Botta, L., Saladino, R., Bizzarri, B. M., Cobucci-Ponzano, B., Iacono, R., Avino, R., et al. (2018). Formamide-based prebiotic chemistry in the phlegrean fields. *Adv. Space Res.* 62, 2372–2379. doi:10.1016/j.asr.2017.07.017
- Boys, S. F., and Bernardi, F. (1970). The calculation of small molecular interactions by the differences of separate total energies. Some procedures with reduced errors. *Mol. Phys.* 19, 553–566. doi:10.1080/00268977000101561
- Bunkan, A. J. C., Mikoviny, T., Nielsen, C. J., Wisthaler, A., and Zhu, L. (2016). Experimental and theoretical study of the OH-initiated photo-oxidation of formamide. *J. Phys. Chem. A* 120, 1222–1230. doi:10.1021/acs.jpca.6b00032
- Dai, N., Shah, A. D., Hu, L., Plewa, M. J., McKague, B., and Mitch, W. A. (2012). Measurement of nitrosamine and nitramine formation from NO_x reactions with amines during amine-based carbon dioxide capture for postcombustion carbon sequestration. *Environ. Sci. Technol.* 46, 9793–9801. doi:10.1021/es301867b
- Dash, M. R., and Ali, M. A. (2022). Effect of a single water molecule on $\text{CH}_2\text{OH} + {}^3\text{O}_2$ reaction under atmospheric and combustion conditions. *Phys. Chem. Chem. Phys.* 24, 1510–1519. doi:10.1039/D1CP03911C
- Dash, M. R., and Ali, M. A. (2023). Can a single ammonia and water molecule enhance the formation of methanimine under tropospheric conditions? kinetics of $\bullet\text{CH}_2\text{NH}_2 + \text{O}_2 (+\text{NH}_3/\text{H}_2\text{O})$. *Front. Chem.* 11, 1243235. doi:10.3389/fchem.2023.1243235
- Deschamps, G. (1931). Preparation of formamide and its conversion into hydrocyanic acid. *Chimie Industrielle*, 589–597.
- Evans, M. G., and Polanyi, M. (1938). Inertia and driving force of chemical reactions. *Trans. Faraday Soc.* 34, 11. doi:10.1039/tf9383400011
- Fabiano, E., Keal, T. W., and Thiel, W. (2008). Implementation of surface hopping molecular dynamics using semiempirical methods. *Chem. Phys.* 349, 334–347. doi:10.1016/j.chemphys.2008.01.044
- Feldmann, M. T., Widicus, S. L., Blake, G. A., Kent, D. R., and Goddard, W. A. (2005). Aminomethanol water elimination: theoretical examination. *J. Chem. Phys.* 123, 034304. doi:10.1063/1.1935510
- Ferus, M., Knížek, A., Cassone, G., Rimmer, P. B., Changela, H., Chatzitheodoridis, E., et al. (2023). Simulating asteroid impacts and meteor events by high-power lasers: from the laboratory to spaceborne missions. *Front. Astron. Space Sci.* 10. doi:10.3389/fspas.2023.1186172
- Ferus, M., Nesvorný, D., Šponer, J., Kubelík, P., Michalčíková, R., Shestivská, V., et al. (2015). High-energy chemistry of formamide: a unified mechanism of nucleobase formation. *Proc. Natl. Acad. Sci.* 112, 657–662. doi:10.1073/pnas.1412072111
- Firaha, D. S., Döntgen, M., Berkels, B., and Leonhard, K. (2018). Pressure-dependent rate constant predictions utilizing the inverse Laplace transform: a victim of deficient input data. *ACS Omega* 3, 8212–8219. doi:10.1021/acsomega.8b00311
- Franco, B., Blumenstock, T., Cho, C., Clarisse, L., Clerbaux, C., Coheur, P.-F., et al. (2021). Ubiquitous atmospheric production of organic acids mediated by cloud droplets. *Nature* 593, 233–237. doi:10.1038/s41586-021-03462-x
- Frisch, M. J., Pople, J. A., and Binkley, J. S. (1984). Self-consistent molecular orbital methods 25. Supplementary functions for Gaussian basis sets. *J. Chem. Phys.* 80, 3265–3269. doi:10.1063/1.447079
- Frisch, M. J., Trucks, G. W., Schlegel, H. B., Scuseria, G. E., Robb, M. A., Cheeseman, J. R., et al. (2019). *Gaussian 16, revision C.01*. Wallingford CT: Gaussian, Inc.
- Ge, X., Wexler, A. S., and Clegg, S. L. (2011a). Atmospheric amines – Part I. A review. *Atmos. Environ.* 45, 524–546. doi:10.1016/j.atmosenv.2010.10.012
- Ge, X., Wexler, A. S., and Clegg, S. L. (2011b). Atmospheric amines – Part II. Thermodynamic properties and gas/particle partitioning. *Atmos. Environ.* 45, 561–577. doi:10.1016/j.atmosenv.2010.10.013
- Gerakines, P. A., Moore, M. H., and Hudson, R. L. (2004). Ultraviolet photolysis and proton irradiation of astrophysical ice analogs containing hydrogen cyanide. *Icarus* 170, 202–213. doi:10.1016/j.icarus.2004.02.005
- Goldsmith, C. F., Green, W. H., and Klippenstein, S. J. (2012). Role of $\text{O}_2 + \text{QOOH}$ in low-temperature ignition of propane. 1. Temperature and pressure dependent rate coefficients. *J. Phys. Chem. A* 116, 3325–3346. doi:10.1021/jp210722w
- González, D., Lema-Saavedra, A., Espinosa, S., Martínez-Núñez, E., Fernández-Ramos, A., Canosa, A., et al. (2022). Reaction of OH radicals with CH_3NH_2 in the gas phase: experimental (11.7–177.5 K) and computed rate coefficients (10–1000 K). *Phys. Chem. Chem. Phys.* 24, 23593–23601. doi:10.1039/D2CP03414J
- Grimme, S., Antony, J., Ehrlich, S., and Krieg, H. (2010). A consistent and accurate *ab initio* parametrization of density functional dispersion correction (DFT-D) for the 94 elements H–Pu. *J. Chem. Phys.* 132, 154104. doi:10.1063/1.3382344
- Gröger, H. (2003). Catalytic enantioselective strecker reactions and analogous syntheses. *Chem. Rev.* 103, 2795–2828. doi:10.1021/cr020038p
- Hammes-Schiffer, S., and Tully, J. C. (1994). Proton transfer in solution: molecular dynamics with quantum transitions. *J. Chem. Phys.* 101, 4657–4667. doi:10.1063/1.467455
- Hays, B. M., Weaver, W., and Susanna, L. (2013). Theoretical examination of $\text{O}(^1\text{D})$ insertion reactions to form methanediol, methoxymethanol, and aminomethanol. *J. Phys. Chem. A* 117, 7142–7148. doi:10.1021/jp400753r
- Kapteina, S., Slowik, K., Verevkin, S. P., and Heintz, A. (2005). Vapor pressures and vaporization enthalpies of a series of ethanolamines. *J. Chem. Eng. Data* 50, 398–402. doi:10.1021/je049761y
- Karl, M., Dye, C., Schmidbauer, N., Wisthaler, A., Mikoviny, T., D’Anna, B., et al. (2012). Study of OH-initiated degradation of 2-aminoethanol. *Atmos. Chem. Phys.* 12, 1881–1901. doi:10.5194/acp-12-1881-2012
- Koike, T., Kaneko, T., Kobayashi, K., Miyakawa, S., and Takano, Y. (2003). Formation of organic compounds from simulated Titan atmosphere: perspectives of the Cassini mission. *Biol. Sci. Space* 17, 188–189.
- Lee, T. J., and Taylor, P. R. (1989). A diagnostic for determining the quality of single-reference electron correlation methods. *Int. J. Quantum Chem.* 36, 199–207. doi:10.1002/qua.560360824

- Lis, D. C., Mehringer, D. M., Benford, D., Gardner, M., Phillips, T. G., Bockelée-Morvan, D., et al. (1997). New molecular species in comet C/1995 O1 (Hale-Bopp) observed with the caltech submillimeter observatory. *Earth Moon Planets* 78, 13–20. doi:10.1023/A:1006281802554
- Manthe, U., Meyer, H.-D., and Cederbaum, L. S. (1992). Wave-packet dynamics within the multiconfiguration Hartree framework: general aspects and application to NOCl. *J. Chem. Phys.* 97, 3199–3213. doi:10.1063/1.463007
- Mazarei, E., and Barker, J. R. (2022). CH₂ + O₂: reaction mechanism, biradical and zwitterionic character, and formation of CH₂OO, the simplest Criegee intermediate. *Phys. Chem. Chem. Phys.* 24, 914–927. doi:10.1039/D1CP04372B
- Meyer, H. (2012). Studying molecular quantum dynamics with the multiconfiguration time-dependent Hartree method. *WIREs Comp. Mol. Sci.* 2, 351–374. doi:10.1002/wcms.87
- Nájera, C., and Sansano, J. M. (2007). Catalytic asymmetric synthesis of α -amino acids. *Chem. Rev.* 107, 4584–4671. doi:10.1021/cr050580o
- Navarro-González, R., and Raulin, F. (2004). Steps toward the origin(s) of life: endogenous sources and chemistry. *Adv. Space Res.* 33, 79–80. doi:10.1016/j.asr.2003.11.002
- Nguyen, T. L., Ruscic, B., and Stanton, J. F. (2019). A master equation simulation for the \bullet OH + CH₃OH reaction. *J. Chem. Phys.* 150, 084105. doi:10.1063/1.5081827
- Nielsen, A. T., Moore, D. W., Ogan, M. D., and Atkins, R. L. (1979). Structure and chemistry of the aldehyde ammonias. 3. Formaldehyde-ammonia reaction. 1,3,5-Hexahydrotriazine. *J. Org. Chem.* 44, 1678–1684. doi:10.1021/jo01324a021
- Onel, L., Blitz, M. A., and Seakins, P. W. (2012). Direct determination of the rate coefficient for the reaction of OH radicals with monoethanol amine (MEA) from 296 to 510 K. *J. Phys. Chem. Lett.* 3, 853–856. doi:10.1021/jz300200c
- Onel, L., Thonger, L., Blitz, M. A., Seakins, P. W., Bunkan, A. J. C., Solimannejad, M., et al. (2013). Gas-phase reactions of OH with methyl amines in the presence or absence of molecular oxygen. An experimental and theoretical study. *J. Phys. Chem. A* 117, 10736–10745. doi:10.1021/jp406522z
- Pastorek, A., Hrnčirová, J., Jankovič, L., Nejd, L., Civiš, S., Ivanek, O., et al. (2019). Prebiotic synthesis at impact craters: the role of Fe-clays and iron meteorites. *Chem. Comm.* 55, 10563–10566. doi:10.1039/C9CC04627E
- Priya, A. M., and Lakshminpathi, S. (2017). DFT study on abstraction reaction mechanism of OH radical with 2-methoxyphenol. *J. Phys. Org. Chem.* 30, e3713. doi:10.1002/poc.3713
- Raghavachari, K., Trucks, G. W., Pople, J. A., and Head-Gordon, M. (1989). A fifth-order perturbation comparison of electron correlation theories. *Chem. Phys. Lett.* 157, 479–483. doi:10.1016/S0009-2614(89)87395-6
- Rahbar, A., Zahedi, E., Aghaie, H., Giah, M., and Zare, K. (2021). DFT insight into the kinetics and mechanism of the OH \cdot -initiated atmospheric oxidation of catechol: OH \cdot Addition and hydrogen abstraction pathways. *Chem. Sel.* 6, 3875–3883. doi:10.1002/slct.202100524
- Rissanen, M. P., Eskola, A. J., Nguyen, T. L., Barker, J. R., Liu, J., Liu, J., et al. (2014). CH₂NH₂ + O₂ and CH₃CHNH₂ + O₂ reaction kinetics: photoionization mass spectrometry experiments and master equation calculations. *J. Phys. Chem. A* 118, 2176–2186. doi:10.1021/jp411238e
- Robertson, S. H., Pilling, M. J., Baulch, D. L., and Green, N. J. B. (1995). Fitting of pressure-dependent kinetic rate data by master equation/inverse Laplace transform analysis. *J. Phys. Chem.* 99, 13452–13460. doi:10.1021/j100036a020
- Rubin, R. H., Swenson Jr, G. W., Benson, R. C., Tigelaar, H. L., and Flygare, W. H. (1971). Microwave detection of interstellar formamide. *Astrophysical J.* 169, L39. doi:10.1086/180810
- Saitta, A. M., and Saija, F. (2014). Miller experiments in atomistic computer simulations. *Proc. Natl. Acad. Sci.* 111, 13768–13773. doi:10.1073/pnas.1402894111
- Saladino, R., Botta, G., Pino, S., Costanzo, G., and Di Mauro, E. (2012a). Genetics first or metabolism first? The formamide clue. *Chem. Soc. Rev.* 41, 5526. doi:10.1039/c2cs35066a
- Saladino, R., Crestini, C., Cicciello, F., Costanzo, G., and Di Mauro, E. (2007). Formamide chemistry and the origin of informational polymers. *Chem. Biodivers.* 4, 694–720. doi:10.1002/cbdv.200790059
- Saladino, R., Crestini, C., Costanzo, G., and DiMauro, E. (2005). “On the prebiotic synthesis of nucleobases, nucleotides, oligonucleotides, pre-RNA and pre-DNA molecules,” in *Prebiotic chemistry*. Editor P. Walde (Berlin/Heidelberg: Springer-Verlag), 29–68. doi:10.1007/b136152
- Saladino, R., Crestini, C., Pino, S., Costanzo, G., and Di Mauro, E. (2012b). Formamide and the origin of life. *Phys. Life Rev.* 9, 84–104. doi:10.1016/j.plrev.2011.12.002
- Schade, G. W., and Crutzen, P. J. (1995). Emission of aliphatic amines from animal husbandry and their reactions: potential source of N₂O and HCN. *J. Atmos. Chem.* 22, 319–346. doi:10.1007/BF00696641
- Schutte, W. A., Allamandola, L. J., and Sandford, S. A. (1993). An experimental study of the organic molecules produced in cometary and interstellar ice analogs by thermal formaldehyde reactions. *Icarus* 104, 118–137. doi:10.1006/icar.1993.1087
- Schutte, W. A., Boogert, A. C. A., Tielens, A., Whittet, D. C. B., Gerakines, P. A., Chiar, J. E., et al. (1999). Weak ice absorption features at 7.24 and 7.41 μ m in the spectrum of the obscured young stellar object W 33A. *Astron Astrophys.* 343, 966–976.
- Silva, G. D. (2012). Atmospheric chemistry of 2-aminoethanol (MEA): reaction of the NH₂•CHCH₂ OH radical with O₂. *J. Phys. Chem. A* 116, 10980–10986. doi:10.1021/jp307726w
- Silva, G. da, Bozzelli, J. W., Liang, L., and Farrell, J. T. (2009). Ethanol oxidation: kinetics of the α -hydroxyethyl radical + O₂ reaction. *J. Phys. Chem. A* 113, 8923–8933. doi:10.1021/jp903210a
- Simon, S., Duran, M., and Dannenberg, J. J. (1996). How does basis set superposition error change the potential surfaces for hydrogen-bonded dimers? *J. Chem. Phys.* 105, 11024–11031. doi:10.1063/1.472902
- Singh, S. K., Zhu, C., La Jeunesse, J., Fortenberry, R. C., and Kaiser, R. I. (2022). Experimental identification of aminomethanol (NH₂CH₂OH)—the key intermediate in the Strecker Synthesis. *Nat. Commun.* 13, 375. doi:10.1038/s41467-022-27963-z
- Solomon, P. M. (1973). Interstellar molecules. *Phys. Today* 26, 32–40. doi:10.1063/1.3127983
- Strecker, A. (1850). Ueber die künstliche Bildung der Milchsäure und einen neuen, dem Glycocol homologen Körper. *Justus Liebigs Ann. Chem.* 75, 27–45. doi:10.1002/jlac.18500750103
- Takano, Y., Tsuboi, T., Kaneko, T., Kobayashi, K., and Marumo, K. (2004). Pyrolysis of high-molecular-weight complex organics synthesized from a simulated interstellar gas mixture irradiated with 3 MeV proton beam. *Bull. Chem. Soc. Jpn.* 77, 779–783. doi:10.1246/bcsj.77.779
- Tian, W., Wang, W., Zhang, Y., and Wang, W. (2009). Direct dynamics study on the mechanism and the kinetics of the reaction of CH₃NH₂ with OH. *Int. J. Quantum Chem.* 109, 1566–1575. doi:10.1002/qua.22000
- Tully, J. C., and Preston, R. K. (1971). Trajectory surface hopping approach to nonadiabatic molecular collisions: the reaction of H \cdot with D₂. *J. Chem. Phys.* 55, 562–572. doi:10.1063/1.1675788
- VandeVondele, J., Krack, M., Mohamed, F., Parrinello, M., Chassaing, T., and Hutter, J. (2005). Quickstep: fast and accurate density functional calculations using a mixed Gaussian and plane waves approach. *Comput. Phys. Commun.* 167, 103–128. doi:10.1016/j.cpc.2004.12.014
- Wang, J., Liu, X., and Feng, X. (2011). Asymmetric strecker reactions. *Chem. Rev.* 111, 6947–6983. doi:10.1021/cr200057t
- Woon, D. E. (2002). *Ab initio* quantum chemical studies of reactions in astrophysical ices. 4. Reactions in ices involving HCOOH, CH₂NH, HCN, HNC, NH₃, and H₂O. *Int. J. Quantum Chem.* 88, 226–235. doi:10.1002/qua.10082
- Xie, H.-B., Li, C., He, N., Wang, C., Zhang, S., and Chen, J. (2014). Atmospheric chemical reactions of monoethanolamine initiated by OH radical: mechanistic and kinetic study. *Environ. Sci. Technol.* 48, 1700–1706. doi:10.1021/es405110t
- Xu, L., Tsonea, N. T., Tang, S., Li, J., and Du, L. (2019). Role of (H₂O)_n ($n = 1-2$) in the gas-phase reaction of ethanol with hydroxyl radical: mechanism, kinetics, and products. *ACS Omega* 4, 5805–5817. doi:10.1021/acsomega.9b00145
- Yamada, H. (2021). Amine-based capture of CO₂ for utilization and storage. *Polym. J.* 53, 93–102. doi:10.1038/s41428-020-00400-y
- Yang, S., and Martínez, T. J. (2011). “*Ab initio* multiple spawning: first principles dynamics around conical intersections,” in *Conical intersections* (Singapore: World Scientific), 347–374. doi:10.1142/9789814313452_0009
- Zhao, Y., and Truhlar, D. G. (2008). The M06 suite of density functionals for main group thermochemistry, thermochemical kinetics, noncovalent interactions, excited states, and transition elements: two new functionals and systematic testing of four M06-class functionals and 12 other functionals. *Theor. Chem. Acc.* 120, 215–241. doi:10.1007/s00214-007-0310-x



OPEN ACCESS

EDITED BY

Steve Suib,
University of Connecticut, United States

REVIEWED BY

Maria Rosaria Romano,
GlaxoSmithKline, Italy
Roberto Adamo,
GlaxoSmithKline, Italy

*CORRESPONDENCE

Nikolay E. Nifantiev,
✉ nen@ioc.ac.ru

RECEIVED 27 April 2024

ACCEPTED 30 May 2024

PUBLISHED 21 June 2024

CITATION

Tsvetkov YE, Volkov TM, Eremin SA,
Sklyarov OD, Kulakov YK, Krylov VB and
Nifantiev NE (2024), New synthesis of
oligosaccharides modelling the M epitope of
the *Brucella* O-polysaccharide.
Front. Chem. 12:1424157.
doi: 10.3389/fchem.2024.1424157

COPYRIGHT

© 2024 Tsvetkov, Volkov, Eremin, Sklyarov,
Kulakov, Krylov and Nifantiev. This is an open-
access article distributed under the terms of the
[Creative Commons Attribution License \(CC BY\)](https://creativecommons.org/licenses/by/4.0/).
The use, distribution or reproduction in other
forums is permitted, provided the original
author(s) and the copyright owner(s) are
credited and that the original publication in this
journal is cited, in accordance with accepted
academic practice. No use, distribution or
reproduction is permitted which does not
comply with these terms.

New synthesis of oligosaccharides modelling the M epitope of the *Brucella* O-polysaccharide

Yury E. Tsvetkov¹, Timur M. Volkov¹, Sergei A. Eremin²,
Oleg D. Sklyarov³, Yuri K. Kulakov⁴, Vadim B. Krylov^{1,5} and
Nikolay E. Nifantiev^{1*}

¹Laboratory of Glycoconjugate Chemistry, N.D. Zelinsky Institute of Organic Chemistry, Russian Academy of Sciences, Moscow, Russia, ²Faculty of Chemistry, M.V. Lomonosov Moscow State University, Moscow, Russia, ³Russian State Centre of Quality and Standardization of Veterinary Drugs and Feeds, Moscow, Russia, ⁴Laboratory of Brucellosis, N.F. Gamaleya National Research Center of Epidemiology and Microbiology, Moscow, Russia, ⁵Laboratory of Synthetic Glycovaccines, N.D. Zelinsky Institute of Organic Chemistry, Russian Academy of Sciences, Moscow, Russia

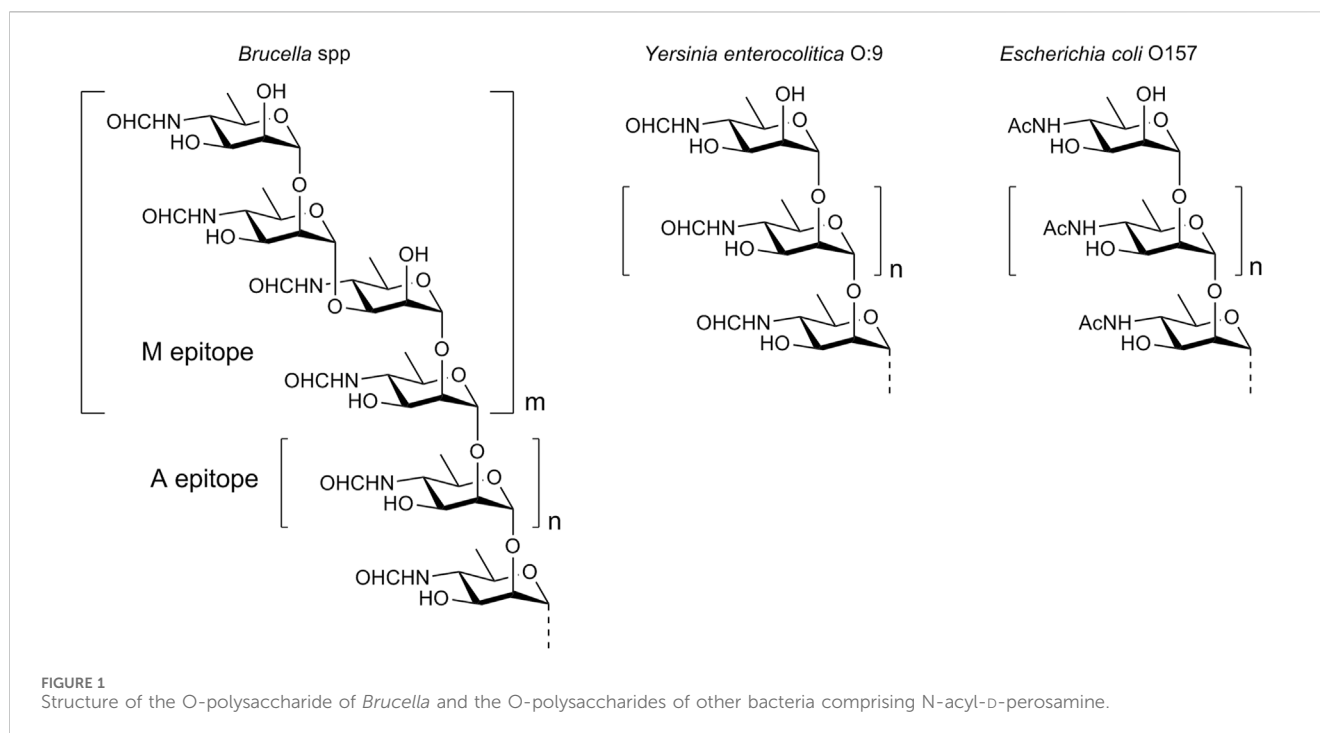
Brucellosis is a dangerous zoonotic disease caused by bacteria of the genus *Brucella*. Diagnosis of brucellosis is based on the detection in animal and human sera of antibodies to the O-polysaccharide of *Brucella* lipopolysaccharide. The currently employed serodiagnosis of brucellosis relies on the use of the *Brucella* O-polysaccharide as a diagnostic antigen. However, the existence of bacterial species, which also express O-polysaccharides structurally similar to that of *Brucella*, may decrease the specificity of the brucellosis detection due to false-positive test results. It has been shown that the efficiency of the test can be significantly improved by using synthetic oligosaccharides that correspond to the so-called M epitope of the *Brucella* O-antigen. This epitope is characterized by an α -(1→3)-linkage between D-perosamine units and is unique to *Brucella*. Here we report on an efficient approach to the synthesis of oligosaccharides that model the M epitope of the *Brucella* O-polysaccharide. The approach is based on the use of the α -(1→3)-linked disaccharide thioglycoside as the key donor block. Its application allowed the straightforward assembly of a set of four protected oligosaccharides, which includes a disaccharide, two trisaccharides, and a tetrasaccharide, in five glycosylation steps. The synthesized oligosaccharides are planned to be used in the development of diagnostic tools for identifying brucellosis in humans and domestic animals, as well as a potential vaccine against it.

KEYWORDS

Brucella, lipopolysaccharide, O-polysaccharide, M epitope, 4-formamido, 4,6-dideoxy-D-mannose, oligosaccharides

Introduction

Brucellosis is a bacterial infection of domestic animals, including cattle, sheep, goats, pigs and others. It is caused by Gram-negative bacteria of the genus *Brucella*. The disease can lead to abortions, infertility, weight loss, and reduced productivity in infected animals. When humans come into contact with infected animals or their products, such as milk, contaminated meat or organs, they can become infected with brucellosis. This can lead to



serious acute and chronic illness with non-specific symptoms similar to malaria or influenza, and is therefore a significant public health concern (Franco et al., 2007).

One of the main virulence factors of *Brucella* is a lipopolysaccharide (LPS), which is located on the surface of the bacterial cell. The lipid part of LPS is embedded in the cell membrane, while the polysaccharide component (O-polysaccharide) extends outwards into the external environment, and thus determines the immunologic properties of the bacterium. O-Polysaccharide is a homopolymer of N-formylated 4-amino-4,6-dideoxy-D-mannose, also known as D-perosamine. N-Formyl-D-perosamine forms an α -(1 \rightarrow 2)-linked linear chain terminated with one or more tetrasaccharide units that contain two α -(1 \rightarrow 2)- and one central α -(1 \rightarrow 3)-glycosidic bonds (Figure 1) (Kubler-Kielb and Vinogradov, 2013). The O-polysaccharide chain has a relatively low molecular weight, with a maximum of 25–30 monosaccharide units (Kubler-Kielb and Vinogradov, 2013). The antigenic determinants, represented by the α -(1 \rightarrow 2)-linked chain and the terminal tetrasaccharide with the α -(1 \rightarrow 3)-bond, are referred to as the A epitope (prevails in most strains of *B. abortus*) and the M epitope (is characteristic of *B. melitensis*), respectively.

The detection of antibodies specific to the O-polysaccharide in animal and human sera is the basis for the diagnosis of brucellosis (Nielsen, 2002; Godfroid et al., 2010). However, this biopolymer is not readily available through bacterial cultivation. Although the chemical synthesis of polysaccharides is in principle possible (Kochetkov et al., 1987; Tsvetkov et al., 1989), this task is often too complex. It is important that the specificity of the serodiagnosis using *Brucella* O-polysaccharide as a diagnostic antigen may not be high enough, as there are some bacteria that have O-polysaccharides made up of N-acylated D-perosamine. A prominent example of these bacteria is *Yersinia enterocolitica* O:9. Its O-polysaccharide consists

of α -(1 \rightarrow 2)-linked N-formyl-D-perosamine units only (Caroff et al., 1984), and is structurally identical to the A epitope of *Brucella*. Another example is *Escherichia coli* O157, whose O-polysaccharide contains α -(1 \rightarrow 2)-linked N-acetyl-D-perosamine (Perry and Bundle, 1990). Sera obtained from animals or humans infected with such bacteria may contain antibodies that cross-react with the *Brucella* O-polysaccharide, leading to false-positive test results.

An increase in the specificity of the serodiagnosis of brucellosis can be achieved through the use of antigens related to the epitope M, which is unique to *Brucella* and is absent in the O-polysaccharides of other bacteria. It is evident that obtaining such antigens from the natural O-polysaccharide is challenging, if not impossible, and the most promising way to produce them is through chemical synthesis. Nowadays, synthetic oligosaccharides of virtually any structure are accessible and find application in immunological studies, including the development of diagnostic tools and vaccines, as a good alternative for antigenic polysaccharides (for recent examples see Argunov et al., 2015; Gening et al., 2015; Kazakova et al., 2020; Komarova et al., 2018; Krylov et al., 2019; Laverde et al., 2020; Solovov et al., 2023; Wong et al., 2020).

The use of synthetic oligosaccharides that mimic the M epitope of the *Brucella* O-polysaccharide for serodiagnosis has recently been investigated by Bundle et al. A large group of oligosaccharides with the characteristic for the M epitope (1 \rightarrow 3)-glycoside bond between N-formyl-D-perosamine residues, was synthesized (Guiard et al., 2013; Ganesh et al., 2014; Bundle and McGiven, 2017). BSA conjugates of these synthetic oligosaccharides, particularly the (1 \rightarrow 3)-linked disaccharide and the tetrasaccharide with the central (1 \rightarrow 3)-glycoside bond, have shown high diagnostic sensitivity and specificity, as well as the ability to reliably differentiate between the sera of infected animals and those that give false-positive results when tested using conventional methods (McGiven et al., 2015; Bundle and McGiven, 2017).

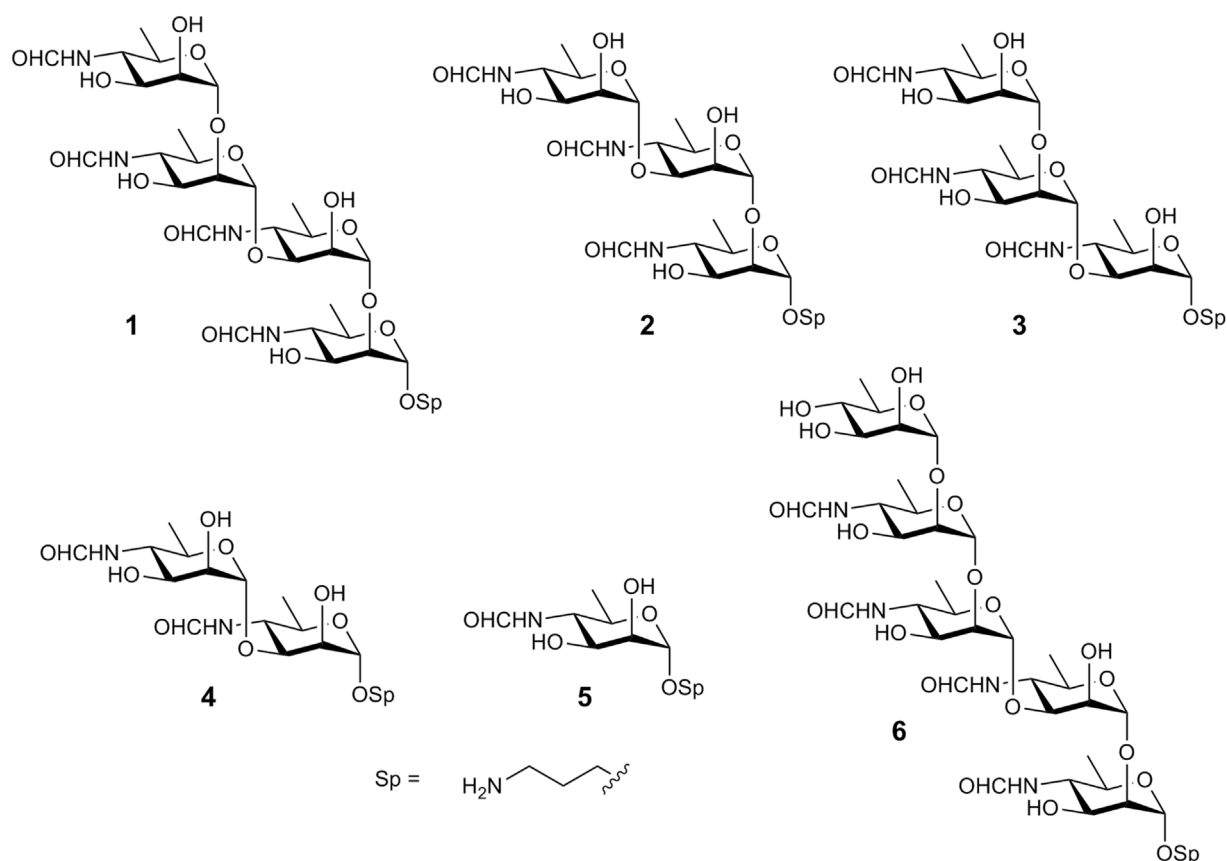


FIGURE 2
Oligosaccharides synthesized in this work.

However, the use of BSA as a carrier protein may carry risks of obtaining overestimated results. This is due to the presence in human sera of antibodies capable of recognizing BSA (Mogues et al., 2005; Sjöwall et al., 2011) and false-positive signals caused by multimeric presentation of glycoligands in the BSA conjugates (Grant et al., 2014; Temme et al., 2019). In addition, there may be a risk of non-specific interactions with hydrophobic spacers, for example, the 5-carboxypentyl spacer used in the works by Bundle et al. (Guiard et al., 2013; Ganesh et al., 2014; Mandal et al., 2017a; Mandal et al., 2017b; Bundle and McGiven, 2017).

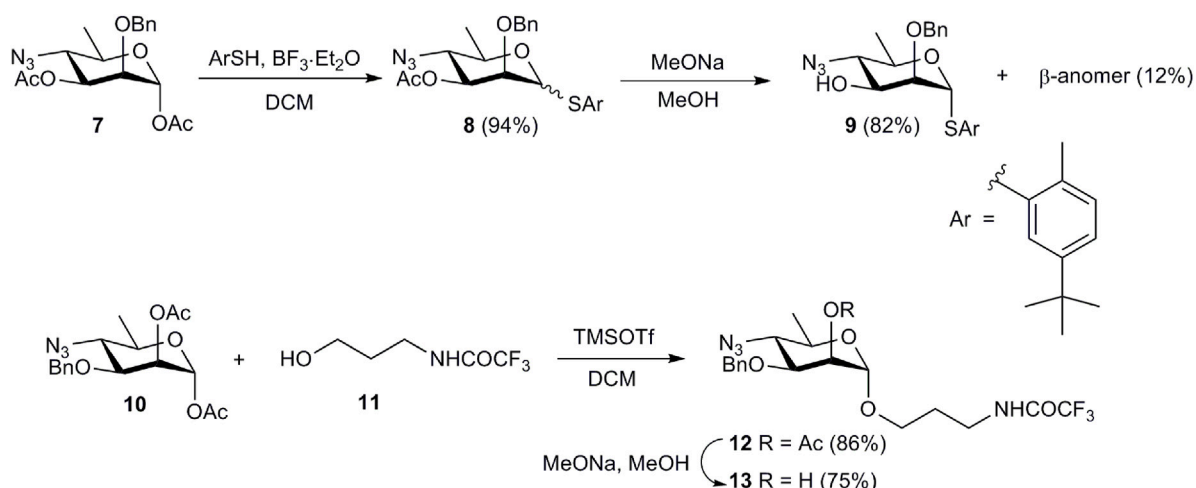
α -(1 \rightarrow 2)-Linked oligomers of N-(3-deoxy-L-glycero-tetronoyl)-D-perosamine related to the O-polysaccharide of *Vibrio cholerae* O1 have been synthesized by the Kováč's group (Hou and Kováč, 2010; Mukherjee et al., 2019). Recently, we reported the synthesis of the (1 \rightarrow 3)-linked disaccharide 4 (Figure 2) (Tsvetkov and Nifantiev, 2023), which corresponds to the unique structural element of the M epitope of the *Brucella* O-polysaccharide. Here, we report on the synthesis of larger oligosaccharides 1-3 that comprise the (1 \rightarrow 3)-linked disaccharide as a fragment. They were prepared with the aim of developing fluorescence polarization-based and other types of diagnostic assays to identify brucellosis in animals and humans and as potential ligands for the design of corresponding vaccines. Additionally, pentasaccharide 6 has been synthesized, representing tetrasaccharide 1 devoid of terminal unsubstituted D-perosamine through its capping with a D-rhamnose residue.

We have also prepared monosaccharide 5, as it has been reported that sera from mice immunized with conjugate immunogens based on (1 \rightarrow 2)-linked *Brucella* oligosaccharides and sera from naturally *Brucella*-infected cattle contained high titers of antibodies specific to the terminal D-perosamine unit (Mandal et al., 2017a; Duncombe et al., 2022). The synthesized compounds were equipped with a short 3-aminopropyl spacer group, which was thought to be less hydrophobic than the 5-carboxypentyl group used by Bundle et al. We hypothesized that the use of the 3-aminopropyl spacer would minimize hydrophobic interactions, which could interfere with antigen-antibody recognition processes.

Results and discussion

Oligosaccharides 1-4 were synthesized using a disaccharide (1 \rightarrow 3)-linked glycosyl donor 15 as the key synthetic block. This choice of the donor allowed the assembly of all four oligosaccharides in a straightforward manner. The synthesis of monosaccharide derivatives, which were used as glycosyl acceptors in the preparation of the target structures, is shown in Scheme 1.

Treatment of known 1,3-diacetate 7 (Mandal et al., 2017b) with 5-(*tert*-butyl)-2-methylthiophenol in the presence of $\text{BF}_3 \cdot \text{Et}_2\text{O}$ produced an inseparable mixture of α - and β -thioglycosides 8. After conventional deacetylation of 8, the anomers were



SCHEME 1
Preparation of monosaccharide acceptor blocks **9** and **13**.

separated and pure α -anomer **9** was isolated in 82% yield. Similarly, TMSOTf-promoted glycosylation of alcohol **11** with 1,2-diacetate **10** (Bundle et al., 1988) and subsequent deacetylation of glycoside **12** afforded glycosyl acceptor **13**.

Using acceptors **9** and **13**, and the known trichloroacetimidate **14** (Ariosa-Alvarez et al., 1998) as a glycosyl donor, all oligosaccharides were assembled in five glycosylation steps (Scheme 2).

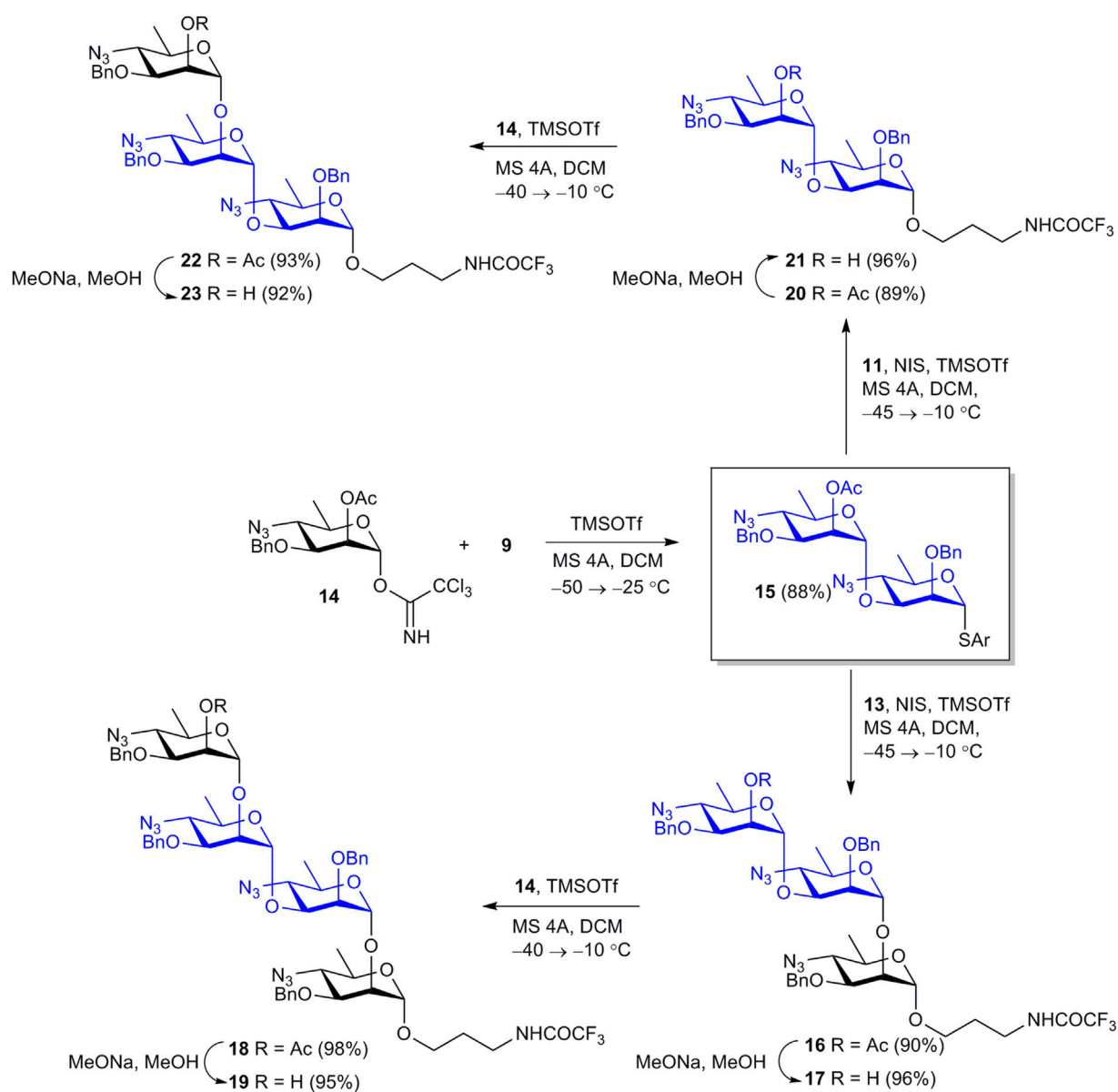
Orthogonal glycosylation of thioglycoside acceptor **9** with imidate **14** smoothly gave key intermediate **15** in 88% yield. Further NIS-TMSOTf-promoted glycosylation of acceptors **11** and **13** with thioglycoside **15** efficiently produced disaccharide **20** and trisaccharide **16**. The $^1J_{C-1,H-1}$ coupling constant values (170–172 Hz) for the 3-substituted monosaccharide residues in products **16** and **20** confirmed the α -configuration of the newly formed glycoside bonds (Bock and Pedersen, 1974). Despite the presence of a non-participating benzyl group at O-2, donor **15** ensured high α -stereoselectivity of glycosylation, in agreement with published data (Hou and Kovač, 2010). Removal of sole acetyl groups from **16** and **20** provided glycosyl acceptors **17** and **21** almost quantitatively. Final glycosylation of these acceptors with imidate **14** afforded tetrasaccharide **18** and trisaccharide **22** in excellent yields. Deacetylation of **18** and **22** gave alcohols **19** and **23**. The structure of protected oligosaccharides **15–23** was confirmed by data of fully assigned 1H and ^{13}C NMR spectra (see Supplementary Material) and high resolution MS.

Then oligosaccharides **17**, **19**, **21**, **23**, and monosaccharide **13** were transformed to final products **1–5**. The reaction sequence employed for this transformation included reduction of azide groups, N-formylation, hydrogenolytic debenzilation and removal of the N-trifluoroacetyl group. This sequence is shown in Scheme 3 in relation to disaccharide **21**. Intermediate products **24–26** on the way from **21** to unprotected **4** were characterized by high resolution mass-spectrometry. Each of the four protected compounds **13**, **17**, **19**, and **23** was processed similarly (for details see Supplementary Material).

As hydrogen sulfide applied by Bundle et al. for the reduction of azide moieties (Guiard et al., 2013; Ganesh et al., 2014; Mandal et al., 2017b; Bundle and McGiven, 2017) is toxic and has an unpleasant odor, we used catalytic hydrogenation over $Pd(OH)_2/C$ at this step instead. Thus, catalytic reduction of diazide **21** proceeded with only minor affecting benzyl protections (Ariosa-Alvarez et al., 1998) and provided, after chromatographic purification, diamine **24** in 81% yield. N-Formylation of the latter with formic anhydride generated *in situ* from formic acid and DCC produced bis(formamide) **25** (88%), which was subjected to catalytic debenzilation with the formation of triol **26** (92%). Final basic removal of the N-trifluoroacetyl group and purification by size-exclusion chromatography gave target 3-aminopropyl glycoside **4** in 87% yield.

E/Z-Isomerism of the formamido groups results in the existence of compounds **1–5** as mixtures of 2^n isomers, where n is the number of monosaccharides in the molecule (Peters et al., 1990). This strongly complicated the full assignment of NMR spectra, making it virtually impossible for oligosaccharides larger than the disaccharide. Nevertheless, the NMR data of **1–5** provided confirmation of the presence of the main functionalities such as formyl groups, anomeric centers, the spacer moiety, etc. (see Supplementary Material). Particularly, signals for *Z*- (δ_H 8.24–8.18 ppm; δ_C 166.1, 165.8 ppm) and *E*-isomers (δ_H 8.06–7.99 ppm; δ_C 169.0, 168.9 ppm) of the formyl groups, four anomeric centers of the prevailing isomer (δ_H 5.09, 5.02, 4.98, 4.92 ppm; δ_C 103.4, 102.9, 101.8; 99.6 ppm), and C-4 of *E*- (δ_C 58.2, 58.0, 57.9, 56.7 ppm) and *Z*-isomers (53.3, 53.1, 52.9, 52.1 ppm) were observed, *inter alia*, in the 1H and ^{13}C NMR spectra of tetrasaccharide **1**.

Pentasaccharide **6**, in which the D-perosamine chain is terminated by a D-rhamnose unit, was prepared from tetrasaccharide acceptor **19** (Scheme 4). This pentasaccharide was thought to lose the ability to be recognized by antibodies specific to the terminal unsubstituted D-perosamine residue (Mandal et al., 2017a). Thioglycoside **27**, which was used as the glycosyl donor, was synthesized by the reaction of known 1,2-diacetate **26** (Zhang et al.,



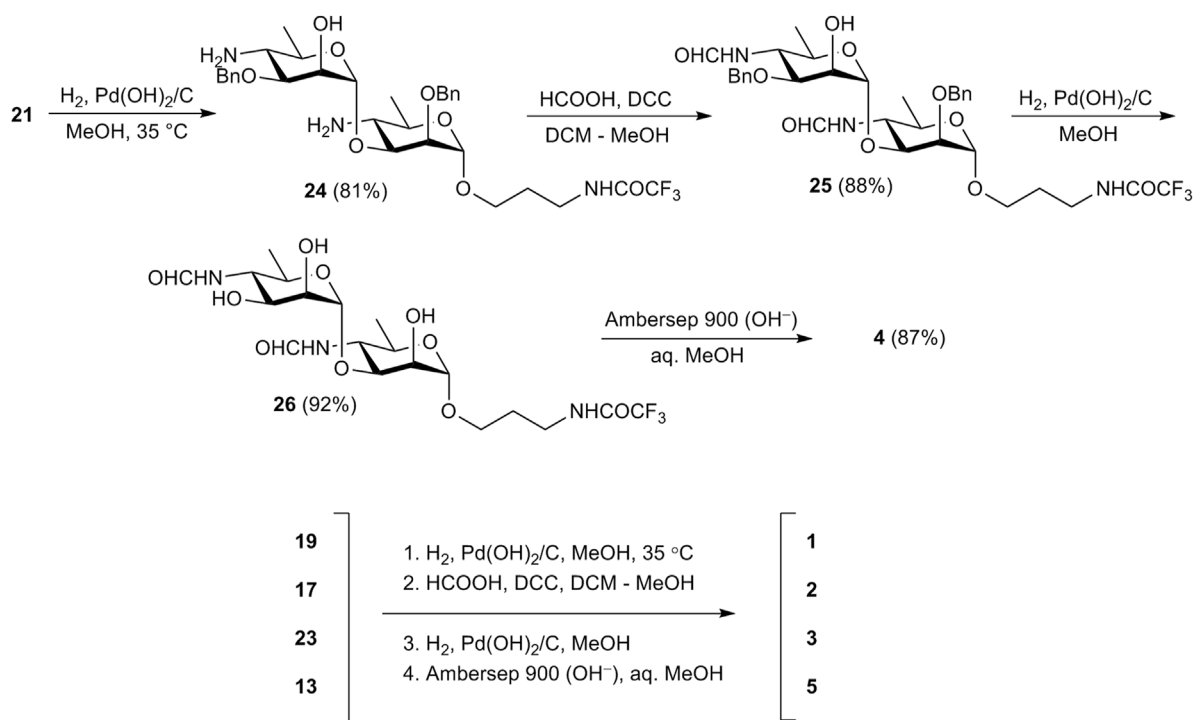
SCHEME 2
Assembly of protected oligosaccharides **16**, **18**, **20**, **22**.

2015) with 5-(*tert*-butyl)-2-methylthiophenol in the presence of $\text{BF}_3 \cdot \text{Et}_2\text{O}$. Following NIS-TMSOTf-promoted glycosylation of **19** with **27** produced pentasaccharide **28** in excellent yield. After deacetylation of **28**, product **29** was subjected to deprotection with the use of the common reaction sequence (Scheme 4) resulting in the formation of target pentasaccharide **6**.

Conclusion

In conclusion, an efficient approach to the synthesis of oligosaccharides related to the M epitope of the *Brucella* O-polysaccharide has been developed. The approach is based on the use of the (1→3)-linked disaccharide thioglycoside as the key donor block. This disaccharide donor mimics the unique structural

fragment of the M epitope with the (1→3)-linkage between two N-formyl-D-perosamine residues. Its application allowed the straightforward assembly of a set of four protected oligosaccharides, which comprised the disaccharide, two trisaccharides, and the tetrasaccharide, in five glycosylation steps. Following deprotection included reduction of azido groups, N-formylation, O-debenzylation, and de-N-trifluoroacetylation and produced free oligosaccharides as 3-aminopropyl glycosides. Using the partially protected tetrasaccharide as the glycosyl acceptor, the pentasaccharide devoid of terminal D-perosamine through its capping with a D-rhamnose residue has been also prepared. The synthesized oligosaccharides will be used for development of a diagnostic assay to identify brucellosis in animals and humans as well as the potential ligands to design vaccine candidates.



SCHEME 3
Synthesis of free mono-(5) and oligosaccharides (1–4).

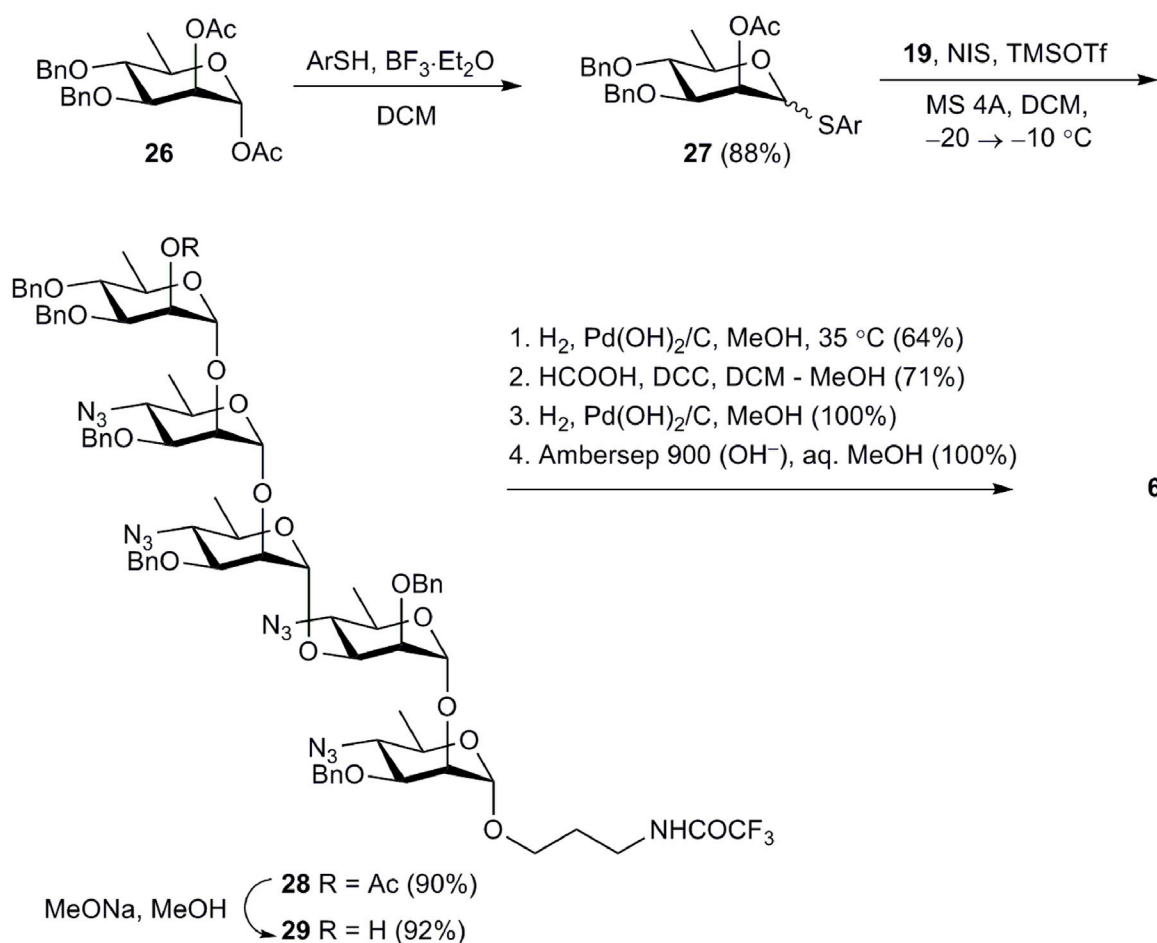
Experiment

General

NMR spectra were recorded on a Bruker Avance 600 NMR spectrometer. Protected oligosaccharides were measured in chloroform- d (CDCl_3), and ^1H NMR chemical shifts were referenced to the solvent residual signal (δ_{H} 7.27). ^{13}C chemical shifts were referenced to the central resonance of CDCl_3 (δ_{C} 77.0). Free oligosaccharides were measured in deuterium oxide (D_2O) with suppression of the HOD signal. Acetone (δ_{H} 2.225, δ_{C} 31.45) was used as an internal standard. Signal assignment was made using COSY, TOCSY, HSQC, and ROESY experiments. In the presentation of NMR data, monosaccharide residues in oligosaccharides are denoted by the capital letters (A, B, C, etc.) starting from the reducing end. NMR spectra of synthesized compounds are presented in the **Supplementary Material**. High-resolution mass spectrometry (HRMS) with electrospray ionization (ESI) was performed on a MicroTOF II (Bruker Daltonics) instrument. Optical rotations were measured using a JASCO P-2000 polarimeter at 20°C–25°C in chloroform (protected oligosaccharides) or water (free oligosaccharides). TLC was performed on Silica Gel 60 F_{254} plates (Merck) and visualization was accomplished using UV light or by charring at $\sim 150^\circ\text{C}$ with orcinol–phosphoric acid (180 mg of orcinol in a mixture of 85% H_3PO_4 (10 mL), ethanol (5 mL), and water (85 mL)). Column chromatography was carried out using Silica Gel 60 (40–63 μm ; Merck Millipore). Gel-permeation chromatography of free oligosaccharides was performed on a Toyopearl TSK HW-40(S) column (2.8 \times 80 cm) in 0.1 M acetic acid. A K-2401 refractive index

detector (Knauer) was used to monitor gel-permeation chromatography. All moisture-sensitive reactions were carried out using dry solvents under dry argon. Powdered molecular sieve 4 Å was activated at 300°C under vacuum (~ 1 mbar) for 30 min directly prior to the reaction. Solutions were concentrated under reduced pressure using a rotatory evaporator at 40°C (bath temperature).

5-(*tert*-Butyl)-2-methylphenyl 4-azido-2-O-benzyl-4,6-dideoxy-1-thio- α -D-mannopyranoside (9). $\text{BF}_3\cdot\text{Et}_2\text{O}$ (84 μL , 0.67 mmol) was added to a solution of 1,3-diacetate 7 (203 mg, 0.56 mmol) and 5-(*tert*-butyl)-2-methylthiophenol (153 μL , 0.84 mmol) in DCM (4 mL) upon chilling in an ice bath. The mixture was stirred for 10 min. with chilling and then at room temperature for 1.5 h. The resulting mixture was diluted with chloroform (50 mL), washed with water (30 mL) and saturated aqueous NaHCO_3 (30 mL). The solvent was evaporated and the residue was purified by column chromatography (petroleum ether–EtOAc, 0 \rightarrow 5%) to give thioglycoside 8 (255 mg, 94%) as a colorless syrup; α,β ratio $\sim 6.3:1$. ^1H NMR (600 MHz, CDCl_3): δ 7.62–7.13 (m, 9.3 H, Ar), 5.44 (s, 1 H, H-1 $_{\alpha}$), 5.15 (dd, 1 H, $J_{2,3} = 3.2$ Hz, $J_{3,4} = 10.4$ Hz, H-3 $_{\alpha}$), 4.91 (d, 0.16 H, $J = 11.8$ Hz, PhCHaHb_{β}), 4.84 (dd, 0.16 H, $J_{2,3} = 3.2$ Hz, $J_{3,4} = 10.2$ Hz, H-3 $_{\beta}$), 4.78 (d, 0.16 H, $J = 11.8$ Hz, PhCHaHb_{β}), 4.73 (s, 1 H, H-1 $_{\beta}$), 4.70 (d, 1 H, $J = 12.2$ Hz, PhCHaHb_{α}), 4.52 (d, 1 H, $J = 12.2$ Hz, PhCHaHb_{α}), 4.25 (d, 0.16 H, $J_{2,3} = 3.2$ Hz, H-2 $_{\beta}$), 4.16–4.11 (m, 2 H, H-2 $_{\alpha}$, H-5 $_{\alpha}$), 3.76–3.71 (m, 1.16 H, H-4 $_{\alpha}$, H-4 $_{\beta}$), 3.30 (dq, 0.16 H, $J_{5,6} = 6.3$ Hz, $J_{4,5} = 9.8$ Hz, H-5 $_{\beta}$), 2.38 (s, 0.5 H, Ar- CH_3_{β}), 2.36 (s, 3 H, Ar- CH_3_{α}), 2.10 (s, 3 H, $\text{CH}_3\text{CO}_{\alpha}$), 2.05 (s, 0.5 H, $\text{CH}_3\text{CO}_{\beta}$), 1.46 (d, 0.5 H, $J_{6,5} = 6.3$ Hz, H-6 $_{\beta}$), 1.40 (d, 3 H, $J_{6,5} = 6.1$ Hz, H-6 $_{\alpha}$), 1.32 (s, 10.4 H, Ar- $\text{C}(\text{CH}_3)_{\alpha\beta}$). ^{13}C NMR (150 MHz, CDCl_3): δ 169.9 (CH_3CO), 149.8, 137.2, 136.4,



SCHEME 4
Synthesis of pentasaccharide 6.

132.7, 130.0, 129.8, 129.4, 129.0, 128.5, 128.1, 128.0, 124.8 (Ar), 87.1 ($\text{C}-1_{\alpha}$), 84.8 ($\text{C}-1_{\beta}$), 77.6 ($\text{C}-2_{\beta}$), 76.4 ($\text{C}-2_{\alpha}$), 76.0 ($\text{PhCH}_2\beta$), 75.9 ($\text{C}-3_{\beta}$), 75.3 ($\text{C}-5_{\beta}$), 72.7 ($\text{C}-3_{\alpha}$), 72.5 ($\text{PhCH}_2\alpha$), 68.3 ($\text{C}-5_{\alpha}$), 62.9 ($\text{C}-4_{\alpha}$), 62.3 ($\text{C}-4_{\beta}$), 31.2 ($\text{C}(\text{CH}_3)_3$), 20.9 (CH_3CO), 20.2 ($\text{CH}_3\text{-Ar}$), 18.7 ($\text{C}-6_{\beta}$), 18.4 ($\text{C}-6_{\alpha}$).

1 M Sodium methoxide in MeOH (50 μL) was added to a solution of 3-acetate **8** (255 mg, 0.53 mmol) in MeOH (5 mL), and the mixture was stirred for 2 h at room temperature. The mixture was neutralized with Amberlite IR-120 (H^+), the resin was filtered off and washed with MeOH ($4 \times 4 \text{ mL}$), and the filtrate was concentrated. The residue was subjected to column chromatography (petroleum ether–EtOAc, 2→8%) to produce α -anomer **9** (192 mg, 82%) and β -anomer (29 mg, 12%).

α -Anomer **9**, colorless syrup, $[\alpha]_{\text{D}} +95$ (c 1, CHCl_3). ^1H NMR (600 MHz, CDCl_3): δ 7.56–7.16 (m, 8 H, Ar), 5.53 (s, 1 H, H-1), 4.77 (d, 1 H, $J = 11.8 \text{ Hz}$, PhCHaHb), 4.55 (d, 1 H, $J = 11.8 \text{ Hz}$, PhCHaHb), 4.07 (dq, 1 H, $J_{4,5} = 9.9 \text{ Hz}$, $J_{5,6} = 6.3 \text{ Hz}$, H-5), 4.02 (d, 1 H, $J_{2,3} = 3.7 \text{ Hz}$, H-2), 3.94 (dd, 1 H, $J_{2,3} = 3.7 \text{ Hz}$, $J_{3,4} = 9.8 \text{ Hz}$, H-3), 3.40 (t, 1 H, $J = 9.8 \text{ Hz}$, H-4), 2.37 (s, 3 H, Ar- CH_3), 1.37 (d, 3 H, $J_{6,5} = 6.3 \text{ Hz}$, H-6), 1.33 (s, 9 H, Ar- $\text{C}(\text{CH}_3)_3$). ^{13}C NMR (150 MHz, CDCl_3): δ 149.8, 136.9, 136.4, 132.6, 130.0, 129.6, 128.7, 128.3, 128.1, 125.0 (Ar), 84.3 (C-1), 78.9 (C-2), 72.3 (PhCH_2), 70.9 (C-3), 67.9 (C-5), 66.8 (C-4), 31.3 ($\text{C}(\text{CH}_3)_3$), 20.1 ($\text{CH}_3\text{-Ar}$), 18.3 (C-6). HRMS

(ESI): calcd. for $\text{C}_{24}\text{H}_{31}\text{N}_3\text{O}_3\text{S}$ $[\text{M} + \text{Na}]^+ m/z$ 464.1978; found m/z 464.1968.

β -Anomer, colorless syrup, $[\alpha]_{\text{D}} -96$ (c 0.5, CHCl_3). ^1H NMR (600 MHz, CDCl_3): δ 7.63–7.14 (m, 8 H, Ar), 5.16 (d, 1 H, $J = 11.5 \text{ Hz}$, PhCHaHb), 4.80 (d, 1 H, $J = 11.5 \text{ Hz}$, PhCHaHb), 4.72 (s, 1 H, H-1), 4.10 (d, 1 H, $J_{2,3} = 3.5 \text{ Hz}$, H-2), 3.61 (dd, 1 H, $J_{2,3} = 3.6 \text{ Hz}$, $J_{3,4} = 9.7 \text{ Hz}$, H-3), 3.35 (t, 1 H, $J = 9.8 \text{ Hz}$, H-4), 3.23 (dq, 1 H, $J_{4,5} = 9.8 \text{ Hz}$, $J_{5,6} = 6.3 \text{ Hz}$, H-5), 2.40 (s, 3 H, Ar- CH_3), 1.44 (d, 3 H, $J_{6,5} = 6.3 \text{ Hz}$, H-6), 1.33 (s, 9 H, Ar- $\text{C}(\text{CH}_3)_3$). ^{13}C NMR (150 MHz, CDCl_3): δ 149.6, 137.5, 135.7, 133.6, 129.8, 128.7, 128.5, 128.3, 128.1, 124.6 (Ar), 87.1 (C-1), 80.1 (C-2), 76.5 (PhCH_2), 75.2 (C-5), 74.3 (C-3), 66.2 (C-4), 31.3 ($\text{C}(\text{CH}_3)_3$), 20.2 ($\text{CH}_3\text{-Ar}$), 18.7 (C-6). HRMS (ESI): calcd. for $\text{C}_{24}\text{H}_{31}\text{N}_3\text{O}_3\text{S}$ $[\text{M} + \text{Na}]^+ m/z$ 464.1978; found m/z 464.1981.

3-Trifluoroacetamidopropyl 2-O-acetyl-4-azido-3-O-benzyl-4,6-dideoxy- α -D-mannopyranoside (12). TMSOTf (0.59 mL, 3.24 mmol) was added to a chilled (ice bath) solution of 1,2-diacetate **10** (906 mg, 2.49 mmol) and alcohol **11** (554 mg, 3.24 mmol) in DCM (15 mL). The mixture was stirred for 20 min. upon chilling and then 2.5 h at room temperature. After dilution with DCM (100 mL), the mixture was washed with saturated aqueous NaHCO_3 (50 mL) and water ($2 \times 50 \text{ mL}$), and concentrated. The residue was purified by column chromatography

(petroleum ether–EtOAc, 15→30%) to yield glycoside **12** (1.02 g, 86%) as a colorless syrup, $[\alpha]_D^{+88}$ (c 1, CHCl₃). ¹H NMR (600 MHz, CDCl₃): δ 7.39–7.29 (m, 5 H, Ar), 6.77 (br. s, 1 H, CF₃CONH), 5.32 (br. s, 1 H, H-2), 4.76 (s, 1 H, H-1), 4.68 (d, 1 H, J = 11.0 Hz, PhCHaHb), 4.54 (d, 1 H, J = 11.0 Hz, PhCHaHb), 3.82–3.78 (m, 1 H, OCHaHbCH₂CH₂N), 3.77 (dd, 1 H, $J_{2,3}$ = 3.3 Hz, $J_{3,4}$ = 9.8 Hz, H-3), 3.54–3.45 (m, 4 H, OCHaHbCH₂CH₂N, H-5), 3.44 (t, 1 H, J = 9.8 Hz, H-4), 2.14 (s, 3 H, CH₃CO), 1.96–1.84 (m, OCH₂CH₂CH₂N), 1.34 (d, 3 H, $J_{6,5}$ = 6.1 Hz, H-6). ¹³C NMR (150 MHz, CDCl₃): δ 170.2 (CH₃CO), 137.1, 128.4, 128.2, 128.0 (Ar), 97.9 (C-1), 76.2 (C-3), 71.7 (PhCH₂), 67.3 (C-2), 76.2 (C-5), 66.1 (OCH₂CH₂CH₂N), 63.8 (C-4), 38.1 (OCH₂CH₂CH₂N), 28.3 (OCH₂CH₂CH₂N), 20.9 (CH₃CO), 18.4 (C-6). HRMS (ESI): calcd. for C₂₀H₂₅F₃N₄O₆ [M + Na]⁺ m/z 497.1618; found m/z 497.1609.

3-Trifluoroacetamidopropyl 4-azido-3-O-benzyl-4,6-dideoxy- α -D-mannopyranoside (13). 1 M Sodium methoxide in MeOH (100 μ L) was added to a solution of 2-acetate **12** (1.02 g, 2.15 mmol) in MeOH (15 mL) and the mixture was stirred for 5 h at room temperature. Amberlite IR-120 (H⁺) was added until neutrality, the resin was filtered off and washed with MeOH (5 \times 4 mL), and the filtrate was concentrated. Column chromatography of the residue (toluene–EtOAc, 15→30%) provided compound **13** (700 mg, 75%) as a colorless syrup, $[\alpha]_D^{+104}$ (c 1, CHCl₃). ¹H NMR (600 MHz, CDCl₃): δ 7.43–7.33 (m, 5 H, Ar), 6.82 (br. s, 1 H, CF₃CONH), 4.83 (s, 1 H, H-1), 4.71 (d, 1 H, J = 11.0 Hz, PhCHaHb), 4.67 (d, 1 H, J = 11.0 Hz, PhCHaHb), 3.99 (br. s, 1 H, H-2), 3.85–3.80 (m, 1 H, OCHaHbCH₂CH₂N), 3.68 (dd, 1 H, $J_{2,3}$ = 3.3 Hz, $J_{3,4}$ = 9.3 Hz, H-3), 3.56–3.42 (m, 5 H, OCHaHbCH₂CH₂N, H-4, H-5), 2.58 (br. s, 1 H, OH), 1.94–1.83 (m, OCH₂CH₂CH₂N), 1.34 (d, 3 H, $J_{6,5}$ = 5.9 Hz, H-6). ¹³C NMR (150 MHz, CDCl₃): δ 137.1, 128.6, 128.2, 128.0 (Ar), 99.2 (C-1), 78.5 (C-3), 72.1 (PhCH₂), 67.1 (C-2), 67.0 (C-5), 66.3 (OCH₂CH₂CH₂N), 63.8 (C-4), 38.4 (OCH₂CH₂CH₂N), 28.2 (OCH₂CH₂CH₂N), 18.4 (C-6). HRMS (ESI): calcd. for C₁₈H₂₃F₃N₄O₅ [M + Na]⁺ m/z 455.1513; found m/z 455.1506.

4-(tert-Butyl)-2-methylphenyl 2-O-acetyl-4-azido-3-O-benzyl-4,6-dideoxy- α -D-mannopyranosyl-(1→3)-4-azido-2-O-benzyl-4,6-dideoxy-1-thio- α -D-mannopyranoside (15). A mixture of acceptor **9** (168 mg, 0.381 mmol), donor **14** (204 mg, 0.438 mmol) and mol. sieve 4 Å (400 mg) in DCM (6 mL) was stirred for 1.5 h at room temperature and cooled to –55°C. TMSOTf (16 μ L, 0.088 mmol) was added and the mixture was stirred for 30 min. at –55 \rightarrow –50°C. Then, over the next 30 min., the temperature was gradually increased to –25°C and the mixture was stirred at this temperature for another 30 min. The reaction was quenched by adding Et₃N (50 μ L), the mixture was diluted with chloroform (50 mL), the solids were filtered off through a Celite layer and washed with chloroform. The filtrate was washed with water (50 mL), and the solvent was evaporated. The residue was subjected to gel-permeation chromatography on a Bio-Beads S-X3 column (3.5 \times 70 cm) in toluene; fractions containing disaccharide **15** were pooled and concentrated. The product obtained was additionally purified by silica gel column chromatography (petroleum ether–EtOAc, 5→8%) to produce disaccharide **15** (251 mg, 88%) as a colorless syrup, $[\alpha]_D^{+129}$ (c 1, CHCl₃). ¹H NMR (600 MHz, CDCl₃): δ 7.52–7.14 (m, 13 H, Ar), 5.53 (br. s, 1 H, H-2^B), 5.48 (s, 1 H, H-1^A), 5.12 (s, 1 H, H-1^B), 4.72 (d, 1 H, J = 11.0 Hz, PhCHaHb), 4.68 (d, 1 H, J = 12.0 Hz, PhCHaHb'), 4.54 (d, 1 H, J = 11.0 Hz, PhCHaHb), 4.53 (d, 1 H, J = 12.0 Hz, PhCHaHb'), 4.04 (dq, 1 H, $J_{4,5}$ = 9.8 Hz, $J_{5,6}$ = 6.1 Hz, H-5^A), 4.01 (br. s, 1 H, H-2^A), 3.96

(dd, 1 H, $J_{2,3}$ = 3.0 Hz, $J_{3,4}$ = 10.0 Hz, H-3^A), 3.88 (dd, 1 H, $J_{2,3}$ = 3.2 Hz, $J_{3,4}$ = 9.8 Hz, H-3^B), 3.72 (t, 1 H, J = 9.8 Hz, H-4^A), 3.67 (dq, 1 H, $J_{4,5}$ = 10.2 Hz, $J_{5,6}$ = 6.3 Hz, H-5^B), 3.46 (t, 1 H, J = 10.0 Hz, H-4^B), 2.36 (s, 3 H, Ar-CH₃), 2.17 (s, 3 H, CH₃CO), 1.39 (d, 3 H, $J_{6,5}$ = 6.1 Hz, H-6^A), 1.32 (s, 9 H, Ar-C(CH₃)), 1.28 (d, 3 H, $J_{6,5}$ = 6.3 Hz, H-6^B). ¹³C NMR (150 MHz, CDCl₃): δ 170.0 (CH₃CO), 149.9, 137.2, 136.4, 132.6, 130.0, 129.4, 128.6, 128.4, 128.3, 128.0, 127.9, 127.5, 125.0 (Ar), 99.8 (C-1^B), 84.3 (C-1^A), 79.6 (C-3^A), 78.5 (C-2^A), 75.8 (C-3^B), 71.7, 71.5 (2 PhCH₂), 68.5 (C-5^A), 67.9 (C-5^B), 67.3 (C-2^B), 64.4 (C-4^A), 63.8 (C-4^B), 31.3 (C(CH₃)₃), 20.9 (CH₃CO), 20.2 (CH₃-Ar), 18.6 (C-6^B), 18.4 (C-6^A). HRMS (ESI): calcd. for C₃₉H₄₈N₆O₇S [M + NH₄]⁺ m/z 762.3643; found m/z 762.3636.

3-Trifluoroacetamidopropyl 2-O-acetyl-4-azido-3-O-benzyl-4,6-dideoxy- α -D-mannopyranosyl-(1→3)-4-azido-2-O-benzyl-4,6-dideoxy- α -D-mannopyranosyl-(1→2)-4-azido-3-O-benzyl-4,6-dideoxy- α -D-mannopyranoside (16). A mixture of donor **15** (251 mg, 0.337 mmol), acceptor **13** (132 mg, 0.306 mmol) and mol. sieve 4 Å (500 mg) in DCM (6 mL) was stirred for 1 h at room temperature, and then was cooled to –45°C. NIS (152 mg, 0.674 mmol) and TMSOTf (12 μ L) were added and the mixture was stirred for 1 h, gradually increasing the temperature to –10°C. The reaction was quenched by adding pyridine (50 μ L), the mixture was diluted with chloroform (10 mL), the mol. sieve was filtered off and washed with chloroform (4 \times 5 mL). The filtrate was washed with 0.5 M Na₂S₂O₃ solution (30 mL) and water (50 mL), and concentrated. Two consecutive column chromatographies (first in toluene–EtOAc (10→15%) and then in petroleum ether–EtOAc (15→25%)) resulted in trisaccharide **16** (273 mg, 90%) as a colorless foam, $[\alpha]_D^{+75}$ (c 1, CHCl₃). ¹H NMR (600 MHz, CDCl₃): δ 7.39–7.12 (m, 15 H, Ar), 6.68 (poorly resolved t, 1 H, NHCOCF₃), 5.49 (br. s, H-2^C), 5.08 (s, 1 H, H-1^B), 5.06 (br. s, 1 H, H-1^C), 4.72–4.68 (m, 3 H, H-1^A, PhCHaHb, PhCHaHb'), 4.57 (d, 1 H, J = 10.8 Hz, PhCHaHb), 4.50 (d, 1 H, J = 11.0 Hz, PhCHaHb'), 4.24 (d, 1 H, J = 11.8 Hz, PhCHaHb''), 4.15 (d, 1 H, J = 11.8 Hz, PhCHaHb''), 3.99 (br. s, 1 H, H-2^A), 3.90 (dd, 1 H, $J_{2,3}$ = 3.0 Hz, $J_{3,4}$ = 9.8 Hz, H-3^B), 3.82–3.78 (m, 2 H, H-3^C, OCHaHbCH₂CH₂N), 3.72–3.68 (m, 2 H, C-2^B, C-3^A), 3.61 (t, 1 H, J = 10.0 Hz, H-4^B), 3.58–3.43 (m, 6 H, H-5^A, H-5^B, H-5^C, OCHaHbCH₂CH₂N), 3.41 (t, 1 H, J = 9.8 Hz, H-4^C), 3.38 (t, 1 H, J = 10.0, H-4^A), 2.14 (s, 3 H, CH₃CO), 1.93–1.85 (m, 2 H, OCH₂CH₂CH₂N), 1.35 (d, 3 H, $J_{6,5}$ = 6.2 Hz, H-6^B), 1.34 (d, 3 H, $J_{6,5}$ = 6.3 Hz, H-6^A), 1.29 (d, 3 H, $J_{6,5}$ = 6.1 Hz, H-6^C). ¹³C NMR (150 MHz, CDCl₃): δ 170.0 (CH₃CO), 137.3, 137.2, 137.1, 128.5, 128.4, 128.3, 128.2, 128.0, 127.9, 127.8, 127.4, 99.6 (C-1^C), 99.1 (C-1^A), 98.2 (C-1^B), 78.4 (C-3^A), 78.3 (C-3^B), 76.2 (C-2^B), 75.8 (C-3^C), 72.9 (C-2^A), 72.5, 71.7, 71.5 (3 PhCH₂), 68.0 (C-5^B), 67.7 (C-5^C), 67.5 (C-5^A), 67.3 (C-2^C), 65.9 (OCH₂CH₂CH₂N), 64.4 (C-4^A), 64.1 (C-4^B), 63.7 (C-4^C), 38.1 (OCH₂CH₂CH₂N), 28.3 (OCH₂CH₂CH₂N), 20.9 (CH₃CO), 18.6, 18.5 (\times 2) (C-6^A, C-6^B, C-6^C). HRMS (ESI): calcd. for C₄₆H₅₅F₃N₁₀O₁₂ [M + NH₄]⁺ m/z 1014.4291; found m/z 1014.4291.

3-Trifluoroacetamidopropyl 4-azido-3-O-benzyl-4,6-dideoxy- α -D-mannopyranosyl-(1→3)-4-azido-2-O-benzyl-4,6-dideoxy- α -D-mannopyranosyl-(1→2)-4-azido-3-O-benzyl-4,6-dideoxy- α -D-mannopyranoside (17). 1 M sodium methoxide in MeOH (60 μ L) was added to a solution of monoacetate **16** (273 mg, 0.337 mmol) in MeOH (6 mL), and the mixture was stirred for 4 h at room temperature. The solution was made neutral by

adding Amberlite IR-120 (H^+), the resin was filtered off and washed with MeOH (4×4 mL). The filtrate was concentrated, and the residue was purified by column chromatography (toluene-EtOAc, 15→25%) to produce deacetylated trisaccharide **17** (250 mg, 96%) as a colorless foam, $[\alpha]_D +57$ (c 1, $CHCl_3$). 1H NMR (600 MHz, $CDCl_3$): δ 7.42–7.13 (m, 15 H, Ar), 6.70 (poorly resolved t, 1 H, $NHCOCF_3$), 5.11 (s, 1 H, $H-1^C$), 5.10 (s, 1 H, $H-1^B$), 4.74–4.65 (m, 4 H, $H-1^A$, $PhCH_2$, $PhCHaHb'$), 4.58 (d, 1 H, $J = 10.8$ Hz, $PhCHaHb'$), 4.23 (d, 1 H, $J = 11.8$ Hz, $PhCHaHb''$), 4.17 (br. s, 1 H, $H-2^C$), 4.13 (d, 1 H, $J = 11.8$ Hz, $PhCHaHb''$), 4.00 (br. s, 1 H, $H-2^A$), 3.92 (dd, 1 H, $J_{2,3} = 2.8$ Hz, $J_{3,4} = 9.6$ Hz, $H-3^B$), 3.82–3.78 (m, 1 H, $OCHaHbCH_2CH_2N$), 3.72–3.69 (m, 3 H, $H-2^B$, $H-3^A$, $H-3^C$), 3.60 (t, 1 H, $J = 9.8$ Hz, $H-4^B$), 3.58–3.44 (m, 6 H, $H-5^A$, $H-5^B$, $H-5^C$, $OCHaHbCH_2CH_2N$), 3.43 (t, 1 H, $J = 10.0$ Hz, $H-4^C$), 3.39 (t, 1 H, $J = 9.8$ Hz, $H-4^A$), 2.50 (s, 1 H, OH), 1.94–1.85 (m, 2 H, $OCH_2CH_2CH_2N$), 1.36–1.33 (m, 6 H, $H-6^A$, $H-6^B$), 1.20 (d, 3 H, $J_{6,5} = 6.1$ Hz, $H-6^C$). ^{13}C NMR (150 MHz, $CDCl_3$): δ 137.4, 137.2, 128.6, 128.5, 128.3, 128.2, 128.1, 128.0, 127.8, 127.4 (Ar), 101.2 ($C-1^C$), 99.1 ($C-1^A$), 98.2 ($C-1^B$), 78.5, 78.1 ($\times 2$) ($C-3^A$, $C-3^B$, $C-3^C$), 76.4 ($C-2^A$), 72.6, 71.9, 71.7 (3 $PhCH_2$), 68.0 ($C-5^B$), 67.5 ($C-5^A$), 67.4 ($C-5^C$), 67.2 ($C-2^C$), 65.9 ($OCH_2CH_2CH_2N$), 64.5 ($C-4^A$), 64.2 ($C-4^B$), 63.6 ($C-4^C$), 38.1 ($OCH_2CH_2CH_2N$), 28.3 ($OCH_2CH_2CH_2N$), 18.6, 18.5 ($C-6^A$, $C-6^B$), 18.4 ($C-6^C$). HRMS (ESI): calcd. for $C_{44}H_{53}F_3N_{10}O_{11}$ [$M + NH_4$] $^+$ m/z 972.4186; found m/z 972.4195.

3-Trifluoroacetamidopropyl 2-O-acetyl-4-azido-3-O-benzyl-4,6-dideoxy- α -D-mannopyranosyl-(1→2)-4-azido-3-O-benzyl-4,6-dideoxy- α -D-mannopyranosyl-(1→3)-4-azido-2-O-benzyl-4,6-dideoxy- α -D-mannopyranosyl-(1→2)-4-azido-3-O-benzyl-4,6-dideoxy- α -D-mannopyranoside (18). A mixture of imidate **14** (53 mg, 0.113 mmol), acceptor **17** (90 mg, 0.094 mmol) and mol. sieve 4 Å (200 mg) in DCM (2 mL) was stirred for 1 h at room temperature and cooled to $-40^\circ C$. TMSOTf (4.2 μ L, 23 μ mol) was added, and the mixture was stirred for 1.5 h, while the temperature was gradually increased to $-10^\circ C$. After adding Et_3N (20 μ L), the mixture was diluted with chloroform (10 mL), the solids were filtered off and washed with chloroform (4×4 mL). The filtrate was washed with 1 M HCl (10 mL), water (30 mL), and the solvent was evaporated. The residue was purified by column chromatography (petroleum ether-EtOAc, 20→25%) to give tetrasaccharide **18** (116 mg, 98%) as a colorless foam, $[\alpha]_D +59$ (c 1, $CHCl_3$). 1H NMR (600 MHz, $CDCl_3$): δ 7.40–7.25 (m, 20 H, Ar), 6.64 (poorly resolved t, 1 H, $NHCOCF_3$), 5.43 (br. s, 1 H, $H-2^D$), 5.09 (s, 1 H, $H-1^B$), 5.00 (s, 1 H, $H-1^C$), 4.90 (s, 1 H, $H-1^D$), 4.75–4.69 (m, 3 H, $H-1^A$, $PhCHaHb$, $PhCHaHb'$), 4.65 (d, 1 H, $J = 11.6$ Hz, $PhCHaHb''$), 4.62 (d, 1 H, $J = 11.6$ Hz, $PhCHaHb'''$), 4.57 (d, 1 H, $J = 11.2$ Hz, $PhCHaHb$), 4.55 (d, 1 H, $J = 11.8$ Hz, $PhCHaHb'$), 4.25 (d, 1 H, $J = 12.0$ Hz, $PhCHaHb''$), 4.15 (d, 1 H, $J = 12.0$ Hz, $PhCHaHb'''$), 4.05 (br. s, 1 H, $H-2^C$), 4.00 (br. s, 1 H, $H-2^A$), 3.85 (dd, 1 H, $J_{2,3} = 3.0$ Hz, $J_{3,4} = 9.4$ Hz, $H-3^B$), 3.82–3.78 (m, 2 H, $H-3^D$, $OCHaHbCH_2CH_2N$), 3.71 (dd, 1 H, $J_{2,3} = 3.0$ Hz, $J_{3,4} = 9.6$ Hz, $H-3^A$), 3.69 (dd, 1 H, $J_{2,3} = 3.0$ Hz, $J_{3,4} = 9.6$ Hz, $H-3^C$), 3.64–3.59 (m, 2 H, $H-2^B$, $H-5^D$), 3.59–3.52 (m, 2 H, $H-4^B$), $H-5^B$), 3.50–3.38 (m, 6 H, $H-4^D$, $H-5^A$, $H-5^C$, $OCHaHbCH_2CH_2N$), 3.36 (t, 1 H, $J = 10.0$ Hz, $H-4^A$), 3.35 (t, 1 H, $J = 10.0$ Hz, $H-4^C$), 2.09 (s, 3 H, CH_3CO), 1.93–1.85 (m, 2 H, $OCH_2CH_2CH_2N$), 1.35–1.32 (m, 9 H, $H-6^A$, $H-6^B$, $H-6^D$), 1.18 (d, 3 H, $J_{6,5} = 6.1$ Hz, $H-6^C$). ^{13}C NMR (150 MHz, $CDCl_3$): δ 169.7

(CH_3CO), 137.4, 137.3, 137.1, 128.6, 128.5, 128.4, 128.2, 128.0, 127.8, 127.5 (Ar), 100.7 ($C-1^C$), 99.4 ($C-1^D$), 99.1 ($C-1^A$), 98.3 ($C-1^B$), 78.4 ($C-3^A$), 77.5 ($C-3^C$), 77.3 ($C-3^B$), 76.3 ($C-2^B$), 75.5 ($C-3^D$), 73.3 ($C-2^C$), 72.8 ($C-2^A$), 72.5, 71.9, 71.8, 71.6 (4 $PhCH_2$), 68.0, ($C-5^B$), 67.8 ($C-5^C$), 67.7 ($C-5^D$), 67.5 ($C-5^A$), 67.1 ($C-2^D$), 65.9 ($OCH_2CH_2CH_2N$), 64.5 ($C-4^B$), 64.4 ($C-4^A$), 63.8 ($C-4^D$), 63.7 ($C-4^C$), 38.1 ($OCH_2CH_2CH_2N$), 28.4 ($OCH_2CH_2CH_2N$), 20.9 (CH_3CO), 18.5 ($\times 2$), 18.4 ($\times 2$) ($C-6^A$, $C-6^B$, $C-6^C$, $C-6^D$). HRMS (ESI): calcd. for $C_{59}H_{70}F_3N_{13}O_{15}$ [$M + NH_4$] $^+$ m/z 1275.5405; found m/z 1275.5399.

3-Trifluoroacetamidopropyl 4-azido-3-O-benzyl-4,6-dideoxy- α -D-mannopyranosyl-(1→2)-4-azido-3-O-benzyl-4,6-dideoxy- α -D-mannopyranosyl-(1→3)-4-azido-2-O-benzyl-4,6-dideoxy- α -D-mannopyranosyl-(1→2)-4-azido-3-O-benzyl-4,6-dideoxy- α -D-mannopyranoside (19). 1 M sodium methoxide (50 μ L) was added to a solution of compound **18** (298 mg, 0.237 mmol) in MeOH (5 mL), and the mixture was stirred for 4.5 h at room temperature. The solution was made neutral by adding Amberlite IR-120 (H^+), the resin was filtered off and washed with MeOH (4×4 mL). The filtrate was evaporated, and the residue was subjected to column chromatography (toluene-EtOAc, 10→25%) to produce deacetylated tetrasaccharide **19** (274 mg, 95%) as a colorless foam, $[\alpha]_D +73$ (c 1, $CHCl_3$). 1H NMR (600 MHz, $CDCl_3$): δ 7.43–7.26 (m, 20 H, Ar), 6.65 (br. s, 1 H, $NHCOCF_3$), 5.09 (s, 1 H, $H-1^B$), 5.03 (s, 1 H, $H-1^C$), 5.00 (s, 1 H, $H-1^D$), 4.74 (d, 1 H, $J = 11.2$ Hz, $PhCHaHb$), 4.72 (s, 1 H, $H-1^A$), 4.71 (d, 1 H, $J = 10.8$ Hz, $PhCHaHb'$), 4.69 (d, 1 H, $J = 11.2$ Hz, $PhCHaHb$), 4.63 (s, 2 H, $PhCH_2$), 4.68 (d, 1 H, $J = 10.8$ Hz, $PhCHaHb'$), 4.25 (d, 1 H, $J = 12.0$ Hz, $PhCHaHb'''$), 4.16 (d, 1 H, $J = 12.0$ Hz, $PhCHaHb''$), 4.09 (br. s, 1 H, $H-2^C$), 4.00 (br. s, 2 H, $H-2^A$, $H-2^D$), 3.86 (dd, 1 H, $J_{2,3} = 3.0$ Hz, $J_{3,4} = 9.5$ Hz, $H-3^B$), 3.83–3.78 (m, 1 H, $OCHaHbCH_2CH_2N$), 3.75–3.69 (m, 3 H, $H-3^A$, $H-3^C$, $H-3^D$), 3.66–3.60 (m, 2 H, $H-2^B$, $H-5^D$), 3.60–3.52 (m, 3 H, $H-4^B$, $H-5^B$, $OCHaHbCH_2CH_2N$), 3.51–3.39 (m, 5 H, $H-4^D$, $H-5^A$, $H-5^C$, $OCH_2CH_2CH_2N$), 3.37 (t, 1 H, $J = 10.0$ Hz, $H-4^A$), 3.32 (t, 1 H, $J = 9.8$ Hz, $H-4^C$), 2.32 (br. s, 1 H, OH), 1.94–1.86 (m, 2 H, $OCH_2CH_2CH_2N$), 1.36–1.33 (m, 9 H, $H-6^A$, $H-6^B$, $H-6^D$), 1.19 (d, 3 H, $J_{6,5} = 6.1$ Hz, $H-6^C$). ^{13}C NMR (150 MHz, $CDCl_3$): δ 137.4, 137.1, 128.6, 128.5, 128.4, 128.3, 128.2, 128.0, 127.8, 127.5 (Ar), 100.8 ($C-1^C$), 100.7 ($C-1^D$), 99.1 ($C-1^A$), 98.4 ($C-1^B$), 78.4 ($C-3^A$), 77.7, 77.6 ($C-3^C$, $C-3^D$), 77.4 ($C-3^B$), 76.3 ($C-2^B$), 73.3 ($C-2^C$), 72.8 ($C-2^A$), 72.5, 72.1, 72.0, 71.8 ($PhCH_2$), 68.1 ($C-5^B$), 67.9 ($C-5^C$), 67.5 ($C-5^A$), 67.4 ($C-5^D$), 67.1 ($C-2^D$), 65.9 ($OCH_2CH_2CH_2N$), 64.5 ($\times 2$) ($C-4^A$, $C-4^B$), 63.9 ($C-4^C$), 63.8 ($C-4^D$), 38.1 ($OCH_2CH_2CH_2N$), 28.4 ($OCH_2CH_2CH_2N$), 18.5 ($\times 3$), 18.4 ($C-6^A$, $C-6^B$, $C-6^C$, $C-6^D$). HRMS (ESI): calcd. for $C_{57}H_{68}F_3N_{13}O_{14}$ [$M + Na$] $^+$ m/z 1238.4853; found m/z 1238.4854.

3-Trifluoroacetamidopropyl 3-O-acetyl-4-azido-3-O-benzyl-4,6-dideoxy- α -D-mannopyranosyl-(1→3)-4-azido-2-O-benzyl-4,6-dideoxy- α -D-mannopyranoside (20). A mixture of thiglycoside **15** (220 mg, 0.295 mmol), alcohol **11** (76 mg, 0.444 mmol) and mol. sieve 4 Å in DCM (5 mL) was stirred for 1 h at room temperature and then cooled to $-45^\circ C$. NIS (132 mg, 0.587 mmol) and TMSOTf (22 μ L, 0.121 mmol) were added, and the mixture was stirred for 1 h with gradual increase of the temperature to $-10^\circ C$. Pyridine (50 μ L) was added, the

mixture was diluted with chloroform (10 mL), the solids were filtered off and washed with chloroform (4 × 4 mL). The filtrate was washed with 0.5 M Na₂S₂O₃ solution (30 mL) and water (50 mL), and concentrated. Column chromatography of the residue (petroleum ether–EtOAc, 20→30%) produced glycoside **20** (194 mg, 89%) as a colorless syrup, [α]_D +83 (c 1, CHCl₃). ¹H NMR (600 MHz, CDCl₃): δ 7.39–7.27 (m, 10 H, Ar), 6.57 (br. s, 1 H, NHCOCF₃), 5.48 (br. s, 1 H, H-2^B), 5.04 (s, 1 H, H-1^B), 4.78 (s, 1 H, H-1^A), 4.70 (d, 1 H, *J* = 11.2 Hz, PhCHaHb), 4.65 (d, 1 H, *J* = 11.8 Hz, PhCHaHb'), 4.60 (d, 1 H, *J* = 11.8 Hz, PhCHaHb'), 4.53 (d, 1 H, *J* = 11.2 Hz, PhCHaHb), 3.86 (dd, 1 H, *J*_{2,3} = 3.2 Hz, *J*_{3,4} = 9.8 Hz, H-3^B), 3.83 (dd, 1 H, *J*_{2,3} = 3.2 Hz, *J*_{3,4} = 10.2 Hz, H-3^A), 3.78–3.74 (m, 1 H, OCHaHbCH₂CH₂N), 3.71 (br. s, 1 H, H-2^A), 3.69 (dq, 1 H, *J*_{4,5} = 10.0 Hz, *J*_{5,6} = 6.1 Hz, H-5^B), 3.62 (t, 1 H, *J* = 10.0 Hz, H-4^A), 3.53–3.38 (m, 5 H, H-4^B, H-5^A, OCHaHbCH₂CH₂N), 2.14 (s, 3 H, CH₃CO), 1.88–1.83 (m, 2 H, OCH₂CH₂CH₂N), 1.35 (d, 3 H, *J*_{6,5} = 6.1 Hz, H-6^A), 1.27 (d, 3 H, *J*_{6,5} = 6.1 Hz, H-6^B). ¹³C NMR (150 MHz, CDCl₃): δ 170.1 (CH₃CO), 137.5, 137.2, 128.5, 128.4, 128.3, 128.0, 127.9, 127.5 (Ar), 99.7 (C-1^B), 97.2 (C-1^A), 79.2 (C-3^A), 76.5 (C-2^A), 75.8 (C-3^B), 72.6, 71.5 (2 PhCH₂), 67.9 (C-5^B), 67.6 (C-5^A), 67.4 (C-2^B), 65.7 (OCH₂CH₂CH₂N), 64.2 (C-4^A), 63.8 (C-4^B), 37.9 (OCH₂CH₂CH₂N), 28.4 (OCH₂CH₂CH₂N), 20.9 (CH₃CO), 18.6 (C-6^B), 18.5 (C-6^A). HRMS (ESI): calcd. for C₃₃H₄₀F₃N₇O₉ [M + Na]⁺ *m/z* 758.2732; found *m/z* 758.2732.

3-Trifluoroacetamidopropyl 4-azido-3-O-benzyl-4,6-dideoxy-α-D-mannopyranosyl-(1→3)-4-azido-2-O-benzyl-4,6-dideoxy-α-D-mannopyranoside (21). 1 M sodium methoxide (25 μL) was added to a solution of compound **20** (77 mg, 0.105 mmol) in MeOH (2.5 mL), and the mixture was stirred for 3 h at room temperature. The solution was made neutral by adding Amberlite IR-120 (H⁺), the resin was filtered off and washed with MeOH (4 × 4 mL). The filtrate was evaporated, and the residue was subjected to column chromatography (toluene–EtOAc, 15→25%) to give deacetylated product **21** (70 mg, 96%) as a colorless syrup, [α]_D +89 (c 1, CHCl₃). ¹H NMR (600 MHz, CDCl₃): δ 7.43–7.32 (m, 10 H, Ar), 6.60 (br. s, 1 H, NHCOCF₃), 5.09 (s, 1 H, H-1^B), 4.80 (s, 1 H, H-1^A), 4.70 (d, 1 H, *J* = 11.6 Hz, PhCHaHb), 4.68 (d, 1 H, *J* = 11.6 Hz, PhCHaHb), 4.67 (d, 1 H, *J* = 11.6 Hz, PhCHaHb'), 4.60 (d, 1 H, *J* = 11.6 Hz, PhCHaHb'), 4.19 (br. s, 1 H, H-2^B), 3.84 (dd, 1 H, *J*_{2,3} = 3.2 Hz, *J*_{3,4} = 10.0 Hz, H-3^A), 3.79–3.74 (m, 2 H, H-3^B, OCHaHbCH₂CH₂N), 3.72 (br. s, 1 H, H-2^A), 3.68 (dq, 1 H, *J*_{4,5} = 10.0 Hz, *J*_{5,6} = 6.3 Hz, H-5^B), 3.60 (t, 1 H, *J* = 10.2 Hz, H-4^A), 3.52–3.40 (m, 5 H, H-4^B, H-5^A, OCHaHbCH₂CH₂N), 2.49 (s, 1 H, OH), 1.89–1.84 (m, 2 H, OCH₂CH₂CH₂N), 1.35 (d, 3 H, *J*_{6,5} = 6.3 Hz, H-6^A), 1.28 (d, 3 H, *J*_{6,5} = 6.3 Hz, H-6^B). ¹³C NMR (150 MHz, CDCl₃): δ 137.5, 137.2, 128.6, 128.5, 128.2, 128.1, 128.0, 127.5 (Ar), 101.4 (C-1^B), 97.2 (C-1^A), 78.9 (C-3^A), 78.0 (C-3^B), 76.8 (C-2^A), 72.6, 71.9 (2 PhCH₂), 67.5 (×2) (C-5^A, C-5^B), 67.2 (C-2^B), 65.7 (OCH₂CH₂CH₂N), 64.3 (C-4^A), 63.7 (C-4^B), 37.9 (OCH₂CH₂CH₂N), 28.4 (OCH₂CH₂CH₂N), 18.5 (×2) (C-6^A, C-6^B). HRMS (ESI): calcd. for C₃₁H₃₈F₃N₇O₈ [M + Na]⁺ *m/z* 716.2626; found *m/z* 716.2628.

3-Trifluoroacetamidopropyl 2-O-acetyl-4-azido-3-O-benzyl-4,6-dideoxy-α-D-mannopyranosyl-(1→2)-4-azido-3-O-benzyl-4,6-dideoxy-α-D-mannopyranosyl-(1→3)-4-azido-2-O-benzyl-4,6-dideoxy-α-D-mannopyranoside (22). Mol. sieve 4 Å

(500 mg) was added to a solution of imidate **14** (150 mg, 0.32 mmol) and acceptor **21** (195 mg, 0.28 mmol) in DCM (5 mL), the resulting mixture was stirred for 1 h at room temperature, and then cooled to –40°C. TMSOTf (11.6 μL, 0.064 mmol) was added, and the mixture was stirred for 1 h with gradual increasing the temperature to –10°C, after which the reaction was quenched with Et₃N (20 μL). The mixture was diluted with chloroform (10 mL), and the solids were filtered off and washed with chloroform (4 × 4 mL). The filtrate was washed with 1 M HCl (20 mL) and water (30 mL), and the solvent was evaporated. The residue was purified by column chromatography (petroleum ether–EtOAc, 20→30%) to yield trisaccharide **22** (260 mg, 93%) as a colorless foam, [α]_D +70 (c 1, CHCl₃). ¹H NMR (600 MHz, CDCl₃): δ 7.40–7.27 (m, 15 H, Ar), 6.55 (poorly resolved t, 1 H, NHCOCF₃), 5.44 (br. s, 1 H, H-2^C), 5.00 (s, 1 H, H-1^B), 4.92 (s, 1 H, H-1^C), 4.79 (s, 1 H, H-1^A), 4.74 (d, 1 H, *J* = 11.0 Hz, PhCHaHb), 4.68 (d, 1 H, *J* = 11.6 Hz, PhCHaHb'), 4.65 (d, 1 H, *J* = 11.8 Hz, PhCHaHb''), 4.64 (d, 1 H, *J* = 11.6 Hz, PhCHaHb'), 4.60 (d, 1 H, *J* = 11.8 Hz, PhCHaHb''), 4.55 (d, 1 H, *J* = 11.0 Hz, PhCHaHb), 4.07 (br. s, 1 H, H-2^B), 3.81–3.74 (m, 4 H, H-3^A, H-3^B, H-3^C, OCHaHbCH₂CH₂N), 3.65 (br. s, 1 H, H-2^A), 3.62–3.54 (m, 3 H, H-4^A, H-5^B, H-5^C), 3.53–3.40 (m, 5 H, H-4^C, H-5^A, OCHaHbCH₂CH₂N), 3.38 (t, 1 H, *J* = 9.8 Hz, H-4^B), 2.10 (s, 3 H, CH₃CO), 1.89–1.84 (m, 2 H, OCH₂CH₂CH₂N), 1.35 (d, 3 H, *J*_{6,5} = 6.3 Hz, H-6^A), 1.33 (d, 3 H, *J*_{6,5} = 6.1 Hz, H-6^C), 1.26 (d, 3 H, *J*_{6,5} = 6.1 Hz, H-6^B). ¹³C NMR (150 MHz, CDCl₃): δ 169.8 (CH₃CO), 137.4, 137.1, 128.6, 128.5, 128.4, 128.0, 127.9, 127.6 (Ar), 101.0 (C-1^B), 99.3 (C-1^C), 97.4 (C-1^A), 78.2 (C-3^A), 77.4 (C-3^B), 76.7 (C-2^A), 75.4 (C-3^C), 73.2 (C-2^B), 72.7, 71.9, 71.6 (3 PhCH₂), 68.0 (C-5^B), 67.7 (C-5^C), 67.6 (C-5^A), 67.1 (C-2^C), 65.7 (OCH₂CH₂CH₂N), 64.7 (C-4^A), 63.8 (×2) (C-4^B, C-4^C), 37.8 (OCH₂CH₂CH₂N), 28.4 (OCH₂CH₂CH₂N), 18.6, 18.5, 18.4 (C-6^A, C-6^B, C-6^C). HRMS (ESI): calcd. for C₄₆H₅₅F₃N₁₀O₁₂ [M + Na]⁺ *m/z* 1019.3845; found *m/z* 1019.3846.

3-Trifluoroacetamidopropyl 4-azido-3-O-benzyl-4,6-dideoxy-α-D-mannopyranosyl-(1→2)-4-azido-3-O-benzyl-4,6-dideoxy-α-D-mannopyranosyl-(1→3)-4-azido-2-O-benzyl-4,6-dideoxy-α-D-mannopyranoside (23). 1 M sodium methoxide (70 μL) was added to a solution of compound **22** (347 mg, 0.348 mmol) in MeOH (7 mL). After being stirred for 4 h at room temperature, the mixture was made neutral with Amberlite IR-120 (H⁺) and the resin was filtered off and washed with MeOH (4 × 4 mL). The filtrate was concentrated, and the residue was purified by column chromatography (toluene–EtOAc, 10→20%) to afford deacetylated trisaccharide **23** (306 mg, 92%) as a colorless foam, [α]_D +86 (c 1, CHCl₃). ¹H NMR (600 MHz, CDCl₃): δ 7.43–7.30 (m, 15 H, Ar), 6.58 (poorly resolved t, 1 H, NHCOCF₃), 5.03 (s, 1 H, H-1^B), 5.01 (s, 1 H, H-1^C), 4.79 (s, 1 H, H-1^A), 4.74 (d, 1 H, *J* = 11.2 Hz, PhCHaHb), 4.70 (d, 1 H, *J* = 11.2 Hz, PhCHaHb), 4.65 (s, 2 H, PhCH₂'), 4.65 (d, 1 H, *J* = 11.8 Hz, PhCHaHb''), 4.61 (d, 1 H, *J* = 11.8 Hz, PhCHaHb''), 4.12 (br. s, 1 H, H-2^B), 4.01 (s, 1 H, H-2^C), 3.81–3.74 (m, 3 H, H-3^A, H-3^B, OCHaHbCH₂CH₂N), 3.73 (dd, 1 H, *J*_{2,3} = 3.2 Hz, *J*_{3,4} = 9.8 Hz, H-3^C), 3.66 (br. s, 1 H, H-2^A), 3.64–3.55 (m, 3 H, H-4^A, H-5^B, H-5^C), 3.54–3.40 (m, 5 H, H-4^C, H-5^A, OCHaHbCH₂CH₂N), 3.36 (t, 1 H, *J* = 9.8 Hz, H-4^B), 2.35 (br. s, 1 H, OH), 1.90–1.84 (m, 2 H, OCH₂CH₂CH₂N), 1.36 (d, 3 H, *J*_{6,5} = 6.1 Hz, H-6^A), 1.34 (d, 3 H, *J*_{6,5} = 6.1 Hz, H-6^C), 1.27 (d, 3 H, *J*_{6,5} = 6.3 Hz,

H-6^B). ¹³C NMR (150 MHz, CDCl₃): δ 137.4, 137.3, 137.1, 128.6, 128.5, 128.3, 128.2, 128.0, 127.6 (Ar), 101.1 (C-1^B), 100.7 (C-1^C), 97.4 (C-1^A), 78.2 (C-3^A), 77.6 (C-3^C), 77.5 (C-3^B), 76.7 (C-2^A), 73.2 (C-2^B), 72.7, 72.0 (×2) (3 PhCH₂), 67.9 (C-5^B), 67.6 (C-5^A), 67.4 (C-5^C), 67.1 (C-2^C), 65.7 (OCH₂CH₂CH₂N), 64.7 (C-4^A), 64.0 (C-4^B), 63.8 (C-4^C), 37.9 (OCH₂CH₂CH₂N), 28.4 (OCH₂CH₂CH₂N), 18.6 (C-6^B), 18.5 (C-6^A), 18.3 (C-6^C). HRMS (ESI): calcd. for C₄₄H₅₃F₃N₁₀O₁₁ [M + NH₄]⁺ *m/z* 972.4186; found *m/z* 972.4170.

5-(*tert*-Butyl)-2-methylphenyl 2-O-acetyl-3,4-di-O-benzyl-1-thio-α,β-D-rhamnopyranoside (27). BF₃·Et₂O (68 μL, 0.55 mmol) was added to a chilled (ice bath) solution of 1,2-diacetate **27** (195 mg, 0.455 mmol) and 5-(*tert*-butyl)-2-methylthiophenol in DCM (4 mL). The mixture was stirred for 15 min., then the cooling bath was removed and stirring was continued at room temperature for next 2 h. The mixture was diluted with chloroform (30 mL), washed with water (30 mL) and saturated NaHCO₃ solution, and concentrated. Column chromatography of the residue (petroleum ether–EtOAc, 0→10%) produced an anomeric mixture (α:β ratio ~1.3:1) of thiglycosides **27** (219 mg, 88%) as a colorless syrup. ¹H NMR (600 MHz, CDCl₃): δ 7.67–7.13 (m, 30 H, Ar), 5.84 (d, 1H, *J*_{2,3} = 3.2 Hz, H-2_β), 5.68 (br. s, 1.3 H, H-2_α), 5.37 (s, 1.3 H, H-1_α), 4.97 (d, 1.3 H, *J* = 11.0 Hz, PhCHaHb_α), 4.95 (d, 1 H, *J* = 11.0 Hz, PhCHaHb_β), 4.84 (d, 1 H, *J* = 11.0 Hz, PhCHaHb_α'), 4.81 (s, 1 H, H-1_β), 4.77 (d, 1.3 H, *J* = 11.2 Hz, PhCHaHb_α'), 4.67 (d, 1.3 H, *J* = 11.0 Hz, PhCHaHb_β'), 4.65 (d, 1 H, *J* = 11.0 Hz, PhCHaHb_β'), 4.61 (d, 1.3 H, *J* = 11.2 Hz, PhCHaHb_α'), 4.53 (d, 1 H, *J* = 11.0 Hz, PhCHaHb_β'), 4.32 (dq, 1.3 H, *J*_{4,5} = 9.4 Hz, H-5_α), 4.00 (dd, 1.3 H, *J*_{2,3} = 3.2 Hz, *J*_{3,4} = 9.4 Hz, H-3_α), 3.68 (dd, 1 H, *J*_{3,4} = 8.7 Hz, H-3_β), 3.55 (t, 1.3 H, *J* = 9.4 Hz, H-4_α), 3.51 (t, 1 H, *J* = 9.2 Hz, H-4_β), 3.49 (dq, 1 H, *J*_{4,5} = 9.2 Hz, H-5_β), 2.42 (s, 4 H, CH₃-Ar_α), 2.39 (s, 3 H, CH₃-Ar_β), 2.28 (s, 3 H, CH₃CO_β), 2.18 (s, 4 H, CH₃CO_α), 1.49 (d, 3 H, *J*_{5,6} = 5.7 Hz, H-6_β), 1.38 (d, 3 H, *J*_{5,6} = 6.1 Hz, H-6_α), 1.33 (s, 21 H, C(CH₃)₃). ¹³C NMR (150 MHz, CDCl₃): δ 170.4, 170.3 (CH₃CO), 149.7, 149.6, 138.4, 138.2, 137.7, 137.6, 136.7, 135.8, 133.2, 132.6, 130.0, 129.8, 128.4, 128.3, 128.1, 128.0, 127.8, 127.7, 125.0, 124.5 (Ar), 85.8 (C-1_α), 84.8 (C-1_β), 81.3 (C-3_β), 80.2 (C-4_α), 79.3 (C-4_β), 78.5 (C-3_α), 76.1 (C-5_β), 75.5, 71.9, 71.8 (PhCH₂), 70.9 (C-2_α), 70.7 (C-2_β), 69.1 (C-5_α), 31.3 (C(CH₃)₃), 21.1 (CH₃CO_α), 20.9 (CH₃CO_β), 20.2 (CH₃-Ar), 18.3 (C-6_β), 17.9 (C-6_α). HRMS (ESI): calcd. for C₃₃H₄₀O₅S [M + Na]⁺ *m/z* 571.2489; found *m/z* 571.2482.

3-Trifluoroacetamidopropyl 2-O-acetyl-3,4-di-O-benzyl-α-D-rhamnopyranosyl-(1→2)-4-azido-3-O-benzyl-4,6-dideoxy-α-D-mannopyranosyl-(1→2)-4-azido-3-O-benzyl-4,6-dideoxy-α-D-mannopyranosyl-(1→3)-4-azido-2-O-benzyl-4,6-dideoxy-α-D-mannopyranosyl-(1→2)-4-azido-3-O-benzyl-4,6-dideoxy-α-D-mannopyranoside (28). A mixture of thiglycoside **27** (58 mg, 0.106 mmol), acceptor **19** (103 mg, 0.085 mmol) and vol. sieve 4 Å (150 mg) in DCM (3 mL) was for 1 h at room temperature and then cooled to –20°C. NIS (48 mg, 0.212 mmol) and TMSOTf (3.8 μL, 0.021 mmol) were added, and stirring was continued for 1 h at –20°C. The reaction was quenched with pyridine (20 μL), the mixture was diluted with chloroform (10 mL), and the solids were filtered off and washed with chloroform (4 × 4 mL). The filtrate was washed with 0.5 M Na₂S₂O₃ solution (20 mL) and water (30 mL), and concentrated. Column chromatography of the residue

(toluene–EtOAc, 8→13%) produced pentasaccharide **28** (121 mg, 90%) as a colorless foam, [α]_D +49 (c 1, CHCl₃). ¹H NMR (600 MHz, CDCl₃): δ 7.42–7.22 (m, 30 H, Ar), 6.66 (poorly resolved t, 1 H, NHCOCF₃), 5.46 (br. s, 1 H, H-2^E), 5.08 (s, 1 H, H-1^B), 5.04 (s, 1 H, H-1^D), 4.99 (s, 1 H, H-1^C), 4.90 (d, 1 H, *J* = 10.8 Hz, benzylic H), 4.85 (s, 1 H, H-1^E), 4.76–4.51 (m, 10 H, 9 benzylic H, H-1^A), 4.23 (d, 1 H, *J* = 11.8 Hz, PhCHaHb), 4.15 (d, 1 H, *J* = 11.8 Hz, PhCHaHb), 4.03 (br. s, 1 H, H-2^C), 4.00 (br. s, 1 H, H-2^A), 3.94–3.90 (m, 2 H, H-2^D, H-3^E), 3.85 (dd, 1 H, *J*_{3,2} = 2.8 Hz, *J*_{3,4} = 9.4 Hz, H-3^B), 3.83–3.78 (m, 1 H, OCHaHbCH₂CH₂N), 3.78–3.69 (m, 3 H, H-3^A, H-3^D, H-5^E), 3.66 (dd, 1 H, *J*_{3,2} = 2.8 Hz, *J*_{3,4} = 10.0 Hz, H-3^C), 3.61 (br. s, 1 H, H-2^B), 3.59–3.52 (m, 4 H, H-4^B, H-5^B, H-5^D, OCH₂CH₂CHaHbN), 3.51–3.32 (m, 7 H, H-4^A, H-4^D, H-4^E, H-5^A, H-5^C, OCHaHbCH₂CH₂N, OCH₂CH₂CHaHbN), 3.25 (t, 1 H, *J* = 9.8 Hz, H-4^C), 2.14 (s, 3 H, CH₃CO), 1.93–1.88 (m, 2 H, OCH₂CH₂CH₂N), 1.36–1.33 (m, 6 H, H-6^A, H-6^D), 1.31 (d, 3 H, *J*_{6,5} = 6.1 Hz, H-6^B), 1.22 (d, 3 H, *J*_{6,5} = 6.3 Hz, H-6^E), 1.17 (d, 3 H, *J*_{6,5} = 6.3 Hz, H-6^C). ¹³C NMR (150 MHz, CDCl₃): δ 169.9 (CH₃CO), 138.4, 137.0, 137.5, 137.3, 137.1, 128.6, 128.5, 128.4, 128.3, 128.2, 128.1, 128.0, 127.9, 127.8, 127.7, 127.6, 127.5 (Ar), 100.8 (C-1^C), 100.5 (C-1^D), 99.3 (C-1^E), 99.1 (C-1^A), 98.4 (C-1^B), 79.9 (C-4^E), 78.4 (C-3^A), 77.5 (C-3^E), 77.2 (C-3^B), 77.1 (C-3^C), 76.9 (C-3^D), 76.2 (C-2^B), 75.4 (PhCH₂), 72.8 (C-2^A), 72.5 (PhCH₂), 71.9, 71.8 (×2), 71.7 (4 PhCH₂), 68.8 (C-2^E), 68.1, 67.9, 67.8 (C-5^B, C-5^C, C-5^D), 67.5 (C-5^A), 65.9 (OCH₂CH₂CH₂N), 64.6 (C-4^B), 64.4 (C-4^A), 64.0, 63.9 (C-4^C, C-4^D), 38.1 (OCH₂CH₂CH₂N), 28.4 (OCH₂CH₂CH₂N), 21.1 (CH₃CO), 18.0 (×4) (C-6^A, C-6^B, C-6^C, C-6^D), 17.8 (C-6^E). HRMS (ESI): calcd. for C₇₉H₉₂F₃N₁₃O₁₉ [M + NH₄]⁺ *m/z* 1601.6923; found *m/z* 1601.6906.

3-Trifluoroacetamidopropyl 3,4-di-O-benzyl-α-D-rhamnopyranosyl-(1→2)-4-azido-3-O-benzyl-4,6-dideoxy-α-D-mannopyranosyl-(1→2)-4-azido-3-O-benzyl-4,6-dideoxy-α-D-mannopyranosyl-(1→3)-4-azido-2-O-benzyl-4,6-dideoxy-α-D-mannopyranosyl-(1→2)-4-azido-3-O-benzyl-4,6-dideoxy-α-D-mannopyranoside (29). 1 M sodium methoxide (20 μL) was added to a solution of compound **28** (121 mg, 0.076 mmol) in MeOH (2 mL). After being stirred for 4 h at room temperature, the mixture was made neutral with Amberlite IR-120 (H⁺) and the resin was filtered off and washed with MeOH (4 × 4 mL). The filtrate was concentrated, and the residue was purified by column chromatography (toluene–EtOAc, 8→15%) to yield deacetylated pentasaccharide **29** (109 mg, 92%) as a colorless foam, [α]_D +59 (c 1, CHCl₃). ¹H NMR (600 MHz, CDCl₃): δ 7.42–7.23 (m, 30 H, Ar), 6.63 (br. s, 1 H, NHCOCF₃), 5.08 (s, 1 H, H-1^B), 5.05 (s, 1 H, H-1^D), 5.00 (s, 1 H, H-1^C), 4.97 (s, 1 H, H-1^E), 4.88 (d, 1 H, *J* = 11.0 Hz, benzylic H), 4.75–4.62 (m, 8 H, H-1^A, 7 benzylic H), 4.57 (d, 1 H, *J* = 11.0 Hz, benzylic H), 4.54 (d, 1 H, *J* = 11.6 Hz, benzylic H), 4.24 (d, 1 H, *J* = 11.8 Hz, PhCHaHb), 4.17 (d, 1 H, *J* = 11.8 Hz, PhCHaHb), 4.06 (br. s, 1 H, H-2^B), 4.03 (br. s, 1 H, H-2^C), 4.00–3.97 (m, 2 H, H-2^A, H-2^D), 3.87–3.82 (m, 2 H, H-3^B, H-3^E), 3.82–3.77 (m, 1 H, OCHaHbCH₂CH₂N), 3.77–3.69 (m, 3 H, H-3^A, H-3^D, H-5^E), 3.67 (dd, 1 H, *J*_{3,2} = 2.6 Hz, *J*_{3,4} = 9.8 Hz, H-3^C), 3.61 (br. s, 1 H, H-2^B), 3.58–3.51 (m, 4 H, H-4^B, H-5^B, H-5^D, OCH₂CH₂CHaHbN), 3.51–3.43 (m, 4 H, H-4^E, H-5^A, OCHaHbCH₂CH₂N, OCH₂CH₂CHaHbN), 3.40–3.34 (m, 3 H, H-4^A, H-4^D, H-5^C), 3.27 (t, 1 H, *J* = 9.8 Hz, H-4^C), 2.40 (br. s, 1 H, OH), 1.94–1.85 (m, 2 H, OCH₂CH₂CH₂N), 1.36–1.32 (m, 6 H, H-6^A, H-6^D), 1.31 (d, 3 H, *J*_{6,5} = 6.1 Hz, H-6^B), 1.20 (d, 3 H, *J*_{6,5} = 6.1 Hz, H-6^E), 1.17 (d, 3 H, *J*_{6,5} = 6.1 Hz, H-6^C). ¹³C NMR (150 MHz, CDCl₃): δ 138.4, 137.9, 137.4, 137.3, 137.2, 128.6, 128.5, 128.4, 128.3, 128.2, 128.1, 128.0, 127.8,

127.7, 127.5 (Ar), 100.8 (C-1^C), 100.7 (×2), (C-1^D, C-1^E), 99.1 (C-1^A), 98.5 (C-1^B), 79.9 (C-4^E), 79.5 (C-3^E), 78.4 (C-3^A), 77.2 (C-3^B), 77.1 (×2) (C-3^C, C-3^D), 76.4 (C-2^B), 75.4 (PhCH₂), 73.4 (C-2^C), 73.2 (C-2^D), 72.9 (C-2^A), 72.5, 72.2, 72.1, 71.9, 71.8 (5 PhCH₂), 68.6 (C-2^E), 68.1 (×2), 67.9 (×2) (C-5^B, C-5^C, C-5^D, C-5^E), 67.5 (C-5^A), 65.9 (OCH₂CH₂CH₂N), 64.6 (C-4^B), 64.5 (C-4^A), 64.2 (C-4^D), 64.0 (C-4^C), 38.1 (OCH₂CH₂CH₂N), 28.4 (OCH₂CH₂CH₂N), 18.5 (×4) (C-6^A, C-6^B, C-6^C, C-6^D), 17.7 (C-6^E). HRMS (ESI): calcd. for C₇₇H₉₀F₃N₁₃O₁₈ [M + NH₄]⁺ *m/z* 1559.6817; found *m/z* 1559.6804.

3-Aminopropyl 4,6-dideoxy-4-formamido-α-D-mannopyranosyl-(1→3)-4,6-dideoxy-4-formamido-α-D-mannopyranoside (4). A mixture of diazide **21** (95 mg, 0.137 mmol) and Pd(OH)₂/C (30 mg) in MeOH was stirred in a hydrogen atmosphere at 35°C for 1.5 h. The catalyst was filtered off and washed with MeOH (4 × 4 mL), and the filtrate was concentrated. Column chromatography (DCM–MeOH, 0→8%) of the residue produced diamine **24** (71 mg, 81%) as a colorless syrup. HRMS (ESI): calcd. for C₃₁H₄₂F₃N₃O₈ [M + H]⁺ *m/z* 642.2997; found *m/z* 642.2991.

Formic acid (25.5 μL, 0.663 mmol) and DCC (69 mg, 0.334 mmol) were added to a solution of diamine **24** (71 mg, 0.111 mmol) in a mixture of DCM–MeOH (9:1, 4 mL). The mixture was stirred for 1 h, the solvents were evaporated, and the residue was suspended in DCM (4 mL). Dicyclohexylurea was filtered off and washed with DCM (3 × 3 mL), the filtrate was concentrated, and the residue was purified by column chromatography (DCM–MeOH, 0→7%) to give bis(formamide) **25** (68 mg, 88%) as a white amorphous solid. HRMS (ESI): calcd. for C₃₃H₄₂F₃N₃O₁₀ [M + NH₄]⁺ *m/z* 715.3161; found *m/z* 715.3167.

A mixture of compound **25** (68 mg, 0.097 mmol) and Pd(OH)₂/C (20 mg) in MeOH (3 mL) was stirred under hydrogen for 2 h at room temperature. The catalyst was removed by filtration and washed with MeOH (4 × 4 mL), and the filtrate was concentrated. Column chromatography of the residue afforded triol **26** (46 mg, 92%) as a white amorphous solid. HRMS (ESI): calcd. for C₁₉H₃₀F₃N₃O₁₀ [M + Na]⁺ *m/z* 540.1775; found *m/z* 540.1780.

Ambersep 900 (OH[−]) (3 mL) was added to a solution of compound **26** (46 mg, 0.089 mmol) in 50% aqueous MeOH (2 mL). The mixture was kept for 1 h with periodic shaking, and then the resin was filtered off and washed with 50% aqueous MeOH (6 × 3 mL). The filtrate was concentrated and the residue was subjected to gel-permeation chromatography to give title compound **4** (36 mg, 92%) as a white amorphous solid. The data of NMR and mass-spectra were identical to those described previously (Tsvetkov and Nifantiev, 2023).

3-Aminopropyl 4,6-dideoxy-4-formamido-α-D-mannopyranosyl-(1→2)-4,6-dideoxy-4-formamido-α-D-mannopyranosyl-(1→3)-4,6-dideoxy-4-formamido-α-D-mannopyranosyl-(1→2)-4,6-dideoxy-4-formamido-α-D-mannopyranoside (1). The title compound was synthesized in four steps from protected precursor **19** in total yield of 55% (for details see [Supplementary Material](#)). A white fluffy solid; contained a non-stoichiometric amount (0.45 equiv.) of AcOH; [α]_D +55 (c 1, water). ¹H NMR (600 MHz, D₂O): δ 8.24–8.18 (m, 2.8 H, H_ZCON), 8.06–7.99 (m, 1.2 H, H_ECON), 5.11–4.92 (m, 4 H, 4 H-1), 4.20–3.77 (m, 15.8 H, 4 H-2, 4 H-3, 4 H-4_Z, 4 H-5, CHaHbCH₂CH₂N), 3.61–3.56 (m, 1 H, OCHaHbCH₂CH₂N), 3.51–3.35 (m, 1.2 H, 4 H-4_E), 3.16–3.07 (m, 2 H, OCH₂CH₂CH₂N), 2.02–1.95 (m, 2 H, OCH₂CH₂CH₂N), 1.90

(s, ~1.4 H, CH₃COOH), 1.30–1.21 (m, 12 H, 4 H-6). ¹³C NMR (150 MHz, D₂O): δ 169.0, 168.9 (H_ECON), 166.1, 165.8 (H_ZCON), 103.5, 103.4, 103.1, 102.9, 101.9, 99.6 (4 C-1), 79.4, 79.2, 79.0, 78.7, 78.6, 78.4, 77.5 (C-2^A, C-2^C, C-3^B), 70.1, 70.0, 69.9, 69.6, 69.5, 69.2, 69.0, 68.9, 68.7, 68.6, 68.5, 68.3 (C-3^A, C-5^A, C-2^B, C-5^B, C-3^C, C-5^C, C-2^D, C-3^D, C-5^D), 66.4 (OCH₂CH₂CH₂N), 58.2, 58.0, 57.9, 56.7 (4 C-4_E), 53.3, 53.1, 52.9, 52.2, 52.1 (4 C-4_Z), 38.6 (OCH₂CH₂CH₂N), 27.9 (OCH₂CH₂CH₂N), 18.4, 18.2, 18.1, 18.0, 17.9 (4 C-6). HRMS (ESI): calcd. for C₃₁H₅₃N₅O₁₇ [M + H]⁺ *m/z* 768.3509; found *m/z* 768.3510.

3-Aminopropyl 4,6-dideoxy-4-formamido-α-D-mannopyranosyl-(1→3)-4,6-dideoxy-4-formamido-α-D-mannopyranosyl-(1→2)-4,6-dideoxy-4-formamido-α-D-mannopyranoside (2). The title compound was obtained in four steps from protected progenitor **17** in total yield of 54% (for details see [Supplementary Material](#)). A white fluffy solid; contained a non-stoichiometric amount (0.40 equiv.) of AcOH; [α]_D +60 (c 1, water). ¹H NMR (600 MHz, D₂O): δ 8.23–8.18 (m, 2.1 H, 3 H_ZCON), 8.06–8.01 (m, 0.9 H, 3 H_ECON), 5.04–4.92 (m, 3 H, 3 H-1), 4.21–3.79 (m, 12.1 H, 3 H-2, 3 H-3, 3 H-4_Z, 3 H-5, OCHaHbCH₂CH₂N), 3.61–3.56 (m, 1 H, OCHaHbCH₂CH₂N), 3.48 (t, 0.3 H, *J* = 10.1 Hz, H-4_E), 3.43 (t, 0.3 H, *J* = 10.3 Hz, H-4_E), 3.36 (t, 0.3 H, *J* = 10.5 Hz, H-4_E), 3.17–3.07 (m, 2 H, OCH₂CH₂CH₂N), 2.02–1.95 (m, 2 H, OCH₂CH₂CH₂N), 1.91 (s, 1.2 H, 0.4 CH₃COOH), 1.30–1.21 (m, 9 H, 3 H-6). ¹³C NMR (150 MHz, D₂O): δ 169.0, 168.9 (3 H_ECON), 165.9, 165.8 (3 H_ZCON), 103.4, 103.2, 103.1, 102.9 (C-1^B, C-1^C), 99.4 (C-1^A), 78.8, 77.8, 77.5, 77.4 (C-2^A, C-3^B), 70.3, 70.0, 69.8, 69.7, 69.2, 69.1, 69.0, 68.8, 68.7, 68.6, 68.2, (C-2^B, C-2^C, C-3^A, C-3^C, C-5^A, C-5^B, C-5^C), 66.2 (OCH₂CH₂CH₂N), 57.9, 57.7, 56.5 (C-4_E^A, C-4_E^B, C-4_E^C), 53.1, 52.7, 51.6 (C-4_Z^A, C-4_Z^B, C-4_Z^C), 38.4 (OCH₂CH₂CH₂N), 27.7 (OCH₂CH₂CH₂N), 24.3 (CH₃COOH), 17.9, 17.7 (C-6^A, C-6^B, C-6^C). HRMS (ESI): calcd. for C₂₄H₄₂N₄O₁₃ [M + H]⁺ *m/z* 595.2821; found *m/z* 595.2819.

3-Aminopropyl 4,6-dideoxy-4-formamido-α-D-mannopyranosyl-(1→2)-4,6-dideoxy-4-formamido-α-D-mannopyranosyl-(1→3)-4,6-dideoxy-4-formamido-α-D-mannopyranoside (3). The title trisaccharide was synthesized in four steps from protected precursor **23** in overall yield of 52% (for details see [Supplementary Material](#)). A white fluffy solid; contained a non-stoichiometric amount (0.35 equiv.) of AcOH; [α]_D +65 (c 1, water). ¹H NMR (600 MHz, D₂O): δ 8.22–8.19 (m, 2.2 H, 3 H_ZCON), 8.05–8.01 (m, 0.8 H, 3 H_ECON), 5.09–4.98 (m, 2 H, 2 H-1), 4.83 (d, 1 H, *J*_{1,2} = 2.0 Hz, H-1), 4.15–3.91 (m, 12.2 H, 3 H-2, 3 H-3, 3 H-4_Z, 3 H-5, OCHaHbCH₂CH₂N), 3.62–3.57 (m, 1 H, OCHaHbCH₂CH₂N), 3.46 (t, 0.25 H, *J* = 10.3 Hz, H-4_E), 3.43–3.35 (m, 0.5 H, 2 H-4_E), 3.17–3.07 (m, 2 H, OCH₂CH₂CH₂N), 2.03–1.95 (m, 2 H, OCH₂CH₂CH₂N), 1.91 (s, ~1 H, 0.35 CH₃COOH), 1.29–1.20 (m, 9 H, 3 H-6). ¹³C NMR (150 MHz, D₂O): δ 169.1, 169.0 (3 H_ECON), 166.2, 166.1, 165.9 (3 H_ZCON), 103.6, 103.5, 103.1, 102.1, 102.0, 100.9, 100.8 (C-1^A, C-1^B, C-1^C), 79.4, 79.3, 78.7, 78.3, 77.9 (C-3^A, C-2^B), 70.2, 70.0, 69.7, 69.5, 69.3, 69.2, 69.1, 69.0, 68.9, 68.7, 68.6, 68.5, 68.2, 68.1 (C-2^A, C-5^A, C-3^B, C-5^B, C-2^C, C-3^C, C-5^C), 66.2 (OCH₂CH₂CH₂N), 58.1, 57.9, 56.7 (C-4_E^A, C-4_E^B, C-4_E^C), 53.1, 53.0, 52.4 (C-4_Z^A, C-4_Z^B, C-4_Z^C), 38.6 (OCH₂CH₂CH₂N), 27.9 (OCH₂CH₂CH₂N), 24.4 (CH₃COOH), 18.4, 18.3, 18.2, 18.0 (C-6^A, C-6^B, C-6^C). HRMS (ESI): calcd. for C₂₄H₄₂N₄O₁₃ [M + H]⁺ *m/z* 595.2821; found *m/z* 595.2815.

3-Aminopropyl 4,6-dideoxy-4-formamido- α -D-mannopyranoside (5). The title glycoside was synthesized in four steps from protected compound **13** in total yield of 57% (for details see [Supplementary Material](#)). A colorless glassy solid; contained a non-stoichiometric amount (0.4 equiv.) of AcOH; $[\alpha]_D +42$ (c 1, water). ^1H NMR (600 MHz, D_2O): δ 8.19 (s, 0.7 H, H_ZCON), 8.02 (s, 0.4 H, H_ECON), 4.85–4.84 (m, 1 H, H-1), 3.98 (dd, 0.3 H, $J_{2,1} = 2.0$ Hz, $J_{2,3} = 3.2$ Hz, H-2 $_E$), 3.96 (t, 0.7 H, $J = 2.4$ Hz, H-2 $_Z$), 3.91–3.77 (m, 3.7 H, H-3, H-4 $_Z$, H-5, $\text{OCHaHbCH}_2\text{CH}_2\text{N}$), 3.62–3.57 (m, 1 H, $\text{OCHaHbCH}_2\text{CH}_2\text{N}$), 3.36 (t, 0.3 H, $J = 10.1$ Hz, H-4 $_E$), 3.17–3.08 (m, 2 H, $\text{OCH}_2\text{CH}_2\text{CH}_2\text{N}$), 2.03–1.95 (m, 2 H, $\text{OCH}_2\text{CH}_2\text{CH}_2\text{N}$), 1.90 (s, 1.2 H, CH_3COO^-), 1.26 (d, 0.9 H, $J_{6,5} = 6.4$ Hz, H-6 $_E$), 1.22 (d, 2.1 H, $J_{6,5} = 6.3$ Hz, H-6 $_Z$). ^{13}C NMR (150 MHz, D_2O): δ 169.0 (H_ECON), 166.1 (H_ZCON), 100.9 (C-1), 70.3 (C-2), 69.2 (C-3), 68.5 (C-5 $_Z$), 68.2 (C-5 $_E$), 66.2 ($\text{OCH}_2\text{CH}_2\text{CH}_2\text{N}$), 57.9 (C-4 $_E$), 53.2 (C-4 $_Z$), 38.7 ($\text{OCH}_2\text{CH}_2\text{CH}_2\text{N}$), 27.8 ($\text{OCH}_2\text{CH}_2\text{CH}_2\text{N}$), 18.0 (C-6 $_Z$), 17.9 (C-6 $_E$). HRMS (ESI): calcd. for $\text{C}_{10}\text{H}_{20}\text{N}_2\text{O}_5$ $[\text{M} + \text{H}]^+$ m/z 249.1445; found m/z 249.1449.

3-Aminopropyl α -D-rhamnopyranosyl-(1 \rightarrow 2)-4,6-dideoxy-4-formamido- α -D-mannopyranosyl-(1 \rightarrow 2)-4,6-dideoxy-4-formamido- α -D-mannopyranosyl-(1 \rightarrow 3)-4,6-dideoxy-4-formamido- α -D-mannopyranosyl-(1 \rightarrow 2)-4,6-dideoxy-4-formamido- α -D-mannopyranoside (6). The title pentasaccharide was obtained in four steps from protected precursor **29** in total yield of 45% (for details see [Supplementary Material](#)). A white fluffy solid; contained a non-stoichiometric amount (0.35 equiv.) of AcOH; $[\alpha]_D +55$ (c 1, water). ^1H NMR (600 MHz, D_2O): δ 8.25–8.19 (m, 2.9 H, 3 H_ZCON), 8.07–8.00 (m, 1.1 H, 3 H_ECON), 5.19–4.93 (m, 5 H, 5 H-1), 4.20–3.73 (m, 20 H, 5 H-2, 5 H-3, 4 H-4 $_Z$, H-4 $_E$, 5 H-5, $\text{OCHaHbCH}_2\text{CH}_2\text{N}$), 3.62–3.57 (m, 1 H, $\text{OCHaHbCH}_2\text{CH}_2\text{N}$), 3.52–3.39 (m, 1.1 H, 4 H-4 $_E$), 3.15–3.06 (m, 2 H, $\text{OCH}_2\text{CH}_2\text{CH}_2\text{N}$), 2.01–1.95 (m, 2 H, $\text{OCH}_2\text{CH}_2\text{CH}_2\text{N}$), 1.91 (s, 1.4 H, CH_3COOH), 1.31–1.22 (m, 15 H, 5 H-6). ^{13}C NMR (150 MHz, D_2O): δ 169.0, 168.9 (3 H_ECON), 166.1, 165.7 (3 H_ZCON), 103.3, 103.1, 103.0, 102.1, 102.0, 101.9, 101.7, 99.6 (5 C-1), 79.0, 78.8, 78.6, 78.2, 77.9, 77.6, 77.4 (C-2 $_A$, C-3 $_B$, C-2 $_C$, C-2 $_D$), 73.2, 71.4, 71.3, 70.4, 70.0, 69.9, 69.7, 69.5, 69.4, 68.9, 68.7, 68.4 (C-3 $_A$, C-5 $_A$, C-2 $_B$, C-5 $_B$, C-3 $_C$, C-5 $_C$, C-3 $_D$, C-5 $_D$, C-2 $_E$, C-3 $_E$, C-4 $_E$, C-5 $_E$), 66.4 ($\text{OCH}_2\text{CH}_2\text{CH}_2\text{N}$), 58.2, 58.1, 58.0, 56.6 (4 C-4 $_E$), 53.3, 53.2, 53.1, 52.2, 52.1 (4 C-4 $_Z$), 38.6 ($\text{OCH}_2\text{CH}_2\text{CH}_2\text{N}$), 28.1 ($\text{OCH}_2\text{CH}_2\text{CH}_2\text{N}$), 18.5, 18.3, 18.1, 18.0, 17.9, 17.8 (5 C-6). HRMS (ESI): calcd. for $\text{C}_{37}\text{H}_{63}\text{N}_5\text{O}_{21}$ $[\text{M} + \text{H}]^+$ m/z 914.4088; found m/z 914.4089.

Data availability statement

The original contributions presented in the study are included in the article/[Supplementary Material](#), further inquiries can be directed to the corresponding author.

References

- Argunov, D. A., Krylov, V. B., and Nifantiev, N. E. (2015). Convergent synthesis of isomeric heterosaccharides related to the fragments of galactomannan from *Aspergillus fumigatus*. *Org. Biomol. Chem.* 13, 3255–3267. doi:10.1039/c4ob02634a
- Ariosio-Alvarez, A., Arencibia-Mohar, A., Madrazo-Alonso, O., Garcia-Imia, L., Sierra-Gonzalez, G., and Verez-Bencomo, V. (1998). Synthesis of the *Vibrio*

Author contributions

YT: Investigation, Writing–original draft. TV: Investigation, Writing–original draft. SE: Investigation, Writing–original draft. OS: Writing–original draft, Investigation. YK: Investigation, Writing–original draft. VK: Investigation, Writing–original draft. NN: Conceptualization, Funding acquisition, Writing–original draft.

Funding

The author(s) declare that financial support was received for the research, authorship, and/or publication of this article. This work was supported by the Russian Science Foundation (Grant 19-73-30017-P).

Acknowledgments

The authors are grateful to Dr. A. S. Dmitrenok and Dr. A. O. Chizhov for recording NMR and mass spectra of synthesized compounds, respectively.

Conflict of interest

The authors declare that the research was conducted in the absence of any commercial or financial relationships that could be construed as a potential conflict of interest.

The author(s) declared that they were an editorial board member of *Frontiers*, at the time of submission. This had no impact on the peer review process and the final decision.

Publisher's note

All claims expressed in this article are solely those of the authors and do not necessarily represent those of their affiliated organizations, or those of the publisher, the editors and the reviewers. Any product that may be evaluated in this article, or claim that may be made by its manufacturer, is not guaranteed or endorsed by the publisher.

Supplementary material

The Supplementary Material for this article can be found online at: <https://www.frontiersin.org/articles/10.3389/fchem.2024.1424157/full#supplementary-material>

cholerae O1 ogawa and inaba terminal disaccharides with dioxolane-type spacers and their coupling to proteins. *J. Carbohydr. Chem.* 17, 1307–1320. doi:10.1080/07328309808002355

Bock, K., and Pedersen, C. (1974). A study of ^{13}C coupling constants in hexopyranoses. *J. Chem. Soc. Perkin Trans. 2*, 293–297. doi:10.1039/P29740000293

- Bundle, D. R., Gerken, M., and Peters, T. (1988). Synthesis of antigenic determinants of the Brucella A antigen, utilizing methyl 4-Azido-4,6-Dideoxy- α -D-Mannopyranoside efficiently derived from D-mannose. *Carbohydr. Res.* 174, 239–251. doi:10.1016/0008-6215(88)85094-8
- Bundle, D. R., and McGiven, J. (2017). Brucellosis: improved diagnostics and vaccine insights from synthetic glycans. *Acc. Chem. Res.* 50, 2958–2967. doi:10.1021/acs.accounts.7b00445
- Caroff, M., Bundle, D. R., and Perry, M. B. (1984). Structure of the O-chain of the phenol-phase soluble cellular lipopolysaccharide of *Yersinia enterocolitica* serotype O:9. *Eur. J. Biochem.* 139, 195–200. doi:10.1111/j.1432-1033.1984.tb07994.x
- Duncombe, L., Howells, L., Haughey, A., Taylor, A. V., Kaveh, D., Gürbilek, S. E., et al. (2022). The tip of Brucella O-polysaccharide is a potent epitope in response to brucellosis infection and enables short synthetic antigens to be superior diagnostic reagents. *Microorganisms* 10, 708. doi:10.3390/microorganisms10040708
- Franco, M. P., Mulder, M., Gilman, R. H., and Smits, H. L. (2007). Human brucellosis. *Lancet Infect. Dis.* 7, 775–786. doi:10.1016/S1473-3099(07)70286-4
- Ganesh, V. N., Sadowska, J. M., Sarkar, S., Howells, L., McGiven, J., and Bundle, D. R. (2014). Molecular recognition of Brucella A and M antigens dissected by synthetic oligosaccharide glycoconjugates leads to a disaccharide antigenic for brucellosis. *J. Am. Chem. Soc.* 136, 16260–16269. doi:10.1021/ja5081184
- Gening, M. L., Kurbatova, E. A., Tsvetkov, Y. E., and Nifantiev, N. E. (2015). Development of approaches to a third-generation carbohydrate-conjugate vaccine against *Streptococcus pneumoniae*: the search for optimal oligosaccharide ligands. *Russ. Chem. Rev.* 84, 1100–1113. doi:10.1070/RCR4574
- Godfroid, J., Nielsen, K., and Saegerman, C. (2010). Diagnosis of brucellosis in livestock and wildlife. *Croat. Med. J.* 51, 296–305. doi:10.3325/cmj.2010.51.296
- Grant, O. C., Smith, H. M. K., Firsova, D., Fadda, E., and Woods, R. J. (2014). Presentation, presentation, presentation! Molecular-level insight into linker effects on glycan array screening data. *Glycobiology* 24, 17–25. doi:10.1093/glycob/cwt083
- Guiard, J., Paszkiewicz, E., Sadowska, J. M., and Bundle, D. R. (2013). Design and synthesis of a universal antigen to detect brucellosis. *Angew. Chem. Int. Ed.* 52, 7181–7185. doi:10.1002/anie.201302303
- Hou, S.-j., and Kovač, P. (2010). Enhanced stereoselectivity of α -mannosylation under thermodynamic control using trichloroacetimidates. *Carbohydr. Res.* 345, 999–1007. doi:10.1016/j.carres.2010.03.025
- Kazakova, E. D., Yashunsky, D. V., Krylov, V. B., Bouchara, J.-P., Cornet, M., Valsecchi, I., et al. (2020). Biotinylated oligo- α -(1→4)-D-galactosamines and their N-acetylated derivatives: α -stereoselective synthesis and immunology application. *J. Am. Chem. Soc.* 142, 1175–1179. doi:10.1021/jacs.9b11703
- Kochetkov, N. K., Nifant'ev, N. E., and Backinowsky, L. V. (1987). Synthesis of the capsular polysaccharide of type 14. *Tetrahedron* 43, 3109–3121. doi:10.1016/S0040-4020(01)86852-6
- Komarova, B. K., Wong, S. S., Orekhova, M. V., Tsvetkov, Y. E., Krylov, V. B., Beauvais, A., et al. (2018). Chemical synthesis and application of biotinylated oligo- α -(1→3)-D-glucosides to study the antibody and cytokine response against the cell wall α -(1→3)-D-glucan of *Aspergillus fumigatus*. *J. Org. Chem.* 83, 12965–12976. doi:10.1021/acs.joc.8b01142
- Krylov, V. B., Solovov, A. S., Argunov, D. A., Latgé, J.-P., and Nifantiev, N. E. (2019). Reinvestigation of carbohydrate specificity of EB-A2 monoclonal antibody used in the immune detection of *Aspergillus fumigatus* galactomannan. *Heliyon* 5, e01173. doi:10.1016/j.heliyon.2019.e01173
- Kubler-Kielbaso, J., and Vinogradov, E. (2013). Reinvestigation of the structure of Brucella O-antigens. *Carbohydr. Res.* 378, 144–147. doi:10.1016/j.carres.2013.03.021
- Laverde, D., Romero-Saavedra, F., Argunov, D. A., Enotarpi, J., Krylov, V. B., Kalfopoulou, E., et al. (2020). Synthetic oligomers mimicking capsular polysaccharide diheteroglycan are potential vaccine candidates against encapsulated enterococcal infections. *ACS Infect. Dis.* 6, 1816–1826. doi:10.1021/acsinfectdis.0c00063
- Mandal, S. S., Duncombe, L., Ganesh, N. V., Sarkar, S., Howells, L., Hogarth, P. J., et al. (2017a). Novel solutions for vaccines and diagnostics to combat brucellosis. *ACS Cent. Sci.* 3, 224–231. doi:10.1021/acscentsci.7b00019
- Mandal, S. S., Ganesh, N. V., Sadowska, J. M., and Bundle, D. R. (2017b). Synthetic glycoconjugates characterize the fine specificity of Brucella A and M monoclonal antibodies. *Org. Biomol. Chem.* 15, 3874–3883. doi:10.1039/c7ob00445a
- McGiven, J., Howells, L., Duncombe, L., Stack, J., Ganesh, N. V., Guiard, J., et al. (2015). Improved serodiagnosis of bovine brucellosis by novel synthetic oligosaccharide antigens representing the capping M epitope elements of Brucella O-polysaccharide. *J. Clin. Microbiol.* 53, 1204–1210. doi:10.1128/JCM.03185-14
- Mogues, T., Li, J., Coburn, J., and Kuter, D. J. (2005). IgG antibodies against bovine serum albumin in humans—their prevalence and response to exposure to bovine serum albumin. *J. Immunol. Methods* 300, 1–11. doi:10.1016/j.jim.2005.01.022
- Mukherjee, M. M., Xu, P., Stevens, E. D., and Kováč, P. (2019). Towards the complete synthetic O-antigen of *Vibrio cholerae* O1, serotype inaba: improved synthesis of the conjugation-ready upstream terminal hexasaccharide determinant. *RSC Adv.* 9, 36440–36454. doi:10.1039/c9ra08232h
- Nielsen, K. (2002). Diagnosis of brucellosis by serology. *Vet. Microbiol.* 90, 447–459. doi:10.1016/S0378-1135(02)00229-8
- Perry, M. B., and Bundle, D. R. (1990). Antigenic relationships of the lipopolysaccharides of *Escherichia hermannii* strains with those of *Escherichia coli* O157:H7, *Brucella melitensis*, and *Brucella abortus*. *Infect. Immun.* 58, 1391–1395. doi:10.1128/iai.58.5.1391-1395.1990
- Peters, V., Brisson, J.-R., and Bundle, D. R. (1990). Conformational analysis of key disaccharide components of Brucella A and M antigens. *Can. J. Chem.* 68, 979–988. doi:10.1139/v90-154
- Sjöwall, C., Kastbom, A., Almroth, G., Wetterö, J., and Skogh, T. (2011). Beware of antibodies to dietary proteins in “antigen-specific” immunoassays! False positive anticytokine antibody tests due to reactivity with bovine serum albumin in rheumatoid arthritis (the Swedish TIRA project). *J. Rheumatol.* 38, 215–220. doi:10.3899/jrheum.100690
- Solovov, A. S., Denisova, E. M., Kurbatova, E. A., Kutsevalova, O. Y., Boronina, L. G., Ageevets, V. A., et al. (2023). Synthesis of methylphosphorylated oligomannosides structurally related to lipopolysaccharide O-antigens of *Klebsiella pneumoniae* serotype O3 and their application for detection of specific antibodies in rabbit and human sera. *Org. Biomol. Chem.* 21, 8306–8319. doi:10.1039/d3ob01203d
- Temme, J. S., Campbell, C. T., and Gildersleeve, J. C. (2019). Factors contributing to variability of glycan microarray binding profiles. *Faraday Discuss.* 219, 90–111. doi:10.1039/c9fd00021f
- Tsvetkov, Y. E., Backinowsky, L. V., and Kochetkov, N. K. (1989). Synthesis of a common polysaccharide antigen of *Pseudomonas aeruginosa* as the 6-aminohexyl glycoside. *Carbohydr. Res.* 193, 75–90. doi:10.1016/0008-6215(89)85108-0
- Tsvetkov, Y. E., and Nifantiev, N. E. (2023). Synthesis of a spacer-armed disaccharide structurally related to the M antigenic fragment of Brucella O-polysaccharides. *Russ. Chem. Bull.* 72, 2731–2737. doi:10.1007/s11172-023-4079-4
- Wong, S. S. W., Krylov, V. B., Argunov, D. A., Karelin, A. A., Bouchara, J.-P., Fontaine, T., et al. (2020). Potential of chemically synthesized oligosaccharides to define the carbohydrate moieties of the fungal cell wall responsible for the human immune response, using *Aspergillus fumigatus* galactomannan as a model. *Ex. Aspergillus fumigatus Cell wall galactomannan. mSphere* 5 (e5), e00688. doi:10.1128/mSphere.00688-19
- Zhang, X., Gu, G., and Guo, Z. (2015). Synthesis of a trisaccharide repeating unit of the O-antigen from *Burkholderia multivorans* and its oligomers. *Eur. J. Org. Chem.* 2015, 7075–7085. doi:10.1002/ejoc.201500964



OPEN ACCESS

EDITED BY

Jean-Claude Guillemin,
UMR6226 Institut des Sciences Chimiques de
Rennes (ISCR), France

REVIEWED BY

Barbara Michela Giuliano,
Max Planck Institute for Extraterrestrial Physics,
Germany
Nicola Tasinato,
Normal School of Pisa, Italy

*CORRESPONDENCE

Malgorzata Biczysko,
✉ malgo.biczysko@gmail.com

RECEIVED 27 May 2024

ACCEPTED 12 August 2024

PUBLISHED 03 September 2024

CITATION

Xu Y and Biczysko M (2024) Toward the
identification of cyano-astroCOMs via
vibrational features: benzonitrile as a test case.
Front. Chem. 12:1439194.
doi: 10.3389/fchem.2024.1439194

COPYRIGHT

© 2024 Xu and Biczysko. This is an open-access
article distributed under the terms of the
[Creative Commons Attribution License \(CC BY\)](#).
The use, distribution or reproduction in other
forums is permitted, provided the original
author(s) and the copyright owner(s) are
credited and that the original publication in this
journal is cited, in accordance with accepted
academic practice. No use, distribution or
reproduction is permitted which does not
comply with these terms.

Toward the identification of cyano-astroCOMs via vibrational features: benzonitrile as a test case

Yanting Xu and Malgorzata Biczysko*

International Centre for Quantum and Molecular Structures, Department of Physics, College of Sciences, Shanghai University, Shanghai, China

The James Webb Space Telescope (JWST) opened a new era for the identification of molecular systems in the interstellar medium (ISM) by vibrational features. One group of molecules of increasing interest is cyano-derivatives of aromatic organic molecules, which have already been identified in the ISM on the basis of the analysis of rotational signatures, and so, are plausible candidates for the detection by the JWST. Benzonitrile considered in this work represents a suitable example for the validation of a computational strategy, which can be further applied for different, larger, and not-yet observed molecules. For this purpose, anharmonic simulations of infrared (IR) spectra have been compared with recent FTIR experimental studies. The anharmonic computations using the generalized second-order vibrational perturbation theory (GVPT2) in conjunction with a hybrid force field combining the harmonic part of revDSD-PBEP86-D3/jun-cc-pVTZ with anharmonic corrections from B3LYP-D3/SNSD show very good agreement with those in the experiment, with a mean error of 11cm^{-1} for all fundamental transitions overall and only 2cm^{-1} for the $\text{C}\equiv\text{N}$ stretching fundamental at $4.49\text{ }\mu\text{m}$. The inclusion of overtones up to three-quanta transitions also allowed the prediction of spectra in the near-infrared region, which shows distinct features due to $\text{C}\equiv\text{N}$ overtones at the $2.26\text{ }\mu\text{m}$ and $1.52\text{ }\mu\text{m}$. The remarkable accuracy of the GVPT2 results opens a pathway for the reliable prediction of spectra for a broader range of cyano-astroCOMs.

KEYWORDS

vibrational spectra, density functional theory, second-order vibrational perturbation theory, near-infrared, James Webb Space Telescope

1 Introduction

Despite being initially considered too harsh and diluted for molecule creation and survival, it is now recognized that several chemical processes can happen in astronomic environments leading to more than 310 molecules already detected in the interstellar medium (ISM) or circumstellar shells (Endres et al., 2016). Several of these molecules have been detected in the last decade, in particular, a number of complex organic species (COMs), defined as astrophysically relevant organic molecules consisting of six or more atoms. Some COMs that contain C, H, N, O, and possibly also S atoms can be claimed as prebiotic (Fulvio et al., 2021). To date, more than 30 prebiotic molecules have been detected in Taurus molecular cloud 1 (TMC-1), a dust-enshrouded gaseous cloud located 400 light-years from the Sun in the Taurus constellation. Such progress and fast increase in new detections has become possible due to advances in instrumentation, in particular the sub-

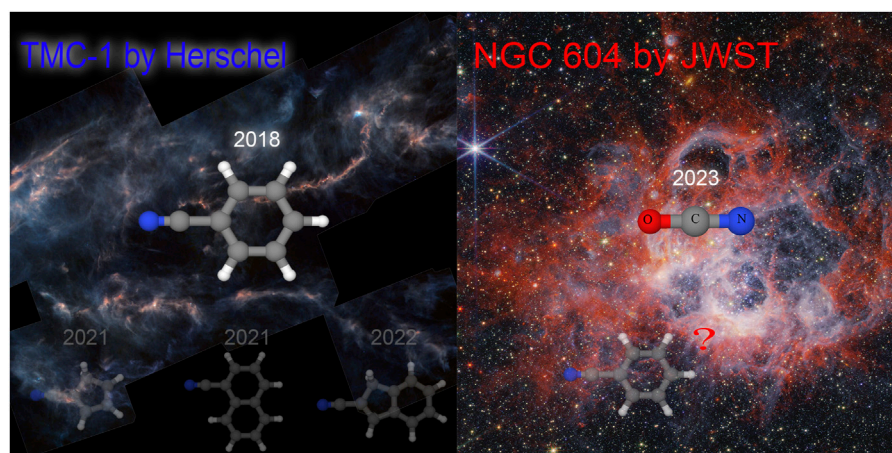


FIGURE 1

Cyano-derivatives in the ISM and the year of detection by rotational (left panel) or vibrational (right panel) features. Left panel: astro-COMs and Herschel's view of TMC-1 (Herschel Space Observatory, 2017) (credit: ESA/Herschel/NASA/JPL-Caltech TMC-1). Right panel: OCN⁻ recently detected by the JWST and NGC 604 NIRC image (Webb Space Telescope, 2024) (credit: NASA/ESA/CSA/STScI).

millimeter and radio domains, allowing the analysis of the lowest rotational lines where radiation can pass through dust-enshrouded clouds (Guélin and Cernicharo, 2022).

However, rotational transitions are not always suitable and accessible for a study, for instance, for exoplanet atmospheres or dense dark regions, for which vibrational spectroscopies are often the methods of choice. The increasing importance of vibrational transitions in astrochemical context is clearly represented by the James Webb Space Telescope (JWST), which, with the infrared (IR) (Frost et al., 2022) observations obtained by the mid-infrared (MIR) and near-IR (NIR) instruments integrated within the Integrated Science Instrument Module (ISIM, Near-Infrared Camera [NIRCam], Near-Infrared Spectrograph [NIRSpec], Mid-Infrared Instrument [MIRI], and Jet Propulsion Laboratory [JPL]), already provides superlative sensitivity, spectral resolution, and wavelength coverage compared to previous space telescopes, such as Herschel, that observe in the visible and ultraviolet spectra (see Figure 1). These emerging experimental data already provide new information about the major ices in molecular cloud cores just prior to their collapse to form protostars (McClure et al., 2023). Currently, the Mars 2020 Perseverance rover also searches for signs of organic matter, in the contexts of the emergence of life, as well as its consideration as a habitable planet, performing, among others, NIR studies using SuperCam (Perez et al., 2017; Eigenbrode et al., 2018; Lasne, 2021; Sharma et al., 2023; McIntosh et al., 2024). These missions yield a huge amount of new significant results, which need to be analyzed, also highlighting the urgent need for accurate reference data in the MIR-to-NIR (0.6–28 μm) range (Öberg, 2016; Nazari et al., 2021; Zapata Trujillo et al., 2023; Fortenberry, 2024b).

Spectroscopic techniques are the key for the analysis of astronomical observations and the detection of molecules in the interstellar medium and other astrochemical environments, such as atmospheres or soils of exoplanets or planetary moons (Loru et al., 2022; Lemmens et al., 2022; Mackie et al., 2022; Peeters et al., 2021; K. Lemmens et al., 2023; Pettrignani and Candian, 2022; Puzzarini et al., 2023). However, the investigation of the chemical composition

of “astrochemical samples” is complicated due to the concomitant presence of many, possibly unknown species. The detection of molecules is based on the comparison of spectra from spectroscopic observations in space with reference experiments from the laboratory (Puzzarini et al., 2023). Unfortunately, the latter might be limited, incomplete, or difficult to obtain under appropriate conditions (Barone et al., 2015c; Fortenberry, 2024b). The optimal strategy is represented by the combination of experiments with the theoretical approaches (Barone et al., 2021; Puzzarini, 2022), supporting and/or complementing laboratory studies (Biczysko et al., 2018a; Barone and Puzzarini, 2023; Fortenberry, 2024a). An increasing role of computational spectroscopy is related to its increasing accuracy (Yang et al., 2021; Barone and Puzzarini, 2023), as well as the possibility to match different, often extreme environmental conditions possible in space (Barone et al., 2015c; Biczysko et al., 2018b; Zapata Trujillo et al., 2023; Fortenberry, 2024b).

Among all the molecules detected to date in the ISM, over 30% bear a nitrogen atom, which usually bonds to carbon, in a large fraction (over 80% of species) by the triple $\text{C}\equiv\text{N}$ bond (Endres et al., 2016). This is in line with the increased dipole moment that facilitates detection by rotational features, as well as the abundance of the CN radical in the ISM (McGuire, 2022) and its extreme reactivity (McGuire et al., 2018; 2021) leading to the abundance of cyano-substituted derivatives (cyano-astroCOMs and $\text{C}\equiv\text{N}$ -astroCOMs) in the ISM. Indeed, benzonitrile ($\text{BC}\equiv\text{N}$, cyano-benzene, $\text{C}_6\text{H}_5\text{C}\equiv\text{N}$), was the first six-membered aromatic compound detected in 2018 in the ISM (McGuire et al., 2018), toward the dark molecular cloud TMC-1, a well-studied region where most molecules were first observed. This detection was possible as the $\text{C}\equiv\text{N}$ group attachment creates a permanent dipole moment, which is null in otherwise “silent” (poly-) aromatic hydrocarbons (PAHs). This breakthrough intensified the search for aromatic $\text{C}\equiv\text{N}$ -astroCOMs, leading to the detection in the TMC-1 of 1- and 2-cyanonaphthalene ($\text{C}_{10}\text{H}_7\text{C}\equiv\text{N}$) isomers (McGuire et al., 2021) in 2021 and 2-cyanoindene ($\text{C}_9\text{H}_7\text{C}\equiv\text{N}$) (Sita et al., 2022) in 2022. Following

the observation of the six-membered rings, 1- and 2-cyanocyclopentadiene ($C_5H_5C\equiv N$) (McCarthy et al., 2021; Lee et al., 2021), which contains a five-membered cycle, were also detected in the same source (see Figure 1). Further searches extending to other hetero-aromatic and bridged bicyclic compounds (Martin-Drumel et al., 2023) also aim at establishing the abundance ratio between $C\equiv N$ -PAHs and their parent PAHs (Barone and Lazzari, 2023). To date, none of these molecules have been identified by their vibrational features, but the first cyano-compound, i.e., the $OC\equiv N^-$ anion, which is one of the most well-detected species in astrophysical ices, has been detected in the low-mass star-forming region Chameleon I by the JWST based on the peak centered at 2165.9 cm^{-1} ($4.62\text{ }\mu\text{m}$) (McClure et al., 2023) (see Figure 1).

In this work, we focus on the first observed cyano-astroCOM, i.e., benzonitrile (McGuire et al., 2018). The experimental microwave spectrum of benzonitrile was first studied simultaneously by Erlandsson (1954) and Lide (1954). Bak et al. conducted comprehensive analyses of benzonitrile utilizing infrared and centimeter-wave techniques, also including feasible mono-substituted isotopologs (Bak and Nielsen, 1960; Bak et al., 1962). This led to the first derivation of a substitution structure, r_s , which was further refined by Casado et al. by incorporating multiple Q-branch transitions for the majority of mono-substituted isotopologs (Casado et al., 1971). Green and Harrison subsequently enhanced the analysis of the experimental IR spectrum, taking into account the lowest wavenumber modes (Green and Harrison, 1976). Recently, these initial spectroscopic investigations have been improved, also in view of the increasing accuracy and spectrum coverage requirements due to the astrochemical importance of $BC\equiv N$ (Yamamoto et al., 2000; Kwon et al., 2003; Burova and Anashkin, 2007; Rajasekhar et al., 2022). The accurate equilibrium structure of benzonitrile has been determined by Rudolph et al. (2013) using two different, complementary techniques, namely, the theoretical estimate r_{BO} and semi-experimental r_e^{SE} . The most extended study is the 2022 synchrotron investigation of $BC\equiv N$ in a very broad spectrum range, up to $90'000\text{ cm}^{-1}$ (11.1 eV), which also included the new detection of the gas-phase IR spectra at a resolution of 0.5 cm^{-1} (Rajasekhar et al., 2022). This work, along with the high-resolution far-infrared spectra collected in the $65 - -695\text{ cm}^{-1}$ range using synchrotron radiation at the SOLEIL facility (Zdanovskaia et al., 2022), represents the reference for the anharmonic computations of IR spectra.

This work focuses on the IR spectra in the MIR-NIR region, first comparing the simulated infrared spectra with the available experimental counterparts and then providing the prediction of not yet available spectral data, which can support either laboratory or astrochemical studies.

2 Computational details

In order to simulate the spectroscopic parameters of benzonitrile in its electronic ground state \tilde{X}^1A_1 , the geometry optimization and harmonic and anharmonic vibrational computations are performed using GAUSSIAN 16 (Frisch et al., 2016). In geometry optimization, the tight convergence criteria (maximum forces and displacements

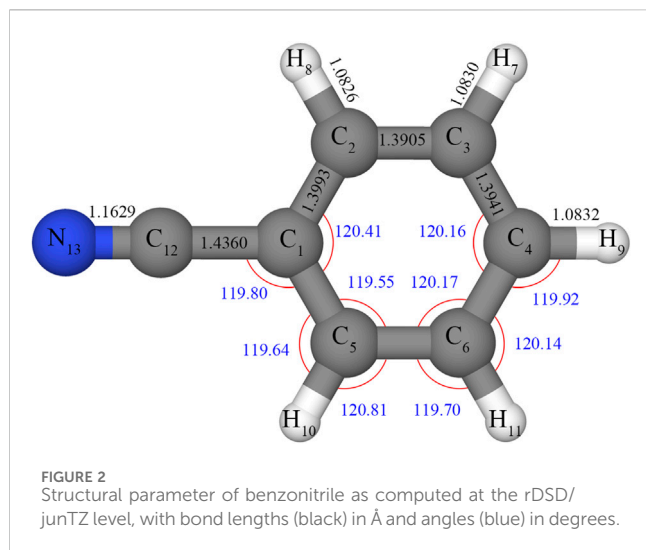
smaller than 1.5×10^{-5} Hartree/Bohr and $6.0 \times 10^{-5}\text{ \AA}$, respectively), as required for the anharmonic computations, are used. The equilibrium structure, harmonic force constants, and first-order electric dipole moment derivatives have been computed using the double-hybrid density functional revDSD-PBEP86 (Santra et al., 2019), which has been recommended for spectroscopic studies of medium-sized biomolecules (Barone et al., 2020; Yang et al., 2021; Mehta et al., 2023). These computations have been performed in conjunction with the jun-cc-pVTZ (denoted hereafter as junTZ) basis set (Papajak et al., 2011), which provides the optimal accuracy/cost ratio, as recently discussed by Xu et al. (2024). Moreover, the B3LYP (Becke, 1993)/SNSD (Barone et al., 2014) level has been used in the anharmonic computations. For both density functional theory (DFT) functionals, the dispersion correction proposed by Grimme (2011) has been added using the D3 (Grimme et al., 2010) version with Becke–Johnson (BJ) damping (Grimme et al., 2011; Najibi and Goerigk, 2018). For brevity, hereafter, the revDSD-PBE86-D3/jun-cc-pVTZ and B3LYP-D3/SNSD levels will be denoted as revDSD and B3LYP.

Computations of the third- and fourth-order derivatives of the potential energy surface have been performed at the B3LYP level by the numerical differentiation (Barone, 2005; Bloino, 2015) of analytic second-order derivatives, while the cubic electric dipole moment surfaces have been obtained through numerical differentiations of the dipole moment derivatives. The revDSD equilibrium and harmonic computations have been combined with B3LYP anharmonic computations to create a hybrid model used in spectroscopic simulations. The consistency of these two sets of data has been checked automatically, as implemented in GAUSSIAN 16. In other words, the overlap between two sets of normal modes (two different levels of theory) is defined using the linear transformation, as proposed by Duschinsky (1937):

$$Q = JQ' + K,$$

where Q and Q' represent the two sets of mass-weighted normal coordinates. The Duschinsky matrix J describes the projection of normal coordinate basis vectors on those of the other, allowing the automatic check of the normal mode consistency between the two levels of theory used to define the hybrid method. To ensure that the two sets of normal modes computed at different levels of theory are equivalent, a 90% cut-off for each coordinate was required.

This cost-effective (Xu et al., 2024) hybrid revDSD/B3LYP scheme has been further used to compute spectroscopic parameters using the second-order vibrational perturbation theory (VPT2) (Nielsen, 1951; Mills, 1972). The ground vibrational state rotational constants have been obtained from the revDSD equilibrium structure by adding vibrational corrections computed at the revDSD/B3LYP level, which also provided data allowing the determination of the quartic and sextic centrifugal-distortion constants (Puzzarini et al., 2010; Puzzarini, 2013). For the vibrational spectra, it is also necessary to account for the possible presence of anharmonic resonances (Amos et al., 1991; Martin et al., 1995; Barone, 2005; Vázquez and Stanton, 2007; Rosnik and Polik, 2014; Barone et al., 2014; Bloino et al., 2015; Bloino, 2015; Krasnoshchekov et al., 2015; Franke et al., 2021; Mendolicchio et al., 2021; Franke et al., 2021) by the generalized VPT2 (GVPT2) model (Bloino and Barone, 2012;



Bloino et al., 2015), where nearly resonant contributions are removed from the perturbative treatment (leading to the deperturbed model, DVPT2) and treated in a second step variationally. Resonance definition and general recommendations

on the applied computational procedures are described in detail in the tutorial review by Bloino et al. (2016). It should be noted that, although improved criteria to define automatic resonances have been proposed recently, they would have negligible impacts on the energies (Yang and Bloino, 2022). Overall, the GVPT2 scheme employed in this work has been successfully applied to medium-sized or larger biomolecules with up to 100 atoms (Fornaro et al., 2015; Fusè et al., 2019; Yatsyna et al., 2019; Green and Improta, 2020; Yang et al., 2021; Sheng et al., 2021), also in the astrochemical context (Zhao et al., 2021; McIntosh et al., 2024; Alberini et al., 2024), so it is a valuable tool to be employed also for significantly larger cyano-astroCOMs.

3 Results and discussion

3.1 Equilibrium structure and rotational parameters

Selected equilibrium structural parameters of benzonitrile calculated at the revDSD/junTZ level are shown in Figure 2, while Table 1 compares all equilibrium parameters with the semi-experimental equilibrium structure r_e^{SE} (Pulay et al., 1978)

TABLE 1 Equilibrium parameters of benzonitrile (bond lengths in Å; angles in degrees).

	r_e^{SE} ^a	r_e^{BO} ^b	CCSD(T)/ANO1 ^c	rDSD/junTZ
C ₁ -C ₂	1.3968	1.3962	1.4012	1.3993
C ₂ -C ₃	1.3884	1.3882	1.3934	1.3905
C ₃ -C ₄	1.3917	1.3917	1.3967	1.3941
C ₁ -C ₁₂	1.4347	1.4359	1.4393	1.4360
C ₂ -H ₈	1.0780	1.0803	1.0823	1.0826
C ₃ -H ₇	1.0799	1.0803	1.0824	1.0830
C ₄ -H ₉	1.0800	1.0806	1.0828	1.0832
C ₁₂ -N ₁₃	1.1582	1.1583	1.1646	1.1629
MAX ^d	.	0.0023	0.0064	0.0047
MAE ^d	.	0.0007	0.0043	0.0030
C ₁ C ₂ C ₃	119.42	119.52	119.54	119.55
C ₂ C ₃ C ₄	120.27	120.13	120.13	120.17
C ₃ C ₄ C ₆	120.07	120.22	120.19	120.16
C ₂ C ₁ C ₅	120.55	120.50	120.46	120.41
C ₁ C ₂ H ₈	119.77	119.61	119.61	119.64
C ₄ C ₃ H ₇	120.10	120.16	120.16	120.14
MAX ^d	.	0.16	0.16	0.15
MAE ^d	.	0.09	0.09	0.08

^aSemi-experimental r_e^{SE} from Rudolph et al. (2013), obtained by combining the experimental ground-state rotational constants for a set of isotopologs with rovibrational corrections derived from cubic force fields determined at the B3LYP level.

^bTheoretical best estimated from r_e^{BO} Rudolph et al. (2013), obtained using a composite *ab initio* approach based on CCSD(T) and MP2 all-electron optimizations with basis sets up to quintuple-zeta quality.

^cTheoretical structure obtained at the CCSD(T)/ANO1 level from Zdanovskaia et al. (2022).

^dLargest absolute (|MAX|) and mean absolute errors (MAEs) of the bond length and angles compared to the r_e^{SE} from Rudolph et al. (2013).

TABLE 2 Rotational spectroscopic constants for the ground vibrational state of benzonitrile.

	Experiment ^a	CCSD(T)/ANO1 ^b	rDSD/junTZ//B3LYP/SNSD
A_0 (MHz)	5,655.265,428	5,616.	5,638.
B_0 (MHz)	1,546.8757715	1535.	1,541.
C_0 (MHz)	1,214.4040832	1,205.	1,210.
Δ_J (kHz)	0.0452858	0.0437	0.0433
Δ_{JK} (kHz)	0.937983	0.923	0.922
Δ_K (kHz)	0.24411	0.241	0.226
δ_J (kHz)	0.01101116	0.0106	0.0106
δ_K (kHz)	0.609187	0.593	0.592
Φ_J (Hz)	0.000002486	0.00000230	0.00000226
Φ_{JK} (Hz)	0.0015586	0.00149	0.00150
Φ_{KJ} (Hz)	-0.007863	-0.00761	-0.00769
Φ_K (Hz)	[0.0066915]	0.0066915	0.0067529
ϕ_J (Hz)	0.000001159	0.00000110	0.00000105
ϕ_{JK} (Hz)	0.0007398	0.000755	0.000757
ϕ_K (Hz)	0.007480	0.00712	0.00714

^aSpectroscopic constants derived by Zdanovskaia et al. (2022) using the single-state approach based on the ground state

^bSpectroscopic constants obtained by Zdanovskaia et al. (2022) using the VPT2 computations at the CCSD(T)/ANO1 level.

derived in the reference (Rudolph et al., 2013) by combining the experimental ground-state rotational constants for a set of isotopologs with rovibrational corrections derived from cubic force fields determined at the B3LYP level (Piccardo et al., 2015). Moreover, Table 1 reports the best estimated theoretical structure r_{BO} obtained using the composite scheme employing all-electron CCSD(T) and MP2 geometry optimizations, with basis sets up to the quintuple-zeta, reaching this way the complete basis set (CBS) limit, as well as computations at the CCSD(T)/ANO1 level (Rajasekhar et al., 2022). Structural parameters computed by all combinations of revDSD and B3LYP functionals with the junTZ and SNSD basis sets are provided in Supplementary Material, along with the Cartesian coordinates by revDSD/junTZ. All DFT structures agree very well with the r_e^{SE} reference, among which revDSD/junTZ shows the smallest mean absolute errors (MAEs) of approximately 0.0030 Å° for bond lengths and 0.08° for the angles, which, in terms of the largest discrepancies, correspond to approximately 0.005 Å° and $\pm 0.15^\circ$, respectively. The good quality structure with MAEs of 0.0045 Å° and 0.13°, respectively, is also observed for B3LYP/SNSD, justifying its application in the hybrid scheme. Interestingly, the revDSD/junTZ structure is closer to the r_e^{SE} reference than the CCSD(T)/ANO1 structure, further proving the reliability of revDSD as a cost-effective computational model, allowing to derive accurate geometrical parameters (Ceselin et al., 2021; Barone and Lazzari, 2023).

The final validation is provided by the direct comparison with the experiment, i.e., spectroscopic constants from Watson's asymmetric rotor Hamiltonian (A-reduction, I' representation), which are given in Table 2. Interestingly, the vibrational ground-state rotational constants obtained based on the revDSD structures with anharmonic corrections computed at the revDSD/B3LYP level

agree with experiment within 0.4%, which is even better than the CCSD(T)/ANO1 obtained by Zdanovskaia et al. (2022). Moreover, good agreement, again similar to the CCSD(T)/ANO1 results, is also obtained for the quartic and sextic centrifugal-distortion constants. Notably, in some cases, such as the Φ_J sextic constant, very good agreement with the most recent global fit including previous and expanded mm-wave measurements (Zdanovskaia et al., 2022) is obtained, while older experimental data reported values smaller by 50%.

3.2 Vibrational properties and IR spectra

Table 3 compares harmonic vibrational wavenumbers and IR intensities with those computed at the CCSD(T)/ANO1 level, showing very good agreement with the average error of approximately 6 cm^{-1} and largest differences of approximately 18 cm^{-1} , as well as qualitative agreement for IR intensities, with a MAE below 1 km/mol, and largest discrepancies of approximately ± 7 km/mol observed for the most intense bands ν_{18} and ν_{19} . Thus, the good accuracy of revDSD harmonic wavenumbers is also demonstrated for benzonitrile, in accordance with what has been observed based on the comparison with CCSD(T) results with the CBS extrapolation from MP2 computations (Pietropolli Charmet et al., 2022; Tasinato et al., 2022; Xu et al., 2024). In Table 3 and following, we have adapted mode numbering, mode description, and Wilson notation, as done by Rajasekhar et al. (2022).

Table 4 lists all fundamental anharmonic wavenumbers and IR intensities of benzonitrile computed at the rDSD/junTZ//B3LYP/SNSD GVPT2 level, while selected overtones and combination bands are given in Table 5. The accuracy of the simulated IR

TABLE 3 Harmonic wavenumbers (ω, cm^{-1}) and IR intensities (km/mol) compared with reference computed data.

Sym	CCSD(T)/ANO1 ^a		rDSD/junTZ	
	ω	IR int.	ω	IR int.
A1				
ν_1	3,219	3.53	3,221	3.85
ν_2	3,206	5.43	3,208	6.29
ν_3	3,189	0.01	3,189	0.00
ν_4	2,277	6.14	2,263	11.32
ν_5	1,645	0.12	1,653	0.12
ν_6	1,520	9.82	1,530	8.75
ν_7	1,213	0.16	1,221	0.30
ν_8	1,195	0.55	1,202	0.72
ν_9	1,043	2.67	1,051	3.34
ν_{10}	1,010	0.12	1,018	0.23
ν_{11}	763	1.38	769	1.49
ν_{12}	459	0.00	462	0.00
A2				
ν_{13}	987	0.00	996	0.00
ν_{14}	860	0.00	866	0.00
ν_{15}	402	0.00	405	0.00
B1				
ν_{16}	1,006	0.01	1,009	0.00
ν_{17}	939	2.81	945	2.83
ν_{18}	769	48.33	770	56.01
ν_{19}	696	26.77	679	19.74
ν_{20}	550	15.42	556	15.05
ν_{21}	378	0.69	382	0.64
ν_{22}	143	1.70	144	1.79
B2				
ν_{23}	3,214	6.27	3,217	6.86
ν_{24}	3,198	1.94	3,200	2.52
ν_{25}	1,620	1.33	1,628	1.24
ν_{26}	1,471	6.71	1,481	6.18
ν_{27}	1,348	0.96	1,358	1.15
ν_{28}	1,314	1.97	1,329	1.46
ν_{29}	1,175	0.26	1,182	0.24
ν_{30}	1,096	2.96	1,104	3.60
ν_{31}	629	0.12	633	0.12
ν_{32}	546	0.14	552	0.24
ν_{33}	162	4.44	162	4.65

(Continued on following page)

TABLE 3 (Continued) Harmonic wavenumbers (ω, cm^{-1}) and IR intensities (km/mol) compared with reference computed data.

Sym	CCSD(T)/ANO1 ^a		rDSD/junTZ	
	ω	IR int.	ω	IR int.
MAX	-		15	7.7
MIN	-		-18	-7.0
MAE	-		6	0.8

^aRef. (Zdanovskaia et al., 2022).^bLargest positive (MAX), negative (MIN), and mean absolute errors (MAEs) of the harmonic wavenumbers compared with the CCSD(T)/ANO1 reference (Zdanovskaia et al., 2022).

spectra of benzonitrile in the 500 cm^{-1} – $4,000 \text{ cm}^{-1}$ range can be assessed by comparing with experimental results recorded in the gas phase (Kwon et al., 2003; Rajasekhar et al., 2022). Table 4 provides both spectra, with the latter showing a higher resolution of 0.5 cm^{-1} . This increased resolution allows us to identify and assign non-fundamental transitions, as shown in Figure 3. The GVPT2 computations show overall good agreement with the experiment with a MAE of approximately 11 cm^{-1} and the largest positive and negative errors of approximately $\pm 44 \text{ cm}^{-1}$. Moreover, the largest errors are all related to the C-H stretching vibrations, which contribute to the broad band with some additional side peaks, which has not been assigned. Considering that our simulation agrees within 12 cm^{-1} with the most intense peak assigned as ν_2 , it could be expected that further analysis of experimental data, including non-fundamental transitions, would lead to some re-assignments. Excluding all C-H stretching vibrations from the statistics leads to the average errors of 8 cm^{-1} and maximum discrepancies within 31 cm^{-1} . The most important result is extremely good agreement, within 2 cm^{-1} , for the $\nu_{\text{C}\equiv\text{N}}$, the fingerprint vibration of benzonitrile, which is predicted at 2227 cm^{-1} ($4.49 \mu\text{m}$). This result can be compared with the very recent study where the B3LYP/N07D quadratic force field was combined with VPT2 computations with resonances included (see Esposito et al. (2024) for details) but performed with the SPECTRO code, yielding $\nu_{\text{C}\equiv\text{N}}$ of 2298 cm^{-1} . Indeed, GVPT2 B3LYP-D3/N07D computations in GAUSSIAN 16 lead to a similar result, with $\nu_{\text{C}\equiv\text{N}}$ of 2305 cm^{-1} . Such a huge discrepancy of approximately 70 cm^{-1} was not expected based on previous benchmark tests, highlighting the need for a dedicated validation. We hope that the proposed GVPT2 revDSD/B3LYP methodology will allow us to distinguish between the different cyano-astroCOMs observed in the ISM using the $\nu_{\text{C}\equiv\text{N}}$ vibrations normally occurring in the broader region $2,200$ – $2,400 \text{ cm}^{-1}$ (Császár and Fogarasi, 1989).

A direct comparison between the spectra given in Figure 3 highlights that the GVPT2 computation not only correctly predicts fundamental bands but also a pattern of five distinct non-fundamental bands in the 1650 – 1980 cm^{-1} range, allowing to correct their assignment with respect to the tentative one reported by Rajasekhar et al. (2022). These non-fundamental bands are reported in Table 5, together with those observed in the far-infrared spectra in a high-resolution FTIR experiment (Zdanovskaia et al., 2022). The overestimated intensity of the ν_{18} band at the 758 cm^{-1} should be noted (computed as 746 cm^{-1}), while the experimental spectra show two similar intensity peaks in this range, the second one being ν_{19} at 686 cm^{-1} . However, this discrepancy needs to be linked to the harmonic values, which already predict the intensity of ν_{18} as twice that of ν_{19} . Notably,

CCSD(T)/ANO-1 harmonic IR intensities yield the same pattern of these two bands as revDSD/junT. In order to provide more information about this discrepancy, a dedicated benchmark analysis, which would require appropriate numerical data on integrated intensities Charmet et al. (2013), not available at present, would be required.

Overall, the good accuracy of our simulations, for both fundamental and non-fundamental transitions, allows us to predict the spectra in the NIR region, which is shown in Figures 4A and B for 4000 – 6500 cm^{-1} and 6500 – 10000 cm^{-1} , respectively (the whole 100 – 9000 cm^{-1} spectrum is also reported in Supplementary Material). The most pronounced bands in 4040 – 4300 cm^{-1} and 6000 – 6180 cm^{-1} are related to the combinations of ν_{CH} with in-plane ring deformations and $2\nu_{\text{CH}}$ overtones, respectively. Similarly, at the higher energies, there are combinations of ν_{CH} two quanta transitions with in-plane ring deformations (7070 – 7350 cm^{-1}) and $3\nu_{\text{CH}}$ second overtones (9000 – 9200 cm^{-1}). Although it is expected that the accuracy of GVPT2 results decreases for the higher-quanta transitions, the error bars for the first and second overtones can be estimated based on the fundamental bands (Barone et al., 2015a). For instance, in the case of formaldehyde (Biczysko et al., 2018a), good accuracy within 1 cm^{-1} has been obtained for fundamentals and first overtones of ν_6 and ν_2 , while a lower accuracy of ν_4 of approximately 10 cm^{-1} transfers to errors of 20 cm^{-1} and 26 cm^{-1} for $2\nu_4$ and $3\nu_4$, respectively. This allows us to provide a reliable prediction of $\nu_{\text{C}\equiv\text{N}}$ overtones, with distinct $2\nu_{\text{C}\equiv\text{N}}$ transition at $4,426 \pm 2 \text{ cm}^{-1}$ ($2.26 \mu\text{m}$) and a significantly weaker second overtone $3\nu_{\text{C}\equiv\text{N}}$ at $6,598 \pm 5 \text{ cm}^{-1}$ ($1.52 \mu\text{m}$).

4 Conclusion and astrochemical implications

Good accuracy of simulated MIR spectra, confirmed by a comparison with available experimental results, allowed us to provide predictions regarding the “missing” data on relevance for the astrochemical observations, in particular, concerning the NIR region.

The availability of NIR references is important for the interpretation of data collected during the Mars 2020 (Williford et al., 2018) space mission by instruments such as SuperCam, for incoming ExoMars 2022 (ESZ-Roscosmos) (Vago et al., 2017), as well as for the JWST observations by the NIRSpec (McClure et al., 2023). The advantage of NIR is its lower spectrum congestion than MIR, which is also clearly visible in Figures 3, 4. However, these reference NIR data are often very scarce and were not available even

TABLE 4 Fundamental wavenumbers (ν, cm^{-1}) and IR intensities (km/mol) computed at the GVPT2//revDSD/junTZ//B3LYP/SNSD level for benzonitrile compared with reference experimental and computed data.

Sym	Mode description ^a Wilson notation		Ref. ^a		Ref. ^b			Current work		Assignments (PED) ^c
			Expt	Theory ^d	Expt	Theory ^e	IR Int. scaled	ν	IR int	
A1										
ν_1	20a	ν CH	3,080	3,207	3,106	3,210	2.40	3,148	2.19	ν CH
ν_2	2	ν CH	3,071	3,196	3,066	3,208	6.54	3,078	3.90	ν CH
ν_3	7a	ν CH	3,042	3,178	3,043	3,198	8.46	2,999	1.20	ν CH
ν_4	ν CN	ν CN	2,232	2,332	2,229	2,323	34.02	2,227	7.44	ν CN, ν CC
ν_5	8a	ν CC	1,599	1,641	1,599	1,643	0.62	1,610	0.01	ν CC, β CCH
ν_6	19a	ν CC	1,492	1,582	1,491	1,509	8.39	1,496	6.98	β HCC, β R sym, ν CC
ν_7	13	X-sens	1,191	1,220	1,193	1,214	0.33	1,202	0.08	ν CC, β CCH, β R sym
ν_8	9a	Ring	1,178	1,203	1,178	1,192	0.93	1,185	0.84	β CCH, ν CC
ν_9	18a	β CH	1,027	1,050	1,027	1,045	3.79	1,039	1.90	ν CC, β R sym, β CCH
ν_{10}	12	β CH	1,001	1,019	1,001	1,010	0.00	1,008	0.14	ω CCCH, τ R asy
ν_{11}	1	X-sens	769	774	758	769	2.05	764	1.11	β R tri, ν CC
ν_{12}	6a	X-sens	461	467	459	463	0.00	458	0.00	β R tri, ν CC
A2										
ν_{13}	17a	γ CH	978	1,002	975	984	0.00	968	0.00	ω CCCH, τ R asy
ν_{14}	10a	γ CH	848	863	844	849	0.00	841	0.00	ω CCCH
ν_{15}	16a	ϕ CC	401	410	398	408	0.00	395	0.00	τ R asy, ω CCCH
B1										
ν_{16}	5	γ CH	987	1,021	1,001	1,008	0.37	977	0.00	β R asy, ν CC
ν_{17}	17b	γ CH	925	954	926	935	2.50	917	2.86	ω CCCH
ν_{18}	11	γ CH	758	781	758	773	34.79	746	50.72	ω CCCH, τ R tri, ω CCCC
ν_{19}	4	ϕ CC	686	706	687	704	38.87	656	23.67	τ R asy, ω CCCH
ν_{20}	16b	X-sens	548	573	547	566	17.79	531	12.09	β CCN, ω CCCH, τ R asy
ν_{21}	γ CN	X-sens	381	392	372	388	0.61	371	0.72	τ R asy, β CCN
ν_{22}	10b	γ CN	172	147	141	147	1.93	138	1.90	ω CCCC, β CCN, τ R tri
B2										
ν_{23}	20b	ν CH	3,039	3,188	3,093	3,208	6.54	3,093	7.49	ν CH
ν_{24}	7b	ν CH	3,027	3,204	3,027	3,190	3.95	3,068	0.86	ν CH
ν_{25}	8b	ν CC	1,584	1,615	1,583	1,614	0.80	1,591	0.89	ν CC
ν_{26}	19b	ν CC	1,448	1,481	1,448	1,462	6.69	1,454	5.73	β CCH, ν CC
ν_{27}	14	ν CC	1,337	1,361	1,335	1,351	1.79	1,337	0.25	ν CC, β CCH
ν_{28}	3	β CH	1,298	1,319	1,288	1,322	0.46	1,298	1.58	β CCH, ν CC
ν_{29}	9b	β CH	1,163	1,188	1,163	1,176	0.16	1,172	0.13	β CCH, ν CC
ν_{30}	18b	β CH	1,071	1,105	1,071	1,099	4.35	1,093	2.52	β CCH, ν CC
ν_{31}	6b	α CCC	629	641		633	0.12	628	0.11	β R sym

(Continued on following page)

TABLE 4 (Continued) Fundamental wavenumbers (ν, cm^{-1}) and IR intensities (km/mol) computed at the GVPT2//revDSD/junTZ//B3LYP/SNSD level for benzonitrile compared with reference experimental and computed data.

Sym	Mode description ^a Wilson notation		Ref. ^a		Ref. ^b			Current work		Assignments (PED) ^c
			Expt	Theory ^d	Expt	Theory ^e	IR Int. scaled	ν	IR int	
ν_{32}	β CN	β CN	551	570	547	559	0.27	547	0.09	β CCC, ω CCCN
ν_{33}	15	X-sens	162	169		167	4.65	158	4.69	β R asy, ω CCCN
All		MAX ^f	42							
		MIN ^f	-44							
		MAE ^f	11							
Exclude all ν CH		MAX ^g	22							
		MIN ^g	-31							
		MAE ^g	8							

^aRef (Kwon et al., 2003).
^bRef (Rajasekhar et al., 2022).
^cNormal mode assignments, ν , β , ω , τ , and tri denote the stretching, in-plane bending, out-of-plane bending, torsion, and trigonal deformation, respectively. “sym” and “asy” stand for symmetrical and asymmetric deformation, respectively.
^dScaled harmonic computations at the B3LYP/6-311++G(2df,2pd) level of theory.
^eScaled harmonic computations at the B3LYP/aug-cc-pVDZ level of theory.
^fLargest positive (MAX), negative (MIN), and mean absolute errors (MAEs) of the benzonitrile fundamental wavenumbers compared with the experiment by Rajasekhar et al. (2022).
^gLargest positive (MAX), negative (MIN), and mean absolute errors (MAEs) in the benzonitrile fundamental wavenumbers, with all C-H stretching excluded, compared with the experiment by Rajasekhar et al. (2022).

TABLE 5 Non-fundamental band wavenumbers (ν, cm^{-1}) and IR intensities (km/mol) computed at the GVPT2//revDSD/junTZ//B3LYP/SNSD level for benzonitrile compared with reference experimental data.

Experiment		Current work		
Assign.	ν	Assign.	ν	IR int.
$2\nu_{22}$	282 ^a	$2\nu_{22}$	275	0.007
$\nu_{22}+\nu_{33}$	303 ^a	$\nu_{22}+\nu_{33}$	296	0
$2\nu_{33}$	323 ^a	$2\nu_{33}$	315	0.01
$2\nu_{32}+2\nu_{22}$	1,393 ^b	$\nu_{18}+\nu_{19}$	1,397	0.41
$2\nu_{18}+\nu_{22}$	1,688 ^b	$\nu_{17}+\nu_{18}$	1,658	1.37
$\nu_{26}+\nu_{22}$	1,769 ^b	$\nu_{14}+\nu_{17}$	1,754	1.30
$\nu_{26}+3\nu_{22}$	1,816 ^b	$\nu_{13}+\nu_{14}$	1,803	1.69
$\nu_{26}+\nu_{12}$	1,900 ^b	$\nu_{16}+\nu_{17}, \nu_{13}+\nu_{17}$	1,883	2.83
$\nu_{26}+\nu_{32}$	1,970 ^b	$\nu_{13}+\nu_{16}, 2\nu_{15}$	1,942	3.23
$\nu_{32}+\nu_{18}$	2,178 ^b	$2\nu_{30}$	2,178	0.02

^aHigh-resolution IR spectra in the gas phase obtained by Zdanovskaia et al. (2022).
^bGas-phase IR spectra obtained by Rajasekhar et al. (2022).

for benzonitrile prior to this work. It has been already highlighted that anharmonic computations provide significant support in the analysis of experimental results and identification of plausible molecules by NIR features (Fornaro et al., 2020; Alberini et al., 2024). Computational spectroscopy can also support the identification of $\text{BC}\equiv\text{N}$ in other spectral regions, also considering effects due to the interactions with cosmic rays (Öberg, 2016; Arumainayagam et al., 2021), relevant for different astrochemical environments, from

the ISM to planetary atmospheres or soil. These interactions can initiate different processes within molecules, depending on the photon energies, and can lead to electronic excitation within neutral molecules or create ions by ejecting off the valence or even inner-layer electrons. Interactions with photons can lead to the creation of new molecules, or their damage, but are also relevant for extending observable spectral ranges (Öberg, 2016). Extensive laboratory experimental investigation of the photoabsorption spectra of benzonitrile recorded using synchrotron radiation in $35'000 - 90'000\text{cm}^{-1}$ (4.3–11.1 eV, 0.111–0.286 μm), which encompasses several neutral and ionic excited states, as recently reported by Rajasekhar et al. (2022). From a computational perspective, these processes can be simulated by means of vibronic computations (Bloino et al., 2016; Barone et al., 2021), which have been demonstrated to allow us to decipher a broad range of energies by the combination of two-state electronic transitions for a series of halogenated benzene (Palmer et al., 2015a; b). Moreover, first-principle spectral simulations also allow us to obtain reference data for unstable species difficult to study in the laboratories and to improve the resolution and predict spectra at a broad range of temperatures (Zhao et al., 2021). Computational spectroscopy studies combining anharmonic vibrational and vibronic simulations covering the broad range from MIR at approximately 20 μm up to even 20 nm in a high-energy photoelectron range can be extended toward other cyano-astroCOMs, supporting their possible detection. The most relevant are those based on aromatic systems, such as 1- and 2-cyanocyclopentadiene (McCarthy et al., 2021; Lee et al., 2021), and 1- and 2-cyanonaphthalene (McGuire et al., 2021), which have been already discovered in TMC-1. However, it can be expected that similar accuracy can also be obtained for aliphatic systems, for

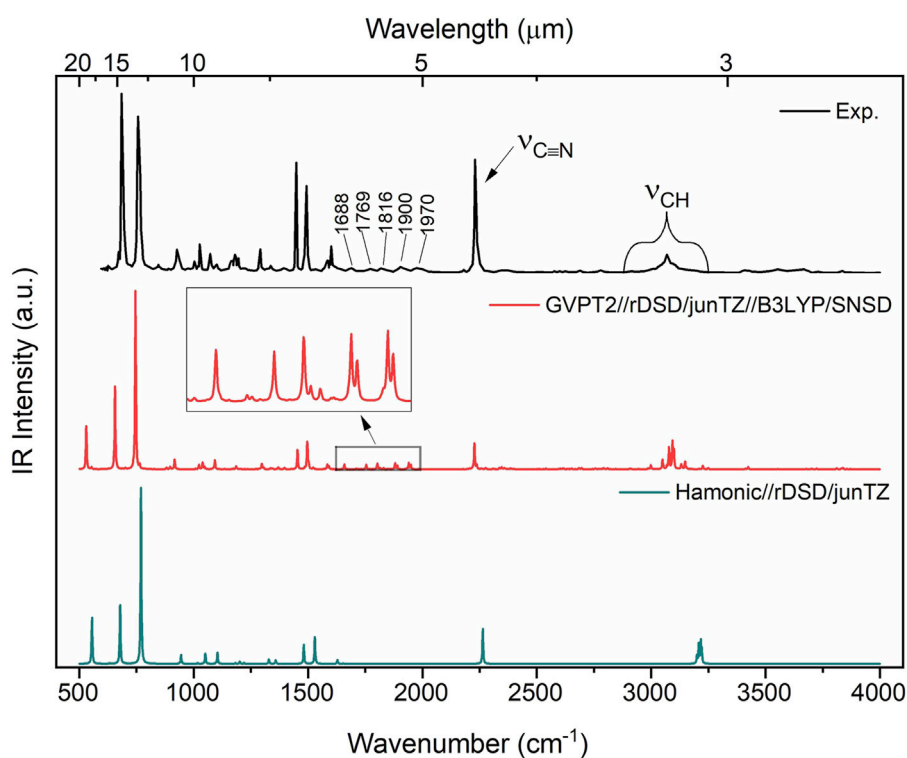


FIGURE 3
IR spectrum of benzonitrile in the range 500–4,000 cm^{-1} . Computed stick spectra were broadened by Lorentzian functions with half-width at half-maximum (HWHM) of 2 cm^{-1} . The experimental IR gas-phase spectrum of benzonitrile (Rajasekhar et al., 2022) is shown for comparison.

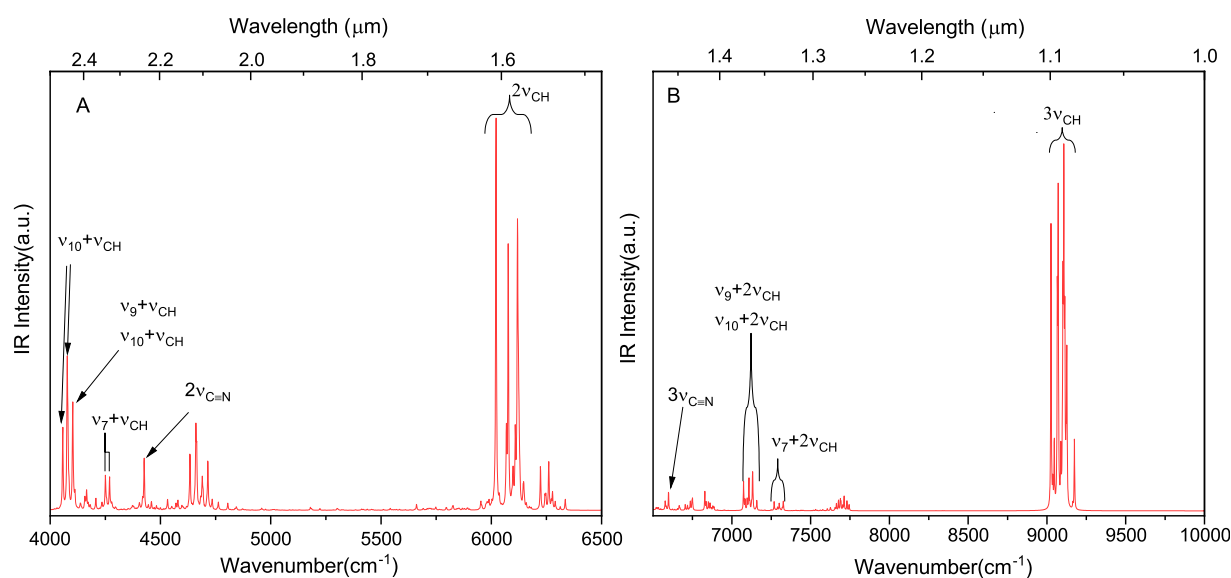


FIGURE 4
NIR spectra simulated at the GVPT2//rDSD/junTZ//B3LYP/SNSD level. The spectra were broadened by Lorentzian functions with HWHM of 2 cm^{-1} .

which several conformers can be present (Barone et al., 2013; 2015b). This situation was highlighted by the recent discovery of five cyano-derivatives of propene (CH_2CHCH_3), based on the QUIJOTE line survey of TMC-1 (Cernicharo et al., 2022). Such

computations, including electronic spectra for benzonitrile and MIR to PES spectra for other $\text{C}\equiv\text{N}$ -astroCOM species, are deferred to subsequent works, within the framework of development of the COSY-ASTRO dataset (COSY COST Action CA21101, 2024).

Data availability statement

The original contributions presented in the study are included in the article/Supplementary Material; further inquiries can be directed to the corresponding author.

Author contributions

YX: formal analysis, investigation, validation, writing—original draft, writing—review and editing, data curation, and visualization. MB: formal analysis, investigation, validation, writing—original draft, writing—review and editing, conceptualization, funding acquisition, methodology, project administration, resources, and supervision.

Funding

The author(s) declare that financial support was received for the research, authorship, and/or publication of this article. This work was performed within COST Action CA21101 “Confined molecular systems: from a new generation of materials to the stars” (COSY) supported by COST (European Cooperation in Science and Technology). This work was supported by the National Natural Science Foundation of China (Grant No. 31870738).

Acknowledgments

MB acknowledges support from the COST Action “COSY,” in particular, discussions with Action Chair Prof. María Pilar de Lara-

Castells, Action Vice-Chair Prof. Cristina Puzzarini, and WG5 “Confined Systems in Astrochemistry” Leader Prof. Lauri Halonen. MB and XY thank Prof. Julien Bloino for fruitful discussions on anharmonic computations.

Conflict of interest

The authors declare that the research was conducted in the absence of any commercial or financial relationships that could be construed as a potential conflict of interest.

The author(s) declared that they were an editorial board member of Frontiers, at the time of submission. This had no impact on the peer review process and the final decision.

Publisher's note

All claims expressed in this article are solely those of the authors and do not necessarily represent those of their affiliated organizations, or those of the publisher, the editors, and the reviewers. Any product that may be evaluated in this article, or claim that may be made by its manufacturer, is not guaranteed or endorsed by the publisher.

Supplementary material

The Supplementary Material for this article can be found online at: <https://www.frontiersin.org/articles/10.3389/fchem.2024.1439194/full#supplementary-material>

References

- Alberini, A., Fornaro, T., García-Florentino, C., Biczysko, M., Poblacion, I., Aramendia, J., et al. (2024). Investigating the stability of aromatic carboxylic acids in hydrated magnesium sulfate under uv irradiation to assist detection of organics on mars. *Sci. Rep.* 14, 15945. doi:10.1038/s41598-024-66669-8
- Amos, R. D., Handy, N. C., Green, W. H., Jayatilaka, D., Willetts, A., and Palmieri, P. (1991). Anharmonic vibrational properties of CH_2F_2 : a comparison of theory and experiment. *J. Chem. Phys.* 95, 8323–8336. doi:10.1063/1.461259
- Arumainayagam, C. R., Herbst, E., Heays, A. N., Mullikin, E., Farrah, M., and Mavros, M. G. (2021). “Extraterrestrial photochemistry: principles and applications,” in *Prebiotic photochemistry: from urey-miller-like experiments to recent findings*. Editors F. Saija and G. Cassone (Cambridge, UK: The Royal Society of Chemistry), 9–36. doi:10.1039/9781839164354-00009
- Bak, B., Christensen, D., Dixon, W. B., Hansen-Nygaard, L., and Rastrup-Andersen, J. (1962). Benzene ring distortion by one substituent. Microwave determination of the complete structure of benzonitrile. *J. Chem. Phys.* 37, 2027–2031. doi:10.1063/1.1733422
- Bak, B., and Nielsen, J. T. (1960). Infrared absorption spectra of benzonitrile and its monodeuterated derivatives: tentative assignment of fundamentals. *Z. Elektrochem. Ber. Bunsenges. Phys. Chem.* 64, 560–562. doi:10.1002/bbpc.196000003
- Barone, V. (2005). Anharmonic vibrational properties by a fully automated second-order perturbative approach. *J. Chem. Phys.* 122, 014108. doi:10.1063/1.1824881
- Barone, V., Alessandrini, S., Biczysko, M., Cheeseman, J. R., Clary, D. C., McCoy, A. B., et al. (2021). Computational molecular spectroscopy. *Nat. Rev. Methods Prim.* 1, 38–27. doi:10.1038/s43586-021-00034-1
- Barone, V., Biczysko, M., and Bloino, J. (2014). Fully anharmonic ir and Raman spectra of medium-size molecular systems: accuracy and interpretation. *Phys. Chem. Chem. Phys.* 16, 1759–1787. doi:10.1039/C3CP53413H
- Barone, V., Biczysko, M., Bloino, J., Cimino, P., Penocchio, E., and Puzzarini, C. (2015a). CC/DFT route toward accurate structures and spectroscopic features for observed and elusive conformers of flexible molecules: pyruvic acid as a case study. *J. Chem. Theory Comput.* 11, 4342–4363. doi:10.1021/acs.jctc.5b00580
- Barone, V., Biczysko, M., Bloino, J., Cimino, P., Penocchio, E., and Puzzarini, C. (2015b). CC/dft route toward accurate structures and spectroscopic features for observed and elusive conformers of flexible molecules: pyruvic acid as a case study. *J. Chem. Theory Comput.* 11, 4342–4363. doi:10.1021/acs.jctc.5b00580
- Barone, V., Biczysko, M., Bloino, J., and Puzzarini, C. (2013). Glycine conformers: a never-ending story? *Phys. Chem. Chem. Phys.* 15, 1358–1363. doi:10.1039/C2CP43884D
- Barone, V., Biczysko, M., and Puzzarini, C. (2015c). Quantum chemistry meets spectroscopy for astrochemistry: increasing complexity toward prebiotic molecules. *Acc. Chem. Res.* 48, 1413–1422. doi:10.1021/ar5003285
- Barone, V., Ceselin, G., Fusè, M., and Tasinato, N. (2020). Accuracy meets interpretability for computational spectroscopy by means of hybrid and double-hybrid functionals. *Front. Chem.* 8, 584203. doi:10.3389/fchem.2020.584203
- Barone, V., and Lazzari, F. (2023). Hunting for complex organic molecules in the interstellar medium: the role of accurate low-cost theoretical geometries and rotational constants. *J. Phys. Chem. A* 127, 10517–10527. doi:10.1021/acs.jpca.3c06649
- Barone, V., and Puzzarini, C. (2023). Gas-phase computational spectroscopy: the challenge of the molecular bricks of life. *Annu. Rev. Phys. Chem.* 74, 29–52. doi:10.1146/annurev-physchem-082720-103845
- Becke, A. D. (1993). Density-functional thermochemistry. iii. the role of exact exchange. *J. Chem. Phys.* 98, 5648–5652. doi:10.1063/1.464913
- Biczysko, M., Bloino, J., and Puzzarini, C. (2018a). Computational challenges in astrochemistry. *WIREs Comput. Mol. Sci.* 8, e1349. doi:10.1002/wcms.1349
- Biczysko, M., Krupa, J., and Wierzejewska, M. (2018b). Theoretical studies of atmospheric molecular complexes interacting with NIR to UV light. *Faraday Discuss.* 212, 421–441. doi:10.1039/C8FD00094H
- Bloino, J. (2015). A vpt2 route to near-infrared spectroscopy: the role of mechanical and electrical anharmonicity. *J. Phys. Chem. A* 119, 5269–5287. doi:10.1021/jp509985u

- Bloino, J., Baiardi, A., and Biczysko, M. (2016). Aiming at an accurate prediction of vibrational and electronic spectra for medium-to-large molecules: an overview. *Int. J. Quantum Chem.* 116, 1543–1574. doi:10.1002/qua.25188
- Bloino, J., and Barone, V. (2012). A second-order perturbation theory route to vibrational averages and transition properties of molecules: general formulation and application to infrared and vibrational circular dichroism spectroscopies. *J. Chem. Phys.* 136, 124108. doi:10.1063/1.3695210
- Bloino, J., Biczysko, M., and Barone, V. (2015). Anharmonic effects on vibrational spectra intensities: infrared, Raman, vibrational circular dichroism and Raman optical activity. *J. Phys. Chem. A* 119, 11862–11874. doi:10.1021/acs.jpca.5b10067
- Burova, T. G., and Anashkin, A. A. (2007). Quantum-mechanical calculation of the intensity distribution in the resonance Raman spectrum of benzonitrile. *Opt. Spectrosc.* 102, 825–828. doi:10.1134/S0030400X07060045
- Casado, J., Nygaard, L., and Sørensen, G. O. (1971). Microwave spectra of isotopic benzonitriles. Refined molecular structure of benzonitrile. *J. Molec. Struct.* 8, 211–224. doi:10.1016/0022-2860(71)80056-X
- Cernicharo, J., Fuentetaja, R., Cabezas, C., Agúndez, M., Marcelino, N., Tercero, B., et al. (2022). Discovery of five cyano derivatives of propene with the QUIJOTE line survey. *Astron. Astrophys.* 663, L5. doi:10.1051/0004-6361/202244255
- Ceselin, G., Barone, V., and Tasinato, N. (2021). Accurate biomolecular structures by the nano-LEGO approach: pick the bricks and build your geometry. *J. Chem. Theory Comput.* 17, 7290–7311. doi:10.1021/acs.jctc.1c00788
- Charmet, A. P., Stoppa, P., Tasinato, N., Giorgianni, S., Barone, V., Biczysko, M., et al. (2013). An integrated experimental and quantum-chemical investigation on the vibrational spectra of chlorofluoromethane. *J. Chem. Phys.* 139, 164302. doi:10.1063/1.4825380
- COSY COST Action CA21101 (2024). COSY Confined molecular systems: from a new generation of materials to the stars CA21101 COST Action.
- Császár, A. G., and Fogarasi, G. (1989). Scaled quantum mechanical (SQM) force field and theoretical vibrational spectrum for benzonitrile. *Spectrochim. Acta A* 45, 845–854. doi:10.1016/0584-8539(89)80222-3
- [Dataset] Herschel Space Observatory (2017). *Herschel's view of the Taurus molecular cloud annotated*. Available at: <https://www.herschel.caltech.edu/image/nhsc2017-003a>.
- Duschinsky, F. (1937). The importance of the electron spectrum in multi atomic molecules. concerning the franck-condon principle. *Acta Physicochim. URSS* 7, 551.
- Eigenbrode, J. L., Summons, R. E., Steele, A., Freissinet, C., Millan, M., Navarro-González, R., et al. (2018). Organic matter preserved in 3-billion-year-old mudstones at Gale crater, Mars. *Science* 360, 1096–1101. doi:10.1126/science.aas9185
- Endres, C. P., Schlemmer, S., Schilke, P., Stutzki, J., and Müller, H. S. P. (2016). The Cologne database for molecular spectroscopy, CDMS, in the virtual atomic and molecular data centre, VAMDC. *J. Mol. Spectrosc.* 327, 95–104. doi:10.1016/j.jms.2016.03.005
- Erlandsson, G. (1954). Microwave spectrum of benzonitrile. *J. Chem. Phys.* 22, 1152. doi:10.1063/1.1740313
- Esposito, V. J., Fortenberry, R. C., Boersma, C., Maragkoudakis, A., and Allamandola, L. J. (2024). CN stretches around 4.4 microns dominate the IR absorption spectra of cyano-polycyclic aromatic hydrocarbons. *Mon. Not. R. Astron. Soc. Lett.* 531, L87–L93. doi:10.1093/mnrasl/slae037
- Fornaro, T., Brucato, J. R., Poggiali, G., Corazzi, M. A., Biczysko, M., Jaber, M., et al. (2020). UV irradiation and near infrared characterization of laboratory mars soil analog samples. *Front. Astron. Space Sci.* 7. doi:10.3389/fspas.2020.539289
- Fornaro, T., Carnimeo, I., and Biczysko, M. (2015). Toward feasible and comprehensive computational protocol for simulation of the spectroscopic properties of large molecular systems: the anharmonic infrared spectrum of uracil in the solid state by the reduced dimensionality/hybrid vpt2 approach. *J. Phys. Chem. A* 119, 5313–5326. doi:10.1021/jp510101y
- Fortenberry, R. C. (2024a). Quantum chemistry and astrochemistry: a match made in the heavens. *J. Phys. Chem. A* 128, 1555–1565. doi:10.1021/acs.jpca.3c07601
- Fortenberry, R. C. (2024b). A vision for the future of astrochemistry in the interstellar medium by 2050. *ACS Phys. Chem. Au* 4, 31–39. doi:10.1021/acsphyschemau.3c00043
- Franke, P. R., Stanton, J. F., and Doublerly, G. E. (2021). How to VPT2: accurate and intuitive simulations of CH stretching infrared spectra using VPT2+K with large effective Hamiltonian resonance treatments. *J. Phys. Chem. A* 125, 1301–1324. doi:10.1021/acs.jpca.0c09526
- Frisch, M. J., Trucks, G. W., Schlegel, H. B., Scuseria, G. E., Robb, M. A., Cheeseman, J. R., et al. (2016). *Gaussian 16 rev. C.01*. Wallingford CT: Gaussian, Inc.
- Frost, A. J., Lau, R. M., Burtcher, L., Packham, C., Tasker, E. J., Rees, G. A., et al. (2022). IR 2022: an infrared-bright future for ground-based IR observatories in the era of JWST. *Nat. Astron.* 6, 772–773. doi:10.1038/s41550-022-01733-9
- Fulvio, D., Potapov, A., He, J., and Henning, T. (2021). Astrochemical pathways to complex organic and prebiotic molecules: experimental perspectives for *in situ* solid-state studies. *Life* 11, 568. doi:10.3390/life11060568
- Fusè, M., Mazzeo, G., Longhi, G., Abbate, S., Masi, M., Evidente, A., et al. (2019). Unbiased determination of absolute configurations by vis-à-vis comparison of experimental and simulated spectra: the challenging case of diplopyrone. *J. Phys. Chem. B* 123, 9230–9237. PMID: 31580674. doi:10.1021/acs.jpcc.9b08375
- Green, J. A., and Improta, R. (2020). Vibrations of the guanine-cytosine pair in chloroform: an anharmonic computational study. *Phys. Chem. Chem. Phys.* 22, 5509–5522. doi:10.1039/C9CP06373K
- Green, J. H. S., and Harrison, D. J. (1976). Vibrational spectra of benzene derivatives—XVII. Benzonitrile and substituted benzonitriles. *Spectrochim. Acta A* 32, 1279–1286. doi:10.1016/0584-8539(76)80166-3
- Grimme, S. (2011). Density functional theory with london dispersion corrections. *WIREs Comput. Mol. Sci.* 1, 211–228. doi:10.1002/wcms.30
- Grimme, S., Antony, J., Ehrlich, S., and Krieg, H. (2010). A consistent and accurate *ab initio* parametrization of density functional dispersion correction (dft-d) for the 94 elements h-pu. *J. Chem. Phys.* 132, 154104. doi:10.1063/1.3382344
- Grimme, S., Ehrlich, S., and Goerigk, L. (2011). Effect of the damping function in dispersion corrected density functional theory. *J. Comput. Chem.* 32, 1456–1465. doi:10.1002/jcc.21759
- Guélin, M., and Cernicharo, J. (2022). Organic molecules in interstellar space: latest advances. *Front. Astron. Space Sci.* 9. doi:10.3389/fspas.2022.787567
- Krasnoshchekov, S. V., Vogt, N., and Stepanov, N. F. (2015). *Ab initio* anharmonic analysis of vibrational spectra of uracil using the numerical-analytic implementation of operator Van Vleck perturbation theory. *J. Phys. Chem. A* 119, 6723–6737. doi:10.1021/acs.jpca.5b03241
- Kwon, C. H., Kim, H. L., and Kim, M. S. (2003). Vibrational analysis of vacuum ultraviolet mass-analyzed threshold ionization spectra of phenylacetylene and benzonitrile. *J. Phys. Chem. A* 107, 10969–10975. doi:10.1021/jp036391w
- Lasne, J. (2021). Heterogeneous physical chemistry in the atmospheres of earth, mars, and venus: perspectives for rocky exoplanets. *ACS Earth Space Chem.* 5, 149–162. doi:10.1021/acsearthspacechem.0c00126
- Lee, K. L. K., Changala, P. B., Loomis, R. A., Burkhardt, A. M., Xue, C., Cordiner, M. A., et al. (2021). Interstellar detection of 2-cyanocyclopentadiene, C₅H₅CN, a second five-membered ring toward TMC-1. *Astrophys. J. Lett.* 910, L2. doi:10.3847/2041-8213/abe764
- Lemmens, A. K., Rap, D. B., Brünken, S., Buma, W. J., and Rijs, A. M. (2022). Polycyclic aromatic hydrocarbon growth in a benzene discharge explored by IR-UV action spectroscopy. *Phys. Chem. Chem. Phys.* 24, 14816–14824. doi:10.1039/D2CP01631A
- Lemmens, K., Mackie, C., Candian, A., Lee, J., Tielens, M., Anouk, M. R., et al. (2023). Size distribution of polycyclic aromatic hydrocarbons in space: an old new light on the 11.2/3.3 m intensity ratio. *Faraday Discuss.* 245, 380–390. doi:10.1039/D2FD00180B
- Lide, D. R. (1954). Microwave spectrum and structure of benzonitrile. *J. Chem. Phys.* 22, 1577–1578. doi:10.1063/1.1740461
- Loru, D., Steber, A. L., Thunnissen, J. M. M., Rap, D. B., Lemmens, A. K., Rijs, A. M., et al. (2022). New potential candidates for astronomical searches discovered in the electrical discharge of the PAH naphthalene and acetonitrile. *J. Mol. Spectrosc.* 386, 111629. doi:10.1016/j.jms.2022.111629
- Mackie, C. J., Candian, A., Lee, T. J., and Tielens, A. G. G. M. (2022). Anharmonicity and the IR emission spectrum of neutral interstellar PAH molecules. *J. Phys. Chem. A* 126, 3198–3209. doi:10.1021/acs.jpca.2c01849
- Martin, J. M. L., Lee, T. J., Taylor, P. M., and François, J.-P. (1995). The anharmonic force field of ethylene, C₂H₄, by means of accurate *ab initio* calculations. *J. Chem. Phys.* 103, 2589–2602. doi:10.1063/1.469681
- Martin-Drumel, M.-A., Spaniol, J.-T., Hölzel, H., Agúndez, M., Cernicharo, J., Moth-Poulsen, K., et al. (2023). Searches for bridged bicyclic molecules in space—norbornadiene and its cyano derivatives. *Faraday Discuss.* 245, 284–297. doi:10.1039/D3FD00016H
- McCarthy, M. C., Lee, K. L. K., Loomis, R. A., Burkhardt, A. M., Shingledecker, C. N., Charnley, S. B., et al. (2021). Interstellar detection of the highly polar five-membered ring cyanocyclopentadiene. *Nat. Astron.* 5, 176–180. doi:10.1038/s41550-020-01213-y
- McClure, M. K., Rocha, W. R. M., Pontoppidan, K. M., Crouzet, N., Chu, L. E. U., Dartois, E., et al. (2023). An Ice Age JWST inventory of dense molecular cloud ices. *Nat. Astron.* 7, 431–443. doi:10.1038/s41550-022-01875-w
- McGuire, B. A. (2022). 2021 census of interstellar, circumstellar, extragalactic, protoplanetary disk, and exoplanetary molecules. *Astrophys. J. Suppl. Ser.* 259, 30. doi:10.3847/1538-4365/ac2a48
- McGuire, B. A., Burkhardt, A. M., Kalenskii, S., Shingledecker, C. N., Remijan, A. J., Herbst, E., et al. (2018). Detection of the aromatic molecule benzonitrile (c-C₆H₅CN) in the interstellar medium. *Science* 359, 202–205. doi:10.1126/science.aao4890
- McGuire, B. A., Loomis, R. A., Burkhardt, A. M., Lee, K. L. K., Shingledecker, C. N., Charnley, S. B., et al. (2021). Detection of two interstellar polycyclic aromatic hydrocarbons via spectral matched filtering. *Science* 371, 1265–1269. doi:10.1126/science.abb7535
- McIntosh, O., García-Florentino, C., Fornaro, T., Marabello, D., Alberini, A., Siljeström, S., et al. (2024). Undecanoic acid and L-phenylalanine in vermiculture: detection, characterization, and UV degradation studies for biosignature identification on mars. *Astrobiology* 24, 518–537. doi:10.1089/ast.2023.0088

- Mehta, N., Santra, G., and Martin, J. M. (2023). Is explicitly correlated double-hybrid density functional theory advantageous for vibrational frequencies? *Can. J. Chem.* 101, 656–663. doi:10.1139/cjc-2022-0277
- Mendolicchio, M., Bloino, J., and Barone, V. (2021). General perturb-then-diagonalize model for the vibrational frequencies and intensities of molecules belonging to abelian and non-abelian symmetry groups. *J. Chem. Theory Comput.* 17, 4332–4358. doi:10.1021/acs.jctc.1c00240
- Mills, I. M. (1972). *Molecular spectroscopy: modern research (academic press, New York), chap. Vibration-rotation structure in asymmetric- and symmetric-top molecules*, 115–140.
- Najibi, A., and Goerigk, L. (2018). The nonlocal kernel in van der waals density functionals as an additive correction: An extensive analysis with special emphasis on the B97M-v and B97M-V approaches. *J. Chem. Theory Comput.* 14, 5725–5738. doi:10.1021/acs.jctc.8b00842
- Nazari, P., van Gelder, M. L., van Dishoeck, E. F., Tabone, B., van 't Hoff, M. L. R., Ligterink, N. F. W., et al. (2021). Complex organic molecules in low-mass protostars on Solar System scales - II. Nitrogen-bearing species. *Astron. Astrophys.* 650, A150. doi:10.1051/0004-6361/202039996
- Nielsen, H. H. (1951). The vibration-rotation energies of molecules. *Rev. Mod. Phys.* 23, 90–136. doi:10.1103/RevModPhys.23.90
- Öberg, K. I. (2016). Photochemistry and astrochemistry: photochemical pathways to interstellar complex organic molecules. *Chem. Rev.* 116, 9631–9663. doi:10.1021/acs.chemrev.5b00694
- Palmer, M. H., Ridley, T., Hoffmann, S. V., Jones, N. C., Coreno, M., de Simone, M., et al. (2015a). Interpretation of the vacuum ultraviolet photoabsorption spectrum of iodobenzene by *ab initio* computations. *J. Chem. Phys.* 142, 134302. doi:10.1063/1.4916121
- Palmer, M. H., Ridley, T., Hoffmann, S. V., Jones, N. C., Coreno, M., de Simone, M., et al. (2015b). The ionic states of iodobenzene studied by photoionization and *ab initio* configuration interaction and DFT computations. *J. Chem. Phys.* 142, 134301. doi:10.1063/1.4916120
- Papajak, E., Zheng, J., Xu, X., Leverenz, H. R., and Truhlar, D. G. (2011). Perspectives on basis sets beautiful: seasonal plantings of diffuse basis functions. *J. Chem. Theory Comput.* 7, 3027–3034. doi:10.1021/ct200106a
- Peeters, E., Mackie, C., Candian, A., and Tielens, A. G. G. M. (2021). A spectroscopic view on cosmic PAH emission. *Acc. Chem. Res.* 54, 1921–1933. doi:10.1021/acs.accounts.0c00747
- Perez, R., Parès, L. P., Newell, R., Robinson, S., Bernardi, P., Réess, J.-M., et al. (2017). The supercam instrument on the NASA Mars 2020 mission: optical design and performance. *International Conf. Space Opt. — ICSSO 2016 (SPIE)* 10562, 744–752. doi:10.1117/12.2296230
- Petrignani, A., and Candian, A. (2022). “Chapter 3 - astrochemistry: ingredients of life in space,” in *New Frontiers in astrobiology*. Editors R. Thombre and P. Vaishampayan (Elsevier), 49–66. doi:10.1016/B978-0-12-824162-2.00007-5
- Piccardo, M., Penocchio, E., Puzzarini, C., Biczysko, M., and Barone, V. (2015). Semi-experimental equilibrium structure determinations by employing b3lyp/snsd anharmonic force fields: validation and application to semirigid organic molecules. *J. Phys. Chem. A* 119, 2058–2082. doi:10.1021/jp511432m
- Pietropolli Charmet, A., Ceselin, G., Stoppa, P., and Tasinato, N. (2022). The spectroscopic characterization of halogenated pollutants through the interplay between theory and experiment: application to R1122. *Molecules* 27, 748. doi:10.3390/molecules27030748
- Pulay, P., Meyer, W., and Boggs, J. E. (1978). Cubic force constants and equilibrium geometry of methane from Hartree-Fock and correlated wavefunctions. *J. Chem. Phys.* 68, 5077–5085. doi:10.1063/1.435626
- Puzzarini, C. (2013). Rotational spectroscopy meets theory. *Phys. Chem. Chem. Phys.* 15, 6595–6607. doi:10.1039/C3CP44301A
- Puzzarini, C. (2022). Gas-phase chemistry in the interstellar medium: the role of laboratory astrochemistry. *Front. Astron. Space Sci.* 8. doi:10.3389/fspas.2021.811342
- Puzzarini, C., Alessandrini, S., Bizzocchi, L., Melosso, M., and Rivilla, V. M. (2023). From the laboratory to the interstellar medium: a strategy to search for exotic molecules in space. *Front. Astron. Space Sci.* 10. doi:10.3389/fspas.2023.1211784
- Puzzarini, C., Stanton, J. F., and Gauss, J. (2010). Quantum-chemical calculation of spectroscopic parameters for rotational spectroscopy. *Int. Rev. Phys. Chem.* 29, 273–367. doi:10.1080/01442351003643401
- Rajasekhar, B. N., Dharmarpu, V., Das, A. K., Shastri, A., Veeraiya, A., and Krishnakumar, S. (2022). A spectroscopic study of benzonitrile. *J. Quant. Spectrosc. Radiat. Transf.* 283, 108159. doi:10.1016/j.jqsrt.2022.108159
- Rosnik, A. M., and Polik, W. F. (2014). Vpt2+k spectroscopic constants and matrix elements of the transformed vibrational Hamiltonian of a polyatomic molecule with resonances using Van Vleck perturbation theory. *Mol. Phys.* 112, 261–300. doi:10.1080/00268976.2013.808386
- Rudolph, H. D., Demaison, J., and Császár, A. G. (2013). Accurate determination of the deformation of the benzene ring upon substitution: equilibrium structures of benzonitrile and phenylacetylene. *J. Phys. Chem. A* 117, 12969–12982. doi:10.1021/jp408208s
- Santra, G., Sylvetsky, N., and Martin, J. M. L. (2019). Minimally empirical double-hybrid functionals trained against the GMTKN55 database: revDSD-PBEP86-D4, revDOD-PBE-D4, and DOD-SCAN-D4. *J. Phys. Chem. A* 123, 5129–5143. doi:10.1021/acs.jpca.9b03157
- Sharma, S., Roppel, R. D., Murphy, A. E., Beegle, L. W., Bhartia, R., Steele, A., et al. (2023). Diverse organic-mineral associations in Jezero crater, Mars. *Nature* 619, 724–732. doi:10.1038/s41586-023-06143-z
- Sheng, M., Silvestrini, F., Biczysko, M., and Puzzarini, C. (2021). Structural and vibrational properties of amino acids from composite schemes and double-hybrid dft: hydrogen bonding in serine as a test case. *J. Phys. Chem. A* 125, 9099–9114. doi:10.1021/acs.jpca.1c06993
- Sita, M. L., Changala, P. B., Xue, C., Burkhardt, A. M., Shingledecker, C. N., Lee, K. L. K., et al. (2022). Discovery of interstellar 2-cyanoindene (2-C9H7CN) in GOTHAM observations of TMC-1. *Astrophys. J. Lett.* 938, L12. doi:10.3847/2041-8213/ac92f4
- Tasinato, N., Pietropolli Charmet, A., Ceselin, G., Salta, Z., and Stoppa, P. (2022). *In vitro* and *in silico* vibrational-rotational spectroscopic characterization of the next-generation refrigerant HFO-1123. *J. Phys. Chem. A* 126, 5328–5342. doi:10.1021/acs.jpca.2c04680
- Vago, J. L., Westall, F., Coates, A. J., Jaumann, R., Korabel, O., Ciarletti, V., et al. (2017). Habitability on early mars and the search for biosignatures with the ExoMars rover. *Astrobiology* 17, 471–510. doi:10.1089/ast.2016.1533
- Vázquez, J., and Stanton, J. F. (2007). Treatment of fermi resonance effects on transition moments in vibrational perturbation theory. *Mol. Phys.* 105, 101–109. doi:10.1080/00268970601135784
- Webb Space Telescope (2024). *NGC 604 (NIRCam image)*. Available at: <https://webbtelescope.org/contents/media/images/2024/110/01HQNV4G6PR6E7ZSJXRRBQQDS>.
- Williford, K. H., Farley, K. A., Stack, K. M., Allwood, A. C., Beaty, D., Beegle, L. W., et al. (2018). “Chapter 11 - the NASA mars 2020 rover mission and the search for extraterrestrial life,” in *From habitability to life on Mars*. Editors N. A. Cabrol and E. A. Grin (Elsevier), 275–308. doi:10.1016/B978-0-12-809935-3.00010-4
- Xu, R., Jiang, Z., Yang, Q., Bloino, J., and Biczysko, M. (2024). Harmonic and anharmonic vibrational computations for biomolecular building blocks: benchmarking DFT and basis sets by theoretical and experimental IR spectrum of glycine conformers. *J. Comput. Chem.* 45, 1846–1869. doi:10.1002/jcc.27377
- Yamamoto, R., Ishikawa, S., Ebata, T., and Mikami, N. (2000). Vibrational spectra and relaxation of benzonitrile and its clusters using time-resolved stimulated Raman-UV double resonance spectroscopy. *J. Raman Spectrosc.* 31, 295–304. doi:10.1002/(sici)1097-4555(200004)31:4<295::aid-jrs542>3.0.co;2-y
- Yang, Q., and Bloino, J. (2022). An effective and automated processing of resonances in vibrational perturbation theory applied to spectroscopy. *J. Phys. Chem. A* 126, 9276–9302. doi:10.1021/acs.jpca.2c06460
- Yang, Q., Mendolicchio, M., Barone, V., and Bloino, J. (2021). Accuracy and reliability in the simulation of vibrational spectra: a comprehensive benchmark of energies and intensities issuing from generalized vibrational perturbation theory to second order (GVPT2). *Front. Astron. Space Sci.* 8. doi:10.3389/fspas.2021.665232
- Yatsyna, V., Mallat, R., Gorn, T., Schmitt, M., Feifel, R., Rijs, A. M., et al. (2019). Competition between folded and extended structures of alanylalanine (ala-ala) in a molecular beam. *Phys. Chem. Chem. Phys.* 21, 14126–14132. doi:10.1039/C9CP00140A
- Zapata Trujillo, J. C., Pettyjohn, M. M., and McKemmish, L. K. (2023). High-throughput quantum chemistry: empowering the search for molecular candidates behind unknown spectral signatures in exoplanetary atmospheres. *Mon. Not. R. Astron. Soc.* 524, 361–376. doi:10.1093/mnras/stad1717
- Zdanovskaia, M. A., Martin-Drumel, M.-A., Kisiel, Z., Piralí, O., Esselman, B. J., Woods, R. C., et al. (2022). The eight lowest-energy vibrational states of benzonitrile: analysis of Coriolis and Darling-Dennison couplings by millimeter-wave and far-infrared spectroscopy. *J. Mol. Spectrosc.* 383, 111568. doi:10.1016/j.jms.2021.111568
- Zhao, Y., Hochlaf, M., and Biczysko, M. (2021). Identification of DNA bases and their cations in astrochemical environments: computational spectroscopy of thymine as a test case. *Front. Astron. Space Sci.* 8. doi:10.3389/fspas.2021.757007



OPEN ACCESS

EDITED BY
Steve Suib,
University of Connecticut, United States

REVIEWED BY
Xiang Ma,
Taiyuan Institute of Technology, China
Andrey E. Krauklis,
University of Latvia, Latvia

*CORRESPONDENCE
Pellegrino Musto,
✉ pellegrino.musto@cnr.it

RECEIVED 06 August 2024
ACCEPTED 25 September 2024
PUBLISHED 30 October 2024

CITATION
Pannico M, Mensitieri G and Musto P (2024) *In-situ* FTIR spectroscopy of epoxy resin degradation: kinetics and mechanisms. *Front. Chem.* 12:1476965. doi: 10.3389/fchem.2024.1476965

COPYRIGHT
© 2024 Pannico, Mensitieri and Musto. This is an open-access article distributed under the terms of the [Creative Commons Attribution License \(CC BY\)](https://creativecommons.org/licenses/by/4.0/). The use, distribution or reproduction in other forums is permitted, provided the original author(s) and the copyright owner(s) are credited and that the original publication in this journal is cited, in accordance with accepted academic practice. No use, distribution or reproduction is permitted which does not comply with these terms.

In-situ FTIR spectroscopy of epoxy resin degradation: kinetics and mechanisms

Marianna Pannico¹, Giuseppe Mensitieri² and Pellegrino Musto^{1*}

¹Institute of Polymers, Composites and Biomaterials, National Research Council of Italy, Pozzuoli, Italy, ²Department of Chemical, Materials and Production Engineering, University of Naples Federico II, Naples, Italy

We report on an *in situ* FTIR study of the thermo-oxidative degradation of a flexible epoxy resin. Different and complementary approaches to the analysis of the spectral data were employed, providing a detailed description of the process in terms of kinetics and mechanisms. A preliminary normal coordinate analysis, based on the DFT method, allowed for a reliable interpretation of the observed spectrum, increasing the amount of available structural information. Two-dimensional correlation spectroscopy provided details on the evolution of the reacting network structure. The relative stability of the various functional groups was ranked, and the most likely sites of initiation were identified. Oxygen fixation on the network chains produced amide and ketone groups, with the latter developing at a higher rate. The kinetic profiles of various functional groups were accurately simulated by a first-order, biexponential model, which allowed a quantitative comparison among their relative stabilities. The spectroscopic analysis allowed us to propose likely mechanisms and to identify those that occur preferentially.

KEYWORDS

FTIR, epoxy, degradation, kinetics, DFT, mechanism

1 Introduction

Epoxy resins find application in a number of technological sectors owing to their excellent properties and versatility. They represent the main class of matrices for structural composites and are widely used as adhesives, surface coatings, and laminates. Their cured networks exhibit high strength, low creep, negligible cure shrinkage, excellent resistance to corrosion, and reasonable thermal stability (Ratna, 2009; Pascault et al., 2013; Ashcroft et al., 1993). The versatility of epoxy resins stems from the wide choice of available amine hardeners which can be aliphatic or aromatic and give rise to materials with properties ranging from those of rubber to those of a very rigid and brittle network, with glass transition temperatures (T_g 's) of 230–503 K (Ashcroft et al., 1993; Ellis and Ellis, 1993; Bonnaud et al., 2000). A recent development is their application in the field of vibrational damping (Ratna et al., 2004). Vibration is a major concern in dynamic systems as it produces several undesired effects, including noise, fatigue, degraded performance, and the eventual failure of the structure (Barber, 2002; Jones, 2001). Vibration control may be achieved by coupling a viscoelastic material (typically a polymer) with the vibrating surface. The vibrational energy is thus converted into heat and dissipated by the damping polymer (Murayama, 1978; Ferry, 1980). The formulation presented in this study was specifically designed for this purpose, exploiting the viscoelastic behaviour of the network, coupled with its excellent adhesive properties. A mixture of short- and long-chain aliphatic

polyetheramines (jeffamines) has been used as the curing blend, resulting in a rubbery network with a T_g of -33°C . In this application, a main requirement is thermooxidative stability; in fact, continuous mechanical cycling usually induces large temperature excursions, which become more pronounced when the efficiency of the dynamic structure degrades. In general, the thermal stability of epoxies is a major factor affecting their shelf life and the maximum service temperature for any kind of application. A large body of research already exists on the thermo-oxidative degradation of epoxy resin, mainly concerned with the rigid networks produced by aromatic curing agents (Lee et al., 2001; Musto et al., 2001; Lee, 1965a; Rose et al., 1993; Li et al., 2021; Zhou et al., 2020). Much less information is available on systems cured with aliphatic diamines (Lee et al., 2001; Ratna et al., 2024; Xia et al., 2014; Mailhot et al., 2005a; Krauklis and Echtermeyer, 2018) and, in particular, with flexible, high molecular mass polyetheramines (Ratna et al., 2004; Ratna et al., 2024; Mailhot et al., 2005a; Krauklis and Echtermeyer, 2018). Among the available research literature, a noteworthy contribution (Krauklis and Echtermeyer, 2018) investigated the hygrothermal degradation of a flexible epoxy network employing a combination of complementary characterization techniques, including FT-NIR, ATR-FTIR, energy-dispersive X-ray analysis (EDX), high-resolution-inductively coupled plasma-mass spectrometry (HR-ICP-MS), optical microscopy, scanning electron microscopy (SEM), and dynamic mechanical thermal analysis (DMTA). It was concluded that in the investigated aging conditions (water immersion, 60°C), chain-scission does not occur, and the oxidative process only produces in-chain carbonyls. No amide terminals were detected nor a depletion of aromatic moieties. Conversely, in more drastic conditions (UV irradiation and high-T exposure), different spectral features and alternative degradation pathways were detected (Mailhot et al., 2005a; Mailhot et al., 2005b), prompting us to reconsider system stability under specific service conditions by using a different experimental approach which emphasizes the kinetics of the process. The degradation of solids is customarily investigated by thermogravimetric analysis (TGA) in the isothermal or non-isothermal mode (Vyazovkin and Linert, 1994; Ozawa, 1965; Doyle, 1962). Other techniques are frequently used to complement TGA, among which are gas chromatography (Bishop and Smith, 1970), mass spectroscopy (Lee, 1965b), radiochemical analysis (Bishop and Smith, 1970), and combinations of these. A common issue of the above experimental approaches is that they rely on volatile products generated upon thermo-oxidation. Reaching a detectable amount of such volatiles requires very high degradation temperatures, which may cause intricate processes, such as the rearrangement of degradation fragments and further decomposition of primary products. Thus, analysis of volatile products provides relevant information on temperature stability but is hard to interpret mechanistically. These issues are alleviated by the use of a solid-state spectroscopic approach such as Fourier transform infrared (FTIR). In this case, the technique considers the evolution of the network rather than the evolved volatiles; due to its sensitivity, it is able to detect weak features occurring in the early stages of the process, related to the initiation step(s) (Musto et al., 2001; Mailhot et al., 2000; Koenig, 1975). We adopted transmission sampling in place of the more widespread attenuated total reflection mode

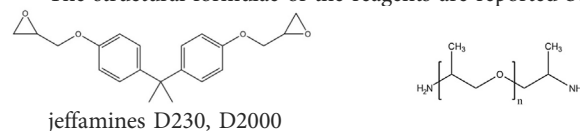
(ATR) because it allows full contact of the sample surfaces with the environment and facilitates *in situ*, time-resolved data collection. Furthermore, the transmission mode is the best choice for an accurate and reproducible quantitative analysis (Chalmers and Griffiths, 2002). Clean kinetic data can thus be gathered, allowing us to compare the chemical stability of the different functional groups of the network. Large collections of dynamically changing datasets also permit advanced spectral-analysis approaches such as two-dimensional correlation spectroscopy (2D-COS), least squares curve fitting (LSCF) analysis, and difference spectroscopy (DS). Among other advantages, such tools are able to improve the band-shape resolution, which is frequently poor in systems undergoing photo- or thermo-oxidative processes (Musto et al., 2008; Musto et al., 2012; Musto, 2003). QM-based normal coordinate analysis (QM-NCA) is the tool for a quantitative interpretation of the spectral features, making it possible to extract the maximum amount of information at the molecular level from the vibrational pattern. The kinetic data coupled with the structural insights provided by spectroscopic analysis allowed us to propose likely mechanisms for the degradation process. A further scope of the present contribution is to highlight the potential of FTIR spectroscopy, in connection with its advanced interpretative tools, for the molecular characterization of complex transient phenomena in polymeric materials.

2 Materials and methods

2.1 Materials

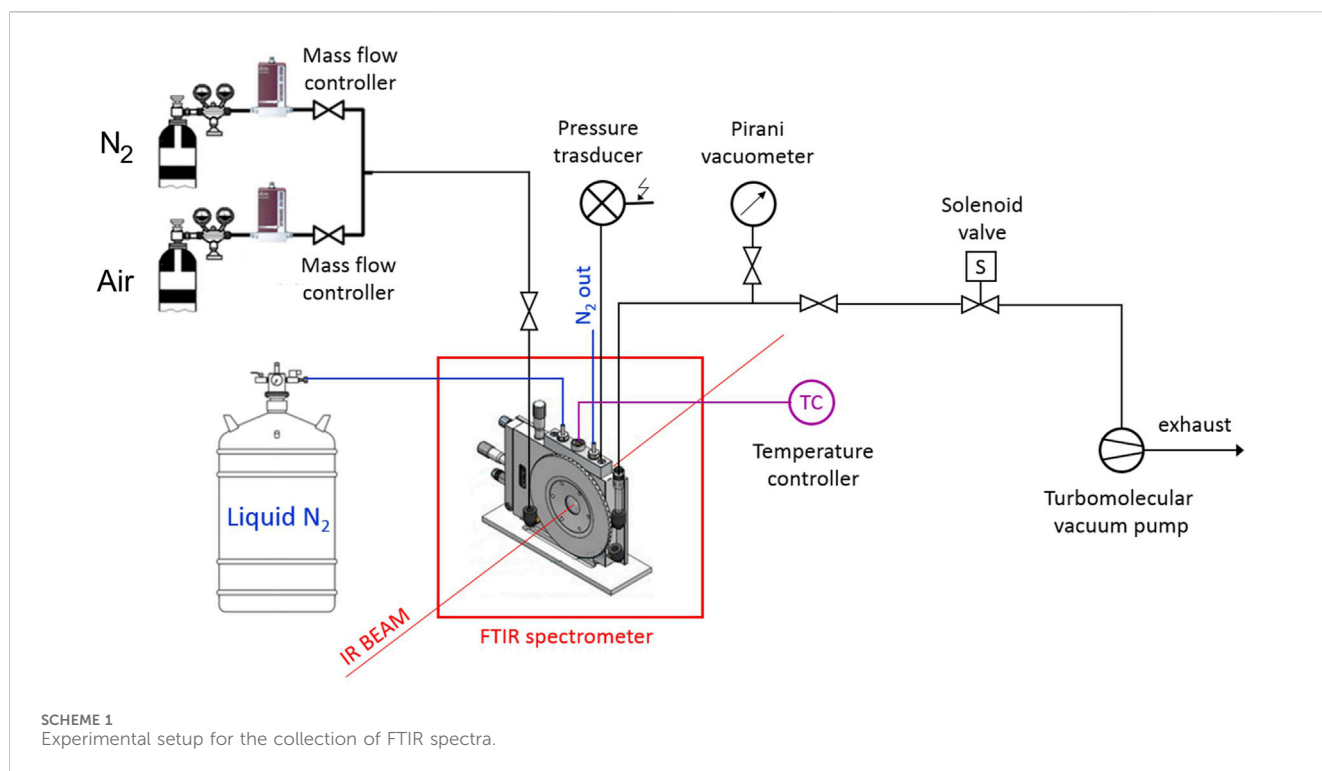
Diglycidyl ether of bisphenol-A (DGEBA) M.W. = 355 Da, polyetheramine (jeffamine) D230 M.W. = 230 Da, and polyetheramine D2000 M.W. 2000 Da were purchased from Sigma-Aldrich, Italy. These products were used as received, with no further purification.

The structural formulae of the reagents are reported below:



2.2 Preparation protocol

The epoxy network to be investigated was obtained by curing the DGEBA precursor with an equimolar mixture of D230 and D2000 jeffamines. We transferred 6.00 g (16.9 mmol) of DGEBA, 0.972 g (4.226 mmol) of D200, and 8.452 g (4.226 mmol) of D2000 were to a round flask and kept this under mechanical stirring at 60°C until complete homogenisation. The viscous, transparent mixture thus obtained was degassed under vacuum until air bubbles completely disappeared (30 min), and it was cooled to RT. Two glass plates were treated with a releasing agent (Lubrolene E6) and preheated at 60°C . A small amount of the resin precursor was squeezed between the hot plates and gently pressed at 5.0 bar to obtain a film thickness suitable for transmission IR measurements. The film was cured at 80°C for 2 h and post-cured at 140°C for 6 h. All thermal treatments were performed under an



N_2 atmosphere to prevent premature oxidation. After cooling to RT, the mould was opened, and a film $8 \pm 2 \mu\text{m}$ thick was recovered. It was rinsed with dichloromethane to eliminate residual releasing agent from the surfaces and dried in air prior to introduction into the environmental chamber of the spectrometer. The T_g of the fully cured resin as detected by DSC was -33°C .

2.3 FTIR spectroscopy

The isothermal collection of transmission FTIR spectra was performed *in situ*, in the *time-resolved* mode. The measurements were made under gas flow ($50 \text{ cm}^3 \text{ s}^{-1}$) using a modified Linkam cell, THMS350V (Surrey, UK), equipped with temperature control ($-180 \div 350^\circ\text{C}$) and a vacuum system. The cell was operated through service lines connected to mass flow controllers (MKS Type GM50A (Andover, MA)) for setting the gas flux, while a solenoid valve regulated the pressure inside the cell. The system was equipped with a Pirani vacuumeter and a MKS Baratron 121 pressure transducer (produced by MKS Instruments, Andover, MA, full-scale 1,000 Torr, resolution 0.01 Torr, accuracy equal to $\pm 0.5\%$ of the reading). The environmental chamber was fluxed with dry N_2 up to stabilization at the test temperature (180°C); thereafter, the flowing gas was switched to air. The switching time marks the origin of the kinetic time-scale. During the interval to stabilize the test temperature ($\approx 15 \text{ min}$), no modifications of the IR spectrum were observed. Prolonged exposure (1 h) at 180°C under nitrogen confirmed the stability of the spectrum in the absence of oxygen.

The FTIR instrument was a Spectrum-100 spectrometer (Perkin-Elmer, Norwalk, CT, United States) equipped with a Ge on KBr beam splitter and a wide-band DTGS detector. Instrumental parameters were set as follows: resolution, 2 cm^{-1} ; optical path

difference (OPD) velocity, 0.20 cm/s ; frequency range, $4,000\text{--}450 \text{ cm}^{-1}$. A schematic diagram of the experimental apparatus is reported in Scheme 1.

2.4 Computational details

A preliminary exploration of the potential energy surface of the model compound was made by Molecular Mechanics (MM) using the MMFF94 force field (Merck Molecular Force Field, from Merck Co, Kenilworth, NJ, United States) (Halgren, 1996). A Metropolis–Monte Carlo method (Rappè and Casewit, 1997) was adopted for the systematic variation of multiple dihedral angles. Four conformational degrees of freedom were considered (Supplementary Figure S1, Supplementary Material—SM). Quantum mechanical (QM) calculations were performed on the minima identified by the MM conformational search using density functional theory (DFT) based on linear combination of atomic orbitals (LCAO) with the unrestricted spin polarization method. The adopted Hamiltonian was the B3LYP global hybrid functional (Becke, 1992; Lee et al., 1988) as implemented in the Gaussian16 program package (Frisch et al., 2016) (Gaussian Inc., Pittsburgh, PA) in connection with the standard 3-21G basis set. Larger basis sets were also checked and were found to provide limited improvements in the simulation of the vibrational spectrum. After geometry optimization, a normal coordinate analysis at the same level of theory was performed, comprising the calculation of the Hessian matrix (F) by analytical evaluation of the first and second derivatives of the potential energy with respect to the Cartesian displacement coordinates. The F matrix was then transformed in terms of mass-weighted coordinates and diagonalized to obtain the corresponding eigenvalues (normal frequencies) and eigenvectors (displacement vectors, L matrix). Finally, a transformation into a set of non-

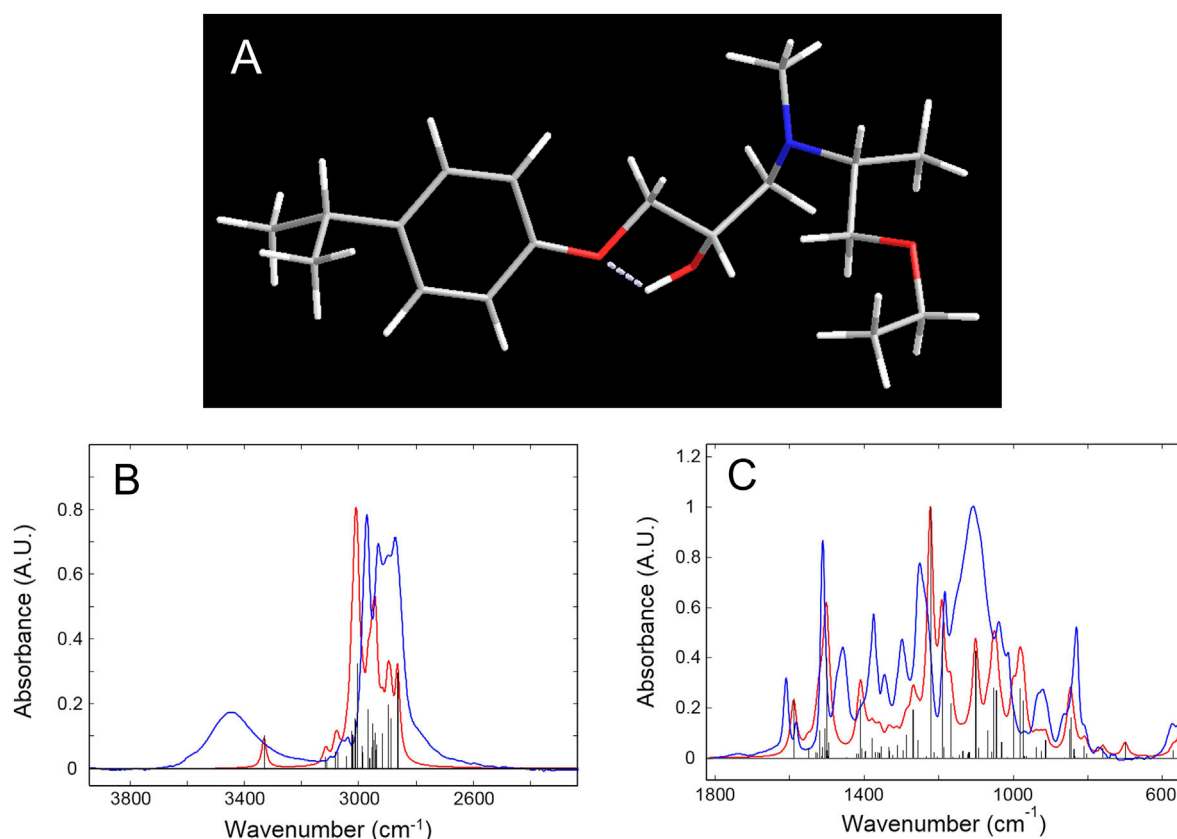


FIGURE 1

(A): Geometry of the model compound optimized at the B3LYP/3-21G level of theory. (B, C) Blue trace: experimental spectrum of the epoxy network. Red trace: calculated spectrum of the network's model compound with a Lorentz broadening function. Black bar graph: calculated spectrum without broadening. All spectra are normalized with respect to their maximum absorbance values.

redundant internal coordinates of both the **F** and **L** matrices was accomplished in order to characterize the normal modes in terms of their potential energy distribution (PED), expressed, in normalized form, as Wilson et al. (1955).

$$(PED)_{jk} = \frac{F_{jj}L_{jk}^2}{\sum_i F_{ii}L_{ik}^2} \cdot 100.$$

PED % refers to the contribution of the j^{th} internal coordinate to the k^{th} normal mode, F_{jj} is the j^{th} diagonal force constant, and L_{jk} is the corresponding element of the **L** matrix.

3 Results and discussion

3.1 QM-based normal coordinate analysis

The as-collected IR spectrum of the epoxy network is reported in Figure 2 (red trace) and Figure 1 (blue trace) after normalization with respect to the maximum absorbance value (Figure 1B refers to the frequency range 3,900–2,200 cm^{-1} ; Figure 1C to the 1800–550 cm^{-1} range).

The pattern displays numerous features, providing abundant structural information. The specific sample preparation has ensured that the whole spectrum lies well within the

absorbance-concentration linearity range (less than 1.5 absorbance units) which allows for the use any peak for quantitative analysis. The amount of available molecular information depends on the interpretative level, ideally providing a normal mode description to any observed feature of the spectrum. So far, despite the relevance of epoxy resins and the widespread use of vibrational spectroscopies for their characterization, only qualitative assignments are available, based on correlative approaches (Musto et al., 2001; Ratna et al., 2024; Ngono et al., 1999; Ngono and Maréchal, 2000; Rivaton et al., 1997a). Furthermore, in the main reference papers (Ngono et al., 1999; Zhang et al., 1994; Mertz and Koenig, 2005), conflicting assignments are often reported, even for the major peaks, which prompted us to adopt a more rigorous approach based on the currently available QM methods.

The choice of the model compound was made by considering the network structure depicted in Supplementary Figure S2, SM. A molecular fragment representative of the polymer chains forming the 3D network was identified, containing all the relevant functional groups. It was truncated by a H atom on the isopropylidene site and the tertiary amine group, and with a methyl group on the ether terminal. Owing to the complexity of the molecular structure, a preliminary survey of the potential energy surface was accomplished by a Metropolis–Monte Carlo method (Rappè and Casewit, 1997) for the systematic variation of multiple dihedral angles; the τ_1 , τ_2 , τ_3 ,

TABLE 1 Experimental and calculated frequencies, percent error, potential energy distribution, and description of the vibrational modes in the spectrum of the investigated epoxy network.

Exp (cm ⁻¹)	Calc (cm ⁻¹)	Err (%)	PED (%)	Description
-	3,331 (w)	-	s1 (100)	v(OH)
3,097 (w)	3,116 (w)	0.6	s4 (95), s3 (90)	v(CH) _{Ar}
3,057 (w)	3,076 (w)	0.6	s2 (91), s5 (96)	v(CH) _{Ar}
2,970 (s)	3,004 (s)	1.3	s8 (78), s23 (83), s20 (77) s23 (11)	v _{asym} (CH) ₃ /v _{asym} (CH) ₂ (α to N)
2,930 (s)	2,945 (m)	0.5	s17 (12) s31 (78), s9 (84)	v _{sym} (CH) ₃ (all)
2,895 (s)	2,895 (m)	0	s28 (85), s26 (75) s28 (11)	v(CH) ₂ (α to O)
2,872 (s)	2,865 (m)	0.2	s24 (94)	v(CH) (α to N)
		$\overline{Err} = 0.5 \pm 0.44$		
1,608 (m)	1,588 (m)	1.2	s33 (52) s57 (16) s87 (11)	in-plane ring def/v(CO)
1,582 (m)	1,550 (w)	2.0	s32 (50) s59 (16)	in-plane ring def
1,510 (vs.)	1,500 (s)	0.7	s55 (53)	sc (CH ₂) α to O
1,457 (m)	-	-		-
1,373 (m)	1,408 (m)	2.5	s54 (31) s78 (10) s147 (13)	δ(COH)/δ(CCH)
1,343 (m)	1,360 (w)	1.3	s80 (15) s128 (19) s130 (24)	δ(CCH) (next to N)
1,297 (m)	1,267 (m)	2.3	s51 (57)	in-plane ring def [v(CC)]
1,249 (s)	1,221 (vs.)	2.2	s36 (46) s57 (11)	v(O-Ar)
1,183 (m)	1,190 (m)	0.6	s33 (13) s57 (40)	δ(CCH) _{Ar}
1,153 (sh, m)	1,167 (m)	1.2	s66 (10)	skeletal (R)
1,106 (vs.)	1,100 (m), 1,070, 1,052	0.5	s35 (27) s42 (16), s49 (13) s132 (16) s40 (26) s125 (16)	v(O-CH ₂)/δ(CH ₃)
1,038 (m)	1,046 (m)	0.6	s42 (23) s44 (13) s116 (13)	v(C-N)/tw (CH ₂)
1,013 (m)	1,000 (m)	1.3	s39 (12) s41 (12)	δ(COH)/v(C-N)
934 (m)	938 (w)	0.4	s43 (35) s50 (15) s52 (13)	v(O-CC ₂ H ₅)
920 (m)	926, 913 (w)	0.05	s51 (12) s118 (14)	tw (CH ₂)
862 (sh)	850 (sh)	1.4	s46 (50)	-
830 (m)	845 (m)	2.0	s107 (64)	w (CCH) _{Ar}
805 (w)	809, 805 (w)	0.2	s35 (27) s37 (15)	in-plane ring def [v(CC)]
773 (vw)	760 (w)	1.7	s45 43	v _{sym} (CN)
572 (w)	570 (m)	0.3	s85 18 s86 43 s87 12	skeletal (L)
559 (w)	550, 543 (w)	2.2	s106 12 s152 18 s153 -24 s92 -15 s101 -18	w (CCH) _{Ar} /w (COH)
		$\overline{Err} = 1.2 \pm 0.78$		

Err % = $\frac{|v_{exp}-v_{calc}|}{v_{exp}} \times 100$; v = stretching; δ = bending; sc = scissoring; tw = twisting; w = wagging; Ar = aromatic. Figures in round brackets in column 4 (PED) are the % contributions of the internal coordinates to the total PE. Contributions lower than 10% were neglected. Contributions separated by commas indicate the occurrence of unresolved normal modes at the observed frequency. R and L in column 5 (Description) denote right and left side of the molecular model as indicated in [Supplementary Figure S1](#), SM.

and τ_4 torsions were considered ([Supplementary Figure S1](#), SM). Then, the most promising structures were fully optimized at the B3LYP/3-21G level of theory, leading in all cases to the relaxed structure represented in [Figure 1A](#) and in [Supplementary Figure S1](#), SM, with the relative atom numbering. Normal coordinate analysis (NCA) according to the Wilson GF method ([Wilson et al., 1955](#)) was

performed next, whose results are compared to the experimental values in [Figures 1B and C](#). [Table 1](#) summarizes the NCA, also reporting the normal-mode description of the observed peaks, along with their potential energy distribution (PED).

The correlation between the calculated and experimental frequencies is reported in [Supplementary Figure S3](#), SM. The

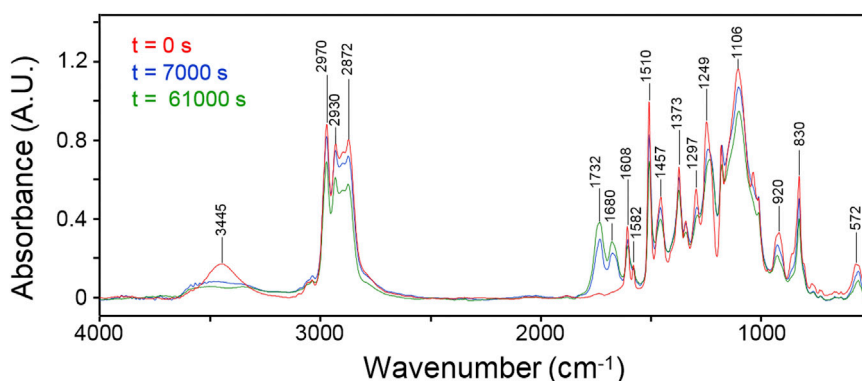


FIGURE 2
FTIR spectra of the network collected at different times during the thermo-degradation experiment. Collection times as indicated.

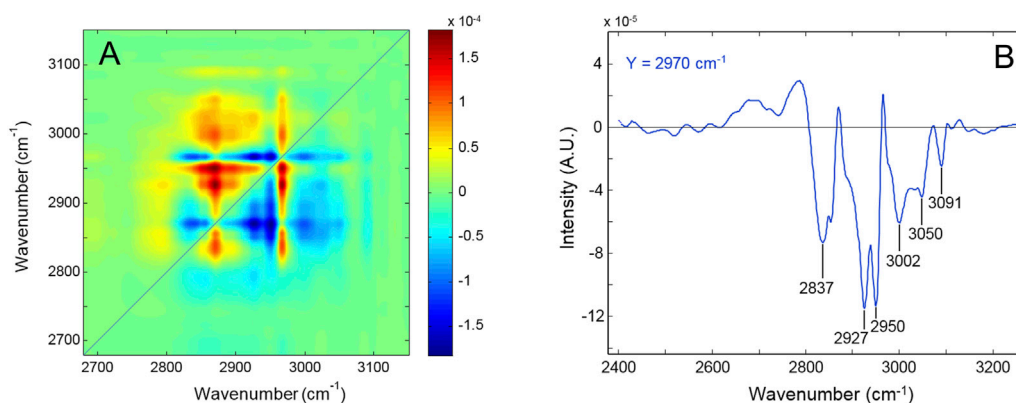


FIGURE 3
(A) Asynchronous spectrum in the 2,700–3,000 cm^{-1} range of the network subjected to thermo-oxidation at 180° . (B) Y-isofrequency plot at 2,970 cm^{-1} .

linearity with zero intercept extends over the whole range ($R^2 = 0.9995$), and the slope, representing the correction factor to compensate for neglecting the exact treatment of the electron correlation, is 0.963 ± 0.004 . This value is in excellent agreement with the benchmark value of 0.965 reported in the literature (Kesharwani et al., 2015; Precomputed vibrational scaling factors, 2019). This analysis confirms the soundness of the NCA and of the proposed assignments and shows that anharmonicity, which produces non-linearity effects in the high-frequency side (CH/OH stretchings), is negligible in the present case.

In the high-frequency side, the calculated $\nu(\text{OH})$ vibration occurs as a sharp peak at $3,331 \text{ cm}^{-1}$, while the observed spectrum displays a broad absorption centered at $3,445 \text{ cm}^{-1}$. The lack of correlation in this region is due to incomplete molecular modeling; the chain fragment is considered to be isolated *in vacuo* and does not take into account intermolecular H-bonding interactions with neighboring chains that are responsible, in the actual network, for the broadening of the observed $\nu(\text{OH})$ band. In the model, only an intramolecular H-bonding with the ether oxygen (O_{10}) is formed, having a conspicuous interaction energy, as demonstrated by the position of the relative normal mode. The

$\nu(\text{CH})$ range between $3,250$ and $2,800 \text{ cm}^{-1}$ is reproduced with remarkable accuracy by the adopted model chemistry, with an average error of 0.5%, well within the predictive capabilities of the method ($\approx 2\%$) (Kesharwani et al., 2015); this affords the interpretation of the complex profile in this interval. In particular, as well as the aromatic signals above $3,000 \text{ cm}^{-1}$, the two components at $2,970$ and $2,930 \text{ cm}^{-1}$ are due to the methyl groups, with the latter mainly localized on the isopropyl terminal. The $2,895$ and $2,865 \text{ cm}^{-1}$ peaks originate, respectively, from the CH_2 in α to the ether oxygen (C_{21}) and the CH in α to the nitrogen ($\text{C}_{18}\text{--H}_{46}$). These assignments afford a signature of specific molecular sites to monitor the initiation and advancement of the degradation process.

In the range below $1,800 \text{ cm}^{-1}$ the experimental-to-calculated correlation worsens slightly (average error = 1.2%), as generally occurs when there is a significant degree of mixing among the basic vibrations (Wilson et al., 1955). However, considering both the positions and the intensities of the simulated spectrum, a reliable description of the observed features can be achieved. The doublet at $1,608\text{--}1,582 \text{ cm}^{-1}$ is due to the aromatic ring with a minor contribution from the $\text{C}_4\text{--O}_{10}$ stretch. The prominent peak at

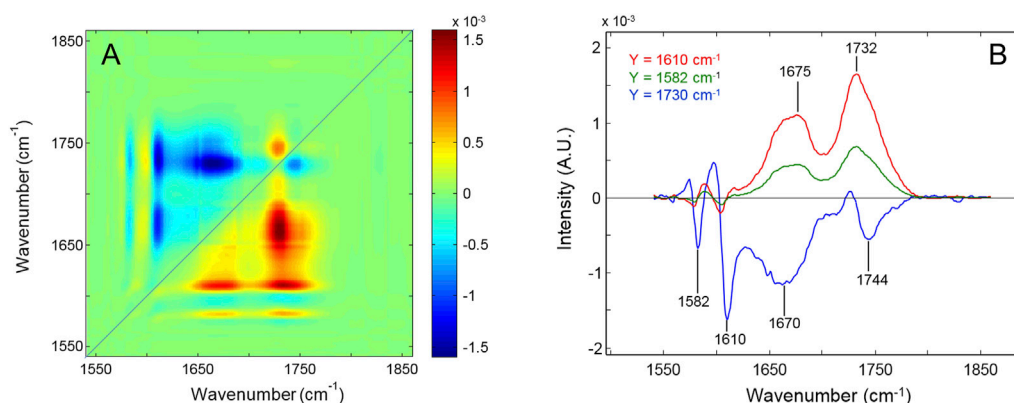


FIGURE 4
(A) Asynchronous spectrum in the 1,550–1,850 cm^{-1} range of the network subjected to thermo-oxidation at 180°. (B) Y-isofrequency plots at 1,610 cm^{-1} (red trace), 1,582 cm^{-1} (green trace), and 1,730 cm^{-1} (blue trace).

1,510 cm^{-1} is mainly due to the CH_2 scissoring at C_{11} , while the equally intense feature at 1,249 cm^{-1} is a mixed vibration with a prevailing O–Ar character. These rather localized modes are also diagnostic for the recognition of the degradation mechanism. The most intense band in the experimental spectrum, centered at 1,106 cm^{-1} , is broad and asymmetric—likely due to an unresolved multicomponent structure. The calculated spectrum in this range displays lesser intensity and a simpler structure (three fully resolved components at 1,100, 1,070 and 1,052 cm^{-1}). These modes are extensively mixed (see PED in Table 1) and are of limited utility in the present context. In addition, of interest for the spectroscopic analysis are the 1,183 cm^{-1} peak (aromatic) and the partially resolved doublet at 862–830 cm^{-1} assigned, respectively, to a skeletal mode with prevalent N_{15} – C_{16} character and to a ring mode (CCH wagging). The remaining features are either too weak or too mixed to be useful for analytical purposes.

3.2 2D-correlation spectroscopy

Two-dimensional correlation spectroscopy (2D-COS) is a powerful tool for investigating dynamic processes that produce extensively overlapped patterns with limited or no resolution (Noda and Ozaki, 2004). It has been successfully applied to investigate thermo- and photo-oxidative degradation kinetics (Musto et al., 2008; Musto et al., 2012; Musto, 2003). The method, rooted in the principles of time-series analysis, improves the resolution by spreading the data over a second frequency axis; at the same time, it can characterize the dynamics of the evolving system at a finer level than conventional 1D-spectroscopy. We briefly summarize the principles of the method for convenience (Noda and Ozaki, 2004). The analysis produces two maps denoted as “synchronous” and “asynchronous”, which convey different information. Along the main diagonal (power spectrum), the synchronous spectrum highlights the signals that are more sensitive to the applied perturbation. If the response function can be expressed in the form of an exponential decay, as in the present case (*vide infra*), then the cross-correlation peaks at off-diagonal positions reflect any couple of signals undergoing intensity changes in the sampling interval. Their sign is positive if both peaks change in the same direction (they both

increase or decrease) and are otherwise negative. The asynchronous spectrum displays a peak at x - y coordinates $[v_1, v_2]$ when the two corresponding IR signals change at different rates and zero intensity if they change at the same rate. This effect produces the resolution enhancement and the specific shape of the asynchronous pattern. In addition, the sign of the asynchronous peaks defines the relative rate of the correlated signals according to the so-called Noda’s rules (Noda and Ozaki, 2004; Noda, 2000). The most important are the following: an asynchronous cross-peak located at coordinates $[v_1, v_2]$ is positive if the intensity change at v_1 is accelerated with respect to that at v_2 and is negative otherwise. This remains true as long as the synchronous spectrum at $[v_1, v_2]$ is positive; otherwise, the above relationship is to be reversed.

Figure 2 displays the initial spectrum of the network (red trace) and those collected after 7,000 and 61,000 s (blue and green traces, respectively). An intensity decrease of most peaks is observed as a consequence of functional group depletion, and the emergence of two well-resolved components in the carbonyl range (1,732–1,680 cm^{-1}) assigned, respectively, to ester and amide functionalities.

Figure 3A displays the asynchronous pattern in the 2,700–3,000 cm^{-1} range obtained from the *time-resolved* spectra collected during the degradation process. The full sequence of spectra employed for the 2D-COS analysis is displayed in Supplementary Figures S4 and S5, SM. Figure 3B represents the Y-isofrequency line at 2,970 cm^{-1} . The resolution enhancement brought about by the 2D approach is evident. The main feature is represented by the negative correlations of the peak at 2,970 cm^{-1} with the components at 2,837, 2,927, 2,950, 3,002, 3,050, and 3,091 cm^{-1} (Figure 3B). The NCA assigned the 2,970 cm^{-1} peak to unresolved CH_3/CH_2 stretching, which implies that the aromatic signals (3,050–3,091 cm^{-1}) decrease faster than the aliphatic ones. It is noted that the number of components detected by 2D-COS largely exceeds the spectroscopic resolution and, hence, the level of detail achievable with the QM vibrational analysis. For instance, the maximum observed at 2,970 cm^{-1} is found to comprise three components at 2,838, 2,853, and 2,970 cm^{-1} . A full account of the features observed in the asynchronous map is therefore unfeasible; however, relevant information on the relative rate of depletion

(i.e., the relative stability) of the different functional groups can be achieved. Thus, the 2,970 and the 2,870 cm^{-1} components display zero asynchronous correlation, which implies that they originate from the same functional group. This result is consistent with the NCA, as the two normal modes display a substantial contribution from the alkyl substituent in the alpha position with respect to the nitrogen (C_{18} , internal coordinates s20 and s24, respectively). The negative asynchronous correlation of both peaks with the rest of the features in the range indicates that the concentration of this group falls at a slower rate than that of the other alkyl substituents. This implies, in turn, that C_{18} is not the preferred site of initiation for the degradation process.

In the 1,550–1,850 cm^{-1} range (Figure 4), the two sharp peaks at 1,608 and 1,582 cm^{-1} display zero asynchronous intensity according to the NCA assignments to in-plane ring modes. The carbonyl components at 1,675–1,732 cm^{-1} are positively correlated with both the aromatic modes (see Y-isofrequency plots in Figure 4B). Considering that the synchronous spectrum is negative at the corresponding coordinates, this result indicates that aromatic group depletion starts earlier and proceeds faster than oxygen fixation on the network chains. Furthermore, the intensity is positive at (1,730, 1,677), implying a faster rate of formation of the ester carbonyls compared to amides. Finally, a well-resolved correlation pattern is observed at [1,745, 1,730 (–)], which reveals the two-component structure of the ester band and demonstrates that the high-frequency shoulder evolves independently (more slowly) than the main component.

3.3 Thermal degradation kinetics

The spectra collected *in situ*, by time-resolved sampling, have been employed to characterize the kinetics of the degradation process. IR quantitative analysis requires the identification of isolated peaks or bands and a consistent, preferentially linear baseline. Among the numerous spectral features, those relevant to the kinetic analysis were chosen accordingly. Different methods were employed depending on the characteristics of the frequency range. Thus, the concentrations of aromatic rings and CH_2 groups next to the ether oxygen were evaluated, respectively, from the height of the peaks at 830 and 1,510 cm^{-1} . In the 3,000–2,800 cm^{-1} range, owing to the lack of resolution, integration over the entire band area was performed, which is representative of the overall concentration of alkyl groups and, therefore, monitors the degradation of the whole chain forming the 3D network. In the carbonyl region, the analysis was made by considering the difference spectra $A_{diff}(\nu) = A_t(\nu) - K \cdot A_0(\nu)$, where A is the absorbance and the subscripts *diff*, *t*, and *0* refer, respectively, to the difference spectrum and to those collected at times *t* and *0*. The subtraction factor K was considered equal to unity for the whole data set, assuming a negligible variation of the sample thickness during the experiment.

The relative conversion, α , of a functional group is defined as (Khawam and Flanagan, 2006):

$$\alpha = \frac{C_0 - C_t}{C_0 - C_\infty}$$

or in terms of absorbance:

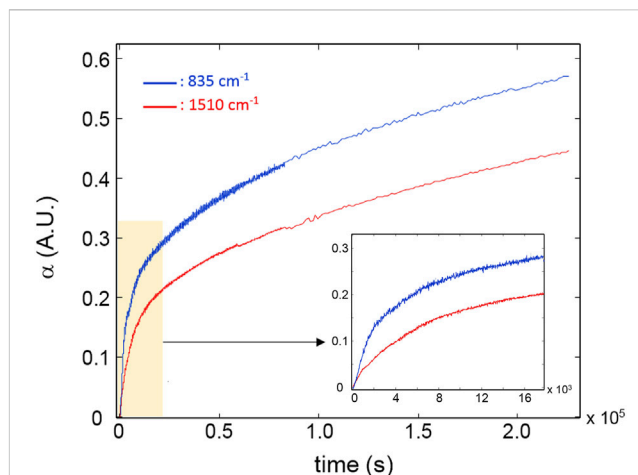


FIGURE 5
Kinetic profiles for the peaks at 835 cm^{-1} (blue curve) and 1,510 cm^{-1} (red curve). The inset highlights the early stages of the degradation process.

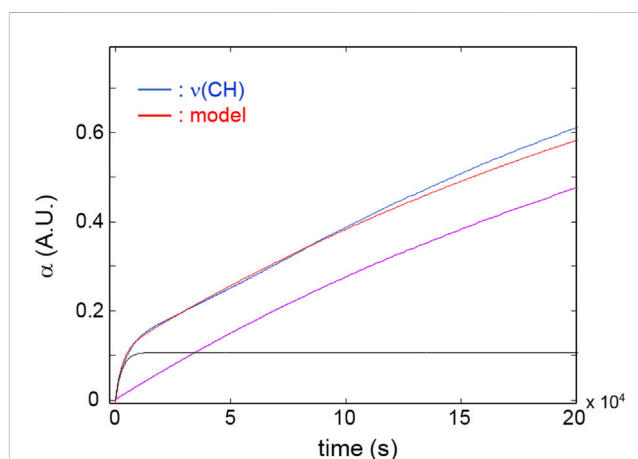


FIGURE 6
Red curve: kinetic profiles for the band area in the 3,000–2,700 cm^{-1} range. Blue curve: model simulation. Black and purple curves: simulated profiles of the exponential components.

$$\alpha = \frac{A_0 - A_t}{A_0 - A_\infty}$$

where C is the molar concentration and the subscript ∞ refers to the time corresponding to final conversion.

Solid-state kinetics is usually approached by using reaction models suitably developed for describing specific processes. This is because of the heterogeneous character of the investigated phenomenon and the difficulty in obtaining information about the individual reaction steps (Khawam and Flanagan, 2006; Galwey and Brown, 1999; Jacobs and Tompkins, 1955).

The rate of a solid-state reaction can be generally described as

$$\frac{d\alpha}{dt} = P \cdot e^{-\frac{E_a}{RT}} \cdot f(\alpha),$$

where P is a pre-exponential (frequency) factor, E_a is the activation energy, R is the gas constant, T is the absolute temperature, and $f(\alpha)$

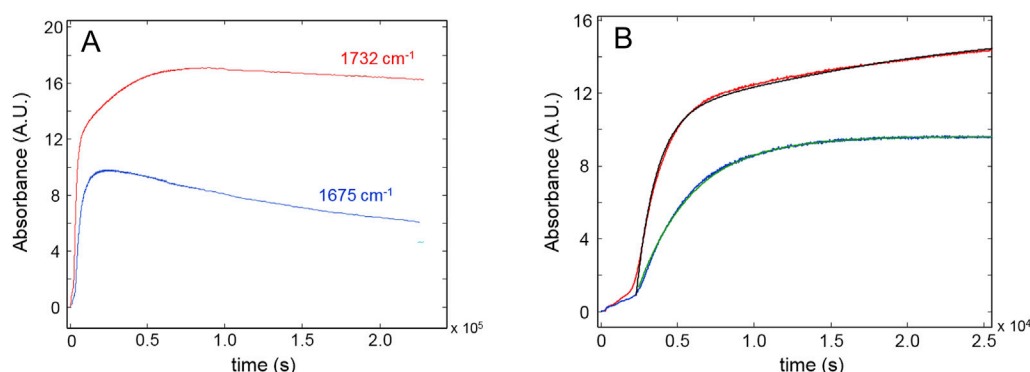


FIGURE 7
(A): Kinetic profiles for the peaks at 1732 cm^{-1} (red curve) and 1,675 cm^{-1} (blue curve). (B) The early stages of the process. Black and green curves represent the model simulations.

is the kinetic model. Kinetic parameters (P , E_a , model) can be obtained from isothermal data by applying the above rate law. The photo- and thermo-oxidative processes in polymeric substrates have been successfully described by order-based models in which, analogous to homogeneous kinetics, the reaction rate is proportional to the residual reactant concentration (i.e., the conversion) raised to a certain power (integer or fractional):

$$\frac{d\alpha}{dt} = k(1 - \alpha)^n,$$

where k is an Arrhenius-type kinetic constant and n is the reaction order. If $n = 0$, separating the variables and integrating gives $\alpha = kt$, while for first-order kinetics, $\alpha = 1 - e^{-kt}$. Integral expressions for reaction orders 2 and 3 are available in Khawam and Flanagan (2006). Regressing the model against the experimental data provides the values of the limiting conversion (i.e., A_∞). Looking at the process from the side of the products (the carbonyls), the same kinetic model identified for the depletion of the reactants is assumed, with a concentration parameter in place of a conversion (C_t or, equivalently, A_t instead of α). Occasionally, it is observed that the kinetic profile of a specific functional group displays a more complex shape than those predicted by order-based models, suggesting that multiple independent mechanisms are operating concurrently. In these cases, the simulation of the kinetic behavior can be attempted by assuming full conversion of the reacting species by the end of the process and a sum of first-order exponential terms:

$$\alpha = \sum_i \alpha_{i,f} (1 - e^{-k_i t}), \quad (1)$$

where each term of the summation accounts for a specific reaction pattern and $\alpha_{i,f}$ represents the limiting conversion of the i^{th} mechanism.

Figure 5 reports the kinetic profiles for the aromatic rings (850 cm^{-1}) and the CH_2 next to the ether oxygen (C_{11} , 1,510 cm^{-1}). The single-order model is unable to simulate the two curves due to the pronounced increasing trend following the initial fast step

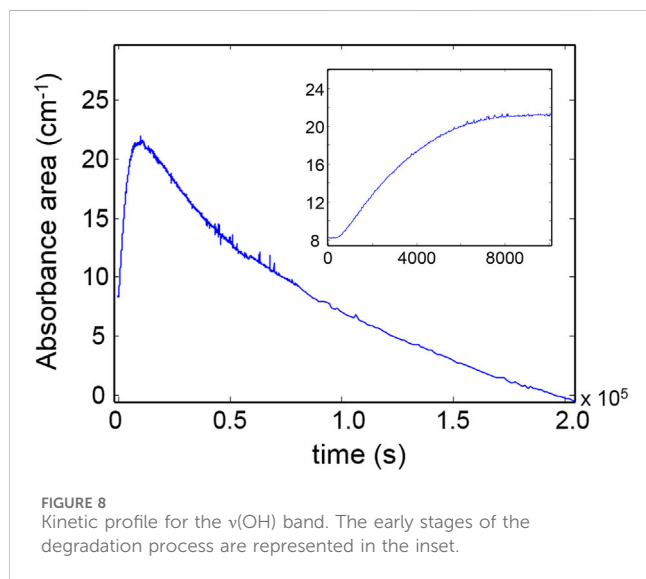
(Figure 5). However, an excellent fit is obtained by a two component first-order model (Equation 1, $i = 2$) which provides correlation coefficients exceeding 0.995. This result suggests the occurrence of two independent reaction pathways that contribute to the depletion of the above functional groups, characterized by a largely different reaction rate (the first is more than 30 times faster than the second). A further relevant observation is that in the early stages of the process, the rate of consumption of the aromatics is considerably higher than that of the C_{11} methylenes (see inset, Figure 5), in agreement with the results of the 2D-COS analysis. Figure 6 reports the kinetic behaviour of the alkyl groups as a whole (band in the $\nu(\text{CH})$ range) along with the simulation of the first-order, two-component model and the curves relative to the single exponentials. In this case, the fit is satisfactory ($R^2 = 0.996$) at least up to 1.2×10^5 s (33 h); thereafter, the model simulation gradually departs from the experimental curve, likely due to a further complication of the degradation mechanism which possibly involves diffusion control. The analysis based on the overall concentration of alkyl groups cannot provide detailed mechanistic information but affords a robust parameter to monitor the degradation kinetics.

Figure 7A depicts the evolution of the carbonyl bands at 1732 and 1,675 cm^{-1} . Oxidative reactions producing ester and amide groups (1732 and 1,675 cm^{-1} , respectively) are active in the initial 20,000 s ($\sim 5\text{h } 30'$) and proceed at a slower rate in the next 6.0×10^4 s with the generation of ester groups only. Thence, the fixation of oxygen onto the network's chains is found to end. At longer times, the concentration of carbonyls, especially those of amidic nature, is found to decrease, likely because of weight-loss steps involving these species.

Figure 7B highlights the initial period of the thermo-oxidative process, comparing the experimental data with the simulations of the kinetic models. The occurrence of an induction period lasting 3,000 s is detected for both carbonyl groups, which is not observed in the case of the conversion curves. Neglecting the initial induction period, the behavior of the amide curve can be well described by a single first-order model, at least up to the pseudo-plateau, before the decreasing trend. This suggests the prevalence of a single mechanism

TABLE 2 Kinetic parameters and correlation coefficients for the different functional groups.

Functional group	k_1 (s^{-1})	k_2 (s^{-1})	R^2
(O)CH ₂	1.8×10^{-4}	0.8×10^{-5}	0.999
Aromatic	3.3×10^{-4}	1.1×10^{-5}	0.996
CH	3.5×10^{-4}	0.3×10^{-5}	0.996
C=O ester	7.8×10^{-4}	4.3×10^{-5}	0.995
C=O amide	2.7×10^{-4}	-	0.998

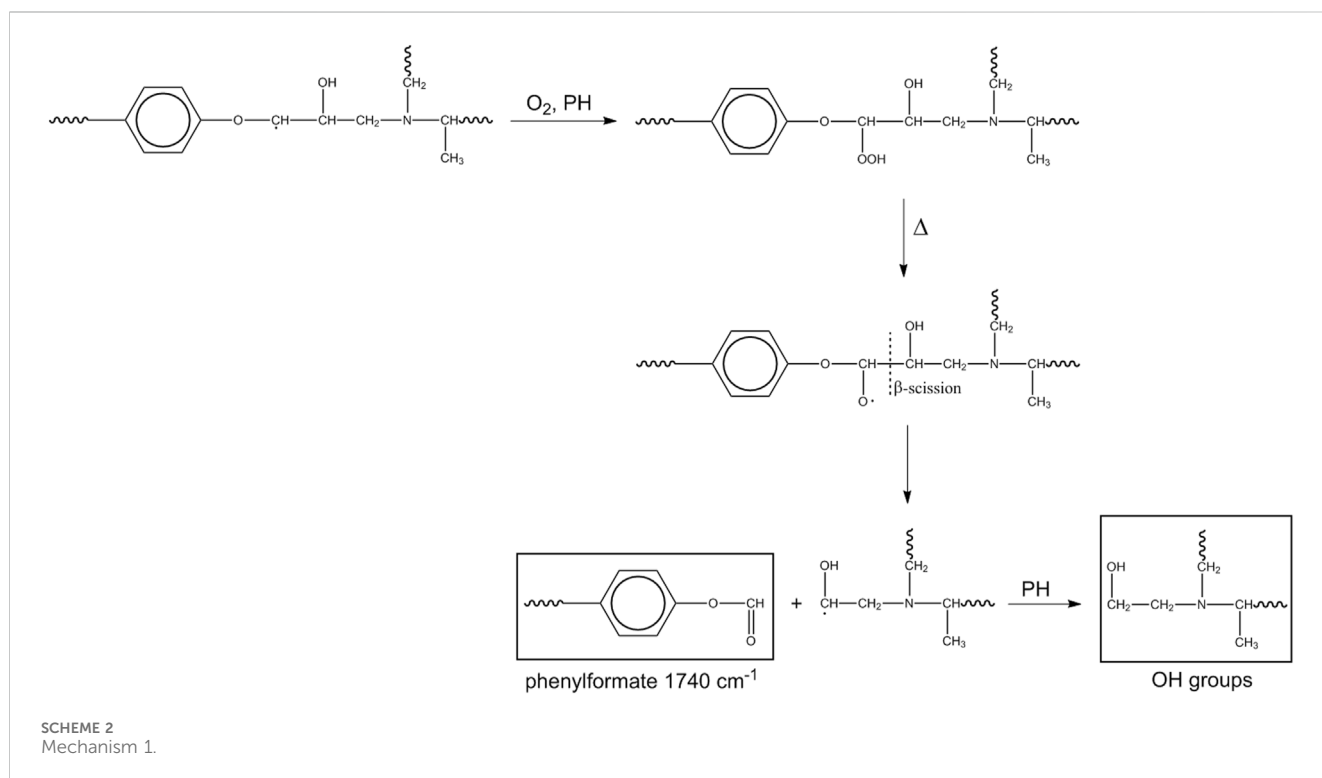


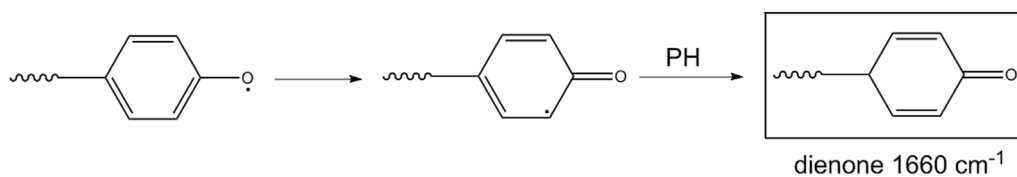
for the production of these groups. Conversely, the concentration of ester carbonyls is simulated by two exponential components with largely different kinetic constants (the first is 18 times larger than the second). This observation suggests that esters and amides originate from independent reaction mechanisms. Table 2 summarizes the results of the kinetic analysis in terms of rate constants and correlation coefficients.

It is noted that a direct comparison between the k values of reagents and products is not feasible since the reaction rate for products contains additional unknown terms with respect to the rate of depletion of the reagents. However, assuming similar values for the molar absorptivity for the $\nu(\text{CO})$ vibration of ester and amides, their rate of production can be compared. It was found that the concentration of ester groups in the network grows at a significantly higher rate than the amides. This result is in accordance with the 2D-COS analysis. Finally, Figure 8 displays the absorbance of the $\nu(\text{OH})$ band as a function of time. The kinetic behavior is complex and cannot be described by the models adopted so far. In the early stages of the process, when the oxidative processes prevail, the concentration of hydroxyl groups increases, reaching a pseudo-plateau at around 10,000 s (see inset, Figure 8); thereafter, a second, slower mechanism induces a gradual depletion of OH groups until full loss.

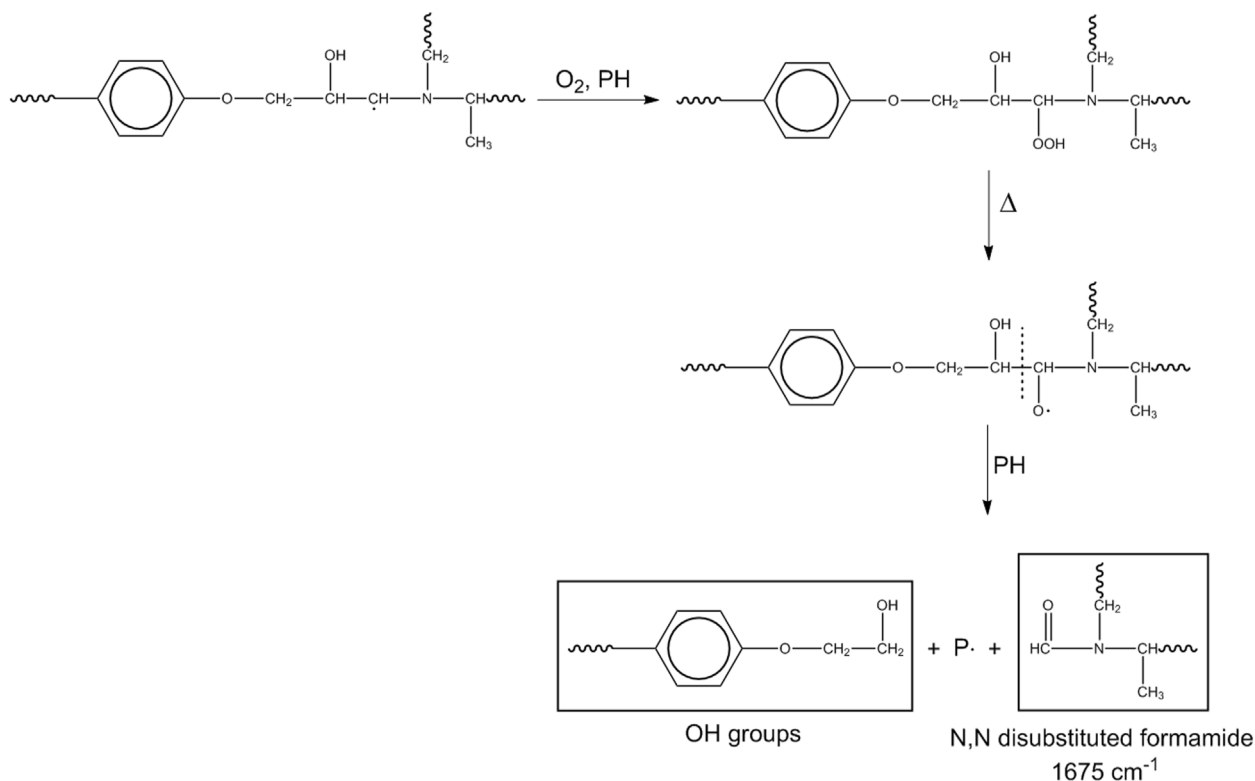
3.4 Mechanism

In this section, we propose some of the most likely mechanisms for the thermo-oxidative degradation of the investigated network based on earlier literature studies (Musto et al., 2001; Rose et al., 1993; Musto et al., 2012; Musto, 2003; Rivaton et al., 1997a; Rivaton





SCHEME 3
Mechanism 2.



SCHEME 4
Mechanism 3.

et al., 1997b) and the present experimental evidence, which can be summarized as follows.

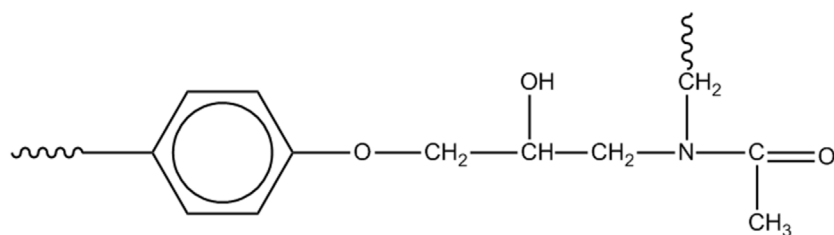
- The methylene and methyl groups are both involved in the chain-scission process through concurrent and competitive reaction pathways. These groups likely represent the main sites of initiation.
- The aromatic ring of DGEBA is involved in a fast process which causes the loss of aromaticity; in fact, a pathway limited to modifying the ring substitution would produce a frequency shift of the associated peaks rather than the observed intensity decrease.
- Oxygen is fixed on the network chains through the formation of amide and ester groups, the latter species being produced at a faster rate and in a larger amount. 2D-COS analysis unambiguously identified two distinct ester groups evolving at different rates.

The thermo-oxidation of polymers initiates with the formation of radical species (frequently from impurities) that are able to abstract hydrogen from a backbone chain (PH) (Rivaton et al., 1997a), forming a macroradical ($P\cdot$). The latter reacts with oxygen to form hydroperoxides, which initiate the so-called basic autoxidation scheme (BAS) (Kelen, 1983).

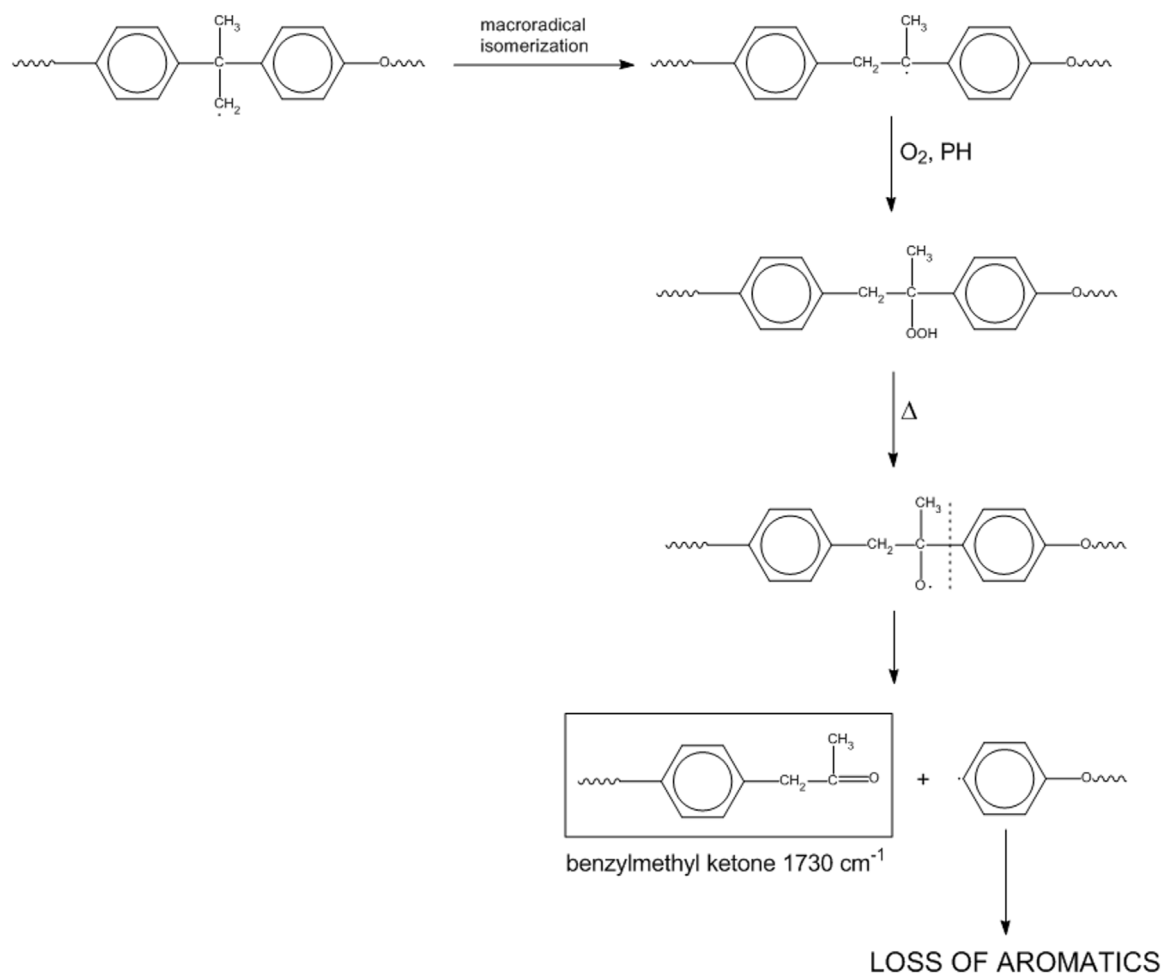
A first pathway (Scheme 2) starts at the methylene of the alkyl-aryl ether.

This mechanism accounts for the production of hydroxyls in the early stages of the process and for the high-frequency shoulder of the carbonyl band (phenylformate). If the β -scission occurs on the opposite site (toward the ether oxygen), the macroradical thus formed evolves by hydrogen abstraction from PH, with the formation of a cyclic dienone and loss of the aromatic character of the aryl group (Scheme 3).

This route accounts for the observed depletion of aromatic groups and suggests that the signals in the 1,700–1,630 cm^{-1}



SCHEME 5
N,N-disubstituted acetamide.



SCHEME 6
Mechanism 4.

range may not originate solely from amides but also from a conjugated ketonic structure.

Another mechanism initiates at the methylene next to the nitrogen.

This pathway produces the amide linkages (N,N-disubstituted formamide) and further hydroxyls (Scheme 4).

A further amidic species can be formed by initiation at the methylene next to the nitrogen, leading to Scheme 5.

If initiation starts at the isopropylidene site, we may have Scheme 6.

This mechanism represents a second route for the loss of aromatics and accounts for the peak observed at 1732 cm^{-1} (benzylmethyl-ketone).

In the light of the kinetic analysis and of the 2D-COS results, Mechanisms 1 and 4 seem to be the preferred paths, since the consumption of the methylenes of the alkylaryl ether moiety is

faster than the consumption of alkyl groups bound to the nitrogen atom and because the keto groups develop faster than the amides. In particular, Mechanism 4 is favored over Mechanism 1, as demonstrated by 2D-COS in the carbonyl range. The higher rate of depletion of aromatic groups compared to different alkyl units may be ascribed to multiple reaction pathways, leading to loss of aromaticity (Mechanisms 1 and 4).

4 Conclusion

We performed *in situ*, FTIR measurements in the *time-resolved* mode under controlled conditions of temperature and environment to elucidate the kinetics and mechanisms of the thermo-oxidative degradation of a flexible epoxy network.

The main findings of the present contribution can be summarized thus.

- The NC analysis routed on the DFT method allowed a reliable interpretation of the complex infrared spectrum of the network, improving the level of structural detail that can be accessed by this spectroscopic technique.
- The relative stability of the various functional groups was ranked. In agreement with previous literature, it was found that initiation occurs at the aliphatic moieties and at the isopropylidene unit. Aryl groups are also involved with loss of the aromatic character. The oxidation of the network chains produces amide and ketone groups, with the latter developing at a higher rate.
- The kinetic behavior of the system was suitably simulated by a first-order, biexponential model, which afforded the evaluation of the kinetic constants for the main functional groups involved in the process.
- On the basis of the spectroscopic analysis, the most likely thermo-oxidative mechanisms were proposed and discussed. The 2D-COS results coupled with the kinetic analysis allowed us to identify those that occur preferentially.

Data availability statement

The raw data supporting the conclusions of this article will be made available by the authors, without undue reservation.

References

- Ashcroft, W., and Ellis, B. (1993). in *Chemistry and technology of epoxy resins*. Editor B. Ellis, 37–71.
- Barber, A. (2002). *Handbook of noise and vibration control*. New York: Elsevier Science.
- Becke, A. D. (1992). Density-functional thermochemistry. I. The effect of the exchange-only gradient correction. *J. Chem. Phys.* 96 (3), 2155–2160. doi:10.1063/1.462066
- Bishop, D., and Smith, D. (1970). Combined pyrolysis and radiochemical gas chromatography for studying the thermal degradation of epoxy resins and polyimides. I. The degradation of epoxy resins in nitrogen between 400°C and 700°C. *J. Appl. Polym. Sci.* 14 (1), 205–223. doi:10.1002/app.1970.070140120
- Bonnaud, L., Pascault, J. P., and Sautereau, H. (2000). Kinetic of a thermoplastic-modified epoxy-aromatic diamine formulation: modeling and influence of a trifunctional epoxy prepolymer. *Eur. Polym. J.* 36 (7), 1313–1321. doi:10.1016/s0014-3057(99)00197-4
- Chalmers, J. M., and Griffiths, P. R. (2002) *Quantitative analysis in handbook of vibrational spectroscopy*, 3. Chichester, U.K.: Wiley.
- Doyle, C. D. (1962). Estimating isothermal life from thermogravimetric data. *J. Appl. Polym. Sci.* 6 (24), 639–642. doi:10.1002/app.1962.070062406
- Ellis, B. (1993). "Introduction to the chemistry, synthesis, manufacture and characterization of epoxy resins," in *Chemistry and technology of epoxy resins*. Editor B. Ellis (Netherlands: Dordrecht: Springer), 1–36.

Author contributions

MP: data curation, formal analysis, methodology, and writing–review and editing. GM: conceptualization, resources, supervision, and writing–review and editing. PM: conceptualization, data curation, formal analysis, investigation, methodology, supervision, writing–original draft, and writing–review and editing.

Funding

The authors declare that no financial support was received for the research, authorship, and/or publication of this article.

Acknowledgments

Mr. G. Orefice is acknowledged for his assistance in performing the FTIR measurements.

Conflict of interest

The authors declare that the research was conducted in the absence of any commercial or financial relationships that could be construed as a potential conflict of interest.

The author(s) declared that they were an editorial board member of *Frontiers*, at the time of submission. This had no impact on the peer review process and the final decision.

Publisher's note

All claims expressed in this article are solely those of the authors and do not necessarily represent those of their affiliated organizations, or those of the publisher, the editors, and the reviewers. Any product that may be evaluated in this article, or claim that may be made by its manufacturer, is not guaranteed or endorsed by the publisher.

Supplementary material

The Supplementary Material for this article can be found online at: <https://www.frontiersin.org/articles/10.3389/fchem.2024.1476965/full#supplementary-material>

- Ferry, J. D. (1980). *Viscoelastic properties of polymers*. John Wiley and Sons.
- Frisch, M. J., Trucks, G. W., Schlegel, H. B., Scuseria, G. E., Robb, M. A., Cheeseman, J. R., et al. (2016). *Gaussian 16W*. Wallingford CT: Gaussian Inc.
- Galwey, A. K., and Brown, M. E. (1999). *Thermal decomposition of ionic solids: chemical properties and reactivities of ionic crystalline phases*. Elsevier.
- Halgren, T. A. (1996). Merck molecular force field. I. Basis, form, scope, parameterization, and performance of MMFF94. *J. Comput. Chem.* 17 (5-6), 490–519. doi:10.1002/(sici)1096-987x(199604)17:5/6<490::aid-jcc1>3.0.co;2-p
- Jacobs, P., and Tompkins, F. (1955). Chemistry of the solid state. *Surfaces Solids*, 91–122.
- Jones, D. I. (2001). *Handbook of viscoelastic vibration damping*. John Wiley and Sons.
- Kelen, T. (1983). *Polymer degradation*. New York: Van Nostrand Reinhold Co.
- Kesharwani, M. K., Brauer, B., and Martin, J. M. (2015). Frequency and zero-point vibrational energy scale factors for double-hybrid density functionals (and other selected methods): can anharmonic force fields be avoided? *J. Phys. Chem. A* 119 (9), 1701–1714. doi:10.1021/jp508422u
- Khawam, A., and Flanagan, D. R. (2006). Solid-state kinetic models: basics and mathematical fundamentals. *J. Phys. Chem. B* 110 (35), 17315–17328. doi:10.1021/jp062746a
- Koenig, J. L. (1975). Application of Fourier transform infrared spectroscopy to chemical systems. *Appl. Spectrosc.* 29 (4), 293–308. doi:10.1366/000370275774455888
- Krauklis, A. E., and Echtermeyer, A. T. (2018). Mechanism of yellowing: carbonyl formation during hygrothermal aging in a common amine epoxy. *Polymers-Basel* 10 (9), 1017. doi:10.3390/polym10091017
- Lee, C., Yang, W., and Parr, R. G. (1988). Development of the Colle-Salvetti correlation-energy formula into a functional of the electron density. *Phys. Rev. B* 37 (2), 785–789. doi:10.1103/physrevb.37.785
- Lee, J. Y., Shim, M. J., and Kim, S. W. (2001). Thermal decomposition kinetics of an epoxy resin with rubber-modified curing agent. *J. Appl. Polym. Sci.* 81 (2), 479–485. doi:10.1002/app.1460
- Lee, L.-H. (1965a). Mechanisms of thermal degradation of phenolic condensation polymers. II. Thermal stability and degradation schemes of epoxy resins. *J. Polym. Sci. Part A General Pap.* 3 (3), 859–882. doi:10.1002/pol.1965.100030303
- Lee, L.-H. (1965b). Mechanisms of thermal degradation of phenolic condensation polymers. III. Cleavage of phenolic segments during the thermal degradation of uncured epoxy resins. *J. Appl. Polym. Sci.* 9 (5), 1981–1989. doi:10.1002/app.1965.070090529
- Li, H., Wang, N., Han, X., Yuan, H., and Xie, J. (2021). Mechanism identification and kinetics analysis of thermal degradation for carbon fiber/epoxy resin. *Polymers-Basel* 13 (4), 569. doi:10.3390/polym13040569
- Mailhot, B., Morlat, S., and Gardette, J. L. (2000). Photooxidation of blends of polystyrene and poly(vinyl methyl ether): FTIR and AFM studies. *Polymer* 41 (6), 1981–1988. doi:10.1016/s0032-3861(99)00204-9
- Mailhot, B., Morlat-Thérias, S., Bussière, P. O., and Gardette, J. L. (2005b). Study of the degradation of an epoxy/amine resin, 2. *Macromol. Chem. Phys.* 206 (5), 585–591. doi:10.1002/macp.200400394
- Mailhot, B., Morlat-Thérias, S., Ouahioune, M., and Gardette, J. L. (2005a). Study of the degradation of an epoxy/amine resin, 1. *Macromol. Chem. Phys.* 206 (5), 575–584. doi:10.1002/macp.200400395
- Mertzel, E., and Koenig, J. L. (2005). Application of FT-IR and NMR to epoxy resins. *Epoxy resins Compos. II*, 73–112. doi:10.1007/bfb0017915
- Murayama, T. (1978). *Dynamic mechanical analysis of polymeric material*. New York: Elsevier Science, Materials Science Monographs.
- Musto, P. (2003). Two-Dimensional FTIR spectroscopy studies on the thermal-oxidative degradation of epoxy and epoxy-bis (maleimide) networks. *Macromolecules* 36 (9), 3210–3221. doi:10.1021/ma0214815
- Musto, P., Abbate, M., Pannico, M., Scarinzi, G., and Ragosta, G. (2012). Improving the photo-oxidative stability of epoxy resins by use of functional POSS additives: a spectroscopic, mechanical and morphological study. *Polymer* 53 (22), 5016–5036. doi:10.1016/j.polymer.2012.08.063
- Musto, P., Ragosta, G., Abbate, M., and Scarinzi, G. (2008). Photo-oxidation of high performance epoxy networks: correlation between the molecular mechanisms of degradation and the viscoelastic and mechanical response. *Macromolecules* 41 (15), 5729–5743. doi:10.1021/ma8005334
- Musto, P., Ragosta, G., Russo, P., and Mascia, L. (2001). Thermal-Oxidative degradation of epoxy and epoxy-Bismaleimide networks: kinetics and mechanism. *Macromol. Chem. Phys.* 202 (18), 3445–3458. doi:10.1002/1521-3935(20011201)202:18<3445::aid-macp3445>3.3.co;2-e
- Ngono, Y., and Maréchal, Y. (2000). Epoxy-amine reticulates observed by infrared spectrometry. II. Modifications of structure and of hydration abilities after irradiation in a dry atmosphere. *J. Polym. Sci. Part B Polym. Phys.* 38 (2), 329–340. doi:10.1002/(sici)1099-0488(20000115)38:2<329::aid-polb5>3.0.co;2-t
- Ngono, Y., Maréchal, Y., and Mermilliod, N. (1999). Epoxy- Amine reticulates observed by infrared spectrometry. I: hydration process and interaction configurations of embedded H₂O molecules. *J. Phys. Chem. B* 103 (24), 4979–4985. doi:10.1021/jp984809y
- Noda, I. (2000). Determination of two-dimensional correlation spectra using the Hilbert transform. *Appl. Spectrosc.* 54 (7), 994–999. doi:10.1366/0003702001950472
- Noda, I., and Ozaki, Y. (2004). *Two-dimensional correlation spectroscopy: applications in vibrational and optical spectroscopy*. New York: John Wiley and Sons.
- Ozawa, T. (1965). A new method of analyzing thermogravimetric data. *Bull. Chem. Soc. Jpn.* 38 (11), 1881–1886. doi:10.1246/bcsj.38.1881
- Pascault, J. P., Williams, R. J., and Thermoetting, polymers (2013). *Handb. Polym. Synthesis, Charact. Process.*, 519–533.
- Precomputed vibrational scaling factors, in *Computational chemistry comparison and benchmark data base*, (2019). Gaithersburg, MD: National Institute of Standards and Technology. Available at: <https://cccbdb.nist.gov/vibscalejust.asp>
- Rappé, A. K., and Casewit, C. J. (1997). *Molecular Mechanics across chemistry*. Sausalito, CA: University Science Books.
- Ratna, D. (2009). *Handbook of thermoset resins*. Shawbury, UK: ISmithers.
- Ratna, D., Jagtap, S., Nimje, R., and Chakraborty, B. (2024). Cure kinetics and thermal degradation characteristics of epoxy/polyetheramine systems. *J. Therm. Anal. Calorim.* 149 (3), 1073–1087. doi:10.1007/s10973-023-12737-6
- Ratna, D., Manoj, N., Chandrasekhar, L., and Chakraborty, B. (2004). Novel epoxy compositions for vibration damping applications. *Polym. Adv. Technol.* 15 (10), 583–586. doi:10.1002/pat.513
- Rivatón, A., Moreau, L., and Gardette, J.-L. (1997a). Photo-oxidation of phenoxy resins at long and short wavelengths—I. Identification of the photoproducts. *Polym. Degrad. Stabil.* 58 (3), 321–332. doi:10.1016/s0141-3910(97)00089-x
- Rivatón, A., Moreau, L., and Gardette, J.-L. (1997b). Photo-oxidation of phenoxy resins at long and short wavelengths—II. Mechanisms of formation of photoproducts. *Polym. Degrad. Stabil.* 58 (3), 333–339. doi:10.1016/s0141-3910(97)00088-8
- Rose, N., Le Bras, M., Delobel, R., Costes, B., and Henry, Y. (1993). Thermal oxidative degradation of an epoxy resin. *Polym. Degrad. Stabil.* 42 (3), 307–316. doi:10.1016/0141-3910(93)90226-9
- Vyazovkin, S., and Linert, W. (1994). Evaluation and application of isokinetic relationships: the thermal decomposition of solids under nonisothermal conditions. *J. Chem. Inf. Comput. Sci.* 34 (6), 1273–1278. doi:10.1021/ci00022a008
- Wilson, E. B., Decius, J. C., and Cross, P. C. (1955). *Molecular vibrations*. New York: McGraw-Hill.
- Xia, L., Zuo, L., Wang, X., Lu, D., and Guan, R. (2014). Non-isothermal kinetics of thermal degradation of DGEBA/TU-DETA epoxy system. *J. Adhesion Sci. Technol.* 28 (18), 1792–1807. doi:10.1080/01694243.2014.922454
- Zhang, G., Pitt, W., Goates, S., and Owen, N. (1994). Studies on oxidative photodegradation of epoxy resins by IR-ATR spectroscopy. *J. Appl. Polym. Sci.* 54 (4), 419–427. doi:10.1002/app.1994.070540402
- Zhou, G., Mikinka, E., Golding, J., Bao, X., Sun, W., and Ashby, A. (2020). Investigation of thermal degradation and decomposition of both pristine and damaged carbon/epoxy samples with thermal history. *Compos. Part B Eng.* 201, 108382. doi:10.1016/j.compositesb.2020.108382

Frontiers in Chemistry

Explores all fields of chemical science across the periodic table

Advances our understanding of how atoms, ions, and molecules come together and come apart. It explores the role of chemistry in our everyday lives - from electronic devices to health and wellbeing.

Discover the latest Research Topics

[See more →](#)

Frontiers

Avenue du Tribunal-Fédéral 34
1005 Lausanne, Switzerland
frontiersin.org

Contact us

+41 (0)21 510 17 00
frontiersin.org/about/contact

